PHYSICS OF THE SOLID STATE VOLUME 41, NUMBER 10 OCTOBER 1999

METALS. SUPERCONDUCTORS

Electronic structure of Y and Pr in Laves phases with Mg, Al, Fe, Co, and Ni

A. E. Sovestnov, V. A. Shaburov, Yu. P. Smirnov, and A. V. Tyunis

B. P. Konstantinov St. Petersburg Nuclear Physics Institute, Russian Academy of Sciences, 188350 Gatchina, Russia

(Submitted February 1, 1999)
Fiz. Tverd. Tela (St. Petersburg) **41**, 1721–1723 (October 1999)

The electronic structure (population of the valence d and s shells) of Y and Pr in the RM_2 Laves phases with Mg, Al, Fe, Co, and Ni has been determined experimentally by the x-ray K-line shift method. It was found that the Y and Pr electronic structures in RM_2 with Mg and Al are practically the same as in metals, but the distribution of the three outer electrons between the d and s shells in Y is essentially different from that in Pr. In the Laves phases with $3d$ metals (Fe, Co, or Ni), the outer-electron distributions between the d and s shells in Y and Pr are practically identical and do not depend on the d metal. © *1999 American Institute of Physics.* [S1063-7834(99)00110-0]

It is believed that the similarity in the physical and chemical properties among rare-earth (RE) compounds is determined by their outer (valence) s and d electrons, and the difference, by the localized f electrons. The population of the $4f$ states in RE compounds was studied adequately by various methods, whereas that of the outer s and d states, whose knowledge is also important for understanding the properties of compounds, is practically unknown. Direct experimental data are actually lacking, while indirect information does not, as a rule, allow unambiguous interpretation.

It was shown that the electronic structure of elements in a compound [i.e. the population of the outer $s(p)$, d, and f shells] can be studied to advantage by the direct microscopic method of x-ray line shift.[1,2] A change in the number of the valence electrons in an atom results in a shift (energy change) of the x-ray lines, whose magnitude and sign can be used to determine the type and number of the electrons $[s(p),d,f]$ involved in the chemical bonding. It is essential that such effects can be calculated with a satisfactory accuracy by Dirac–Fock formalism.

The Laves phases RM_2 with a $MgCu_2$-type structure ($C15$) are a convenient subject for studying the physics of RE compounds. These phases form with a large variety of M elements (s, p, and d elements). Among such RM_2 compounds, one has discovered all kinds of magnetic interactions, superconductivity (including the one coexisting with ferromagnetism), Kondo lattices, heavy-fermion and fluctuating-valence systems. While these intermetallic compounds have been investigated thoroughly for a number of years by various techniques (see, e.g., Refs. 3,4), there is still no full understanding of their structure on a microscopic level.

This work makes use of the x-ray line shift method to experimentally determine the electronic structure of Y and Pr in the Laves phases with Mg, Al, Fe, Co, and Ni (i.e. with s, p, and d elements). This choice of the RE elements was based on the following consideration: while Pr is a $4f$ element, and Y is not an f element, they are both believed to have similar outer sd shells, which determine the main physical properties of the substances they are part of.

The compounds we prepared by arc melting were practically single phase and close in crystallographic characteristics to those described in literature.[3,4]

The x-ray line shift method, the measurement procedure, and the processing of experimental data were described in detail elsewhere (see, e.g., Ref. 1).

This work deals with a measurement of the $K\alpha_1$- and $K\beta_1$-line shifts of Y and Pr in the Laves phases relative to the corresponding metal. To establish their electronic structure in the metal, similar measurements were carried out on RF_3 ionic compounds (R=Y, Pr). The results of these measurements are given in Table I.

As seen from Table I, $K\alpha_1$- and $K\beta_1$-line shifts of Y and Pr in compounds with Al and Mg are close to zero, whereas compounds with Fe, Co, and Ni reveal effects of $\sim 20-50$ meV, negative for Y and positive for Pr, which are practically independent of the $3d$ element. This implies that when bound with s and p elements (Mg and Al) in Laves phases, these RE elements have nearly the same electronic structure as in metals, but when combined with $3d$ elements (Fe, Co, Ni), it is different.

The electronic configurations of Y and Pr in the Laves phases and in metals were derived from experimental shifts and Dirac–Fock calculations made in the Koopmans single-electron approximation (DF–K).[5]

The electronic structure of an RE element in the metal can be obtained by least-squares solving the coupled equations

$$\Delta E_K^{\mathrm{cal}}(N_d, N_s, n_d, n_s) = \Delta E_K^{\mathrm{exp}}, \quad K = K\alpha_1 \text{ and } K\beta_1,$$

$$N_s + N_d = 3,$$

TABLE I. X-ray *K*-line shifts of Y and Pr (relative to the metal) and occupation of their outer shells in the metal and Laves phases RM_2 in the absence of charge transfer from the RE to the M element, and (in parentheses) with a transfer $q=0.3$ el/R atom.

	$\Delta E_{\alpha 1}$, meV		$\Delta E_{\beta 1}$, meV		Outer shell population, el/R atom	
Compound	exp.	calc.	exp.	calc.	$5s$(Y) or $6s$(Pr)	$4d$(Y) or $5d$(Pr)
Y-MET.	184 ± 5	176	78 ± 9	98	1.20 ± 0.05	1.80 ± 0.05
YAl_2	12 ± 6	12	15 ± 11	15	1.08 ± 0.05	1.92 ± 0.05
YFe_2	-28 ± 6	-29	-40 ± 12	-36	1.46 ± 0.05	1.54 ± 0.05
		(-29)		(-37)	(1.23 ± 0.04)	(1.46 ± 0.04)
YCo_2	-17 ± 6	-22	-43 ± 12	-27	1.40 ± 0.05	1.60 ± 0.05
		(-21)		(-28)	(1.18 ± 0.04)	(1.52 ± 0.04)
YNi_2	-26 ± 6	-32	-55 ± 11	-39	1.48 ± 0.04	1.52 ± 0.04
		(-31)		(-40)	(1.26 ± 0.04)	(1.44 ± 0.04)
Pr-MET.	42 ± 5	37	-34 ± 9	20	1.86 ± 0.07	1.14 ± 0.07
$PrMg_2$	-6 ± 7	-15	-52 ± 14	-16	2.08 ± 0.09	0.92 ± 0.09
$PrAl_2$	8 ± 7	-1	-37 ± 14	-2	1.88 ± 0.09	1.12 ± 0.09
$PrCo_2$	46 ± 7	45	44 ± 14	48	1.16 ± 0.11	1.86 ± 0.11
		(45)		(47)	(0.94 ± 0.10)	(1.79 ± 0.10)
$PrNi_2$	36 ± 7	34	30 ± 14	36	1.33 ± 0.10	1.67 ± 0.10
		(34)		(36)	(1.11 ± 0.10)	(1.59 ± 0.10)

Note: The shifts for the R=Y, Pr metals are relative to RF_3.

$$n_s+n_d=3(1-i),$$

where $\Delta E_K^{\mathrm{cal}}(N_d,N_s,n_d,n_s)$ are calculated shifts approximated by a second-order polynomial, $\Delta E_K^{\mathrm{exp}}$ are the experimental values, $i=0.9$ is the Pauling ionicity, N_s and N_d are the outer-shell occupation numbers of Y and Pr in the metal, and n_s and n_d are those in the compound (here and in what follows, s refers to the $5s$ and $6s$ shells of Y and Pr, respectively, and d, to their $4d$ and $5d$ shells).

The occupation numbers of the s and d shells of Y and Pr obtained in this way and the calculated $\Delta E_K^{\mathrm{cal}}$ shifts for the metal-fluoride pair are listed in Table I. As seen from a comparison of $\Delta E_K^{\mathrm{cal}}$ with $\Delta E_K^{\mathrm{exp}}$, our experimental results are fitted satisfactorily by DF–K–type calculations.

A comparison of the Y and Pr electronic structures in metals shows that the outer electron distribution between their s and d shells is noticeably different, namely, in Y it is close to d^2s^1, and in Pr, to d^1s^2.

The electronic structures of Y and Pr in the Laves phases were determined in a similar manner. The only difference consisted in N_s and N_d being considered already established (see Table I), while the last equation (for n_s and n_d) was different, depending on the mechanism of the assumed change in the RE electronic structure associated with the transfer from the metal to the compound. Two versions were analyzed.

1. The redistribution of the three outer electrons of an RE element between its s and d states follows from band calculations.[6] These calculations showed that the magnetic properties of YM_2 (M=Fe, Co, Ni) can be well accounted for without invoking electron transfer from yttrium to a $3d$ element. Experimental evidence for such a mechanism may be provided by Mössbauer measurements on Gd and Dy in Laves phases, which are explained, without any quantitative evaluation, as due to the $s\rightarrow d$ transition in the RE element.[7]

In this case the last equation in the system acquires the form $n_d+n_s=3$. The results of a solution of the system are presented in Table I. A comparison of the experimental with calculated shifts δE_K again shows them to be in satisfactory agreement.

As seen from Table I, the occupation numbers of the outer RE s and d shells in Laves phases with Mg and Al, as well as in metals, differ strongly for Y and Pr. The situation for Laves phases with $3d$ metals is different; indeed, the populations of the outer d shells (and, hence, of the s shells as well) in Y and Pr are close to one another, with the mean values $n_d=1.57\pm0.03$ and $n_s=1.43\pm0.03$.

Thus experimental x-ray K-line shifts of Y and Pr in Laves phases can be described satisfactorily in terms of the redistribution of their outer s and d electrons, without invoking any charge transfer to the partner in the compound. Note also that the population of the Y $4d$ states in Laves phases with $3d$ metals, $n_d=1.7$, quoted in Ref. 6, is close to the one obtained by us.

2. The mechanism mostly discussed in the literature is electron transfer from RE to d elements (see, e.g., Refs. 3,4,8), but, as a rule, without any specific conclusions on the type and number of transferred electrons. This mechanism is hardly likely for Laves phases with Mg and Al, because they have practically the same electronegativities as the RE elements.

It can be shown that our data are capable of elucidating the type of the electron (s,d) transferred from an RE to the d element in Laves phases. It is known that removal of an s electron results in a positive shift of the x-ray $K\alpha_1$ and $K\beta_1$ lines, while removal of a d electron, to negative ones (see, e.g., Ref. 2). Because the effects observed for Y and Pr in Laves phases with $3d$ elements are of opposite signs (see Table I), one may conclude that our experimental data cannot be reconciled by assuming that charge transfer from any RE element to the M element is effected by only d or only s electrons.

A general case of q sd electrons transferred from an RE element to an M element, with the other $3-q$ distributed between the s and d states of the RE element, is more complex, because it allows satisfactory description of experimental data within a relatively broad range of q.

The results of solution of the coupled equations for the Laves phases of Y and Pr performed under the condition $n_d+n_s=2.7$ (i.e. for the maximum possible $q=0.3$, see Ref. 8) are presented in Table I in parentheses.

As seen from Table I, even a charge transfer of $q=0.3$ provides as good an agreement with the experimental data as in the case of electron redistribution between the outer s and d states of the RE element $(q=0)$. In the $q=0.3$ case the occupation numbers n_d and n_s for Y and Pr in Laves phases turn out to be smaller than those in the preceding case. However their differences (0.08 and 0.22 for the d and s states, respectively) lie practically within experimental accuracy. Note also that the outer electron distributions between the Y and Pr s and d shells, in the case of charge transfer, are also close.

Thus it has been shown that the electronic structure of Y and Pr practically does not change in a transition from a pure metal to Laves phases with Mg and Al, whereas transition to Laves phases with $3d$ elements brings about substantial rearrangement. The outer-electron distributions in Y and Pr between the s and d shells in the metal and the Laves phases with Mg and Al differ considerably, and in the Laves phases with $3d$ elements they are similar.

The authors are indebted to O. I. Sumbaev for fruitful criticisms.

Support of the Russian Fund for Fundamental Research (Grant 96-02-17811) is gratefully acknowledged.

[1] O. I. Sumbaev, Usp. Fiz. Nauk **124**, 281 (1978) [Sov. Phys. Usp. **21**, 141 (1978)].

[2] O. I. Sumbaev, Zh. Éksp. Teor. Fiz. **57**, 1716 (1969) [Sov. Phys. JETP **30**, 927 (1969)].

[3] K. H. J. Buschow, Rep. Prog. Phys. **40**, 1179 (1977).

[4] K. H. J. Buschow, Rep. Prog. Phys. **42**, 1373 (1979).

[5] I. M. Band and V. I. Fomichev, LNPI Preprint No. 498 (1979).

[6] H. Yamada, J. Inoue, K. Terao, S. Kanda, and M. Shimizu, J. Phys. F **14**, 1943 (1984).

[7] E. R. Bauminger, G. M. Kalvis, and I. Nowik, in *Mössbauer Isomer Shifts*, edited by G. K. Shenoy and F. E. Wagner (North-Holland, Amsterdam, 1978), p. 661.

[8] T. W. Capehart, J. F. Herbst, R. K. Mishra, and F. E. Pinkerton, Phys. Rev. B **52**, 7907 (1995).

Translated by G. Skrebtsov

Atomic charges in $RBa_2Cu_4O_8$ lattices derived from a comparison of experimental and calculated nuclear-quadrupole coupling parameters

V. F. Masterov,*) F. S. Nasredinov, N. P. Seregin, and P. P. Seregin

St. Petersburg State Technical University, 195251 St. Petersburg, Russia

(Submitted February 2, 1999)
Fiz. Tverd. Tela (St. Petersburg) **41**, 1724–1728 (October 1999)

The nuclear-quadrupole coupling parameters at the rare-earth metal and copper sites in the $RBa_2Cu_4O_8$ lattices (R=Sm, Y, Er) have been determined by $^{67}Cu(^{67}Zn)$ and $^{67}Ga(^{67}Zn)$ Mössbauer emission spectroscopy. The crystal electric-field-gradient tensor has been calculated for all sites of the above lattices in the point-charge approximation. A comparison of the experimental with calculated parameters shows that holes in the $RBa_2Cu_4O_8$ lattices are localized primarily at chain-oxygen sites. *© 1999 American Institute of Physics.* [S1063-7834(99)00210-5]

By comparing the experimental with calculated nuclear-quadrupole coupling parameters describing the interaction of the electric quadrupole moment of a probe nucleus with the electric-field gradient (EFG) tensor at the nucleus one can determine the charges on lattice atoms. The most revealing results are obtained when such a comparison is performed with ''crystalline'' probes (the EFG at such probes is generated primarily by lattice ions). This is why we proposed and used for experimental determination of the nuclear quadrupole coupling parameters at copper sites in high-T_c cuprates Mössbauer emission spectroscopy (MES) on the $^{67}Cu(^{67}Zn)$ isotope; indeed, in this case the crystal-field probe $^{67}Zn^{2+}$ resides in copper sites, and the EFG tensor at ^{67}Zn nuclei, which is completely determined by the lattice ions, can be calculated using the point-charge model.[1] This method is particularly efficient when applied to lattices having several crystallographically inequivalent positions for the copper atoms, because one can avoid in this case the problems associated with the uncertainty in the Sternheimer coefficient for $^{67}Zn^{2+}$ centers.[1] This situation arises, in particular, in $RBa_2Cu_4O_8$ high-T_c superconductors [R stands here for a rare-earth metal (REM) or yttrium], whose structure has two different copper sites, Cu(1) and Cu(2). Note that for REM sites one can determine also the parameters of nuclear quadrupole interaction at the crystal-field probe $^{67}Zn^{2+}$ using $^{67}Ga(^{67}Zn)$ MES.[2] Besides, the $RBa_2Cu_4O_8$ compound was studied in considerable detail by NMR and NQR on the ^{17}O and ^{63}Cu isotopes (Refs. 3 and 4, respectively). This offers new possibilities for experimentally validating the proposed interpretation of ^{67}Zn Mössbauer emission spectroscopy data.

The objective of this work was experimental determination of the nuclear quadrupole coupling parameters for the copper and REM sites in the $RBa_2Cu_4O_8$ lattices by $^{67}Cu(^{67}Zn)$ and $^{67}Ga(^{67}Zn)$ Mössbauer emission spectroscopy, and calculation of the crystal EFG tensor parameters for these sites, with subsequent comparison of experimental with calculated values to derive information on the charge state of atoms in the above lattices.

1. EXPERIMENTAL TECHNIQUE

In studying $RBa_2Cu_4O_{8+x}$ (R=Sm, Y, Er) we used ceramic samples. The ^{67}Cu and ^{67}Ga isotopes were introduced into the ceramic by diffusion doping in an oxygen environment at 700 °C for two hours. In the $RBa_2Cu_3O_7$ compound subjected to a similar procedure, ^{67}Ga enters the REM sites, and ^{67}Cu, the Cu(1) and Cu(2) sites, in accordance with their natural occupation.[1,2] Note that control annealing of a $YBa_2Cu_4O_8$ sample made under similar conditions did not result in a change of $T_c \approx 80$ K. The $^{67}Cu(^{67}Zn)$ and $^{67}Ga(^{67}Zn)$ Mössbauer spectra were measured at 4.2 K with a ^{67}ZnS absorber.

2. EXPERIMENTAL RESULTS

$^{67}Cu(^{67}Zn)$ Mössbauer spectra were sets of six lines of approximately equal intensity [Fig. 1(a)], which were unfolded into two equal-intensity quadrupole triplets. The selection of the particular spectral unfolding version into the triplets and identification of the latter with the $^{67}Zn^{2+}$ centers at the Cu(1) and Cu(2) sites were made based on the Cu(2) environment in $RBa_2Cu_4O_8$ being similar to that in $RBa_2Cu_3O_7$. Therefore it appeared natural to require a zero asymmetry parameter of the EFG tensor for the Cu(2) sites in $RBa_2Cu_4O_8$, as this is observed[1] for the Cu(2) sites in $RBa_2Cu_3O_7$. It was found that only the (1–3–5) triplet satisfies this requirement, and it is this triplet that should be assigned to the $^{67}Zn^{2+}$ centers in the Cu(2) sites (Fig. 1a). Accordingly, the (2–4–6) triplet in Fig. 1a relates to these centers at the Cu(1) sites. The equal intensities of the two triplets corresponds to equal populations of the two sites. The nuclear-quadrupole coupling parameters for $^{67}Zn^{2+}$ centers at the Cu(1) and Cu(2) sites are listed in Table I.

The $^{67}Ga(^{67}Zn)$ spectra are quadrupole triplets (Fig. 1b) corresponding to the only state of the $^{67}Zn^{2+}$ center. Based on the data of Ref. 2, we assumed these spectra to be due to the $^{67}Zn^{2+}$ centers occupying REM sites. Table I presents the nuclear-quadrupole coupling parameters for $^{67}Zn^{2+}$ centers at the R sites.

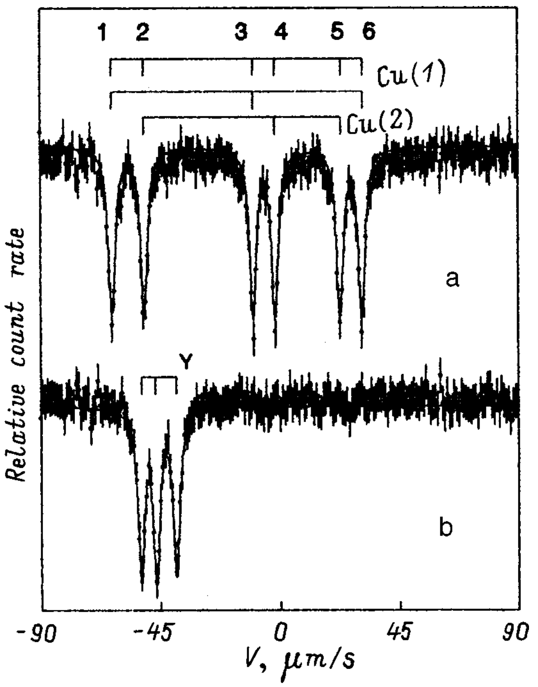

FIG. 1. (a) ^{67}Cu(^{67}Zn) and (b) ^{67}Ga(^{67}Zn) Mössbauer emission spectra of $YBa_2Cu_4O_8$ measured at 4.2 K. The positions of all (labeled) lines in the ^{67}Cu(^{67}Zn) spectrum and of components of the quadrupole triplets corresponding to the $^{67}Zn^{2+}$ probe at the Cu(1), Cu(2), and Y sites are identified.

3. DISCUSSION OF EXPERIMENTAL RESULTS

To determine the atomic charges at the $RBa_2Cu_4O_8$ lattice sites, one has to compare the experimental with calculated nuclear-quadrupole coupling parameters for the $^{67}Zn^{2+}$ probe at the copper sites. In a general case, the measured quadrupole coupling constant C is a sum of two terms

$$C=eQU_{zz}=eQ(1-\gamma)V_{zz}+eQ(1-R_0)W_{zz}, \qquad (1)$$

where eQ is the quadrupole moment of the probe nucleus, U_{zz}, V_{zz}, and W_{zz} are the principal tensor components of the total, crystal-field (generated by the lattice ions), and valence (created by the nonspherical valence electrons of the probe atom) EFG, and γ and R_0 are the Sternheimer coefficients for the probe atom.

For the $^{67}Zn^{2+}$ probe, the valence-electron contribution to the total EFG tensor may be neglected,[1] so that one obtains from Eq. (1)

$$C(\mathrm{Zn})\approx eQ(1-\gamma)V_{zz}. \qquad (2)$$

TABLE I. Parameters of ^{67}Cu(^{67}Zn) and ^{67}Ga(^{67}Zn) Mössbauer emission spectra.

Compound	Site	C(Zn), MHz	η
$SmBa_2Cu_4O_8$	Cu(1)	14.1(2)	0.75(5)
	Cu(2)	12.0(2)	<0.2
$YBa_2Cu_4O_8$	Y	−2.5(2)	0.30(5)
	Cu(1)	14.3(1)	0.70(5)
	Cu(2)	12.3(1)	<0.2
$ErBa_2Cu_4O_8$	Cu(1)	14.4(2)	0.68(5)
	Cu(2)	12.2(2)	<0.2

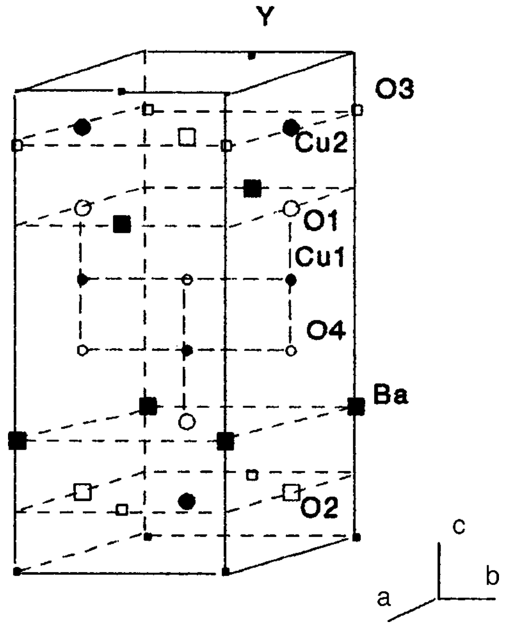

FIG. 2. The unit cell of $RBa_2Cu_4O_8$ compounds with atomic positions identified.

The crystal EFG tensor was calculated in the point-charge approximation. Its components were derived from the following expressions

$$V_{pp}=\sum_k e_k^*\sum_i (1/r_{ki}^3)[(3p_{ki}^2/r_{ki}^2)-1]=\sum_k e_k^* G_{ppk},$$

$$V_{pq}=\sum_k e_k^*\sum_i (3p_{ki}q_{ki}/r_{ki}^5)=\sum_k e_k^* G_{pqk}, \qquad (3)$$

where k is the index of summation over the sublattices, i is that over the sublattice sites, q, p are the Cartesian coordinates, e_k^* are the atomic charges on the k-sublattice, and r_{ki} is the distance from the k_i ion to the site of interest.

The lattice sums G_{ppk} and G_{pqk} were computed within a sphere of radius 30 Å (using a larger summation radius did not change the result). The structural data needed were taken from Ref. 5, and the lattice was presented in the form $RBa_2Cu(1)_2Cu(2)_2O(1)_2O(2)_2O(3)_2O(4)_2$.

Figure 2 shows a unit cell of the $RBa_2Cu_4O_8$ lattice with notation of all atomic sites. The values assigned to summation index k in Eq. (3) ranged from 1 to 8 for the sublattices for R, Ba, Cu(1), Cu(2), O(1), O(2), O(3), and O(4) respectively.

The atomic charges on the $RBa_2Cu_4O_8$ sublattices can be derived from ^{67}Cu(^{67}Zn) Mössbauer emission spectroscopy using four coupled equations:[1]

(1) an equation for the ratio of quadrupole coupling constants for the $^{67}Zn^{2+}$ centers at the Cu(1) and Cu(2) sites, $P_{34}=eQU_{zz3}/eQU_{zz4}$,

$$\sum_k e_k^*[G_{zzk3}-P_{34}G_{zzk4}]=0, \qquad (4)$$

(2) two equations for the EFG tensor asymmetry parameters at the Cu(1) and Cu(2) sites, η_3 and η_4, respectively

$$\sum_k e_k^*[G_{xxk3}-G_{yyk3}-\eta_3 G_{zzk3}]=0, \tag{5}$$

$$\sum_k e_k^*[G_{xxk4}-G_{yyk4}-\eta_4 G_{zzk4}]=0, \tag{6}$$

(3) charge neutrality condition

$$e_1^*+2e_2^*+2e_3^*+2e_4^*+2e_5^*+2e_6^*+2e_7^*+2e_8^*=0. \tag{7}$$

Equations (4)–(7) are all homogeneous so that the system they form can determine the atomic charges only in units of charge of one of them. One can conveniently take for it the charge on the R ions, which may be expected to be close to their formal chemical charge $(+3e)$. This is supported by direct Mössbauer spectroscopy data on the ^{155}Gd isotope,[6] by which the gadolinium atoms in $GdBa_2Cu_4O_8$ are trivalent.

Equations (4)–(7) are not sufficient to find the atomic charges on seven sublattices. However taking into account that the coefficients of the anion charges exceed by an order of magnitude or even more those of the cation charges, system (4)–(7) permits one to determine the anion charges to within small corrections depending on the cation charges. We made a number of assumptions concerning the cation charges, namely, that the R/Ba charge ratio is 3:2 (this follows from the traditional chemical relations for the REM and barium valence states in their compounds); that charges on Ba and O(1) should be equal in absolute magnitude (to conserve charge neutrality in the Ba–O layers in the lattice); and that the Cu(1)/Cu(2) charge ratio may vary from 1:3 to 3:1 (in accordance with the possible valence states of copper).

One also has to bear in mind that the local environment symmetry of the Cu(2) sites requires that the *z* axis of the crystal EFG tensor coincides with the crystallographic axis **c**, and that our measurements yield $V_{zz4}>0$. For the Cu(1) sites one can isolate two regions within which the experimental conditions $\eta_3\approx 0.7$ and $V_{zz3}>0$ are satisfied, namely, region *A* near $e_5^*/e_8^*\approx 1.5$ (where $|V_{bb3}|<|V_{cc3}|$), and region *B* near $e_5^*/e_8^*\approx 0.3$ (where $|V_{bb3}|>|V_{cc3}|$).

In accordance with these assumptions, there exist two sets of e_k^* satisfying the experimental values of P_{34}, η_3, and η_4. Assuming the R, Ba, and Cu atoms to have standard valences ($e_1^*=3$, $e_2^*=2$, $e_3^*=2$, and $e_4^*=2$), one obtains for region *A*:

$$e_5^*=-2.025,\quad e_6^*=-2.035,$$
$$e_7^*=-1.986,\quad e_8^*=-1.454, \tag{A1}$$

and for region *B*:

$$e_5^*=-0.715,\quad e_6^*=-2.076,$$
$$e_7^*=-2.031,\quad e_8^*=-2.678 \tag{B1}$$

(with all charges given in units of the electronic charge).

One has to have independent criteria for choosing between the solutions of type *A* and *B*. For the $RBa_2Cu_3O_7$ compounds, we chose[1] ^{17}O NMR data as such criteria. Because for $YBa_2Cu_4O_8$ there also exist ^{17}O NMR measurements,[3] one can try to use them as a criterion for selecting physically reasonable solutions.

An analysis of solution (A1) shows that atoms O(1), O(2), and O(3) have effective charges corresponding to nearly filled oxygen valence shells, i.e. that the EFG at ^{17}O nuclei in the O(1), O(2), and O(3) sites should be generated by lattice ions. Hence Eqs. (4)–(6) for region *A* can be complemented by three equations of the type (4)–(6) constructed for any pair of the sites O(1) and O(2), O(1) and O(3), O(2) and O(3):

$$\sum_k e_k^*[G_{xxkl}-G_{yykl}-\eta_l G_{zzkl}]=0, \tag{8}$$

$$\sum_k e_k^*[G_{xxkm}-G_{yykm}-\eta_m G_{zzkm}]=0, \tag{9}$$

$$\sum_k e_k^*[G_{zzkl}-P_{lm}G_{zzkm}]=0, \tag{10}$$

where indices *l* and *m* label the oxygen sites to which the ^{17}O NMR data[3] relate, and can have the values 5 and 6, 5 and 7, 6 and 7 for the above pairs of sites; η_m and η_l are experimental values of the EFG tensor asymmetry parameters; and $P_{lm}=eQU_{zzl}/eQU_{zzm}$ is the ratio of the experimental quadrupole coupling constants for ^{17}O occupying the corresponding sites.

According to model (B1), the valence shell of the O(2), O(3), and O(4) oxygens can be nearly filled. Hence Eqs. (8)–(10) for region *B* can be written for the O(2) and O(3), O(2) and O(4), and O(3) and O(4) site pairs.

Thus we have seven coupled equations (4)–(10) for seven unknowns, $e_2^*-e_8^*$ (the charge of the R atoms is assumed to be $+3e$). The coefficients of this system were calculated taking into account that the principal axes of the crystal-field EFG tensor for the O(1), O(2), O(3), and O(4) sites having filled shells should coincide with the *c*, *b*, *a*, *b* crystallographic axes.[3] The *x* and *y* EFG tensor axes were chosen coinciding with the *b* and *a*, *c* and *a*, *c* and *b*, and *c* and *a* axes for the O(1), O(2), O(3), and O(4) sites, respectively.[3] The uncertainty of the eQU_{zz} sign for ^{17}O forced us to substitute P_{lm} into Eqs. (8)–(10) with both positive and negative signs. The solutions yielding a negative charge for cations or a positive one for anions were dropped as unphysical.

However, when six experimental figures are introduced, for all physically acceptable solutions in regions *A* and *B* one observes substantial differences between the calculated and experimental values of the remaining parameters. Besides, the charge states of the ^{17}O probes whose NMR data were used in the (4)–(10), equations were found to be at odds with the starting assumption that these probes feel only the crystal field, and the charge state of barium atoms always differed considerably from the traditional value of +2. All this implies that one cannot use ^{17}O NMR data for $YBa_2Cu_4O_8$ as a criterion for selecting between the *A* and *B* solutions.

One can try to use as criteria for choosing between the *A*- and *B*-type solutions the correlations established between the ^{67}Cu(^{67}Zn) MES and ^{63}Cu NMR data for copper sites in the cuprate lattices. Figure 3(a) presents a $C(\mathrm{Cu})-C(\mathrm{Zn})$ diagram constructed[7] using the quadrupole coupling constant $C(\mathrm{Cu})$ measured by ^{63}Cu NMR spectroscopy for the ^{63}Cu

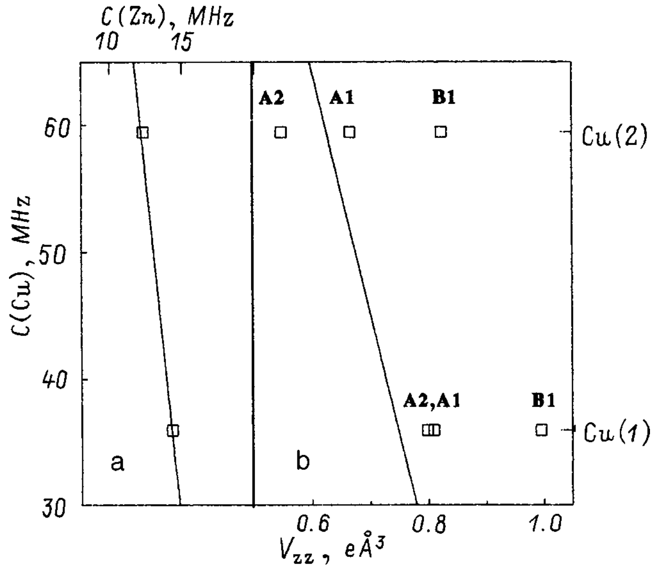

FIG. 3. (a) $C(\mathrm{Cu})-C(\mathrm{Zn})$ and (b) $C(\mathrm{Cu})-V_{zz}$ diagrams for cuprates. The points are data obtained for the Cu(1) and Cu(2) sites in $\mathrm{YBa_2Cu_4O_8}$. The indices (A1), (A2), and (B1) refer to the charge distribution models used in V_{zz} calculations.

probe, and the $C(\mathrm{Zn})$ values obtained by Mössbauer emission spectroscopy for the ^{67}Zn probe residing in copper sites of the same cuprates. It was found that most of the data fit on a straight line

$$C(\mathrm{Cu})=197-11.3C(\mathrm{Zn}), \tag{11}$$

where $C(\mathrm{Cu})$ and $C(\mathrm{Zn})$ are in MHz.

This linear dependence is a consequence of the constant valence contribution of $^{63}\mathrm{Cu}^{2+}$ centers to the EFG in different cuprates. The main reason for the deviation from the straight line (11) is that the copper valence differs from $+2$. Besides, the quantities $C(\mathrm{Cu})$ and V_{zz} were found[7] to be related through

$$C(\mathrm{Cu})=179-191.4V_{zz}, \tag{12}$$

where V_{zz} are the principal components of the crystal EFG tensor calculated for the copper sites in which $C(\mathrm{Cu})$ were measured by ^{63}Cu NMR.

The $C(\mathrm{Cu})-V_{zz}$ diagram is shown in Fig. 3b; another reason why it could deviate from the straight line (11) is a wrong calculation of the crystal EFG tensor because of an inappropriate choice for the atomic charges. Therefore the position of the points in the $C(\mathrm{Cu})-C(\mathrm{Zn})$ and $C(\mathrm{Cu})-V_{zz}$ diagrams corresponding to the same copper site can be used to choose possible versions of charge distribution over the lattice.

Figure 3a displays the Cu(1) and Cu(2) sites in $\mathrm{YBa_2Cu_4O_8}$ (the ^{63}Cu data were taken from Ref. 4). Both points are seen to fit satisfactorily the straight line (11), thus supporting the divalent state of copper in the $\mathrm{YBa_2Cu_4O_8}$ lattice. The points for Cu(1) and Cu(2) for which V_{zz} was calculated on model (A1) lie near the straight line (11) in Fig. 3b, whereas the calculation made within model (B1) results in a considerable deviation of both points from straight line (12). This obviously may serve as supportive evidence for the validity of model (A1).

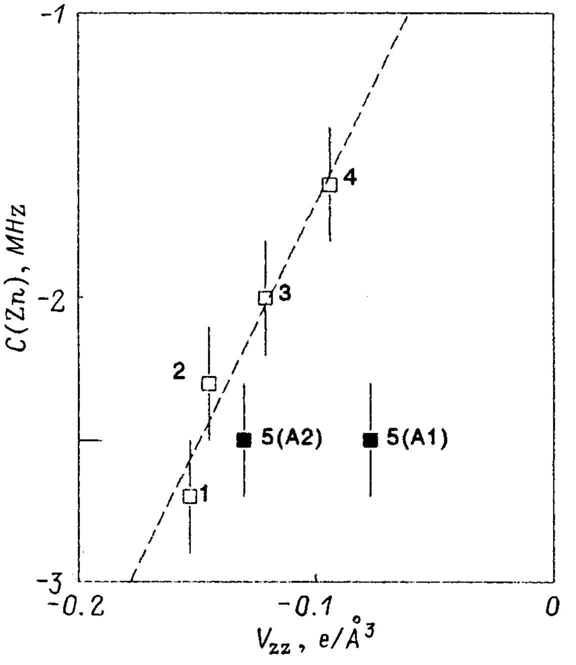

FIG. 4. $C(\mathrm{Zn})-V_{zz}$ diagram for the REM sites of (*1*) $\mathrm{EuBa_2Cu_3O_7}$, (*2*) $\mathrm{YBa_2Cu_3O_7}$, (*3*) $\mathrm{GdBa_2Cu_3O_7}$, (*4*) $\mathrm{TmBa_2Cu_3O_7}$, and (*5*) $\mathrm{YBa_2Cu_4O_8}$. The indices (A1) and (A2) refer to the charge distribution models used in V_{zz} calculations. The data for $\mathrm{RBa_2Cu_3O_7}$ are from Ref. 2.

It was found[2] that the values of $C(\mathrm{Zn})$ determined by $^{67}\mathrm{Ga}(^{67}\mathrm{Zn})$ Mössbauer emission spectroscopy for the REM sites in the $\mathrm{RBa_2Cu_3O_7}$ lattices are related linearly to the principal component of the crystal-field EFG tensor V_{zz} calculated for the REM sites in the point-charge approximation. This linear relation is a consequence of the ''crystalline'' nature of the $^{67}\mathrm{Zn}^{2+}$ probe. As seen from Fig. 4, the point corresponding to the $\mathrm{YBa_2Cu_4O_8}$ compound does not fit this relation (in the latter case, V_{zz} was calculated by model (A1)).

This deviation requires introducing corrections into model (A1) of charge distribution over the $\mathrm{YBa_2Cu_4O_8}$ lattice sites. To achieve the required increase of V_{zz}, one has to localize holes on the O(2) and O(3) sublattices. Because there are no known sources of holes in $\mathrm{RBa_2Cu_4O_8}$-type lattices, we redistributed the charges among the O(1), O(2), O(3), and Cu(1) sublattices (leaving $e_1^*=3$, $e_2^*=2$, and $e_4^*=2$) to finally obtain

$$e_3^*=1.85,\quad e_5^*=-2.15,\quad e_6^*=-1.9,$$

$$e_7^*=-1.85,\quad e_8^*=-1.45. \tag{A2}$$

As seen from Fig. 4, model (A2) demonstrates a satisfactory agreement with the $C(\mathrm{Zn})-V_{zz}$ relationship. Note that model (A2) practically does not change the position of the Cu(1) point in Fig. 3b while displacing slightly the Cu(2) point, but this displacement is of a reasonable magnitude.

The noticeable deviation of the effective charges of all oxygen atoms from $-2e$ in model (A2) excludes the possibility of using ^{17}O NMR data to solve Eqs. (3)–(9), which require that the oxygen probe be ‘‘crystalline.’’

Support of the Russian Fund for Fundamental Research (Grant 97-02-16216) is gratefully acknowledged.

*⁾Deceased.

---

[1] V. F. Masterov, P. P. Seregin, F. S. Nasredinov, N. P. Seregin, and M. A. Sagatov, Phys. Status Solidi B **196**, 11 (1996).

[2] V. F. Masterov, F. S. Nasredinov, N. P. Seregin, and P. P. Seregin, Fiz. Tverd. Tela (St. Petersburg) **38**, 1986 (1996) [Phys. Solid State **38**, 1094 (1996)].

[3] I. Mangelschots, M. Mali, J. Roos, D. Brinkmann, S. Rusiecki, J. Karpinski, and E. Kaldis, Physica C **194**, 277 (1992).

[4] D. Brinkmann, Z. Naturforsch., A: Phys. Sci. **45**, 393 (1990).

[5] D. E. Morris, J. H. Nickel, J. Y. T. Wei, N. G. Asmar, J. S. Scott, U. M. Scheven, C. T. Hultgren, A. G. Markelz, J. E. Post, P. J. Heaney, D. R. Veblen, and R. M. Hazen, Phys. Rev. B **39**, 7347 (1989).

[6] H. J. Bornemann, D. E. Morris, C. Steinleitner, and G. Czjzek, Phys. Rev. B **44**, 12567 (1991).

[7] P. P. Seregin, V. F. Masterov, F. S. Nasredinov, and N. P. Seregin, Phys. Status Solidi B **201**, 269 (1997)

Translated by G. Skrebtsov

PHYSICS OF THE SOLID STATE VOLUME 41, NUMBER 10 OCTOBER 1999

Influence of interatomic forces on the lattice dynamics of $YBa_2Cu_3O_7$ (molecular dynamics method)

E. B. Dolgusheva, V. G. Chudinov,*) and A. G. Chirkov

Physicotechnical Institute, Ural Branch, Russian Academy of Sciences, 426001 Izhevsk, Russia

(Submitted August 27, 1998; accepted for publication January 10, 1999)
Fiz. Tverd. Tela (St. Petersburg) **41**, 1729–1733 (October 1999)

The method of molecular dynamics is used to study the dynamic properties of the high-temperature superconductor $YBa_2Cu_3O_7$. It is shown in the system $La_{2-x}Sr_xCuO_4$ that, due to the presence of strong anharmonism and a substantial difference in the interatomic forces, local ''hot'' regions arise around the Ba^{4+} charge defects in the CuO_2 and CuO planes, where the mean kinetic energy of the vibrations of the oxygen atoms reaches ~ 0.5 eV. All other types of defects: oxygen and copper vacancies, substitutional atoms, and charge defects, do not lead to such effects. [S1063-7834(99)00310-X]

In the infrared scattering spectra of all high-temperature superconductors (HTSC) peaks have been discovered in the superconducting phase, with energies ~ 0.4 eV in $La_{2-x}Sr_xCuO_4$ (Ref. 1), ~ 0.7 eV in $YBa_2Cu_3O_7$ (Ref. 2), 0.8–1.2 eV in $BiSr_2Ca_{n-1}Cu_nO_y$ $(n=1,2,3)$ (Ref. 3). The correlation of these peaks with the transition temperature T_c is noteworthy: the higher the peak energy, the higher is T_c. The nature of these peaks is insufficiently clear. Most authors associate them with excitations in the electron subsystem in the presence of polarons. But in this case, as the density of current carriers varies, the frequency of these oscillations according to the Drude model $\omega \sim n^{1/2}$, where n is the number of carriers, should also vary.[1] However, this is not observed, and the positions of the peaks remain unchanged within the limits of measurement error. Nevertheless, some theoretical works have provided a possible explanation by assuming that these absorption peaks are due to interband electron transitions.[4] No attempts have been made to identify them with vibrations of the crystal lattice, and it would be complicated, methodologically speaking, to detect them experimentally with the help of slow neutron scattering.

Experiments have been performed which indirectly indicate the existence in these systems of local high-frequency vibrations. As is well known, the Debye temperature in lanthanum compounds is ~ 400 K. However, the authors of Ref. 5, in neutron-scattering measurements of the partial kinetic energy of the atoms in La_2CuO_4 and $YBa_2Cu_3O_7$, discovered that the Debye temperature for oxygen is 1400 K (120 meV) and 1500 K, respectively, in these compounds. They suggested that unrecorded high-frequency vibrations can play an important role in the HTSC mechanism. At room temperature, the specific heat of $La_{1.85}Sr_{0.15}CuO_4$ and $YBa_2Cu_3O_7$ reaches only $\sim 85\%$ of its maximum value in the classical limit $3Nk$ (Ref. 6), which also may suggest the existence of high-frequency modes of the lattice vibrations which do not contribute to the specific heat at room temperature. Raman scattering by the compounds $La_{1.85}Sr_{0.15}CuO_4$ and $YBa_2Cu_3O_7$ show bands in the 100–150 meV region (Ref. 7). The authors link these bands with peculiarities of the crystal structure and the phonon spectra of these systems. Phonon features are also observed in the tunneling spectra up to ~ 180 meV in bismuth compounds in which the electrical characteristics of point tunneling contacts were investigated.[8] Only a direct experiment using inelastic scattering of slow neutrons can give an unambiguous answer on the nature of these peculiarities since the diversity of these properties and the complexity of HTSC structures complicate an interpretation of the experimental results.

On this level, the method of molecular dynamics (MMD) is of special interest. The use of MMD allows one to determine both the structural and the dynamic characteristics of solids. It requires a knowledge of the crystal structure and the pairwise interaction potentials (PIP). Studies conducted with the aid of this method for the most part assume that all the bonds in the HTSC's in question are ionic.[9–11] It seems to us that such an approach is incorrect since it does not take into account the actual properties of copper-containing HTSC's. All HTSC's of this class have a layered structure in which CuO layers with pronounced ''metallic'' bonding alternate with ''dielectric'' layers. The distinguishing feature of our potentials is that they meet this requirement. Calculations show[12] that the depths of the potential wells in the CuO layers are comparable in order of magnitude with ordinary metallic potentials, but in the transverse direction, due to weak screening, they are similar to ionic potentials. In the present work we use model potentials calculated according to a pseudopotential scheme using the Heine–Abarenkov–Animalu form factor with Zhou exchange-correlation corrections.[13] Their construction is described in detail in Ref. 12.

In Refs. 14–16, for the anharmonic system $La_{2-x}Sr_xCuO_4$ it was shown that using potentials reflecting the physical properties of layered structures leads to the appearance of local high-frequency vibrations with energy ~ 0.4 eV of the oxygen atoms in the CuO_2 layer near the Sr impurity atoms. For small Sr concentrations the kinetic energy of the atoms of the system undergoes a spatial redistribution. ''Hot'' regions are formed, imbedded in a ''cold'' matrix through which, in principle, a superconducting current can flow. This steady-state picture did not depend on the initial conditions and did not vary, even if the system persisted for up to 10^{-9} s, which is ~ 1000 times longer than the relaxation time. The question arises, how general are these results for other copper-containing HTSC's. The aim of the present work is to study the influence of peculiarities in the interatomic forces on the lattice dynamics of another high-temperature superconductor, $YBa_2Cu_3O_7$. This system also exhibits strongly anharmonic properties.[17]

1. EXPERIMENTAL TECHNIQUE

The unit cell of the model crystallite had the parameters $a=0.382$, $b=0.388$, and $c=1.168$ mm. Due to limitations of the program and the computer and the complexity of the crystal lattice, the simulation was performed in one case for five layers: $BaO–CuO_2–Y–CuO_2–BaO$ and in the second case, for three layers: BaO–CuO–BaO. The BaO layers were rigidly fixed in place, and cyclic boundary conditions were imposed along the X and Y axes. The model crystallite contained around 700 mobile atoms in the first case, and around 800 mobile atoms in the second. In the initial state the valences were taken to be Y^{3+}, Ba^{2+}, Cu^{2+}, and O^{2-} (in the BaO layer) and O^{1-} (in the CuO_2 layer). As defects, we investigated O^{2-}, Cu^{1+}, and Cu^{3+}, which figure in speculations about high-temperature superconductivity more than once, copper and oxygen vacancies (in the CuO_2 layer), and the charge defect Ba^{4+} (in the BaO layer, substitution of Y for Ba and Ba for Y). In the case of CuO chains, the valences in the initial state were taken to be Cu^{1+}, O^{1-} (in the CuO layer), and Ba^{2+}, O^{2-} (in the BaO layer). As defects in the chains, we investigated oxygen and copper vacancies, and the charge defects O^{2-}, Cu^{2+}, Cu^{3+} (in the CuO chains), and Ba^{4+} (in the BaO layer).

The procedure for forming the crystallite consisted in the following operations: translation of the atoms in the unit cell, assignment of the potentials and interaction forces, minimization of the potential energy, consisting in a choice of the equilibrium size of the unit cell, and prescription of the initial conditions of the calculation. After this, we refined the positions of the atoms using relaxation and by holding the crystallite for $\sim 10^{-12}$ s at $T \approx 0$ without any external influence on the system. If the structure remained stable during the calculation time, the dynamic characteristics were calculated. The lattice constant was reproduced with an accuracy of up to 5%.

In the calculation of the potentials, we take account of the fact that the entire cell is not ''metallic,'' only the CuO_2 and CuO layers, and the well-known fact that the electron density in this system is about one electron per unit cell. All of the electrons are located in a narrow layer ($\sim r_b$ — the Bohr radius). In calculations of the electronic structure[18] and a study of the Fermi surface by photoelectron spectroscopy[19] it was shown that the electron density at the Fermi level is ~ 0.7 in the CuO_2 layers and ~ 0.3 in the CuO chains. All pairwise interaction potentials in these layers have a depth of the potential well of the order of ~ 0.1 eV. Potentials between the ''metallic'' and ''dielectric'' layers were of the order of several eV. The depth of the $Ba^2–O^{1-}$ potential was ~ 6 eV, and of the $Ba^{2+}–Cu^{2+}$ potential, ~ 3 eV. The potentials with Ba had a much larger well depth than the remaining PIP's of this system. This apparently is because Ba has a large ionic radius, which in turn correlates with the model radius. The model radius is one of the parameters for calculating the PIP's in the Heine–Abarenkov–Animalu method. Such atoms include, in addition to Ba, Sr and Ca, which are also present in all copper-containing HTSC's.

The temperature was introduced into the system in the usual way for MMD: a velocity was assigned to all the atoms, equal in magnitude but random in direction, with subsequent playout to equilibrium. The system was assumed to have reached equilibrium when the velocity distribution function ceased to vary with time and the main parameters of the system (kinetic energy, potential energy, total energy, minimum distance between atoms, etc.) fluctuated due to the finite dimensions of the system about some mean value, which did not vary over a time $\sim 10^{-11}$ s.

To analyze the dynamic properties, we calculated the density of vibrational states $G(\omega)$ as the Fourier transform of the autocorrelation function $\gamma(\tau)$ (Ref. 20)

$$G(\omega)=\int_0^\infty \gamma(\tau)\exp(-i\omega\tau)\,d\tau, \tag{1}$$

where

$$\gamma(\tau)=\sum_i \langle \boldsymbol{\nu}_i(\tau)\boldsymbol{\nu}_i(0)\rangle/\nu_i^2(0)$$

is the autocorrelation function, $\boldsymbol{\nu}_i(\tau)$ is the velocity vector of the ith atom at the time τ, and $\langle \dots \rangle$ denotes averaging over various time intervals.

2. RESULTS OF CALCULATIONS AND DISCUSSION

2.1. Dynamics of the CuO_2 layer

Figure 1 depicts the partial (Cu, Y, O) and total density of vibrational states, calculated for the CuO_2 layer at $T=90$ K. The negative values and small oscillations are due to calculational error and the finite dimensions of the crystallite. Information about the density of vibrational states (DVS) for the yttrium system was obtained in Refs. 21–24 with the help of inelastic neutron scattering. Note that in their general outline the results of these different works coincide. The limiting frequency of the DVS in all of these works lies in the vicinity of 100 meV, and the positions of the main peaks practically coincide. Figure 1 (*5*), for comparison, presents the experimental DVS from Ref. 21. Since our results were obtained for only three mobile layers, they cannot be compared directly with experiment; however, qualitative agreement does obtain. The presence of an upper edge to the phonon spectrum at ~ 100 meV and peaks in the range 60–90 meV due to oxygen atoms agrees with experiment. The copper peaks are found mainly in the ranges 20–50 and 75–80 meV. The contribution to $G(\omega)$ from the yttrium atoms is

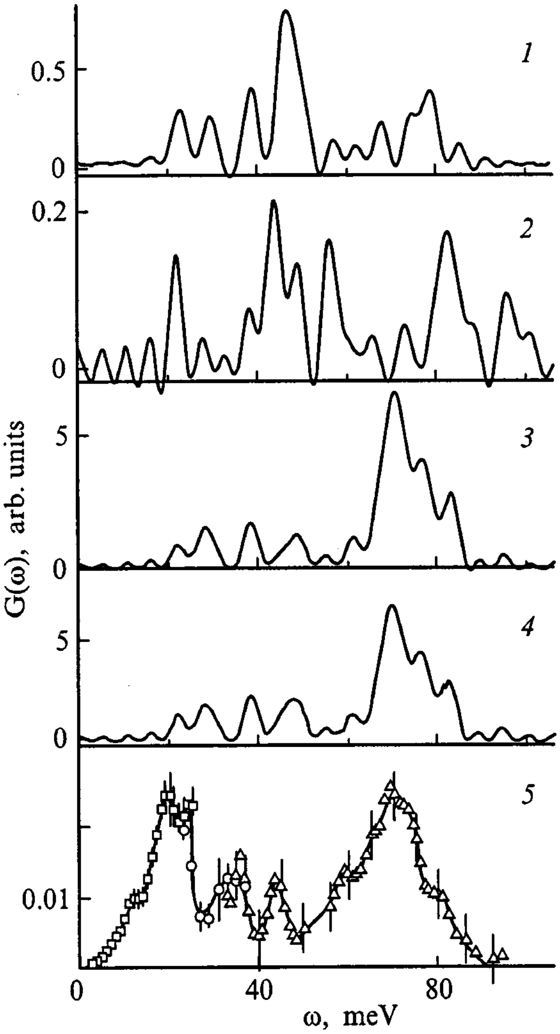

FIG. 1. Densities of vibrational states: partial Cu — (*1*), Y — (*2*), O — (*3*), and complete — (*4*) for the Cu–O_2 layer at $T=90$ K without defects. Inelastic neutron scattering experiment (Ref. 15) for $YBa_2Cu_3O_7$ — (*5*).

found in the energy range 20–100 meV. The experimental peaks in the range $\sim 12-15$ meV are probably due to the heavy Ba atoms.

The authors of Ref. 25 proposed that the appearance of a Ba^{4+} charge defect is possible in a reversible oxidation–reduction reaction. Direct experiments using high-resolution x-ray electron spectroscopy made it possible to observe such a valence state of Ba (Ref. 26). Ba^{4+} appeared in the transition to the superconducting state, accompanied by a structural deformation of the lattice. The qualitative behavior of the potentials of Ba^{4+} with copper and oxygen atoms from the CuO_2 layer is analogous to the behavior of the PIP's with Sr^{2+} in the lanthanum system. The Ba^{4+}–Cu^{2+} pairwise potential is characterized by a well depth of 8 eV, and the Ba^{4+}–O^{1-} potential, by a well depth of 36 eV.

We introduced 5% Ba^{4+} into the BaO layer. The abrupt change in the nature of the PIP led to the appearance of local vibrations with an energy of $\sim 0.17-0.18$ eV and an energy of ~ 0.5 eV. The density of vibrational states for the CuO_2 layer at $T=90$ eV with Ba^{4+} (5%) defects is shown in Fig. 2. Simultaneously, we observed a redistribution of the kinetic energy in the system. ''Hot'' regions in a ''cold'' matrix appeared in analogy with the situation we observed earlier in the lanthanum system.[14] We also modeled the situation with the simultaneous presence of Ba^{4+} ions and 10% Cu^{3+} ions in the CuO_2 layer. This led to the disappearance of the peak at $\sim 0.17-0.18$ eV with the preservation of the peak at 0.5 eV. The well depth of the potentials with Cu^{3+} are roughly 3–4 times deeper than the corresponding PIP's with Cu^{2+}. A study of the lattice dynamics of the CuO_2 layer in the presence of all the enumerated defects other than Ba^{4+} did not lead to the appearance of local high-frequency vibrations.

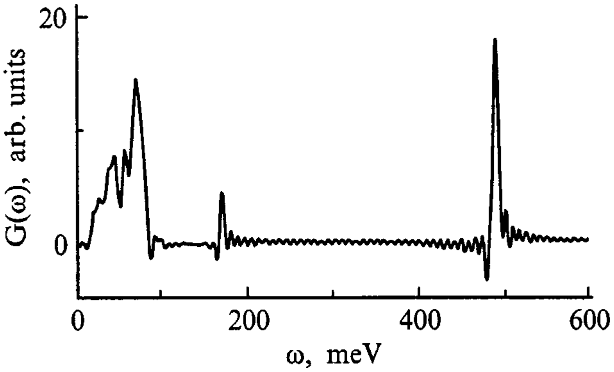

FIG. 2. Density of vibrational states for the CuO_2 layer at $T=90$ K with the charge defect Ba^{4+} (5%).

Great attention has been given to monitoring the state of the system since all physical characteristics can be calculated only after the system has reached steady state. The steady-state setup time, defined as the ''decay'' time of the autocorrelation function, for our specific system, is $\sim 4\times 10^{-13}$ s. In the calculations we ran the system for times always much longer than $\sim 10^{-11}$ s, after which we calculated the velocity distribution functions; if they did not vary with time (within the limits of error), then we calculated the DVS. In the initial state and in the presence of all the investigated defects other than Ba^{4+}, the velocity distribution function is described by a Maxwell distribution. When Ba^{4+} ions are present in the system, on the other hand, noticeable deviations from the Maxwell distribution are observed in the high-energy region, especially for the oxygen atoms. For a rough estimate of the temperature of the ''hot'' and ''cold'' regions, we used an expansion in Maxwell distributions with weighting factors.[27] Figure 3 plots velocity distribution functions for the times $\tau_1=8\times 10^{-11}$ s, $\tau_2=9\times 10^{-11}$ s, and $\tau_3=10^{-10}$ s at $T=90$ K. The low-energy part of the distribution is described by two Maxwell distributions—one with characteristic temperature $T_1=85$ K and a weighting factor of 0.5, and one with characteristic temperature $T_2=90$ K and a weighting factor of 0.45 (curve *1* in Fig. 3), and in the high-energy region there are two peaks corresponding to temperatures of ~ 2600 K and ~ 5700 K (see inset). The deviations from a Maxwell distribution in the copper and yttrium subsystems are insignificant. Oxygen atoms with large energies are found near the Ba^{4+} ions. Their mean kinetic energy is 15–20 times larger than in the rest of the matrix. The effect is substantially less than in the lanthanum system, but identical to it from the point of view of its physical content.

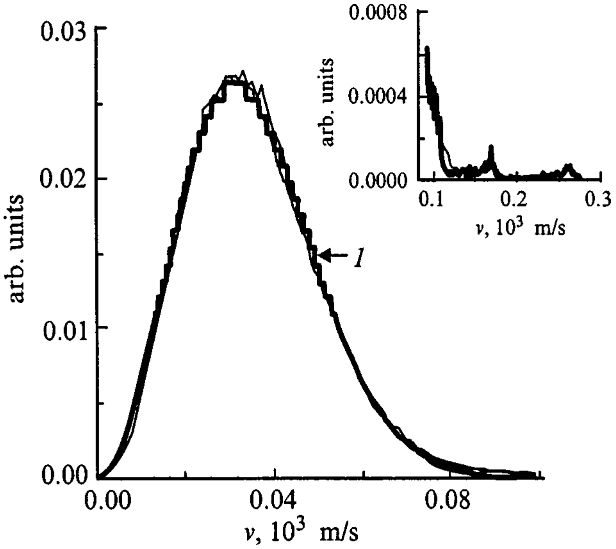

FIG. 3. Velocity distribution function of the oxygen atoms in the CuO_2 layer for times $\tau_1=8\times10^{-11}$ s, $\tau_2=9\times10^{-11}$ s, and $\tau_3=10^{-10}$ s (thin curves) at $T=90$ K in the presence of Ba^{4+} defects (5%). Theoretical distribution: thick curve *1* — for $T=T_1A_1+T_2A_2$, where $T_1=85$, $T_2=90$ K, $A_1=0.5$, and $A_2=0.45$.

2.2. Dynamics of the CuO chains

The partial (Cu, O) and total density of vibrational states for the CuO chains at $T=90$ K having no defects were calculated in a similar way. The peaks at 30 and 65–70 meV are due to vibrations of the oxygen atoms, and the peaks at 40 and 50 meV are due to vibrations of the copper atoms. When the charge defect Ba^{4+} (5%) is introduced into the BaO plane, the copper and oxygen atoms located near the defect are shifted out of their equilibrium positions by $\sim 10-15\%$ in the direction of the Ba^{4+} defect. Local peaks appear in the density of vibrational states with energies of ~ 0.2 eV and ~ 0.52 eV, due to vibrations of the oxygen atoms.

As in the CuO_2 plane, the velocity distribution functions in the CuO chains, in the initial state with all defects except Ba^{4+}, are well described by the corresponding Maxwell distributions. In the presence of Ba^{4+} in the chains, the deviation of the velocity distribution functions from a Maxwell distribution is very large and much greater than in the CuO_2 plane. Figure 4 plots velocity distribution functions at $T=90$ K for oxygen atoms at different time steps. The low-energy part for the oxygen atoms can be described by two Maxwell distributions—one with $T_1=8$ K (with weighting factor equal to 0.4), and the other with $T_2=45$ K (with weighting factor 0.55) (curve *1* in Fig. 4), and the high-energy part can be described by a Maxwell distribution with $T=1000$ K (curve *2* in the inset). The velocity distribution function of the copper atoms differs from a Maxwell distribution much more than in the CuO_2 layer. The high-energy atoms in the CuO chains are found, as in the CuO_2 layer, in the close vicinity of the Ba^{4+} ions and form ''hot'' regions in which the mean kinetic energy of the atoms is $\sim 15-20$ times greater than in the matrix.

When all of the Ba^{2+} ions have been replaced by Ba^{4+} ions in the model experiment, the velocity distribution again turns out to be near to a Maxwell distribution, but in this case the local high-frequency peaks (LHP) in the DVS are preserved, and the ''hot'' points ''wander'' over the entire plane with a lifetime of $\sim 10^{-12}$ s.

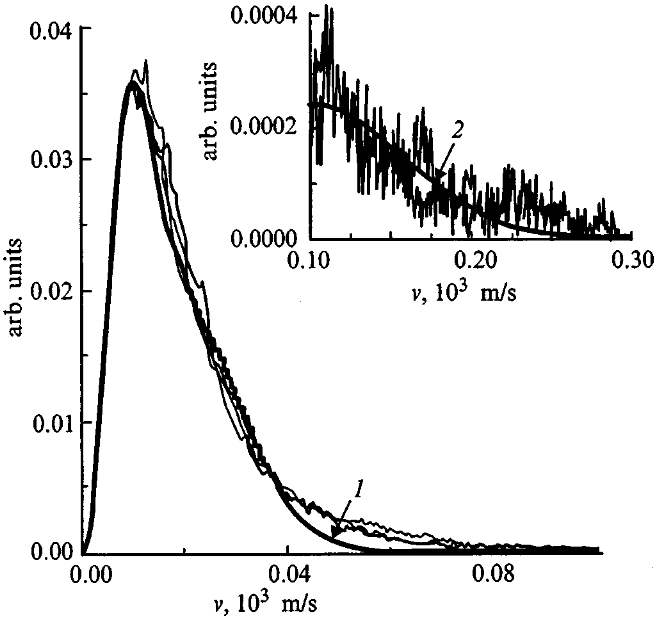

FIG. 4. Velocity distribution function of the oxygen atoms in the CuO chains for times $\tau_1=4\times10^{-11}$ s, $\tau_2=5\times10^{-11}$ s, and $\tau_3=6\times10^{-11}$ s (thin curves) at $T=90$ K in the presence of Ba^{4+} defects (5%). Theoretical distribution: thick curve *1* — for $T=T_1A_1+T_2A_2$, where $T_1=8$, $T_2=45$, $A_1=0.4$, and $A_2=0.55$; thick curve *2* — for $T=1000$ K.

As in the CuO_2 plane, we investigated the effect of various point defects (oxygen and copper vacancies, replacement of Cu^{1+} by Cu^{2+} and Cu^{3+}) on the dynamics of the CuO chains, but the local high-frequency peaks appeared only for the Ba^{4+} charge defect.

In Ref. 12 it was noted that the PIP's of corresponding layers in the lanthanum and yttrium systems are very similar, both in their overall character and in order of magnitude. In the lanthanum system the Sr–O potential had a very deep minimum (~ 30 eV), which led to the appearance of local high-frequency peaks of the oxygen atoms while in the yttrium system such a role is played by the Ba^{4+} charge defect, whose potential with oxygen also has a very deep well (36 eV). Both in that case and in the other case, local high-frequency peaks of oxygen atoms having large energy ($\sim 0.4-0.5$ eV) arise around defects having a deep and anharmonic PIP (Sr^{3+}, Ba^{4+}). The mean kinetic energy of these atoms is substantially greater than in the matrix, i.e., ''hot'' regions arise. The effect of ''hot'' points is observed only when the velocity distribution function deviates from the Maxwell distribution. Therefore it can be said that the dynamics of the crystal lattice of the CuO_2 and CuO conducting layers, both in the lanthanum system and in the yttrium system, are quite general.

It should be noted that it has been experimentally shown[28–30] in thallium and bismuth systems that thallium is present in two valence states Tl^{1+} and Tl^{2+} while in bismuth systems Bi has the valences Bi^{3+} and Bi^{5+}. It is possible that this charge difference of the Tl(Bi) ions induces the same charge defects in the BaO planes as in the lanthanum and yttrium systems. Judging from our results, these defects should have a radically different interaction potential with oxygen, and such a potential is characteristic of atoms having a large ionic radius (Sr, Ba, Ca).

To summarize, using the molecular dynamics method we have shown that certain types of defects (Ba^{4+}) in a model crystal lattice of the system $YBa_2Cu_3O_7$ lead to the excitation of local high-frequency peaks with energy ~0.5 eV. The ions responsible for the appearance of the local high-frequency peaks, as in the lanthanum system, are ions with large ionic radius, whose potential is unusually deep. In the lanthanum system these were Sr atoms, and in the yttrium system these were the Ba^{4+} defect. Thus, in the yttrium system the same situation can be realized, in principle, as in the lanthanum system, in which the dominant fraction of the energy of the thermal vibrations is concentrated in comparatively small (0.5 nm) regions of the copper-containing planes near the defects.

*)E-mail: chud@fti.udmurtia.su

---

[1] S. Tayima, S. Uchida, S. Tanaka, S. Kanbe, K. Kitazawa, and K. Fueki, Jpn. J. Appl. Phys., Part 2 **26**, L432 (1987).

[2] H. L. Dewing, E. K. H. Solje, K. Scott, and A. P. Mackenzie, J. Phys.: Condens. Matter **4**, L109 (1992).

[3] A. Maeda, M. Hase, I. Tsukada, K. Noda, S. Takebayashi, and K. Uchinokura, Phys. Rev. B **41**, 6418 (1990).

[4] V. M. Loktev, Sverkhprovodimost: Fiz., Khim., Tekh. **6**, 1972 (1993).

[5] S. Ikeda, M. Misawa, S. Tomiyoshi, M. Omori, and T. Suzuki, Phys. Lett. A **134**, 191 (1988).

[6] J. A. Unod, A. Berzinge, D. Cattani, J. Cors, M. Decroux, O. Fisher, P. Genoud, L. Hoffmann, J. L. Jorda, J. Muller, and E. Walker, Jpn. J. Appl. Phys., Suppl. **26**, Suppl. 26–3, 1119 (1987).

[7] V. P. Preobrazhenskiĭ, V. D. Klimov, Sh. Sh. Nabiev, A. P. Osipov, V. P. Ushakov, I. Yu. Arnol'd, S. E. Voinova, Yu. I. Vereshchagin, R. S. Larina, and V. I. Ozhogin, *Problems of High-Temperature Superconductivity*, Pt. 2 (Academy of Sciences of the USSR, Ural Branch, Sverdlovsk, 1987), p. 34.

[8] M. Ohachi, D. Shimada, and N. Tsuda, Jpn. J. Appl. Phys., Part 2 **32**(28), L251 (1993).

[9] X. Zhang and C. R. A. Catlow, Phys. Rev. B **46**, 457 (1992).

[10] R. C. Baetzold, Phys. Rev. B **38**(16A), 11 304 (1988).

[11] S. L. Chaplot, Phys. Rev. B **42**, 2149 (1990).

[12] V. G. Chudinov, E. B. Dolgusheva, and A. A. Yur'ev, Sverkhprovodimost: Fiz., Khim., Tekh. **4**, 2086 (1991).

[13] *The Interparticle Interaction in Liquid Metals*, edited by O. A. Esin (Nauka, Moscow, 1979).

[14] V. G. Chudinov, A. G. Chirkov, E. B. Dolgusheva, and V. M. Dyadin, Sverkhprovodimost: Fiz., Khim., Tekh. **6**, 204 (1993).

[15] A. G. Chirkov and V. G. Chudinov, Sverkhprovodimost: Fiz., Khim., Tekh. **7**, 800 (1994).

[16] V. G. Chudinov and A. G. Chirkov, Sverkhprovodimost: Fiz., Khim., Tekh. **8**, 243 (1995).

[17] L. M. Volkova, S. A. Polishchuk, S. A. Magarill, and S. V. Borisov, Sverkhprovodimost: Fiz., Khim., Tekh. **2**, 127 (1989).

[18] W. E. Pickett, Rev. Mod. Phys. **61**, 433 (1989).

[19] H. Haghighi, J. H. Kaiser, S. Rayner, R. N. West, J. Z. Liu, R. Shelton, R. H. Howell, F. Solal, and M. J. Fluss, Phys. Rev. Lett. **67**, 382 (1991).

[20] J. M. Dickey and A. Paskin, Phys. Rev. **188**, 1407 (1969).

[21] J. J. Rhyne, D. A. Neumann, J. A. Gotaas, F. Beech, L. Toth, S. Lawrence, S. Wolf, M. Osofsky, and D. U. Gubser, Phys. Rev. B **36**, 2294 (1987).

[22] P. P. Parshin, M. G. Zemlyanov, I. A. Chernoplekov, I. É. Graboĭ, and A. R. Kaul', Sverkhprovodimost: Fiz., Khim., Tekh. **201**, 30 (1988).

[23] I. Natkanets, A. V. Belushkin, E. A. Goremychkin, Ya. Maĭer, I. L. Sashin, V. K. Fedotov, R. K. Nikolaev, E. G. Ponyatovskiĭ, and N. S. Sidorov, JETP Lett. **48**, 181 (1989).

[24] L. Pintschovius, N. Pyka, W. Reichardt, A. Yu. Rumiantsev, N. L. Mitrofanov, A. S. Ivanov, G. Collin, and P. Bourges, Physica C **185–189**, 156 (1991).

[25] G. P. Kostikova, D. V. Korol'kov, and Yu. P. Kostikov, Dokl. RAN Khimiya. **331**(3), 318 (1993).

[26] I. N. Shabanova, O. V. Popova, V. I. Kukuev, and V. I. Kormilets, Surf. Rev. Lett. **5**, 347 (1998).

[27] Yu. L. Klimontovich, *Statistical Physics*, Nauka, Moscow (1982), p. 158.

[28] T. Suzuki, M. Nagoshi, Y. Fuhuda, S. Nakajima, M. Kikuchi, Y. Syono, and M. Tachiki, Physica C **162–164**, 1387 (1989).

[29] A. Manthiram, M. Paranthaman, and J. B. Goodenough, Physica C **171**, 135 (1990).

[30] S. Kambe, T. Matsuoka, M. Takahasi, M. Kawai, and T. Kawai, Phys. Rev. B **42**, 2669 (1990).

Translated by Paul F. Schippnick

PHYSICS OF THE SOLID STATE VOLUME 41, NUMBER 10 OCTOBER 1999

Mössbauer study of the $HgBa_2Ca_{n-1}Cu_nO_{2n+2}$ ceramics

V. F. Masterov,*) F. S. Nasredinov, N. P. Seregin, and P. P. Seregin

St. Petersburg State Technical University, 195251 St. Petersburg, Russia

(Submitted February 2, 1999)
Fiz. Tverd. Tela (St. Petersburg) **41**, 1734–1738 (October 1999)

The parameters of the electric-field gradient tensor at the copper, barium, and mercury sites in the $HgBa_2Ca_{n-1}Cu_nO_{2n+2}$ lattices ($n=1,2,3$) have been determined by Mössbauer emission spectroscopy on the $^{67}Cu(^{67}Zn)$, $^{133}Ba(^{133}Cs)$, and $^{197}Hg(^{197}Au)$ isotopes, and calculated in the point-charge approximation. An analysis of these results combined with available ^{63}Cu NMR data showed that the experimental and theoretical data can be reconciled by assuming that the holes originating from defects in the material are localized primarily on the sublattice of the oxygen lying in the copper plane [for $HgBa_2Ca_2Cu_3O_8$, in the plane of the Cu(2) atoms]. © *1999 American Institute of Physics.* [S1063-7834(99)00410-4]

$HgBa_2Ca_{n-1}Cu_nO_{2n+2}$ compounds (HgBaCaCuO) ($n=1,2,3$) exhibit record-high superconducting transition temperatures T_c, which makes determination of the charge states of the oxygen atoms in HgBaCaCuO lattices responsible for the phenomenon of high-T_c superconductivity in these ceramics an important problem. This paper reports the use of Mössbauer emission spectroscopy on the $^{67}Cu(^{67}Zn)$, $^{133}Ba(^{133}Cs)$, and $^{197}Hg(^{197}Au)$ isotopes to determine the charge states of atoms in the HgBaCaCuO lattices.

The Mössbauer sources $HgBa_2Ca_{n-1}{}^{67}Cu_nO_{2n+2}$ and $^{197}HgBa_2Ca_{n-1}Cu_nO_{2n+2}$ were prepared by diffusion doping of the compounds $HgBa_2Ca_2Cu_3O_8$ (1223, $T_c=112$ K), $HgBa_2CaCu_2O_6$ (1212, $T_c=93$ K), and $HgBa_2CuO_4$ (1201, $T_c=79$ K) by the ^{67}Cu and ^{197}Hg radioactive isotopes at 450 °C for 2 hours in an oxygen atmosphere. The ^{133}Ba radioactive isotope was introduced into the $HgBa_2Ca_{n-1}Cu_nO_{2n+2}$ ceramics during the preparation. The $^{67}Cu(^{67}Zn)$ and $^{133}Ba(^{133}Cs)$ Mössbauer spectra were obtained at 4.2 K with ^{67}ZnS and CsCl absorbers, respectively. The $^{197}Hg(^{197}Au)$ Mössbauer spectra were measured at 80 K with metallic gold serving as an absorber. Figures 1–3 present typical spectra, and Table I lists the results of their treatment.

It was assumed that the ^{67}Cu, ^{133}Ba, and ^{197}Hg parent isotopes occupy during diffusion doping the copper, barium, and mercury sites, respectively, with the daughter isotopes ^{67}Zn, ^{133}Cs, and ^{197}Au turning up in the same lattice sites. Because barium and mercury atoms occupy unique sites in all HgBaCaCuO lattices,[1,2] it was expected that $^{133}Ba(^{133}Cs)$ and $^{197}Hg(^{197}Au)$ Mössbauer spectra would reflect the only state of the corresponding probes. As seen from Figs. 2 and 3, this is what is observed in experimental spectra. In the (1201) and (1212) compounds, copper atoms also reside in unique sites,[1,2] so that the $^{67}Cu(^{67}Zn)$ spectra of these compounds correspond to the only state of the ^{67}Zn probe [see Figs. 1a and 1b]. Finally, in the (1223) lattice, the copper atoms reside in two crystallographically inequivalent sites,[2] so that the $^{67}Cu(^{67}Zn)$ Mössbauer spectra of this ceramic should be assigned to the two states of the ^{67}Zn Mössbauer probe occupying the Cu(1) and Cu(2) sites [Fig. 1c].

The local symmetry of all sites in the HgBaCaCuO lattices is lower than cubic, and interaction of the quadrupole moment of the probe nucleus eQ with the electric-field gradient (EFG) splits the Mössbauer spectrum into several components. In the case of the ^{67}Zn isotope, the experimental spectrum splits into three components, and the spectrum allows determination of the quadrupole coupling constant for the ^{67}Zn probe, $C(\mathrm{Zn})=eQU_{zz}/h$, of its sign, and of the EFG tensor asymmetry parameter η, with the measured quantity eQU_{zz} being a sum of two terms

$$eQU_{zz}=eQ(1-\gamma)V_{zz}+eQ(1-R_0)W_{zz}, \tag{1}$$

where U_{zz}, V_{zz}, and W_{zz} are the principal components of the total, crystal-field, and valence EFGs, respectively, and γ and R_0 are the Sternheimer coefficients for the probe atom.

The zinc daughter atom left after the radioactive decay of the ^{67}Cu parent isotope stabilizes in the divalent state (the only valence state of zinc possible in oxide systems); in the case of the $^{67}Zn^{2+}$ probe the valence-electron contribution to the total EFG tensor may be neglected, which yields

$$C(\mathrm{Zn})\approx eQ(1-\gamma)V_{zz}/h. \tag{2}$$

The crystal-field EFG tensor can be calculated within the point-charge model, so that by comparing the experimental $C(\mathrm{Zn})$ and calculated $eQ(1-\gamma)V_{zz}$ quantities one can determine the effective charges of atomic centers at lattice sites.

We calculated the crystal-field EFG tensors for the HgBaCaCuO lattices represented as superpositions of several sublattices:

$$[\mathrm{Hg}][\mathrm{Ba}_2][\mathrm{Cu}][\mathrm{O}(1)_2][\mathrm{O}(2)_2],$$

$$[\mathrm{Hg}][\mathrm{Ba}_2][\mathrm{Ca}][\mathrm{Cu}_2][\mathrm{O}(1)_4][\mathrm{O}(2)_2],$$

$$[\mathrm{Hg}][\mathrm{Ba}_2][\mathrm{Ca}_2][\mathrm{Cu}(1)][\mathrm{Cu}(2)_2][\mathrm{O}(1)_2][\mathrm{O}(2)_4][\mathrm{O}(3)_2].$$

Figure 4 presents parts of unit cells of the HgBaCaCuO compounds. The structural data required for the calculations were taken from Refs. 1 and 2. The lattice

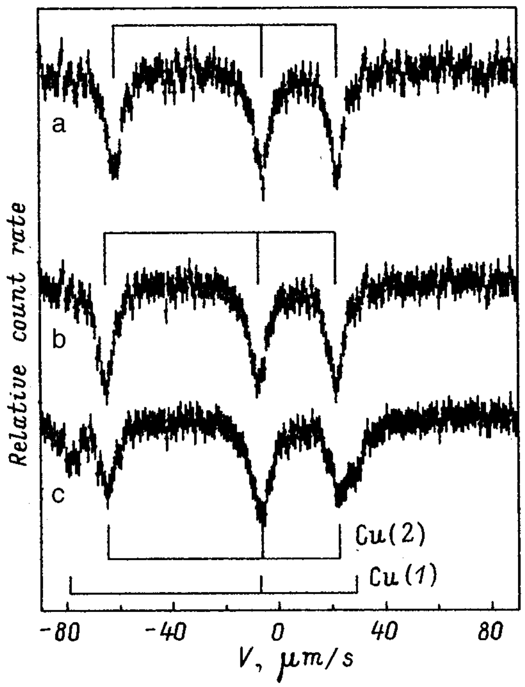

FIG. 1. ^{67}Cu(^{67}Zn) Mössbauer spectra of (a) (1201), (b) (1212), and (c) (1223) compounds. The position of the quadrupole triplet components corresponding to ^{67}Zn^{2+} centers at copper sites is identified.

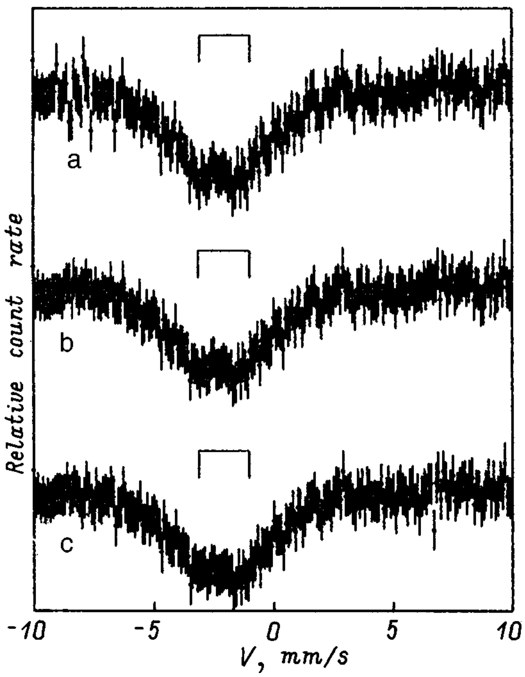

FIG. 3. ^{197}Hg(^{197}Au) Mössbauer spectra of (a) (1201), (b) (1212), and (c) (1223) compounds. The position of the quadrupole doublet components corresponding to ^{197}Au centers at mercury sites is identified.

sum tensors were found to be diagonal along the crystallographic axes and axially symmetric for all sites.

If one uses the values $\gamma = -12.2$ (Ref. 3) and $Q = 0.17$b (Ref. 4) for the ^{67}Zn^{2+} centers, then taking model *A* corresponding to the standard valence states (Hg^{2+}, Ba^{2+}, Ca^{2+}, Cu^{2+}, O^{2-}) one obtains for the $HgBa_2Ca_2Cu_3O_8$ lattice $eQ(1-\gamma)V_{zz1} \approx 79$ MHz for the Cu(1) sites and $eQ(1-\gamma)V_{zz2} \approx 72$ MHz for the Cu(2) sites. These values differ substantially from the experimental C(Zn) figures for the Cu(1) and Cu(2) sites [C(Zn1) and C(Zn2), accordingly]. To exclude the error caused by a wrong choice of the value for γ, one can compare the ratios $S = C(\mathrm{Zn1})/C(\mathrm{Zn2}) = 1.23(8)$ and $s = V_{zz1}/V_{zz2} = 1.08$. In this case, however, the difference between the measured and calculated values is also substantial. Similar discrepancies are observed for the other compounds as well.

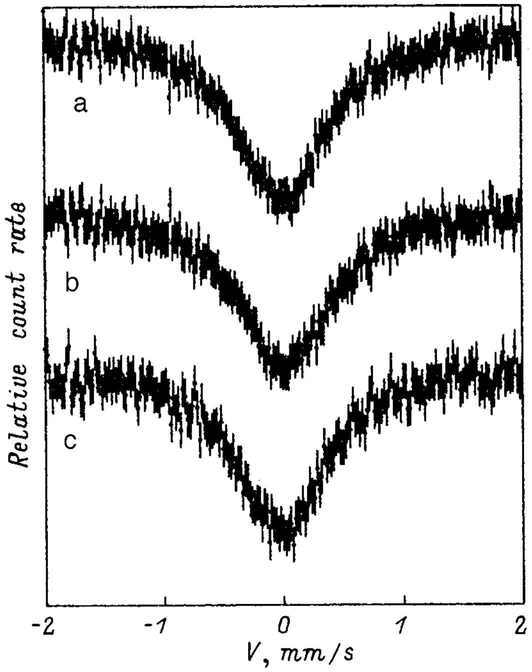

FIG. 2. ^{133}Ba(^{133}Cs) Mössbauer spectra of (a) (1201), (b) (1212), and (c) (1223) compounds.

The nature of the discrepancies can be established by a combined analysis of ^{67}Cu(^{67}Zn) MES data and ^{63}Cu NMR measurements for copper sites in the copper cuprate lattices. Figure 5a presents a $C(\mathrm{Cu})-C(\mathrm{Zn})$ diagram constructed in Ref. 5. The experimental data obtained for divalent copper compounds fit onto a straight line

$$C(\mathrm{Cu}) = 197 - 11.3\,C(\mathrm{Zn}), \tag{3}$$

where C(Cu) and C(Zn) are in MHz.

The main reason for the deviation from straight line (3) is the difference of the copper valence from $+2$.

One can obtain additional information from a $C(\mathrm{Cu})-V_{zz}$ diagram proposed in Ref. 5 [Fig. 5b]. Plotted along the horizontal axis here are the calculated principal components V_{zz} of the crystal-field EFG tensor for the copper sites for which C(Cu) was measured by ^{63}Cu NMR. The $C(\mathrm{Cu})-V_{zz}$ plot can be fitted by the expression

$$C(\mathrm{Cu}) = 179 - 191.4\,V_{zz}, \tag{4}$$

where C(Cu) is given in MHz, and V_{zz}, in $e/\text{Å}^3$.

TABLE I. Nuclear quadrupole coupling parameters of the ^{67}Zn, ^{133}Cs, and ^{197}Au probes at the cation sites of the $HgBa_2Ca_{n-1}Cu_nO_{2n+2}$ lattices.

							V_{zz}	
Compound	Site	Probe	C(Zn)	η	$\lvert C(\mathrm{Cs})\rvert$	$\lvert C(\mathrm{Au})\rvert$	A	B
$HgBa_2CuO_4$	Cu	^{67}Zn	14.0(5)	⩽0.2			0.858	0.737
	Ba	^{133}Cs			⩽40		0.080	0.076
	Hg	^{197}Au				262(6)	−1.078	−1.032
$HgBa_2CaCu_2O_6$	Cu	^{67}Zn	14.5(5)	⩽0.2			0.937	0.753
	Ba	^{133}Cs			⩽40		0.088	0.093
	Hg	^{197}Au				268(6)	−1.100	−0.961
$HgBa_2Ca_2Cu_3O_8$	Cu(1)	^{67}Zn	18.0(5)	⩽0.2			1.010	1.006
	Cu(2)	^{67}Zn	14.6(5)	⩽0.2			0.931	0.766
	Ba	^{133}Cs			⩽40		0.064	0.071
	Hg	^{197}Au				264(6)	−1.138	−1.010

Note: C are the quadrupole coupling constants (MHz), η is the asymmetry parameter, and V_{zz} is the crystal-field EFG principal component for models A and B (in e/Å^3).

There is one more reason for a deviation of the $C(\mathrm{Cu})-V_{zz}$ plot from straight line (4), namely, a wrongly calculated EFG tensor caused by an erroneous choice of the atomic charges.

^{63}Cu NQR data for the (1201), (1212), and (1223) compounds (Refs. 6–8, respectively) are plotted on the $C(\mathrm{Cu})-C(\mathrm{Zn})$ diagram together with our ^{67}Cu(^{67}Zn) MES data [Fig. 5a]. We readily see that all points fit satisfactorily onto relation (3), which implies that copper in the HgBaCaCuO compounds is divalent.

At the same time the $C(\mathrm{Cu})-V_{zz}$ graph in Fig. 5b does not follow the linear relation (4) if V_{zz} was calculated assuming standard atomic charges (model A). The deviation of the data from the straight line (4) obviously should be attributed to the inadequacy of the model chosen for V_{zz} calculation. This conclusion is also supported by the considerable difference between the values $S=C(\mathrm{Zn1})/C(\mathrm{Zn2})$ and $s=V_{zz1}/V_{zz2}$. An agreement can be reached within B-type models; namely, for the (1201) and (1212) compounds one should localize holes at the O(1) atoms, and for (1223), they should be localized on the O(2) sublattice. Holes in these compounds may appear as a result of part of the mercury atoms being stabilized in a univalent state. When calculating

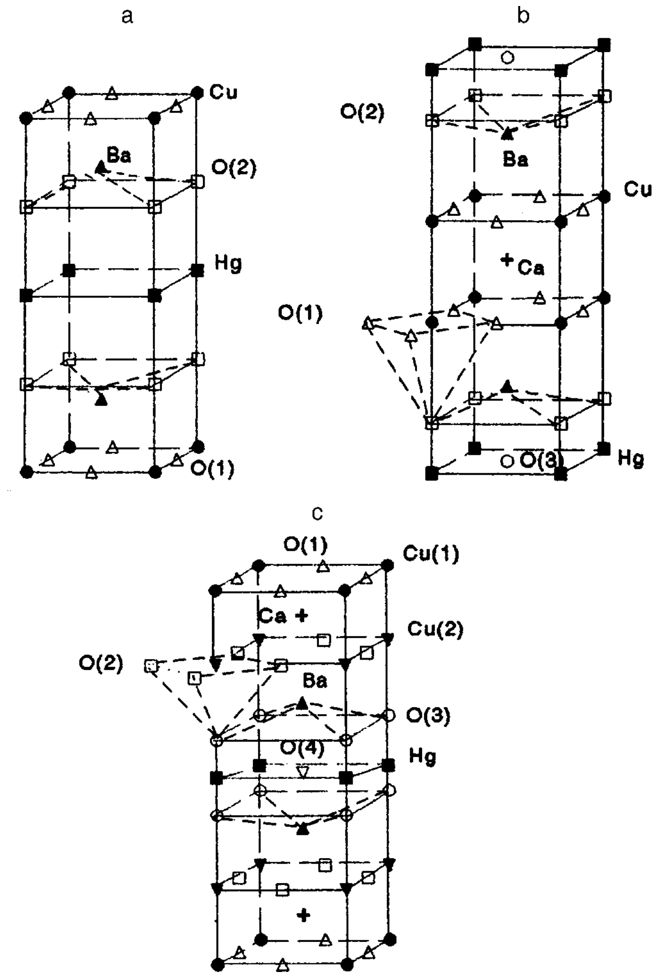

FIG. 4. Parts of the unit cells of (a) (1201), (b) (1212), and (c) (1223) compounds.

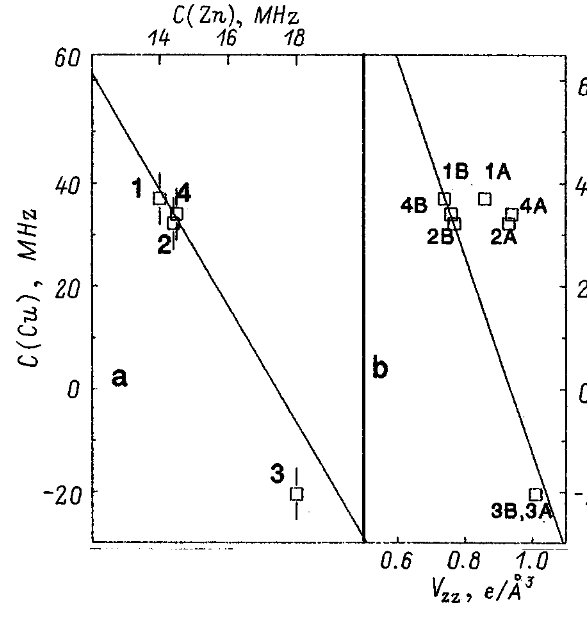

FIG. 5. (a) $C(\mathrm{Cu})-C(\mathrm{Zn})$ diagram for compounds of divalent copper (solid line). (b) $C(\mathrm{Cu})-V_{zz}$ diagram for compounds of divalent copper. The points relate to: *1*—Cu in (1201), *2*—Cu in (1212), *3*—Cu(1) in (1223), and *4*—Cu(2) in (1223). Indices A and B refer to the V_{zz} calculation models used.

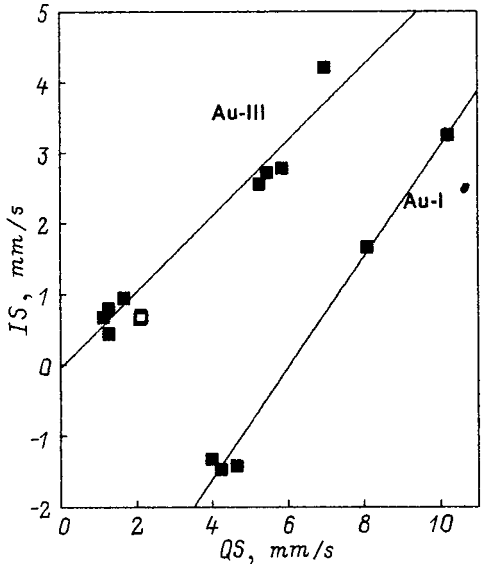

FIG. 6. I.S. vs Q.S. graph for compounds of univalent (Au–I) and trivalent (Au–III) gold (the experimental data for the various gold compounds presented by filled squares are from Ref. 10). The open squares relate to the data for $HgBa_2CuO_4$, $HgBa_2CaCu_2O_6$, and $HgBa_2Ca_2Cu_3O_8$ (these values coincide).

the EFG tensor within models B, it was assumed that mercury is univalent in the (1201), (1212), and (1223) compounds in amounts of 30, 90, and 80%, respectively. For the B model the discrepancy between the values of S and s is smaller too. It should be noted, however, that XPS measurements do not support mercury stabilization in a univalent state (see, e.g., Ref. 9), and one will possibly have to invoke defects in the material to account for the presence of holes at the oxygen sublattices.

^{197}Hg(^{197}Au) measurements show that interaction of the quadrupole moment of the ^{197}Au nucleus with the EFG splits the Mössbauer spectrum into two components spaced by $\mathrm{Q.S.}=(1/2)|eQU_{zz}|(1+\eta^2/3)^{1/2}$, and that an experimental spectrum does not allow separate determination of C and η, as well as the sign of C. Besides, ^{197}Au Mössbauer spectroscopy does not permit one to identify the valence (charge) state of gold atoms from the magnitude of the isomer shift I.S. only. As shown in Ref. 10, however, such identification can be made by a combined analysis of the isomer shifts and quadrupole splittings of ^{197}Au Mössbauer spectra. Figure 6 shows, in particular, I.S. vs Q.S. graphs for compounds of uni- and trivalent gold, which exhibit a good agreement of the data on HgBaCaCuO compounds with those for trivalent gold. In other words, the ^{197}Au daughter atoms produced in the decay of the ^{197}Hg parent isotope are stabilized at mercury sites of the HgBaCaCuO lattices, formally in trivalent state. Because the Au^{3+} ion is not a crystal-field probe, the Q.S. values obtained do not permit determination of the lattice contribution to the total ^{197}Au EFG. However taking into account that EFG tensor calculations yield $\eta=0$ for the mercury sites, one can find the quadrupole coupling constant for the ^{197}Au nucleus as $|C(\mathrm{Au})|=2$ Q.S. (see Table I). Note also that the values of $C(\mathrm{Au})$ for all HgBaCaCuO compounds are very similar (see Table I), and this is in accord with V_{zz} calculations for mercury sites in models B.

There is obviously a direct relation between the valence state of the ^{197}Hg parent atoms and that of the ^{197}Au daughter atom; indeed, electron capture in $^{197}Hg^{+}$ and $^{197}Hg^{2+}$ produces, accordingly, $^{197}Au^{+}$ and $^{197}Au^{2+}$. However the Au^{2+} state is unstable and decays into the Au^{+} and Au^{3+} states, the ratio of the uni- to trivalent gold atoms being determined by the type and concentration of carriers in the material. Because the conduction in HgBaCaCuO ceramics is typically p-type, the presence in the ^{197}Hg(^{197}Au) Mössbauer emission spectra of the trivalent gold only implies evidently the divalent state of the mercury atoms. This agrees with XPS data[9] and may be considered as additional evidence for the existence in HgBaCaCuO compounds of residual defects resulting in hole localization at the oxygen sublattices.

Finally, ^{133}Ba(^{133}Cs) experimental spectra represent single lines without any fine structure, and therefore one can only make an estimate of the quadrupole coupling constant $|C(\mathrm{Cs})|$ for the ^{133}Cs probe. This can be accounted for by the small magnitude of V_{zz} at barium sites in all HgBaCaCuO compounds (see Table I).

Support of the Russian Fund for Fundamental Research (Grant 97-02-16216) is gratefully acknowledged.

[*)] Deceased.

---

[1] J. L. Wagner, P. G. Radaelli, D. G. Hinks, J. D. Jorgensen, J. F. Mitchell, B. Dabrowski, G. S. Knapp, and M. A. Beno, Physica C **210**, 447 (1993).
[2] L. W. Finger, R. M. Hazen, R. T. Downs, R. L. Meng, and C. W. Chu, Physica C **226**, 216 (1994).
[3] R. Sternheimer, Phys. Rev. **146**, 140 (1966).
[4] A. Forster, W. Potzel, and G. M. Kalvius, Z. Phys. B **37**, 209 (1980).
[5] V. F. Masterov, F. S. Nasredinov, N. P. Seregin, and P. P. Seregin, Fiz. Tverd. Tela (St. Petersburg) **37**, 3400 (1995) [Phys. Solid State **37**, 1868 (1995)].
[6] T. Machi, R. Usami, H. Yamauchi, N. Koshizuka, and H. Yasuoka, Physica C **235–240**, 1675 (1994).
[7] M. Horvatić, C. Berthier, P. Carretta, J. A. Gillet, P. Ségransan, Y. Berthier, and J. J. Capponi, Physica C **235–240**, 1669 (1994).
[8] K. Magishi, Y. Kitaoka, G.-q. Zheng, K. Asayama, K. Tokiwa, A. Iyo, and H. Ihara, Phys. Rev. B **53**, R8906 (1996).
[9] R. P. Vasquez, M. Rupp, A. Gupta, and C. C. Tsuei, Phys. Rev. B **51**, 15657 (1995).
[10] G. Kaindl, K. Leary, and M. Bartlett, J. Chem. Phys. **59**, 5050 (1973)

Translated by G. Skrebtsov

PHYSICS OF THE SOLID STATE VOLUME 41, NUMBER 10 OCTOBER 1999

The statistical distribution of magnetic critical currents determined by HTSC film morphology

Yu. I. Kuz'min and I. V. Pleshakov

A. F. Ioffe Physicotechnical Institute, Russian Academy of Sciences, 194021 St. Petersburg, Russia

S. V. Razumov

St. Petersburg State Electrotechnical University, 197022 St. Petersburg, Russia

(Submitted February 9, 1999)
Fiz. Tverd. Tela (St. Petersburg) **41**, 1739–1742 (October 1999)

An analysis is made of the geometric and morphological properties of YBCO superconducting films and of their effect on the magnetic and transport phenomena. A study is presented of the statistical characteristics of critical currents derived from the variation of trapped magnetic flux induced by passing a pulsed transport current. It is shown that the critical currents in the materials under study have a specific statistical distribution, whose main properties are due to the morphology of their structure and can be determined by geometric-probability analysis. The superconducting film is considered as a percolation system. An empirical normal-phase cluster-area distribution function was used to derive the distribution function of magnetic critical currents, which describes adequately the experimental data on how transport current affects trapped magnetic flux. The critical current for transition of a film to the resistive state has been calculated. © *1999 American Institute of Physics.* [S1063-7834(99)00510-9]

Development of superconducting composites with high critical currents is an important problem in cryoelectronics.[1] One of the promising methods to increase the critical current consists in using hard superconductors (i.e. type-II superconductors with pinning centers) possessing microscopic inhomogeneities. Being only partially superconducting because of the presence of normal-phase fragments, such materials can support high currents in magnetic fields far in excess of the thermodynamic critical field of a ''pure'' bulk superconductor. It is these inclusions of the normal phase that act as pinning centers inhibiting the motion of vortices under the action of the Lorentz force.

This work studies critical currents in YBCO superconducting films containing normal-phase inclusions with a given texture. The structure of the inhomogeneities does not vary over the film thickness, and all magnetic-flux distributions are two-dimensional. The critical currents at liquid-nitrogen temperature were measured magnetically from the variation of the trapped magnetic flux induced by the transport current. We shall call such critical currents magnetic in order to distinguish them from the critical current determined from the sample transition to resistive state.

The object of the work was to study the statistical nature of magnetic critical currents and to establish their relation to the geometric-morphological properties of the superconducting film structure.

The YBCO superconducting films were prepared by magnetron sputtering in pure oxygen at a pressure of 1 Torr. The discharge current was increased from 100 to 400 mA during the first 30 min and not varied subsequently. The substrate was an [1102] sapphire crystal (the *r*-cut) with a 0.02-μm thick cerium oxide buffer layer. The substrate temperature was maintained at 650 °C during the whole growth period (8 h). The thickness of the films thus prepared was 0.4 μm. Figure 1 displays a fragment of an electron photomicrograph of such a film. One readily sees a characteristic texture created during the growth due to surface defects at the film/substrate interface. The bright regions correspond to the $YBa_2Cu_3O_{7-x}$ superconducting phase, and the dark ones, to normal-phase CuO inclusions and voids in the bulk of the material. The normal-phase inclusions have a columnar structure oriented along the *c* axis. The total film area scanned for subsequent statistical treatment was 200 μm^2. The fraction of the area occupied by the superconducting phase is 80%, which is considerably in excess of the electric-current percolation threshold (50% for two-dimensional continuum percolation[2]). Thus a sufficiently dense superconducting cluster providing in-plane transport-current flow formed in the film. At the same time the fraction of surface area occupied by the normal phase and, hence, subject to magnetic-flux penetration, is 20%. This is less than the percolation threshold for magnetic-flux transport in the transverse direction so that the fragments of the normal phase merged to form final clusters, and vortices cannot move in the film plane without crossing an infinite superconducting cluster. A superconducting film with a two-dimensional magnetic-flux distribution is an example of a two-dimensional system where the electric and magnetic percolation cannot coexist. Such a superconducting structure ensures efficient pinning, because when a transport current is passed, there is no percolation of the magnetic-flux directed perpendicular to the film plane.

We showed earlier[3] that the statistical properties of pinning centers play an important part in the determination of

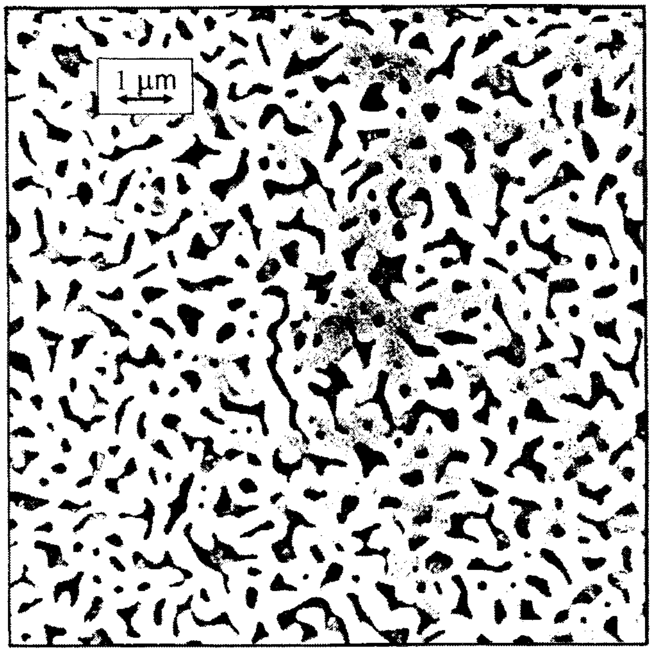

FIG. 1. Part of an electron photomicrograph of an YBCO superconducting film. The a and b axes lie in the plane of the figure, and the c axis is perpendicular to the latter.

critical currents. When a film with a texture like that in Fig. 1 is magnetized, the magnetic flux is trapped by normal-phase fragments acting as pinning centers. Therefore it is essential to know the geometric-statistical nature of the clusters formed by normal-phase fragments. Figure 2 shows an empirical distribution function $F(S)$ of normal-phase cluster areas, which was calculated as the relative number of clusters whose area did not exceed a given area S for each order statistic. Also shown in Fig. 2 is a histogram of a sample of normal-phase cluster areas constructed with an area step of $0.02113\,\mu\mathrm{m}^2$. Plotted along the vertical axis is the number of clusters N falling in a given area step, and along the horizontal axis, the number of this group n. The sample size is 526. The maximum and minimum normal-phase cluster areas were 0.4015 and $0.002\,\mu\mathrm{m}^2$, respectively. The asymmetry of the distribution is 1.743. The discrepancy between the sample mean $(0.07750\,\mu\mathrm{m}^2)$ and standard deviation $(0.07389\,\mu\mathrm{m}^2)$ does not exceed 5%, which suggests an exponential distribution of normal-phase clusters in area. Least-squares fitting of the distribution function

$$F(S)=1-\exp\left(-\frac{S}{S_0}\right) \tag{1}$$

yields $S_0=0.07381\,\mu\mathrm{m}^2$ for the average normal-phase cluster area.

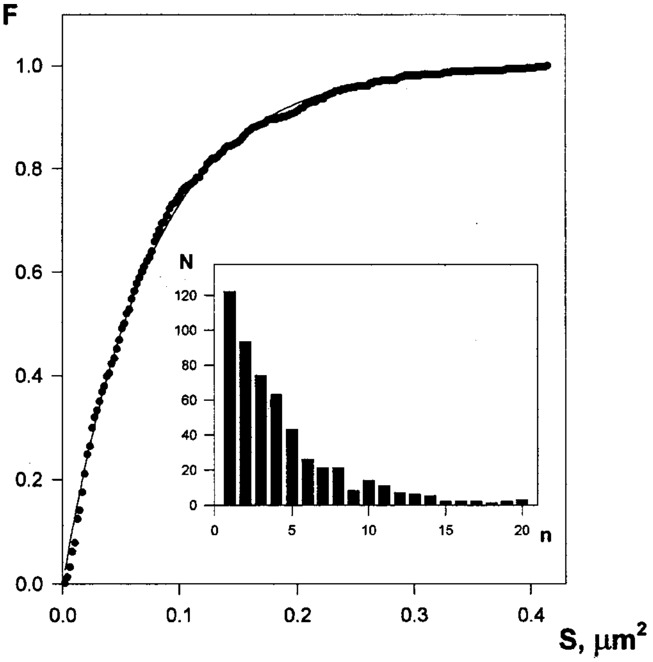

FIG. 2. An empirical distribution function and a histogram of a normal-phase cluster area sample. The points correspond to order statistics, and the line is a fit with a $F(S)=1-\exp(-S/S_0)$ function.

We next proceed with critical current measurement by the following scheme. First the film is magnetized by cooling it below the critical temperature in a magnetic field oriented along the c axis. The magnetic flux will be trapped in clusters of the normal phase. Next a transport current is passed through the film in the (a,b) plane. The film magnetization will not change until the Lorentz force becomes higher than the pinning force of the weakest pinning center. As the current is increased, the magnetization will vary as the magnetic flux is depinned from the normal-phase clusters whose pinning strength does not exceed the Lorentz force generated by the given transport current. After the current has reached the critical level, vortex depinning will grow to an avalanche rate, and the sample will transform to the resistive state. At the same time each pinning center will be identified with its particular critical current capable of depinning the magnetic flux trapped by it. Because the pinning centers represent, in this case, clusters of the normal phase, the vortices depinned from such a center will cross the infinite superconducting cluster whose cells contain finite normal clusters. The vortices will traverse the superconducting region along weak links, for instance, along twin boundaries, which are always present in the superconducting phase.[4,5] The larger a cluster, the more such weak links in the surrounding superconducting space and, hence, the smaller is the corresponding critical current. Based on these geometric considerations, we assume the critical current to be inversely proportional to the perimeter of a normal-phase cluster, which, in its turn, is proportional to $S^{1/2}$, namely, $I\propto S^{-1/2}$, where S is the normal-phase cluster area. This is valid in the case where the weak-link concentration per unit perimeter length is the same for all normal clusters, irrespective of their area and in any part of the film, and where all clusters are similar in shape. The condition of geometrical similarity is not rigorous; indeed, as seen from the photograph (Fig. 1), clusters of larger sizes, which formed by coalescence of smaller clusters, are much more diverse in shape. At the same time taking variations in cluster shape into account does not change the main physical conclusions. To simplify the analysis, we assume all clusters of the same area to have the same pinning strength and, hence, the same critical current. Note that $I=\beta S^{-1/2}$, where the form factor β takes into account both the microscopic

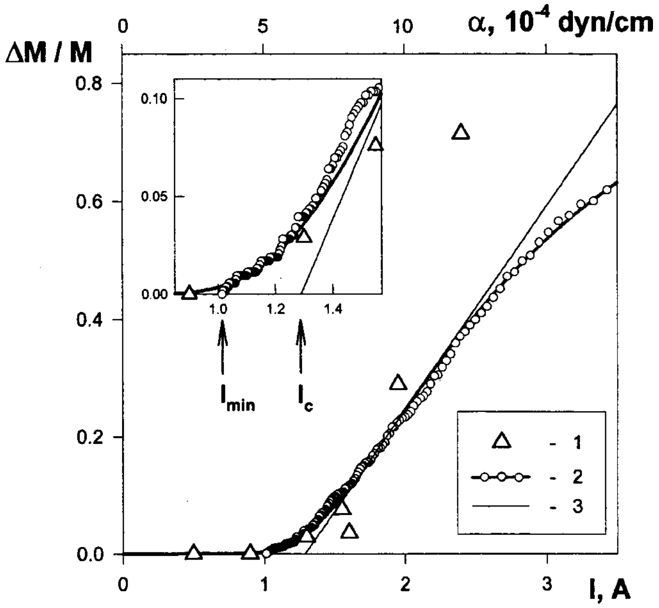

FIG. 3. Statistical distribution of magnetic critical currents. *1* — Variation of the magnetization induced by passing pulsed transport currents; *2* — the fraction of the normal-phase clusters whose pinning strength does not exceed a given Lorentz force; *3* — a tangent to the magnetic critical-current distribution curve. Plotted along the upper axis is the linear pinning-strength density. $I_{\min}$ is the magnetic critical current for the largest normal-phase cluster in the sample, and I_c is the critical current of transition to the resistive state.

properties of a pinning center, including the shape of a normal-phase cluster, and the sample geometry, which determines the transport-current density of the given pinning center. It is assumed also that the β coefficient is the same for all normal-phase clusters.

When a transport current flows through the sample, its magnetization will change by the amount of the magnetic flux depinned only from the normal-phase clusters whose pinning strength is less than or equal to the given Lorentz force. In accordance with this assumption, as the transport current is increased, the first to be freed of the magnetic flux will be clusters with a larger perimeter and, hence, with a larger area. Therefore the relative change in magnetization M can be expressed through the distribution function of normal-phase cluster areas and is equal to the fraction of clusters with the area exceeding a given value: $\Delta M/M = 1 - F(S)$. Because $S = \beta^2/I^2$, we obtain for an exponential distribution (1)

$$\frac{\Delta M}{M} = \exp\left(-\frac{\beta^2}{S_0 I^2} \right) . \tag{2}$$

Thus, by passing transport currents of various amplitude through a sample and measuring the corresponding changes in magnetization, one can not only determine the critical current but also the pinning-strength distribution, which is determined by the statistical properties of normal-phase clusters.

Figure 3 presents the results of an experiment performed by the above scheme. The sample was cooled to the liquid nitrogen temperature. The transport current pulses used in the measurements were 100 ms long. This permitted one to prevent film overheating, which would be unavoidable if a dc current of the same magnitude was passed. Besides, thermomagnetic instability does not develop during such a short transport-current pulse, and the sample remains superconducting with currents as high as the maximum pulse amplitude of 2.5 A. To check a possible influence of thermal effects on the magnetization measurements, calculations of the thermal action of the transport current were carried out, which took into account the contact resistances ($0.1\,\Omega$ at liquid nitrogen temperature) and thermal diffusivity of the film. It was found that, even in the absence of efficient heat removal and for current pulses having maximum amplitude, the sample heating in the near-contact region is negligible and does not affect the trapped flux. An experimental check was also made of the absence of parasitic thermal effects; variation of pulse duration from 50 to 200 ms did not affect noticeably the results of magnetic measurements.

Each of points *1* in Fig. 3 shows the change in magnetization induced by passing a single current pulse. Figure 3 presents also the average linear pinning-strength density $\alpha = (\Phi_0/c)j$ corresponding to the critical current with a density j (Φ_0 is the magnetic flux quantum, and c is the velocity of light). The film cross-sectional area was $4\times10^{-5}\,\mathrm{cm}^2$. The measurements were performed with a Hall sensor having a sensitivity of $30\,\mu\mathrm{V}\cdot\mathrm{G}^{-1}$, the lowest magnetic field measured being 0.02 G. The Hall sensor was placed on the sample surface between the current contacts, at a distance of 7 mm from each of them.

The results of magnetic measurements were fitted by function (2) characterizing the distribution of normal-phase clusters in their magnetic critical currents. The β coefficient played the part of a fitting parameter, whose magnitude, calculated by the least-squares procedure, was found to be $\beta = 0.6434\,\mathrm{A}\cdot\mu\mathrm{m}$. The distribution function of the critical magnetic currents obtained in this way is shown in Fig. 3; each point on curve *2* corresponds to its order statistics in the graph of the empirical distribution function of Fig. 2, and the line connecting them is the function (1) replotted in $(1-F)$ vs $\beta S^{-1/2}$ coordinates. Note that the points of curve *2* are also experimental and reflect the geometric-statistical properties of the film superconducting structure.

As seen from Fig. 3, the geometric approximation (2) fits satisfactorily to the magnetic measurements made in the critical current range up to 2 A. At high currents, a deviation can be noticed, which may originate from a number of reasons. First, as the transport current increases, violations of the geometric similarity in the shape of normal-phase clusters play an ever increasing role. Smaller clusters, which have less weak links along the perimeter, are characterized by a larger pinning strength. The less there are weak links in a cluster, the more important is where exactly on the perimeter they are located, in a ''hollow'' or a ''protruding'' part of an inkspot-shaped cluster. This is the factor that influences the probability of a vortex attaching to this weak spot. Therefore the initial assumption that the β coefficient is the same for all clusters is here no longer valid. Second, the assumption of the weak-link concentration per unit perimeter length being the same for all normal-phase clusters reflects purely statistical relationships and holds well for large clusters, where there are many such links. Deviations due to the violation of the law of large numbers become inevitable as the cluster size decreases. This also results in the form factor β depending, strictly speaking, on cluster size, with this dependence becoming more significant for small-area clusters which have a larger pinning strength. The third reason originates from structural distortions in the superconducting cluster, which inevitably arise when large currents are passed through a film. Each subsequent point of curve *1* in Fig. 3 is obtained on the same sample without its remagnetization. After passing an ever larger current pulse, some regions in the sample may transform to normal state, and then the superconducting infinite cluster becomes less dense. This gives rise to coalescence of some normal-phase clusters of finite size, which will result in an additional decrease of the trapped flux.

Note the complete coincidence of the ''magnetic'' (*1*) with ''geometric'' (*2*) data for currents below 1 A. Transport currents in this region leave the magnetization unchanged, because there are no pinning centers for such low magnetic critical currents. Large clusters are characterized by weak pinning forces. The area of the largest normal-phase cluster in the sampling $S_{\max}=0.4015\,\mu\mathrm{m}^2$, which corresponds to a critical current $I_{\min}=\beta S_{\max}^{-1/2}=1.015\,\mathrm{A}$. It is with this value that the magnetic critical-current curve *2* starts, because the trapped flux is not depinned within the current range from zero to $I_{\min}$.

As seen from Fig. 3, each normal-phase cluster is characterized by its specific magnetic critical current, which contributes to the statistical distribution. One might ask what is the critical current I_c which will drive a sample to the resistive state if passed continuously. The magnitude of I_c can be found most easily from the intercept on the horizontal axis of the tangent (line *3* in Fig. 3) passing through the inflection point of the magnetic critical-current distribution *2*: $I_c=(2/3)^{3/2}\beta S_0^{-1/2}$. This estimate for the sample under study yields $I_c=1.3\,\mathrm{A}$, which agrees well with the experiment.

Thus we have shown that the statistical distribution of magnetic critical currents is due to geometric-morphological properties of the superconducting structure of the material. The technology used to prepare the YBCO films under investigation creates an exponential distribution of normal-phase clusters in area. It appears essential for practical applications that one can draw conclusions from the statistical properties of the geometric structure of a superconducting film regarding the parameters of the statistical critical-current distribution, and to use this information to predict the characteristics of superconducting materials, to monitor their quality, and to optimize their technology. One of the directions pursued in this optimization is the development of superconducting composites with a given pinning-strength distribution, which would provide the largest possible critical current.

Partial support of the ''Integration'' program (Grant 679) is gratefully acknowledged.

[1] M. R. Beasley, in *Percolation, Localization, and Superconductivity*, edited by A. M. Goldman and S. A. Wolf, NATO ASI Series, Ser. B, Vol. 109 (Plenum Press, New York, 1984), p. 115.

[2] R. Zallen and H. Scher, Phys. Rev. B **4**, 4474 (1971).

[3] Yu. I. Kuzmin, A. P. Paugurt, I. V. Pleshakov, and S. V. Rasumov, Supercond. Sci. Technol. **7**, 41 (1994).

[4] S. Senoussi, J. Phys. III **2**, 1041 (1992).

[5] M. J. M. E. de Nivelle, G. J. Gerritsma, and H. Rogalla, Phys. Rev. Lett. **70**, 1525 (1993).

Translated by G. Skrebtsov

PHYSICS OF THE SOLID STATE VOLUME 41, NUMBER 10 OCTOBER 1999

Josephson and quasiparticle currents in tunneling junctions between partially dielectrized (partially gapped) superconductors with spin density waves

A. I. Voĭtenko and A. M. Gabovich

Institute of Physics, Ukrainian Academy of Sciences, 252022 Kiev, Ukraine

(Submitted February 10, 1999)
Fiz. Tverd. Tela (St. Petersburg) **41**, 1743–1749 (October 1999)

The current–voltage characteristics (CVC) are calculated for the Josephson, interference, and quasiparticle components of the current through a tunneling junction formed by two superconductors with spin density waves (SDW). The treatment is based on the model of partial dielectrization (gapping) of the Fermi surface and the assumption of pinning of the spin density waves. The following particular cases are studied in detail: asymmetric SDW superconductor–ordinary superconductor junctions and symmetric junctions between two identical SDW superconductors. The positions and nature of the singularities in the CVC are determined. For a symmetric contact the possibility of the existence of asymmetric CVC's is predicted. The calculations are in qualitative agreement with the experimentally observed behavior of the CVC's of tunneling junctions and microcontacts containing the SDW superconductor with heavy fermions URu_2Si_2. *© 1999 American Institute of Physics.* [S1063-7834(99)00610-3]

It is well known that an external magnetic field or the exchange field of a ferromagnet has a negative effect on spin-singlet superconductivity. First of all, diamagnetic Meissner currents arise, and second, a paramagnetic effect is manifested consisting in an electron spin flip breaking a Cooper pair. The conditions for the coexistence of superconductivity and antiferromagnetism, on the other hand, are much more favorable since the intracrystal magnetic field of an antiferromagnet averaged over a volume having the characteristic dimension of a Cooper pair is equal to zero. Spin density waves (SDW) are related to antiferromagnetism.[1] Spin density waves arise at temperatures T below a critical temperature (the Néel temperature T_N) due to a divergence of the spin susceptibility of the conduction electrons for some wave vector $\mathbf{Q}$. This logarithmic singularity is a consequence of the instability of the system due to the presence on the Fermi surface (FS) of congruent (nested) segments $(i=1,2)$ on which the electron spectrum $\xi(\mathbf{p})$ is degenerate: $\xi_1(\mathbf{p})=-\xi_2(\mathbf{p}+\mathbf{Q})$. On the remainder of the Fermi surface $(i=3)$, the electron spectrum is nondegenerate. In this case, a spin-triplet dielectric gap arises on the nested segments. In this respect, spin density waves are similar to charge density waves (CDW) except that in the case of charge density waves the dielectric gap is a spin-singlet.

The coexistence of superconductivity with spin density waves was observed in the compounds $(TMTSF)_2ClO_4$ and $(TMTSF)_2PF_6$ at a pressure of 6 kbar (Ref. 2), in RRh_2Si_2 $(R=La,Y)$ (Ref. 3), in the alloys $Cr_{1-x}Re_x$ (Ref. 4), in the compound with heavy fermions URu_2Si_2 (Refs. 5 and 6), and in other materials. In these materials the electrons that participate in the Cooper pairing are the ones that are found near the Fermi surface and are responsible for formation of the spin density waves. In fact, a struggle goes on between these two phenomena, and this struggle is expressed as a competition for occupation of the Fermi surface. Usually, the spin density waves are the stronger competitor since they are formed as a result of the exchange interaction between the electrons in contrast to superconductivity, where pairing between electrons occurs through virtual phonons. Therefore, spin density waves are capable, generally speaking, of completely suppressing superconductivity. For this to occur, the dielectric gap would have to encompass the entire Fermi surface. However, the anisotropic character of spin density waves and the specific topology of the Fermi surface lead to the result that only partial dielectrization (gapping) of the Fermi surface is possible, as is observed for all presently known SDW superconductors. In addition, the critical temperature of the superconducting transition T_c, as a rule, is less than T_N. Therefore, when the temperature is lowered below T_c, a superconducting gap Δ is formed on the non-nested, non-dielectrized (nd) (non-gapped) segments of the Fermi surface, which according to the model of strong mixing of electronic states[7] propagates over the entire Fermi surface, including the dielectrized (d) (gapped) regions. In this case, the superconducting gap Δ and the dielectric gap are modified in comparison to the Bardeen–Cooper–Schrieffer (BCS) theory.[8]

In the present work, on the basis of the Bilbro–MacMillan model[7] later applied to spin density waves and charge density waves,[9–12] we investigate tunneling between partially dielectrized (partially gapped) SDW superconductors with s-pairing. We calculate the current–voltage characteristics (CVC's) of the unsteady Josephson current and the quasiparticle tunneling current. Singularities in the CVC's for symmetric and asymmetric junctions are identified and classified. To compare with experiment, we adduce data for a superconductor with heavy fermions, URu_2Si_2, since this is the only compound for which measurements of the parameters repaired by the theory have been made.[5,6]

1. GENERAL THEORY

The initial formulation of the problem is analogous to that considered earlier[13] with substitution of the CDW superconductor by its SDW analog. The model Hamiltonian H of a partially dielectrized (partially gapped) SDW superconductor in the mean-field approximation is equal to[9,10,14]

$$H=H_0+H_{\mathrm{BCS}}+H_{\mathrm{SDW}}, \tag{1}$$

where H_0 is the Hamiltonian of the free electrons, H_{BCS} is the BCS Hamiltonian, which is responsible for the superconductivity, and

$$H_{\mathrm{SDW}}=-2\Sigma\sum_{i=1}^{2}\sum_{\mathbf{p}\alpha}\alpha a_{i\mathbf{p}\alpha}^{+}a_{i,\mathbf{p}+\mathbf{Q},\alpha}+\mathrm{h.c.} \tag{2}$$

is the SDW Hamiltonian, which describes the spin-triplet electron–hole pairing. We again stress that in the given model a single, common superconducting gap exists everywhere on the Fermi surface while dielectrization (gapping) of the Fermi surface (with the corresponding appearance of a dielectric order parameter Σ) takes place only on its nested segments [the summations in expression (2) are only over $i=1,2$].

The inequality $T_N\gg T_c$ holds for all the SDW superconductors considered below. Moreover, calculations show[9] that the presence of a superconducting gap stabilizes the amplitude of Σ at some level analogous to the situation obtaining for CDW superconductors.[7] Proceeding from this fact, we did not carry out self-consistent calculations of the dependences $\Sigma(T)$ and $\Delta(T)$. As was shown in Ref. 13, the quantity Σ can be chosen as a Δ-independent function of T. Moreover, in microcontact measurements it was found that for the SDW superconductor $\mathrm{URu_2Si_2}$ (Refs. 15 and 16) the dependence $\Sigma(T)$ almost completely corresponds to the classical dependence of BCS theory. Therefore, for $\Sigma(T)$ we chose the Mühlschlegel function,[8] which also applies to a spin-triplet exciton insulator with spin density waves.[17] Note that the specific choice that we have made is not important from a conceptual point of view. In what follows, we assume pinning of the spin density waves so that the parameter Σ is a real quantity with arbitrary sign.

Another important parameter of the theory is the degree of dielectrization (gapping) of the Fermi surface, which it is standard to define as the ratio of the density of states on the nd- and d-segments of the Fermi surface (N_{nd} and N_{d}, respectively)

$$\nu=N_{\mathrm{nd}}(0)/N_{\mathrm{d}}(0). \tag{3}$$

For prescribed ν and $\Sigma(T)$ it is easy to calculate the dependence $\Delta(T)$ on the interval $0<T<T_c$ (Refs. 10, 18–20).

The normal $G_{ij}^{\alpha\beta}(\mathbf{p};\omega_n)$ and anomalous $F_{ij}^{\alpha\beta}(\mathbf{p};\omega_n)$ Matsubara Green's functions corresponding to the Hamiltonian (1) can be determined from the Dyson–Gor'kov equations for SDW superconductors, which were obtained earlier.[10–12,19] Taking the matrix structure of the initial superconducting and dielectric order parameters into account, the desired solutions have the form

$$G_{\mathrm{nd}}(\mathbf{p};\omega_n)=-[i\omega_n+\xi_3(\mathbf{p})]\mathrm{Det}_1^{-1}, \tag{4}$$

$$F_{nd}(\mathbf{p};\omega_n)=\Delta\ \mathrm{Det}_1^{-1}, \tag{5}$$

$$G_{\mathrm{d}}(\mathbf{p};\omega_n)=-[i\omega_n+\xi_1(\mathbf{p})][\omega_n^2+\xi_1^2(\mathbf{p})+\Delta^2+\Sigma^2]\mathrm{Det}_2^{-1}, \tag{6}$$

$$F_{\mathrm{d}}(\mathbf{p};\omega_n)=\Delta[\omega_n^2+\xi_1^2(\mathbf{p})+D_+D_-]\mathrm{Det}_2^{-1}, \tag{7}$$

$$G_{\mathrm{is}}(\mathbf{p};\omega_n)=\Sigma[\omega_n^2+\xi_1^2(\mathbf{p})-D_+D_-]\mathrm{Det}_2^{-1}, \tag{8}$$

$$F_{\mathrm{is}}(\mathbf{p};\omega_n)=-2\Delta\Sigma[-i\omega_n+\xi_1(\mathbf{p})]\mathrm{Det}_2^{-1}. \tag{9}$$

Here

$$\mathrm{Det}_1=\omega_n^2+\xi_3^2(\mathbf{p})+\Delta^2, \tag{10}$$

$$\mathrm{Det}_2=[\omega_n^2+\xi_1^2(\mathbf{p})+D_+^2][\omega_n^2+\xi_1^2(\mathbf{p})+D_-^2], \tag{11}$$

$$D_\pm=\Delta\pm\Sigma, \tag{12}$$

and the subscript ''is'' corresponds to intersectional ($1\leftrightarrow 2$) electron–hole pairing.

The tunneling current I is calculated using the method of the tunneling Hamiltonian.[21,22] The matrix elements of the tunneling Hamiltonian are assumed to be equal and independent of Δ and Σ. This assumption is natural within the framework of a scheme of BCS type, i.e., in a treatment of Cooper and electron–hole pairing in the weak-binding approximation (see the discussion in Ref. 13). Thus, it is possible to introduce a universal tunneling resistance parameter R. We assume that the voltage on the tunneling contact $V(\tau)$, where τ is time, varies adiabatically in comparison with energies of order T_c, i.e., $V^{-1}dV/d\tau\ll T_c$. Taking this into account, the expression for the current I in terms of the tunneling contact takes the form

$$I[V(\tau)]=\sum_{i,i'=\mathrm{d,nd,is}}[I_{(i,i')}^{1}(V)\sin 2\varphi+I_{(i,i')}^{2}(V)\cos 2\varphi+J_{(i,i')}(V)], \tag{13}$$

where $\varphi=\int^{\tau}eV(\tau)d\tau$, e is the elementary charge, $I^1(V)=\Sigma_{i,i'}I_{(i,i')}^{1}(V)$ is the amplitude of the Josephson current, $I_2(V)=\Sigma_{i,i'}I_{(i,i')}^{2}(V)$ is the amplitude of the interference current, and $J(V)=\Sigma_{i,i'}J_{(i,i')}(V)$ is the quasiparticle current. This equation is a generalization of the corresponding expression obtained for a junction between BCS superconductors[21] to the case of SDW superconductors. Each quantity of the type $I_{(i,i')}^{1}(V)$ in Eq. (13) is an integral of some expression including a pairwise product of Fourier transforms of temporal Green's functions $F_i^{+}(\omega)F_{i'}(\omega')$ or $G_i(\omega)G_{i'}(\omega')$ for the left and right electrodes, where the right-electrode quantities are indicated by primed indices. The required temporal Green's functions were obtained from the corresponding temperature functions (4)–(9) by a standard technique.[9] To calculate $I_{(i,i')}^{1,2}(V)$ only the anomalous Green's functions are needed, and to calculate $J_{(i,i')}(V)$ only the normal Green's functions are needed. Explicit expressions for the amplitudes are not given due to their cumbersomeness.

It is important for what follows that the nine terms of each amplitude can be divided into two groups differing in their symmetry properties with respect to variation of the polarity V, specifically terms related in the usual way

$$I^{1,2}_{(i,i')}(-V)=\pm I^{1,2}_{(i,i')}(V),\quad J_{(i,i')}(-V)=-J_{(i,i')}(V),\tag{14}$$

where the upper and lower signs pertain to the Josephson and interference currents, respectively, and terms related in the opposite way

$$I^{1,2}_{(i,i')}(-V)=\mp I^{1,2}_{(i,i')}(V),\quad J_{(i,i')}(-V)=J_{(i,i')}(V).\tag{15}$$

This ''nonstandard'' behavior of the latter group follows from the fact that the expressions for calculating them contain products of ''intersectional'' Green's functions of one electrode, obtained from Eqs. (8) and (9), and Green's functions for the second electrode, obtained from Eqs. (4) and (5), i.e., the combinations (d, is), (nd, is), (is, d), and (is, nd). Thus, the CVC's of all three currents through an asymmetric tunneling junction formed by different SDW superconductors turn out to be sensitive to the polarity of the applied voltage in contrast to the well-known independence on this polarity of the CVC's of asymmetric contacts consisting of different BCS superconductors.[22]

2. CURRENT–VOLTAGE CHARACTERISTICS

The expressions for the currents can be simplified in two cases: for an asymmetric junction, where one of the electrodes is a BCS superconductor or a normal metal, and where the junction is formed by two identical SDW superconductors.

If one of the electrodes is a BCS superconductor (an ns-contact), then only Green's functions (4) and (5) are characteristic for it. Correspondingly, only three terms remain in the sum (13) for each current

$$I_{\mathrm{ns}}=\sum_{i=\mathrm{d,nd,is}}\left[I^{1}_{(i,\mathrm{nd})}(V)\sin 2\varphi+I^{2}_{(i,\mathrm{nd})}(V)\cos 2\varphi+J_{(i,\mathrm{nd})}(V)\right].\tag{16}$$

For the (d, nd) and (nd, nd) terms of each component symmetry relations (14) are satisfied, and for the (is, nd) terms, equalities (15). Thus, the CVC's of all three currents through an asymmetric tunneling contact formed by a SDW superconductor and an ordinary superconductor (or a normal metal), turn out to be asymmetric and sensitive to the polarity of the applied voltage.

Table I lists the characteristics of the singularities of the CVC's of each current component for an ns-contact. Type 1 corresponds to a logarithmic singularity proportional to $Y_+(eV,D_1,D_2)$ for the Josephson component and to jumps proportional to $Z_+(D_1,D_2)$ for the interference and quasiparticle components. Type 2 corresponds to a jump proportional to $Z_-(D_1,D_2)$ for a Josephson component and to logarithmic singularities proportional to $Y_-(eV,D_1,D_2)$ for the interference and quasiparticle components. Here

$$Z_\pm(D_1,D_2)=\sqrt{|D_1D_2|}\left|\tanh\frac{|D_1|}{2T}\pm\tanh\frac{|D_2|}{2T}\right|,\tag{17}$$

$$Y_\pm(eV,D_1,D_2)=Z_\pm(D_1,D_2)\ln\left|\left|\frac{eV}{|D_1|\pm|D_2|}\right|-1\right|.\tag{18}$$

Specific values of the quantities D_1 and D_2 are also listed in Table I.

TABLE I. Positions and characteristics of singularities of the CVC's of terms of the currents through an asymmetric tunneling junction between a SDW semiconductor and a BCS semiconductor.

Singularity	Type (see text)	Temperature region	Components	D_1	D_2
$K_\pm=\lvert D_\pm\rvert+\Delta_{\mathrm{BCS}}$	1	$T\geqslant 0$	(d,nd), (is,nd)	$D_\pm$	Δ_{BCS}
$K=\Delta+\Delta_{\mathrm{BCS}}$	1	$T\geqslant 0$	(nd,nd)	Δ	Δ_{BCS}
$L_\pm=\lvert\lvert D_\pm\rvert-\Delta_{\mathrm{BCS}}\rvert$	2	$T\neq 0$	(d,nd), (is,nd)	$D_\pm$	Δ_{BCS}
$L=\lvert\Delta-\Delta_{\mathrm{BCS}}\rvert$	2	$T\neq 0$	(nd,nd)	Δ	Δ_{BCS}

Figure 1 plots the V dependence of the dimensionless Josephson current $i^1_{\mathrm{ns}}=I^1_{\mathrm{ns}}eR/\Delta_0$ and the differential conductivity $g^{\mathrm{diff}}_{\mathrm{ns}}=RdJ_{\mathrm{ns}}/dV$, calculated for an ns-junction. Here Δ_0 is the value of the superconducting order parameter for zero temperature in the absence of dielectrization (gapping) $(\nu\to\infty)$. The graphs also show curves calculated for $T=0$. This was done in order to avoid cluttering up Fig. 1b with divergences generated by products of logarithmic singularities of type 2 showing up at finite temperatures. Note that in a real experiment logarithmic singularities of this type should be strongly smoothed out for various reasons, e.g., inhomogeneities of the order parameters over the cross section of the tunneling junction.[23]

The case of a Josephson junction consisting of two identical SDW superconductors ($\nu=\nu'$, $\Delta=\Delta'$, $\Sigma=\pm\Sigma'$) turns out to be much more interesting. In analogy with CDW superconductors,[24] we should consider separately the cases where the dielectric order parameters on the two sides of the junction are identical and where they have different signs. Such a difference exists due to the fact that, in both electrodes under conditions of pinning of the spin density waves (which we have assumed to be the case), states of a SDW superconductor are possible differing only in the sign of Σ, which are thermodynamically identical.

In the case where $\Sigma=\Sigma'$ (s-junction), those terms of each amplitude pairwise compensate which exhibit ''nonstandard'' symmetry properties (15), specifically (d, is) with (is, d) and (nd, is) with (is, nd). The remaining terms as a result form currents obeying Eqs. (14). Figure 2 plots the V dependence of the dimensionless Josephson current $i^1_{\mathrm{s}}=I^1_{\mathrm{s}}eR/\Delta_0$ and the differential conductivity $g^{\mathrm{diff}}_{\mathrm{s}}=RdJ_{\mathrm{s}}/dV$, calculated for an s-junction.

For $\Sigma=-\Sigma'$ (bs-junction) such compensation does not occur. On the contrary, these currents mutually add, and to such an extent that for a certain polarity of the voltage on the junction the singularities of the ''nonstandard'' terms compensate the singularities of the other terms, as a result of

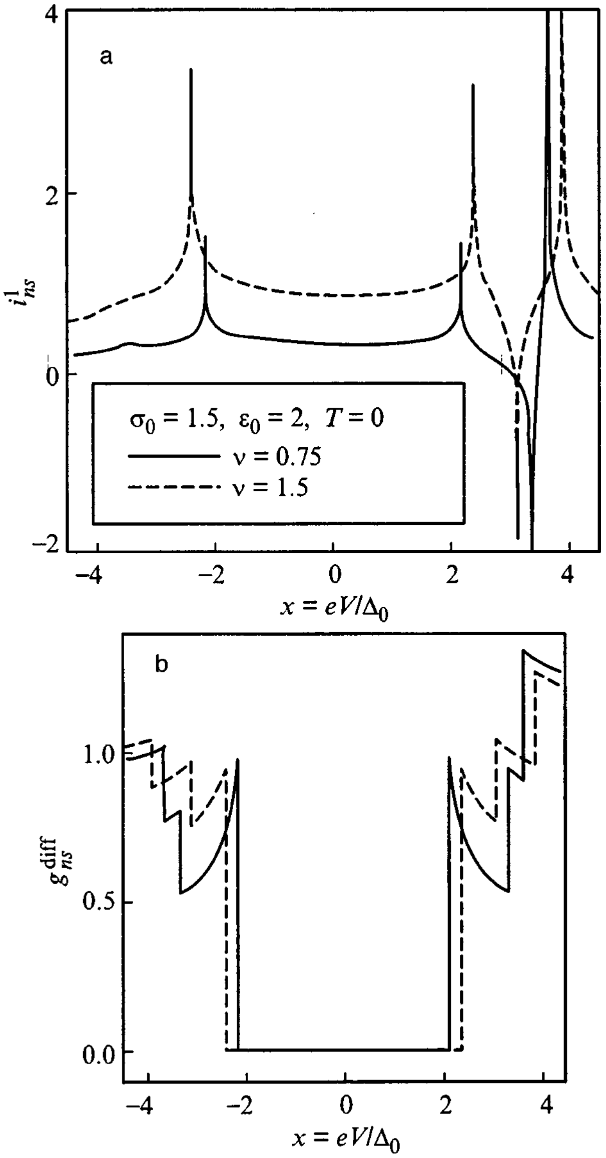

FIG. 1. Dependence of dimensionless Josephson currents $i^1_{\text{ns}} = I^1_{\text{ns}} eR/\Delta_0$ (a) and dimensionless conductivities $g^{\text{diff}}_{\text{ns}} = RdJ_{\text{ns}}/dV$ for quasiparticle currents J_{ns} (b) on the dimensionless voltage $x = eV/\Delta_0$ on an asymmetric tunneling junction of the type SDW superconductor–BCS superconductor for different values of the degree of dielectrization (gapping) of the electronic spectrum $\nu = N_{\text{nd}}(0)/N_{\text{d}}(0)$. Here e is the elementary charge, R is the resistance of the junction in the normal state, Δ_0 is the superconducting gap of the SDW superconductor at $T = 0$ in the absence of dielectrization (gapping), σ_0 is the value of $\sigma = \Sigma/\Delta_0$ at $T = 0$, $\Sigma(T)$ is the dielectric order parameter, $N_{\text{nd(d)}}(0)$ is the density of electron states on non-dielectrized (dielectrized) segments of the Fermi surface, $\varepsilon_0 = \Delta_{\text{BCS}}(T = 0)/\Delta_0$, and Δ_{BCS} is the superconducting gap of the BCS superconductor.

which the total CVC of each of the currents has a pronounced asymmetric character (Fig. 3). Such a phenomenon is a new type of symmetry breaking in a many-particle system, manifested only when the corresponding junction is included in the electrical circuit.

For simultaneous variation of the signs of Σ on both sides of the bs-junction, the corresponding CVC switches its branches corresponding to different polarity of the bias voltage. Thus, for a tunneling junction between SDW superconductors considered initially as identical, e.g., a break junction, in principle it is possible to observe three different CVC's. A number of associated circumstances can be imagined (inhomogeneities in the impurity distribution, external conditions, the temperature prehistory, etc.) favoring one or the other state. These circumstances operate directly below the Néel point. For $T \ll T_N$ switches between different branches of the CVC caused by thermal fluctuations become impossible since this would require a large energy to restructure the spin density waves. However, increasing the voltage on the junction could stimulate such a switch. On the other hand, heating the junction above T_N with subsequent cooling could lead to a CVC different from the original one if the states in question are energetically degenerate. It is significant that a change in the state of the spin density waves will

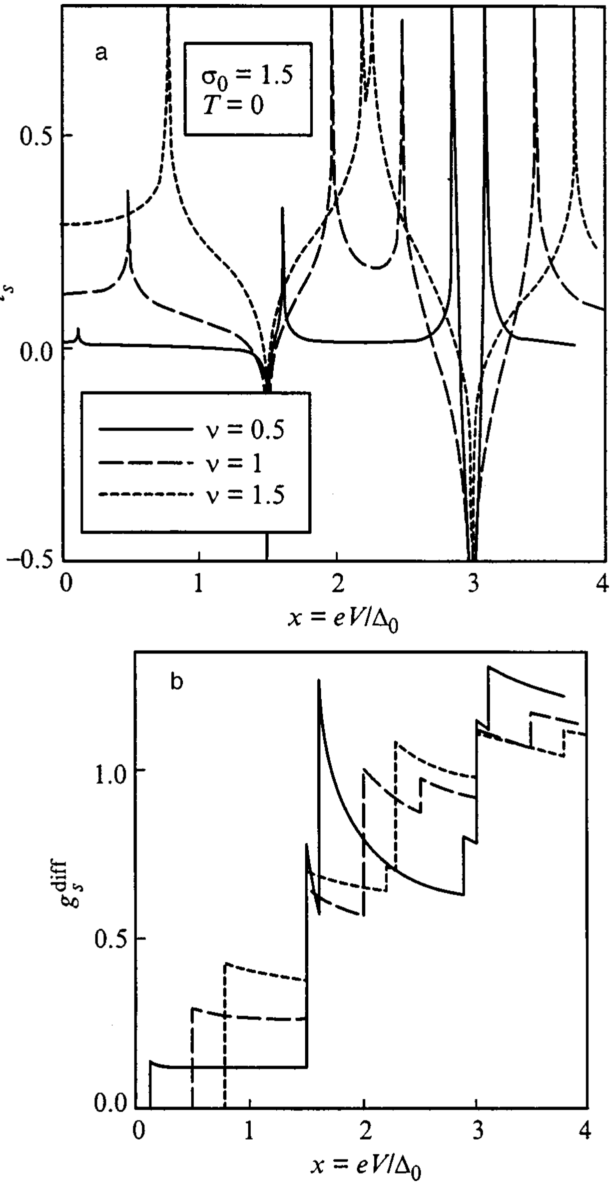

FIG. 2. Dependence of the dimensionless Josephson currents $i^1_{\text{s}}(x) = I^1_{\text{s}}(V)eR/\Delta_0$ (a) and the dimensionless conductivities $g^{\text{diff}}_{\text{s}}(x) = RdJ_{\text{s}}/dV$ for quasiparticle currents J_{s} (b) in the case of a purely symmetric tunneling junction between a SDW superconductors for different values of ν.

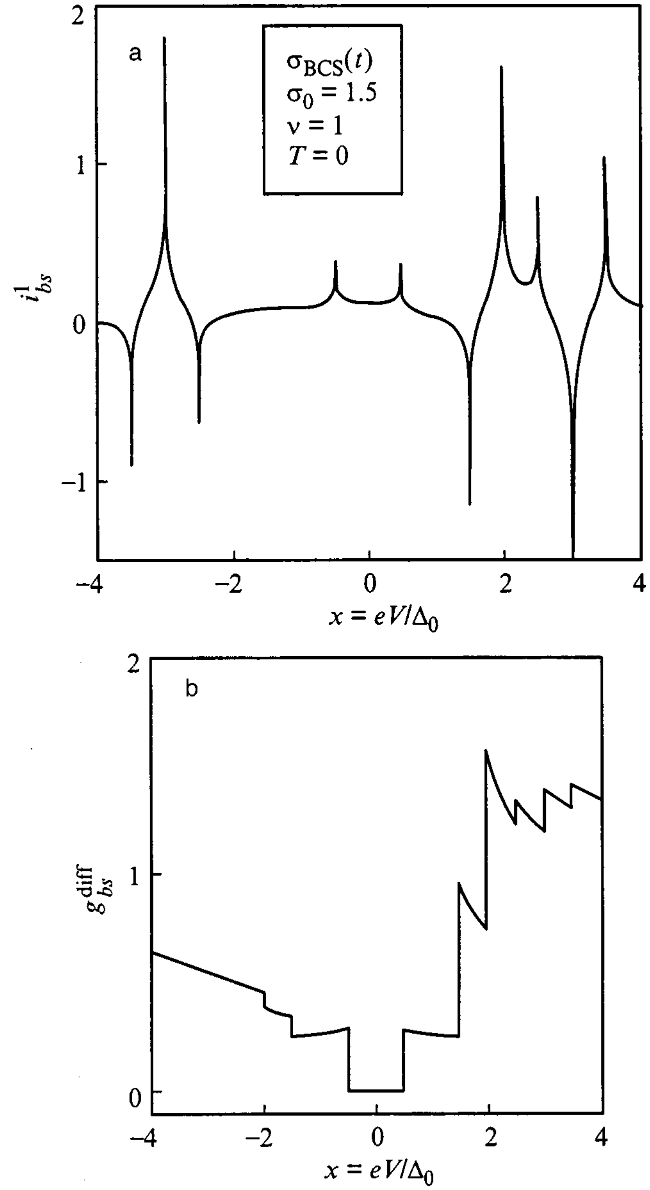

FIG. 3. Dependence of the dimensionless Josephson current $i^1_{\mathrm{bs}}(x) = I^1_{\mathrm{bs}}(V)eR/\Delta_0$ (a) and the dimensionless conductivity $g^{\mathrm{diff}}_{\mathrm{bs}}(x) = RdJ_{\mathrm{bs}}/dV$ for the quasiparticle current J_{bs} (b) in the case of a symmetric tunneling junction with broken symmetry between SDW superconductors for $\nu = 1$.

have an effect on the superconducting currents which appear only upon further cooling below $T_c \ll T_N$.

Table II lists the characteristics of the singularities of the various current components for s- and bs-junctions. As can be seen from the table, by virtue of the fact that the parameters $D_\pm$ depend linearly on Δ and Σ [see Eq. (12)], for tunneling junctions between identical SDW superconductors, alongside compensation of some singularities the superposition of singularities of the CVC's of different types (jumps and logarithmic singularities) is also possible, which does not happen in the case of CDW superconductors.[13,24]

3. DISCUSSION

Unfortunately, the amount of experimental data on SDW superconductors is negligible. Nevertheless, the available data are in satisfactory agreement with our theory. For example, the CVC's for UNi_2Al_3 break junctions (i.e., symmetric junctions in their very essence!) can be asymmetrical.[25] However, for a quantitative comparison of the theoretically obtained dependences to the experimental data, it is necessary to know the values of the dielectric and superconducting gaps, and also the dielectrization (gapping) parameter of the Fermi surface ν.

The most widely studied SDW superconductor of interest to us is URu_2Si_2. According to various sources,[5,6,26] its temperature characteristics are $T_c \approx 1.3 - 1.5\,\mathrm{K}$ and $T_N \approx 17 - 17.5\,\mathrm{K}$. As for the parameters Σ and ν, here there is a significant spread. For example, according to specific heat measurements the values of the desired parameters are $\Sigma \approx 115\,\mathrm{K}$ and $\nu \approx 0.4$ according to Ref. 5, and $\Sigma \approx 129\,\mathrm{K}$ and $\nu \approx 1.5$ according to Ref. 6. Other studies of the thermal properties[26] also give the value $\Sigma \approx 115\,\mathrm{K}$.

Tunneling and microcontact measurements of the conductivity of symmetric and asymmetric junctions containing URu_2Si_2 were conducted relatively recently.[15,16] The resulting CVC's distinctly manifest gaplike singularities disappearing at temperatures above T_N, which confirms the presence of partial dielectrization (gapping) of the Fermi surface associated with spin density waves. A gaplike singularity is also observed below T_c, associated with T_c by the BCS relation. It should be noted that direct tunneling and micro-

TABLE II. Positions and characteristics of singularities of the CVC's of components of the currents through a symmetric tunneling junction and an asymmetric tunneling junction with broken symmetry between SDW semiconductors.

Singularity	Value for $\Delta < \Sigma$	Type	Temperature region	Components*)	D_1	D_2
2Δ	2Δ	1	$T \geqslant 0$	(nd,nd)	Δ	Δ_{BCS}
$2\lvert D_\pm \rvert$	$2(\Sigma \pm \Delta)$	1	$T \geqslant 0$	(d,d), (is,is),(d,is), (is,d)	$D_\pm$	$D_\pm$
$H_+ = \lvert\lvert D_+ \rvert + \lvert D_- \rvert\rvert$	2Σ	1	$T \neq 0$	(d,nd), (is,nd)	D_+	D_-
$K_\pm = \lvert D_\pm \rvert + \Delta_{\mathrm{BCS}}$	2Δ	2	$T \neq 0$	(d,d), (is,is) ,(d,is), (is,d)	D_+	D_-
$M_+ = \lvert D_+ \rvert + \Delta$	$2\Delta + \Sigma$	1	$T \geqslant 0$	(d,nd), (nd,d) ,(is,nd), (nd,is)	D_+	Δ
$K_\pm = \lvert D_\pm \rvert + \Delta_{\mathrm{BCS}}$	Σ	1	$T \geqslant 0$	(d,nd), (nd,d) ,(is,nd), (nd,is)	D_-	Δ
$K_\pm = \lvert D_\pm \rvert + \Delta_{\mathrm{BCS}}$	Σ	2	$T \neq 0$	(d,nd), (is,nd)	D_+	Δ
$L = \lvert\lvert \Delta - \Delta_{\mathrm{BCS}} \rvert$	$\lvert 2\Delta - \Sigma \rvert$	2	$T \neq 0$	(nd,nd)	D_-	Δ

*)The (d,is), (is,d), (nd,is), and (is,nd) components of all currents appear only for broken symmetry in the junction.

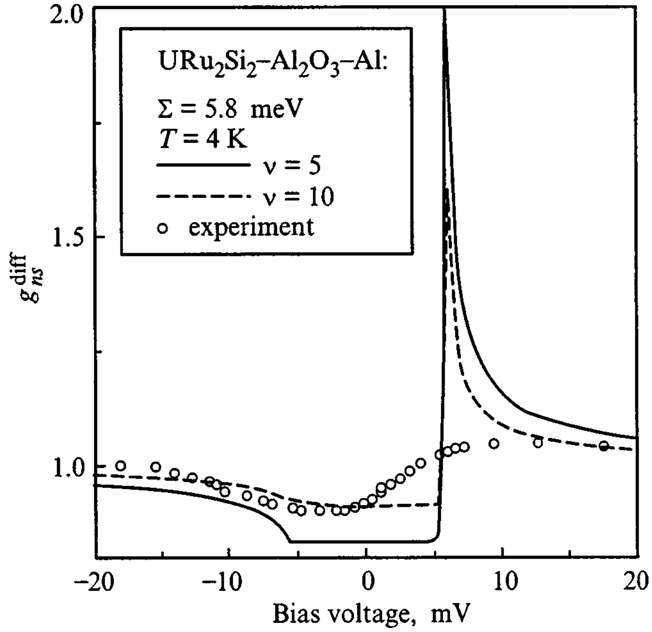

FIG. 4. Dependence of $g_{\rm ns}^{\rm diff}(V)$ for a $\mathrm{URu_2Si_2-Al_2O_3-Al}$ asymmetric tunneling junction in the normal state, obtained from experiment and calculated for different values of ν.

contact measurements of the dielectric gap[15] give the value $\Sigma \approx 68\,\mathrm{K}$, which differs dramatically from the values given above. At the same time, these measurements can be considered as a direct proof of partial dielectrization (gapping) of the electronic spectrum in $\mathrm{URu_2Si_2}$.

Symmetry breaking in the CVC's of symmetric junctions similarly was also already manifested in point homojunctions with $\mathrm{URu_2Si_2}$ (Ref. 16). Specifically, CVC's were sporadically observed having a characteristic asymmetric distortion at which singularities in dV/dJ associated with Σ were more sharply pronounced for one polarity of the voltage V than for the other. This agrees with the above theoretical arguments.

As for a direct experimental confirmation of the conclusions of our theory, unfortunately the overwhelming majority of the available data was obtained by the microcontact method, so that a comparison with theory is possible only for the observed positions of the CVC singularities and not for their profiles. There is one study[15] which reports tunneling measurements of the conductivity $G^{\rm diff}(V) = dJ/dV$ of the asymmetric junction $\mathrm{URu_2Si_2-Al_2O_3-Al}$. However, the CVC presented in this paper was obtained at $T = 4$ K, which lies significantly above the critical temperatures both for $\mathrm{URu_2Si_2}$ (see above) and for Al (≈ 1.19 K). Thus, both electrodes were in the normal state. Figure 4 compares the corresponding dependence with our calculations. Qualitatively, the overall dependence of the experimental curve is reproduced. The smoothing of the singularities can be related to procedural averaging of the data, which cannot be avoided in experiments of this type. Note that fitting of the theoretical results would require much larger values of the parameter ν than those obtained in the thermal measurements.[5,6,26]

This work was carried out with the partial support of the State Fund for Fundamental Research of Ukraine (Grant No. 2.4/100).

[1] G. Grüner, Rev. Mod. Phys. **66**, 1 (1994).

[2] J. Friedel and D. Jerome, Contemp. Phys. **23**, 583 (1982).

[3] I. Felner and I. Nowik, Solid State Commun. **47**, 831 (1983).

[4] E. Fawcett, H. L. Alberts, V. Yu. Galkin, D. R. Noakes, and J. V. Yakhmi, Rev. Mod. Phys. **66**, 25 (1994).

[5] T. T. M. Palstra, A. A. Menovsky, J. van der Berg, A. I. Dirkmaat, P. H. Kes, G. J. Niewenhuys, and J. A. Mydosh, Phys. Rev. Lett. **55**, 2727 (1985).

[6] M. B. Maple, J. W. Chen, Y. Dalichaouch, T. Kohara, C. Rossel, M. S. Torikachvili, M. W. McElfresh, and J. D. Thompson, Phys. Rev. Lett. **56**, 185 (1986).

[7] G. Bilbro and W. L. McMillan, Phys. Rev. B **14**, 1887 (1976).

[8] A. A. Abrikosov, L. P. Gor'kov, and I. E. Dzyaloshinskiĭ, *Methods of Quantum Field Theory in Statistical Physics* (Prentice-Hall, Englewood Cliffs, N.J., 1963).

[9] K. Machida, J. Phys. Soc. Jpn. **50**, 2195 (1981); **51**, 1420 (1982); **52**, 1333 (1983).

[10] A. M. Gabovich and A. S. Shpigel', Fiz. Tverd. Tela (Leningrad) **26**, 1569 (1984) [Sov. Phys. Solid State **26**, 956 (1984)]; J. Phys. F **14**, 1031 (1984).

[11] A. M. Gabovich and A. S. Shpigel', Fiz. Tverd. Tela (Leningrad) **24**, 1006 (1982) [Sov. Phys. Solid State **24**, 571 (1982)]; Zh. Éksp. Teor. Fiz. **84**, 694 (1983) [Sov. Phys. JETP **57**, 400 (1983)].

[12] A. M. Gabovich and A. S. Shpigel', Metallofizika (Kiev) **8**(5), 12 (1986); Phys. Rev. B **38**, 297 (1988).

[13] A. I. Voĭtenko and A. M. Gabovich, Fiz. Tverd. Tela (St. Petersburg) **39**, 991 (1997) [Phys. Solid State **39**, 889 (1997)]; A. M. Gabovich and A. I. Voitenko, Phys. Rev. B **55**, 1081 (1997).

[14] A. M. Gabovich and A. I. Voitenko, Phys. Rev. B **52**, 7437 (1995); A. I. Voĭtenko, A. M. Gabovich, Fiz. Tverd. Tela (St. Petersburg) **38**, 1107 (1996) [Phys. Solid State **38**, 613 (1996)].

[15] R. Escudero, F. Morales, and P. Lejay, Phys. Rev. B **49**, 15 271 (1994).

[16] Yu. G. Naĭdyuk, O. E. Kvitnitskaya, A. Novak, I. K. Yanson, and A. A. Menovski, Fiz. Nizk. Temp. **21**, 310 (1995) [Low Temp. Phys. **21**, 236 (1995)].

[17] N. I. Kulikov and V. V. Tugushev, Usp. Fiz. Nauk **144**, 643 (1984) [Sov. Phys. Usp. **27**, 954 (1984)].

[18] A. M. Gabovich, A. S. Gerber, and A. S. Shpigel, Phys. Status Solidi B **141**, 575 (1987).

[19] A. M. Gabovich, D. P. Moiseev, A. S. Shpigel, and A. I. Voitenko, Phys. Status Solidi B **161**, 293 (1990).

[20] A. I. Voĭtenko, A. M. Gabovich, and A. S. Shpigel', Fiz. Nizk. Temp. **18**, 108 (1992) [Sov. J. Low Temp. Phys. **18**, 75 (1992)].

[21] A. I. Larkin and Yu. N. Ovchinnikov, Zh. Éksp. Teor. Fiz. **51**, 1535 (1966) [Sov. Phys. JETP **24**, 1035 (1966)].

[22] A. Barone and G. Paterno, *Physics and Applications of the Josephson Effect* (Wiley, New York, 1982).

[23] B. Barbiellini, Ø. Fischer, M. Peter, Ch. Renner, and M. Weger, Physica C **220**(1/2), 55 (1994); G. T. Jeong, J. I. Kye, S. H. Chun, S. Lee, S. I. Lee, and Z. G. Khim, Phys. Rev. B **49**, 15 416 (1994).

[24] A. M. Gabovich and A. I. Voitenko, J. Phys.: Condens. Matter **9**, 3901 (1997); Europhys. Lett. **38**, 371 (1997).

[25] K. Gloos, F. B. Anders, B. Buschinger, and C. Geibel, Physica B **230–232**, 391 (1997).

[26] S. A. M. Mentink, U. Wyder, J. A. A. J. Perenboom, A. de Visser, A. A. Menovsky, G. J. Nieuwenhuys, J. A. Mydosh, and T. E. Mason, Physica B **230–232**, 74 (1997).

Translated by Paul F. Schippnick

PHYSICS OF THE SOLID STATE VOLUME 41, NUMBER 10 OCTOBER 1999

SEMICONDUCTORS. DIELECTRICS

Trends in the kinetic and magnetic properties of $Pb_{0.8}Sn_{0.2}Te$ single crystals of high structural perfection

M. V. Radchenko, G. V. Lashkarev, E. I. Slyn'ko, and A. P. Malysheva

Institute for Problems of Materials Science, Ukrainian Academy of Sciences, 252680 Kiev, Ukraine

(Submitted July 29, 1998; accepted for publication January 10, 1999)
Fiz. Tverd. Tela (St. Petersburg) **41**, 1750–1752 (October 1999)

In the temperature interval 4.2–300 K and magnetic fields up to 4 T, we have investigated the electrical, thermal-electrical, thermal-magnetic, and magnetic properties of single crystals of the solid solution $Pb_{0.8}Sn_{0.2}Te$. It is shown that an enhancement of its level of structural perfection leads to the appearance of a second structural phase transition (SPT), and also to an increase in the temperature of the first structural phase transition. © *1999 American Institute of Physics.* [S1063-7834(99)00710-8]

Solid solutions of lead telluride and tin telluride are of considerable interest for infrared optoelectronics applications. The efficiency of devices based on these compounds depends to a significant degree on their chemical homogeneity and degree of structural perfection. The latter is a function of the dislocation density, the number of large-angle boundaries, etc.

It is well known that, in the narrow-band semiconductors $Pb_{1-x}Sn_xTe$ in the composition and temperature intervals $0.2 \leqslant x \leqslant 1.0$ and $4.2 < T < 300$ K, an instability of the crystal lattice is observed which leads to a second-order ferroelectric structural phase transition (SPT) from the cubic (O_h) to the rhombohedral (C_{3v}) phase.[1,2] Using x-ray analysis, the authors of Ref. 3 detected the existence of three structural phase transitions, in two of which the crystal lattice undergoes a change of symmetry. Free current carriers and structural defects of the crystal lattice have a substantial effect on the phase transition. The strong scattering of the current carriers during the structural phase transition[4] is caused by local fluctuations of the polarization associated with the presence of inhomogeneities and with fluctuations of the order parameter at the critical point.

The present paper reports results of a study of the Hall coefficient R, the resistivity, thermal voltage α, and magnetic susceptibility (MS) χ in the temperature interval 4.2–300 K and Shubnikov oscillations of α in magnetic fields H down to 4 K.

The Hall coefficient, the resistivity, and the thermal emf were varied by the compensation method at constant current. The temperature of the sample and its gradient (~ 2 K/cm) were measured using a copper–gold (iron doped) thermocouple. In the liquid-helium and liquid-hydrogen temperature range we recorded the absolute thermal voltage of copper. The magnetic susceptibility was measured using the relative Faraday method with the help of an electronic microbalance with automatic compensation.[5]

Single crystals of $Pb_{0.8}Sn_{0.2}Te$, 40 mm in diameter, were prepared from the vapor phase. In their synthesis we used tin of purity 99.9999% and tellurium of purity 99.999999%. To lower the concentration of current carriers, the samples were isothermally annealed in vapors containing an excess of metal. The samples were cut along the (100) plane. Removal of the surface layer of the sample, damaged by mechanical polishing, was accomplished by electrochemical polishing and chemical processing in a mixture of Br and HBr.

Studies of the structure of the $Pb_{0.8}Sn_{0.2}Te$ crystals showed that the dislocation density did not exceed $2 \times 10^4\ \mathrm{cm}^{-2}$, and that small-angle boundaries were absent. The homogeneity of the samples was monitored by measuring the thermal emf in a magnetic field by the technique described in Ref. 6. All of the samples had hole-type conductivity.

Figure 1 plots the temperature dependence of the thermal emf on one of the samples with Hall hole concentration $p = 2.12 \times 10^{17}\ \mathrm{cm}^{-3}$ and mobility $\mu = 5.2 \times 10^5\ \mathrm{cm}^2/\mathrm{V \cdot s}$. The same figure plots the dependence $\alpha(T)$ of a PbTe sample ($p = 3 \times 10^{18}\ \mathrm{cm}^{-3}$), in which, as is well known,[1] there are no structural phase transitions. In the temperature interval $6 < T < 35$ K the thermal emf of the $Pb_{0.8}Sn_{0.2}Te$ crystals is linear and reveals a salient point at $T_{c1} = 35$ K. The dependence $\alpha(T)$ for $\mu H/c \gg 1$ (α_∞) also has a salient point at the same temperature as α_0. This fact indicates that processes of current-carrier scattering participate in the formation of this salient point. We observed this feature in α earlier at $T = 20$ K for crystals having a similar concentration of current carriers undergoing a structural phase transition.[2,7,8]

At $T_{c2} = 115$ K we detected a singularity in the dependence which we associate with the second structural phase transition, where the thermal emf describes a hysteresis loop of small area in the temperature range $T_{c1} < T < T_{c2}$, which, in our opinion, confirms the structural instability of the crystal in this temperature range. This is the first observation of a hysteresis loop in the thermal emf associated with a structural phase transition of shift type to our knowledge. The

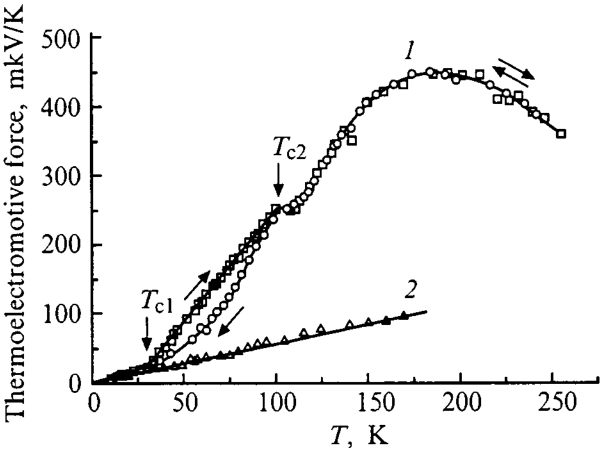

FIG. 1. Temperature dependence of the thermal emf of sample 3 (*1*) and PbTe (*2*).

presence of a maximum in $\alpha(T)$ at $T \approx 180\,\mathrm{K}$ with subsequent decrease of α with increasing temperature is associated with the onset of intrinsic conductivity.

Note that a break in the linear dependence of $\alpha(T)$ is observed at T_{c1}, where the electron gas is found in the degenerate state, while the singularity in $\alpha(T)$ at T_{c2}, where the degeneracy is removed, has the character of an inflection point. We already noticed such trends in previous studies, for $Pb_{0.8}Sn_{0.2}Te$ samples[2] and $Pb_{0.94}Ge_{0.06}Te$ samples,[8] which is an additional indication that we have indeed observed a structural phase transition here.

The temperature of the first structural phase transition in $Pb_{0.8}Sn_{0.2}Te$ samples prepared from the vapor phase is substantially higher than in the case of crystals grown by the Bridgman method ($\sim 25\,\mathrm{K}$). This is in line with the data of Ref. 9, which show that crystal defects lower the phase transition temperature.

Measurements of the Hall coefficient in the investigated samples showed that R is essentially independent of the temperature and has no singularities associated with structural phase transitions since the hole concentration is small and the Fermi level in the temperature interval 4.2–120 K is found in the light-hole band and does not penetrate into the heavy-hole band,[10] as a result of which the light-hole concentration in these samples does not vary at the phase transition.

Earlier, for $Pb_{0.18}Sn_{0.82}Te$ and $Pb_{1-x}Sn_xTe$ we showed[2,7,8] that at a structural phase transition the magnetic

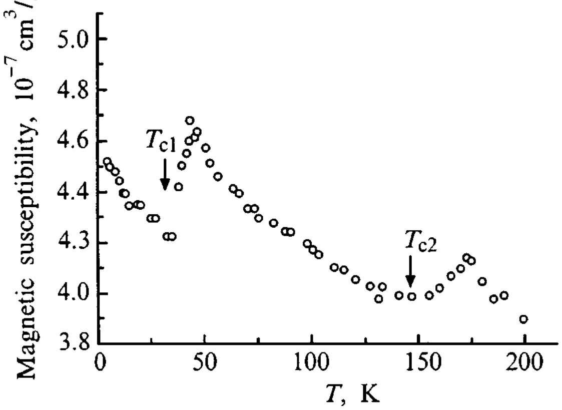

FIG. 2. Temperature dependence of the magnetic susceptibility (sample 3).

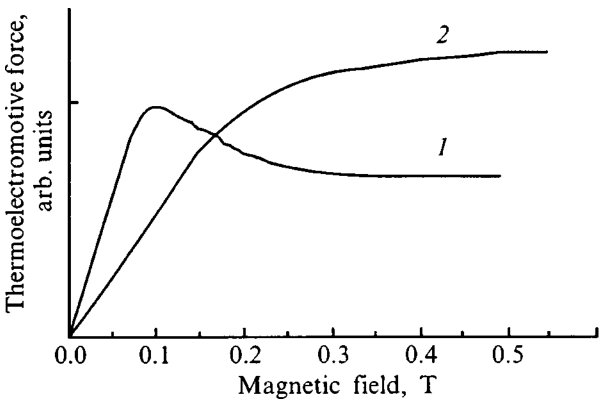

FIG. 3. Dependence of the thermal emf in a longitudinal (*1*) and a transverse (*2*) magnetic field at $T = 5.1$ K (sample 3).

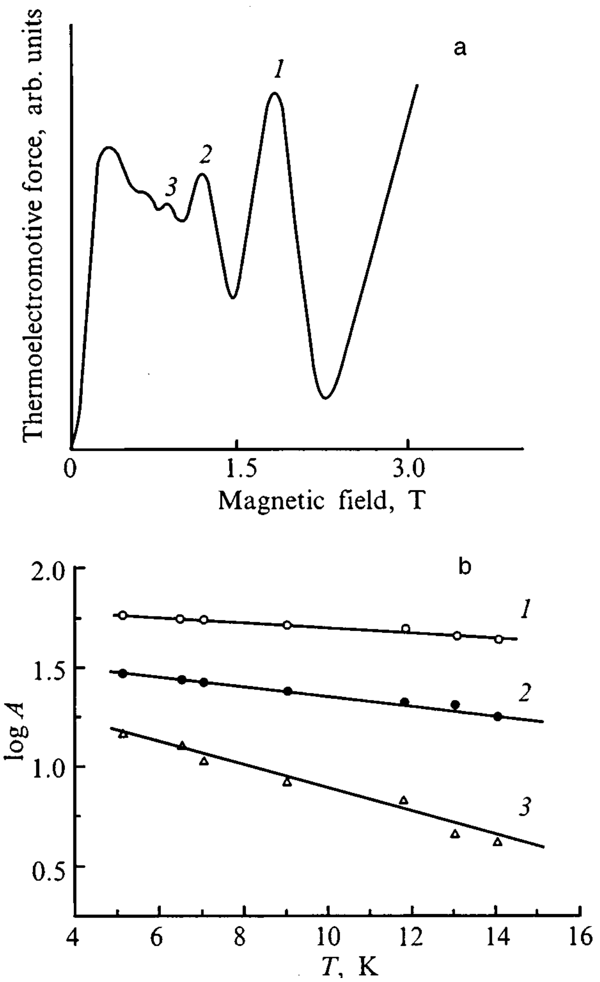

FIG. 4. a — Quantum oscillations of the thermal emf in a longitudinal magnetic field at $T = 5.1$ K (sample 3); b — temperature dependence of the amplitude of the oscillations of the thermal emf in a longitudinal magnetic field. The figures labeling the straight lines in figure b correspond to the figures labeling the oscillation peaks in figure a.

TABLE I. Characteristics of the samples at $T=4.2$ K.

Samples	$p\times10^{-7}$ cm^{-3}, from the Hall coeff.	$p\times10^{-7}$ cm^{-3}, from the Shubnikov oscillations α	$\mu\times10^{5}$, cm^{2}/V·s	$m^{*}/m_{0}\times10^{2}$	K	T_c, K	γ
1	2.03	1.8	1.5	1.83	10	20	2.3
2	3.11	2.5	2.0	1.82	10	22	2.0
3	2.12	1.9	5.8	1.76	10.5	35	2.5
4	3.81	3,5	5.2	1.75	10.4	36	2.4

Note: Samples 1 and 2 were obtained by the Bridgman method; samples 3 and 4 were obtained from the vapor phase; γ was determined from the relation $\mu\sim T^{-\gamma}$.

susceptibility has a singularity with a minimum. The temperature dependence of the magnetic susceptibility of the samples examined in the present study has two singularities which take the form of a decrease in paramagnetism against a diamagnetic background (Fig. 2). The temperature of the first singularity is close to the value of T_{c1} determined from the temperature dependence of the thermal voltage. Therefore, we associate it with the structural phase transition, as we did in Refs. 2, 7, and 8. Indeed, at the structural phase transition a temperature-dependent correction to the width of the band gap E_g arises. In connection with the smallness of E_g in the narrow-gap (narrow-band) semiconductor $Pb_{0.8}Sn_{0.2}Te$ renormalization of the band spectrum should lead to changes in its magnetic and kinetic properties: a correction to the magnetic susceptibility appears, due to fluctuations of the order parameter in the vicinity of the structural phase transition.[11] The temperature at which the second phase transition shows up in the magnetic susceptibility ($T_{c2}\sim140$ K) is higher than the temperature of the singularity in $\alpha(T)$; this is apparently due to the different nature of this phase transition.

Figure 3 shows the experimental dependence of α in a magnetic field aligned with the temperature gradient ($\alpha_{\parallel}$) and transverse to it ($\alpha_{\perp}$) at $T=5.1$ K. Using the calculational technique described in Ref. 12, we determined the anisotropy coefficient of the effective masses $K=m_{\parallel}^{*}/m_{\perp}^{*}$ ($m_{\parallel}^{*}$ is the longitudinal effective mass, and $m_{\perp}^{*}$ is the transverse effective mass of the current carriers, respectively).

The high degree of structural perfection of the investigated crystals, the large mobilities and small effective masses of the current carriers in the presence of a degenerate hole gas enabled us to investigate Shubnikov oscillations of α in the $Pb_{0.8}Sn_{0.2}Te$ samples.

The thermal emf in a quantizing longitudinal magnetic field was measured on samples oriented so that the magnetic field vector and the temperature gradient were parallel to the high-symmetry axis $H\|\nabla T\|\langle100\rangle$ under the conditions $\Omega H/kT>1$ and $\zeta/kT>1$ (Ω is the cyclotron frequency, ζ is the chemical potential).

Figure 4 plots the thermal emf as a function of the magnetic field at $T=5.1$ K. Pronounced single-frequency oscillations of $\alpha(H)$ are observed, where the location of the oscillations is determined by the current-carrier concentration (i.e., by the Fermi energy).

We determined the frequency of the oscillations F from the slope of the dependence $1/H_{\text{extr}}$ on the number of the Landau level (H_{extr} is the magnitude of the magnetic field at the maximum of the thermal emf). The extremal area of the intersection of the Fermi surface S_{extr} by the set of planes perpendicular to the magnetic field vector is related to F by the equation

$$S_{\text{extr}}=(2\pi he/c)F. \tag{1}$$

The hole concentration at an L-extremum can be calculated from the dependence of the period of the oscillations $\Delta=(1/H_{n+1})-(1/H_n)$ on the reciprocal magnitude of the magnetic field using the formula

$$\Delta(1/H)=3.18\times10^{6}K^{1/2}/p^{2/3}. \tag{2}$$

From an analysis of the temperature dependence of the amplitudes of the oscillations A we determined the magnitude of the cyclotron effective mass at the Fermi level m_c^{*} at the L-minimum. The values of m_c^{*} and the current-carrier concentration, calculated from the oscillations of the thermal voltage at $T=5.1$ K, are listed in Table I. It can be seen that the total hole concentration at the four L-extrema coincide to within 10% with the Hall current-carrier concentration.

To summarize, increasing the degree of structural perfection in single crystals of the solid solution $Pb_{0.8}Sn_{0.2}Te$ led to an increase in the temperature of the first structural phase transition, the appearance of a second structural phase transition, and hysteresis of the thermal emf in the temperature interval between the first and second structural phase transitions. We also detected an increase in the exponent γ of the temperature dependence of the mobility $\mu\sim T^{-\gamma}$ from 2.1–2.3 to 2.5, which is evidence of a decrease in the scattering of current carriers by lattice defects.

The authors thank A. V. Brodskiĭ and A. L. Mirets for measuring the magnetic susceptibility.

[1] K. L. I. Kobayashi, Y. Kato, Y. Katayama, and K. F. Komatsubara, Phys. Rev. Lett. **37**, 772 (1976).

[2] G. V. Lashkarev, V. M. Baginsky, R. O. Kikodze, and M. V. Radchenko, Inst. Phys. Conf. Ser. No. 43, Ch. 18. Edinburgh (1978), p. 597.

[3] O. V. Aleksandrov, K. V. Kiseleva, and Yu. A. Gorina, Zh. Tekh. Fiz. **50**, 2473 (1980) [Tech. Phys. Lett. **25**, 1449 (1980)].

[4] A. P. Levanyuk, V. V. Osipov, Yu. I. Épifanov, and A. S. Sigov, Zh. Éksp. Teor. Fiz. **76**, 345 (1979) [Sov. Phys. JETP **49**, 176 (1979)].

[5] G. V. Lashkarev, D. F. Migley, A. D. Shevchenko, and K. D. Tovstyuk, Phys. Status Solidi B **63**, 663 (1974).

[6] G. V. Lashkarev and M. V. Radchenko, *International Workshop on Semimagnetic Semiconductors. Abstracts. Johannes Kepler University, Linz, Austria (1994)*, p. 207; G. V. Lashkarev, M. V. Radchenko, and V. V. Asotskiĭ, Funktsional'nye Materialy **1**(2), 67 (1994).

[7] G. V. Lashkarev, R. O. Kikodze, M. V. Radchenko, V. B. Orletskiĭ, E. I. Slin'ko, and I. Z. Marchuk, Fiz. Tekh. Poluprovodn. **13**, 1548 (1979) [Sov. Phys. Semicond. **13**, 902 (1979)].

[8] G. V. Lashkarev, M. V. Radchenko, V. B. Orletskiĭ, E. I. Slin'ko, and R. M. Starik, Fiz. Tekh. Poluprovodn. (St. Petersburg) **14**, 490 (1980); **21**, 1921 (1987) [Sov. Phys. Semicond. **14**, 290 (1980); **21**, 1165 (1987)].

[9] W. Jantsch and A. Lopez-Otero, *Proceedings of the Thirteenth International Conference on the Physics of Semiconductors, Rome (1976)*, p. 148.

[10] G. V. Lashkarev and M. V. Radchenko, Ukr. Fiz. Zh. **27**, *5*, 747 (1982).

[11] V. I. Litvinov and V. K. Dugaev, J. Exp. Theor. Phys. **77**, 335 (1979).

[12] C. A. Nemov, Fiz. Tekh. Poluprovodn. **13**, 1439 (1979) [Sov. Phys. Semicond. **13**, 842 (1979)].

Translated by Paul F. Schippnick

Electron–phonon entrainment, thermodynamic effects, and the thermal conductivity of degenerate conductors

I. G. Kuleev*)

Institute for Metal Physics, Ural Branch, Russian Academy of Sciences, 620219 Ekaterinburg, Russia

(Submitted June 22, 1998; accepted for publication October 23, 1998)
Fiz. Tverd. Tela (St. Petersburg) **41**, 1753–1762 (October 1999)

A method is proposed for calculating the kinetic coefficients of degenerate conductors that takes into account in a self-consistent way the mutual influence of the nonequilibrium state of the electron and phonon subsystems. The calculated expressions for the kinetic coefficients satisfy Onsager symmetry relations. The influence of the nonequilibrium character of the electron–phonon subsystem on the electrical conductivity, thermal voltage, and electronic thermal conductivity is analyzed.
[S1063-7834(99)00810-2]

The electron–phonon interaction in solids leads to an exchange of momentum between the electron and phonon subsystems and correspondingly to mutual entrainment effects.[1] A large number of works have been dedicated to a study of electron–phonon entrainment effects (see Refs. 2–6 and the references cited therein). An exact solution of the system of kinetic equations for electron–phonon systems taking into account the mutual influence of the nonequilibrium state of the electrons and phonons on each other even under simplifying assumptions of spherical energy surfaces and isotropic relaxation times has still not been found. Approximate solutions for nondegenerate semiconductors were found in Refs. 7 and 8 by expanding the perturbed distribution functions in power series in a small parameter defined by the effect of the nonequilibrium state of the electrons on the phonon distribution function. Such studies are described in Refs. 5, 9, and 10 for metals. In Refs. 11 and 12 the system of kinetic equations was solved for degenerate conductors in a magnetic field. In Ref. 11 the solution was found for a particular form of the dependence of the phonon relaxation time on the wave vector in the zeroth approximation of the degeneracy of the electron gas. Reference 12 considered a more general case. References 9 and 10 showed that in a treatment of the influence of entrainment effects on thermoelectric phenomena it is necessary to solve the system of kinetic equations for the current carriers and the phonons together with a rigorous account of deviations of both distribution functions from their equilibrium values. In the opposite case, the Onsager symmetry relations for the thermoelectric coefficients will not be satisfied, as was the case in a number of works.[13,14]

Here I propose a method for calculating the kinetic coefficients of degenerate conductors with allowance for the mutual influence of the nonequilibrium state of the electrons and phonons on each other. Here I use only the condition of strong degeneracy $k_BT/\zeta \ll 1$ (ζ is the Fermi energy), and the inelastic character of electron–phonon scattering is taken into account in the first nonvanishing order. The calculation does not assume any specific form of the time dependence of non-electron mechanisms of phonon relaxation on the wave number. The contributions to the relaxation frequencies of the longitudinal and transverse acoustic phonons are identified. The electron spectrum is assumed to be isotropic. The influence of mutual entrainment on the electrical conductivity, thermal voltage, and thermal conductivity is considered, along with some physical aspects of the theory of electron–phonon entrainment which previously had received insufficient attention.

1. SYSTEM OF KINETIC EQUATIONS FOR THE ELECTRONS AND PHONONS

In this section I analyze the momentum balance and the mutual influence of the nonequilibrium state of the electrons and phonons. A diagram illustrating the redistribution and relaxation of the momentum received by the electron–phonon system on the temperature gradient is shown in Fig. 1. Mechanisms of electron–phonon relaxation characterized by the frequencies ν_{eph} ν_{phe} lead to a redistribution of the momentum within the electron–phonon system. Mechanisms of electron scattering by impurities ν_{ei}, phonon scattering by boundaries ν_{phL}, phonon scattering by impurities (the Rayleigh mechanism) ν_{phR}, and Herring phonon–phonon scattering ν_{phH} lead to relaxation of the total momentum of the electron–phonon system. Expressions for the corresponding relaxation frequencies are given below. We start with the system of kinetic equations for the nonequilibrium electron $f(\mathbf{k},\mathbf{r})$ and phonon $N^{\lambda}(\mathbf{q},\mathbf{r})$ distribution functions, which has the standard form[3,11]

$$\frac{e}{\hbar}\mathbf{E}_0\frac{\partial f_{\mathbf{k}}}{\partial \mathbf{k}}+(\mathbf{v}_{\mathbf{k}}\nabla_{\mathbf{r}})f_{\mathbf{k}}=I_{\mathrm{ei}}(f_{\mathbf{k}})+I_{\mathrm{eph}}(f_{\mathbf{k}},N_{\mathbf{q}}^{\lambda}),$$

$$\mathbf{v}_q^{\lambda}\boldsymbol{\nabla}_{\mathbf{r}}N_q^{\lambda}=-(N_{\mathbf{q}}^{\lambda}-N_{\mathbf{q}\lambda}^{0})\nu_{\mathrm{ph}}^{(1)\lambda}+I_{\mathrm{phe}}(N_{\mathbf{q}}^{\lambda},f_{\mathbf{k}}). \tag{1}$$

Here $\mathbf{v}_q^{\lambda}=\partial\omega_q^{\lambda}/\partial\mathbf{q}$ is the group velocity of the acoustic phonons with polarization λ, $\mathbf{v}_q^{\lambda}=s_{\lambda}\mathbf{q}/q$, $N_{\mathbf{q}\lambda}^{0}$ is the Planck function, the relaxation frequency $\nu_{\mathrm{ph}}^{(1)\lambda}(q)$ includes all non-electron mechanisms of phonon scattering: phonon scattering by phonons, defects, and the boundaries of the sample. The

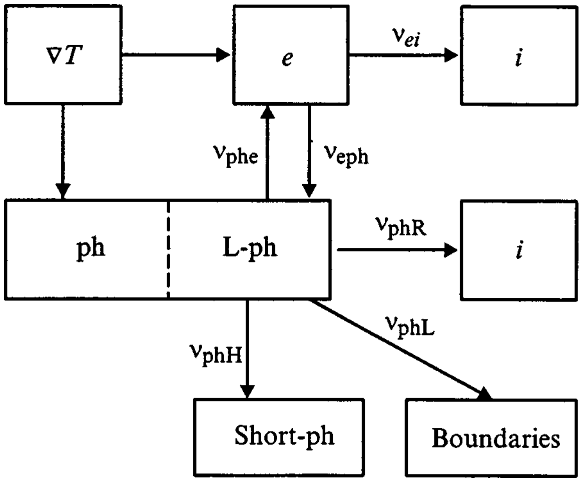

FIG. 1. Diagram illustrating relaxation of the momentum of an electron–phonon system in the presence of a temperature gradient. Here ν_{phR}, ν_{phL}, and ν_{phH} are the frequencies of relaxation of the phonons at the impurities (Rayleigh mechanism), boundaries, and other phonons (Herring mechanism), respectively.

collision integrals of the electrons with impurities I_{ei} and with phonons I_{eph}, and of the phonons with electrons I_{phe} are given in Refs. 3 and 11.

We represent the electron and phonon distribution functions as

$$f_{\mathbf{k}}=f_0(\varepsilon_k)+\delta f_{\mathbf{k}},\quad N^\lambda_{\mathbf{q}}=N^0_{\mathbf{q}\lambda}+g_\lambda(\mathbf{q}), \tag{2}$$

where $f_0(\varepsilon_k)$ and $N^0_{\mathbf{q}\lambda}$ are the local equilibrium functions of the electrons and phonons, and $\delta f_{\mathbf{k}}$ and $g_\lambda(\mathbf{q})$ are the nonequilibrium corrections to the distribution functions, which are linear in the external actions. We linearize the collision integrals in these correction terms

$$I_{eph}(f_{\mathbf{k}},N^\lambda_{\mathbf{q}})=I_{eph}(\delta f_{\mathbf{k}},N^0_{\mathbf{q}\lambda})+I_{eph}(f_0(\varepsilon_k),g_\lambda(\mathbf{q})),$$
$$I_{phe}(f_{\mathbf{k}},N^\lambda_{\mathbf{q}})=I_{phe}(\delta f_{\mathbf{k}},N^0_{\mathbf{q}\lambda})+I_{phe}(f_0(\varepsilon_k),g_\lambda(\mathbf{q})). \tag{3}$$

We represent the collision integrals $I_{ei}(\delta f_{\mathbf{k}})$, $I_{phe}(f_0,g_\lambda(\mathbf{q}))$, and $I_{eph}(\delta f_{\mathbf{k}},N^0_{\mathbf{q}}\lambda)$ in the approximation of elastic scattering of the electrons by the phonons in terms of the relaxation frequencies[3,11,12]

$$I_{ei}(\delta f_{\mathbf{k}})=-\nu_{ei}(k)\delta f_{\mathbf{k}},\quad I_{phe}(f_0,g_\lambda(\mathbf{q}))=-\nu^\lambda_{phe}(q)g_\lambda(\mathbf{q}),$$
$$I_{eph}(\delta f_{\mathbf{k}},N^0_{\mathbf{q}\lambda})\cong-\nu_{eph}(k)\delta f_{\mathbf{k}}. \tag{4}$$

Here $\nu_{ei}(k)$ is the relaxation frequency of the electrons on the impurities,[3] $\nu^\lambda_{phe}(k_F,q)=|C^\lambda_q|^2 m_F^2 s_\lambda f_0(\varepsilon_{q/2})/\pi\hbar^4$ is the relaxation frequency of the phonon momentum on the electrons, $|C^\lambda_q|^2=E^2_{0\lambda}\hbar q/s_\lambda\rho=C^2_{0\lambda}q$, ρ is the density of the crystal, $E_{0\lambda}$ is the constant of the deformation potential, and s_λ is the speed of sound of the acoustic phonons with polarization λ. $f_0(\varepsilon_{q/2})$ is the Fermi distribution function of the energy $\varepsilon_{q/2}$, and $\nu_{eph}(k)$ is the electron collision frequency with the phonons,

$$\nu_{eph}(k)=\sum_\lambda\int_0^{z^\lambda_{2k}}dz^\lambda_q\,\nu^\lambda_{eph}(k,q)\equiv\frac{\tilde m(\varepsilon)}{\tilde k^3}\sum_\lambda\langle\nu^\lambda_{eph}(k_F,q)\rangle_{z^\lambda_{2k}}, \tag{5}$$

where

$$\nu^\lambda_{eph}(k,q)=\frac{m(\varepsilon)(C^\lambda_0)^2}{2\pi\hbar^3k^3}q^5_{T\lambda}(z^\lambda_q)^5N^0_{q\lambda}(N^0_{q\lambda}+1)$$
$$=\frac{\tilde m(\varepsilon)}{\tilde k^3}\nu^\lambda_{eph}(k_F,q),$$

$$z^\lambda_q=\frac{\hbar\omega_{q\lambda}}{k_BT}=\frac{q}{q^\lambda_T},\quad q^\lambda_T=\frac{k_BT}{\hbar s_\lambda},\quad z^\lambda_{2k}=\frac{2k}{q^\lambda_T},\quad \tilde m(\varepsilon)=\frac{m(\varepsilon)}{m_F},$$

$m_F=m(\zeta)$ is the effective mass of the electron at the Fermi level, $\tilde k=k/k_F$, and $\hbar k_F$ is the Fermi momentum.

In the calculation of the collision integral $I_{eph}(f_0,g_\lambda(\mathbf{q}))$ we take account of the inelastic nature of the collisions of the electrons with the phonons in the first-order perturbation theory

$$I_{eph}(f_0,g_\lambda(\mathbf{q}))=\frac{2\pi}{\hbar}\frac{1}{V}\sum_{\mathbf{q},\lambda}|C_{q\lambda}|^2\hbar\omega_{q\lambda}g_\lambda(\mathbf{q})\left(\frac{\partial f_0}{\partial\varepsilon_k}\right)$$
$$\times[\delta(\varepsilon_{\mathbf{k}+\mathbf{q}}-\varepsilon_{\mathbf{k}})-\delta(\varepsilon_{\mathbf{k}-\mathbf{q}}-\varepsilon_{\mathbf{k}})]. \tag{6}$$

As a result, the equation for the phonon distribution takes the form

$$g_\lambda(\mathbf{q})=-\frac{N^0_{q\lambda}(N^0_{q\lambda}+1)}{\nu^\lambda_{ph}(q)}\frac{\hbar\omega_{q\lambda}}{k_BT}(\mathbf{v}^\lambda_q\nabla T)$$
$$+\frac{1}{\nu^\lambda_{ph}}I_{phe}(\delta f_{\mathbf{k}},N^{(0)}_{q\lambda})=g^{(1)}_\lambda(\mathbf{q})+g^{(2)}_\lambda(\mathbf{q}), \tag{7}$$

where $\nu^\lambda_{ph}=\nu^{(1)\lambda}_{ph}+\nu^\lambda_{phe}$ is the total relaxation frequency of the phonons with wave vector q and polarization λ. The function $g^{(1)}_\lambda(\mathbf{q})$ is due to the direct action of the temperature gradient on the phonon subsystem, and the correction term $g^{(2)}_\lambda(\mathbf{q})$ takes into account the influence of the nonequilibrium state of the electrons

$$g^{(2)}_\lambda(\mathbf{q})=\frac{1}{\nu^\lambda_{ph}(q)}I_{phe}(\delta f_{\mathbf{k}},N^0_{q\lambda})$$
$$=\frac{4\pi}{\hbar}\frac{|C_{q\lambda}|^2}{\nu^\lambda_{ph}(q)}\frac{\hbar\omega_{q\lambda}}{k_BT}N^0_{q\lambda}(N^0_{q\lambda}+1)$$
$$\times\frac{1}{V}\sum_{\mathbf{k}'}\delta f_{\mathbf{k}'}[\delta(\varepsilon_{\mathbf{k}'-\mathbf{q}}-\varepsilon_{\mathbf{k}'})-\delta(\varepsilon_{\mathbf{k}'+\mathbf{q}}-\varepsilon_{\mathbf{k}'})]. \tag{8}$$

We substitute expression (8) for $g_\lambda(\mathbf{q})$ into Eq. (6); then, taking formulas (3) and (4) into account we obtain a closed integral equation for the nonequilibrium correction to the electron distribution function

$$\delta f_{\mathbf{k}}=\delta f^{(1)}_{\mathbf{k}}+\tau(\varepsilon_k)I_{eph}(f_0,g^{(2)}_\lambda)=\delta f^{(1)}_{\mathbf{k}}+\delta f^{(2)}_{\mathbf{k}}. \tag{9}$$

The function $\delta f^{(1)}_{\mathbf{k}}$ takes into account the entrainment of electrons by phonons, and also the direct action of the electric field and temperature gradient on the electron subsystem. It has the well-known form[3]

$$\delta f_{\mathbf{k}}^{(1)}=\left(-\frac{\partial f_0}{\partial \varepsilon_k}\right)(\mathbf{v}_k\mathbf{\Phi}_1)\,\tau(\varepsilon_k),$$

$$\mathbf{\Phi}_1(\varepsilon_k)=-e\left(\mathbf{E}+\frac{k_\mathrm{B}}{e}\left(\frac{\widetilde{m}(\varepsilon)}{\widetilde{k}^3}A_\mathrm{ph}(\varepsilon)+\frac{\varepsilon_k-\zeta}{k_\mathrm{B}T}\right)\boldsymbol{\nabla} T\right),$$

$$A_\mathrm{ph}(\varepsilon)=\sum_\lambda \frac{m_\mathrm{F}s_\lambda^2}{k_\mathrm{B}T}\left\langle \frac{\nu_\mathrm{eph}^\lambda(k_\mathrm{F},q)}{\nu_\mathrm{ph}^\lambda(q)}\right\rangle_{z_{2k}^\lambda}. \tag{10}$$

Here $\tau(\varepsilon)$ is the total relaxation time of the electrons $\tau^{-1}(\varepsilon_k)=\nu_e(k)=\nu_\mathrm{ei}(k)+\nu_\mathrm{eph}(k)$, and the function $A_\mathrm{ph}(\varepsilon)$ depends on the energy ε only through the upper limit of integration $2k(\varepsilon)$. The correction term $\delta f_{\mathbf{k}}^{(2)}$ takes account of the influence of the nonequilibrium state of the electrons via the phonons on the electron distribution function

$$\begin{aligned}\delta f_k^{(2)}&=\tau(\varepsilon_k)I_\mathrm{eph}(f_0,g_\lambda^{(2)})\\&=\left(\frac{2\pi}{\hbar}\right)^2\frac{2}{V}\tau(\varepsilon_k)\sum_{\mathbf{k}',\mathbf{q},\lambda}\frac{|C_q^\lambda|^4}{\nu_\mathrm{ph}^\lambda(q)}\frac{(\hbar\omega_{q\lambda})^2}{k_\mathrm{B}T}N_{q\lambda}^0(N_{q\lambda}^0+1)\\&\quad\times\frac{\partial f_0}{\partial\varepsilon_k}[\delta(\varepsilon_{\mathbf{k}+\mathbf{q}}-\varepsilon_{\mathbf{k}})-\delta(\varepsilon_{\mathbf{k}-\mathbf{q}}-\varepsilon_{\mathbf{k}})]\,\delta f_{\mathbf{k}'}\\&\quad\times[\delta(\varepsilon_{\mathbf{k}'-\mathbf{q}}-\varepsilon_{\mathbf{k}'})-\delta(\varepsilon_{\mathbf{k}'+\mathbf{q}}-\varepsilon_{\mathbf{k}'})].\end{aligned} \tag{11}$$

Calculation of the conduction current with distribution function $\delta f_{\mathbf{k}}^{(1)}$ gives the general effect of electron entrainment by phonons.[3] Calculation of the electron fluxes with the help of the function $\delta f_{\mathbf{k}}^{(1)}$ (see the following section) shows that the symmetry relations between the Onsager kinetic coefficients in this case are not satisfied. Therefore, in solving the system of kinetic equations it is necessary to take into account the terms $\delta f_{\mathbf{k}}^{(2)}$ and $g_\lambda^{(2)}(\mathbf{q})$, which take into account the mutual influence of the nonequilibrium state of the electrons and phonons on each other. The term $\delta f_{\mathbf{k}}^{(2)}$ takes account of the influence of the nonequilibrium state of the electrons on the phonon subsystem, which in turn alters the electron distribution function. For degenerate semiconductors with a high concentration of charged defects, as a rule, the ratio of frequencies $\nu_\mathrm{eph}/\nu_\mathrm{ei}\ll 1$, and the contribution of the term $\delta f_{\mathbf{k}}^{(2)}$ to the kinetic coefficients in this case is small; however, for pure enough semimetals and gapless semiconductors its role can be significant. Below I present a new way of calculating the kinetic coefficients without direct solution of Eq. (9).

2. CALCULATION OF THE KINETIC COEFFICIENTS

The experimentally measured quantities are not the electron and phonon distribution functions, but mean values of physical quantities, defined with the help of these distribution functions. In the given case, we are interested in the charge fluxes and heat fluxes due to external forces, namely an electric field and a temperature gradient. Therefore, using Eqs. (9)–(11), we find that the conduction current $\mathbf{j}$ and the electronic heat flux $\mathbf{W}_e$ are expressed in terms of the same function, the equation for which can be rigorously solved without resorting to an expansion in a small parameter associated with the interaction

$$\mathbf{j}=-\frac{2e}{V}\sum_{\mathbf{k}}\mathbf{v}_{\mathbf{k}}(\delta f_{\mathbf{k}}^{(1)}+\delta f_{\mathbf{k}}^{(2)})=\mathbf{j}_1+\mathbf{j}_2, \tag{12}$$

$$\begin{aligned}\mathbf{W}&=\frac{2}{V}\sum_{\mathbf{k}}(\varepsilon_k-\zeta)\mathbf{v}_k\delta f_{\mathbf{k}}+\frac{1}{V}\sum_{\mathbf{q},\lambda}\hbar\omega_{q\lambda}\mathbf{v}_q^\lambda g_\lambda(\mathbf{q})\\&=\mathbf{W}_\mathrm{e}+\mathbf{W}_\mathrm{ph}.\end{aligned} \tag{13}$$

The electron $\mathbf{W}_\mathrm{e}$ and phonon $\mathbf{W}_\mathrm{ph}$ heat fluxes can also be broken down into two parts proportional to the nonequilibrium corrections to the electron $\delta f_{\mathbf{k}}^{(1)}$, $\delta f_{\mathbf{k}}^{(2)}$ and phonon $g_\lambda^{(1)}(\mathbf{q})$, $g_\lambda^{(2)}(\mathbf{q})$ distribution functions

$$\mathbf{W}_\mathrm{e}=\frac{2}{V}\sum_{\mathbf{k}}(\varepsilon_{\mathbf{k}}-\zeta)\mathbf{v}_k(\delta f_{\mathbf{k}}^{(1)}+\delta f_{\mathbf{k}}^{(2)})=\mathbf{W}_\mathrm{e}^{(1)}+\mathbf{W}_\mathrm{e}^{(2)}, \tag{14}$$

$$\mathbf{W}_\mathrm{ph}=\frac{1}{V}\sum_{\mathbf{q},\lambda}\hbar\omega_{q\lambda}\mathbf{v}_q^\lambda(g_\lambda^{(1)}(\mathbf{q})+g_\lambda^{(2)}(\mathbf{q}))=\mathbf{W}_\mathrm{ph}^0+\mathbf{W}_\mathrm{phe}. \tag{15}$$

The heat flux $\mathbf{W}_\mathrm{ph}^0$ is caused by the direct action of the temperature gradient on the phonon subsystem while the heat flux $\mathbf{W}_\mathrm{phe}$ is the result of the mutual influence of the nonequilibrium state of the electrons and phonons. It leads to a renormalization of both the electron and phonon heat fluxes.

The fluxes $\mathbf{j}_1$, $\mathbf{W}_\mathrm{e}^{(1)}$, and $\mathbf{W}_\mathrm{ph}^0$ are easily calculated since analytical expressions are known for the corresponding distribution functions (9) and (12)

$$\begin{aligned}\mathbf{j}_1&=\sigma_{xx}^0\left\{\mathbf{E}+\frac{k_\mathrm{B}}{e}\left(A_\mathrm{ph}(\zeta)+\frac{\pi^2}{3}\left(\frac{k_\mathrm{B}T}{\zeta}\right)D_1\right)\nabla T\right\}\\&=\mathbf{j}_\mathrm{dr}+\mathbf{J}_\mathrm{drag}+\mathbf{j}_\mathrm{dif},\end{aligned} \tag{16}$$

$$\mathbf{W}_\mathrm{e}^{(1)}=-L_0\sigma_{xx}^0T\left\{\frac{eT}{\zeta}D_1\mathbf{E}+\left(1+\frac{k_\mathrm{B}T}{\zeta}A_\mathrm{ph}D_2\right)\nabla T\right\}, \tag{17}$$

where

$$\sigma_{xx}^0=\frac{e^2n_e\tau_\mathrm{F}}{m_\mathrm{F}},\quad L_0=\frac{\pi^2}{3}\left(\frac{k_\mathrm{B}}{e}\right)^2,$$

$$D_1=\zeta\frac{d}{d\varepsilon}\left[\ln\left(\frac{k^3(\varepsilon)\tau(\varepsilon)}{m(\varepsilon)}\right)\right]_{\varepsilon=\zeta},$$

$$D_2=\zeta\frac{d}{d\varepsilon}[\ln(\tau(\varepsilon)A_\mathrm{ph}(\varepsilon))]_{\varepsilon=\zeta}.$$

It can be seen from formula (16) that the charge flux (like the heat flux) is made up of three contributions: the drift current $\mathbf{j}_\mathrm{dr}$ and the diffusion current $\mathbf{j}_\mathrm{dif}$ are formed by the direct action of the electric field and the temperature gradient on the electron subsystem while the drag current $\mathbf{j}_\mathrm{drag}$ is the result of entrainment of electrons by phonons.

The heat flux $\mathbf{W}_\mathrm{phe}$ conveyed by the phonons, but due to the influence of the nonequilibrium state of the electrons on the phonon subsystem, can also be separated into two parts

$$\mathbf{W}_{\text{phe}}=\frac{1}{V}\sum_{\mathbf{q},\lambda} s_\lambda^2\hbar\mathbf{q}g_\lambda^{(2)}(\mathbf{q})$$
$$=\frac{k_BT}{m_F}\frac{2}{V}\sum_{\mathbf{k}}\frac{\tilde{m}(\varepsilon)}{\tilde{k}^3}A_{\text{ph}}(\varepsilon)\hbar\mathbf{k}(\delta f_{\mathbf{k}}^{(1)}+\delta f_{\mathbf{k}}^{(2)})$$
$$=\mathbf{W}_{\text{phe}}^{(1)}+\mathbf{W}_{\text{phe}}^{(2)}. \tag{18}$$

Calculation of the flux $\mathbf{W}_{\text{phe}}^{(1)}$ due to the nonequilibrium correction $\delta f_{\mathbf{k}}^{(1)}$ gives

$$\mathbf{W}_{\text{phe}}^{(1)}=-\frac{k_BT}{e}\sigma_{xx}^0A_{\text{ph}}(\zeta)\left\{\mathbf{E}+\frac{k_B}{e}\left[A_{\text{ph}}(\zeta)+\frac{\pi^2}{3}\left(\frac{k_BT}{\zeta}\right)D_A\right]\nabla T\right\}, \tag{19}$$

where $D_A=\zeta(d/d\varepsilon)[\ln(m(\varepsilon)\tau(\varepsilon)A_{\text{ph}}(\varepsilon))]_{\varepsilon=\zeta}$. As can be seen from Eq. (10), for $\delta f_{\mathbf{k}}^{(1)}$ and relation (19) the drift and diffusion components of the heat flux $\mathbf{W}_{\text{phe}}^{(1)}$ [first and last terms in expression (19)] are connected with the influence of the nonequilibrium state of the electrons, and these terms should be included in the electronic heat flux. The second term in expression (19) is the result of the influence of the entrainment current (which is caused by the nonequilibrium state of the phonons) on the phonon subsystem. It should be included in the phonon heat flux $\mathbf{W}_{\text{ph}}^{(1)}$. As a result, we have

$$\mathbf{W}_{\text{ph}}^{(1)}=-\kappa_{\text{ph}}^{(1)}\nabla T,\quad \kappa_{\text{ph}}^{(1)}=\kappa_{\text{ph}}^0+\kappa_{\text{phe}}^{(1)},$$
$$\kappa_{\text{ph}}^{(1)}=\sum_\lambda\frac{k_Bs_\lambda^2q_T^3}{6\pi^2}\int_0^{z_d^\lambda}dz_q^\lambda(z_q^\lambda)^4N_{q\lambda}^0(N_{q\lambda}^0+1)$$
$$\times\left\{1+\frac{\nu_{\text{phe}}^\lambda(q)}{\nu_e(\zeta)}\frac{k_BT}{s_\lambda^2}A_{\text{ph}}(\zeta)\right\}, \tag{20}$$

where $z_d^\lambda=\hbar\omega_{d\lambda}/k_BT$, and $\omega_{d\lambda}$ is the Debye frequency for phonons of polarization λ.

Assuming that the electric field and the temperature gradient are aligned with the x axis, we write down expressions for the fluxes in terms of the kinetic coefficients

$$j_x=\sigma_{xx}E_x-\beta_{xx}\nabla_xT,\quad W_{etx}=\gamma_{xx}E_x-\kappa_{xx}^e\nabla_xT. \tag{21}$$

It is not hard to convince oneself that if the contribution of $\mathbf{W}_{\text{phe}}^{(1)}$ to the electronic heat flux is taken into account, the Onsager relations for the thermoelectric coefficients $\gamma_{xx}^{(1)}$ and $\beta_{xx}^{(1)}$ are satisfied

$$\gamma_{xx}^{(1)}=T\beta_{xx}^{(1)}=-\sigma_{xx}^0T\frac{k_B}{e}\left\{A_{\text{ph}}(\zeta)+\frac{\pi^2}{3}\left(\frac{k_BT}{\zeta}\right)D_1\right\}, \tag{22}$$

and the expression for the electronic thermal conductivity $\kappa_{xx}^{e(1)}$ has the form

$$\kappa_{xx}^{e(1)}=L_0\sigma_{xx}^0T\left\{1+\left(\frac{k_BT}{\zeta}\right)A_{\text{ph}}(\zeta)(D_2+D_A)\right\}. \tag{22a}$$

Thus, a necessary condition for the satisfaction of the microscopic reversibility relations is that the heat flux communicated by the phonons and due to the nonequilibrium state of the electrons must be taken into account in the calculation of the total electronic heat flux. For the kinetic coefficients calculation including the entrainment effect,[3] the Onsager relations are not satisfied since the flux $\mathbf{W}_{\text{phe}}^{(1)}$ was not taken into account.

The fluxes $\mathbf{j}_2$, $\mathbf{W}_e^{(2)}$, and $\mathbf{W}_{\text{phe}}^{(2)}$ contain the unknown functions $\delta f_{\mathbf{k}}^{(2)}$ and $g_\lambda^{(2)}(\mathbf{q})$, which are expressed as integral transforms of the total nonequilibrium correction to the electron distribution function $\delta f_{\mathbf{k}}$. We substitute expression (11) for $\delta f_{\mathbf{k}}^{(2)}=\tau(\varepsilon_k)I_{\text{eph}}(f_0,g_\lambda^{(2)})$ into formulas (12), (15), and (18) and sum over the electron wave vectors. As a result, all three fluxes can be represented in terms of the same function $\boldsymbol{\varphi}(\varepsilon)$

$$\mathbf{j}_2=-\frac{e}{m_F}\int_0^\infty d\varepsilon\left(-\frac{\partial f_0}{\partial\varepsilon}\right)\tilde{m}(\varepsilon)\tau(\varepsilon)\boldsymbol{\varphi}(\varepsilon),$$
$$\mathbf{W}_e^{(2)}=\frac{1}{m_F}\int_0^\infty d\varepsilon\left(-\frac{\partial f_0}{\partial\varepsilon}\right)(\varepsilon-\zeta)\tilde{m}(\varepsilon)\tau(\varepsilon)\boldsymbol{\varphi}(\varepsilon),$$
$$\mathbf{W}_{\text{phe}}^{(2)}=\frac{k_BT}{m_F}\int_0^\infty d\varepsilon\left(-\frac{\partial f_0}{\partial\varepsilon}\right)\left(\frac{\tilde{m}(\varepsilon)}{\tilde{k}(\varepsilon)}\right)^3\tau(\varepsilon)A_{\text{ph}}(\varepsilon)\boldsymbol{\varphi}(\varepsilon),$$
$$\boldsymbol{\varphi}(\varepsilon)=\frac{1}{V}\sum_{|\mathbf{q}|<2k,\lambda}\nu_{\text{phe}}^\lambda\hbar\mathbf{q}g_\lambda^{(2)}(\mathbf{q}). \tag{23}$$

$\boldsymbol{\varphi}(\varepsilon)$ depends on the energy through the upper limit of integration $2k(\varepsilon)$. Substituting expression (8) in the expression for $\boldsymbol{\varphi}(\varepsilon)$, we take the integral over the angular variables $d\Omega_q$ with the help of the δ functions and interchange the order of integration over the wave vectors q and k' after dividing the region of integration in k' into two regions: $q/2<k'<k$ and $q/2<k<k'$. As a result, we obtain

$$\boldsymbol{\varphi}(\varepsilon)=\boldsymbol{\varphi}^<(\varepsilon)+\Phi_{2k}(\varepsilon)\boldsymbol{\varphi}^>(\varepsilon),$$
$$\boldsymbol{\varphi}^<(\varepsilon)=\frac{2}{V}\sum_{|\mathbf{k}'|<k}\frac{\tilde{m}(\varepsilon')}{\tilde{k}'^3}\Phi_{2k'}\hbar\mathbf{k}'\delta f_{\mathbf{k}'},$$
$$\boldsymbol{\varphi}^>(\varepsilon)=\frac{2}{V}\sum_{|\mathbf{k}'|>k}\frac{\tilde{m}(\varepsilon')}{\tilde{k}'^3}\hbar\mathbf{k}'\delta f_{\mathbf{k}'}, \tag{24}$$

where

$$\Phi_{2k}(\varepsilon)=\sum_\lambda\left\langle\frac{\nu_{\text{phe}}^\lambda(k_F,q)\nu_{\text{eph}}^\lambda(k_F,q)}{\nu_{\text{ph}}^\lambda(q)}\right\rangle_{z_{2k}^\lambda}$$

also depends on ε through the upper limit of integration $z_{2k(\varepsilon)}^\lambda$. The inverse quantity Φ_{2k}^{-1} characterizes the time during which the momentum transferred by the electrons to the phonon subsystem is returned to the electrons. Making use of Eqs. (9)–(11), we express the functions $\boldsymbol{\varphi}^<(\varepsilon)$ and $\boldsymbol{\varphi}^>(\varepsilon)$ in terms of $\boldsymbol{\varphi}(\varepsilon)$

$$\boldsymbol{\varphi}^<(\varepsilon)=\int_0^\varepsilon d\varepsilon'\left(-\frac{\partial f_0}{\partial\varepsilon'}\right)\Phi_{2k}(\varepsilon')\tilde{\boldsymbol{\varphi}}(\varepsilon'),$$
$$\boldsymbol{\varphi}^>(\varepsilon)=\int_\varepsilon^0 d\varepsilon'\left(-\frac{\partial f_0}{\partial\varepsilon'}\right)\tilde{\boldsymbol{\varphi}}(\varepsilon'), \tag{25}$$

where

$$\tilde{\boldsymbol{\varphi}}(\varepsilon)=\tau(\varepsilon)\left[n_{\mathrm{e}}\tilde{m}(\varepsilon)\boldsymbol{\Phi}_1(\varepsilon)+\left(\frac{\tilde{m}(\varepsilon)}{\tilde{k}(\varepsilon)}\right)^3\boldsymbol{\varphi}(\varepsilon)\right].$$

Substituting expressions (25) into Eq. (24) gives an inhomogeneous Volterra integral equation for $\boldsymbol{\varphi}(\varepsilon)$, which can be represented in the following form:

$$\boldsymbol{\varphi}(\varepsilon)=\int_0^\infty d\varepsilon'\left(-\frac{\partial f_0}{\partial\varepsilon'}\right)\Phi_{2k}(\varepsilon')\tilde{\boldsymbol{\varphi}}(\varepsilon')+\int_\varepsilon^\infty d\varepsilon'\left(-\frac{\partial f_0}{\partial\varepsilon'}\right)(\Phi_{2k}(\varepsilon)-\Phi_{2k}(\varepsilon'))\tilde{\boldsymbol{\varphi}}(\varepsilon'). \tag{26}$$

The kernel of integral equation (26) is defined in terms of a single integral whereas the kernel of the integral equation derived earlier in Refs. 7, 8 and 11, 12 has a more complicated form: first, the unknown function appears inside the double integral and, second, to solve the equation it is necessary to specify the dependence of the relaxation frequencies on the phonon wave vector.[11]

The solution of Eq. (26) in the linear approximation in the degeneracy parameter $k_{\mathrm{B}}T/\zeta$ is found in two steps. First, we determine the energy dependence of the function $\boldsymbol{\varphi}(\varepsilon)$. Toward this end, we expand the function $\varphi(\varepsilon)$ in a series in the parameter $\varepsilon-\zeta$ since the main contribution to the integrals (26) comes from a narrow band of energies $|\varepsilon-\zeta|\leqslant k_{\mathrm{B}}T$.

$$\boldsymbol{\varphi}(\varepsilon)=\boldsymbol{\varphi}(\zeta)+\sum_{n=1}^{\infty}\frac{(\varepsilon-\zeta)^n}{n!}\boldsymbol{\varphi}^{(n)}(\zeta),$$

$$\boldsymbol{\varphi}^{(n)}(\zeta)=\left(\frac{d^n\boldsymbol{\varphi}(\varepsilon)}{d\varepsilon^n}\right)_{\varepsilon=\zeta}. \tag{27}$$

We can write expressions for the first three derivatives of $\boldsymbol{\varphi}(\varepsilon)$ with respect to the energy using the derived integral equation

$$\boldsymbol{\varphi}^{(1)}(\varepsilon)=\Phi_{2k}'\boldsymbol{\varphi}^{>}(\varepsilon),$$

$$\boldsymbol{\varphi}^{(2)}(\varepsilon)=\Phi_{2k}''(\varepsilon)\boldsymbol{\varphi}^{>}(\varepsilon)-\Phi_{2k}'\left(-\frac{\partial f_0}{\partial\varepsilon}\right)\tilde{\boldsymbol{\varphi}}(\varepsilon),$$

$$\boldsymbol{\varphi}^{(3)}(\varepsilon)=\Phi_{2k}'''(\varepsilon)\boldsymbol{\varphi}^{>}(\varepsilon)-2\Phi_{2k}''(\varepsilon)\left(-\frac{\partial f_0}{\partial\varepsilon}\right)\tilde{\boldsymbol{\varphi}}(\varepsilon)-\Phi_{2k}'(\varepsilon)\times\left[\left(-\frac{\partial^2 f_0}{\partial\varepsilon^2}\right)\tilde{\boldsymbol{\varphi}}(\varepsilon)+\left(-\frac{\partial f_0}{\partial\varepsilon}\right)\boldsymbol{\varphi}^{(1)}(\varepsilon)\right]. \tag{28}$$

As can be seen from Eqs. (28), the integral equation (26) is equivalent to an inhomogeneous second-order differential equation. Therefore, all higher derivatives $\varphi^{(n)}(\varepsilon)$ can be expressed in terms of the two functions $\boldsymbol{\varphi}^{>}(\varepsilon)$ and $\boldsymbol{\varphi}(\varepsilon)$, specifically

$$\boldsymbol{\varphi}^{(n)}(\varepsilon)=A_n(\varepsilon)\boldsymbol{\varphi}^{>}(\varepsilon)+B_n(\varepsilon)\boldsymbol{\varphi}(\varepsilon)+\mathbf{C}_n(\varepsilon). \tag{29}$$

The derivatives in expansion (27) are evaluated at $\varepsilon=\zeta$; therefore, let us analyze the coefficients $A_n(\zeta)$, $B_n(\zeta)$, and $C_n(\zeta)$ and separate out the terms whose contributions are linear in the parameter $k_{\mathrm{B}}T/\zeta$. Then, for the derivatives of the function $\boldsymbol{\varphi}(\varepsilon)$ for $n\geqslant 2$ we find

$$\boldsymbol{\varphi}^{(n)}(\zeta)\approx-\Phi_{2k}'(\zeta)\left\{\left[\frac{\partial^{n-1}f_0}{\partial\varepsilon^{n-1}}\right]_{\varepsilon=\zeta}\tilde{\boldsymbol{\varphi}}(\zeta)+\frac{n-2}{k_{\mathrm{B}}T}\left[\frac{\partial^{n-2}f_0}{\partial\varepsilon^{n-2}}\right]_{\varepsilon=\zeta}\tau_{\mathrm{F}}(-k_{\mathrm{B}}\nabla T)\right\}. \tag{29a}$$

Here $\tilde{\boldsymbol{\varphi}}(\zeta)=\tau_{\mathrm{F}}[\boldsymbol{\varphi}(\zeta)+n_{\mathrm{e}}\boldsymbol{\Phi}_1(\zeta)]$. Substituting expression (29a) in Eq. (27) gives

$$\boldsymbol{\varphi}(\varepsilon)=\boldsymbol{\varphi}(\zeta)+k_{\mathrm{B}}T\Phi_{2k}'(\zeta)\left\{\boldsymbol{\varphi}^{>}(\zeta)\eta-\sum_{n=1}^{\infty}\left(-\frac{\partial^n f_0(\eta)}{\partial\eta^n}\right)_{\eta=0}\times\left[\frac{\eta^{n+1}}{(n+1)!}\tilde{\boldsymbol{\varphi}}(\zeta)+\frac{n\eta^{n+2}}{(n+2)!}\tau_{\mathrm{F}}n_{\mathrm{e}}(-k_{\mathrm{B}}\nabla T)\right]\right\}, \tag{30}$$

where $\eta=(\varepsilon-\zeta)/k_{\mathrm{B}}T$ is in fact the parameter of the energy expansion. In the vicinity of the Fermi level, the inequality $|\eta|\ll 1$ is not satisfied. Therefore, the alternating series (30) are asymptotic, which prevents us from restricting them to a finite number of terms. Summing the infinite series gives

$$\boldsymbol{\varphi}(\varepsilon)=\boldsymbol{\varphi}(\zeta)+k_{\mathrm{B}}T\Phi_{2k}'(\zeta)\{\eta\boldsymbol{\varphi}^{>}(\zeta)-f_1(\eta)\tau_{\mathrm{F}}[\boldsymbol{\varphi}(\zeta)+n_{\mathrm{e}}\boldsymbol{\Phi}_1(\zeta)]-f_2\tau_{\mathrm{F}}n_{\mathrm{e}}(-k_{\mathrm{B}}\nabla T)\},$$

$$f_1(\eta)=\ln(1+\exp(-\eta))-\ln(2)+\eta/2,$$

$$f_2(\eta)=\eta f_1(\eta)-2\int_0^\eta d\eta' f_1(\eta'). \tag{31}$$

Thus, employing expansion (27) and expressions (28)–(30), we find the dependence of the function $\boldsymbol{\varphi}(\varepsilon)$ on the energy and the two constants $\boldsymbol{\varphi}(\zeta)$ and $\boldsymbol{\varphi}^{>}(\zeta)$, which remain to be determined. Note that the function $f_1(\eta)$ is symmetric with respect to substitution of η by $-\eta$ while the function $f_2(\eta)$ is antisymmetric with respect to this substitution; therefore, $\boldsymbol{\varphi}(\varepsilon)$ can also be divided into two parts: a symmetric part $\boldsymbol{\varphi}_{\mathrm{s}}(\varepsilon)$ and an antisymmetric part $\boldsymbol{\varphi}_{\mathrm{a}}(\varepsilon)$.

To determine the function $\boldsymbol{\varphi}(\zeta)$, we employ the expansion $\Phi_{2k}(\varepsilon)-\Phi_{2k}(\zeta)\approx(\varepsilon-\zeta)\Phi_{2k}'(\zeta)$ and rewrite Eq. (26) for $\boldsymbol{\varphi}(\zeta)$ in the form

$$\boldsymbol{\varphi}(\zeta)=\int_{-\infty}^{\infty}d\eta\left(-\frac{\partial f_0}{\partial\eta}\right)\Phi_{2k}(\varepsilon)\tilde{\boldsymbol{\varphi}}(\varepsilon)-\left(\frac{k_{\mathrm{B}}T}{\zeta}\right)\Phi_{2k}(\zeta)D_\Phi\int_0^\infty d\eta\left(-\frac{\partial f_0}{\partial\eta}\right)\eta\tilde{\boldsymbol{\varphi}}(\varepsilon), \tag{32}$$

where $\varepsilon=\zeta+\eta k_{\mathrm{B}}T$ and $D_\Phi=\zeta(d/d\varepsilon)[\ln(\Phi_{2k}(\varepsilon))]_{\varepsilon=\zeta}$. To zeroth order in the degeneracy parameter, the second term in Eq. (32) can be neglected and thus the expression for $\boldsymbol{\varphi}_0(\zeta)$ is found simply as

$$\boldsymbol{\varphi}_0(\zeta)=-\frac{en_{\mathrm{e}}\Gamma}{(1-\Gamma)}\left(\mathbf{E}+\frac{k_{\mathrm{B}}}{e}A_{\mathrm{ph}}(\zeta)\nabla T\right), \tag{33}$$

where $\Gamma=\tau_{\mathrm{F}}\Phi_{2k_F}(\zeta)$ is a parameter characterizing the degree of influence of the nonequilibrium state of the electrons via the phonons on the electron distribution function. It is equal to the ratio of the electron collision time to the time it takes the momentum transferred by the electrons to the phonons to be returned to the electron subsystem. Solution (33) in fact corresponds to the approximation adopted in Ref. 11.

To find the solution of Eq. (32) to first order in the degeneracy parameter, we substitute expression (31) in expression (32) and integrate over η. As a result, we obtain an algebraic equation for the function $\boldsymbol{\varphi}(\zeta)$, the solution of which has the form

$$\boldsymbol{\varphi}(\zeta)=\left(\boldsymbol{\varphi}^{(1)}(\zeta)-\left(\frac{k_{\mathrm{B}}T}{\zeta}\right)J_1\Gamma^2 D_\Phi n_{\mathrm{e}}\mathbf{\Phi}_1(\zeta)\right)\left[1-\Gamma+\left(\frac{k_{\mathrm{B}}T}{\zeta}\right)\Gamma D_\Phi[J_1\Gamma+\ln 2]\right]^{-1}, \tag{34}$$

$$J_1=\int_{-\infty}^{\infty}d\eta\left(-\frac{\partial f_0}{\partial\eta}\right)f_1(\eta)\cong 0.31,$$

$$\left(-\frac{\partial f_0}{\partial\eta}\right)=\frac{\exp(\eta)}{(\exp(\eta)+1)^2},$$

$$\begin{aligned}\boldsymbol{\varphi}^{(1)}(\zeta)&=n_{\mathrm{e}}\int_{-\infty}^{\infty}d\eta\left(-\frac{\partial f_0}{\partial\eta}\right)\Phi_{2k}(\varepsilon)\tau(\varepsilon)\mathbf{\Phi}_1(\varepsilon)\\&\quad+\left(\frac{k_{\mathrm{B}}T}{\zeta}\right)n_{\mathrm{e}}\Phi_{2k}(\zeta)D_\Phi\int_0^{\infty}d\eta\left(-\frac{\partial f_0}{\partial\eta}\right)\eta\tau(\varepsilon)\mathbf{\Phi}_1(\varepsilon)\\&=-en_{\mathrm{e}}\Gamma\left\{\left(\mathbf{E}+\frac{k_{\mathrm{B}}}{e}A_{\mathrm{ph}}(\zeta)\nabla T\right)\left[1-\left(\frac{k_{\mathrm{B}}T}{\zeta}\right)D_\Phi\ln 2\right]\right.\\&\quad\left.+\frac{\pi^2}{3}\frac{k_{\mathrm{B}}}{e}\left(\frac{k_{\mathrm{B}}T}{\zeta}\right)D_3\nabla T\right\},\end{aligned} \tag{35}$$

where $D_3=\zeta(d/d\varepsilon)[\ln(m(\varepsilon)\tau(\varepsilon)\Phi_{2k}^{1/2})]_{\varepsilon=\zeta}$. The solution of the equation for the function $\boldsymbol{\varphi}^{>}(\zeta)$ is found analogously as above: we substitute expression (31) into expression (25) and integrate over η. As a result, we obtain an algebraic equation, whose solution can be represented in the form

$$\begin{aligned}\boldsymbol{\varphi}^{>}(\zeta)&=\left\{\boldsymbol{\varphi}^{(1)>}(\zeta)+\tau_{\mathrm{F}}\boldsymbol{\varphi}(\zeta)\left[\frac{1}{2}+\left(\frac{k_{\mathrm{B}}T}{\zeta}\right)(2\ln 2D_4\right.\right.\\&\quad\left.-J_1D_\Phi\Gamma)\right]-\left(\frac{k_{\mathrm{B}}T}{\zeta}\right)n_{\mathrm{e}}\tau_{\mathrm{F}}\Gamma D_\Phi\left[\frac{1}{2}J_1\mathbf{\Phi}_1(\zeta)\right.\\&\quad\left.\left.+J_2(-k_{\mathrm{B}}\nabla T)\right]\right\}\left(1-\left(\frac{k_{\mathrm{B}}T}{\zeta}\right)\ln 2\Gamma D_\Phi\right)^{-1},\end{aligned}$$

$$\begin{aligned}\boldsymbol{\varphi}^{(1)>}(\zeta)&=-\frac{1}{2}en_{\mathrm{e}}\tau_{\mathrm{F}}\left\{\mathbf{E}+\frac{k_{\mathrm{B}}}{e}\left(A_{\mathrm{ph}}(\zeta)+2\ln 2\right.\right.\\&\quad\left.+\frac{\pi^2}{3}\left(\frac{k_{\mathrm{B}}T}{\zeta}\right)D_5\right)\nabla T+2\ln 2\left(\frac{k_{\mathrm{B}}T}{\zeta}\right)\\&\quad\left.\times\left[\mathbf{E}D_5+\frac{k_{\mathrm{B}}}{e}A_{\mathrm{ph}}D_A\nabla T\right]\right\},\end{aligned}$$

$$J_2=\int_0^{\infty}d\eta\left(-\frac{\partial f_0}{\partial\eta}\right)f_2(\eta)\cong 0.11,$$

$$D_4=\zeta\frac{d}{d\varepsilon}\left[\ln\left(\left(\frac{m(\varepsilon)}{k(\varepsilon)}\right)^3\tau(\varepsilon)\right)\right]_{\varepsilon=\zeta},$$

$$D_5=\zeta\frac{d}{d\varepsilon}[\ln(m(\varepsilon)\tau(\varepsilon))]_{\varepsilon=\zeta}. \tag{36}$$

To zeroth order in the degeneracy parameter we have

$$\begin{aligned}\boldsymbol{\varphi}_0^{>}(\zeta)&=-\frac{1}{2}en_{\mathrm{e}}\tau_{\mathrm{F}}\left\{\left(\mathbf{E}+\frac{k_{\mathrm{B}}}{e}A_{\mathrm{ph}}(\zeta)\nabla T\right)(1-\Gamma)^{-1}\right.\\&\quad\left.+2\ln 2\frac{k_{\mathrm{B}}}{e}\nabla T\right\}.\end{aligned} \tag{36a}$$

Substituting expressions (34)–(36) into expression (31) gives the solution of the integral equation for the function $\boldsymbol{\varphi}(\varepsilon)$, which is valid in the linear approximation in the degeneracy parameter. This solution allows us to calculate fluxes and to analyze the dependence of the kinetic coefficients on the temperature both in the case of weak $(\Gamma\ll 1)$ and strong $(\Gamma\to 1)$ mutual entrainment of the electrons and phonons.

First of all, let us calculate the charge flux $\mathbf{j}_2$ due to the nonequilibrium correction to the electron distribution function $\delta f_{\mathbf{k}}^{(2)}$. Substituting expression (31) into Eq. (23), it is not hard to convince oneself that in the linear approximation in $k_{\mathrm{B}}T/\zeta$ only the symmetric part of the function $\boldsymbol{\varphi}(\varepsilon)$ contributes to the charge flux $\mathbf{j}_2$. Carrying out the integration over η, we obtain

$$\begin{aligned}\mathbf{j}_2&=\sigma_{xx}^0\Gamma\left\{\left(\mathbf{E}+\frac{k_{\mathrm{B}}}{e}A_{\mathrm{ph}}(\zeta)\nabla T\right)\left[1-\left(\frac{k_{\mathrm{B}}T}{\zeta}\right)D_\Phi\right.\right.\\&\quad\left.\left.\times(\ln 2+J_1(1+\Gamma))\right]+\frac{\pi^2}{3}\frac{k_{\mathrm{B}}}{e}\left(\frac{k_{\mathrm{B}}Y}{\zeta}\right)D_5\nabla T\right\}\\&\quad\times\left(1-\Gamma+\left(\frac{k_{\mathrm{B}}T}{\zeta}\right)\Gamma D_\Phi[J_1\Gamma+\ln 2]\right)^{-1}.\end{aligned} \tag{37}$$

Expression (37) enables us to investigate the exotic case of total mutual entrainment of the electrons and phonons,[5] where both the electron and the phonon drift velocities are so close that the inequality $1-\Gamma\ll k_{\mathrm{B}}T/\zeta$ is satisfied. In this case the current $\mathbf{j}_2$ is larger than the current $\mathbf{j}_1$ by a factor of $\zeta/k_{\mathrm{B}}T$, and the resistance of the metal is proportional to T^6 if we ignore the temperature dependence of D_Φ. However, a detailed analysis of this asymptotic limit requires separate study. For the more realistic case in which $(k_{\mathrm{B}}T/\zeta)\ll 1-\Gamma$, expanding the denominator in the small parameter we find

$$\begin{aligned}\mathbf{j}_2&=\frac{\sigma_{xx}^0\Gamma}{1-\Gamma}\left\{\left(\mathbf{E}+\frac{k_{\mathrm{B}}}{e}A_{\mathrm{ph}}(\zeta)\nabla T\right)\left[1-\left(\frac{k_{\mathrm{B}}T}{\zeta}\right)D_\Phi C_\Gamma\right]\right.\\&\quad\left.+\frac{\pi^2}{3}\frac{k_{\mathrm{B}}}{e}\left(\frac{k_{\mathrm{B}}Y}{\zeta}\right)D_3\nabla T\right\},\\C_\Gamma&=(\ln 2+J_1)(1-\Gamma)^{-1}\cong 1/(1-\Gamma).\end{aligned} \tag{38}$$

Here $\Gamma\ll 1$, the current $\mathbf{j}_2\ll\mathbf{j}_1$, and mutual entrainment effects can be neglected. As the parameter Γ increases, the role of the current $\mathbf{j}_2$ grows and for $\Gamma>1/2$ $|\mathbf{j}_2|>|\mathbf{j}_1|$. In this case, neglecting mutual entrainment effects leads to qualitatively invalid results in the interpretation of the experimental data.

As can be seen from relation (38), the drift current (proportional to the electric field intensity **E**) and the entrainment current (proportional to $A_{\mathrm{ph}}\nabla T$) renormalize in the same way due to the influence of the nonequilibrium state of the electrons on the phonon subsystem. The last term in Eq. (38) is a correction to the diffusion current. Combining results (16) and (38), we obtain for the kinetic coefficients σ_{xx} and β_{xx}

$$\sigma_{xx}=\tilde{\sigma}_{xx}\left\{1-\left(\frac{k_{\mathrm{B}}T}{\zeta}\right)\Gamma D_{\Phi}C_{\Gamma}\right\}, \tag{39}$$

$$\beta_{xx}=-\tilde{\sigma}_{xx}\frac{k_{\mathrm{B}}}{e}\left\{A_{\mathrm{ph}}(\zeta)\left[1-\Gamma\left(\frac{k_{\mathrm{B}}T}{\zeta}\right)D_{\Phi}C_{\Gamma}\right]+\frac{\pi^2}{3}\left(\frac{k_{\mathrm{B}}T}{\zeta}\right)\times(D_1+\Gamma(D_3-D_1))\right\}, \tag{40}$$

where $\tilde{\sigma}_{xx}=\sigma^0_{xx}(1-\Gamma)^{-1}=e^2n_{\mathrm{e}}\tilde{\tau}_{\mathrm{F}}/m_{\mathrm{F}}$, and $\tilde{\tau}_{\mathrm{F}}=\tau_{\mathrm{F}}(1-\Gamma)^{-1}=\tilde{\nu}_{\mathrm{e}}^{-1}$ is the renormalized relaxation time of the electrons. It is not difficult to convince oneself that

$$\tilde{\nu}_{\mathrm{e}}=\nu_{\mathrm{ei}}+\nu_{\mathrm{eph}}-\Phi_{2k_{\mathrm{F}}}=\nu_{\mathrm{ei}}+\tilde{\nu}_{\mathrm{eph}},$$

$$\tilde{\nu}_{\mathrm{eph}}=\sum_{\lambda}\left\langle \nu^{\lambda}_{\mathrm{eph}}(k_{\mathrm{F}},q)\left(1-\frac{\nu^{\lambda}_{\mathrm{phe}}(q)}{\nu^{\lambda}_{\mathrm{ph}}(q)}\right)\right\rangle_{z^{\lambda}_{2k_{\mathrm{F}}}}. \tag{41}$$

It follows from (39) that the mutual influence of the nonequilibrium state of the electrons and phonons leads to the appearance of terms linear in the degeneracy parameter in the expression for the electrical conductivity. To zeroth order in this parameter the electrical conductivity $\sigma_{xx}=\tilde{\sigma}_{xx}$, which differs from the expression found in Ref. 11 by separating out the contributions of the longitudinal and transverse phonons and by a more rigorous averaging of the phonon relaxation frequencies entering into the function $\Phi_{2k_{\mathrm{F}}}$.

The renormalized relaxation frequency of the electron by phonons $\tilde{\nu}_{\mathrm{eph}}$ differs from that given in Ref. 15 only in the separation of contributions of the transverse and longitudinal phonons. As can be seen from Eqs. (41), mutual exchange of momenta between the electron and phonon subsystems leads to a decrease of the effective relaxation frequency of the electrons by phonons $\tilde{\nu}_{\mathrm{eph}}$. This renormalization can be important if for actual phonon wave vectors the fraction of the phonon momentum transferred to the electron subsystem and proportional to the ratio $\nu^{\lambda}_{\mathrm{phe}}(q)/\nu^{\lambda}_{\mathrm{ph}}(q)$ is not too small. However, for this effect to have a noticeable effect on the electron mobility it is necessary that the fraction of the electron momentum transferred to the phonon subsystem and proportional to the ratio $\nu_{\mathrm{eph}}/\nu_{\mathrm{e}}$ also not be too small, i.e., the electron relaxation frequency on the phonons should be comparable to the electron relaxation frequency on the impurities.

Let us now consider what effect mutual entrainment has on the thermal electromotive force of a degenerate conductor. Figure 2 shows a diagram illustrating the generation of a thermal voltage in semiconductors. The thermal voltage is found from the condition $j_x=j_{\mathrm{dr}}+j_{\mathrm{dif}}+j_{\mathrm{drag}}=0$; therefore, it follows from Eqs. (21), (39), and (40) that

$$\alpha=-\frac{k_{\mathrm{B}}}{e}\left\{A_{\mathrm{ph}}+\frac{\pi^2}{3}\left(\frac{k_{\mathrm{B}}T}{\zeta}\right)(D_1+\Gamma(D_3-D_1))\right\}=\alpha_{\mathrm{ph}}+\alpha_{\mathrm{dif}}. \tag{42}$$

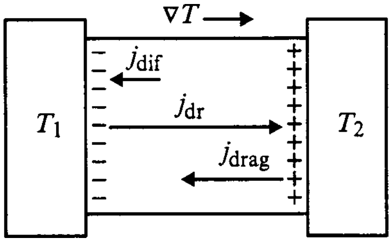

FIG. 2. Diagram illustrating the formation of a thermal voltage in conductors. j_{dif} — Diffusion current, j_{dr} — drift current, j_{drag} — the current due to phonon entrainment.

The first two terms in expression (42) were obtained using the standard theory,[3] the third term inside the braces, which is proportional to Γ, is due to the influence of the nonequilibrium state of the electrons on the phonon subsystem. First of all, note that, as can be seen from (38), the drift current and the entrainment current due to the influence of the nonequilibrium state of the electrons on the phonon subsystem renormalize in the same way; therefore, the contribution of phonon entrainment to the thermal voltage α_{ph} does not renormalize. The appearance of a correction from mutual entrainment to the diffusion component of the thermal voltage is also physically clear. Since the thermal voltage is found from the condition $j_x=0$, the mean velocity of ordered motion of the electrons is zero. Therefore, momentum transfer from the electrons to the phonon subsystem (Fig. 3) occurs due to the dependence of the effective mass, the electron quasimomentum, and the scattering parameters on the electron energy in the vicinity of the Fermi level, i.e., this contribution should be proportional to $k_{\mathrm{B}}T/\zeta$ and to the derivatives of the enumerated parameters in the electron energy.

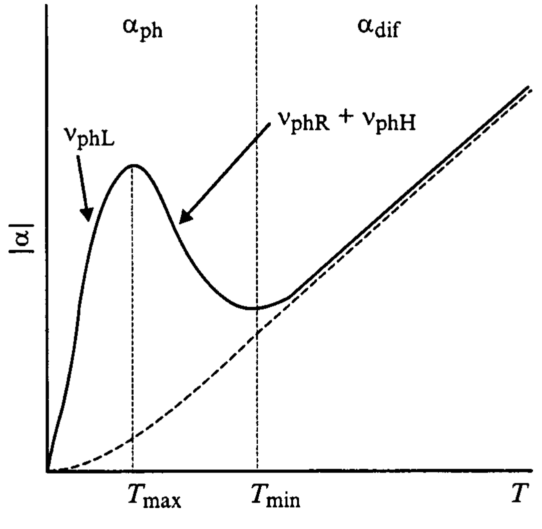

FIG. 3. Typical dependence of the thermal voltage of a degenerate semiconductor on the temperature. The dashed vertical line to the right divides off the temperature region where the phonon entrainment contribution dominates ($T<T_{\min}$) from the region where the diffusion contribution dominates ($T>T_{\min}$).

This also follows from Eq. (42). It may be noted that, in their calculation of the thermal voltage, the authors of Refs. 11 and 12 limited themselves to the zeroth approximation in the degeneracy of the electron gas; therefore, the diffusion contribution to the thermal voltage, and also the contribution of mutual entrainment, completely fell out of their treatment. As a rule, for degenerate semiconductors with a large concentration of charged defects the contribution to the thermal voltage due to mutual entrainment is small by virtue of the smallness of the parameter Γ; however, for semimetals its contribution can be considerable. It can be definitely stated that, in the temperature region (Fig. 3) where the contribution of phonon entrainment dominates, $|\alpha_{\mathrm{ph}}| \gg \alpha_{\mathrm{dif}}$, the term proportional to Γ can be neglected in practically all the calculations. However, in the calculation of the kinetic coefficients (in particular, β_{xx}) in a rigorous theory, this term must be kept. In the opposite case, it will not be possible to satisfy the Onsager relations for the kinetic coefficients.[10]

The heat flux $\mathbf{W}_{\mathrm{e}}^{(2)}$ was calculated analogous to the calculation of the current $\mathbf{j}^{(2)}$. We substitute expression (31) in Eq. (23) and integrate over η, restricting the calculation to the linear approximation in the degeneracy parameter

$$\mathbf{W}_{\mathrm{e}}^{(2)} = -L_0 T \tilde{\sigma}_{xx} \Gamma \left(\frac{k_{\mathrm{B}}T}{\zeta}\right) \left\{ \frac{e}{k_{\mathrm{B}}} \mathbf{E} D_3 + [D_3 A_{\mathrm{ph}} - (1-\Gamma) D_{\Phi} C_2] \nabla T \right\},$$

$$J_3 = \int_0^{\infty} d\eta \left(-\frac{\partial f_0}{\partial \eta}\right) \eta f_2(\eta) \cong 0.381,$$

$$C_2 = \ln 2 - \frac{3}{\pi^2} J_3 \cong 0.577. \tag{43}$$

From (17) and (43) we find for the heat flux

$$\mathbf{W}_{\mathrm{e}} = -L_0 \tilde{\sigma}_{xx} T \left\{ \frac{eT}{\zeta} (D_1 + \Gamma(D_3 - D_1)) \mathbf{E} + \left[(1-\Gamma) \left(1 + \left(\frac{k_{\mathrm{B}}T}{\zeta}\right) D_{\Phi} C_2 \right) + \left(\frac{k_{\mathrm{B}}T}{\zeta}\right) \times \{ A_{\mathrm{ph}} (D_2 + \Gamma(D_3 - D_2)) \} \right] \nabla T \right\}. \tag{44}$$

Comparing the kinetic coefficients in the fluxes $\mathbf{j}$ and $\mathbf{W}_{\mathrm{e}}$, one can convince oneself that the Onsager relation for these two fluxes is not satisfied. It is necessary to take into account the heat flux $\mathbf{W}_{\mathrm{phe}}^{(2)}$ communicated by the phonons but due to the nonequilibrium contribution to the electron distribution function, $\delta f_{\mathbf{k}}^{(2)}$.

In this approximation the heat flux $\mathbf{W}_{\mathrm{phe}}^{(2)}$ is expressed in terms of the current $\mathbf{j}_2$ as follows: $\mathbf{W}_{\mathrm{phe}}^{(2)} = -\frac{k_{\mathrm{B}}}{e} T A_{\mathrm{ph}}(\zeta) \mathbf{j}_2$. As a result, we obtain for the flux $\mathbf{W}_{\mathrm{phe}}$

$$\mathbf{W}_{\mathrm{phe}} = -\frac{k_{\mathrm{B}}T}{e} \tilde{\sigma}_{xx} A_{\mathrm{ph}}(\zeta) \left\{ \left(\mathbf{E} + \frac{k_{\mathrm{B}}}{e} A_{\mathrm{ph}}(\zeta) \nabla T \right) \left[1 - \Gamma D_{\Phi} \times \left(\frac{k_{\mathrm{B}}T}{\zeta}\right) C_{\Gamma} \right] + \frac{\pi^2}{3} \left(\frac{k_{\mathrm{B}}T}{\zeta}\right) (D_A + \Gamma(D_3 - D_A)) \nabla T \right\}. \tag{45}$$

As in the analysis of the contribution $\mathbf{W}_{\mathrm{phe}}^{(1)}$, we include the drift and diffusion components of the heat flux $\mathbf{W}_{\mathrm{phe}}$ in the electronic heat flux. The term proportional to $A_{\mathrm{ph}}(\zeta)\nabla T$ in Eq. (45) is a consequence of the effect of entrainment of electrons by phonons. Therefore, it should be included in the phonon heat flux. As a result of this assignment, the expressions for the kinetic coefficients take the form

$$\gamma_{xx} = T \beta_{xx},$$

$$\kappa_{\mathrm{ph}} = \sum_{\lambda} \frac{k_{\mathrm{B}} s_{\lambda}^2 q_T^3}{6\pi^2} \int_0^{z_d^{\lambda}} dz_q^{\lambda} (z_q^{\lambda})^4 N_{q\lambda}^0 (N_{q\lambda}^0 + 1) \left\{ 1 + \frac{\nu_{\mathrm{phe}}^{\lambda}(z)}{\nu_{\mathrm{e}}(\zeta)} \frac{k_{\mathrm{B}}T}{s_{\lambda}^2} A_{\mathrm{ph}}(\zeta) \left[1 - \left(\frac{k_{\mathrm{B}}T}{\zeta}\right) D_{\Phi} \Gamma C_{\Gamma} \right] \right\},$$

$$\kappa_{xx}^{e} = L_0 \tilde{\sigma}_{xx} T \left\{ (1-\Gamma) \left[1 + \left(\frac{k_{\mathrm{B}}T}{\zeta}\right) D_{\Phi} \Gamma C_2 \right] + \left(\frac{k_{\mathrm{B}}T}{\zeta}\right) A_{\mathrm{ph}}(\zeta) [D_2 + D_A + \Gamma(2D_3 - D_2 - D_A)] \right\}, \tag{46}$$

where β_{xx} is given by (40). Thus, we have shown by direct calculation that the Onsager relations for the critical coefficients γ_{xx} and β_{xx} are fulfilled if the mutual influence of the nonequilibrium state of the electrons and phonons is taken into account. This supports the claim that our method enables one to take correct account of effects of mutual entrainment of electrons and phonons in the calculation of the kinetic coefficients of degenerate conductors. Note that we have not made use of the assumption of smallness of the parameter Γ characterizing the degree of mutual entrainment.

The electronic thermal conductivity is usually found by setting $j_x = 0$. In this case the electronic heat flux is proportional to the temperature gradient

$$\mathbf{W}_{\mathrm{e}} = -\kappa_{\mathrm{e}} \nabla T, \quad \kappa_{\mathrm{e}} = \kappa_{xx}^{e} - T \beta_{xx} \alpha. \tag{47}$$

From relations (46), (40), and (42) we find that

$$\kappa_{\mathrm{e}} = L_0 \tilde{\sigma}_{xx} T \left\{ (1-\Gamma) \left[1 + \left(\frac{k_{\mathrm{B}}T}{\zeta}\right) (D_{\Phi} \Gamma C_2 + A_{\mathrm{ph}}(\zeta)(D_2 + D_A - 2D_1)) \right] - \frac{3}{\pi^2} A_{\mathrm{ph}}^2(\zeta) \left[1 - \Gamma \left(\frac{k_{\mathrm{B}}T}{\zeta}\right) D_{\Phi} C_2 \right] \right\}. \tag{48}$$

In conclusion, we note that for the total thermal conductivity $\kappa = \kappa_{\mathrm{ph}} + \kappa_{\mathrm{e}}$ the interference contribution, proportional to $(A_{\mathrm{ph}})^2$, cancels out

$$\kappa=\kappa_{\mathrm{ph}}^{0}+L_{0}\sigma_{xx}^{0}T\left\{1+\left(\frac{k_{\mathrm{B}}T}{\zeta}\right)\left[D_{\Phi}\Gamma C_{2}+A_{\mathrm{ph}}(\zeta)(D_{2}+D_{A}-2D_{1})\right]\right\}. \qquad (49)$$

This is a consequence of the fact that the increase in the phonon thermal conductivity due to the momentum transferred from the electrons to the phonons is completely canceled out thanks to the reverse process. As can be seen from a comparison of expressions (39) and (48), the Wiedemann–Franz relation is not fulfilled because of the effect of electron entrainment by phonons A_{ph} and the influence of the nonequilibrium state of the electrons on the phonon subsystem (characterized by the parameter Γ). In the elastic scattering approximation ($A_{\mathrm{ph}}=0$ and $\Gamma=0$) the Wiedemann–Franz relation is fulfilled. From Eq. (48) it is possible to determine the effective Lorentz factor $L^{*}=L_{0}\kappa_{e}/\tilde{\sigma}_{xx}T$. It is equal to the expression in braces in formula (48), from which it can be seen that mutual entrainment effects can lead to a substantial decrease in the effective Lorentz factor at low temperatures.

To summarize, a method has been developed for calculating the kinetic coefficients of degenerate conductors which takes account of the mutual influence of the nonequilibrium state of the electron and phonon subsystems. The influence of the mutual entrainment of electrons and phonons on the electrical conductivity, thermal voltage, and thermal conductivity of degenerate conductors has been analyzed in the linear approximation in the degeneracy parameter. Important physical aspects of the theory of electron–phonon entrainment have also been considered, which heretofore had not received sufficient attention. First of all, the drift and diffusion contributions and the contributions of electron entrainment by phonons were isolated in the heat and charge fluxes, and the renormalization of each of these contributions associated with mutual entrainment of electrons and phonons was considered. This made it possible to establish that only the diffusion contribution to the thermal voltage is renormalized due to the mutual entrainment effect. Second, the heat flux conveyed by the phonons but due to the nonequilibrium state of the electrons was analyzed in detail. In it, as in the electron fluxes, we isolated the contributions due to drift, diffusion, and the entrainment effect. We found that this flux leads to renormalization of both the electron and the phonon thermal fluxes. We showed that a necessary condition for the satisfaction of the microscopic Onsager reversibility relations is that the contribution of this flux to the total electronic heat flux must be taken into account.

For future work it is proposed to generalize the method developed here to take account of a magnetic field and to consider the influence of the nonequilibrium state of the electrons and phonons on thermomagnetic effects, such as the longitudinal and transverse Nernst–Ettinghausen effects. Thermomagnetic effects are much finer indicators of scattering mechanisms of current carriers in semiconductors than is the mobility[2]: whereas the mobility varies only in magnitude in response to changes in the current-carrier scattering mechanism, thermomagnetic effects can alter its sign. Therefore, there are grounds to assume that mutual entrainment of electrons and phonons can give a significant contribution to these effects. As an application of the theory developed in this paper, I will consider the thermal voltage and thermal conductivity of HgSe and HgSe : Fe crystals, in which peculiarities due to electron–phonon entrainment are most strikingly manifested.[16,17]

The author expresses his gratitude to I. Yu. Arapova for helpful remarks and assistance in preparing the manuscript, and to A. P. Tankeev and V. I. Okulov for discussions of the results of this work.

This work was carried out with the support of INTAS (Grant No. 93-3657 EXT).

*)E-mail: kuleev@imp.uran.ru

---

[1] É. L. Gurevich, Zh. Éksp. Teor. Fiz. **16**, 193 (1946); **16**, 416 (1946).

[2] I. M. Tsidil'kovskiĭ, *Thermomagnetic Effects in Semiconductors* (Academic Press, New York, 1962).

[3] V. M. Askerov, *Electron Transport Phenomena in Semiconductors* (Nauka, Moscow, 1985).

[4] F. J. Blatt, P. A. Schroeder, C. A. Foiles, and D. Greig, *Thermoelectric Power of Metals* (Plenum Press, New York, 1976).

[5] R. N. Gurzhi, Usp. Fiz. Nauk **94**, 689 (1968) [Sov. Phys. Usp. **94**, 255 (1968)]; R. N. Gurzhi and A. I. Kopeliovich, Usp. Fiz. Nauk **133**, 33 (1981) [Sov. Phys. Usp. **24**, 17 (1981)].

[6] P. S. Zyryanov and G. I. Guseva, Usp. Fiz. Nauk **95**, 565 (1968) [Sov. Phys. Usp. **11**, 538 (1968)]; R. T. Delves, Rep. Prog. Phys. **28**, *2*, 249 (1965).

[7] J. E. Parrott, Proc. Phys. Soc. London, Sect. B **70**, 590 (1957).

[8] J. Appel, Z. Naturforsch. A **12**, 410 (1957); **13**, 386 (1958).

[9] I. I. Hanna and E. H. Sondheimer, Proc. R. Soc. London, Ser. A **238**, 247 (1957).

[10] E. H. Sondheimer, Proc. R. Soc. London, Ser. A **234**, 391 (1956).

[11] É. L. Gurevich and I. Ya. Korenblit, Fiz. Tverd. Tela (Leningrad) **6**, 856 (1964) [Sov. Phys. Solid State **6**, 661 (1964)].

[12] I. G. Lang and S. T. Pavlov, Zh. Éksp. Teor. Fiz. **63**, 1495 (1972) [Sov. Phys. JETP **36**, 793 (1972)].

[13] H. P. R. Frederikse, Phys. Rev. **91**, 491 (1953).

[14] C. Herring, Phys. Rev. **96**, 1163 (1954).

[15] P. S. Zyryanov and M. I. Klinger, *Quantum Theory of Phenomena of Electron Transport in Crystalline Semiconductors* (Nauka, Moscow, 1976).

[16] I. M. Tsidilkovskii and I. G. Kuleyev, Semicond. Sci. Technol. **11**, 625 (1996).

[17] I. G. Kuleev, A. T. Lonchakov, I. Yu. Arapova, and G. I. Kuleev, Zh. Éksp. Teor. Fiz. **114**, 9 (1998) [JETP **87**, 106 (1998)].

Translated by Paul F. Schippnick

PHYSICS OF THE SOLID STATE VOLUME 41, NUMBER 10 OCTOBER 1999

Kinetics of photoluminescence decay of KCl–Yb

V. V. Pologrudov and Z. D. Ibragim

Irkutsk State University, 664003 Irkutsk, Russia

(Submitted January 22, 1999; accepted for publication February 18, 1999)
Fiz. Tverd. Tela (St. Petersburg) **41**, 1763–1765 (October 1999)

We have investigated the kinetics of the luminescence decay of a KCl–Yb crystal excited in one of the long-wavelength absorption bands of the Yb^{2+} ion by nitrogen laser radiation with a power density less than 10^3 W/cm^2. We found that, in both luminescence bands, both the one associated with the allowed transition (399 nm) and the one associated with the forbidden transition (430 nm), there are two stages of decay—an initial exponential stage that gives way to a hyperbolic stage. Non-exponential decay due to the optical electron tunneling back to the luminescence center is treated as evidence of delocalization of the electron upon intracenter excitation and is explained by the formation of an excimer-like molecular bond upon photoexcitation of the crystal. © *1999 American Institute of Physics.* [S1063-7834(99)00910-7]

In Refs. 1 and 2 it was found that, as a result of an $f-d$ transition in a Eu^{2+} ion in the lattice of an alkali-halide[1] or fluorite crystal,[2] the electron can delocalize without falling into the band states of the basis. The results of photoelectric measurements of another $f-d$ system—a KCl–Yb crystal—lead to the same conclusion.[3] In the present work, dedicated to a study of the kinetics of luminescence decay of KCl–Yb, this conclusion is confirmed.

1. EXPERIMENTAL PART

In this work we used KCl crystals containing 0.5% Yb. The luminescence was isolated with a UM-2 monochromator. The signal from the photomultiplier was fed either to a recording potentiometer or to an S8-11 storage oscilloscope. Luminescence was excited with an LGI-21 nitrogen laser ($\lambda = 337$ nm), whose power density did not exceed 10^3 W/cm^2. We used a phosphoroscope to record the late stages of decay ($>10^{-4}$ s), which enabled us to avoid overloading the photomultiplier with the light signal of the initial stage. The luminescence spectrum was corrected for the spectral sensitivity of the photomultiplier and the dispersion of the monochromator. No corrections were made to the excitation spectrum of the red luminescence. For the low-temperature measurements, the crystals were placed in a quartz dewar filled with liquid nitrogen.

2. RESULTS OF EXPERIMENTS

In the KCl–Yb crystal used in this study, the luminescence excited by the nitrogen laser at room temperature consisted of two bands located in the blue (~ 430 nm) and red (~ 650 nm) regions of the spectrum. The blue luminescence predominates, exceeding the red luminescence by more than an order of magnitude. In Refs. 4, 7, and 8 red luminescence of the same spectral composition was observed in x-irradiated crystals and identified with the luminescence of Yb^+ ions. In our experiments the red photoluminescence was recorded in crystals not subjected to irradiation. The excitation spectrum of the red centers is not associated with the main impurity absorption of the ytterbium ions (Fig. 1). The kinetics of the decay of the blue luminescence contains two stages: an initial exponential stage with decay constant $\tau = 315\,\mu$s, over the course of which the luminescence intensity falls by more than two orders of magnitude [Fig. 2a], and a non-exponential stage which follows it, extending into times of tens of seconds [Fig. 2b]. In this stage the decay is described by the empirical Becquerel formula $J = t^{-\alpha}$. For the blue luminescence $\alpha = 1.8$. In a crystal cooled to 77 K the decay constant τ grows to 1 ms and the luminescence intensity falls by a factor of ten during the exponential stage [Fig. 3a], the non-exponential component of the decay also slows down, and at low temperatures $\alpha = 0.49$ [Fig. 3b]. The red luminescence, whose excitation spectrum differs from the spectrum of the impurity absorption, does not contain an exponential component in its decay at room temperature. The exponent of the approximating hyperbola is equal to 1.4 for the red luminescence at room temperature.

At low temperatures, the two above-mentioned bands in the luminescence spectrum are joined by a luminescence band in the near ultraviolet with $\lambda_{\max} = 399$ nm. The initial stage of the decay of this luminescence is exponential with a time constant 2.5 μs and duration encompassing a decay of around one order of magnitude; the final stage is hyperbolic with the same exponent $\alpha = 0.49$ as for the blue band at this temperature [Figs. 4a and 4b].

3. DISCUSSION OF RESULTS

The luminescence characteristics of Yb^{2+} ions in alkali-halide crystals were studied in great detail by Kostenko (Ivakhnenko) and co-authors.[4–8] The luminescence spectra in KCl–Yb, KBr–Yb, and KI–Yb contain two bands, one of which is located in the near ultraviolet (~ 399 nm for KCl and KBr) or in the violet (413 nm for KI–Yb), and the other in the blue (see, e.g., Ref. 5). The ultraviolet bands in KCl and KBr are completely extinguished at room temperature. In the case of the phosphor KI–Yb it was concluded that the luminescence decay time in the case of the short-wavelength

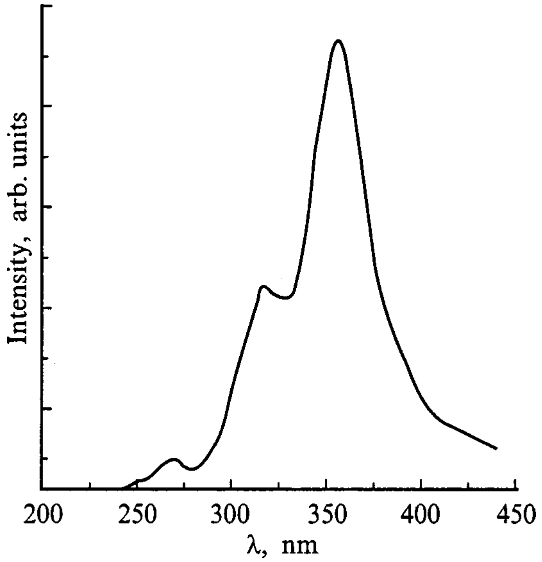

FIG. 1. Excitation spectrum of red luminescence ($\lambda = 650$ nm).

band is quite short ($\tau < 5\ \mu$s). A comparison with the results for the system SrCl$_2$–Yb^{2+} (Refs. 9 and 10) links this band with the allowed transition $A_{lg} - T_{lu}$ of the Yb^{2+} ion in a field with symmetry O_h. For the long-wavelength luminescence band, on the other hand, a complicated form of the decay curves is noted. The author of Ref. 5 comes to the conclusion that the decay curve is composed of two components, the more extended of which is located in the millimeter region. The short component of the long-wavelength band at room temperature is counted in tens of microseconds, and this band is identified with the forbidden transition from the two neighboring levels T_{2u} and E_u or from one of them. In regard to KCl–Yb, this is the 430-nm band, the decay constant of which according to our measurements ($315\ \mu$s at room temperature) corresponds exactly to the characteristics of the forbidden transition. The value we measure for the time constant of the initial exponential stage of decay of the short-wavelength luminescence of KCl–Yb ($2.5\ \mu$s) supports the conclusion of previous authors about the nature of this band. The non-exponential components of luminescence decay were not previously recorded. As can be seen from the presented results, none of the observed occurrences of luminescence of KCl–Yb upon photoexcitation are completely described by an exponential decay—neither at room temperature, nor at lower temperatures.

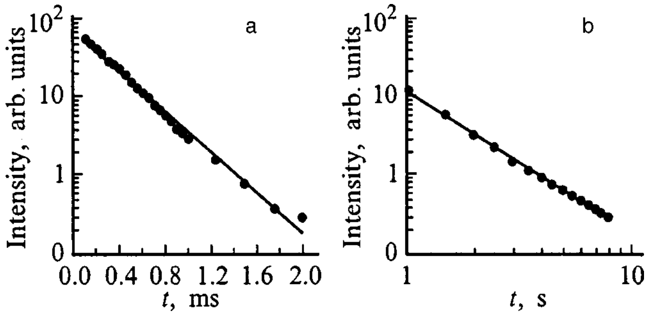

FIG. 2. Luminescence decay of KCl–Yb (0.5%) at 300 K in the 430-nm luminescence band: a—initial exponential stage, b—final ‘‘hyperbolic’’ stage.

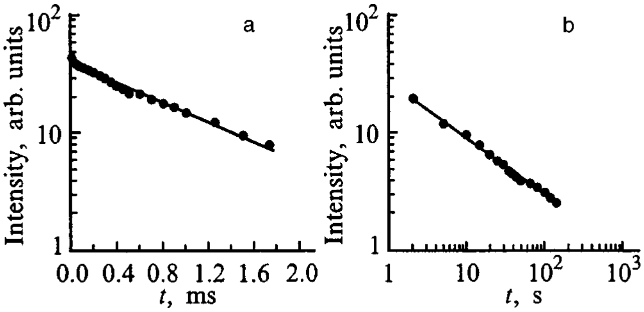

FIG. 3. Luminescence decay of KCl–Yb (0.5%) at 77 K in the 430-nm luminescence band: initial (a) and final (b) stage.

Luminescence decay obeying a hyperbolic law with a power other than 2 is not characteristic of an intracenter process, nor of a recombination process with participation of band states of the charge carriers. Such a time dependence is characteristic of a tunneling process and can be considered as evidence that the electron tunnels back to the radiative state. A theoretical treatment of tunneling does not lead to simple analytical expressions; nevertheless, the possibility of analysis exists since the theoretical decay curves are approximated by hyperbolas, which are characteristic of the Becquerel law.[1] The decrease in the power of the hyperbola α upon cooling can be a consequence of the fact that upon cooling the electron populates the lower vibrational state of the trap, the probability of tunneling from which (the lower state) is less. The same value of the power of the hyperbola α for the blue and ultraviolet luminescence may be considered as evidence that the same tunneling transition of the electron from the capture center to the luminescence center is responsible for both luminescence bands, as is confirmed by the fact that both bands belong to one center. The significant temporal extent of the exponential component of the blue luminescence is obviously due to the fact that the lifetime of the electron in the radiative excited state is longer than the tunneling transition time and thus, in the initial stage of the decay, tunneling transitions whose duration is less than the decay constant are hidden by the exponential component.

The weak red luminescence we recorded at room temperature, coincident with the spectrum of the Yb$^+$ centers,

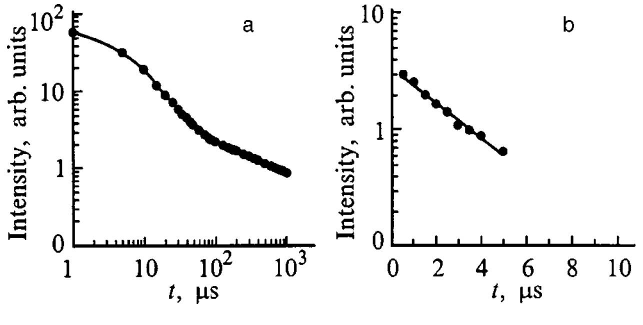

FIG. 4. Luminescence decay of KCl–Yb (0.5%) at 77 K in the 399-nm luminescence band: initial (a) and final (b) stage.

may be due to luminescence centers whose composition includes univalent ytterbium but with a different charge compensation from the case of the x-ray induced Yb^{+} centers investigated in Refs. 4, 7, and 8. However, the completely different excitation region of this luminescence in comparison with the excitation of the induced centers (430 nm, Ref. 7) gives preference to the variant of ''defective'' centers, which in one form or another include the ytterbium ion. An important aspect of the problem in this case is not so much the structure of the centers as the presence of nonexponential decay of centers excited not far away in their short-wavelength absorption band (Fig. 1). The concentration of these centers is substantially smaller than the concentration of the main centers (their presence in the crystal is not reflected in the absorption spectrum), which is in complete agreement (see, e.g., Refs. 11 and 12) with the absence of an exponential component of the decay.

Obviously, the described phenomena are determined by the interaction of spatially separated defects as a result of excitation in the impurity absorption bands.

The presence of tunneling decay reveals another fundamentally important side of the phenomenon, namely that return of the electron is preceded by its rapid transport to the capture center due to intracenter excitation of the activator. Capture of the electron by a trap as a result of activator excitation is also dramatically displayed in photoelectric measurements.[3]

Thus, noteworthy here is the conclusion that the presence of rapid electron transport which originates from a state far from the bottom of the conduction band (in this case excitation takes place in one of the long-wavelength bands) and may be considered as evidence of the formation during excitation of a short-lived single-electron excimer-like molecular bond between spatially separated defects—an excited ion and an electron capture center.[1,2,11,12]

[1] V. V. Pologrudov and E. N. Karnaukhov, Fiz. Tverd. Tela (Leningrad) **31**, 179 (1989) [Sov. Phys. Solid State **31**, 275 (1989)].

[2] V. V. Pologrudov and G. I. Kalinovskiĭ, Fiz. Tverd. Tela (Leningrad) **34**, 2988 (1992) [Sov. Phys. Solid State **34**, 1602 (1992)].

[3] V. V. Pologrudov, Z. D. Ibragim, and E. V. Mal'chukova, in *Proceedings of the Fourth All-Russia School ''Luminescence and Associated Phenomena,''* Irkutsk (1999), p. 25.

[4] S. S. Ivakhnenko, P. S. Ivakhnenko, I. A. Parfianovich, and E. I. Shuraleva, in *Physics of the Condensed State of Matter*, Khabarovsk (1977), p. 48.

[5] S. S. Ivakhnenko, in *Physics of the Condensed State of Matter* (Khabarovsk, 1977), p. 35.

[6] E. I. Shuraleva, S. S. Ivakhnenko, and P. S. Ivakhnenko, in *Physics of the Condensed State of Matter* (Khabarovsk, 1977), p. 57.

[7] C. C. Kostenko, E. I. Shuraleva, and P. S. Ivakhnenko, in *Physics of the Condensed State of Matter* (Khabarovsk, 1977), p. 68.

[8] S. Kostenko, Author's Abstract of Candidate's Dissertation, Sverdlovsk (1980).

[9] T. S. Piper, J. P. Brown, and D. S. McClure, J. Chem. Phys. **46**(4), 1353 (1967).

[10] H. Witzke, D. MacClure, and B. Mitchell, Izv. Akad. Nauk SSSR, Ser. Fiz. **34**(4), 705 (1973).

[11] V. V. Pologrudov and E. N. Karnaukhov, Fiz. Tverd. Tela (Leningrad) **23**, 3033 (1981) [Sov. Phys. Solid State **23**, 1769 (1981)].

[12] V. V. Pologrudov and E. N. Karnaukhov, Fiz. Tverd. Tela (Leningrad) **27**, 1380 (1985) [Sov. Phys. Solid State **27**, 833 (1985)].

Translated by Paul F. Schippnick

The influence of elastic stress fields on ionic transport through a ⟨superionic crystal⟩–⟨electrode⟩ heterojunction

S. I. Bredikhin and M. V. Bogatyrenko

Institute of Solid State Physics, Russian Academy of Sciences, 142432 Chernogolovka, Moscow District, Russia

(Submitted March 12, 1999)
Fiz. Tverd. Tela (St. Petersburg) **41**, 1766–1771 (October 1999)

The appearance of a current in an external circuit has been observed upon elastic deformation of a local region of the superionic crystal $RbAg_4I_5$. The dependence of the magnitude and sign of the deformation current on the region of application of the local load on the sample is examined, and the temporal characteristics of the processes are investigated. The influence of an elastic deformation on processes taking place at the ⟨superionic crystal⟩–⟨electrode⟩ heterojunction is investigated, and a mechanism of generation of the deformation current is proposed. The generation of photostimulated currents upon illumination of a local region of the superionic conductor by light corresponding to intracenter excitation of optically active centers is considered. It is shown that the elastic stress fields arising around photoexcited centers are responsible for the generation of photostimulated currents. © *1999 American Institute of Physics.* [S1063-7834(99)01010-2]

Superionic conductors are a special class of crystals in which structural disordering of one of the ionic sublattices is observed at temperatures significantly below the melting temperature. An important distinguishing feature of superionic crystals is the presence of two types of charge carriers: electrons and ions, the interaction between which leads to an entire list of new phenomena and effects arising at the ⟨superionic crystal⟩–⟨electrode⟩ heterojunction.[1–4] The characteristic properties of superionic materials appear most distinctly in materials that have come to be called ''materials with a melted cation sublattice.'' In the most typical representative of this group—$RbAg_4I_5$ crystals—minimum values of the activation energy are observed for motion of mobile silver cations ($\Delta E_a \simeq 0.1\,\text{eV}$) and maximum values of the ionic conductivity $\sigma_i \simeq 0.32\,(\Omega\cdot\text{cm})^{-1}$ at room temperature.[5]

The presence of a mobile ionic subsystem leads to ion exchange between a superionic conductor and an electrode.[6–8] Thus, the application of a potential difference to the system Ag–$RbAg_4I_5$–Ag leads to the appearance of an ionic current and silver transport from the positive to the negative electrode. The application of mechanical pressures to reverse silver electrodes also leads to an ionic current in the system Ag–$RbAg_4I_5$–Ag.[6,9,10] In the case of closed electrodes an ionic current flows in the system from the electrode under greater pressure. In opened electrodes the appearance of a pressure voltage opposed to the applied pressure was observed.[6,9,10] A distinguishing feature of the pressure voltage, observed and studied in Refs. 6, 9, and 10, is the fact that the pressure voltage depends only on the properties of the electrodes, and a superionic crystal fulfills the function of a semipermeable membrane, letting through ions and not letting through electrons. It should be noted here that in all the studies of all these phenomena processes of ion transport through the ⟨superionic crystal⟩–⟨electrode⟩ heterojunction and processes taking place in the heterojunction itself have remained outside the purview of the investigators. The present paper is dedicated to examining the influence of elastic stresses on processes taking place in a superionic crystal and in a ⟨superionic crystal⟩–⟨electrode⟩ heterojunction.

Many physical phenomena observed in superionic conductors are governed by transport processes of mobile ions through a ⟨superionic crystal⟩–⟨electrode⟩ heterojunction and are connected with the surmounting by the mobile ions of the potential barrier at the heterojunction.[7,8] In the absence of an external potential difference on a ⟨reversible electrode⟩–⟨superionic crystal⟩ heterojunction the thermally activated ion currents flowing through the potential barrier from the superionic crystal to the electrode and from the electrode to the superionic crystal are equal and the total current through the junction is zero.[7,8] Of course, changes in the conditions of equilibrium at the heterojunction upon the application of a potential difference, or as a result of a change in the energy of the cations in the superionic conductor upon its elastic deformation, should be accompanied by the formation of ionic currents in the heterojunction.

With the aim of detecting and studying phenomena associated with the appearance of deformation currents and photostimulated currents, the present work examines the influence of elastic stresses and intracenter excitation of optically active centers on processes taking place on a ⟨superionic crystal⟩–⟨electrode⟩ heterojunction.

1. DEFORMATION CURRENTS IN SUPERIONIC CRYSTALS

Crystalline samples of $RbAg_4I_5$, grown by directed crystallization were studied.[11] Special methods of cleaning and optimal conditions of crystallization enabled us to lower the content of monitored heavy-metal impurities in the samples to concentrations less than $10^{-4}\%$. Samples 6–7 mm in

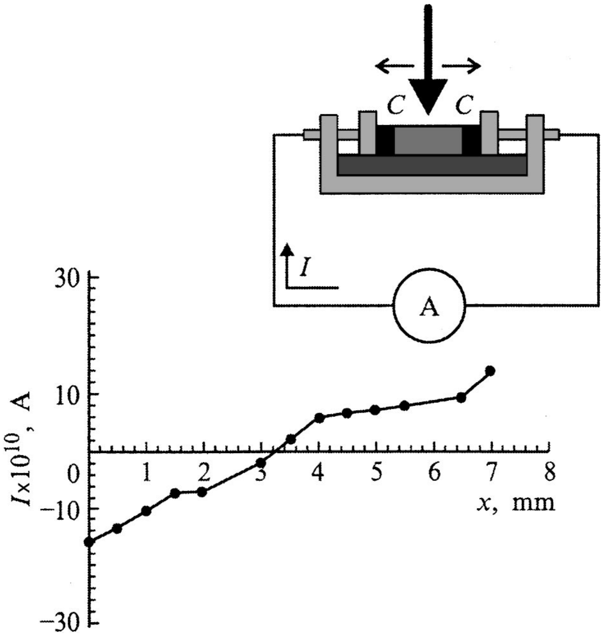

FIG. 1. Dependence of the deformation current on the location of the region of load application in the superionic crystal $RbAg_4I_5$ between graphite electrodes for a fixed value of the external loading $P\simeq5\times10^6$ Pa.

length with cross-sectional area 2×4 mm^2 were cut from boules immediately before the experiments. Finely-dispersed powder electrodes were deposited on the end-faces of the sample. During the measurements the sample was mounted on the surface of a sapphire lamina (Fig. 1) placed in an optical thermostat. The sample was loaded using a punch, whose lower end was outfitted with a sapphire prism with a working surface 0.1×3 mm. An external pressure was applied to a region of the sample 0.1×3 mm^2 in area, located between graphite contacts deposited on the end-face (Fig. 1). During the measurements a load was applied to the sample that was less than the microhardness limit of the $RbAg_4I_5$ crystals, $P\simeq5\times10^8$ Pa (Ref. 6).

As a result of our experiments, we found that a current arose in the external circuit upon elastic deformation of a local region of the investigated $RbAg_4I_5$ sample, whose direction corresponded to electron transport toward the electrode near which the load was applied. It turned out that the magnitude and sign of the deformation current depend on the region of application of the local load. As the region of application of the local load is shifted away from the contact, the magnitude of the current decreases and the deformation current changes sign as the loading region is moved across the center of the sample (Fig. 1). Figure 1 shows a typical plot of the dependence of the deformation current on the position of the loading region in the superionic crystal $RbAg_4I_5$. Note that the deformation current arises in a sample with symmetric graphite or silver electrodes in the absence of an external electric field, and a necessary condition for its appearance is only local elastic deformation of the sample (Fig. 1). We found that, for loading of a local region of the superionic crystal $RbAg_4I_5$ with symmetric graphite electrodes, the C–$RbAg_4I_5$–C cell operates as a current source.

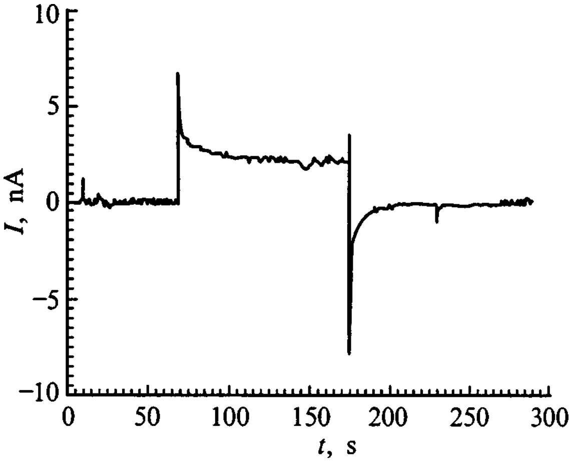

FIG. 2. Jumplike appearance and decline of the deformation current upon application and removal of an external load $P\simeq5\times10^6$ Pa.

The characteristic response of the system C–$RbAg_4I_5$–C to application and removal of pressure is shown in Fig. 2. It can be seen that the application of an external load is accompanied by the jumplike appearance of a deformation current with subsequent partial relaxation (with time constant $\tau\simeq9$ s) to the equilibrium value of the deformation current, which remains practically invariant during the entire time (τ_{def}) of application of the external mechanical load. Removal of the mechanical load is accompanied by a jumplike decrease in the deformation current and its subsequent relaxation with time constant $\tau\simeq9$ s to its initial value. Thus, in our study of the response of the system to a local external load, we observed both a transient response ($\tau\simeq9$ s) and a quasi-steady-state response to elastic deformation of a superionic crystal. The dependence of the steady-state value of the deformation current on the magnitude of the external load, measured on a sample of $RbAg_4I_5$ with symmetric graphite electrodes, is plotted in Fig. 3. It can be seen that the deformation current increases linearly with pressure.

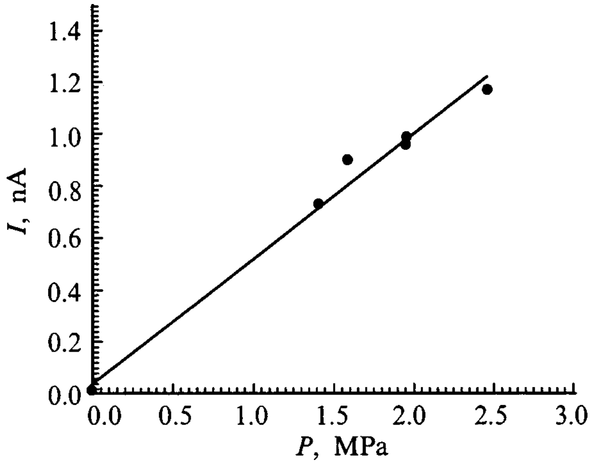

FIG. 3. Dependence of the steady-state magnitude of the deformation current on the external applied load on a $RbAg_4I_5$ sample at a distance of 0.5 mm from one of the graphite electrodes.

2. PROCESSES OF ION EXCHANGE AND RELAXATION PROCESSES AT A ⟨SUPERIONIC CONDUCTOR⟩–⟨ELECTRODE⟩ HETEROJUNCTION

To elucidate the mechanism of the appearance of deformation currents, let us consider the transport of ions and electrons through the heterojunction. Ion transport from the superionic conductor $RbAg_4I_5$ to the electrode is associated with the formation of neutral silver atoms on the surface of the electrode, and the reverse process is associated with the dissolution of these atoms into the bulk of the sample. In this case, processes of silver deposition on the graphite electrode and formation of silver clusters, and also the reverse processes of dissolution of these silver clusters into the bulk of the superionic conductor take place at the ⟨superionic conductor $RbAg_4I_5$⟩–⟨electrode⟩ heterojunction. In equilibrium the silver currents through the heterojunction from the superionic conductor to the electrode (J_p) and from the electrode into the bulk of the superionic conductor (J_d) are equal: $J_d = J_p = J^0$. Expressions for the fluxes of dissolving and depositing silver can be written down with the help of the Butler–Volmer equations[7,8]

$$J_d = C_{\mathrm{Ag}} k_d \exp(-\Delta_d / kT), \tag{1}$$

$$J_p = C_{\mathrm{Ag}^+} k_p \exp(-\Delta_p / kT), \tag{2}$$

where J_d and J_p are the fluxes of dissolving and depositing silver; C_{Ag} and C_{Ag^+} are the concentration of silver in the electrode and in the superionic phase of the $RbAg_4I_5$ crystal; k_d and k_p are the ionization and dissociation constants of silver; Δ_d and Δ_p are the activation energies of the processes of solution and deposition of silver, respectively. An estimate of the activation energy of the dissolution of silver in the bulk of the superionic conductor $RbAg_4I_5$ gives $\Delta_d \simeq (15-20)$ mV (Ref. 10) and for deposition of silver on the graphite electrode with formation of silver clusters $\Delta_p \simeq 460$ mV (Ref. 8). Under equilibrium conditions, the fluxes of dissolving and depositing silver in the heterojunction are equal ($J_d = J_p$); this enables us to estimate the concentration of silver C_{Ag} being liberated at the blocking graphite electrode in contact with the superionic conductor. Assuming equality of the silver ionization and dissociation constants ($k_p \simeq k_d$) at the concentration of silver, C_{Ag}, being liberated at the surface of the blocking graphite electrode under equilibrium conditions for the concentration of model silver cations in the superionic crystal $RbAg_4I_5$ $C_{\mathrm{Ag}^+} \sim 10^{22}\,\mathrm{cm}^{-3}$ is equal in order of magnitude to

$$C_{\mathrm{Ag}} = \frac{C_{\mathrm{Ag}^+} k_p}{k_d} \exp\left(-\frac{\Delta_p - \Delta_d}{kT}\right) \simeq 10^{14}\,\mathrm{cm}^{-3}, \tag{3}$$

i.e., less than a monolayer of silver on the graphite surface. This is another confirmation of the result obtained earlier by us[8] that on a ⟨superionic conductor⟩–⟨graphite electrode⟩ heterojunction a silver island structure appears together with dendritic clusters.

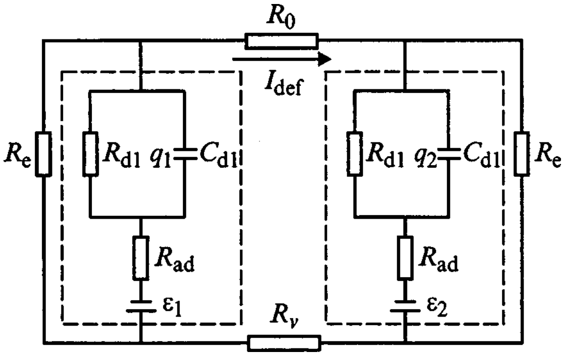

FIG. 4. Equivalent electrical circuit of a C–$RbAg_4I_5$–C cell for application of a local external load on a sample of $RbAg_4I_5$.

An important parameter governing the properties of the mobile defects in superionic crystals is the activation volumes associated with these defects. Detailed measurements of the magnitudes and temperature dependence of these volumes for the diffusion process in $RbAg_4I_5$ superionic crystals were performed in Refs. 12 and 13. Measurements of the activation volume, carried out in the low-temperature nonsuperionic γ phase, gave the value $\Delta V_a \simeq 9\,\mathrm{cm}^3/\mathrm{mol}$, which is comparable to the value of the total activation volume for AgBr crystals ($10.6\,\mathrm{cm}^3/\mathrm{mol}$) and AgCl crystals ($11.6\,\mathrm{cm}^3/\mathrm{mol}$).[12]

Let us consider the influence of elastic stresses on processes taking place in a ⟨superionic conductor⟩–⟨electrode⟩ heterojunction. Let an external pressure P be applied to a C–$RbAg_4I_5$–C cell with symmetric graphite electrodes near one of the heterojunctions. Application of the pressure (P) leads to a change in the potential energy of the mobile cations $\mu_i^d = \mu_i^p + P\Delta V_a$ in the near-electrode region of the superionic conductor $RbAg_4I_5$ and to a decrease in the height of the barrier for the process of silver deposition on the graphite electrode $\Delta_0 - P\Delta V_a$. As a consequence, the silver flux from the superionic conductor to the electrode is increased

$$J_0^d = C_{\mathrm{Ag}^+} k_p \exp\left(-\frac{\Delta_p - P\Delta V_a}{kT}\right) = J^0 \exp(P\Delta V_a / kT), \tag{4}$$

while the silver flux from the electrode into the bulk of the superionic conductor remains unchanged

$$J_d = C_{\mathrm{Ag}} k_d \exp(-\Delta_d / kT) = J^0. \tag{5}$$

Consequently, the application of an external pressure to the near-electrode region of the superionic conductor $RbAg_4I_5$ leads to a breakdown of the conditions of local equilibrium and to the appearance of an ionic current ΔJ_i flowing through the heterojunction into the electrode from the superionic conductor

$$\Delta J_i = J^0\left(\exp\left(\frac{P\Delta V_a}{kT}\right) - 1\right). \tag{6}$$

In turn, the nonequilibrium ionic currents flowing through the heterojunctions lead to the appearance in the external circuit of the experimentally observed deformation current $[I_{\mathrm{def}}(t)]$.

When an external pressure (P) is applied to a local region of the sample, a nonuniform elastic deformation arises in it together with internal elastic stresses (P_1 and P_2) in the heterojunctions. For a C–$RbAg_4I_5$–C cell (Fig. 4), this is equivalent to connecting two voltage sources $\varepsilon_1 = P_1 \Delta V_a / e$ and $\varepsilon_2 = P_2 \Delta V_a / e$ to the cell at the first and second heterojunctions, respectively. To describe the resulting deformation current, let us first consider the equivalent electrical circuit of the cell C–$RbAg_4I_5$–C. A typical circuit of the cell C–$RbAg_4I_5$–C is shown in Fig. 4, where R_{dl} is the resistance of the heterojunction associated with ion transport; R_e is the electronic resistance of the heterojunction; R_{ad} is the resistance of the heterojunction associated with the movement of ions out of the bulk of the sample onto its surface; C_{dl} is the capacitance of the double layer; R_v is the internal resistance of the sample; and R_0 is the load resistance across which the measurement of the deformation current (I_{def}) is made. According to the data of numerous studies, the capacitance of the doubly charged layer at a ⟨superionic conductor $RbAg_4I_5$ ⟨–C heterojunction is significantly higher than at a semiconductor–electrode contact and is equal to $C_{dl} \simeq 5-10\,\mu\mathrm{F/cm}^2$ (Refs. 14 and 15). We obtained an estimate of the electronic resistance of the heterojunction earlier[8] in a study of electron transport in superionic conductors: $R_e \simeq (1-5)\times 10^7 \Omega/\mathrm{cm}^2$. To describe the relaxation processes taking place in a heterojunction, find the parameters of the deformation current flowing through the load resistance R_0 and also the parameters of the time dependence of the charges q_1 and q_2 on the capacitors formed by the double charged layers C_{dl}, it is necessary to solve the following system of first-order differential equations:

$$\dot{q}_1 = \frac{\varepsilon_1}{R_e} + \frac{\varepsilon_1 - \varepsilon_2}{R_0} - \frac{q_1}{C_{dl} R_{dl}} - \frac{q_1}{C_{dl} R_e} - \frac{q_1}{C_{dl} R_0} + \frac{q_2}{C_{dl} R_0},$$

$$\dot{q}_2 = \frac{\varepsilon_2}{R_e} + \frac{\varepsilon_2 - \varepsilon_1}{R_0} - \frac{q_2}{C_{dl} R_{dl}} - \frac{q_2}{C_{dl} R_e} - \frac{q_2}{C_{dl} R_0} + \frac{q_1}{C_{dl} R_0}. \tag{7}$$

Numerical solution of the given system of differential equations enables us to obtain the time dependence of the additive charges $[q_1(t)$ and $q_2(t)]$ arising on the capacitors formed by the doubly charged layers, and to describe the characteristics of the deformation current $[I_{\mathrm{def}}(t)]$ for different initial conditions on the cell C–$RbAg_4I_5$–C. Within the framework of the described model for the appearance of a deformation current, it is possible to estimate the magnitude of this current. Indeed, the application of an external pressure ($P \simeq 5\times 10^6$ Pa) to one of the near-electrode regions of the sample is equivalent to connecting an electromotive force equal to $\varepsilon = P\Delta V_a / e \simeq 0.1$ V to the $RbAg_4I_5$–C heterojunction.

Calculations of the model system's temporal response to the application and removal of pressure on a C–$RbAg_4I_5$–C cell, based on the equivalent circuit described above (Fig. 4), are plotted in Fig. 5. It can be seen that the calculated magnitude of the deformation current (Fig. 5) and the experimentally determined magnitude (Fig. 2) are in good agreement. It should also be noted that the shape of the model deformation-current signal correlates well with the experimentally obtained response of a C–$RbAg_4I_5$–C system to the application and removal of pressure (Fig. 2). Studies of the temporal response of a $RbAg_4I_5$–C heterojunction showed that the time constant of the response (τ_0) is controlled by the capacitance of the doubly charged layer C_{dl} and the resistance of the heterojunction R_{dl} ($\tau_0 \simeq R_{dl} C_{dl}$). Comparison of the experimentally determined relaxation time $\tau \simeq 9$ s (Fig. 2) and the calculated relaxation time $\tau \simeq R_{dl} C_{dl}$ allows us to estimate the magnitude of the ionic resistance of the $RbAg_4I_5$–C heterojunction: $R_{dl} \simeq 5 \times 10^6\,\Omega\cdot\mathrm{cm}^2$.

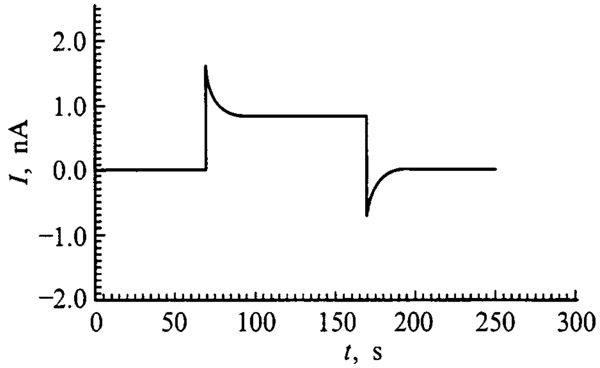

FIG. 5. Results of calculating the temporal response of the deformation current upon application and removal of the pressure in the equivalent electrical circuit of a C–$RbAg_4I_5$–C cell.

Thus, the model calculations confirm the above assumptions that the appearance of a current upon elastic deformation of a local region of a superionic conductor is associated with breakdown of the conditions of local equilibrium the heterojunctions and the appearance of ionic currents flowing through the heterojunctions.

3. PHOTO-INDUCED CURRENTS IN SUPERIONIC CRYSTALS

Earlier, we found that illumination of the superionic crystal $RbAg_4I_5$ leads to the appearance of a current in the external circuit.[3,16] It should be noted that a photocurrent arises in a sample with symmetric graphite or silver contacts in the absence of an external electric field, and a necessary condition for the appearance of a photocurrent is only asymmetric illumination of the sample. Studies were performed on crystalline samples of $RbAg_4I_5$ 6–7 mm in length with cross-sectional area 3×4 mm^2. Electrodes were deposited on the end-faces. These electrodes were prepared using finely disperses silver or graphite powder. The sample was illuminated by a DKSSh-120 xenon lamp with an MDR-4 monochromator or a He–Cd laser ($\lambda = 4416$ Å). An optical system focused the laser beam onto a spot $30\times 300\,\mu\mathrm{m}^2$. The beam scanning rate across the surface of the sample was $\simeq 1.4\,\mu$m/s. During the measurements the sample was located in an optical thermostat.

From these studies we found that, when a region of the $RbAg_4I_5$ crystal near one of the contacts was illuminated, a current arose in the external circuit whose direction corresponded to electron transport toward the illuminated electrode. For a laser power $\simeq 2$ mW ($\lambda = 4416$ Å), the current in the external circuit was $\sim 10^{-10}$ A. It turned out that the photostimulated current depends on the region of the sample that is being illuminated. When scanning the laser beam along the length of the sample starting at one of the elec-

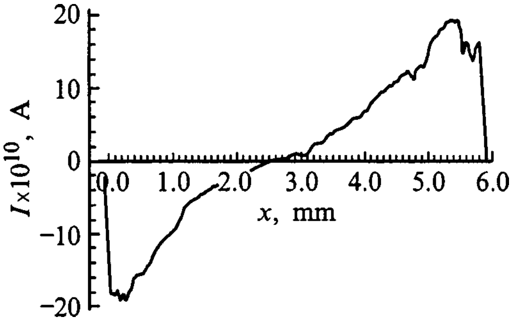

FIG. 6. Typical dependence of the photo-induced current on the location of the illuminated region in a $RbAg_4I_5$ sample between the graphite electrodes.

trodes, the intensity of the photocurrent decreased and the current changed sign as the beam crossed the middle of the sample. To study dependences of this kind, the He–Cd laser beam ($h\nu = 2.81$ eV) was focused on the surface of the sample in a $30\times300\,\mu m^2$ spot. Figure 6 shows a typical dependence of the photo-induced current on the position of the illuminated region of the $RbAg_4I_5$ crystal along the length of the sample between the graphite electrodes.

To elucidate the mechanism of the appearance of the photostimulated current, we examined its spectral and temperature characteristics.[3,16] At room temperature (300 K) three main bands with maxima at 2.85, 2.64, and 2.35 eV are present in the photocurrent spectrum. The positions and halfwidths of the bands in the spectra of the photostimulated current correlate well with the absorption bands arising upon photostimulated coloration[17] of $RbAg_4I_5$ superionic crystals and the bands observed in the ionic photoconductivity quenching spectrum.[4]

An important peculiarity of the spectral characteristics of the photostimulated current in $RbAg_4I_5$ superionic crystals should be noted. It turned out that almost all of the main bands (2.64 and 2.35 eV) were absent in the initial samples. These bands appear in the spectrum of the photostimulated current only after irradiation of a previously unirradiated sample by light with wavelength in the range from 420 to 450 nm. Thus, as was shown earlier,[17,4] these bands are associated with color centers arising during a reversible change in the stoichiometry of the superionic crystals in the Ag mobile subsystem under the action of light with wavelength in the range from 420 to 450 nm.

Earlier,[3,16] in a discussion of the mechanism of the appearance of a photo-induced current, we assumed that the following process is realized. Illumination of a local region of a $RbAg_4I_5$ crystal by light with photon energy corresponding to excitation of the electron centers leads to the generation of nonequilibrium electrons in the conduction band. Mobile Ag^+ cations, by virtue of their high concentration in the superionic phase, screen the electrostatic interaction between ionized centers and electrons. The excess electron concentration in the illuminated region leads to the appearance of diffusion currents of electrons and ions toward the contacts in the ambipolar-diffusion regime. Here we assumed that the physical reason for the appearance of the photo-induced current is analogous to the reason for the appearance of a rectifier photovoltage upon illumination of a p–n junction, where the potential barrier of the junction separates the photoelectron and hole currents and, in the case of a superionic conductor, the Ag^+ cation and electron currents.

At the same time, our experimental data contradicts the model of the separation of Ag^+ cation and electron fluxes at the ⟨superionic conductor⟩–⟨electronic conductor⟩ interface. First of all, the spectral characteristics of photostimulated currents should be included among such data. Thus, in the spectrum of the photostimulated current the band with maximum at $\lambda = 430$ nm, that is is due to ambipolar diffusion of Ag^+ cations and electrons from the illuminated region of the sample toward the contacts, is absent. A second important argument is that the magnitude of the ambipolar diffusion coefficient of Ag^+ cations and electrons in $RbAg_4I_5$ superionic crystals is small ($D_{\mathrm{amb}} \simeq 10^{-8}\,\mathrm{cm^2/s}$).[1,2] Therefore, when a region of the sample a distance $L \simeq 1$ mm from the contact is illuminated, a delay should be observed between the startup of illumination and the appearance of the photocurrent of the order of $\tau \sim L^2/D_{\mathrm{amb}} \simeq 10^{-6}$ s, associated with the time it takes a packet of carriers to move from the illuminated region to the contact. At the same time, we were not able to observe any delay between the startup of illumination and the appearance of the photostimulated current in the $RbAg_4I_5$ superionic crystals. All this argues against invoking a mechanism of the rectifier-photovoltage type to explain the appearance of a photocurrent in $RbAg_4I_5$ superionic crystals.

To elucidate the photocurrent mechanism, let us turn to the spectrum of the photostimulated current. As was noted above, the photostimulated current is not observed in the initial sample and its appearance requires pre-illumination of the $RbAg_4I_5$ crystal with light in the wavelength range 420 to 450 nm, leading to the appearance of color centers. The agreement between the absorption spectra of photo-colored crystals of $RbAg_4I_5$ (Ref. 17) and the ionic photoconductivity quenching spectra[4] with the photostimulated current spectra is connected with intracenter excitation of complexes created as a result of previous illumination of the samples ($\lambda \simeq 430$ nm). Indeed, intracenter excitation of donor–acceptor pairs, brought about by charge transport within the complex, is accompanied by relaxation of the lattice and leads to changes in the elastic stress fields existing around the donor–acceptor pairs. Thus, when a local region of $RbAg_4I_5$ superionic crystals is illuminated by light with photon energy corresponding to intracenter excitation of donor–acceptor pairs created as a result of pre-illumination of the samples ($\lambda \simeq 430$ nm), a change takes place in the elastic stress fields in the illuminated region of the crystal. Consequently, the appearance of photostimulated currents is due to the appearance of elastic stress fields in the illuminated region of the crystal. Indeed, the studies reported here show that the dependence of the photo-induced current on the location of the illuminated region and the temperature characteristics of the photostimulated currents are completely analogous to the corresponding characteristics of the deformation currents arising upon elastic deformation of a local region of the $RbAg_4I_5$ sample.

To summarize, in the present work we have detected and investigated for the first time the appearance of a current in the external circuit upon elastic deformation of a local region of the superionic $RbAg_4I_5$ crystal. We have established that elastic deformation of a local region of this superionic crystal leads to breakdown of the conditions of local equilibrium in the subsystem of mobile Ag cations in a ⟨superionic conductor⟩–⟨electrode⟩ heterojunction and to the appearance of an ionic current flowing through the heterojunction. A mechanism has been proposed for the process, and processes taking place at the ⟨superionic conductor⟩–⟨electrode⟩ heterojunction have been modeled. It has been shown that the shape of a model deformation-current signal correlates well with the experimentally measured response of the system $C-RbAg_4I_5-C$ to the application and removal of pressure, and the calculated and experimentally measured magnitudes of the deformation current are in good agreement.

We have considered the appearance of photostimulated currents upon illumination of a local region of a superionic crystal. We have established that the appearance of photostimulated currents is due to the creation in the illuminated region in the case of $RbAg_4I_5$ crystals of long-lived centers which are donor–acceptor pairs consisting of a silver-cation vacancy $[V]^-_{Ag^+}$ and hole center. We have shown that the elastic stress fields existing around such complexes are responsible for breakdown of the conditions of equilibrium in the heterojunction and for the appearance of an ionic current flowing through the heterojunction. We have also established that the photostimulated currents arise as a result of a change in the elastic stresses P_{elast} in the illuminated region of the superionic crystal upon intracenter excitation of the complexes created as a result of pre-illumination of the samples ($\lambda \simeq 430\,nm$).

We have established that the mechanisms of the photoinduced current and the deformation current are analogous and associated with a change in the energy of the mobile cations in the region of elastic stresses arising in the sample both upon its elastic deformation and upon illumination of a local region.

[1] S. Bredikhin, T. Hattori, and M. Ishigame, Phys. Rev. B **50**, 2444 (1994).
[2] S. Bredikhin, T. Hattori, and M. Ishigame, Solid State Ionics **67**, 311 (1994).
[3] A. V. Boris and S. I. Bredikhin, JETP Lett. **49**, 106 (1989).
[4] M. V. Bogatyrenko and S. I. Bredikhin, Zh. Éksp. Teor. Fiz. **112**, 698 (1997) [JETP **85**, 381 (1997)].
[5] B. B. Owens and G. R. Argue, Science **157**, 308 (1967).
[6] Yu. M. Gerbshteĭn, E. I. Nikulin, and F. A. Chudnovskiĭ, Fiz. Tverd. Tela (Leningrad) **25**, 1148 (1983) [Sov. Phys. Solid State **25**, 659 (1983)].
[7] H. Germain Creighton, *Principles and Applications of Electrochemistry*, Vol. 1., *Principles* (Wiley, New York, 1928).
[8] S. I. Bredikhin, V. N. Bondarev, A. V. Boris, P. V. Pikhitsa, and W. Weppner, Solid State Ionics **81**, 19 (1995).
[9] Yu. M. Gerbshteĭn, S. E. Nikitin, and F. A. Chudnovskiĭ, Fiz. Tverd. Tela (Leningrad) **25**, 3559 (1983) [Sov. Phys. Solid State **25**, 2048 (1983)].
[10] Yu. M. Gerbshteĭn, V. P. Kuznetsov, and S. E. Nikitin, Fiz. Tverd. Tela (Leningrad) **27**, 2996 (1985) [Sov. Phys. Solid State **27**, 1616 (1985)].
[11] V. N. Zagorodnev and N. V. Lichkova, Izv. Akad. Nauk SSSR, Neorg. Mater. **19**, 1031 (1983).
[12] P. C. Allen and D. Lazarus, Phys. Rev. B **17**, 1913 (1978).
[13] G. A. Samara, Solid State Phys. **38**, 80 (1984).
[14] N. G. Bukun and A. E. Ukshe, Elektrokhimiya **29**, 110 (1993).
[15] A. E. Ukshe and S. A. Sherstnov, Fiz. Tverd. Tela (Leningrad) **28**, 2850, (1986) [Sov. Phys. Solid State **28**, 1597 (1986)].
[16] A. V. Boris and S. I. Bredikhin, Fiz. Tverd. Tela (Leningrad) **34**, 219 (1992) [Sov. Phys. Solid State **34**, 115 (1992)].
[17] N. Kovaleva, A. Boris, S. Bredikhin, and T. Awano, Radiat. Eff. Defects Solids **134**, 457 (1995).

Translated by Paul F. Schippnick

PHYSICS OF THE SOLID STATE VOLUME 41, NUMBER 10 OCTOBER 1999

DEFECTS. DISLOCATIONS. PHYSICS OF STRENGTH

Physical model of the interaction of grain-boundary and lattice dislocations

A. K. Emaletdinov

Ufa Technological Institute, 450014 Ufa, Russia

(Submitted January 18, 1999)
Fiz. Tverd. Tela (St. Petersburg) **41**, 1772–1777 (October 1999)

Processes of absorption and creation of lattice dislocations by grain boundaries are examined in a physical model of grain-boundary quasi-dislocations. The dissociation time and the power and energy conditions for generation of dislocations are found and compared to experiment.
[S1063-7834(99)01110-7]

Grain boundaries are one of the main defects of polycrystalline solids that determine their mechanical properties.[1,2] When ultra-small-grain and nanocrystalline materials are deformed in the superplasticity regime, the important microscopic processes are absorption and emission of lattice dislocations by grain boundaries (see, e.g., Refs. 3–6).

The process of absorption depends substantially on the temperature.[1,6] Under cold deformation ($T<T_S\approx(0.5-0.6)T_m$, where T_m is the melting point) lattice dislocations entering into a grain boundary continue to preserve their long-range stress fields and electron-microscope contrast. Under hot deformation ($T>T_S$, where T_S is the equicohesive temperature) the electron-microscope image of the dislocations that have entered into a grain boundary disappear (spread) after a time t_D and their elastic fields relax. Theoretical investigations of the structure of the grain boundaries have been pursued by constructing geometrical models and performing atomic calculations (see, e.g., Refs. 1, 6–8). Two microscopic mechanisms of the spreading process have been proposed:[6] expansion of the dislocation nucleus and its dissociation into grain-boundary dislocations with Burgers vector $b_g=b/n$. Both mechanisms are based on a geometrical model of grain-boundary dislocations (solitons),[7,8] which are assigned long-range stress fields similar to those that lattice dislocations possess,[9] and given by the relation $\sigma_{ij}^{(D)}\sim\mu b/2\pi|\mathbf{r}|$, where $|\mathbf{r}|=\sqrt{x^2+y^2}$ is the length of the radius vector from the dislocation axis and μ is the shear modulus.

Creation of dislocations by grain boundaries was confirmed by electron-microscopy *in situ*.[6] A number of geometrical models have been proposed to describe the generation process.[6–8] But from a geometrical analysis alone it is impossible to derive the elastic properties of grain-boundary dislocations or even prove their existence. An analysis of the conditions of the passage of a lattice dislocation into the body of a grain,[7] for grain-boundary dislocations with long-range stresses, has shown that there are large force and energy barriers in this model associated with the strong attraction of a dislocation to the boundary.

The present work is a study of soliton solutions (dislocations) of the equations of dynamics and the elastic properties of defects in the Frenkel'–Kontorova physical model[9–14] for an arbitrary boundary. The conditions for dissociation of the lattice dislocations entering a grain boundary, into an ensemble of grain-boundary defects, is analyzed and the spreading time is determined. The force and energy conditions of creation of a lattice dislocation on a boundary, upon coalescence of the ensemble of grain-boundary defects, are calculated. Associated problems are solved numerically, and the results compared to experiment.

1. SOLITON SOLUTIONS (GRAIN-BOUNDARY DEFECTS) ON BOUNDARIES

Let us consider a model of a grain-boundary structure consisting of two interacting sublattices, where the sublattice of one grain (with period a) experiences the action of an external periodic (quasiperiodic) potential $V(u)$ created by the sublattice of the second grain (with period b), where $u(u,0,0)$ is the displacement vector of the atoms from their equilibrium positions. The given model has been used in many works.[9–14] The dynamics of the atomic layer of the boundary will be described by the nonlinear sine-Gordon equation with potential $V(u)$ (Ref. 11).

We approximate the potential $V(u)$ by a Fourier series

$$V(u)=V_0\left(1+\sum_{i=1}^{n}a_i\cos(k_iu)\right),\tag{1}$$

where $u=2\pi u/b$ is a new dimensionless variable, k_i are integers or irrational numbers, and $V_0=\mu b^2/4\pi^2$. The potential (1) reflects the main property of the grain boundaries: periodicity (quasiperiodicity) of their structure[1,6–8,10,12–14] [for $n=1$ the potential (1) describes the Frenkel'–Kontorova model[9,11]].

With the help of the Hamiltonian of the lattice with potential (1) we obtain the equations for the dynamics of the atoms of the grain-boundary layer[11]

$$Mu_{tt}-Mc^2u_{xx}=V'_u(u),\tag{2}$$

where M is the mass of the atoms and c is the speed of sound. Grain-boundary dislocations correspond to N-soliton solutions of the stationary equation (2) with boundary conditions (a 2π kink, Refs. 9 and 11): $u(\infty)=-u(-\infty)=-\pi$.

Let us consider three types of boundaries: small-angle, with misorientation angle $\Theta<\pi/10^2\ll 1$; special, with density of the coincident angles Σ and $\Theta>\pi/10^2$; and ordinary, with $\Theta>\pi/10^2$.

In the case of small-angle boundaries, the potential (1) contains only one term $(n=1)$. The values of the periods are related by the expression $a=b(1+\Theta)$, $\Theta\ll 1$. Introducing the new variable $x=2\pi b\Theta$ in the continuum approximation, we obtain from Eqs. (1) and (2) a modified sine-Gordon equation

$$u_{xx}=2V_1\sin(u), \tag{3}$$

where $V_1=V_0(1-\Theta)/Mc^2$, which for $\Theta=0$ goes over to the Frenkel'–Kontorova equation.[9,11] The N-soliton solution of Eq. (3) has the form

$$u(x,0)=4\arctan[\exp(-2\pi(x+\lambda n)/b)],$$

$$\lambda\approx b/\Theta,\quad n=\pm 1,\pm 2,\ \dots\ , \tag{4}$$

where $\lambda=2\zeta K(\zeta)/V_1^{1/2}$, $\zeta=4V_1/(A+2V_1)$, $K(\zeta)$ is the complete elliptic integral of the first kind, λ is the distance (period) between solitons (lattice dislocations) on the boundary, and A is an integration constant. Thus, the given model provides a valid description of a small-angle wall of infinite, rectilinear lattice dislocations with density $\rho_D\propto 1/\lambda\approx\Theta/b$ (Refs. 7 and 9).

If there is a special misorientation of the lattices of the grains and it is possible to introduce a lattice of coincident sites,[1,6,7] then the periods of the sublattices a and b will be commensurate and determined by the ratio $a/b=n/m$, where n and m are integers, i.e., the k_i are rational numbers. The stationary solution of Eq. (2) has the form

$$x-x_0=\int_0^u\frac{du}{\sqrt{A-V_1\sum_{i=1}^{n}a_i\cos(k_iu)/\pi k_i}}. \tag{5}$$

If the expression inside the square-root in Eq. (5) is a polynomial of third or fourth order, or a trigonometric function, then the solution (5) can be expressed in terms of elliptic functions. Periodic solutions obtain when u oscillates between the simple zeros of the expression inside the square root, i.e., the minima of the potential (1).

The case $k_1=1$, $k_2=2$ was considered in Ref. 11, and the solution (5) in the coordinate system moving with the dislocation has the form

$$u(x,0)=4\arctan(\exp(\eta)), \tag{6}$$

where $\eta=2\pi(vt-k_2x)/b$, $v\neq 0$ is the dislocation velocity, which is not equal to zero. Thus, the solution represents a kink soliton (grain-boundary dislocation) with Burgers vector $b_g=b/k_2=b/2$. The physical basis of the solution (6) is the appearance of additional minima in the interatomic potential in comparison with the lattice potential (the period of the grain-boundary potential is equal to $b/2$).

In the case $k_1=1$, $k_2=3$ it is possible to obtain a solution analogous to (6), but with Burgers vector $b_g=b/3$ (two additional minima appear, and the period of the potential (1) becomes equal to $b/3$).

In the general case of rational k_i, the solutions are also expressed in terms of a function of the form (6). Thus, stationary (kink-soliton) grain-boundary dislocations can exist on special grain boundaries. This means that the deformation (grain-boundary slip) is realized by moving grain-boundary dislocations with Burgers vector b_g and velocity $v\neq 0$. Therefore, all geometrical models of grain-boundary dislocations on special boundaries are related to the physically possible soliton states of the boundary structure. Since there are no fixed, stable grain-boundary dislocations on the special boundaries $(v\neq 0)$, their creation must be homogeneous, requiring high stresses.[9] This explains the high hardness of special boundaries and the small value of grain-boundary slip observed in experiment.[6]

On arbitrary high-angle grain boundaries, the coefficients k_i in the interatomic potential (1) will be irrational numbers (quasiperiodic potential). In general, the solution of Eq. (2) with kink-soliton boundary conditions and the potential (1) is not found in explicit form.[11] This follows from the implicit solution (5). The simple zeros and local minima of the potential in the the expression inside the square root in Eq. (5) oscillate; therefore, no stationary solutions, that is to say, solitons (dislocations), exist. To analyze the asymptotic behavior of the solution, we expand the function cos(z) in the potential (1) in a Taylor series. The equation of motion (2), taking into account the first two terms, becomes

$$Mu_{tt}-Mc^2u_{xx}=Au-Bu^3, \tag{7}$$

where $A=\Sigma_{i=1}^{n}a_ik_i^2$ and $B=\frac{1}{6}\Sigma_{i=1}^{n}a_ik_i^4$. To find the grain-boundary ''dislocations,'' it is necessary to examine the stationary equation (7) with boundary conditions corresponding to a 2π kink. Solutions of the following forms are possible: quasiharmonic oscillations with small amplitudes (motion along phase trajectories near equilibrium states); nonlinear periodic waves—cnoidal waves (motion along closed trajectories near the separatrix); and soliton solutions—quasi-grain-boundary dislocations (they correspond to motion along the separatrix).

The general solution of Eq. (7) is expressed by a cnoidal wave[11]

$$u(x,0)=A_0\,\mathrm{sn}[(x-vt)/\Delta_0s], \tag{8}$$

where $\mathrm{sn}(z)$ is the elliptic sine with period $\lambda_0=\sqrt{24B/c^2|A|s}K(s)$, $0<s<1$, s is the modulus of the elliptic function. It is well known that as $s\to 0$ the elliptic sine goes over to the trigonometric sine and, as $s\to 1$, it goes over to the hyperbolic tangent

$$u(x,0)=A_0\tanh[(x-vt)/\Delta_0], \tag{9}$$

where A_0 is the oscillating amplitude and $\Delta_0\approx 3b_g$ is the width of the quasi-soliton. Figure 1 plots the dependence of the displacements on distance to the quasi-dislocation

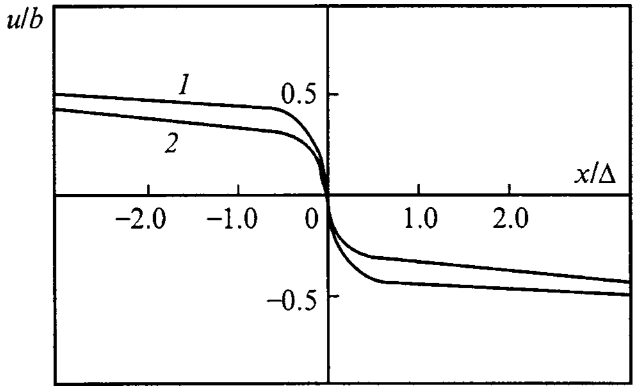

FIG. 1. Dependence of the displacement vector on distance: *1*—grain-boundary quasi-dislocation; *2*—lattice dislocation.

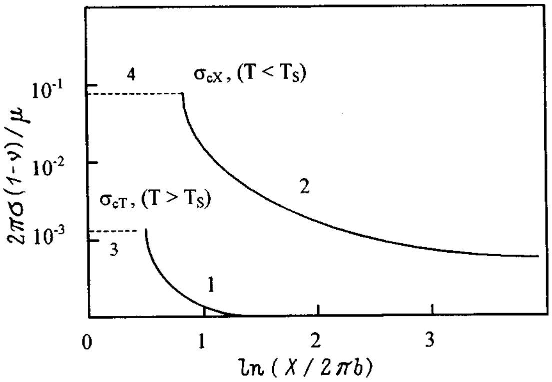

FIG. 2. Dependence of the internal stresses of a grain-boundary quasi-dislocation on distance to the defect: *1*—quasi-dislocations; *2*—for a lattice dislocation. The dashed lines *3, 4* are the critical voltages for creation of a hot and a cold deformation, respectively.

(curve *1*), obtained by numerical solution of Eq. (2), and for comparison, the displacements from the lattice dislocation (curve *2*).

In the second case the cnoidal wave is expressed in the form of a periodic sequence of quasi-stationary packets of *N*-solitons (grain-boundary quasi-dislocations), moving with constant speed at the distance $\lambda \cong \sqrt{24B/c^2|A|s}\,\ln(1-s^2) \approx N\Delta_0$ from one another. Thus, grain-boundary quasi-dislocations (Somiliana dislocations[9]) exist on an arbitrary boundary having a variable ''Burgers vector'' defined by the quasiperiod of the local minima in the grain-boundary potential (1). It can be shown that a stationary lattice dislocation described by expressions of the types (4) and (6) is unstable.[11]

2. ELASTIC STRESS FIELDS AND ENERGY OF GRAIN-BOUNDARY QUASI-DISLOCATIONS

Let us consider the intrinsic stress fields of the grain-boundary quasi-dislocations since they determine the kinetics of the quasi-dislocations and their interaction with the lattice dislocations. We obtain expressions for the intrinsic stresses of the quasi-dislocations with the help of Eq. (9) and the stress function ψ (Ref. 9). In the moving coordinate system bound to the quasi-dislocation, we have

$$\psi = \frac{\mu}{2\pi(1-\nu)} \int_{-\infty}^{\infty} dx' y \ln[(x-x')^2+y^2]^{1/2} \times \left(-2\frac{d}{dx'}[A_0 \tanh(x'/\Delta_0)] \right), \tag{10}$$

where ν is the Poisson coefficient.

The stress tensor of the quasi-dislocation is given by the expressions

$$\sigma_{xx} = -\frac{\mu b_g}{\pi^2(1-\nu)} \frac{\partial^2}{\partial y^2} \int_{-\infty}^{\infty} dx' y \ln[(x-x')^2+y^2]^{1/2} \times \left(-2\frac{d}{dx'}(A_0 \tanh[(x')/\Delta_0]) \right),$$

$$\sigma_{xy} = \frac{\mu b_g}{\pi^2(1-\nu)} \frac{\partial^2}{\partial x \partial y} \int_{-\infty}^{\infty} dx' y \ln[(x-x')^2+y^2]^{1/2} \times \left(-2\frac{d}{dx'}(A_0 \tanh[(x')/\Delta_0]) \right),$$

$$\sigma_{yy} = -\frac{\mu b_g}{\pi^2(1-\nu)} \frac{\partial^2}{\partial x^2} \int_{-\infty}^{\infty} dx' y \ln[(x-x')^2+y^2]^{1/2} \times \left(-2\frac{d}{dx'}(A_0 \tanh[(x')/\Delta_0]) \right). \tag{11}$$

Expressions (11) lead to a more abrupt exponential falloff of the stresses. For example, the stress fields (11) in the asymptotic region are equal to

$$\sigma_{xy}^{(K)}(x,0) \cong \frac{\mu \operatorname{sech}^3(x/\Delta_0)}{2\pi(1-\nu)} \operatorname{sgn}(x), \quad (x \gg b_g). \tag{12}$$

Figure 2 plots curves, obtained by numerical calculation, of expressions (10) and (11) (curve *1*) and, for comparison, the stresses from the lattice dislocation (curve *2*). Thus, the quasi-dislocations on the grain boundaries can easily coalesce thanks to short-range stresses, for example, during creation of lattice dislocations on the grain boundaries. On the other hand, they create an insignificant force barrier to intrusion by lattice dislocations. Refinement of expressions (10) and (11), allowing for variation of the elastic and lattice constants in the region of the boundary, does not alter the order-of-magnitude estimate. The approximation of long-range stresses of the quasi-dislocations, similar to lattice dislocations, leads to exaggerated estimates.[7] A short-range deformation field creates weak electron-microscope contrast.[6]

Let us consider the elastic energy of the quasi-dislocations. The natural elastic energy of a grain-boundary dislocation per unit length, written in the cylindrical coordinate system, is equal to[9]

$$W_g/L=\int_{b_g}^{L} r\,dr\int_0^{2\pi}d\Theta\left[\frac{1}{2\mu}\sigma_{xy}^2\right.$$
$$\left.+\frac{1}{2E}(\sigma_{xx}^2+\sigma_{yy}^2-2\nu\sigma_{xx}\sigma_{yy}-\sigma_{zz}^2)\right], \qquad (13)$$

where E is Young's modulus. Numerical calculation of expressions (10), (11), and (13) shows that the energy of a quasi-dislocation is given by

$$W_g^{(K)}/L\cong C_0\mu b_g^2, \qquad (14)$$

where $C_0\cong 0.1253$. An analogous expression for the long-range stresses leads to the result $W_g^{(D)}\cong 6\mu b_g^2$. Taking the variation of the lattice parameter and the elastic moduli in the boundary layer of width $\delta\cong(6-8)b$ into account leads to an insignificant lowering of the quantity W_g/L by an amount of the order of $\Delta\mu W_g/\mu L$, where $\Delta\mu/\mu\ll 1$. Thus, the natural elastic energy of the quasi-dislocations is almost two orders of magnitude lower than the energy of the dislocations with long-range stresses, which must be taken into account in the geometrical models.

3. DISSOCIATION OF A LATTICE DISLOCATION INTO AN ENSEMBLE OF QUASI-DISLOCATIONS

We describe the dissociation process of a lattice dislocation entering into a grain boundary by the nonstationary equation of motion of the grain boundary (2) with an initial perturbation of the form $u(x,0)=b\arctan(\exp(-2x\pi/b))/2\pi$, which describes the displacement field of a lattice dislocation entering into a grain boundary. The dissociation time t_D must be determined by solving the self-consistent problem of the spreading of the initial perturbation out to the dimensions of the packet, $L\approx 10^{-7}$ m, of N quasi-dislocations. The velocity of the quasi-dislocations is controlled by diffusion processes and to first order can be described by a semi-phenomenological expression of the form[6,9] $v=c_0D_g\Omega(\sigma-\sigma_{0g})(\exp(T-T_S)/T_0)/LkT$ or $v=v_0\sigma$, where c_0 and T_0 are phenomenological constants, D_g is the grain-boundary diffusion coefficient, $\Omega=b^3$, σ is the effective stress acting on the quasi-dislocation, and σ_{0g} is the initial stress. We write the main equations of continuity and dynamics (equation of motion) of the quasi-dislocations[9]

$$\frac{\partial\rho}{\partial t}+\frac{\partial}{\partial x}\rho v=0, \qquad (15)$$

$$v_0\int_{-L}^{L}\rho(x',t)\sigma_{xy}(x'-x)dx'/b_g=v(x,t), \qquad (16)$$

where $\rho(x',t)$ is the density of quasi-dislocations. The initial condition is $\rho(x,0)=b\delta(x)$ and the normalization condition is $\int_{-L}^{L}\rho(x',t)dx'=b$. The dissociation time t_D is found from the condition of uniform distribution of the quasi-dislocations in the interval $[-L,L]$: $\rho(x,t_D)=b/2L$. The numerical solution of system (15), (16) found using the method developed in Ref. 15 is plotted in Fig. 3 for two cases of interaction of the quasi-dislocations:

1) the short-range case, given by expressions (11) and (13), and

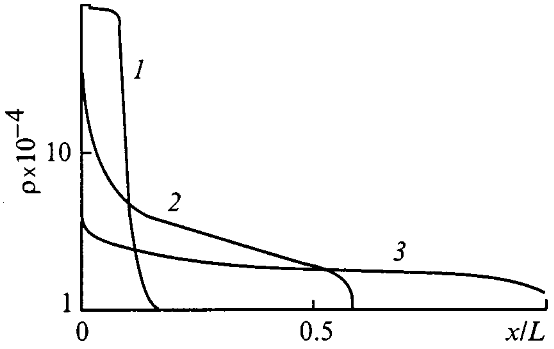

FIG. 3. Dependence of the mean density of quasi-dislocations in an ensemble on time for dissociation of a lattice dislocation. Curves *1, 2, 3* correspond to the times 1, 5, 20 s for interaction with short-range stresses, and 0.02, 0.1, and 0.5 s for interaction with long-range stresses.

2) the long-range lattice case, described by the relation[9] $\sigma_{xy}^D(x,0)=\mu b_b/2\pi x$. As can be seen from the results obtained, the dissociation time in case (1) is almost two orders of magnitude larger and corresponds to the experimental values. The approximate expression for the dissociation time in case (1) has the form

$$t_D^{(K)}\approx\frac{L^2}{b_g v_0\sigma_{0g}}\exp\left(-\frac{T_s-T}{T_0}\right). \qquad (17)$$

Calculating according to Eq. (17) with parameters for Mg gives the order-of-magnitude estimate $t_D^{(K)}\approx 1-10$ s, which is close to the experimental values[6]: $t_D\approx 10-60$ s. In case (2) an order-of-magnitude estimate gives

$$t_D^{(D)}\leqslant\frac{L^2}{\pi b_g v_0\mu}, \qquad (18)$$

and calculating for Mg gives $t_D^{(D)}\approx 10^{-2}-10^{-1}$ s. Such a small value of the dissociation time in case (2) is connected to the very large long-range stresses of mutual repulsion of the quasi-dislocations (Fig. 2).

4. CREATION OF LATTICE DISLOCATIONS ON GRAIN BOUNDARIES

Let us consider the process for creation of a lattice dislocation on a grain boundary of ultra-fine-grained material with grain size $d\leqslant 10^{-6}$ m, which was important in developing the theory of superplasticity.[4] In the geometrical models[7] the creation process is described as the coalescence of n grain-boundary dislocations, during which a ''mismatch dislocation'' remains on the boundary, defined by the condition of preservation of contiguity of the body. The force and energy conditions for coalescence $n=b/b_g$ of quasi-dislocations depend very strongly on the temperature and the dissociation process of the defect (mismatch dislocation) remaining on the boundary after departure of the lattice dislocation, into quasi-dislocations. The energy condition for creation of a lattice-dislocation loop of radius r is determined by the change in the magnitude of the thermodynamic potential[9]

$$\Delta F(r)=2\pi r(W_D/L)+d(W_g/L)+W_V-\pi r^2 b\sigma, \qquad (19)$$

where $W_D/L\cong\mu b^2\ln(r/b)/4\pi$ is the elastic energy of the lattice dislocation, the second term describes the energy of

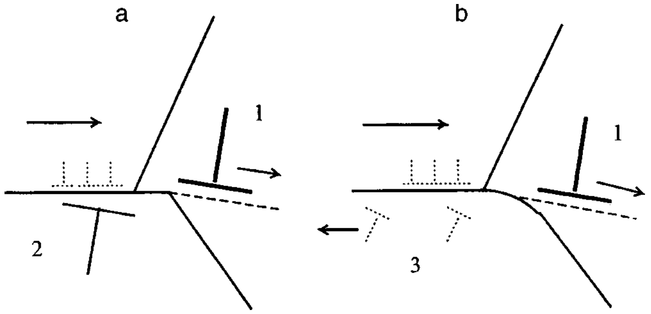

FIG. 4. Diagram of the creation of lattice dislocations at a grain boundary: *a*—at normal temperatures ($T<T_S$), *b*—at temperatures above the equicohesive temperature ($T>T_S$). *1*—Lattice dislocation, *2*—mismatch dislocation, *3*—grain-boundary quasi-dislocations.

the mismatch dislocation, the third term describes the interaction energy of a lattice dislocation and a mismatch dislocation, and the fourth term describes the work expended by external forces in the creation of a dislocation. The function ΔF also has a component which takes account of the action of image forces from all the faces of the grain, an account of which would lead in the final result to small corrections of the order of $\Delta\mu W_D/\mu L$, $\Delta\mu/\mu \ll 1$. The dependence $\Delta F(r)$ is nonmonotonic, and its maximum value $\Delta F_C(r_C)$ determines the activation energy. The radius of a critical loop r_C (distance from the boundary in the case of creation of a rectilinear dislocation) and the critical stress σ_C for creation of a dislocation are found from the system of equations

$$\partial\Delta F(r_C)/\partial r=0, \quad \sigma_C=\sigma_V(r_C), \tag{20}$$

where $\sigma_V(r_C)$ is the stress of self-action of the loop (of attraction to the boundary for a rectilinear dislocation). Substituting expressions (11), (12) and (19) into Eqs. (20), we obtain a system of equations for the critical values. System of equations (11), (12), (19), and (20) was solved numerically for two limiting cases: a) $T<T_S$ — cold deformation, and b) $T>T_S$ — hot, superplastic deformation (Fig. 4). In case (a) the starting stresses of the quasi-dislocations are large and dissociation of a geometrical incompatibility (''mismatch dislocation'') does not occur. Therefore, the conditions for creation of a dislocation are dictated by the long-range stresses and the following estimates are valid:[7] $\sigma_{CX} \leqslant 0.1\mu$ and $E_{CX} \leqslant \mu b^2/4\pi$, where E_{CX} is the height of the energy barrier. In case (b), for example for superplastic deformation of ultra-fine-grained materials, a mismatch dislocation can dissociate into an ensemble of n quasi-dislocations with short-range stresses (11) and (12). The force barrier is equal to $\sigma_{Cg} \cong 0.00421\mu$ and has the order-of-magnitude estimate $\sigma_{Cg} \leqslant \mu\exp(-n)/2\pi \cong 10^{-3}\mu$, i.e., creation is possible under stresses of the order of those applied. The energy barrier is more than two times lower: $E_{Cg} \leqslant E_{CX}/2$. The results of numerical calculation of the force conditions for creation of lattice dislocations on boundaries for cases (a) and (b) are shown by the dashed line in Fig. 2.

5. DEFECTS AND DEFORMATION OF AMORPHOUS METALS AND QUASICRYSTALS

The quasicrystal potential (1) can describe the structure of amorphous and quasicrystalline solids. Therefore, quasi-dislocations (8) and (9) describe defects in such structures. The absence of static quasi-dislocations and the short-range nature of the stress field (11), (12) do not contradict the structural data of Refs. 16 and 17 for a deformation-without-hardening curve.[16] The motion of periodic packets of quasi-dislocations (8) explains the localization and periodicity in the magnitude of the deformation in the shear bands of such materials[16,17] and the appearance of jumps in the deformation curve. Creation of quasi-dislocations by means of a homogeneous mechanism requires high stresses, equal in order of magnitude to $\sigma_T \approx \mu\exp(-2\Delta_0/b_g) \approx (10^{-1}-10^{-2})\mu$. These values correlate well with the yield point of amorphous metals $\sigma_T \approx 2\times10^{-2}\mu$. The small elastic energy of the quasi-dislocations (14) explains the small value of the latent energy ($\sim 4\%$) of the work of deformation in such materials.[16]

[1] H. Gleiter and B. Chalmers, *Large-Angle Grain Boundaries* (Mir, Moscow, 1975).
[2] R. W. K. Honeycombe, *The Plastic Deformation of Metals* (Arnold, London, 1968).
[3] O. A. Kaĭbyshev, *Plasticity and Superplasticity of Metals* (Metallurgiya, Moscow, 1975).
[4] O. A. Kaibyshev, R. Z. Valiev, and A. K. Emaletdinov, Dokl. AN SSSR **279**, 369 (1984) [Sov. Phys. Dokl. **29**, 967 (1984)].
[5] H. Gleiter, Nanostructured Materials (Stuttgart University) **6** (1–4), 3 (1995).
[6] O. A. Kaĭbyshev and R. Z. Valiev, *Grain Boundaries and Properties of Metals* (Metallurgiya, Moscow, 1987).
[7] A. N. Orlov, V. N. Perevezentsev, and V. V. Rybin, *Grain Boundaries in Metals* (Metallurgiya, Moscow, 1980).
[8] *Structure and Properties of the Inner Surfaces of an Interface in Metals* edited by B. S. Bokshteĭn (Nauka, Moscow, 1988).
[9] J. P. Hirth and J. Lothe, *Theory of Dislocations* (McGraw-Hill, New York, 1967).
[10] J. H. Van der Merve, Crit. Rev. Solid State Mater. Sci. **17**, 187 (1991).
[11] A. C. Newell, *Solitons in Mathematics and Physics* (SIAM, Philadelphia, 1985).
[12] Yu. A. Tkhorik and L. S. Khazan, *Plastic Deformation and Mismatch Dislocations in Hetero-Epitaxial Systems* (Naukova Dumka, Kiev, 1983).
[13] D. Gratias and A. Thalal, Philos. Mag. Lett. **57**, *2*, 63 (1988).
[14] I. V. Ovid'ko, Fiz. Tverd. Tela (St. Petersburg) **39**, 306 (1997) [Phys. Solid State **39**, 268 (1997)].
[15] A. K. Emaletdinov and Sh. Kh. Khannanov, Fiz. Met. Metalloved. **44**, 460 (1977).
[16] *Metallic Glasses*, edited by J. J. Gilman and Kh. Dzh. Limi (Metallurgiya, Moscow, 1984).
[17] A. M. Bratkovskiĭ, Yu. A. Danilov, and G. I. Kuznetsov, Fiz. Met. Metalloved. **68**, 1045 (1989).

Translated by Paul F. Schippnick

PHYSICS OF THE SOLID STATE VOLUME 41, NUMBER 10 OCTOBER 1999

Radio-frequency paramagnetic resonance spectra, detected from dislocation displacement in NaCl single crystals

Yu. I. Golovin, R. B. Morgunov, V. E. Ivanov, and A. A. Dmitrievskiĭ

G. R. Derzhavin Tambov State University, 392622 Tambov, Russia

(Submitted March 12, 1999)
Fiz. Tverd. Tela (St. Petersburg) **41**, 1778–1784 (October 1999)

Results are reported here of a study of the resonance effect of a constant magnetic field and a variable magnetic field crossed with it on the rate of macroplastic deformation and motion of edge dislocations in NaCl crystals. The frequencies of the variable magnetic field at which the maximum variations in the plasticity of the crystals are observed correspond to the resonant frequencies for transitions between the Zeeman sublevels in paramagnetic complexes of point defects and complexes consisting of a point defect and a dislocation. Analysis of the radio-frequency spectra obtained enabled us to establish the role of intercrystal reactions in the formation of the mechanical properties of the crystals. © *1999 American Institute of Physics.* [S1063-7834(99)01210-1]

Reference 1 reported the discovery that a constant magnetic field has an effect on the mobility of dislocations in ionic crystals. A detailed study of this magnetoplastic effect[2,3] showed that one possible reason for softening of crystals in a magnetic field is a change in the kinetics of formation and breaking of covalent bonds between paramagnetic defects. This conclusion, on the face of it, leads to a contradiction with thermodynamics. In actual fact, magnetic effects in the equilibrium electronic subsystem of a crystal are possible at temperatures T at which the energy of the Zeeman splitting of the electron levels $g\mu B$ is comparable to or larger than the mean energy of the thermal fluctuations kT (g is the spectroscopic splitting factor, μ is the Bohr magneton, and B is the magnetic induction). For example, if we consider the formation process of a covalent bond between a thermalized donor and a thermalized acceptor, which in an ionic crystal are structural defects, then it is necessary to take into account that the polarization of paramagnetic centers $P=(n_+-n_-)/(n_++n_-)$ created by a magnetic field with induction $B\sim 1$ T, at $T=300$ K, is equal in order of magnitude to $P=\coth(g\mu B/2kT)\sim 10^{-3}$ (n_+ and n_- are the concentrations of defects with spin aligned and anti-aligned with the magnetic field, respectively). The corresponding relative change in the rate of the electronic process in the crystal $\Delta k/k$ can be estimated as the product of the polarizations of the donors and acceptors, i.e., $\Delta k/k\sim P^2\sim 10^{-6}$. At the same time, the effects described in Refs. 1–3 consist in a more-than-twofold increase in the dislocation motion and rate of macroplastic flow of the crystals in a magnetic field with induction $B\sim 1$ T at $T=300$ K.

To overcome this contradiction, the authors of Refs. 4 and 5 proposed an approach analogous to the approach that explains the influence of an energetically weak magnetic field on the evolution of multistep chemical reactions.[6–8] Within the framework of this approach, thermal fluctuations can be neglected if the duration of the magnetically sensitive reaction step is shorter than the spin relaxation time. Therefore, when considering the influence of a magnetic field on the interaction of a paramagnetic point defect P and a dislocation D (the reaction $M\Leftrightarrow D+P$) or about reactions between point defects $K\Leftrightarrow P_1+P_2$, it is necessary to take into account that some steps of these reactions can occur at an effective local temperature $T^*=0$. This is because, during the short time of occurrence of a reaction step, the variable magnetic fields created by phonons ‘‘do not have time’’ to destroy the spin polarization of the electrons, which is usually inherited from the preceding stable state of the complex and can be close to 100% at the time of creation of its intermediate state. The authors of Refs. 4 and 5 advanced the hypothesis that, in contrast to thermally fluctuating magnetic fields, an external magnetic field can mix the states of a pair of defects with different multiplicity during a time, over the course of which the energy difference between the singlet S and triplet T_0 terms, of the complex $\Delta U=U_T-U_S$, is comparable to $g\mu B$. This, in their opinion, influences the probability of bond formation in the pair $D\ldots P$. At present, experimental confirmation of this hypothesis as well as a direct proof of the spin nature of the magnetoplastic effect in ionic crystals is lacking. In addition, it is unclear whether this hypothesis relates to that part of the magnetoplastic effect for which reactions in the pairs $P_1\ldots P_2$ are responsible. To solve these problems, it is possible to create experimental conditions analogous to those that obtain in the widely known method for studying non-thermalized short-lived complexes in chemical reactions, RYDMR (reaction yield detected magnetic resonance).[9,10] Frankevich and coworkers detected a paramagnetic resonance not by absorption of an electromagnetic wave, but by the chemical reaction yield[9] or the fluorescence intensity.[10] RYDMR, in contrast to the well-known method ODMR (optical detection of magnetic resonance),[11] makes it possible to record and study at room temperature less than 10^3 pairs of paramagnetic particles—intermediate reaction products, simultaneously present in the sample.

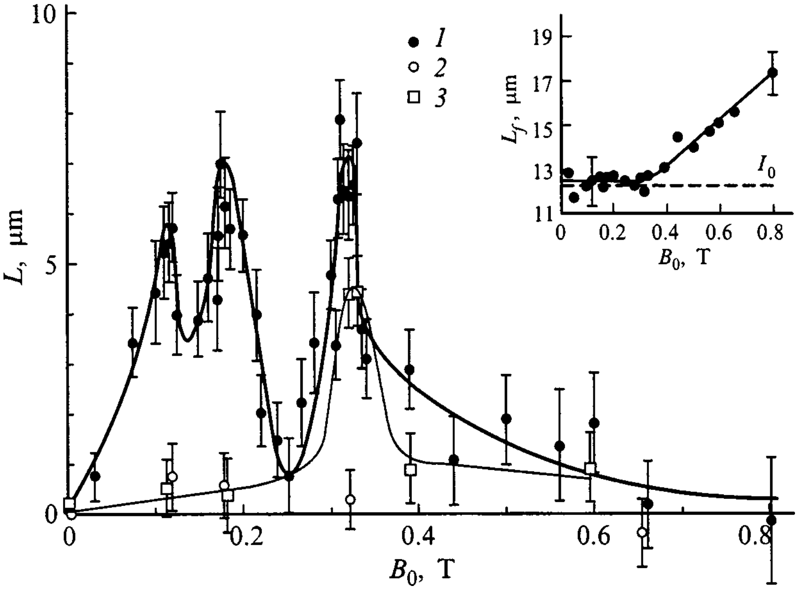

FIG. 1. Dependence of the mean displacement of the dislocations L on the induction of the constant magnetic field B_0 applied for 15 min with simultaneous application of a microwave field ($\nu=9.5$ GHz): *1* — in the configuration $\mathbf{B}_1 \perp \mathbf{B}_0$, where $\mathbf{B}_1$ is the induction of the microwave field, *2* — in the configuration $\mathbf{B}_1 \| \mathbf{B}_0$, *3* — in the configuration $\mathbf{B}_1 \perp \mathbf{B}_0$ in crystals pre-treated with a constant magnetic field pulse with amplitude $B=7$ T. The inset shows a plot of the dependence of the displacement of the dislocations L_f on the induction of the constant magnetic field B_0 applied for 15 min in the absence of the microwave field. The dashed line indicates the value of the displacement L_0 in control runs without the constant and microwave magnetic fields.

In Ref. 12 Molotskii and Fleurov demonstrated theoretically for the first time that the combined action of a constant and a high-frequency magnetic field can lead to resonant plastification of crystals if the frequency of the variable field ν satisfies the paramagnetic resonance condition $h\nu = g\mu B$. Therefore, the aim of the present work consists in studying the mobility of individual edge dislocations and macroplastic flow of crystals under conditions of simultaneous action of a constant magnetic field and a high-frequency magnetic field crossed with it.

1. TECHNIQUE

Plasticity of crystals under an external magnetic field was studied with the help of two standard techniques: measurement of the displacements of individual edge dislocations and recording changes in the macrostrain diagram of crystals placed in a constant magnetic field at the moment the microwave field is switched on. The experiments used NaCl single crystals with a divalent-metal impurity (mainly Ca) with concentration 0.01 at.% (to study microplasticity) and 0.1 at.% (to study macrostrains), annealed at 700 K and cooled to 293 K during 10 h. Samples with freshly introduced edge dislocations were placed inside a H_{10} waveguide connected to a klystron which operated at the frequency ν=9.5 GHz and generated an electromagnetic energy flux through the crystal with power ~10 mW. The waveguide was located between the poles of an electromagnet, which established a constant magnetic field with induction B_0 from 0 to 0.8 T in the vicinity of the crystal. The vector $\mathbf{B}_0$ in all of the runs was directed along the [001] direction.

2. RESULTS

To investigate the effect of a constant magnetic field and a microwave field on the mobility of of individual edge dislocations, their displacements, initiated by the action of the external magnetic fields in the absence of a mechanical load, were measured by the traditional method of double chemical etching. Double etching of the samples in the absence of external effects caused a mean shift of the dislocations $L_0 = 12 \pm 1$ μm. This shift is due to the action of internal mechanical stresses and etching-out of near-surface stoppers.[13] The dislocation displacement in crystals subjected for 15 min to the microwave field in the absence of a constant magnetic field was the same in magnitude, i.e., exposure of the crystals to just the variable magnetic field had no effect on the mobility of the dislocations. Therefore, in processing the results of the experiments, the mean displacement L_0 was subtracted from the mean displacement L_f in crossed constant and microwave fields, and the value of the displacement $L = L_f - L_0$ obtained in this way served as an indicator of the effect of crossed fields on the mobility of the dislocations.

In the first stage of the experiments, on introducing dislocations and first etching the crystals placed in the waveguide were exposed to crossed magnetic fields for 15 min and were subjected to a second etching. Exposure of the crystals in a constant magnetic field with simultaneous action of a microwave field (in the configuration $\mathbf{B}_1 \perp \mathbf{B}_0$, where $\mathbf{B}_1$ is the induction of the microwave magnetic field) led to an increase in L for $B_0 = B_{\mathrm{res1}} = 0.12 \pm 0.02$ T, $B_0 = B_{\mathrm{res2}} = 0.18 \pm 0.02$ T, and $B_0 = B_{\mathrm{res3}} = 0.32 \pm 0.03$ T (Fig. 1). In the region of the peaks we made the measurements with special care: using a smaller step in B_0 and larger statistics (as many as 500 measurements at each point). When the constant field and the microwave field were applied in the configuration $\mathbf{B}_1 \| \mathbf{B}_0$, the peaks disappeared (Fig. 1).

In the absence of the microwave field, the constant magnetic field with $B_0 > 0.35$ T also caused dislocation displacements L_f which were larger than L_0; however, the field dependence of the displacements in this case was monotonic, i.e., peaks were absent (inset to Fig. 1).

In order to convince ourselves that the appearance of peaks was not random, we carried out analogous experiments at the microwave frequency ν=152 MHz, at which for $B \approx 5$ mT we also detected an increase in the dislocation displacements (Fig. 2), where the magnitude of the effect at maximum decreases monotonically as the angle φ between

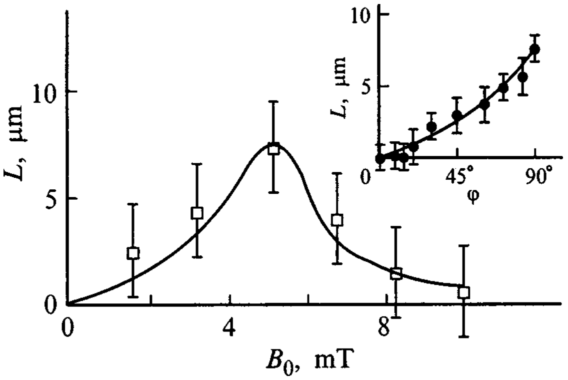

FIG. 2. Dependence of the mean displacement of the dislocations L on the induction of the constant magnetic field B_0 applied for 15 min with simultaneous application of a microwave field (ν=152.2 MHz) in the configuration $\mathbf{B}_1 \perp \mathbf{B}_0$, where $\mathbf{B}_1$ is the induction of the microwave field. The inset shows a plot of the dependence of the displacements of the dislocation in a microwave field for B_0=5mT on the angle φ between the field vectors $\mathbf{B}_1$ and $\mathbf{B}_0$.

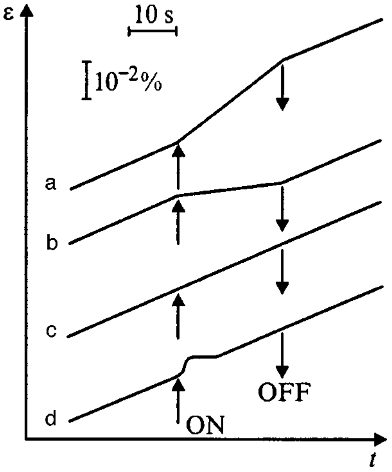

FIG. 3. Typical portions of the dependence of the relative strain of the crystals ε on the loading time t in a constant magnetic field with B_0=0.32 T at the time the microwave field is switched on (ν=9.5 GHz). a — softening; b — hardening; c — no effect of crossed fields; d — deformation ''jump.'' Arrows indicate switching on and off times of the microwave field.

$\mathbf{B}_1$ and $\mathbf{B}_0$ is varied from 90° to 0° (inset to Fig. 2).

We found that, in crossed fields, on average over the crystal, an equiprobable nature of the motion of the individual dislocations is observed in the crystallographic planes $[\bar{1}10]$, $[1\bar{1}0]$, $[\bar{1}\bar{1}0]$, and $[110]$ at the same average distances on all the faces of the sample. Consequently, the role of the external fields in our experiments reduced to a depinning of the dislocations from stoppers, and the motion of the dislocations took place under the action of random internal mechanical stresses.

Thus, measurement of the dislocation displacements allows one to record the radio-frequency spectrum of the electronic transitions in the subsystem of structural defects. Since the mobility of the dislocations can depend not only on their interaction with point defects (the reaction $M \Leftrightarrow D+P$), but also on reactions inside the complexes of point defects themselves and in the dislocation nuclei, it is difficult *a priori* to put the peaks in correspondence with definite types of reactions between defects. Earlier it was established that the dislocation displacements created by placing the crystals in a constant magnetic field in the absence of the microwave field decrease if the crystal is pre-exposed in a constant magnetic field before the dislocations are introduced.[14] It was established that a constant magnetic field stimulates the accelerated relaxation of metastable complexes K by unblocking irreversible first-order reactions of the type $\mathrm{K} \Rightarrow P_1 + P_2$ (Ref. 3). This process in crossed magnetic fields can, in principle, also lead to the appearance of peaks in the dislocation mobility.

To establish the roles of the $\mathrm{K} \Rightarrow P_1 + P_2$ reactions in the formation of the spectra detected from the dislocation displacements, we carried out a second series of measurements in which we studied the influence of pre-exposure of the crystals in a constant magnetic field prior to introducing dislocations on the dependence $L(B_0)$ measured in crossed fields. We found that pre-exposure of the crystals in a constant magnetic field with $B=7$ T for 2×10^{-2} s is sufficient to make the first and second peaks in the dependence $L(B_0)$ disappear completely (Fig. 1). In this case, the third peak at $B_0=0.32$ T is decreased only a little. Consequently, the first and second peaks arise as a consequence of a resonance with complexes formed by magnetically sensitive point defects while the third peak is an indicator of paramagnetic resonance in complexes containing a dislocation. Thus, preliminary treatment of the crystals in a constant magnetic field, which leads to relaxation of metastable, magnetically sensitive point defects, takes reactions of the type $\mathrm{K} \Rightarrow P_1 + P_2$ out of play.

In the third series of runs we investigated the combined action of a constant magnetic field and a microwave field with frequency ν=9.5 GHz, applied in the configuration $\mathbf{B}_1 \perp \mathbf{B}_0$, on the rate of macroplastic flow of the crystals. Macroplastic deformation of the crystals was performed in a ''soft'' machine with quartz rods, creating a mechanical compressive stress that increased linearly with time, $\sigma = st$, where s = const (Ref. 15). In this case, aided by an induction sensor with an accuracy of ±0.1 μm, we continuously recorded the length of the sample. This enabled us to construct a stress/strain diagram on an $X-Y$ plotter, i.e., the dependence of the relative strain ε on σ or the time t elapsed from the commencement of loading.

In the absence of a constant magnetic field, switching on a microwave field did not lead to a change in the strain rate $d\varepsilon/dt$ (Fig. 3). This suggests that any changes in the strain diagram, that could arise when the microwave field is switched in the presence of the constant magnetic field, can be interpreted as a result of the combined action of the constant and variable magnetic fields. In the following experiments, each sample was strained to a relative strain ε=0.5% for 10–15 min with the constant magnetic field switched on. The microwave field was switched on for 20–30 s during application of stress.The combined action of the fields on the macroplasticity was investigated in a comparatively narrow range of strains ($0.1<\varepsilon<0.5\%$) at the easy-slip stage.

We found that, up to the yield point, switching on the microwave field did not lead to a change in the $\varepsilon(t)$ plot. After the yield point was reached, the microwave field could lead with roughly equal probability to three different experimental outcomes: to an increase in $d\varepsilon/dt$, to a decrease in $d\varepsilon/dt$, and to no change in $d\varepsilon/dt$ (Fig. 3). Switching the microwave field off, as a rule, led to a recovery of the plastic flow rate, both in the case of softening and in the case of hardening brought about by switching on the microwave field. In 10% of cases, after switching off the microwave field, $d\varepsilon/dt$ did not recover. Another, significantly more unusual outcome that could occur was a jumplike increase in the strain level by ~ 0.5 μm when the microwave field was switched on [Fig. 3d]. For B_0 close to B_{res2} or B_{res3}, such deformation ''jumps'' were encountered three times more often than for other values of B_0. The different sign of the effect, and also its absence in ~ 30 affected by the crossed magnetic fields, and also to the absence of artifacts caused by the action of the fields on the components of the testing machine.

In what follows, in the quantitative reduction of the experimental results, we did not take into account ''jumps'' and situations in which the diagram did not change when the microwave field was switched on; rather, we only took into account cases in which there was a change in the slope of the curve $\varepsilon(t)$ with its subsequent recovery when the microwave field was switched off. Here we measured the plastic flow rate before switching on the microwave field $(d\varepsilon/dt)_1$ and immediately after switching it on $(d\varepsilon/dt)_2$. We took the ratio $\gamma = (d\varepsilon/dt)_2/(d\varepsilon/dt)_1$ as a measure of the effect of the combined action of the crossed fields on the plasticity, so that softening was characterized by values of this ratio $\gamma = \gamma_+ > 1$, and hardening, by values $\gamma = \gamma_- < 1$. In such an approach, the frequency of appearance of various outcomes is ignored, and only the magnitude of the effects associated with their appearance is taken into account. Each point on the graphs in the third series of runs is the result of 10–20 separate measurements of the quantities γ_+ and γ_-, performed on different crystals under identical conditions.

We found that both dependences $\gamma_+(B_0)$ and $\gamma_-(B_0)$ are nonmonotonic. Both of them have extrema at $B_0 \approx 0.2$ T and $B_0 \approx 0.3$ T (Fig. 4). Thus, the combined action of a microwave magnetic field and a constant magnetic field on the macroplastic flow also has a resonance nature, where the positions of the maxima of the hardening and softening effects are close to the positions observed in the study of the displacements of individual dislocations.

An EPR study of the crystals examined in our experiments did not reveal resonant absorption of microwave power for the above-indicated values of $B_{\mathrm{res}\,i}$. This fact, and also the necessity of extended exposure of the crystals in crossed fields to detect resonances in the mobility of the dislocations indicates that only a small number of defect pairs are simultaneously present in the crystals, which enter into the reaction in an uncorrelated way. Their formation is a rare event, inaccessible for recording with an EPR spectrometer.

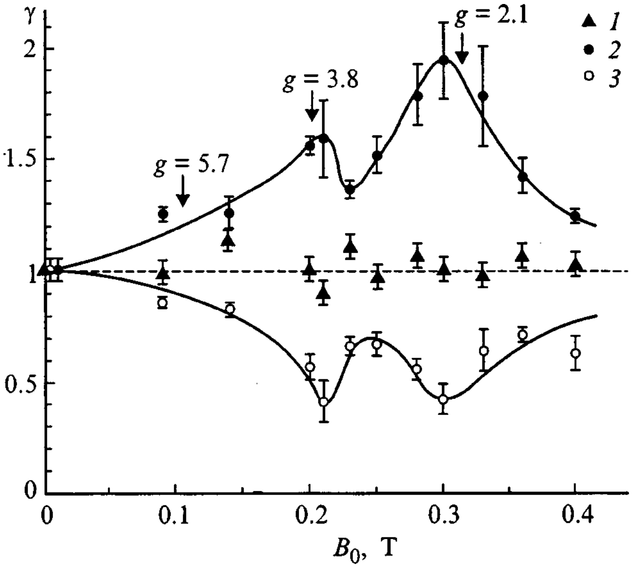

FIG. 4. Dependence of the softening effect of the crystals γ [ratio of the plastic flow rate after switching on the microwave field $(d\varepsilon/dt)_2$ to the plastic flow rate before switching it on $(d\varepsilon/dt)_1$] on the induction of the constant magnetic field B_0 at which deformation occurs: *1* — before the yield point in the range of relative strains $\varepsilon < 0.03\%$ γ_+ for cases of softening observed after the yield point for relative strains $0.1 < \varepsilon < 0.5\%$, *3* — γ_- for cases of hardening observed after the yield point for relative strains $0.1 < \varepsilon < 0.5\%$.

3. DISCUSSION

The setup of the experiment and its results are similar to the usual conditions for observing an EPR signal with the exception that the response consisted of a change in characteristics of the plasticity of the crystal instead of absorption of an electromagnetic wave. The values $B_{\mathrm{res1}} = 0.12 \pm 0.02$, $B_{\mathrm{res2}} = 0.18 \pm 0.02$, and $B_{\mathrm{res3}} = 0.32 \pm 0.03$ obtained in the first series of runs correspond to the field values $B_{\mathrm{th}} = h\nu/\mu B_0 g$ at which resonant transitions occur at the implemented microwave frequency $\nu = 9.5$ GHz between the constant-field split electron-spin sublevels with effective spectroscopic-splitting factors $g_1 = 5.7 \pm 0.7$, $g_2 = 3.8 \pm 0.3$, and $g_3 = 2.1 \pm 0.2$, respectively. An increase in the mobility of the dislocations at the frequency $\nu = 152$ MHz for $B_0 = 5$ mT is additional evidence of the resonance nature of the observed phenomenon.

With less accuracy, it is possible to judge the position of the peaks in the dependence $\gamma(B_0)$ in the runs with macroplastic deformation (Fig. 4); however, within the limits of measurement error, the positions of the two resonance peaks coincide with the positions of the peaks detected from the mobility of individual dislocations in the first series of runs. The low accuracy of measuring of the peak positions in the third series of runs may be due both to instability of the macroplastic deformation and to the wider spectrum of the electronic processes occurring under these conditions than for motion of individual dislocations.

As was indicated in the Introduction, the constant and variable magnetic fields used in our experiments are too weak to alter the state of the thermalized paramagnetic centers or of the covalent bond between the defects. At the same time, it is known that upon deformation of ionic crystals, or when they are damaged, F-like, V_k, and other paramagnetic centers arise, and also metastable complexes of such centers.[16–18] Defects of this kind could also have been formed in our experiments during creation and motion of the dislocations. Relaxation of these metastable defects during interaction of the dislocations with them, like most other solid-state chemical reactions, takes place in several steps, one of which may be too short for thermal fluctuations to have time to influence their course. Apparently, the magnetic fields interfere with the evolution of the structural defects during this short step, whose duration τ should satisfy the condition $\tau_{\rm tr}<\tau<\tau_{\rm rel}$ in order for the magnetic fields to be able to affect the evolution of the defects ($\tau_{\rm tr}$ is the duration of the $S-T$ transition, $\tau_{\rm rel}$ is the duration of spin relaxation caused by thermal vibrations of the crystalline lattice). In the absence of external magnetic fields the time of the transition between states with different multiplicity $\tau_{\rm tr}$ can reach tens of minutes because of spin blocking of such a transition.[19] The role of the magnetic fields reduces to removal of this blockage and a many-fold increase in the rate of the transitions, i.e., to a decrease of $\tau_{\rm tr}$.

If the presence of a threshold value for the induction of the constant magnetic field $B_0\approx 0.35$T, above which an enhanced mobility of the dislocations arises (Fig. 1), is connected with the fact that the inequality $\tau_{\rm tr}<\tau$ ceases to hold (i.e., $\tau_{\rm tr}$ approaches τ for $B_0\approx 0.35$ T), then it is possible to obtain an estimate for τ which, as a rule, does not depend on the presence of the magnetic field. For this it is necessary to know the mechanism of mixing of states with different multiplicity in the magnetic field. At present, the following mechanisms are known in spin chemistry: ''relaxational,'' ''STV,'' and the ''Δg mechanism.''[6–8] The first two are brought about with the participation of the Fermi magnetic field of the nuclei and, as a rule, are characterized by values of the induction of the constant magnetic field $B_0\sim 0.01-0.1$ T, at which the magnetic effects start to saturate.[6] Since saturation of the field dependence of the dislocation displacements has not been observed in studies of the magnetoplastic effect, even at $B\sim 10$ T (Refs. 5 and 20), we are left to assume that the magnetic field affects the multiplicity of the complexes by the ''Δg mechanism.'' In this case, in a constant magnetic field in the absence of the microwave field, inter-Raman transitions take place as a consequence of the difference in the g factors of the two paramagnetic particles of the complex. This difference $\Delta g=g_1-g_2$ may be due to the different nature of the paramagnetic particles of the pair or to different local crystal fields around them. It causes the difference in the frequencies of precession of the spins about the field vector $\mathbf{B}_0$ (Refs. 6–8) and the periodic interconversion of singlet states. For typical values of $\Delta g\sim 10^{-3}$ and the threshold value of $B_0=35$ T we obtain $\tau=\tau_{\rm tr}\sim 1/(\omega_1-\omega_2)=\hbar/\mu B_0(g_1-g_2)\sim 10^{-8}$ s, where ω_1 and ω_2 are the precession frequencies of the spins of particles with g factors g_1 and g_2.

In the absence of the microwave field, for inductions of the constant magnetic field larger than 0.35 T, an inter-Raman transition has sufficient time to occur during the lifetime of a nonequilibrium state of the complex. As a result, products of an interdefect reaction are formed which could not be formed in the absence of the magnetic field. This alters the arrangement of the atoms and covalent bonds between them and leads to a decrease of the braking force on a dislocation produced by stoppers and to a corresponding increase in its displacement.

For inductions of the constant magnetic field less than 0.35 T, an inter-Raman transition does not have sufficient time to occur during the time τ. Therefore, the same reaction products are formed as in the absence of the magnetic field, but the mobility of the dislocations does not change. If in addition to the constant magnetic field a resonant microwave field is present, then τ_{S-T} decreases and softening takes place for B_0 less than threshold.

It is entirely possible that the value of τ found can be less than the spin relaxation time $\tau_{\rm rel}$, which usually lies in the range $10^{-5}-10^{-9}$ s in the investigated crystals at room temperature.[21] This means that the condition $\tau_{\rm tr}<\tau<\tau_{\rm rel}$, necessary for the magnetic field to have a significant effect on the spin state of the structural defects, can in principle be satisfied in our experiments.

Let us discuss the energy-level diagram and possible transitions in crossed fields that can explain the appearance of a resonance in $P\ldots D$ pairs. The presence of only one peak corresponding to the reactions $M\Leftrightarrow P+D$ may mean that the $P\ldots D$ pairs are doublets, i.e., the paramagnetic centers that make them up have spin 1/2 (Ref. 22). Such a pair is characterized by one S and three T states (T_0, T_+, and T_- with projections of the total spin onto the the magnetic field vector $\mathbf{B}_0$ equal to 0, $+1$, and -1, respectively, see Fig. 5). The constant magnetic field mixes the S and T_0 states, which leads to a change in the relative concentrations of final reaction products, which are new stable defect complexes M_1 and M_2 (Fig. 5). This, in turn, increases the probability of depinning of dislocations from stoppers and facilitates plastification of the crystals. The microwave field in the presence of the constant magnetic field can increase or decrease the intensity of the $S-T_0$ transitions indirectly, depending on its amplitude and the multiplicity of the pair.[6–8] In singlet pairs the microwave field stimulates $S-T$ conversion, and in triplet pairs it weakens it. Consequently, the possibility of detecting resonance peaks in our experiments is evidence of a nonequilibrium population of the intermediate pairs over the S and T states. Measurements of the mobility of individual dislocations in crossed magnetic fields makes it possible to determine which of these states is preferentially filled at the moment of creation of the nonequilibrium complexes.

In the absence of the microwave field, the constant magnetic field causes transitions only between the S and T_0 states, thereby causing an increase in the displacements of the dislocations for $B_0>0.35$ T. If in the creation of nonequilibrium complexes the T_0 state is preferentially populated, then the microwave field facilitates its mixing with the T_+ and T_- states, leading thereby to a decrease in the occupation of the T_0 level, a decrease in the spin polarization, and a decrease in the rate of $S-T$ conversion. This, in turn, should lead to a lowering of the mobility of the dislocations under resonance conditions in comparison to the displacements in a constant magnetic field. Since in actual fact an increase in

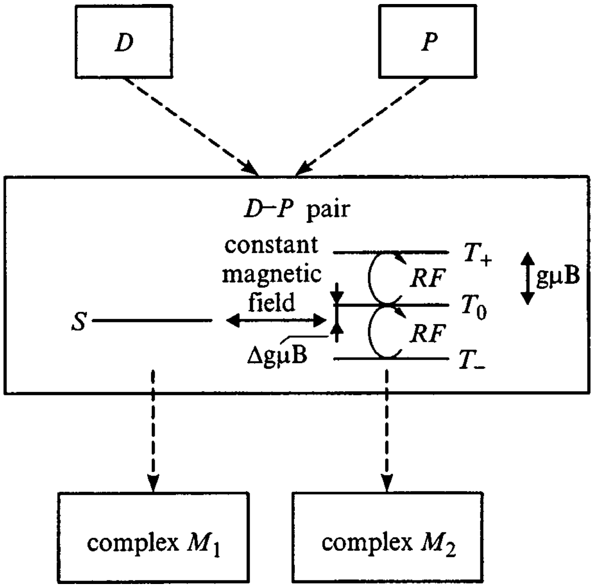

FIG. 5. Diagram of the energy levels in short-lived pairs of defects of the type $D\ldots P$ in crossed constant and microwave fields. The dashed lines indicate processes of formation of a $D\ldots P$ pair from an isolated dislocation D and a point defect P, and also the process of formation of stable complexes of two types M_1 and M_2 from the S and T states. The arrows show mixing of S and T_0 states in a constant magnetic field, and mixing of T_0, T_+, and T_- states in a microwave field.

the dislocation displacements is observed when a microwave field is added to the constant magnetic field (Fig. 1), it may be assumed that the S state is preferentially populated (as is usually the case in short-lived intermediate states whose precursors are metastable complexes of atoms, with a stable covalent bond in the singlet state). Consequently, singlet complexes make the main contribution to the peak with $g=2.1$, corresponding to the reactions $M\Leftrightarrow P+D$. Similar arguments regarding the peaks with $g_1=5.7$ and $g_2=3.8$ corresponding to the reactions $\mathrm{K}\Rightarrow P_1+P_2$ show that the main contribution to the magnetoplasticity in this case also comes from the singlet complexes.

Note that, for ''weak'' microwave fields, a mixing of the T_0 state with the T_+ and T_- states must take place, which lowers the population of the T_0 level and thus favors the $S-T_0$ transitions. For ''strong'' microwave fields, on the contrary, spin locking of the $S-T_0$ must be observed,[23] due to saturation of the $T_0\rightarrow T_+$ and T_- transitions. Consequently, by varying the microwave power it is possible to observe a maximum of the resonance effect of the magnetic field on the plasticity. The presence or absence of this effect on the plasticity can be judged from the dependence of the magnitude of the magnetoplastic effect on the angle φ between $\mathbf{B}_1$ and $\mathbf{B}_0$, with decrease of which the effective value of $\mathbf{B}_1$ falls. Since a monotonic decrease of the peak was observed in our experiments as φ decreased from 90° to 0° (see inset to Fig. 2), it may be assumed that we are dealing here with ''weak'' microwave fields.[1)]

The presence of two peaks corresponding to the reactions $\mathrm{K}\Rightarrow P_1+P_2$ has several possible explanations: the appearance in the crystal of two different types of magnetically sensitive defect–intermediates; the presence in the pair of defects of a paramagnetic center with spin greater than 1/2; a substantial contribution to the Hamiltonian from the dipole–dipole interaction between the paramagnetic centers, which unblocks the transitions with change of spin projection onto $\mathbf{B}_0$ by ± 2.

The possibility of the appearance of both softening and hardening in crossed fields indicates that several competing processes initiated by the crossed magnetic fields take place in the crystals. In a special series of measurements, we verified that the cases of hardening and softening arise with equal probability both in the easy-slip stage, and in later stages of hardening. Consequently, competing processes cannot facilitate mobility of the dislocations in the primary and secondary slip planes, as is usually observed at the end of the easy-slip stage. In addition, in earlier studies of the effect of a constant magnetic field on the macroplasticity of ionic crystals, only a softening effect of the field was observed.[1–3,5,14,15] Consequently, the reason for the appearance of hardening may be the addition of the microwave field to the constant field.

In contrast to the constant field, the microwave field is capable of mixing the singlet state of pairs of S defects with the triplet states T_+ and T_-. At the same time, in fields $B_0\sim 0.1$ T, as was shown theoretically in Ref. 24, the transitions $S\rightarrow T_+$ and $S\rightarrow T_-$ can depend on a hyperfine interaction, an account of which leads not to softening but to hardening of the crystals. Therefore, the sign of the effect of crossed fields on the plasticity can be determined by a competition of the external constant field and the Fermi field of the nuclei of the ions. It may be assumed that the result of this competition can be different, depending on the proximity of the $D\ldots P$ or $P_1\ldots P_2$ pair to the magnetic nuclei. The summation of the positive and negative effects on the various types of pairs apparently leads to the uncontrollable appearance of four possible outcomes in experiments with macroplastic deformation (Fig. 3). The absence of hardening effects in studies of the macroplasticity can be explained by the fact that the level of mechanical stresses and the density of the dislocations, and along with them the degree of distortion of the interionic distances, are markedly lower, which stabilizes the contribution of the hyperfine interaction. Additional studies are needed to test this hypothesis.

In summary, we have established experimentally that spin-dependent, magnetically sensitive reactions in a subsystem of paramagnetic structural defects in ionic crystals make a substantial contribution to their plastic properties, and the kinetics of these reactions can be effectively regulated by a weak constant magnetic field and its combined action with a microwave field. We have shown that the mobility of the dislocations can be used as an indicator of a spin resonance in non-thermalized short-lived complexes of paramagnetic defects. The contributions to the resonance spectrum from point defects in the bulk of the crystal and from pairs formed by a point defect and a dislocation have been isolated. The results can serve as a basis for a new highly-sensitive method for investigating paramagnetic structural defects in crystals, allowing a direct determination of the interrelationship between their plastic properties and the electronic state of the defects. The proposed investigative method can be extended to a wide class of materials in which plastic deformation is accompanied by spin-dependent reactions between the defects.

This work was carried out with the financial support of the Russian Fund for Fundamental Research (Grant No. 97-02-16074), and also the program ''Universities of Russia.''

*) E-mail: golovin@main.tsu.tambox.ru

1) The authors thank A. I. Tyurin for providing these data.

---

[1] V. I. Al'shits, E. V. Darinskaya, T. M. Perekalina, and A. A. Urusovskaya, Fiz. Tverd. Tela (Leningrad) **29**, 467 (1987) [Sov. Phys. Solid State **29**, 265 (1987)].

[2] V. I. Al'shits, E. V. Darinskaya, and O. L. Kazakova, Zh. Éksp. Teor. Fiz. **111**, 615 (1997) [JETP **84**, 338 (1997)].

[3] Yu. I. Golovin and R. B. Morgunov, *Chemistry Reviews*. Gordon and Breach Publishing Group **23** (2), 23 (1998).

[4] M. I. Molotskiĭ, Fiz. Tverd. Tela (Leningrad) **33**, 3112 (1991) [Sov. Phys. Solid State **33**, 1760 (1991)].

[5] V. I. Al'shits, E. V. Darinskaya, and E. A. Petrzhik, Fiz. Tverd. Tela (Leningrad) **33**, 3001 (1991) [Sov. Phys. Solid State **33**, 1694 (1991)].

[6] Ya. L. Zel'dovich, A. L. Buchachenko, and V. L. Frankevich, Usp. Fiz. Nauk **155**, 3 (1988) [Sov. Phys. Usp. **31**, 1 (1988)].

[7] A. L. Buchachenko and I. V. Khudyakov, Usp. Khim. **60**, 1105 (1991).

[8] A. L. Buchachenko, Usp. Khim. **62**, 1139 (1993).

[9] E. L. Frankevich, V. I. Lesin, and A. I. Pristupa, Zh. Éksp. Teor. Fiz. **75**, 415 (1978) [Sov. Phys. JETP **48**, 208 (1978)].

[10] E. L. Frankevich, A. I. Pristupa, and V. I. Lesin, Chem. Phys. Lett. **47** (2), 304 (1977).

[11] G. Liĭd'ya, Izv. AN SSSR **46** (3), 429 (1982).

[12] M. Molotskii and V. Fleurov, Philos. Mag. Lett. **73**, 11 (1996).

[13] V. B. Pariĭskiĭ, A. I. Landau, and V. I. Startsev, Fiz. Tverd. Tela (Leningrad) **5**, 1377 (1963) [Sov. Phys. Solid State **5**, 1002 (1963)].

[14] Yu. I. Golovin and R. B. Morgunov, JETP Lett. **58**, 191 (1993).

[15] Yu. I. Golovin and R. B. Morgunov, JETP Lett. **61**, 596 (1995).

[16] K. Hoffman and E. Linke, Phys. Status Solidi A **32**, K67 (1975).

[17] J. Wollbrant, U. Bruckner, and E. Linke, Phys. Status Solidi A **78**, 163 (1983).

[18] V. A. Zakrevskiĭ and A. V. Shul'diner, Fiz. Tverd. Tela (Leningrad) **27**, 3042 (1985) [Sov. Phys. Solid State **27**, 1826 (1985)].

[19] S. P. McGlynn, T. Azumi, and M. Kinoshita, *Molecular Spectroscopy of the Triplet State* (Prentice-Hall, Englewood Cliffs, N.J., 1969).

[20] Yu. I. Golovin, R. B. Morgunov, S. E. Zhulikov, and D. Yu. Golovin, Fiz. Tverd. Tela (St. Petersburg) **38**, 3047 (1996) [Phys. Solid State **38**, 1667 (1996)].

[21] A. Abragam and B. Bleaney, *Electron Paramagnetic Resonance of Transition Ions* (Clarendon Press, Oxford, 1970).

[22] E. L. Frankevich, A. I. Pristupa, and V. M. Kobryanskiĭ, JETP Lett. **40**, 733 (1984)].

[23] A. E. Ermakova and S. I. Kubarev, Khim. Fiz. **11** (1), 73 (1992).

[24] M. Molotskii and V. Fleurov, Phys. Rev. B **56** (18), 1 (1997).

Translated by Paul F. Schippnick

PHYSICS OF THE SOLID STATE VOLUME 41, NUMBER 10 OCTOBER 1999

Kinetics of high-velocity penetration into high-hardness brittle media

A. S. Vlasov, Yu. A. Emel'yanov,*) E. L. Zil'berbrand, A. A. Kozhushko,
A. I. Kozachuk, G. S. Pugachev, and A. B. Sinani

A. F. Ioffe Physicotechnical Institute, Russian Academy of Sciences, 194021 St. Petersburg, Russia

(Submitted February 11, 1999)
Fiz. Tverd. Tela (St. Petersburg) **41**, 1785–1787 (October 1999)

A study has been made of the kinetics of penetration of deformable steel and tungsten rods into high-hardness brittle media (ceramics and glass) at impact velocities of 1.3–1.6 km/s. The penetration has been established to occur in two stages. In the first stage, the penetration velocity increases as the ceramic is progressively damaged. The second stage corresponds to quasi-steady-state penetration into a zero-strength medium. It is shown that it is the first stage that determines the high resistance of ceramics to intense impact. The dependence of the resistance to penetration on target geometry and impact pressure has also been established.

Recent years have witnessed an intensive interest in studies of high-hardness brittle materials (in particular, ceramics) in view of their possible use as protection against high-velocity impact.[1,2] However, the efficiency of ceramics for this has been estimated, as a rule, from the final results, for instance, from the residual penetration depth into the backup metallic target witness.

Final results are able to provide only some generalized, averaged characteristics of the process, which may prove to be of interest solely for certain specific problems. However they cannot shed light on the mechanism of such a complex, strongly time-dependent process as penetration into a ceramic, and, thus, cannot provide a basis for the use of such materials in high-velocity impact conditions.

To gain understanding of the ceramic behavior under dynamic loading taking into account the kinetics of failure of such brittle media, one should accumulate a large array of experimental data on penetration parameters obtained with a good time resolution within a broad range of experimental conditions.

Studies published to date[3–8] present some information on the investigation of the kinetics of high-velocity penetration into ceramics and glass. An analysis of these data leads one to a conclusion that the ceramic resistance to penetration varies strongly with time, namely, it decreases continually in the course of the ceramic failure. However known publications relate to specific cases and cannot yield complete information on the general relations governing high-velocity penetration into a ceramic.

The aim of the present work was a systematic study of high-velocity penetration into a ceramic during the whole process. It included investigation of the kinetics within a broad range of impact conditions for various ceramic compositions and properties, sample geometries, and impact pressures.

1. EXPERIMENTAL

The impact loading of the materials under study was effected by rods of mild steel and a plastic tungsten alloy (3 mm in diameter, 30 mm in length) at velocities ranging from 1.3 to 1.6 km/s.

The experiments were carried out on samples of alumina (Al_2O_3), silicon carbide (SiC), aluminum nitride with titanium nitride (AlN/TiN-70/30 wt.%), boron carbide (B_4C), and silicate glass, with transverse dimensions of 20×20 and 40×40 mm and 100-mm thickness. The transverse dimensions were varied to follow the effect of damage from the side surfaces. The sample thickness permitted one to exclude the effect of damage from the rear free surface of the sample during the whole interaction process. The properties of the materials studied are listed in Table I.

The studies were made with a four-frame flash x-ray setup with an exposure of $\sim 0.1\,\mu$s (the operating voltage 400–450 kV). The measurements provided data on the rod position in the ceramic to within 0.2 mm at predetermined instants of time fixed to within $0.1\,\mu$s. These data were used to construct graphs relating the position of the projectile/target boundary (penetration depth) and of the projectile back end with time.

2. RESULTS OF EXPERIMENTS AND DISCUSSION

A program based on the Tate–Alekseevskiĭ model[9,10] of penetration of a deformable rod into a continuum was developed to approximate experimental data with a continuous relationship. This program permitted one also to obtain the velocity of penetration U (velocity of the projectile/target interface), projectile rear-end velocity V, and projectile length L as functions of time after impact T or of penetration depth P.

The penetration velocity U and the projectile erosion rate dL/dT are known to be sufficiently complete characteristics of the resistance to penetration. Figure 1 displays $U(T)$ graphs for the materials under study subjected to a steel rod

TABLE I. Physicomechanical characteristics of the materials studied.

Material	Al_2O_3	SiC	AlN/TiN	B_4C	Glass
Density (ρ), g/cm^3	3.88	2.95	3.25	2.44	2.3
Longitudinal wave velocity (C_l), km/s	10.4	10.5	9.3	12.8	5.7
Shear wave velocity (C_t), km/s	6.2	6.6	5.75	7.8	3.4
Bending strength (σ), MPa	230	140	190	350	150
Fracture toughness (K_{1C}), MN$\cdot$m$^{-3/2}$	3.8	3.4	4.2	3.6	0.8

impact at a velocity $V_0 = 1.6$ km/s. All curves can be broken up into three sections.

The first section, the falling part of the curve, corresponds to a transition from the mass velocity at time $T=0$, which is determined by the shock adiabatics of interacting bodies,[11] to the penetration velocity itself. In other words, this branch of the curve reflects the transition from the shock-wave-induced interface displacement to penetration.

The second, rising section describes the initial stage of penetration, which starts from a certain minimum velocity increasing with time to an approximately constant level.

The third section corresponds to constant-velocity penetration.

Thus penetration into a ceramic may be considered as a two-stage process, with the first stage being low-velocity penetration with a progressively increasing velocity, and the second, quasisteady constant-velocity penetration. Because in the given conditions the penetration velocity is determined by the resistance to penetration, the first stage may be called a high-resistance stage. The increase in the penetration velocity (decrease of the resistance) in this stage can be accounted for by the progressively increasing target strength degradation and the transition to the zero-strength state. Hence penetration in the second stage occurs into a fractured, weakened medium, whose resistance to penetration must be determined primarily by the forces of inertia.

The variation of the target resistance to penetration can be followed also from the dependence of the projectile erosion rate dL/dP on penetration depth P (Fig. 2). The initial transient stage corresponds here to the onset of quasi-steady flow of the projectile. After the transient stage one observes intensive projectile erosion (the stage of high resistance to penetration) followed by erosion with a practically constant rate (penetration into a weakened medium). Such a dL/dP relation is in full agreement with the $U(T)$ dependence.

The data displayed in Figs. 1 and 2 indicate that the resistance to penetration is high only in the initial stage of the process. One may consider this stage to come to an end with fracture of the ceramic and complete loss of strength in the medium. Hence the high ceramic resistance to impact must depend on the parameters of this initial stage, in particular on its duration and the initial minimum penetration velocity.

Figure 3 presents dependences of the penetration velocity U on time obtained for various transverse dimensions of the sample. The duration of the low-velocity penetration stage is seen to decrease with decreasing transverse dimensions of the sample. The ceramic comminution in this case occurs faster under the action of the stronger tensile-stress waves propagating from the free side surfaces of the sample.

The dependences of the penetration velocity U on time for various pressures at the interface are shown graphically in Fig. 4. The data obtained show that as the projectile ma-

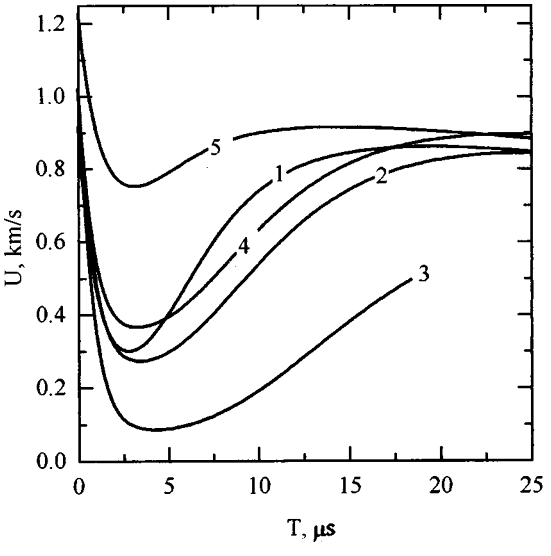

FIG. 1. Dependence of the penetration velocity of a steel projectile ($V_0 = 1.6$ km/s) into ceramic targets (*1*—Al_2O_3, *2*—SiC, *3*—AlN/TiN, *4*—B_4C, *5*—glass) on time.

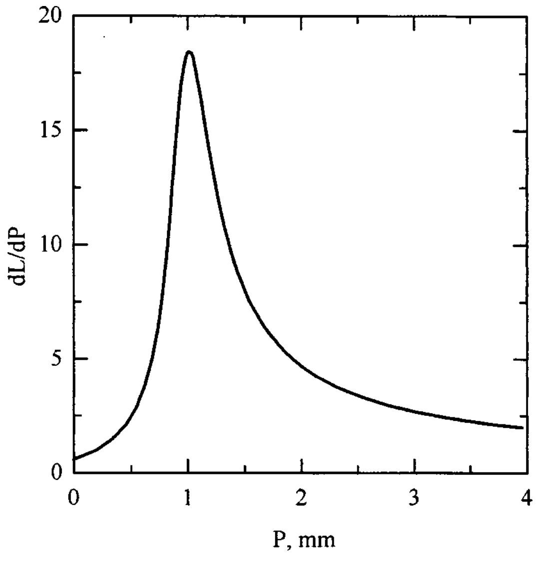

FIG. 2. Dependence of the steel-projectile erosion rate dL/dP ($V_0 = 1.6$ km/s) on penetration depth P.

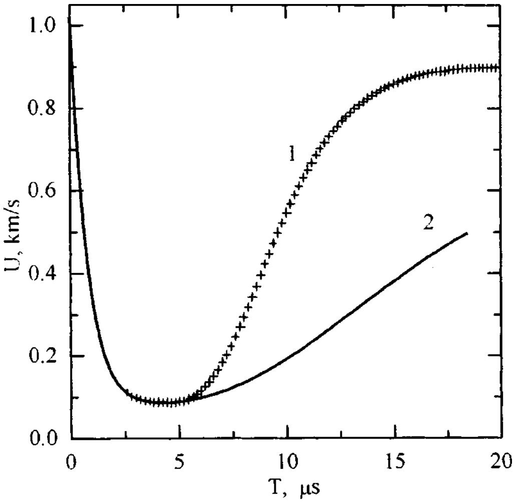

FIG. 3. Dependence of the steel-projectile penetration velocity ($V_0 = 1.6$ km/s) into an AlN/TiN target on time for various transverse dimensions of the target (*1*—20×20 mm, *2*—40×40 mm).

terial density and the impact velocity increase, the minimum penetration velocity increases, and the duration of the low-velocity stage decreases. This is attributed to the increasing level of shock loading of the material, which accelerates initiation and development of brittle fracture in the sample.

As for the effect of the properties of high-hardness brittle media on the parameters of the low-velocity penetration stage, as follows from Fig. 1, the penetration kinetics are essentially different for the materials studied in the work. In particular, this stage of low-velocity penetration (high resistance) in glass, which is characterized by the lowest strength, hardness, and fracture toughness, is less pronounced. However a correlation of the physicomechanical characteristics of ceramic materials with the parameters of the penetration process requires further investigation.

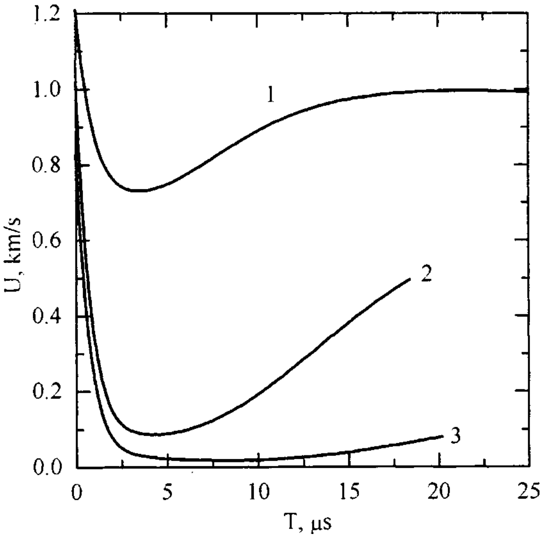

FIG. 4. Dependence of the penetration velocity of a (*1*) tungsten and (*2*,*3*) steel projectile into an AlN/TiN target on time. V_0 (km/s): *1*,*2*—1.6, *3*—1.3.

Thus a systematic experimental study of high-velocity penetration of plastic projectiles into brittle media has established that:

(1) The resistance to penetration into brittle media depends strongly on time;

(2) Penetration into ceramics and glasses occurs as a two-stage process. In the first stage, the penetration proceeds with a velocity increasing in the course of the ceramic fracture. In the second, the penetration velocity is nearly constant and is determined primarily by inertial resistance of the medium;

(3) The duration of the first penetration stage and the minimum penetration velocity determining the ceramic efficiency under high-velocity impact depend on the target material and geometry, as well as on the impact intensity. The way to an increase of the resistance of ceramics and glasses to high-velocity impact lies in increasing the duration of this stage and reducing the minimum penetration velocity.

Support of the Russian Fund for Fundamental Research (Grant 96-01-01207a) is gratefully acknowledged.

*)Deceased.

---

[1] S. J. Bless, Z. Rosenberg, and B. Yoon, Int. J. Impact Eng. **5**, 165 (1987).
[2] J. Sternberg, J. Appl. Phys. **65**, 3417 (1989).
[3] M. Wilkins, C. Cline, and C. Honodel, *Light Armor*, Report UCRL-71817 (Livermore Radiation Lab., Livermore, 1969).
[4] E. L. Zil'berbrand, N. A. Zlatin, A. A. Kozhushko, V. I. Polozenko, G. S. Pugachev, and A. B. Sinani, Zh. Tekh. Fiz. **59**(10), 54 (1989) [Sov. Phys. Tech. Phys. **34**, 1123 (1990)].
[5] G. E. Hauver, P. Netherwood, A. F. Benck, W. A. Gooch, W. J. Perciballi, and M. S. Burkins, *Proceedings of the 13th International Symposium on Ballistics* (*Stockholm, 1992*), p. 257.
[6] C. E. Anderson, Jr., V. Hohler, J. D. Walker, and A. J. Stilp, *Proceedings of the 14th International Symposium on Ballistics* (*Quebec, 1993*), p. 145.
[7] D. Orphal and B. Franzen, Int. J. Impact Eng. **19**, 1 (1997).
[8] H. Ernst, K. Hoog, and V. Wiesner, *Proceedings of the 15th International Symposium on Ballistics* (*Jerusalem, 1995*), p. 11.
[9] V. P. Alekseevskiĭ, Fiz. Goreniya Vzryva **2**(2), 99 (1966).
[10] A. Tate, J. Mech. Phys. Solids **15**, 387 (1967).
[11] Ya. B. Zel'dovich and Yu. P. Raizer, *Physics of Shock Waves and High-Temperature Hydrodynamic Phenomena* (Academic Press, New York, 1967; Nauka, Moscow, 1984).

Translated by G. Skrebtsov

PHYSICS OF THE SOLID STATE VOLUME 41, NUMBER 10 OCTOBER 1999

Interfaces between nanostructures and stepwise creep in highly oriented polymers

E. M. Ivan'kova, V. A. Marikhin, L. P. Myasnikova,*) N. I. Peschanskaya,
and P. N. Yakushev

A. F. Ioffe Physicotechnical Institute, Russian Academy of Sciences, 194021 St. Petersburg, Russia

(Submitted February 11, 1999; resubmitted February 26, 1999)
Fiz. Tverd. Tela (St. Petersburg) **41**, 1788–1791 (October 1999)

A comparative laser-interferometric study of steady creep in oriented ultrahigh-molecular-weight polyethylene films differing in the structure of interfaces between nanosized structural units has been carried out to gain a better understanding of the creep mechanism in oriented polymer materials. In contrast to conventional methods, laser interferometry permits measurement of creep rates from very small strain increments ($0.3\,\mu$m) to within 1%. This technique made it possible to detect the stepwise nature of plastic deformation in creep. The data obtained suggest that the creep rate and its periodic changes are controlled by the structure of the interfaces, and that the plastic deformation itself occurs to a considerable extent through shear of nanosized structural units relative to one another by an ''acceleration-deceleration'' type. It is proposed that the ''deceleration'' phase is due to a glide resistance created by some ''stoppers'' having either physical or chemical nature, which become destroyed and reappear again in the course of creep. © *1999 American Institute of Physics.* [S1063-7834(99)01410-0]

Highly oriented, ultrahigh-molecular-weight polymer fibers prepared by gel spinning[1] possess a high strength and a high elastic modulus combined with a low specific weight, which makes them promising construction materials. However they exhibit also a low creep resistance, which limits substantially their application potential.

There are many publications dealing with creep in polymers. While a variety of models have been proposed thus far to describe this phenomenon, the mechanism of creep still remains unclear. Various combinations of elements of the Newton, Maxwell, Voigt and other models are employed usually in simulation of the process. Most of the authors consider the creep of oriented polymers as a process controlled by deformation of the entangled molecular network and diffusion of defects through crystalline regions.[2,3] Some publications find an analogy between the processes of creep and fracture and suggest the creep to be dominated by scissions of macromolecules.[4] However practically all of them disregard the existence of a complex hierarchy of nanostructures in an oriented material and neglect the possibility of their effect on the long-term characteristics of a material. There are only a few studies considering the possible contribution of interfibrillar slip to the total deformation of an oriented polymer.[5] At the same time it would be difficult to imagine that nanostructural units (micro- and macrofibrils) do not shear in steady creep. Our recent laser-interferometric study revealed a stepped nature of the plastic deformation in highly oriented fibers of ultrahigh-molecular-weight polyethylene (UHMPE) and permitted relating it to a possible shear deformation of microfibrils and microfibrillar layers.[6] It was proposed that interfibrillar slip is controlled by the structure of the interfibrillar regions.

The objective of this work was to learn whether nanostructural morphological units slip with respect to one another in the course of steady creep and what is the part played by the structure of the interfaces separating them. Samples with completely different kinds of nanostructure connections were prepared to study this problem.

1. SAMPLES FOR THE STUDY

The samples of type I were prepared by gel-casting from a 2%-solution of UHMPE in decalin, drying in air, and drawing the films cut from it to various draw ratios λ (24, 64, and 119) by high-temperature multi-stage zone drawing. Besides, the gel films drawn to $\lambda=24$ were modified by chemical cross-linking (type-II films) by impregnating them with a radical initiator $CHCl{=}CCl_2$ (trichloroethylene), followed by UV irradiation for three min for the cross-links to form. Samples of type III were prepared from films crystallized from the melt and drawn by the above procedure. They could not be drawn to more than $\lambda=7.5$. It is known that the nanosized structural units (microfibrils) in type-I samples are connected by a few tie molecules, while in type-III samples their number is much higher.[7] It is these molecules that interfere with reaching high draw ratios. It may be thought that cross-links in type-II samples also form between microfibrils, because the large size of the trichloroethylene molecule makes possible its diffusion apparently only into the interfibrillar space.[7]

Thus the films under study represent model samples with different structural organization of interfaces, namely, with nanostructural units weakly connected and loosely packed in type-I samples with $\lambda=24$, weakly tied but closely packed in type-II samples with $\lambda=119$, cross-linked by many long bent molecular segments in type-III samples with $\lambda=4$, connected by many, predominantly extended, molecular segments in type-III samples with $\lambda=7.35$ and, finally, tied by short cross-links in type-II modified samples with $\lambda=24$.

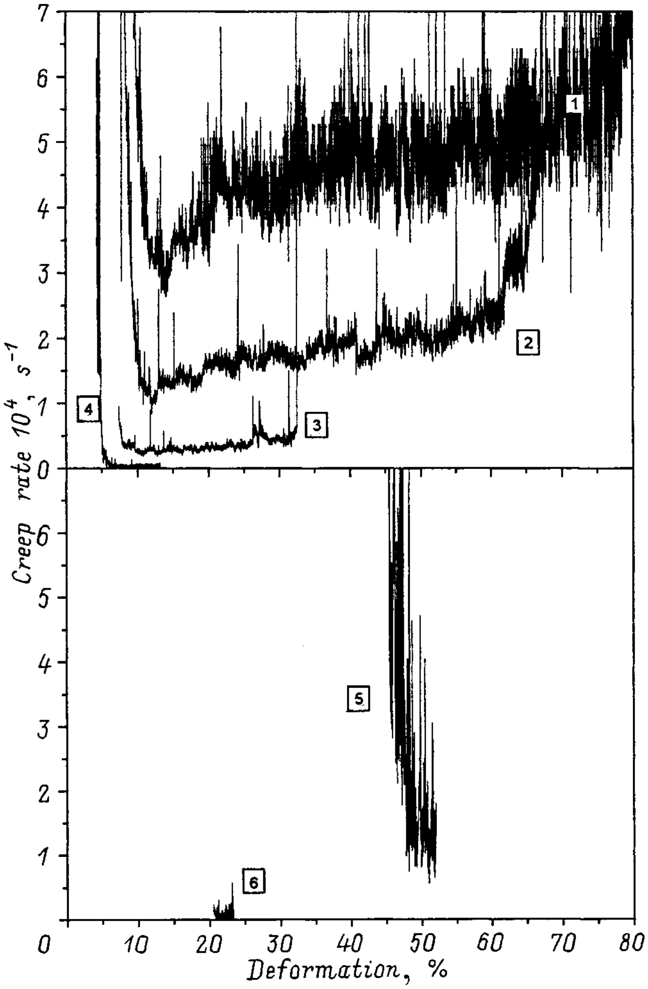

FIG. 1. Room-temperature creep under a constant load equal to 50% of the tensile stress of each sample. Sherby–Dorn plots for gel-spun UHMPE samples drawn to $\lambda = 24$ (*1*), for the same samples cross-linked by trichloroethylene (*2*), gel-spun samples with λ of 64 (*3*) and 119 (*4*), as well as for melt-cast films with λ of 4 (*5*) and 7.35 (*6*).

2. EXPERIMENTAL

The unique laser-interferometric method developed[8] at the Ioffe Physicotechnical Institute was used to measure the steady creep rate under constant load at room temperature. To be able to compare the plastic properties of the materials under study under the same conditions for all samples, the experiments were carried out by applying a stress of 50% of the tensile strength measured separately for each sample. The creep rate was calculated for each minimum increment of the total strain ($0.3\,\mu$m). An analysis was made of the dependence of the strain rate $\dot{\varepsilon}$ on strain ε (the so-called Sherby–Dorn plots).

3. RESULTS

As evident from the Sherby–Dorn plots, all the samples studied exhibited a clearly pronounced nonuniformity in the steady creep rate (Fig. 1). It looks as if plastic deformation develops always in multiple successive jumps, and the strain rate in an individual jump can be either higher or lower than the average creep rate, i.e., the process periodically accelerates and decelerates. However the deviation from the average rate depends on sample type. It is higher for samples with a smaller λ and for samples of type I (curve *1* in Fig. 1) and type II (*5* in Fig. 1). Besides, it decreases with increasing draw ratio. A comparison of curves *1* and *2* in Fig. 1 shows that formation of cross-links acts in a similar way. At the same time both cross-linking and drawing result in a decrease of the average steady-creep rate and of the ultimate strain. The resolution of interferometric strain recording is high enough to permit revealing simultaneous development of jumps on several size scales (a few microns, tens and hundreds of microns), with large jumps being composed of small ones, and their number and interrelation being dependent on the interface structure.

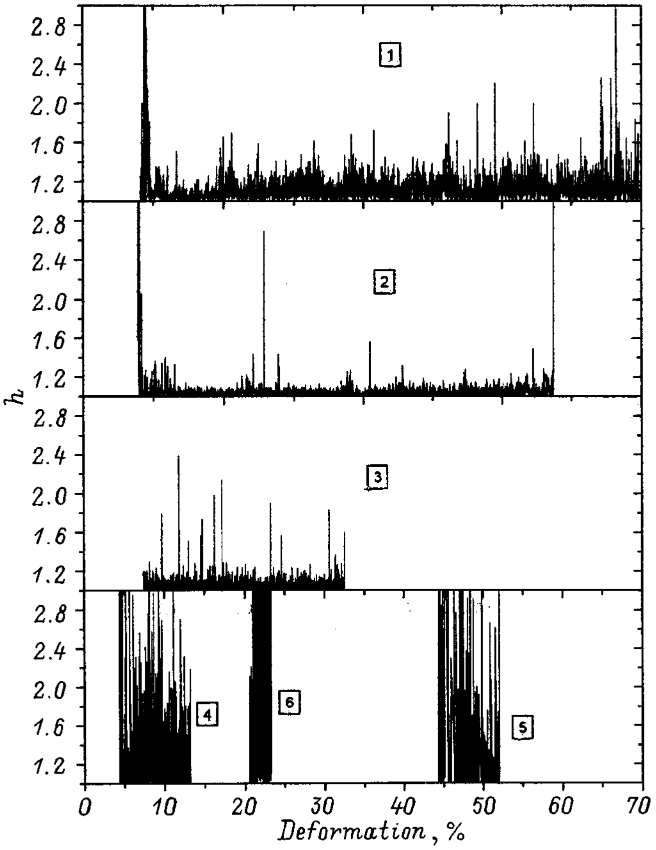

FIG. 2. Parameter *h* vs strain for the same samples. Notation same as in Fig. 1.

It is believed that the stepwise flow nature exists at the deeper structural levels, including molecular, as well.[9] The unresolved microscale (intracrystallite) shear may act as a trigger for a larger-scale (micron-size) strain. The interferometric data were used to calculate the relative change in the steady creep rate, which is characterized by the parameter $h = |\dot{\varepsilon}_{\max}|/|\dot{\varepsilon}_{\min}|$. This ratio was found for each two neighboring points, i.e., in steps of $0.3\,\mu$m (Fig. 2).

The jumps in the absolute creep rate are certainly not adequate for those in the relative rate *h*. For instance, the highest-oriented samples of type I ($\lambda = 119$) and II ($\lambda = 7.35$) (curves *4* and *6* in Fig. 1, respectively) exhibit the smallest scatter in absolute creep rate, while their jumps in the *h* parameter are an order of magnitude larger than those

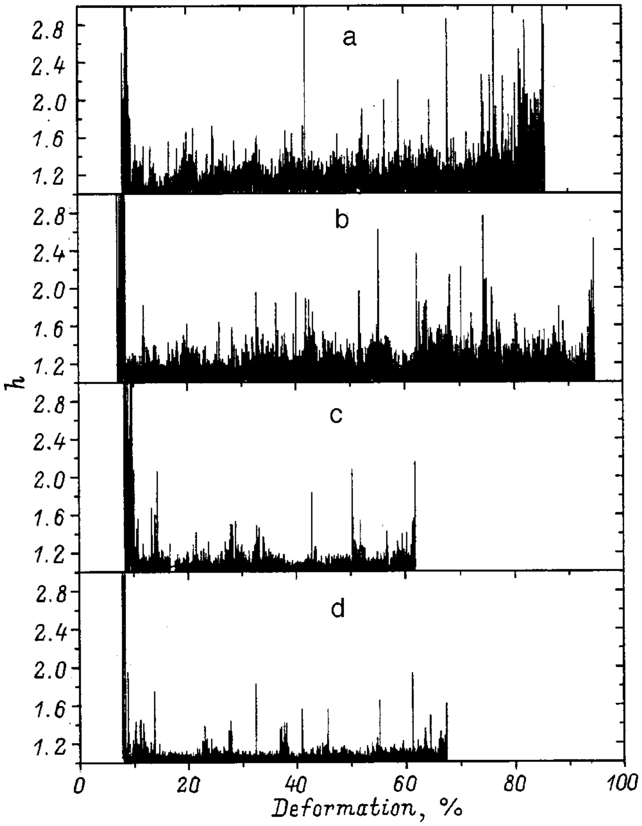

FIG. 3. Parameter *h* vs strain for two original gel-spun UHMPE films drawn to $\lambda = 24$ (a,b) and the same films cross-linked by trichloroethylene (c,d).

observed in all the other samples (curves *4* and *6* in Fig. 2). The smallest changes in the relative creep rate are seen to occur in cross-linked samples (curve *2* in Fig. 1). Note that these results show a good reproducibility (Fig. 3).

The clearly pronounced difference in the jumplike pattern of steady creep among samples having different interface structures provides supportive evidence for the hypothesis[6] that shear deformation of the nanostructural units (micro- and macrofibrils) proceeds stepwise under a constant applied load. It appears reasonable to suggest the existence of some ''stoppers'' inhibiting fibril glide with respect to one another. These stoppers could have both a physical (molecular interaction) and chemical (interfibrillar molecules, chemical cross-links) nature. Creep develops through local microshear of nanostructural units produced in overcoming the potential barriers which prevent destruction of physical knots and covalent bonds. It should be pointed out that the interferometric method is very sensitive to the height of these barriers. For instance, the jumps *h* in the relative creep rate in the highly oriented, strongly cross-linked (strong stoppers) PE fibers manufactured by DSM Co. (Netherlands) studied by us earlier were larger than those in non-modified fibers, whereas in the weakly-tied and weakly oriented (weak stoppers) films investigated here *h* decreased compared to that in the non-modified films.

The above data obtained on model samples provide a convincing argument for the assumption that the creep process consists of jumplike glide of nanostructural morphological units. These observations open up a way for efficient suppression of creep in highly oriented polymer materials by creating strong stoppers inhibiting the motion of the kinetic units.

The authors are indebted to Drs. M. Jacobs and N. Heijnen, DSM Co. (Netherlands), for providing us cross-linked gel-spun samples of UHMPE.

Support of the Russian Fund for Fundamental Research (Grant 98-03-33264a) is gratefully acknowledged.

*)E-mail: Liuba.Myasnikova@pop.ioffe.rssi.ru

---

[1] P. Smith and P. J. Lemstra, Polymer **21**, 1341 (1980).

[2] M. A. Wilding and I. M. Ward, Polymer **19**, 1969 (1978).

[3] M. A. Wilding and I. M. Ward, Polymer **22**, 870 (1981).

[4] S. N. Zhurkov, Int. J. Fract. Mech. **1**, 311 (1965).

[5] B. M. Ginzburg and Sh. Tuichiev, J. Macromol. Sci., Phys. **31**, 291 (1992).

[6] P. N. Yakushev, N. N. Peschanskaya, V. A. Marikhin, L. P. Myasnikova, and M. J. N. Jacobs, Polym. Eng. Sci. **37**, 1286 (1997).

[7] N. N. Peschanskaya, P. N. Yakushev, L. P. Myasnikova, V. A. Marikhin, and M. J. Jacobs, Fiz. Tverd. Tela (St. Petersburg) **39**, 580 (1997) [Phys. Solid State **39**, 505 (1997)].

[8] N. N. Peschanskaya and P. N. Yakushev, Fiz. Tverd. Tela (Leningrad) **30**, 2196 (1988) [Sov. Phys. Solid State **30**, 1264 (1988)].

[9] N. N. Peschanskaya, Fiz. Tverd. Tela (St. Petersburg) **35**, 3019 (1993) [Phys. Solid State **35**, 1484 (1993)].

Translated by G. Skrebtsov

PHYSICS OF THE SOLID STATE VOLUME 41, NUMBER 10 OCTOBER 1999

MAGNETISM AND FERROELECTRICITY

Spin fluctuations and peculiarities of semiconductor–metal electronic transitions in almost ferromagnetic compounds of transition metals

A. G. Volkov, A. A. Povzner, V. V. Kryuk, and P. V. Bayankin

Ural State Technical University, 620002 Ekaterinburg, Russia

(Submitted December 11, 1998)
Fiz. Tverd. Tela (St. Petersburg) **41**, 1792–1796 (October 1999)

The influence of spin fluctuations on the energy spectra of sp and d current carriers in almost ferromagnetic semiconductors based on compounds of d transition metals is examined. It is shown that because electron spectra split in the fluctuating exchange fields in almost ferromagnetic systems, electronic transitions of the type semiconductor–metal are possible, accompanied by the disappearance of energy gaps in the spectra of the sp and d electrons at various temperatures and by a shift of the chemical potential into the region of allowed energies. A specific analysis of similar electronic transitions is presented, based on the almost ferromagnetic compound FeSi. © *1999 American Institute of Physics.* [S1063-7834(99)01510-5]

1. Semiconductor–metal electronic transitions in narrowband, strongly correlated compounds of transition d metals proceed differently and are characterized by peculiarities, the reason for which have not been fully established. For example, in the antiferromagnetic oxides of titanium and vanadium, they are accompanied by a ‘‘collapse’’ of the gap in the d band and a simultaneous jumplike growth of the conductivity by several orders of magnitude.[1,2] At the same time, in the almost ferromagnetic compound FeSi and its alloys with the monosilicides of cobalt and manganese, semiconductor–metal electronic transitions have a completely different nature displayed in a gradual growth with temperature of the electrical conductivity and the magnetic susceptibility, culminating in the formation of a metallic state with a positive resistivity temperature coefficient (RTC).[3–5] Experimental studies of the static and optical conductivities[4] have established that ‘‘collapse’’ of the energy gap in the d spectrum and the change of sign of the RTC take place at different temperatures.

In Refs. 6 and 7, on the basis of an analysis of experimental data on the electronic properties of almost and weakly ferromagnetic compounds, it was shown that spin fluctuations lead to a splitting of the energies of d electrons in fluctuating exchange fields ξ. In semiconductors, such a splitting leads to a change in the energy gap between the valence d band and the conduction d band $[E_g(\xi)=E_g(0)-2\xi]$ with this gap disappearing due to monotonic growth of $\xi(T)$ at $T\geqslant T_g^{(d)}\approx 100\,\mathrm{K}$ (Ref. 7).

This latter circumstance is apparently one of the reasons for the stretched-out (in temperature) electronic transition observed in almost ferromagnetic semiconductors. However, in such a simplified model, which does not consider the influence of spin fluctuations on the spectra of sp electrons (whose spin magnetic moments interact with the fluctuating magnetic moments of the d electrons as a consequence of the sp,d exchange interaction), it is not possible to obtain quantitative agreement with experimentally observed complex temperature dependences of transport properties in the materials considered. In particular, in almost ferromagnetic FeSi, the energy gap in the d band disappears at 100 K, and the electrical resistivity begins to grow above 350 K (Ref. 5), which cannot be explained by any model which only takes account of spin-fluctuation splitting of d states. Therefore, to understand specific features of electron transitions in almost and weakly ferromagnetic compounds of transition metals, we deem it necessary to analyze the spin-fluctuation renormalizations of the energy spectra of sp current carriers.

2. To analyze the role of spin-fluctuation renormalizations of sp electron spectra, we utilize the Hamiltonian of the generalized sd model

$$H=H_0+H_{dd}+H_{int}, \tag{1}$$

in which

$$H_0=\sum_{i,\mathbf{k},\sigma}\varepsilon_{l,\mathbf{k}}a^{+}_{l,\mathbf{k},\sigma}a_{l,\mathbf{k},\sigma} \tag{2}$$

is the Hamiltonian of the noninteracting sp $(l=1)$ and d $(l=2)$ electrons;

$$H_{dd}=U\sum_{\mathbf{q}}N^d_{\mathbf{q},\sigma}N^d_{-\mathbf{q},-\sigma} \tag{3}$$

is the Hamiltonian of the Hubbard model for the d electrons;

$$H_{int}=\sum_{l,l',\mathbf{q}}Q^{l,l'}_{\mathbf{q}}\mathbf{S}^l_{\mathbf{q}}\mathbf{S}^{l'}_{\mathbf{q}} \tag{4}$$

is the Hamiltonian of the exchange interaction of the sp electrons with each other $(Q^{1,1}_{\mathbf{q}}=I_{\mathbf{q}})$ and with the d electrons $(Q^{1,2}_{\mathbf{q}}=Q^{2,1}_{\mathbf{q}}=J_{\mathbf{q}})$.

In Eqs. (2)–(4) $\varepsilon_{l,\mathbf{k}}$ re the one-electron band energies, $a^{+}_{l,\mathbf{k},\sigma}(a_{l,\mathbf{k},\sigma})$ are the creation (annihilation) operators of the sp $(l=1)$ and d $(l=2)$ electrons, $\mathbf{k}$ is the electron momentum, σ is the spin quantum number, U is the parameter of the intra-atomic Coulomb repulsion of the d electrons $(Q^{2,2}_{\mathbf{q}} \equiv U)$, $I_{\mathbf{q}}$ and $J_{\mathbf{q}}$ are the parameters of the sp,sp and sp,d exchange interactions, respectively,

$$N^{d}_{\mathbf{q},\sigma}=\sum_{\mathbf{k}} a^{+}_{2,\mathbf{k},\sigma}a_{2,\mathbf{k}+\mathbf{q},\sigma}$$

is the Fourier-transform of the electron density operator with wave vector $\mathbf{q}$ and spin σ, in the system of d electrons, and $\mathbf{S}^{l}_{\mathbf{q}}$ is the Fourier transform of the spin density vector operator of the sp $(l=1)$ and d $(l=2)$ electrons.

The calculation of the thermodynamic potential and the Green's functions (G) of the system of electrons described by the Hamiltonian (1) is a complicated many-body problem. One of the methods for solving it is based on its reduction with the help of the Stratonovich–Hubbard transformation (see Ref. 8) to a study of electron motion in fluctuating exchange $(\boldsymbol{\xi})$ and charge (η) fields. Earlier,[6,7] this method was used to describe the properties of d electrons in the Hubbard model with the Hamiltonian (2). In the present paper we present a generalization of this method to the two-band sp,d model. Here we use the formalism of Matsubara–Green's functions[9] directly dependent on the density of states and the spectra of sp and d electrons,

$$G_{l,\mathbf{k},\sigma}=\frac{1}{T}\langle T_{\tau}a^{+}_{l,\mathbf{k},\sigma}a_{l,\mathbf{k},\sigma}\sigma(1/T)\rangle_{0}/\langle T_{\tau}\sigma(1/T)\rangle_{0}. \tag{5}$$

Here T is the temperature in energy units, T_{τ} is the ordering operator in imaginary time τ, $k=(\mathbf{k},\omega_n)$, $\omega_n=(2n+1)T$ is the Fermi Matsubara frequency (n is an integer), $\langle\ldots\rangle_0$ denotes quantum-statistical averaging with the Hamiltonian (2), $\sigma(1/T)$ is the scattering matrix, defined in terms of the Hamiltonians (3) and (4) in the Matsubara interaction representation.[9]

To calculate the Green's functions, we introduce the generating functional

$$\Omega(\lambda)=\Omega_{0}-T\ln\left\langle T_{\tau}\exp\left\{-\left[\int_{0}^{1/T}d\tau(H_{dd}(\tau)+H_{int}(\tau))+\sum_{l,\mathbf{k},\sigma}\lambda_{l,\mathbf{k},\sigma}a^{+}_{l,\mathbf{k},\sigma}a_{l,\mathbf{k},\sigma}/T\right]\right\}\right\rangle, \tag{6}$$

which for $\lambda_{l,\mathbf{k},\sigma}\to 0$ coincides with the thermodynamic potential of the system under consideration, Ω_0 is the thermodynamic potential of the noninteracting electrons, $H_{dd}(\tau)$ and $H_{int}(\tau)$ are the interaction Hamiltonians (3) and (4) in the Matsubara interaction representation. We represent the Green's functions (5) in terms of the generating functional (6)

$$G_{l,\mathbf{k},\sigma}=\lim_{\lambda_{l,\mathbf{k},\sigma}\to 0}\partial\Omega(\lambda)/\partial\lambda_{l,\mathbf{k},\sigma}. \tag{7}$$

Next, employing the Stratonovich–Hubbard transformation, in analogy with Refs. 6 and 7 we express Eq. (6) in terms of functional integrals of the fluctuating exchange and charge fields

$$\Omega(\lambda)=T\ln\int_{-\infty}^{\infty}\prod_{l,\mathbf{q},j,\gamma}d\xi^{(\gamma)}_{\mathbf{q},j,l}\exp\left\{-\sum_{l,\mathbf{q}}\left|\boldsymbol{\xi}_{\mathbf{q},l}\right|^{2}+\Psi(\boldsymbol{\xi})\right\}. \tag{8}$$

Here

$$\begin{aligned}\Psi(\xi)=&-\sum_{\mathbf{q}}(X_{\mathbf{q}}|\xi_{\mathbf{q},2}|^{2}+4J_{\mathbf{q}}A_{\mathbf{q}}\boldsymbol{\xi}_{\mathbf{q},2}\boldsymbol{\xi}_{-\mathbf{q},\mathbf{1}})\\&+T\int_{0}^{1/T}d\tau\sum_{n,\mathbf{k}}\ln[(i\omega_{n}-\lambda_{l,\mathbf{k}}-\varepsilon_{l,\mathbf{k}})^{2}\\&-|\boldsymbol{\xi}_{l,\boldsymbol{\nu}}(\tau)|^{2}],\\A_{\mathbf{q}}=&\{(U-J_{\mathbf{q}}/2)(I_{\mathbf{q}}-J_{\mathbf{q}}/2)/[(UI_{\mathbf{q}}+2J_{\mathbf{q}}I_{\mathbf{q}}\\&-5J^{2}_{\mathbf{q}}/4)(UI_{\mathbf{q}}+2J_{\mathbf{q}}U-5J^{2}_{\mathbf{q}}/4)]\}^{1/2},\\c_{l,\mathbf{q}}=&\left[\left(T\det(\mathbf{Q}_{\mathbf{q}})\sum_{l'}Q^{l,l'}_{\mathbf{q}}(-1)^{l'+l}\right)\Big/\left(\det(\mathbf{Q}_{\mathbf{q}})\right.\right.\\&\left.\left.+2J_{\mathbf{q}}\sum_{l'}Q^{l,l'}_{\mathbf{q}}(-1)^{l'+l}\right)\right]^{1/2},\end{aligned}$$

$\boldsymbol{\xi}_{\mathbf{q},l}$ is a complex vector with coordinates $\xi^{\gamma}_{\mathbf{q},l}=\xi^{\gamma}_{\mathbf{q},1,l}+i\xi^{\gamma}_{\mathbf{q},2,l}$, $\gamma=x,y,z$, $\boldsymbol{\xi}_{l,\boldsymbol{\nu}}(\tau)=\Sigma_{\mathbf{q},n}c_{l,\mathbf{q}}\xi_{\mathbf{q},l}\exp(i2nT\tau-i\mathbf{q}\boldsymbol{\nu})/N_0$, N_0 is the number of sites of the crystalline lattice,

$$X(\mathbf{q},\omega)\cong aq^{2}-\frac{ib\omega}{q}, \tag{9}$$

the coefficients a and b are found either from an analysis of neutron scattering data or from magnetic measurements (see Refs. 6–8).

According to Ref. 3, integrals (8) can be calculated by the method of steepest descent in the variables $r^{\gamma}_{\mathbf{q},l}=|\xi^{\gamma}_{\mathbf{q},l}|$. Next, substituting the resulting expression for the generating functional into (7) and restricting the calculation to the case of the weak sp,d exchange interaction $(U\gg J)$, we find the paramagnetic Matsubara Green's function of the sp and d electrons in the form

$$G_{k,l}=\sum_{\alpha=\pm 1}(i\omega_{n}-\varepsilon_{\mathbf{k},l}-\alpha\xi_{l})/2. \tag{10}$$

Here ξ_l is the magnitude of the spin-fluctuation splitting of the energy spectrum of the sp $(l=1)$ and d $(l=2)$ electrons, expressed in terms of the amplitude of the spin fluctuations in the d subsystem

$$\begin{aligned}\xi^{2}_{1}&=\sum_{\mathbf{q}}J^{2}_{\mathbf{q}}\langle m^{2}_{\mathbf{q}}\rangle/N_{0},\\\xi^{2}_{2}&=U^{2}\sum_{\mathbf{q}}\langle m^{2}_{\mathbf{q}}\rangle/N_{0},\\\langle m^{2}_{\mathbf{q}}\rangle&=\int_{-\infty}^{\infty}d\omega(f_{B}(\omega)+1/2)D^{-1}(\mathbf{q},\omega,\xi_{2})/(2U),\end{aligned} \tag{11}$$

where $f_B(\omega)$ is the Bose function,

$$D(\mathbf{q},\omega,\xi_2)=[(D_0^{-1}(\mathbf{q},\omega,\xi_2)-J_q^2/(2U^2))^{-1}+(D_0^{-1}(\mathbf{q},\omega,\xi_2)+J_q^2/(2U^2))^{-1}]/2,$$

$$D_0^{-1}(\mathbf{q},\omega,\xi_2)=D_0^{-1}+X(\mathbf{q},\omega),$$

$$D_0^{-1}=1-2Un_{ef}/(3\xi_2)-U\tilde{g}(\mu,\xi_2)/3,$$

$$n_{ef}=\sum_{\alpha=\pm 1}\alpha\int d\varepsilon g_0^{(2)}(\varepsilon)f(\varepsilon-\mu-\alpha\xi_2)/2,$$

$$\tilde{g}(\mu,\xi_2)=2\prod_{\alpha=\pm 1}g_0^{(2)}(\mu+\alpha\xi_2)/\sum_{\alpha=\pm 1}g_0^{(2)}(\mu+\alpha\xi_2),$$

μ is the chemical potential, found from the condition of electrical neutrality with renormalized densities of states, $f(\varepsilon-\mu)$ is the Fermi–Dirac function, $g_0^{(l)}(\varepsilon)$ is the density of states of the noninteracting sp $(l=1)$ and d $(l=2)$ electrons.

In the region of comparatively high temperatures, where the spin fluctuations are thermal, and zero spin fluctuations can be neglected, according to Ref. 7

$$\xi_1=(J/U)^2\xi_2\cong(J^2/U)bTD_0^{-1/2}(D_0^{-1}+a)^{1/2}, \tag{12}$$

where J is the homogeneous part of the sp,d exchange.

At the same time, for low enough temperatures, where in fact only zero spin fluctuations are realized,[7]

$$\xi_1=(J/U)^2\xi_2\cong(J^2/U)[(3U/\pi b)(1-D_0^{-2}a^{-2})]^{1/2}. \tag{13}$$

Next, performing an analytic continuation of the Matsubara Green's functions (10) onto the real axis $(i\omega_{2n+1}\rightarrow\omega+i0)$ and transforming to the two-time temperature Green's functions,[10] we find the densities of states of the sp and d electrons in the paramagnetic case with the spin-fluctuation renormalizations of the electron energy spectra taken into account

$$g^{(\mathbf{l})}(\varepsilon)=\sum_{\alpha=\pm 1}g_0^{(\mathbf{l})}(\varepsilon+\alpha\xi_{\mathbf{l}})/2$$

$$=\sum_{\alpha=\pm 1}\sum_{\mathbf{k}}\delta(\varepsilon_{\mathbf{k},\mathbf{l}}+\alpha\xi_{\mathbf{l}}-\varepsilon)/N_0. \tag{14}$$

As follows from Eq. (14), the electron spectrum is split by the fluctuating exchange fields, and growth with temperature of the amplitudes of the spin fluctuations in the system of electrons under consideration leads to suppression of the gap not only in the d, but also in the sp bands

$$E_g^{(\mathbf{l})}(T)=E_g^{(l)}(0)-2\xi_{\mathbf{l}}. \tag{15}$$

Here it can be seen that, under conditions of equality of the band gaps in the spectra of the sp and d electrons (as is the case in FeSi) and a weak sp,d exchange interaction, the energy gap in the spectra of the sp electrons disappears at higher temperatures than for the d electrons [see Eq. (15) and Figs. 1 and 2].

3. We perform a specific quantitative analysis of the electronic transition in the instance of almost ferromagnetic FeSi, which, according to the results of band calculations,[11] should be a semiconductor with an energy gap between the valence band and the conduction band (both in the sp and in the d spectra) roughly equal to 0.12 eV. At the same time, the experimental data[12] at temperatures up to 5 K show that a semimetallic state exists in this temperature range which is not described by the one-particle model of Ref. 11. At higher temperatures, at first a semiconducting phase arises, then at 100 K according to measurements of the optical conductivity[4] the energy gap in the d band disappears, and a metallic state begins to form, accompanied by a smooth growth of the magnetic susceptibility, and at $T>350$ K, of the electrical resistivity.

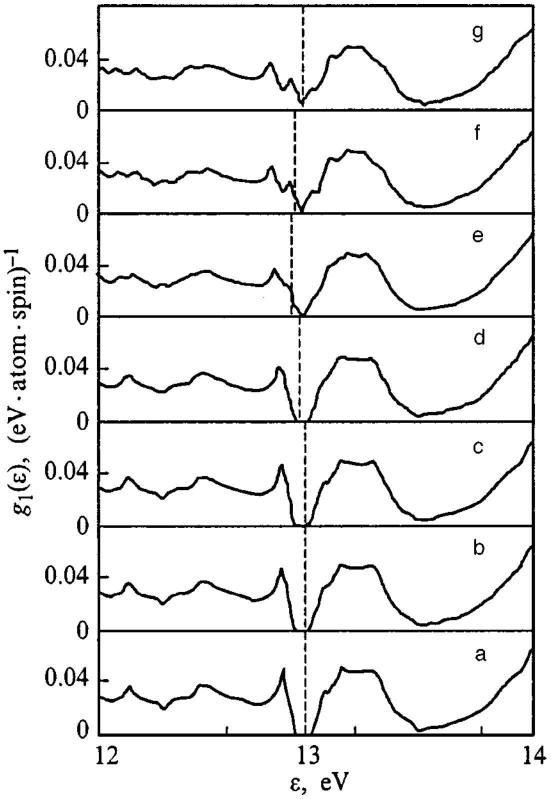

FIG. 1. Density of states of the sp electrons: (a) $U=0$ (Ref. 11), (b) $T=4$ K, (c) $T=100$ K, (d) $T=200$ K, (e) $T=350$ K, (f) $T=600$ K, (g) $T=650$.

To estimate the total conductivity of the sp $(l=1)$ and d $(l=2)$ electrons

$$\sigma=\sum_l\sigma_l \tag{16}$$

we assume, in accordance with Ref. 13, that

$$\sigma_l=4e^2\int_{-\infty}^{\infty}\varphi_l(\varepsilon)(-\partial f(\varepsilon-\mu)/\partial\varepsilon)d\varepsilon/3h^2. \tag{17}$$

Here

$$\varphi_l(\varepsilon_{\mathbf{k},l})=\tau_l\mathbf{k}^2d\mathbf{k}/d\varepsilon_{\mathbf{k},l}, \tag{18}$$

the relaxation time

$$\tau_l\propto\mathbf{k}^{2r-1}(\partial\varepsilon_{\mathbf{k},l}/\partial\mathbf{k})^2, \tag{19}$$

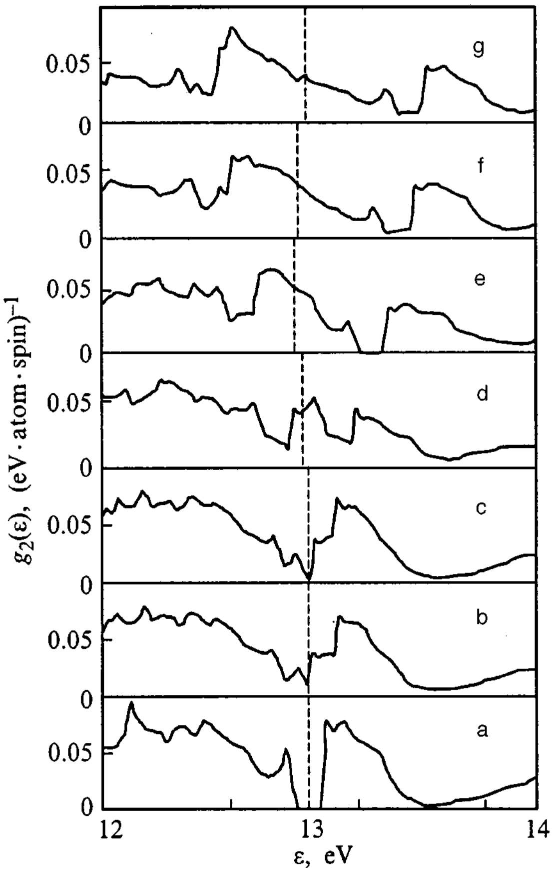

FIG. 2. Density of states of the *d* electrons: (a) $U=0$ (Ref. 11), (b) $T=4$ K, (c) $T=100$ K, (d) $T=200$ K, (e) $T=350$ K, (f) $T=600$ K, (g) $T=650$.

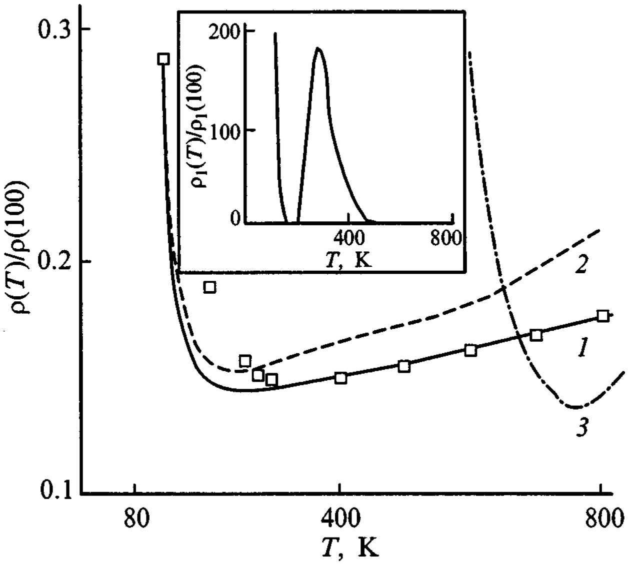

FIG. 3. Temperature dependence of the resistance of FeSi. Points — experiment,[5] lines — calculation: (*1*) total contribution of the *sp* and *d* electrons, (*2*) resistance of the *d* electrons, (*3*) resistance of the *sp* electrons. The inset plots the contribution of the *sp* electrons to the resistance of FeSi at temperatures below 600 K.

r is a parameter of the impurity ($-1/2$) or phonon (3/2) scattering, and the electron *d* and *sp* spectra are modeled on the basis of the formula for the density of states in the effective-mass approximation

$$g^{(l)}(\varepsilon_{\mathbf{k},l})=\mathbf{k}^2(\partial\varepsilon_{\mathbf{k},l}/\partial\mathbf{k})^{-1}. \tag{20}$$

To calculate the amplitudes of the spin fluctuations, we employ relations (11)–(13) and use the values of the spin-fluctuation parameters *a* and *b*, obtained in Ref. 7 from an analysis of neutron scattering data. Specifically, $a=0.1$ and $b=30/U$ in Eq. (13) for the low-temperature region; $a=0$ and $b=10/U$ in Eq. (12) for the region of comparatively high temperatures.

Calculations of the total conductivity (16) using the above procedure show that agreement with experimental data over a wide temperature interval is achieved for $J\approx 0.1U$ (Fig. 3).

Analysis of calculations of the renormalized densities of states of the *d* and *sp* electrons shows that the chemical potential up to $T_g^{(d)}\approx 100$ K is found at the center of the band of forbidden energies of both types of current carriers. Therefore, for $T<T_g^{(d)}$ the temperature dependence of the electrical resistance of FeSi is described by an exponential law. After the disappearance at $T=T_g^{(d)}$ of the energy gap in the spectrum of the *d* electrons, their state metallizes. In turn, the chemical potential (due to asymmetry of the *d* bands) begins to shift to the left along the energy axis (Figs. 1 and 2) and at $T\approx 200$ K falls into the valence band of the *sp* electrons. Here, the forbidden band in the spectrum of *sp* electrons does not disappear although it continues to narrow. Thus, the nature of the temperature dependence of the electrical resistance for *d* electrons above 100 K, and then for *sp* electrons above 200 K, acquires a metallic character. Then, according to our estimates, at $T_g^{(sp)}\cong 350$ K the "collapse" of the energy gap occurs in the spectrum of the *sp* electrons and, as a consequence, a deep dip appears in the corresponding energy region. At the same time, the continuing changes in the density of *d* states (with growth of *T*) lead to the result that the direction of shift of the chemical potential reverses, and it begins to shift toward the newly formed minimum in the density of *sp* states. This latter circumstance results in a significant decrease in the number of *sp* states near the position of the chemical potential and an abrupt increase in the electrical resistivity of these current carriers. It is especially significant that the number of *d* states in the energy region near the chemical potential varies quite weakly, for which reason the temperature dependence of the resistivity of *d* electrons is nearly linear. In addition, over the entire temperature range under discussion, and even up to $T\approx 600$ K, the electrical resistivity of the *sp* electrons is so large that its extremal dependence has no effect on the temperature variation of the total resistivity $\rho(T)$ although it does allow us to improve the quantitative agreement with experiment. With further increase of the temperature, the depth and width of the dip in the density of *sp* states fall off, which again leads to a growth of the *sp* conductivity. Above $T\approx 600$ K the abrupt variation of the number of *sp* states near the position of the chemical potential gives way to a significantly slower variation, which makes it possible to identify the temperature dependence due to scattering of these electrons. The values of the density of states of *sp* electrons near the position of

the chemical potential turn out to be quite large, which together with the smallness of the effective mass of the current carriers of the given type makes their contribution to the total electrical resistivity stand out.

Additional renormalizations of the sp and d states arise in the low-temperature region due to an increase in the zero spin fluctuations. In Ref. 7 it was shown that this leads to the formation of a ''gapless'' energy spectrum of d electrons. However, even at maximum amplitude of the zero spin fluctuations, which is equal to 0.08 (in units of two Bohr magnetons), the narrowing of the gap in the sp spectra turns out to be comparatively small, and a ''gapless'' state does not arise in it. Therefore, the concentration of the d current carriers at $T<T_g^{(sp)}\cong 350\,\mathrm{K}$ is much greater than that of the sp carriers, and the contribution of the latter to the electrical conductivity in the indicated temperature range can be neglected. We associate the temperature dependence of the electrical resistivity at low temperatures ($T<5\,\mathrm{K}$) observed in Ref. 12 with the excess amplitude of of the zero spin fluctuations, the scattering by which here is apparently the strongest. However, at present the spectral functions for the zero spin fluctuations are unknown, and therefore direct calculations of the relaxation times associated with spin-fluctuational scattering of d electrons are not possible.

Analyzing for the case of FeSi electronic transitions in almost ferromagnetic compounds of d metals shows that the formation of a metallic phase in them is accompanied by disappearance of the energy gap, both in the d and in sp bands. In so far as these effects take place at different temperatures, states of intermediate conductivity are formed in certain temperature intervals which cannot be identified as either semiconducting or metallic. In almost ferromagnetic FeSi, such states are formed at $T<5$ K and in the interval 100–350 K. In this case, the semiconducting phase arises only in the temperature interval from 5 to 100 K, and the metallic phase is formed in a region of comparatively high temperatures: $T>350$ K. Similar trends explain the stretched-out (in temperature) electronic transition in FeSi in contrast to compounds of transition metals where the reason for the electronic phase transitions is Coulomb correlations in the system of d electrons, which do not affect the sp electron states. In this regard, in FeSi, where measurements of the optical conductivity have so far been carried out only at temperatures below 300 K (Ref. 4), it would be of interest to perform high-temperature measurements, in particular at the temperatures at which the energy gap in the sp electron spectra disappears.

What is more, taking into account the definite similarity in the properties of FeSi and the so-called Kondo systems based on compounds of rare-earth metals (e.g., CeNiSn, $CeBi_4Pt$, and SmB_6),[12] for these latter compounds the electronic transitions considered here are also a possibility. An analysis of neutron scattering data and spin-fluctuation excitation spectra in this systems over sufficiently wide temperature intervals is needed. Such data, as far as we know, is presently lacking.

[1] N. F. Mott, *Metal–Insulator Transitions* (Taylor & Francis, London, 1974).

[2] A. A. Bugaev, B. P. Zakharchenya, and F. A. Chudnovskiĭ, *The Metal–Semiconductor Phase Transition and Its Applications* (Nauka, Leningrad, 1976).

[3] V. Jaccarino, G. R. Wertheim, J. H. Werneic, L. R. Walker, and S. Arays, Phys. Rev. **160**(3), 46 (1967).

[4] Z. Schlesinger, Z. Fisk, H.-T. Zhang, M. B. Maple, J. F. Di Tusa, and G. Aeppli, Phys. Rev. Lett. **71**, 1748 (1993).

[5] F. A. Sidorenko, E. A. Dmitriev, and P. V. Gel'd, Izv. Vyssh. Uchebn. Zaved. Fiz. **8**, 15 (1972).

[6] P. V. Gel'd, A. A. Povzner, and A. G. Volkov, Dokl. AN SSSR **283**, 358 (1985) [Sov. Phys. Dokl. **30**, 585 (1985)].

[7] A. A. Povzner, A. G. Volkov, and P. V. Bayankin, Fiz. Tverd. Tela (St. Petersburg) **40**, 1437 (1998) [Phys. Solid State **40**, 1305 (1998)].

[8] T. Moriya, *Spin Fluctuations in Itinerant Electron Magnetism*, Springer Series in Solid State Sciences, Vol. 56 (Springer-Verlag, New York, 1985).

[9] A. A. Abrikosov, L. P. Gor'kov, and I. E. Dzyaloshinskiĭ, *Methods of Quantum Field Theory in Statistical Physics* (Prentice-Hall, Englewood Cliffs, N.J., 1963).

[10] S. V. Tyablikov, *Methods of the Quantum Theory of Magnetism* (Nauka, Moscow, 1975).

[11] L. I. Vinokurova, A. V. Vlasov, and É. T. Kulatov, Trudy IOFAN **2**(4), 463 (1991).

[12] M. B. Hunt, M. A. Chernikov, E. Felder, H. R. Ott, Z. Fisk, and P. Canfield, Phys. Rev. B **50**, 14933 (1994).

[13] D. Ziman, *Electrons and Phonons* (Clarendon Press, Oxford, 1960).

Translated by Paul F. Schippnick

PHYSICS OF THE SOLID STATE VOLUME 41, NUMBER 10 OCTOBER 1999

Field-induced magnetic phase transitions in the Yafet–Kittel model

N. P. Kolmakova, S. A. Kolonogiĭ, and M. Yu. Nekrasova

Bryansk State Technical University, 241035 Bryansk, Russia

R. Z. Levitin

M. V. Lomonosov Moscow State University, 119899 Moscow, Russia

(Submitted December 18, 1998)
Fiz. Tverd. Tela (St. Petersburg) **41**, 1797–1799 (October 1999)

The Yafet–Kittel model for a two-sublattice ferrimagnet with an antiferromagnetic exchange interaction in one of the sublattices was developed to describe magnetic-field-induced phase transitions in the isotropic and Ising cases. Depending on the relative values of the exchange parameters of the inter-sublattice interaction and the intra-sublattice interaction in the isotropic case, two types of magnetic phase diagrams with two types of second-order phase transitions are possible: to the noncollinear phase and to the spin-flip phase, and, in the Ising case, three types of magnetic phase diagrams with first-order phase transitions are possible. *© 1999 American Institute of Physics.* [S1063-7834(99)01610-X]

1. In a two-sublattice ferrimagnet with stable sublattices, an external magnetic field induces a transition from the ferrimagnetic state with antiparallel arrangement of the magnetic moments of the sublattices to the ferromagnetic state with parallel magnetic moments via two second-order phase transitions through a noncollinear phase or, in the presence of a large enough uniaxial magnetic anisotropy, via one first-order transition. If there exists an antiferromagnetic exchange interaction inside one of the sublattices of the ferrimagnet, thanks to which that sublattice can decay into two equivalent sublattices, then the magnetic phase diagrams and the magnetization curves become substantially more complicated. The first attempt to describe magnetic systems of such type was the Yafet–Kittel model[1] (see also Ref. 2), which considers a two-sublattice ferrimagnet with an antiferromagnetic exchange interaction in each sublattice. In the molecular field approximation the possible magnetic states of such a system were calculated in the absence of an external magnetic field in the exchange interaction. The idea of triangular ordering was introduced, which corresponds to an orientation of the magnetic moments of all the sublattices at certain angles with respect to each other, and it was shown that its presence entails the possibility of an increase in the saturation magnetization in the presence of an external magnetic field even in the limit $T\to 0\,\mathrm{K}$.

The Yafet–Kittel theory was developed for ferrites with spinel structure. While still remaining relevant for these compounds, if this theory is developed from the case of spontaneous transitions to transitions induced by an external magnetic field, it can be used to describe the magnetic properties of many other compounds, including intermetallics with rare earths, e.g., ternaries of the type $R\mathrm{Mn}_2X_2$, where $X=\mathrm{Si}$ or Ge. The present paper is dedicated to such a development of the Yafet–Kittel theory.

2. Let us consider the two-sublattice ferrimagnet with an antiferromagnetic exchange interaction inside one of the sublattices, thanks to which that sublattice can decay into two equivalent sublattices with magnetic moments $\mathbf{m}_1$ and $\mathbf{m}_2$, where $m_1=m_2=m$. We calculate the magnetic phase diagrams and magnetization curves of such a ferrimagnet in the molecular field approximation, in which the magnetic moments in a state of thermodynamic equilibrium are assumed to be aligned with the effective fields acting in them. We will analyze the signs and magnitudes of these effective fields and chose the states corresponding to minimum values of the thermodynamic potential for a prescribed value of the external magnetic field.

In the exchange approximation (in the absence of magnetic anisotropy) the thermodynamic potential can be written in the form

$$\Phi=J_1\mathbf{m}_1\cdot\mathbf{m}_2/2+J_2\mathbf{M}\cdot\mathbf{m}_1/2+J_2\mathbf{M}\cdot\mathbf{m}_2/2 -\mathbf{H}\cdot(\mathbf{m}_1+\mathbf{m}_2+\mathbf{M}). \quad (1)$$

Here J_1 and J_2 are the parameters of the antiferromagnetic $(J_1,J_2>0)$ exchange interaction inside the unstable sublattice and between the sublattices, respectively; $\mathbf{M}$ is the magnetic moment of the stable sublattice.

We list the phases realized in such a ferrimagnet. There are four of them. Three of them are characterized by parallel orientation of $\mathbf{m}_1$ and $\mathbf{m}_2$, which thus form a common sublattice and are similar to the phases of an ordinary ferrimagnet: a ferrimagnetic phase with antiferromagnetic orientation of $\mathbf{m}_1+\mathbf{m}_2$ and $\mathbf{M}$ (phase A), a ferromagnetic phase (F), and a noncollinear phase (N). The fourth and last phase is the triangular phase, and we denote it as C (canted). In it the moments $\mathbf{m}_1$ and $\mathbf{m}_2$ form an angle θ with the direction of the field which is given by

$$\cos\theta=\frac{2H\mp J_2M}{2J_1m}. \quad (2)$$

This phase is the initial state of the ferrimagnet for $M/2m<J_1/J_2$; the sign in the denominator is minus if $J_1>J_2$ and plus if $J_1<J_2$. In the opposite case $(M/2m>J_1/J_2)$ the A

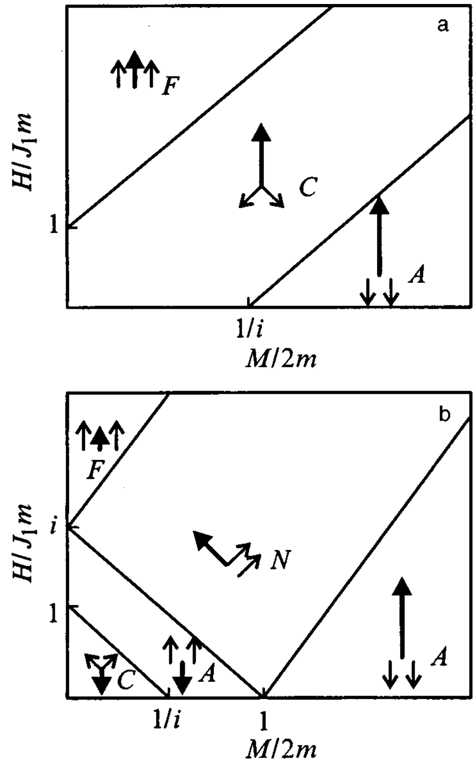

FIG. 1. Magnetic phase diagrams of a ferrimagnet with antiferromagnetic exchange interaction in one of the sublattices (isotropic case): for $J_1>J_2$ (a) and for $J_1<J_2$, $i=J_2/J_1$ (b). The solid lines represent second-order phase transitions.

phase is the initial state. All of the phase transitions are second-order, and the critical fields are given by the following relations:

$$H_{C\leftrightarrow A}=\begin{cases} J_1m-J_2M/2 & \text{for } J_1<J_2, \\ -J_1m+J_2M/2 & \text{for } J_1>J_2; \end{cases}$$

$$H_{C\leftrightarrow F}=J_1m+J_2M/2;$$

$$H_{A\leftrightarrow N}=J_2|M-2m|/2;$$

$$H_{N\leftrightarrow F}=J_2(M+2m)/2. \tag{3}$$

The magnetic phase diagrams are shown in Fig. 1. Figure 2 depicts the most interesting magnetization curve with three second-order phase transitions, which is realized for $J_1<J_2$ and $M/2m<J_1/J_2$. For values of the parameters not satisfying these relations, the magnetization curves contain either one transition $C\rightarrow F$ or two transitions $A\rightarrow C\rightarrow F$ or $F\rightarrow N\rightarrow F$.

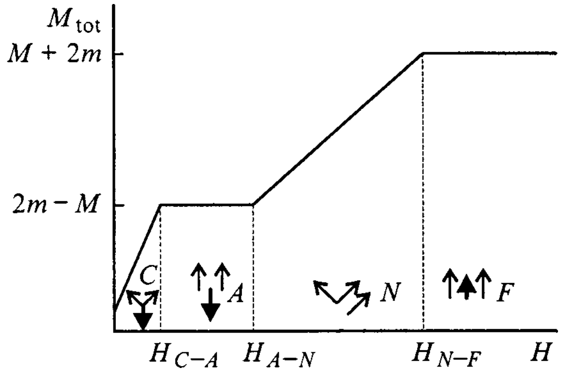

FIG. 2. Schematic magnetization curve in the case of the phase diagram of Fig. 1(b) for $M/2m<J_1/J_2=1/i$.

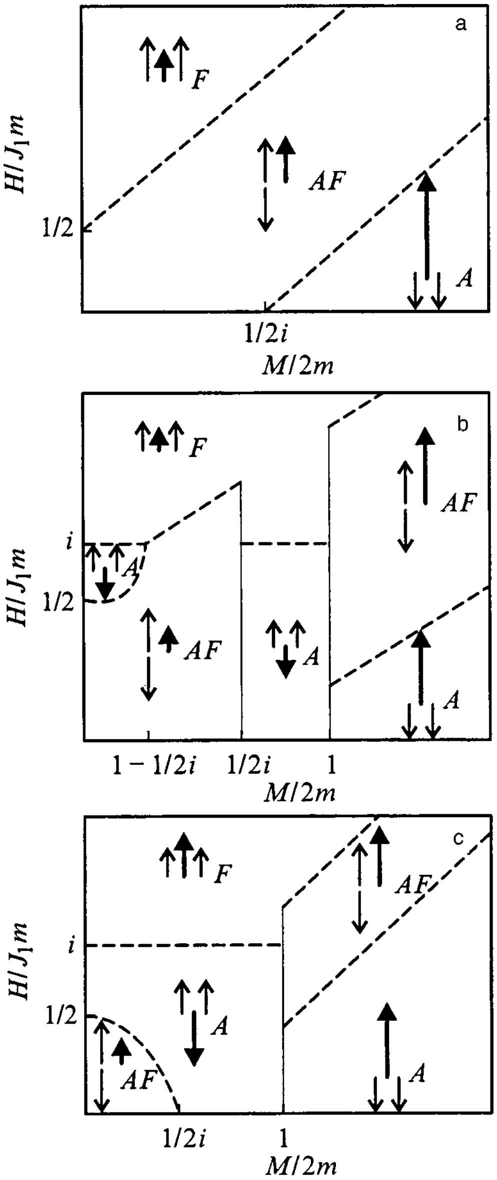

FIG. 3. The same as in Fig. 1 for the Ising model for different relative values of the exchange parameters: $J_1>2J_2$ (a); $J_2<J_1<2J_2$ (b); $J_1<J_2$, $i=J_2/J_1$ (c). The dashed lines represent first-order phase transitions.

3. Going beyond the limits of the exchange approximation and taking the finite anisotropy of both sublattices into account is a very relevant and interesting problem. We have extracted the results for this situation into a separate paper, and in the present paper consider only the limiting case of an infinitely large anisotropy (the Ising case). For this case the scalar products of the magnetic moment vectors in the thermodynamic potential (1) should be replaced by products of the projections of the magnetic moments onto the Ising axis since the remaining projections are equal to zero. In this case, the noncollinear and triangular phases cannot be realized, but the ferrimagnetic phase (A) and the ferromagnetic phase (F) are joined by another collinear phase, in which $\mathbf{m}_1$

and $\mathbf{m}_2$ are ordered antiferromagnetically. We denote this phase as AF. In this case three types of phase diagrams are realized, which are shown in Fig. 3 for different relative values of the exchange parameters J_1 and J_2. All of the phase transitions are first-order. The magnetization curves are characterized by one or two jumps, which occur at the critical fields

$$\begin{aligned} &H_{A\leftrightarrow AF}=(J_2M-J_1m)/2;\\ &H_{AF\leftrightarrow A}=\frac{(J_1m-J_2M)m}{2(m-M)};\\ &H_{AF\leftrightarrow F}=(J_2M+J_1m)/2;\\ &H_{\leftrightarrow F}=J_2m. \end{aligned} \tag{4}$$

Note that the field of the transition between the A and AF phases depends on which of the phases is the initial one; in formulas (4) the expressions for $H_{A\leftrightarrow AF}$ and $H_{AF\leftrightarrow A}$ are different. In the case when the AF phase is the initial phase, the critical field is a nonlinear function of M and m, as can be seen in the phase diagrams shown in Figs. 3b and 3c. All the remaining critical fields are linear functions of the magnetizations of the sublattices. A peculiarity of the phase transition $AF\rightarrow A$ is the fact that in it not one magnetic moment, as in all the other phase transitions, but two magnetic moments change their orientation, with the total magnetization changing from M to $2m-M$.

4. Thus, in this paper, in the effective field model, we have calculated the magnetic phase diagrams of ferrimagnets with an antiferromagnetic exchange interaction in one of the sublattices for the isotropic and Ising cases. A consideration of these limiting (in the magnetic anisotropy) cases is a necessary step in the solution of the problem for a ferrimagnet of such type with arbitrary anisotropy. Ferrimagnets of this type include intermetallic compounds with a rare earth and manganese $R\mathrm{Mn}_2X_2$, which for some pure and diluted rare earths in certain temperature intervals are characterized by an antiferromagnetic exchange interaction, both inside the manganese subsystem and between the rare-earth and manganese subsystems. The rare-earth subsystem in these compounds should be isotropic for $R=\mathrm{Gd}$ since Gd^{3+} is an S-ion, and Ising, e.g., for $R=\mathrm{Dy}$ since such is the single-ion nature of the anisotropy of the Dy^{3+} ion. The available experimental data for the magnetic properties of $R\mathrm{Mn}_2X_2$ compounds (Refs. 3–5) points to the need to consider triangular ordering for the magnetic moments of the rare earth and manganese and, consequently, underscores the urgency of developing the Yafet–Kittel model further along this path.

This work was carried out with the support of the Russian Fund for Fundamental Research (RFBR) (Project No. 96-02-16373) and with the joint support of INTAS–RFBR (Project No. 95-641).

[1] Y. Yafet and C. Kittel, Phys. Rev. **87**, 290 (1952).
[2] S. Krupička, *Physics of Ferrites and Related Magnetic Oxides*, Vol. 1 (Mir, Moscow, 1976).
[3] N. Iwata, K. Hattori, and T. Shigeoka, J. Magn. Magn. Mater. **53**, 318 (1986).
[4] H. Kobayashi, H. Onodera, and H. Yamamoto, J. Magn. Magn. Mater. **79**, 76 (1989).
[5] H. Kobayashi, H. Onodera, Y. Yamaguchi, and H. Yamamoto, Phys. Rev. B **43**, 728 (1991).

Translated by Paul F. Schippnick

PHYSICS OF THE SOLID STATE VOLUME 41, NUMBER 10 OCTOBER 1999

Comparison of negative magnetoresistance mechanisms in manganese perovskites and chromium spinels

V. A. Gavrichkov,*) N. B. Ivanova, S. G. Ovchinnikov, and A. D. Balaev

*L. V. Kirenskiĭ Institute of Physics, Siberian Branch, Russian Academy of Sciences,
660036 Krasnoyarsk, Russia*

T. G. Aminov and G. G. Shabunina

*N. S. Kurnakov Institute of General and Inorganic Chemistry, Russian Academy of Sciences,
117907 Moscow, Russia*

V. K. Chernov and M. V. Petukhov

Krasnoyarsk State Technical University, 660074 Krasnoyarsk, Russia

(Submitted December 22, 1998)
Fiz. Tverd. Tela (St. Petersburg) **41**, 1800–1803 (October 1999)

A transition of the field dependence of the electrical resistivity from a square law ($\sim H^2$) above T_c to a linear function ($\sim H$) below T_c is observed in the degenerate ferromagnetic semiconductor $HgCr_2Se_4(n)$. Together with the large negative magnetoresistance, these magnetoelectric effects correspond to effects observed in the perovskite-type oxides $La_{1-x}Ca_xMnO_\delta$. Inasmuch as the undoped semiconductor $HgCr_2Se_4$ is a ferromagnet with approximately the same critical temperature as the doped semiconductor and in view of the total lack of data on the Jahn–Teller effect in this compound, we infer that our results cast doubt on existing hypotheses (polaron and binary exchange) regarding the origin of the giant magnetoresistance in $La_{1-x}Ca_xMnO_\delta$. Impurity sd scattering is discussed as a possible magnetoresistance mechanism for both compounds. © *1999 American Institute of Physics.* [S1063-7834(99)01710-4]

A detailed analysis of the magnetoresistance of thin films of the perovskite oxide $La_{1-x}Ca_xMnO_\delta$ shows that the temperature and field dependences of the electrical resistivity are dictated entirely by the magnetization at temperatures both above and below T_c (Ref. 1). According to the interpretation of current carriers as small-radius polarons, $\rho(M) \approx \rho(0)(1-\gamma M^2)$ (Refs. 2–4). O'Donnell et al.[1] have observed an abrupt transition in the low-field ($H\rightarrow 0$) dependence of the resistivity from a square law ($\sim H^2$) above T_c to a linear function ($\sim H$) below T_c. According to polaron concepts, the low-field dependence of the electrical resistivity should exhibit a negative curvature at all temperatures, both above T_c and below T_c (Refs. 2–4). However, the experimental curves have a positive curvature below T_c (Ref. 1). Moreover, Eckstein *et al.*[5] have observed a dependence of the resistivity on the direction of magnetization in samples of the same compositions. A similar anisotropy of the magnetoresistance observed much earlier in transition metals has been well understood in terms of sd scattering.[6] These are all new problems for the theory of electrical conductivity in the oxides of transition metals.

The objective of the present study is to compare the experimental magnetoresistance curves of the ferromagnetic semiconductor $HgCr_2Se_4(n)$ at temperatures above and below the magnetic phase transition temperature T_c with the analogous curves for $La_{1-x}Ca_xMnO_\delta$. Like the latter, the degenerate magnetic semiconductor $HgCr_2Se_4(n)$ has a high negative magnetoresistance ($\Delta\rho/\rho \approx 100\%$) with a peak in the vicinity of T_c. According to band calculations,[7] the bottom of the conduction band in this compound has a $4s$-$3d$ nature. We have previously[8] proposed a $4s$-$3d$ mechanism for the impurity scattering of carriers in nonstoichiometric magnetic semiconductors, whereby the temperature and field dependences of the resistivity are governed by the corresponding dependences of the magnetization: $\rho=\rho(M(T,H))$. The results of calculations based on this scattering mechanism[9] for $HgCr_2Se_4(n)$ are quite consistent both with the actual existence of a large negative magnetoresistance and with its temperature dependence for this nonstoichiometric compound. It is reasonable therefore to assume, on the basis of the same sd-scattering mechanism, that the magnetoresistance of this compound could have the above-stated distinctive characteristics.

To identify the scattering mechanism responsible for the giant negative magnetoresistance, we have noted the low-field electrical resistivity curves, analogous to those in Ref. 1, for $HgCr_2Se_4(n)$ both above and below T_c. As in Ref. 1, we have observed a transition from square-law behavior of the magnetoresistance above T_c to linear behavior below T_c. Moreover, in the latter case we have also observed a separate magnetoresistance peak superimposed on the linear field curve, attesting indirectly to a dependence of the resistivity on the direction of the magnetic field. We emphasize that the object in question is a compound that differs altogether from $La_{1-x}Ca_xMnO_\delta$, the only common ground being phase separation into conducting and nonconducting phases[10] and the same scattering mechanism.

The mechanism of binary exchange affecting the magnetoresistance is ruled out: The undoped compound $HgCr_2Se_4$ is a ferromagnetic semiconductor with $T_c = 106$ K. As the doping level or the degree of nonstoichiometry is raised, the Curie temperature increases only slightly, whereas the carrier mobility at T_c increases by roughly two orders of magnitude.[11] Data on the Jahn–Teller effect are nonexistent. Consequently, the concepts of polaron-type carriers must also be excluded for this compound. Realistically, we can contemplate scattering by spin disorder and scattering by nonstoichiometry defects. However, the strong concentration dependence of the mobility at low temperatures[11] strongly supports the latter.

1. SAMPLES AND MEASUREMENT PROCEDURE

Single-crystal samples were prepared by the technology described in Ref. 12 and were subsequently additionally annealed in mercury vapor at a vapor pressure $P = 4.1$ atm and temperature $T = 350$ °C for sample 1 and at $P = 2.7$ atm and $T = 428$ °C for sample 2. This annealing procedure yields degenerate *n*-type $HgCr_2Se_4$ samples with a carrier density that depends only slightly on the temperature. For the resistivity measurements contacts were microwelded to the samples with the subsequent application of a mercury-indium amalgam. Thin silver wire of 6 μm diameter was used for the conducting leads. Four contacts were attached along a single line for the resistivity measurements and at the corners of a square for Hall measurements on the large face of the sample. A magnetic field up to 7 T was generated by a superconducting solenoid.

The Hall emf, which was obtained as the voltage difference on the potential contacts for opposite directions of the field, was found to be essentially constant in the temperature range 4.2–160 K, indicating a weak temperature dependence of the carrier density. Magnetic transport measurements were performed in the range of fields $H = 0 - 6$ T at two temperatures $T = 4.2$ K and 125 K for the first sample and at $T = 4.2$ K and 111 K for the second sample. The magnetic field was applied along the direction of the current. We have analyzed the initial segment of the magnetic field dependence of the resistivity ρ at $H < 0.6$ T. Figures 1a and 1b show the field dependence of the resistivity for the two investigated samples at temperatures $T = 125$ K for the first sample and $T = 111$ K for the second sample, both of which are above $T_c = 106$ K. Figures 2a and 2b show the field dependence of the resistivity at $T = 4.2$ K for the same samples.

2. EXPERIMENTAL RESULTS

In Figs. 1a and 1b, the field curves of the resistivity for the two samples exhibit a square-law behavior: $\rho(H)|_{H\to 0} \sim H^2$. In Figs. 2a and 2b, as the field is increased, the resistivity increases initially until it reaches a maximum, and then decreases monotonically in higher fields. The linear curves extracted from these data are shown in Figs. 2a and 2b, and the remaining peaks are shown in Figs. 2c and 2d. The most noticeable feature out of the entire set of experimental data is the transition from a square-law dependence of the resistivity (Figs. 1a and 1b) above T_c to a linear dependence below T_c (Figs. 2a and 2b). The occurrence of the magnetoresistance peak superimposed on the linear curve at low fields can be attributed to the onset of a resistivity dependence on the angle between the directions of the magnetization and the current in the presence of magnetization rotation processes. The amplitude of the peak tends to zero as $T \to T_c$. Each of the two peaks has its own corresponding field at which the maximum is observed and its own particular amplitude of the maximum. Auxiliary measurements aimed at clarifying the dependence of the magnetoresistance on the angle between the applied field and the current have not been performed. However, existing data reveal a similarity to results obtained for epitaxial $La_{1-x}Ca_xMnO_\delta$ films.[5] We recall that magnetoresistance anisotropy has not been observed to date in bulk $La_{1-x}Ca_xMnO_\delta$ samples.

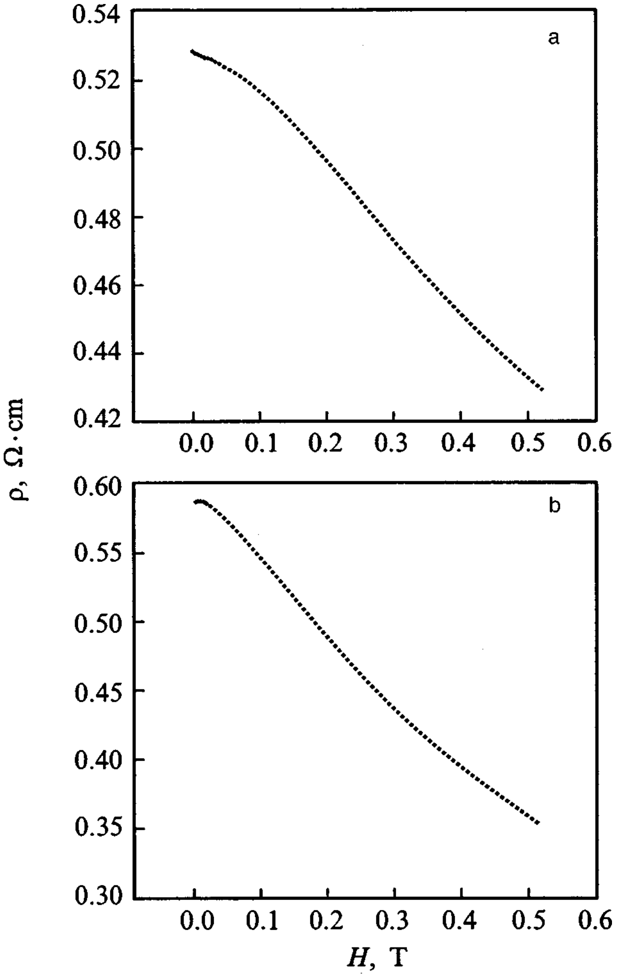

FIG. 1. Field dependence of the electrical resistivity at two temperatures: (a) $T = 125$ for the first sample; (b) $T = 111$ for the second sample.

3. DISCUSSION OF RESULTS

Thus, having observed similar field dependences of the electrical resistivity in the radically different compounds $La_{1-x}Ca_xMnO_\delta$ and $HgCr_2Se_4(n)$, we conclude that, apart from the mechanism of binary exchange affecting the mag-

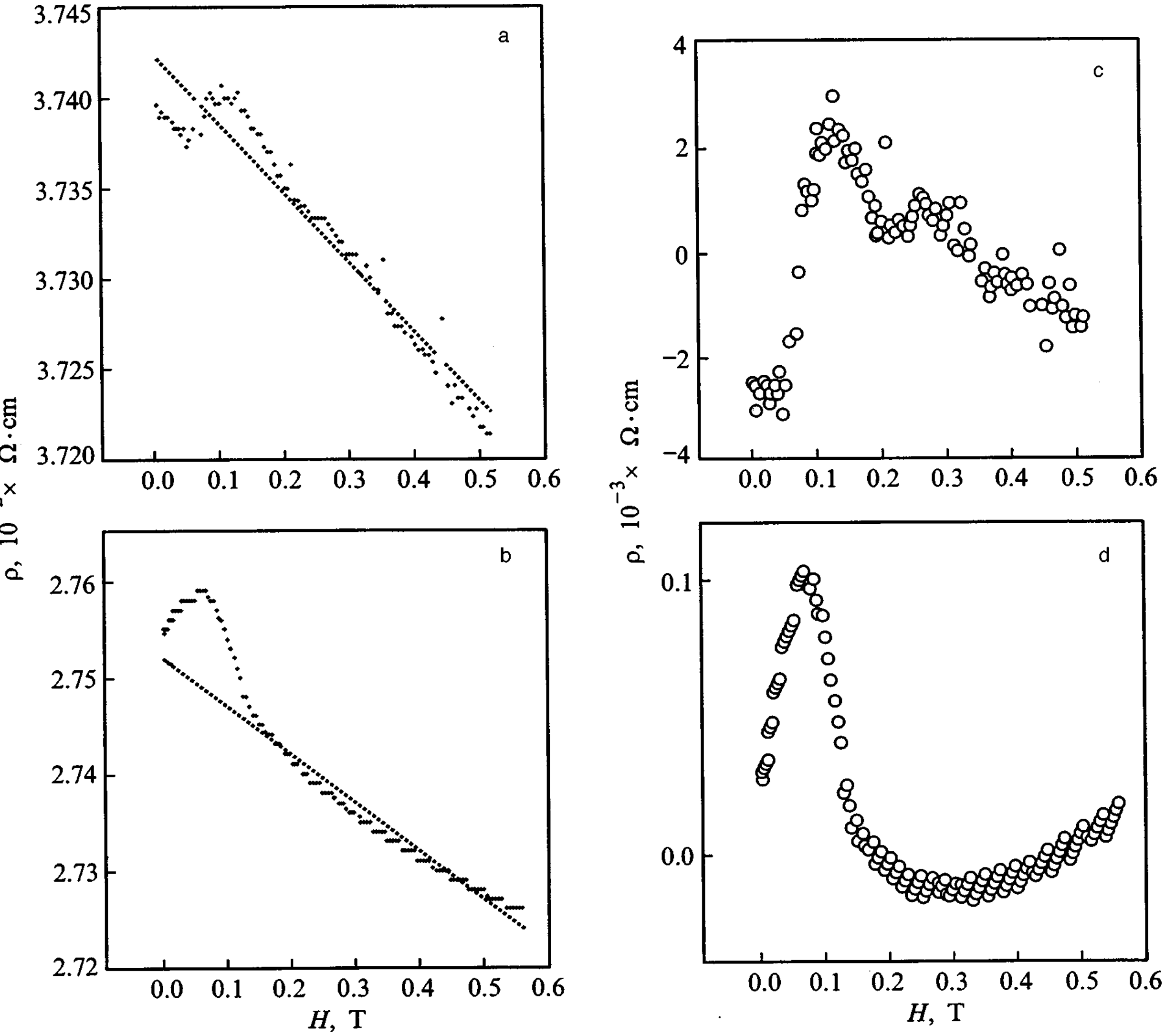

FIG. 2. Field dependence of the resistivity at a temperature $T=4.2$: (a) first sample; (b) second sample. Remaining positive magnetoresistance: (c) first sample; (d) second sample.

netoresistance and carriers of a polaron nature, an impurity mechanism of sd scattering may become the primary source for a large negative magnetoresistance.

The corresponding theory based exclusively on notions of an sd scattering mechanism also reproduces the required transition from a square-law temperature dependence of the resistivity above T_c to a linear dependence below T_c (Ref. 13). These theoretical notions are based on the results of calculating the band structure of a magnetic semiconductor taking into account the strong Coulomb correlation of carriers in the $3d$ states of chromium.[14] According to these calculations, the bands of $4s$ and $3d$ states behave altogether differently: Whereas the band of the more diffuse $4s$ states undergo strong spin splitting as a result of sd exchange when the temperature is lowered, the amplitude of the partial density of $3d$ states corresponding to the $^4A_2\leftrightarrow{}^5E$ transition changes without any change in the energies of the states themselves. Shifts of the d band are possible only through Heisenberg exchange, but they are of the order of $T_c \approx 0.01$ K and are much smaller than for sd-exchange interaction. As a result, the fractions of $4s$ and $3d$ states and the effective hybridization parameter between them vary markedly in correspondence with the magnetization of the semiconductor. In addition, the distribution of carriers between the $4s$ and $3d$ scattering channels also changes, along with the relaxation rate in the latter channel. Calculations have shown[13] that a jump of the temperature dependence of the resistivity and a peak of the magnetoresistance ratio should be observed at $T\leqslant T_c$, the amplitude of the effect depending on the specific nature of carrier scattering in the $3d$ channel. The magnetoresistance anisotropy in this case emerges as a natural consequence of spin-orbit interaction, as found in the ferromagnetic transitions of metals.[6]

*)E-mail: gav@iph.krasnoyarsk.su

---

[1] J. O'Donnell, M. Onellion, M. S. Rzchowski, J. N. Eckstein, and J. Bozovic, Phys. Rev. B **54**, R6841 (1996).
[2] N. Furukawa, J. Phys. Soc. Jpn. **63**, 3214 (1994).
[3] J. Inoue and S. Maekawa, Phys. Rev. Lett. **74**, 3407 (1995).
[4] A. J. Millis, P. B. Littlewood, and B. I. Shraimen, Phys. Rev. Lett. **74**, 5144 (1995).

[5] J. N. Eckstein, I. Bozovic, J. O'Donnell, M. Onellion, and M. S. Rzchowski, Appl. Phys. Lett. **69**, 1312 (1996).

[6] R. I. Potter, Phys. Rev. B **10**, 4626 (1974); A. P. Malozemoff, Phys. Rev. B **32**, 6080 (1985).

[7] T. Kambara, T. Oguchi, G. Yokoyama, and K. I. Gondaira, Jpn. J. Appl. Phys. **19**, 223 (1980).

[8] V. A. Gavrichkov, M. Sh. Erukhimov, and S. G. Ovchinnikov, Preprint No. 452F [in Russian] (L. V. Kirenskiĭ Physics Institute, Krasnoyarsk, 1987).

[9] V. A. Gavrichkov and S. G. Ovchinnikov, Fiz. Tverd. Tela (St. Petersburg) **41**, 68 (1999) [Phys. Solid State **41**, 59 (1999)].

[10] É. L. Nagaev, Fiz. Tverd. Tela (St. Petersburg) **40**, 2069 (1998) [Phys. Solid State **43**, 1873 (1998)].

[11] A. Selmi, A. Mauger, and M. Heritier, J. Appl. Phys. **57**, 3216 (1985); A. Selmi *et al.*, J. Magn. Magn. Mater. **66**, 295 (1988).

[12] T. G. Aminov, V. T. Kalinnikov, V. E. Makhotkin, L. I. Ochertyanova, and G. G. Shabunina, Izv. Akad. Nauk SSSR, Neorg. Mater. **12**, 1299 (1976); V. T. Kalinnikov, T. G. Aminov, A. A. Babitsyna, A. V. Zachatskaya, N. P. Luzhnaya, V. P. Turchanov, M. A. Chernitsina, G. G. Shabunina, and N. P. Shapsheva, *Magnetic Semiconductor Spinels of the Type* $CdCr_2Se_4$ [in Russian] (Shtiintsa, Kishinev, 1978).

[13] V. A. Gavrichkov and S. G. Ovchinnikov, Physica B **259–261**, 828 (1999).

[14] V. A. Gavrichkov, S. G. Ovchinnikov, M. Sh. Erukhimov, and I. S. Édel'man, Zh. Éksp. Teor. Fiz. **90**, 1275 (1986) [Sov. Phys. JETP **63**, 744 (1986)].

Translated by James S. Wood

PHYSICS OF THE SOLID STATE VOLUME 41, NUMBER 10 OCTOBER 1999

Magnetic properties of the compounds $R_2Sc_3Si_4$ (R=Gd, Tb, Dy, Ho, Er)

S. A. Nikitin, A. E. Bogdanov,*) and A. V. Morozkin

M. V. Lomonosov Moscow State University, 119899 Moscow, Russia

(Submitted January 27, 1999)
Fiz. Tverd. Tela (St. Petersburg) **41**, 1804–1805 (October 1999)

The magnetization of $R_2Sc_3Si_4$ compounds is measured in static magnetic fields up to 14 kOe in the temperature range 77–300 K. It is established that all compounds in the given series are paramagnetic at these temperatures. The paramagnetic Curie points are determined, and the effective magnetic moments are calculated. The measurements are performed on polycrystalline samples. © *1999 American Institute of Physics.* [S1063-7834(99)01810-9]

New compounds $R_2Sc_3Si_4$ (R=Gd, Tb, Dy, Ho, Er) have recently been synthesized by arc melting and subsequent high-temperature annealing.[1] An x-ray structural analysis of these compounds on the basis of data obtained on an x-ray diffractometer for polycrystalline samples at room temperature has shown that they have an orthorhombic crystal structure of the Sm_5Ge_4 type (space group Pnma). The parameters of the crystal lattice and the volume of the unit cell decrease as the atomic number of the rare-earth ion increases (lanthanide contraction). The objective of the present study is to investigate the magnetic properties of these compounds and to determine the principal magnetic characteristics. The magnetization was measured on a magnetometer of the Domenicali pendulum type in magnetic fields up to 14 kOe in the temperature range 78–300 K. The measurements were carried out on polycrystalline samples. Figure 1 shows a family of magnetization isotherms of a $Cd_2Sc_3Si_4$ sample. It is evident that the dependence of the magnetization σ on the applied magnetic field in the temperature range 78–300 K is essentially linear. The same behavior is exhibited by the $\sigma(H)$ curves for compounds with R=Tb, Dy, Ho, Er. The temperature curves of the reciprocal susceptibility $1/\chi$ for these compositions are shown in Fig. 2. The $1/\chi(T)$ curves are linear with temperature. This means that the magnetic susceptibility obeys the Curie–Weiss law. We can conclude from the results that the paramagnetic state is present in the investigated compositions in the range 78–300 K. The data obtained for $1/\chi$ have been processed by the least-squares method, permitting the paramagnetic Curie temperatures θ_p to be determined, along with the effective magnetic moments μ_{eff}. The results are shown in Table I. The experimental values of μ_{eff} are close to the theoretical values for trivalent ions of rare-earth elements, but quickly exceed them for all compositions other than the one containing Ho. According to the results of indirect exchange theory,[2] which are consistent with the experimental data on θ_p for rare-earth elements, $\theta_p=(2/3)GA_{\mathrm{ex}}/k_B$, where A_{ex} is the indirect exchange integral. We have used this equation to calculate the values of the indirect $s-f$-exchange interaction integrals A_{ex}. The resulting values of A_{ex} show that the paramagnetic Curie temperatures are not identically proportional to the De Gennes

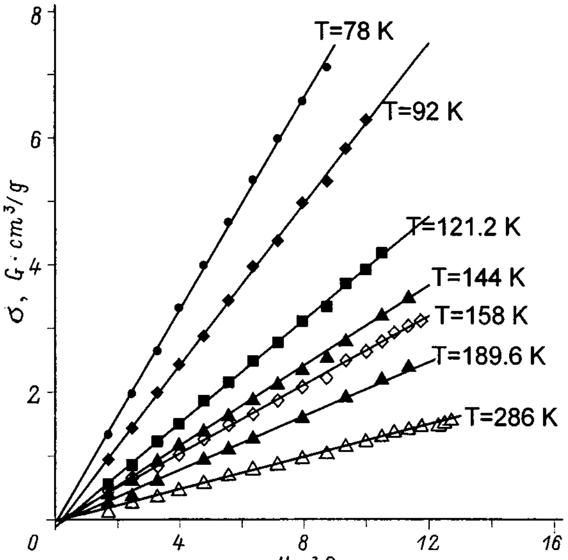

FIG. 1. Magnetization isotherms of the compound $Cd_2Sc_3Si_4$.

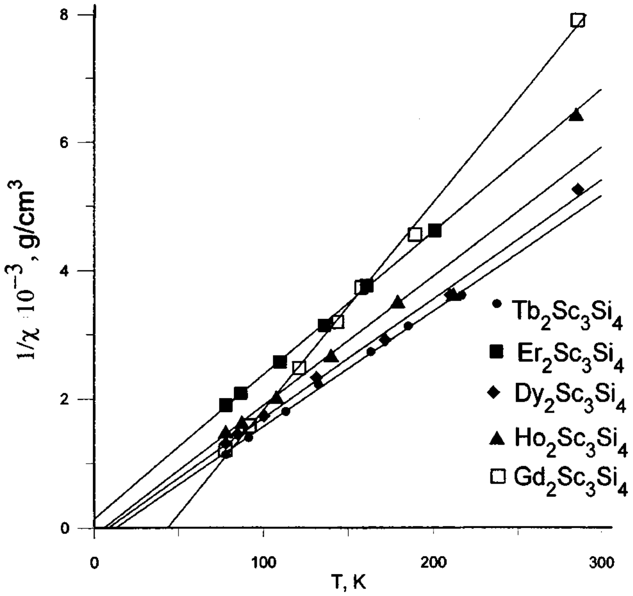

FIG. 2. Temperature curves of the reciprocal magnetic susceptibility of $R_2Sc_3Si_4$ compounds.

TABLE I. Paramagnetic Curie temperatures θ_p, effective magnetic moments μ_{eff}, and exchange interaction integrals A_{ex} for $R_2Sc_3Si_4$ compounds.

		μ_{eff}/μ_B			
Compound	θ_p, K	experiment	theory	G	A_{ex}/k_B, K
$Gd_2Sc_3Si_4$	43.6	8.29	7.98	15.75	4.15
$Tb_2Sc_3Si_4$	12.8	11.15	9.62	10.5	1.83
$Dy_2Sc_3Si_4$	8.4	11.05	10.64	7.08	1.78
$Ho_2Sc_3Si_4$	5.7	10.65	11.2	4.5	1.9
$Er_2Sc_3Si_4$	−6.4	10.16	9.9	2.55	−3.76

factor $G=(g_j-1)^2J(J+1)$ for different samples. Moreover, θ_p is positive for R=Gd, Tb, Dy, Ho, but is negative for R=Er. We can assume that together with $s-f$ interaction between rare-earth ions, other types of indirect interaction play a part as well.

The magnetic behavior of $R_2Sc_3Si_4$ compounds in the investigated temperature range is analogous to published data for the similar compositions $R_2Nb_3Si_4$ (Ref. 3) and $R_2Mo_3Si_4$ (Ref. 4). For $Tb_2Nb_3Si_4$ and $Dy_2Nb_3Si_4$ the Néel temperatures are 19 K and 5 K, respectively.[3] The negative value obtained in the present study for paramagnetic Curie point of $Er_2Sc_3Si_4$ indicates the presence of antiferromagnetic ordering in this compound at low temperatures. The large positive value of $\theta_p=43.6$ K for the compound $Gd_2Sc_3Si_4$ is probably evidence of fairly strong ferromagnetic interaction between Cd ions, which can have various contributions: indirect exchange through conduction electrons, $3d$-band scandium electrons, and silicon atoms.

This work has been supported by the Federal Program to Support Leading Scientific Schools (Grant No. 96-15-96429).

*)E-mail: bogdanov@afrodita.phys.msu.su

---

[1] A. V. Morozkin, Yu. D. Seropegin, V. K. Portnoy, A. V. Leonov, and I. A. Sviridov, J. Alloys Compd. **281**, L1 (1998).
[2] S. A. Nikitin, *Magnetic Properties of Rare-Earth Metals and Their Alloys* (Izd. MGU, Moscow, 1989).
[3] T. Le Bihan, K. Hiebl, and P. Rogl, J. Alloys Compd. **235**, 80 (1996).
[4] O. I. Bodak, Yu. K. Gorelenko, V. I. Yarovets, and R. V. Skoloédra, Izv. Akad. Nauk SSSR, Neorg. Mater. **20**, 853 (1984).

Translated by James S. Wood

PHYSICS OF THE SOLID STATE VOLUME 41, NUMBER 10 OCTOBER 1999

Surface magnetism of Al-substituted Sr–M-type hexagonal ferrites

A. S. Kamzin*)

A. F. Ioffe Physicotechnical Institute, Russian Academy of Sciences, 194021 St. Petersburg, Russia

L. P. Ol'khovik

Kharkov State University, 310077 Kharkov, Ukraine

(Submitted February 1, 1999)
Fiz. Tverd. Tela (St. Petersburg) **41**, 1806–1813 (October 1999)

The surface and bulk magnetic structures of Sr–M-type single-crystal hexagonal ferrites (with the chemical formula $SrFe_{12-x}Al_xO_{19}$) have been directly compared by simultaneous gamma, x-ray, and electron Mössbauer spectroscopy. It was found, that when the magnetic lattice of Sr–M hexagonal ferrites is slightly diluted by diamagnetic Al ions, namely, for $x=1.8$ ($SrFe_{10.2}Al_{1.8}O_{19}$), a ~300-nm thick macroscopic anisotropic layer forms on the crystal surface, wherein iron-ion magnetic moments are oriented differently from those in the bulk of the sample. The reason for the onset of a noncollinear magnetic structure in the surface layer of $SrFe_{10.2}Al_{1.8}O_{19}$ crystals is the additional lowering of the exchange interaction energy caused by the presence of such a ''defect'' as the surface. Thus an anisotropic surface layer predicted theoretically by L. Néel in 1954 has been detected in ferromagnetic crystals.
[S1063-7834(99)01910-3]

Studies of the magnetic properties of surfaces or of a thin near-surface layer, investigation of the processes occurring on the surface in such fundamental phenomena as phase transitions, and of their differences from and relations to those observed in the bulk of a crystal have acquired both scientific and practical significance.

The surface anisotropic layer in ferromagnets was first described theoretically by L. Néel in 1954.[1] It was however much later that the concept of a surface effect on the properties of magnets was used to account for experimental data.[2] Subsequent studies of surface properties made wide use of thin films and powders because reducing the volume of a crystallite increases the fraction of its surface. Another reason for the use of such objects was the lack of experimental methods capable of discriminating the signals from a thin surface layer from those of the bulk of the sample in studies of macroscopic crystals.

An unusual observation was first reported in Ref. 3: the saturation magnetization of a finely dispersed powder is lower than that of the bulk crystal from which it was prepared. The results of Mössbauer studies[4] suggested that this is due to a change in the magnetic structure of the crystallite surface. To explain the magnetic properties of finely dispersed powders, a ''shell'' model was proposed,[5,6] which assumes that the magnetic structure of the inner part of a crystallite is similar to or possibly even identical with that of the bulk, whereas in a thin surface layer (i.e., in the shell) the magnetic moments are oriented in a noncollinear way. This model accounts for the experimental data obtained on finely dispersed powders of α-Fe_2O_3,[5] γ-Fe_2O_3,[6,7] $CrFe_2O_4$,[8] CrO_2,[9] $NiFe_2O_4$, $Y_3Fe_5O_{12}$, and $Dy_2BiFe_5O_{12}$,[10] and $BaFe_{12}O_{19}$ (Refs. 11 and 12).

The shell model is, however, not the only one used to interpret experimental data. There is, for instance, an assumption of angular spin ordering on the surface of $NiFe_2O_4$ particles with a variety of stable configurations, which transforms to the spin-glass state with decreasing temperature.[13] A disordered shell is conjectured to exist on the surface of $CoFe_2O_4$ and Fe_3O_4 crystallites (Refs. 14 and 15, respectively). It is believed[16] that the spins in γ-Fe_2O_3 are arranged noncollinearly throughout the bulk of a particle rather than on its surface only. It is assumed[17] that in order to overcome bulk anisotropy and to reach complete magnetic-moment ordering along the external magnetic field, one should apply substantially higher fields than those used to validate the shell model. On the other hand, the data on textured γ-Fe_2O_3 samples[18] were explained as due to noncollinear spin ordering, and it was shown that a large bulk magnetic anisotropy cannot account for the incomplete magnetic-moment ordering, as was assumed in Ref. 17.

Studies carried out on finely dispersed powders provided a significant contribution to the understanding of the physics of ''surface'' magnetism. The wide use of Mössbauer spectroscopy in surface investigations made on thin films and powders is explained by the possibility offered by this method of enhancing (or suppressing) the signal from the surface layer by enriching the latter with the Fe-57 (or Fe-56) isotope. However the nonuniformity of the particle ensemble in size, the superparamagnetic phenomena, a strong dependence on preparation technology, etc., complicate substantially investigation of surface properties on finely dispersed powders. The above difficulties are removed by employing macroscopic crystals.

The pioneering experimental studies of surface anisotropy on macroscopic crystals were performed by G. S. Krinchik with coworkers,[19] who assumed that the role of surface anisotropy increases in magnets, where the demagnetizing field energy is small (compared to that in ferromagnets), and that there is no magnetic anisotropy in the basal plane. This combination of conditions permitted the first observation[19] of a macroscopic surface anisotropic layer in hematite, a weakly ferromagnetic antiferromagnet. The experimental data obtained suggested[19] that, first, such a surface layer is a transition layer between the crystal and the environment and, second, that within this transition layer the magnetic-moment orientation changes smoothly from the direction along which the bulk magnetic moments are oriented to that on the surface. An anisotropic surface layer was later observed to exist also in macroscopic crystals of $FeBO_3$,[20,21] $ErFeO_3$ and $TbFeO_3$,[22] which, similar to the hematite, exhibit a weak ferromagnetism. The thickness of the transition surface layer measured experimentally for $FeBO_3$ was found to be ~500 nm.[20,21]

New possibilities in surface studies of macroscopic crystals were opened by the method of simultaneous gamma, characteristic x-ray, and electron Mössbauer spectroscopy (SGXEMS), first proposed by the present authors and described in Ref. 23.

The SGXEMS provided the first experimental evidence for the existence of a transition surface layer ~400 nm thick in macroscopic Fe_3BO_6 crystals, which are weakly ferromagnetic antiferromagnets.[24] Layer-by-layer measurements made by SGXEMS established[24] that, as one approaches the crystal surface within the transition layer, the angular deviation of iron-ion magnetic moments from their orientation in the bulk increases smoothly. SGXEMS surface studies of $Fe_{3-x}Ga_xBO_6$ crystals demonstrated that substitution of as little as 9% of iron ions by gallium diamagnetic ions increases the thickness of the transition surface layer by an order of magnitude.[25]

At the same time SGXEMS studies of the M-type hexagonal ferrites ($BaFe_{12}O_{19}$, $SrFe_{12}O_{19}$, and $PbFe_{12}O_{19}$) did not reveal a transition surface layer with a magnetic structure different from that of the bulk.[26] An analysis of model Mössbauer spectra showed that, if such a layer is present in the hexaferrites studied, its thickness cannot be larger than a few nm. This coincides in order of magnitude with the theoretical calculations of Néel[1] and is substantially below the experimental accuracy of ~10 nm. However Ba–M-type hexagonal ferrites diluted weakly by Sc diamagnetic ions (chemical formula $BaFe_{12-x}Sc_xO_{19}$) do exhibit formation of a macroscopic surface layer ~200 nm thick, in which the magnetic moments of iron ions are noncollinear with those in the bulk and are oriented parallel to the crystallographic axis C.[27] Thus the existence in weakly ferromagnetic antiferromagnets of a macroscopic surface layer with a magnetic structure different from that in the bulk (called the transition layer in Ref. 19) was demonstrated experimentally for a number of crystals. Studies of the magnetic properties of ferrite surfaces have to be pursued further.

This work presents the results of a direct experimental comparison of the magnetic structures of a surface layer and the bulk in macroscopic Sr–M-type hexagonal ferrites, $SrFe_{12}O_{19}$, with part of the iron ions replaced by Al diamagnetic ions. The existence of a macroscopic transition layer in such ferrites was assumed for the following reasons. As shown in Ref. 25, substitution in Fe_3BO_5 of only 9% of iron ions by Ga diamagnetic ions increases by an order of magnitude the thickness of this layer as a result of a weakening of intersublattice exchange bonding not only through introduction of diamagnetic ions but due to the presence of the surface as well. It is known also[28–31] that substitution in M-type hexaferrites of In, Sc, Ga, or Al diamagnetic ions for a large fraction of iron ions gives rise to the formation of a noncollinear magnetic structure in the bulk. Thus one can conjecture that, if iron ions in M-type ferrites are replaced by diamagnetic ions in concentrations at which a collinear magnetic structure is retained in the bulk, a macroscopic surface layer with magnetic moments ordered noncollinearly with respect to the orientation of the moments in the bulk will form on the surface of macrocrystals of hexagonal ferrites. The corresponding studies were carried out on the $SrFe_{10.2}Al_{1.8}O_{19}$ hexaferrite. The Al diamagnetic ions were chosen because aluminum introduced in small amounts distributes statistically among all inequivalent sites of the magnetic lattice of a hexagonal ferrite. This distinguishes Al ions from Sc ions, which occupy at low concentrations primarily the $2b$ sites in a $BaFe_{12-x}Sc_xO_{19}$ crystal.[27,31]

The Al concentration in the crystal under study ($x=1.8$) was chosen on the following grounds. The magnetic moments in $SrFe_{12-x}Al_xO_{19}$ crystals remain collinear up to $x=\sim 3$.[28–31] For $x>3$, a noncollinear magnetic structure forms in the bulk of the sample. Thus the concentration $x=1.8$ was chosen so as to make sure that a collinear magnetic structure is retained in the crystal. The $SrFe_{10.2}Al_{1.8}O_{19}$ hexagonal ferrite crystals used in the study were prepared by spontaneous crystallization from a $NaFeO_2$ melt solution. The chemical formula of the synthesized compounds and their belonging to type-M hexagonal ferrites were confirmed by x-ray diffraction measurements, chemical analysis, and the structure of the Mössbauer spectra. The degree of iron substitution was derived also from the dependence of the Curie temperature on Al concentration. The Curie points were found both from temperature dependences of the effective magnetic fields and by temperature scanning at a constant velocity of gamma-ray source motion.

Platelets ~80 μm thick and ~8 mm in diameter were cut from the synthesized single crystals for Mössbauer measurements. The crystallographic c axis was perpendicular to the cut plane. Particular attention was paid to the quality of the platelet surface. The samples chosen for the study of the surface properties were both $SrFe_{10.2}Al_{1.8}O_{19}$ single crystals with the natural specular surface and platelets cut from bulk crystals and chemically etched for 1 min in orthophosphoric acid at 90 °C. Platelets of the unsubstituted ferrite $SrFe_{12}O_{19}$, prepared simultaneously by the above surface treatment, were used as reference samples.

The magnetic structure of the surface layer and of the bulk of crystals was studied by the SGXEMS method. This method is based on simultaneous measurement of Mössbauer spectra of radiations having different mean free paths in material, namely, gamma rays, characteristic x-rays, and secondary (conversion and Auger) electrons bearing information on the properties of the bulk and of surface layers of a few microns and 300 nm thick, respectively. The energy of

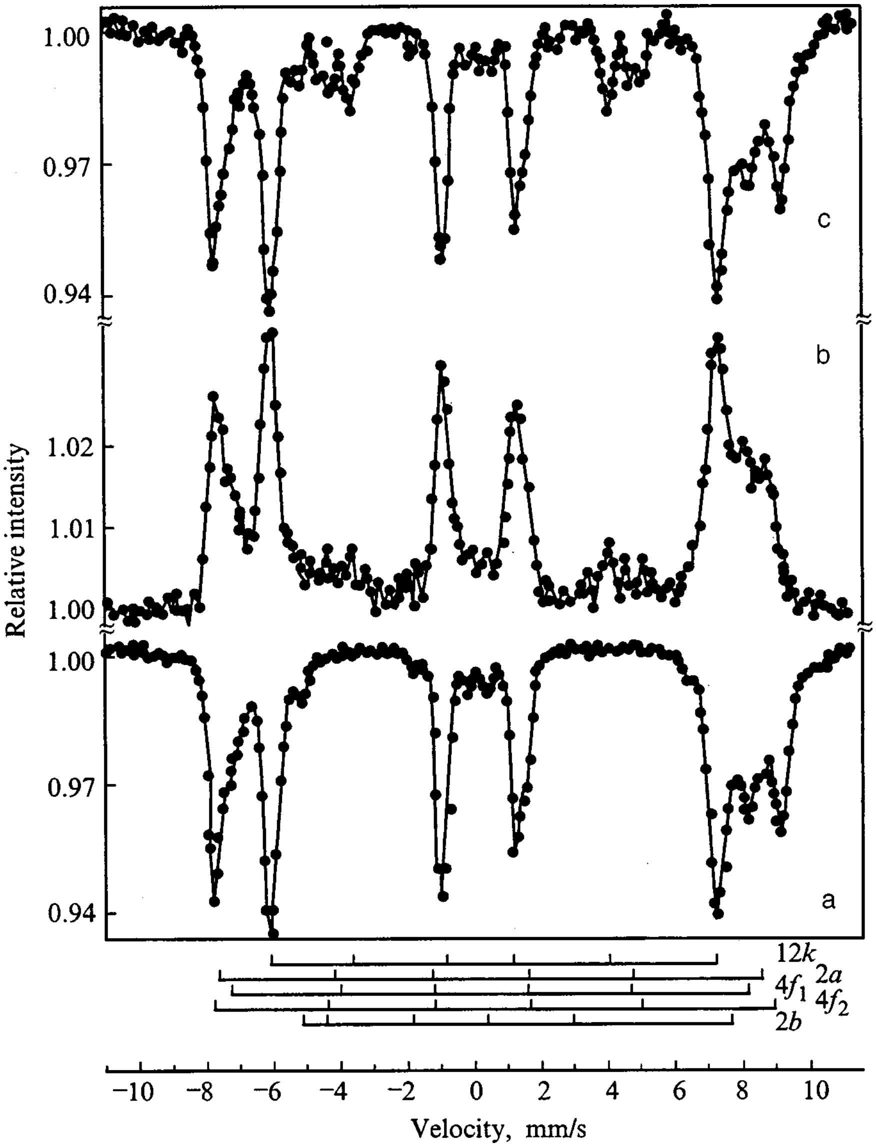

FIG. 1. Mössbauer spectra of $SrFe_{10.2}Al_{1.8}O_{19}$ single-crystal hexaferrite obtained at room temperature; a and c—detection of gamma rays carrying information on the bulk of the crystal; b—detection of secondary electrons from a 0–200-nm thick surface layer. a and b: the crystallographic *c* axis parallel to the gamma-ray wave vector, and c—it is at 28° to the latter.

an electron emerging from the crystal is the lower the deeper the atom from which this electron came, and therefore the secondary electrons used in SGXEMS to study the properties of surface layers less than 300 nm thick are energy selected.[32]

Experimental spectra were obtained by SGXEMS in the temperature range from 300 to 700 K. Figure 1 presents for illustration $SrFe_{10.2}Al_{1.8}O_{19}$ spectra obtained at room temperature by measuring gamma rays and secondary electrons, with the wave vector of the former oriented parallel to the crystallographic axis *C*. The Mössbauer spectra taken with x-rays and carrying information on the layer a few microns thick were similar to those obtained with gamma rays. Therefore in order to make the figures clearer, the x-ray spectra are not displayed. As seen from Fig. 1, the resonance lines are well resolved, which enabled processing the Mössbauer spectra with a high accuracy and to both calculate the hyperfine interaction parameters and determine the magnetic-moment orientation in the crystal.

Mössbauer spectroscopy permits one to calculate the angle Θ determining the magnetic-moment orientation in a crystal with respect to the γ-radiation wave vector from the intensity ratio of the first to second (as well as of the fifth to sixth) Zeeman sextuplet lines by the relation (see, e.g., Ref. 31):

$$\Theta = \arccos\left(\frac{4A_{1.6}-3A_{2.5}}{4A_{1.6}+3A_{2.5}}\right)^{1/2} = \arcsin\left(\frac{(3/2)A_{2.5}/A_{1.6}}{1+(3/4)A_{2.5}/A_{1.6}}\right)^{1/2}. \tag{1}$$

As seen from Fig. 1a, the Mössbauer spectrum of $SrFe_{10.2}Al_{1.8}O_{19}$ obtained with gamma rays is similar to that of the unsubstituted ferrite $SrFe_{12}O_{19}$ [see, e.g., Fig. 2a], hence one does not observe under Al doping the formation of a new sublattice, as occurs in $BaFe_{12}O_{19}$ with Sc ions substituted for the iron ions.[27,30,31] An analysis of gamma-resonance spectra [Fig. 1a] showed that the intensities of the second and fifth lines in the Zeeman sextuplets of each inequivalent position, which correspond to $\Delta m = 0$ transitions, are zero. This means that the Θ angle is zero and, hence, the magnetic moments of the iron ions in the bulk of the crystal are collinear with the gamma-ray wave vector and parallel to the crystallographic *c* axis. This pattern is observed through-

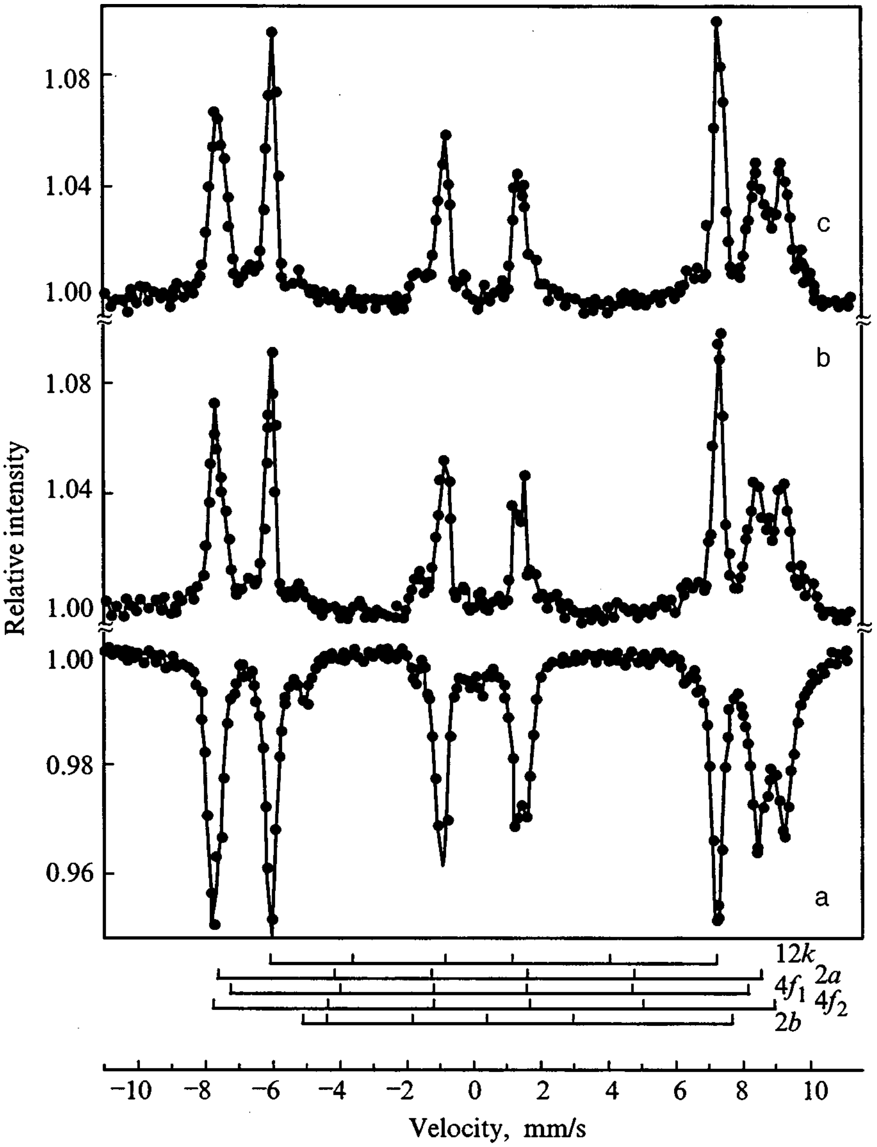

FIG. 2. Mössbauer spectra of single-crystal $SrFe_{12}O_{19}$ obtained at room temperature; a—detection of gamma rays carrying information on the bulk of the crystal; b and c—detection of secondary electrons from the surface layer up to ~200 and ~50 nm thick, respectively. The crystallographic *c* axis is parallel to the gamma-ray wave vector.

out the temperature range studied and agrees with published data on the bulk properties of these crystals (see, e.g., Ref. 31 and references therein).

Spectra taken with secondary electrons [Fig. 1b] exhibit within the regions corresponding to velocities from −4 to −5 and from +4 to +5 mm/s weak lines which are not seen in gamma-ray spectra [Fig. 1a]. Computer processing of the spectra showed these additional lines to be the second and fifth components of the Zeeman sextuplets and to correspond to $\Delta m = 0$ transitions. This implies that the magnetic moments of the iron ions residing in the ~200-nm thick surface layer are deflected from the gamma-ray wave vector and, accordingly, from the crystallographic *c* axis by an angle Θ. This pattern persists up to a temperature ~550 K, above which poor line resolution makes spectral analysis difficult. The deviation of the magnetic moments from the gamma-ray wave vector direction (Θ) calculated from Eq. (1) was found to be $23 \pm 2°$. Thus the magnetic moments of the iron ions residing in a ~200-nm thick surface layer are collinear neither with the crystallographic *c* axis along which the gamma-ray wave vector is aligned nor with the magnetic-moment orientation in the bulk. To check the validity of the calculations using the experimental data of Fig. 1a and 1b, Mössbauer spectra were measured on platelets inclined so that the crystallographic *c* axis forms an angle α with the gamma-ray wave vector. Figure 1c shows such a spectrum obtained with gamma rays for $\alpha = 28 \pm 2°$. We readily see that the deviation of magnetic moments from the gamma-ray propagation direction results in the appearance in the velocity sections of −4 to −5 and from +4 to +5 mm/s, accordingly, of the second and fifth Zeeman-sextuplet lines corresponding to $\Delta m = 0$ transitions. It should be noted that the Mössbauer spectra obtained on samples inclined to the gamma-ray beam are similar to those presented in Refs. 33 and 34. A comparison of Fig. 1b and 1c reveals a good coincidence in position on the velocity scale of the second and fifth gamma-resonance lines measured on an inclined crystal [Fig. 1c] with the second and fifth lines obtained by detecting secondary electrons [Fig. 1b]. Applying Eq. (1) to the gamma-ray spectrum in Fig. 1c yields $\Theta = 29 \pm 2°$. Thus the calculated value of Θ was found to coincide with the experimentally set crystal-tilt angle α within its setting error.

TABLE I. Fe^{3+} ion distribution among the cell sites, ion spin orientation, and Mössbauer effect (the areas under the corresponding spectral lines) for the $SrFe_{12}O_{19}$ and $SrAl_{1.8}Fe_{10.2}O_{19}$ hexaferrites.

	Distribution of Fe^{3+} ions among lattice sites and their spin orientation			Mössbauer effect	
				$SrFe_{12}O_{19}$	$SrAl_{1.8}Fe_{10.2}O_{19}$
Sublattice	Number of ions	Environment	Spin orientation	Area, % (normalized to 24)	Area, % (normalized to 20.4)
$12k$	12	octa	up	9.5 ± 0.4	9.1 ± 0.2
$4f_1$	4	tetra	down	2.9 ± 0.5	3.2 ± 0.3
$4f_2$	4	octa	down	7.7 ± 0.7	4.8 ± 0.2
$2a$	2	octa	up	1.9 ± 0.9	1.7 ± 0.4
$2b$	2	trigonal bipyramid	up	1.9 ± 0.6	1.5 ± 0.2

Our experiments showed that the magnetic-moment orientation of the iron ions residing in a ~200-nm thick surface layer in a $SrFe_{10.2}Al_{1.8}O_{19}$ crystal deviates both from the C axis direction and from the iron ion spins in the bulk of the sample.

One could suggest that the observed magnetic-moment deviation arises due to magnetic ions being etched out of the crystal surface layer in the course of chemical polishing, which would result in an additional lowering of the exchange interaction energy in this layer. To check this assumption, one measured Mössbauer spectra of $SrFe_{12}O_{19}$ single crystals prepared simultaneously with the $SrFe_{10.2}Al_{1.8}O_{19}$ samples under study and using the same chemical polishing procedure. The experimental Mössbauer spectra obtained on these $SrFe_{12}O_{19}$ crystals with the platelets oriented so that the c axis is parallel to the gamma-ray wave vector are displayed in Fig. 2. One readily sees that, first, the spectra obtained by detecting electrons not only from a ~200-nm thick surface layer [Fig. 2b] but even from a ~50-nm thick one [Fig. 2c] are fully identical to the spectrum taken with gamma rays [Fig. 2a]; second, the velocity intervals from -4 to -5 and from $+4$ to $+5$ mm/s in the $SrFe_{12}O_{19}$ secondary-electron spectra [Fig. 1b, c] do not contain any lines observed in the secondary-electron spectrum of $SrFe_{10.2}Al_{1.8}O_{19}$ crystals [Fig. 1b] obtained at the same velocities.

Thus the above experiments show convincingly that, first, the sample preparation technology used by us does not affect in any way the magnetic structure of the surface layer, and, second, on the surface of $SrFe_{10.2}Al_{1.8}O_{19}$ crystals there is a layer within which the magnetic-moment orientation differs from that in the bulk. Consider the reasons for the formation of such a surface layer. The orientation of the magnetic moments of the sublattices is dominated (see, e.g., Ref. 31 and references therein) by exchange interactions in the hexagonal block R between $Fe(2b)-O-Fe(4f_2)$ and $Fe(4f_2)-O-Fe(12k)$. The bond angles between them are fairly large, ~140° and 130°, and the Fe–O bond lengths are ~1.8 and 1.95 Å, respectively. These interactions correspond to the largest exchange integrals. Because the $Fe(2b)-O-Fe(4f_2)-O-Fe(12k)$ interaction is slightly stronger, and the chain consists of two exchange bonds, the spins of the $Fe(2b)$ and $Fe(12k)$ ions are oriented antiparallel to the $Fe(4f^2)$ spin, despite the strong counteracting coupling between the $Fe(2b)$ and $Fe(12k)$ ions, for which the interaction angle ~125°, and the Fe–O distances are 2.3 and 1.87 Å, respectively. In the spinel block the ions interact in the conventional manner to produce the mutual magnetic-moment orientation specified in Table I.

Studies of M-type hexagonal ferrites showed[28–31] that substitution of Al diamagnetic ions for iron ions in such ferrites affects the exchange interaction even in compounds with a comparatively low Al content. Al contents $x>3$ give rise to the formation of a noncollinear magnetic structure.[28–31]

Table I lists the resonance absorption (or Mössbauer effect) probabilities calculated from the areas bounded by spectral lines in experimental Mössbauer spectra. The hyperfine interaction parameters derived from $SrFe_{12}O_{19}$ and $SrFe_{10.2}Al_{1.8}O_{19}$ spectra are presented in Table II. The figures in the tables are in a good agreement with published data[28–31,33–37] for similar ferrites. A comparison of the hyperfine interaction parameters obtained for $SrFe_{12}O_{19}$ and $SrFe_{10.2}Al_{1.8}O_{19}$ shows that they do not change significantly under such $(x=1.8)$ Al substitution for iron. One cannot also maintain that Al ions show any preference for occupying a specific sublattice in the ferrite structure, because the changes in line intensities lie within the error of their determination (see Table I) from poorly resolved sextuplets. Al ion localization at all sites reduces the Curie temperature T_c by 50–60 K per one substituting Al diamagnetic ion (i.e., for $\delta x=1$), whereas, for instance, introduction of Sc ions, which occupy predominantly the $2b$ sites, results in a decrease of T_c by 160–170 K for $\delta x=1$. The experimental data obtained were used to derive the Curie temperatures. The value of T_c obtained by us for the $SrFe_{10.2}Al_{1.8}O_{19}$ ferrite is 647 K, which is in accord with the data quoted by other authors.[37]

Summing up, it can be maintained that, in the $SrFe_{10.2}Al_{1.8}O_{19}$ crystals chosen by us, the Al diamagnetic ions substitute for iron ions and, by rupturing the magnetic bonds, favor the formation of a noncollinear magnetic structure. However the Al ion content of $x=1.8$ is far from being high enough to disrupt the collinearity in the bulk. The exchange interaction energy in the surface layer of the crystals under study decreases not only because of the presence of diamagnetic ions; indeed, in $SrFe_{10.2}Al_{1.8}O_{19}$ it decreases also because of the effect of the surface. It was shown,[26] for instance, that replacement of only 9% iron ions in Fe_3BO_6 by

TABLE II. Effective magnetic fields H_{eff}, isomer shifts δ, and quadrupole splittings ΔE for $\mathrm{SrAl}_x\mathrm{Fe}_{12-x}\mathrm{O}_{19}$ obtained at room temperature (the isomer shift δ determined relative to α-Fe).

Sublattice	H_{eff},Oe		δ,mm/s		ΔE,mm/s	
$x=0$	$[\gamma]$	$[e]$	$[\gamma]$	$[e]$	$[\gamma]$	$[e]$
$12k$	413 ± 1	415 ± 1	0.36 ± 0.01	0.35 ± 0.01	0.40 ± 0.02	0.40 ± 0.02
$4f_1$	498 ± 1	497 ± 3	0.32 ± 0.01	0.31 ± 0.02	0.18 ± 0.02	0.20 ± 0.04
$4f_2$	519 ± 2	529 ± 3	0.44 ± 0.01	0.42 ± 0.03	0.44 ± 0.02	0.43 ± 0.06
$2a$	510 ± 2	516 ± 7	0.31 ± 0.01	0.30 ± 0.06	0.18 ± 0.02	0.18 ± 0.12
$2b$	405 ± 4	400 ± 20	0.37 ± 0.02	0.34 ± 0.07	2.37 ± 0.04	2.25 ± 0.14
$x=1.8$	$[\gamma]$	$[e]$	$[\gamma]$	$[e]$	$[\gamma]$	$[e]$
$12k$	415 ± 1	415 ± 1	0.36 ± 0.01	0.36 ± 0.01	0.42 ± 0.02	0.40 ± 0.02
$4f_1$	482 ± 2	482 ± 2	0.29 ± 0.02	0.26 ± 0.04	0.18 ± 0.04	0.10 ± 0.08
$4f_2$	518 ± 2	513 ± 2	0.44 ± 0.02	0.38 ± 0.02	0.40 ± 0.04	0.20 ± 0.04
$2a$	510 ± 2	-	0.31 ± 0.02	-	0.10 ± 0.04	-
$2b$	405 ± 4	-	0.29 ± 0.02	-	2.22 ± 0.04	

Ga diamagnetic ions increases by an order of magnitude the thickness of the surface transition layer. Thus one may maintain that the formation of a noncollinear magnetic structure in the surface layer of $\mathrm{SrFe}_{10.2}\mathrm{Al}_{1.8}\mathrm{O}_{19}$ crystals originates from an additional decrease of the exchange interaction energy due to the presence of such a ''defect'' as the surface.

Thus it has been demonstrated experimentally that a slight diamagnetic substitution in type Sr–M hexagonal ferrites leads to formation of a thin layer on the surface of the crystal within which the iron-ion magnetic moments are oriented noncollinearly with respect to the *c* axis, whereas the magnetic moments of the bulk ions are aligned with the *c* axis. This layer is ~200 nm thick. Hence this paper reports the first experimental evidence for the presence of an anisotropic surface layer in Sr–M ferrites, whose existence was theoretically predicted[1] by L. Néel in 1954.

The authors are indebted to V. L. Rozenbaum for assistance in the measurements.

Support of the Russian Fund for Fundamental Research (Grants 96-02-10038 and 98-02-18279) is gratefully acknowledged.

*)E-mail: kamzin@kas.ioffe.rssi.ru

---

[1] L. Néel, J. Phys. Radium **15**, 225 (1954).

[2] L. Liebermann, D. R. Fredkin, and H. B. Shore, Phys. Rev. Lett. **22**, 539 (1969); L. Liebermann, J. Clinton, D. M. Edwards, and J. Mathon, *ibid.* **25**, 232 (1970).

[3] A. E. Berkowitz, W. J. Schuele, and P. J. Flanders, J. Appl. Phys. **39**, 1261 (1968).

[4] J. M. D. Coey, Phys. Rev. Lett. **27**, 1140 (1971); Can. J. Phys. **65**, 1210 (1987).

[5] A. N. van der Kraan, Phys. Status Solidi A **18**, 215 (1973).

[6] A. H. Morrish, K. Haneda, and P. J. Schurer, J. Phys. Colloq. **37**, C6–301 (1976).

[7] P. M. de Bakker, E. DeGrave, R. E. Vandenberghe, and L. H. Bowen, Hyperfine Interact. **54**, 493 (1990).

[8] A. E. Berkowitz, J. A. Lahut, and C. E. van Buren, IEEE Trans. Magn. **MAG-16**, 184 (1980).

[9] K. Haneda, H. Kojima, A. H. Morrish, P. J. Picone, and K. Wakai, J. Appl. Phys. **53**, 2686 (1982).

[10] A. H. Morrish and K. Haneda, IEEE Trans. Magn. **MAG-25**, 297 (1989); J. Appl. Phys. **52**, 2496 (1981).

[11] K. Haneda and A. H. Morrish, Nucl. Instrum. Methods Phys. Res. B **76**, 132 (1993).

[12] K. Haneda, Can. J. Phys. **65**, 1233 (1987).

[13] R. H. Kodama, A. E. Berkowitz, E. J. McNiff, Jr., and S. Foner, J. Appl. Phys. **81**, 5552 (1997).

[14] D. Lin, A. C. Nunes, C. F. Majkrzak, and A. E. Berkowitz, J. Magn. Magn. Mater. **45**, 343 (1995).

[15] S. S. P. Parkin, R. Sigsbee, R. Felici, and G. P. Felcher, J. Appl. Phys. **57**, 3771 (1985).

[16] F. T. Parker, M. W. Foster, D. Margulies, and A. E. Berkowitz, Phys. Rev. B **47**, 7885 (1993).

[17] Q. A. Pankhurst and R. J. Pollard, Phys. Rev. Lett. **67**, 248 (1991).

[18] P. V. Hendriksen, S. Linderoth, C. A. Oxborrow, and S. Morup, J. Phys.: Condens. Matter **6**, 3091 (1994).

[19] G. S. Krinchik, A. P. Khrebtov, A. A. Askochenskiĭ, and V. E. Zubov, JETP Lett. **17**, 335 (1973); G. S. Krinchik and V. E. Zubov, Zh. Éksp. Teor. Fiz. **69**, 707 (1975) [Sov. Phys. JETP **42**, 359 (1975)].

[20] V. G. Labushkin, V. V. Rudenko, É. V. Sarkisov, V. A. Sarkisyan, and V. N. Seleznev, JETP Lett. **34**, 544 (1981).

[21] V. E. Zubov, G. S. Krinchik, V. N. Seleznev, and M. B. Strugatskiĭ, Zh. Éksp. Teor. Fiz. **94**(10), 290 (1988) [Sov. Phys. JETP **67**, 2122 (1988)]; V. E. Zubov, G. S. Krinchik, V. N. Seleznyov, and M. B. Strugatsky, J. Magn. Magn. Mater. **86**, 105 (1990).

[22] E. A. Balykina, E. A. Gan'shina, and G. S. Krinchik, Zh. Éksp. Teor. Fiz. **93**, 1879 (1987) [Sov. Phys. JETP **67**, 1073 (1987)]; Fiz. Tverd. Tela (Leningrad) **30**, 570 (1988) [Sov. Phys. Solid State **30**, 326 (1988)].

[23] A. S. Kamzin, V. P. Rusakov, and L. A. Grigoriev, in *Proceedings of the International Conference on Physics of Transition Metals* (Kiev, 1988), Vol. II, p. 271; A. S. Kamzin and L. A. Grigor'ev, Pisma Zh. Tekh. Fiz. **16**, No. 16, 38 (1990) [Sov. Tech. Phys. Lett. **16**, 616 (1990)].

[24] A. S. Kamzin and L. A. Grigor'ev, JETP Lett. **57**, 557 (1993); Zh. Éksp. Teor. Fiz. **104**, 3489 (1993) [JETP **77**, 658 (1993)].

[25] A. S. Kamzin, L. A. Grigor'ev, and S. A. Kamzin, Fiz. Tverd. Tela (St. Petersburg) **36**, 1399 (1994) [Phys. Solid State **36**, 765 (1994)]; *ibid.* **37**, 67 (1995) [Phys. Solid State **37**, 33 (1995)].

[26] A. S. Kamzin, L. P. Ol'khovik, and V. L. Rozenbaum, JETP Lett. **61**, 936 (1995); J. Magn. Magn. Mater. **161**, 139 (1996); Zh. Éksp. Teor. Fiz. **111**, 1426 (1997) [JETP **84**, 788 (1997)].

[27] A. S. Kamzin, L. P. Ol'khovik, and V. L. Rozenbaum, Fiz. Tverd. Tela (St. Petersburg) **41**, 483 (1999) [Phys. Solid State **41**, 433 (1999)].

[28] G. Albanese, J. Phys. Colloq. **38**, 85 (1977); J. Magn. Magn. Mater. **147**, 421 (1995).

[29] G. Albanese, G. Asti, and P. Batti, Nuovo Cimento Soc. Ital. Fis., B **58**, 467, 480 (1968).

[30] V. Florescu, D. Barb, M. Morariu, and D. Tarina, Rev. Roum. Phys. **19**, 249 (1974).

[31] Sh. Sh. Bashkirov, A. B. Liberman, and V. I. Sinyavskiĭ, *Magnetic Microstructure of Ferrites* (Kazan University, 1978).

[32] A. S. Kamzin and L. A. Grigor'ev, Pisma Zh. Tekh. Fiz. **19**, No. 8, 50 (1993) [Tech. Phys. Lett. **19**, 245 (1993)].

[33] G. Albanese, A. Deriu, and D. Cabrini, Hyperfine Interact. **70**, 1087 (1992).

[34] J. Fontcuberta and X. Obrados, J. Phys. C **21**, 2335 (1988).

[35] R. H. Fogel and B. J. Evans, J. Appl. Phys. **49**, 1570 (1978).

[36] B. J. Evans, F. Granjean, A. P. Lilot, R. H. Fogel, and A. Gerard, J. Magn. Magn. Mater. **67**, 123 (1987).

[37] D. R. Taft, J. Appl. Phys. **35**, 776 (1964); G. Albanese, M. Carbucicchio, and A. Deriu, Phys. Status Solidi A **23**, 351 (1974); Nuovo Cimento Soc. Ital. Fis., B **15**, 147 (1973)

Translated by G. Skrebtsov

PHYSICS OF THE SOLID STATE VOLUME 41, NUMBER 10 OCTOBER 1999

Angular dependence of the giant magnetoresistance for a current perpendicular to the plane of the layers in a magnetic sandwich

A. V. Vedyaev, O. A. Kotel'nikova, N. G. Pugach,*) and M. G. Chshiev

M. V. Lomonosov Moscow State University, 119899 Moscow, Russia

(Submitted February 18, 1999)
Fiz. Tverd. Tela (St. Petersburg) **41**, 1814–1818 (October 1999)

A quantum-statistical model using the Kubo formalism is proposed for describing the magnetoresistance of a multilayer structure with the current perpendicular to the plane of the layers. In particular, this model describes the case of noncollinear magnetization of consecutive ferromagnetic layers of the structure. Interference between electron wave functions with different directions of the spin projections onto the magnetization axis, which arises in the noncollinear configuration, is investigated along with the role of electron scattering, not only within the bulk of the layers, but also at their interfaces. © *1999 American Institute of Physics.* [S1063-7834(99)02010-9]

Two main theoretical approaches to the description of giant magnetoresistance (GMR) have evolved since this phenomenon first began to be investigated.[1] One approach places greatest emphasis on the spin-dependent scattering of conduction electrons by the surfaces and in the bulk of the ferromagnetic layers.[2–4] The electrons of each layer are described by the model of a free electron gas.[5] Some of the models incorporate the most characteristic features of the band structure. In particular, the creation of spin-dependent potential barriers at the boundaries of the ferromagnetic layers by the different populations of the valence band in adjacent layers is taken into account, but without regard for the details of the band structure.[6–9] Transport phenomena are described by simple parameters such as the spin-dependent mean free path and the Fermi wave vector.

The second approach is concerned primarily with the influence of the band structure on transport phenomena.[10–12] The electronic structure is calculated from first principles in both the parallel and the antiparallel magnetization configuration of adjacent layers. The magnetization is calculated with allowance for the complete electronic structure of the superlattice. This approach requires complex numerical computations. It is difficult to compare the results of the latter with experimental measurements of the absolute conductivity and magnetoresistance. In particular, the nature of the scattering centers in real multilayer structures is poorly accounted for. The role of such centers can be played by surface defects, magnetic inclusions in the nonmagnetic layers, impurities in the ferromagnetic layers, and finite-temperature phonons. The exact relationship between the electronic structure and the scattering amplitude for each type of defect requires a separate numerical analysis, making it extremely difficult to perform calculations ''from first principles.''

For this reason we prefer the first approach and, while disregarding the complete electronic band structure, we nonetheless take interfacial potential barriers into account, which constitute one of the main features introduced by band-structure calculations.

It has been shown previously[9] that, regardless of whether the current is perpendicular to the plane of the layers (CPP geometry) or is parallel to this plane (in-plane or CIP geometry),[8] the main contribution to the conductivity is from *s*-like electrons, which obey the relation

$$\frac{k_F^{\uparrow}-k_F^{\downarrow}}{k_F^{\uparrow}+k_F^{\downarrow}}\ll 1, \tag{1}$$

where $k_F^{\uparrow}$ and $k_F^{\downarrow}$ are the Fermi quasi-momenta for electrons whose magnetic moments are directed (respectively) in the same and opposite directions as the magnetization. The dependence of the magnetoresistance on the angle γ between the directions of the magnetizations of adjacent layers has been investigated[8,9] with allowance for the above-mentioned potential barriers between adjacent ferromagnetic layers and also the volume scattering of conduction electrons. However, these papers ignore scattering at the layer interfaces, which has been included in a similar analysis[13] confined to strictly parallel and antiparallel magnetization configurations of the adjacent ferromagnetic layers. In such configurations the spin channels do not mix, and the potential barrier (1), which is small in comparison to the Fermi energy, does not play a significant role.

In this paper we present a quantum-statistical analysis of the angular dependence of the magnetoresistance in CPP geometry, taking all the above-indicated mechanisms into account: the spin-dependent potential barrier created by hybridized exchange between the *s* and *d* bands; the spin-dependent scattering of conduction electrons in the bulk of the layers; scattering by the interfaces as distinct from volume scattering. The interfacial type of scattering is caused by roughness of the surfaces between the layers, ''dirt,'' and various kinds of surface defects. The problem is that, when the angle γ between the magnetizations of the layer differs from either 0 or π, mixing takes place between electronic states with spin directions ↑ and ↓ as electrons pass from one layer to another, and surface scattering together with volume scattering contributes to a term that depends on the height of the potential barrier, which is found to be proportional to $\sin^2\gamma$, i.e., describes the deviation of the angular dependence from linearity in $\cos\gamma$.

1. THE MODEL

We consider a sandwich consisting of two identical ferromagnetic layers of thickness a and c separated by a paramagnetic interlayer of thickness b. The electronic system of each layer is described as a gas of free electrons subjected to spin-dependent scattering both in the bulk of the layers and at the interfaces. In the case of a noncollinear configuration of the magnetizations of adjacent ferromagnetic layers it is impossible to diagonalize the electron Green's functions in spin space in both layers simultaneously by choosing the right quantization axis. We therefore choose the direction of the magnetization in one layer (c) as the axis in question. Then upon transition from one ferromagnetic layer to the other a pure electronic state with wave vector $k^{\uparrow(\downarrow)}$ goes over to a mixed state, and the electrons pass through the potential barrier, because $k_F^{\uparrow}\neq k_F^{\downarrow}$.

For the zeroth-approximation Green's functions $G_0^{\alpha\beta}(z,z')$, which describe the system with volume scattering only, we adopt the solutions of the matrix equation[9]

$$\left[\left(\frac{\partial^2}{\partial z^2}+k_F^2-k^2\right)I-\frac{2m}{\hbar^2}\Sigma_{\mathrm{vol}}^{\alpha\beta}\right]G_0^{\alpha\beta}(z,z')=\frac{2m}{\hbar^2}\delta(z-z')I, \tag{2}$$

where m is the effective mass of the conduction electrons, $\delta(z)$ is the Dirac delta function, α and β are the spin indices $(\alpha,\beta=\uparrow,\downarrow)$, and I is the unit matrix. For sandwich calculations, i.e., for a structure with spatial inhomogeneity in one direction, we use a mixed coordinate-momentum representation for all quantities. The coordinate z describes the position of a point on the axis perpendicular to the plane of the sandwich layers, and the vector k is the projection of the quasi-momentum onto this plane. The self-energy part corresponding to volume elastic scattering in layer c, where the quantization axis coincides with the direction of the magnetization, has the diagonal form

$$\Sigma_{\mathrm{vol}}^{\alpha\beta}=\begin{pmatrix}\Sigma_{\mathrm{vol}}^{\uparrow} & 0\\ 0 & \Sigma_{\mathrm{vol}}^{\downarrow}\end{pmatrix}. \tag{3}$$

Upon rotation of the quantization axis through the angle γ in layer a, this matrix is transformed according to the law

$$\Sigma_{\mathrm{vol}}^{\alpha\beta}=\frac{\Sigma_{\mathrm{vol}}^{\uparrow}+\Sigma_{\mathrm{vol}}^{\downarrow}}{2}I^{\alpha\beta}+\frac{\Sigma_{\mathrm{vol}}^{\uparrow}-\Sigma_{\mathrm{vol}}^{\downarrow}}{2}\begin{pmatrix}\cos\gamma & \sin\gamma\\ \sin\gamma & -\cos\gamma\end{pmatrix}. \tag{4}$$

The spin-dependent mean free paths of electrons in the bulk of the ferromagnetic layers are

$$l^{\uparrow(\downarrow)}=\frac{\hbar^2k_F^{\uparrow(\downarrow)}}{m\,\mathrm{Im}\,\Sigma_{\mathrm{vol}}^{\uparrow(\downarrow)}}. \tag{5}$$

Note that $(\Sigma_{\mathrm{vol}}^{\uparrow}-\Sigma_{\mathrm{vol}}^{\downarrow})$ is the energy of exchange interaction between electrons of the subbands with different spin directions. We consider the case in which the potential barrier overcome by electrons crossing from one ferromagnetic layer to the other is small by virtue of relation (1), i.e., is much lower than the Fermi energy. We can therefore disregard the reflection of electrons by the potential barriers and any effects associated with such reflection, and in Eq. (2) we can set $k_F=(k_F^{\uparrow}+k_F^{\downarrow})/2$. However, the presence of a barrier between electronic states with spins ↑ and ↓ must be taken into account in expressions of the type $(k_F^{\uparrow}-k_F^{\downarrow})l^{\uparrow(\downarrow)}$, which can be much larger than unity.

Equation (2) must be augmented by the conditions of continuity of the Green's function and its derivative at the interfaces and by boundary conditions corresponding to the weakening of correlations of the electronic states at infinity.

Taking into account scattering at the interfaces in the sandwich, we find the Green's functions of our system as solutions of the Dyson equation

$$\begin{aligned}G^{\alpha\beta}(z,z')=G_0^{\alpha\beta}(z,z')&+G_0^{\alpha\beta}(z,a)\Sigma_{\mathrm{int}}^{\alpha\beta}(a)G^{\alpha\beta}(a,z')\\&+G_0^{\alpha\beta}(z,a+b)\Sigma_{\mathrm{int}}^{\alpha\beta}(a+b)G^{\alpha\beta}(a+b,z')\end{aligned} \tag{6}$$

in the first approximation, i.e., on the assumption of sufficiently small scattering at the interfaces (with coordinates a and $a+b$ along the z axis). Upon rotation of the quantization axis, the matrix $\Sigma_{\mathrm{int}}^{\alpha\beta}$ is transformed according to the same law (3), (4) as the volume scattering matrix. In Eq. (6) $G_0^{\alpha\beta}(z,z')$ is the zeroth-approximation Green's function (2). If by analogy with (5) we introduce a parameter having the dimensions of length, $\lambda^{\uparrow(\downarrow)}=\hbar^2k_F/m\mathrm{Im}\Sigma_{\mathrm{int}}^{\uparrow(\downarrow)}$, which characterizes the effective mean free path corresponding to spin-dependent scattering at the interfaces, then by assumption this length is much shorter than the lattice constant a_0.

To calculate the two-point conductivity, we use the Kubo equation in the form given in Ref. 14, which appears as follows in the mixed $k-z$ representation:

$$\begin{aligned}\sigma^{\alpha\beta\eta\nu}(z,z')=-\frac{e^2\hbar^3}{4m^2\pi}\sum_{\mathbf{k}}&\,[G^{\beta\eta+}(z,z')-G^{\beta\eta-}(z,z')]\\&\times\nabla^{\leftrightarrow}{}_z\nabla^{\leftrightarrow}{}_{z'}[G^{\nu\alpha+}(z',z)-G^{\nu\alpha-}(z',z)],\end{aligned} \tag{7}$$

where $G^{\alpha\beta\pm}(z,z')$ denotes the advanced and retarded Green's functions (6), the spin indices $\alpha,\beta,\eta,\nu=\uparrow,\downarrow$, $\nabla^{\leftrightarrow}{}_z=\frac{1}{2}\nabla^{\rightarrow}{}_z-\nabla^{\leftarrow}{}_z)$ is the antisymmetric operator of differentiation with respect to the coordinate z, and e is the electron charge. Now the current density at a point z has the form of a second-rank spinor and is given by the expression

$$J^{\alpha\beta}(z)=\int\sigma^{\alpha\beta\eta\nu}(z,z')E^{\eta\nu}(z')dz', \tag{8}$$

where $E^{\eta\nu}(z')$ is the effective electric field, which is also a second-rank spinor. It has been shown[14] that the introduction of this quantity is equivalent to the calculation of a vertex correction to the expression for the conductivity (7).

From the energy conservation law we obtain equations for determining the fields $E^{\eta\nu}(z')$:

$$\frac{\partial}{\partial z}J^{\alpha\beta}(z)=0. \tag{9}$$

Equations (8) and (9) are solved self-consistently on the basis of the assumption that the effective fields $E^{\eta\nu}(z')$ do not depend on the coordinate within each layer, but jump at the interfaces as a result of the surface scattering of electrons:

$$E^{\eta\nu}(z)=E_i^{\eta\nu}+C_1^{\eta\nu}\delta(z-a)+C_2^{\eta\nu}\delta(z-a-b), \tag{10}$$

where $C_1^{\eta\nu}$ and $C_2^{\eta\nu}$ are the voltage drops across the interfaces due to spin-dependent scattering as distinct from volume scattering, $E_i^{\eta\nu}$ denotes quantities that are independent of the coordinate z and differ for different layers ($i=a,b,c$). These quantities are chosen in such a way as to satisfy the conditions of continuity of the expressions for the currents in different layers $J_a^{\alpha\beta}(z)$, $J_b^{\alpha\beta}(z)$, and $J_c^{\alpha\beta}(z)$:

$$\begin{aligned}&J_a^{\alpha\beta}(z)|_{z=a}=J_b^{\alpha\beta}(z)|_{z=a}\,,\\&J_b^{\alpha\beta}(z)|_{z=a+b}=J_c^{\alpha\beta}(z)|_{z=a+b}\,,\end{aligned} \tag{11}$$

and the constants $C_1^{\eta\nu}$ and $C_2^{\eta\nu}$ are chosen so that all coordinate-dependent terms in these expressions will vanish. This choice can be made even though such terms are much greater than the evaluated constants.

To obtain the complete system, Eq. (9) must be augmented with expressions for the total voltage drop

$$\begin{aligned}&aE_a^{\alpha\alpha}+bE_b^{\alpha\alpha}+cE_c^{\alpha\alpha}+C_1^{\alpha\alpha}+C_2^{\alpha\alpha}=U,\\&aE_a^{\alpha\beta}+bE_b^{\alpha\beta}+cE_c^{\alpha\beta}+C_1^{\alpha\beta}+C_2^{\alpha\beta}=0\quad\text{for }\alpha\neq\beta.\end{aligned} \tag{12}$$

We have thus written a system of equations for the quantities $E_i^{\alpha\beta}$, $C_1^{\alpha\beta}$, and $C_2^{\alpha\beta}$, each of which is a second-rank spinor. We can solve this system to obtain the total resistance of the sandwich: $R=U/(J^{\uparrow\uparrow}+J^{\downarrow\downarrow})$.

The final equation for the resistance of the sandwich $(a/b/c)$ has the form

$$\begin{aligned}R=\frac{6\pi^2\hbar}{e^2k_F^2}A^{-1}\Bigg\{\Bigg[&(a+c)^2+(a+c)(l^\uparrow+l^\downarrow)\left(\frac{b}{l}+2\Sigma_0\right)\\&+l^\uparrow l^\downarrow\left(\frac{b}{l}+2\Sigma_0\right)^2+(1-\cos\gamma)ac\frac{(l^\uparrow-l^\downarrow)^2}{2l^\uparrow l^\downarrow}\\&+(1+\cos\gamma)((a+c)(l^\uparrow-l^\downarrow)\Sigma_1-2l^\uparrow l^\downarrow\Sigma_1^2)\Bigg]\\&\times\left[a+c+\frac{2\xi l^\uparrow l^\downarrow}{l^\uparrow+l^\downarrow}\left(\frac{b}{l}+2\Sigma_0\right)\right]+\sin^2\gamma(1-\xi)\\&\times\Bigg[ac\frac{(l^\uparrow+l^\downarrow)^2(1-\xi)}{4l^\uparrow l^\downarrow\xi}\left(a+c+\frac{2l^\uparrow l^\downarrow}{l^\uparrow+l^\downarrow}\left(\frac{b}{l}+2\Sigma_0\right)\right)\\&+\frac{ac(a+c)(l^\uparrow-l^\downarrow)^2}{4l^\uparrow l^\downarrow}+(a+c)l^\uparrow l^\downarrow\Sigma_1^2-ac(l^\uparrow-l^\downarrow)\Sigma_1\Bigg]\Bigg\},\end{aligned} \tag{13}$$

where $1/\xi=1+[(k^\uparrow-k^\downarrow)l^\uparrow l^\downarrow/(l^\uparrow+l^\downarrow)]^2$, l is the mean free path of conduction electrons in the nonmagnetic interlayer, and the following notation has been introduced:

$$\begin{aligned}A=(l^\uparrow+l^\downarrow)\Bigg[&\left(a+c+\frac{2\xi l^\uparrow l^\downarrow(b/l+2\Sigma_0)}{l^\uparrow+l^\downarrow}\right)\\&\times\left(a+c+\frac{2l^\uparrow l^\downarrow(b/l+2\Sigma_0)}{l^\uparrow+l^\downarrow}\right)+ac\sin^2\gamma\frac{(1-\xi)^2}{\xi}\Bigg],\\\Sigma_0=&\frac{ma_0}{\hbar^2k_F}\,\mathrm{Im}(\Sigma_{\mathrm{int}}^\uparrow+\Sigma_{\mathrm{int}}^\downarrow),\\\Sigma_1=&\frac{ma_0}{\hbar^2k_F}\,\mathrm{Im}(\Sigma_{\mathrm{int}}^\uparrow-\Sigma_{\mathrm{int}}^\downarrow).\end{aligned} \tag{14}$$

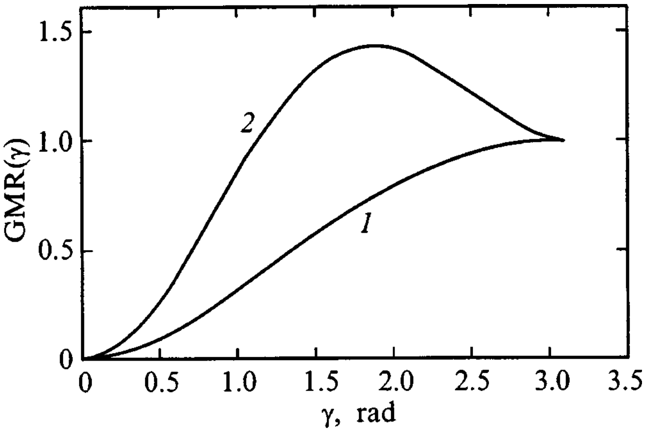

FIG. 1. Dependence of the normalized magnetoresistance on the angle between the directions of the magnetizations of ferromagnetic layers with thicknesses $a=c=23$, $b=11$, $l^\uparrow=60$, $l^\downarrow=20$, $l=180$; (*1*) $\lambda^\uparrow\to\infty$, $\lambda^\downarrow\to\infty$; (*2*) $\lambda^\uparrow=200$, $\lambda^\downarrow=10$.

2. DISCUSSION OF THE RESULTS

We have derived an analytical equation (13) for the resistance of a magnetic sandwich in the case of noncollinear magnetization of the magnetic layers, taking into account spin-dependent scattering that differs in the bulk and at the interfaces of the layers. This property enables us to investigate the role of interfacial scattering in the gigantic magnetoresistance of such multilayer magnetic structures.

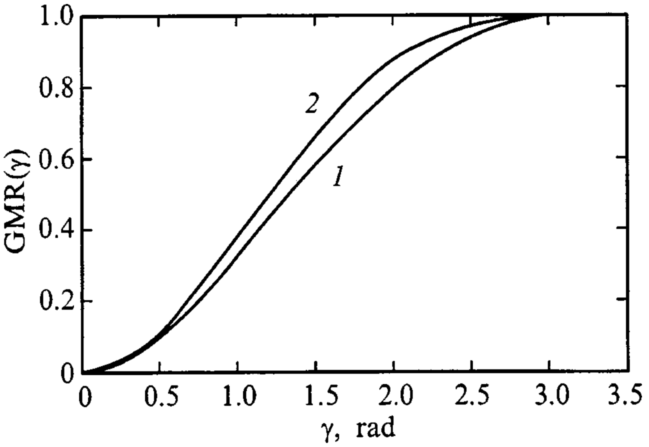

FIG. 2. The same as Fig. 1 for $a=c=39$, $b=11$, $l^\uparrow=60$, $l^\downarrow=20$, $l=180$; (*1*) $\lambda^\uparrow\to\infty$, $\lambda^\downarrow\to\infty$; (*2*) $\lambda^\uparrow=200$ $\lambda^\downarrow=10$.

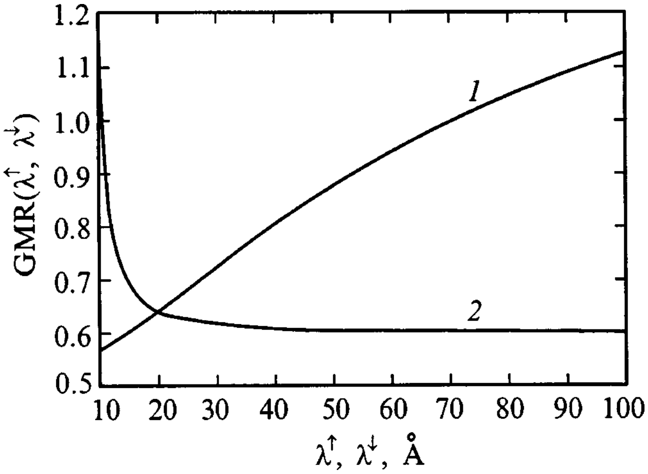

FIG. 3. Dependence of the normalized magnetoresistance on the mean free paths corresponding to scattering at the interfaces: (*1*) $\lambda^\uparrow=100$, $\lambda^\downarrow=10-100$; (*2*) $\lambda^\uparrow=10$, $\lambda^\downarrow=10-100$. The angle between the directions of the magnetizations of the ferromagnetic layers is $\gamma=\pi/2$. The parameters are $a=c=23$, $b=11$, $l^\uparrow=60$, $l^\downarrow=20$, $l=180$. All lengths are given in angstroms.

In the limit without surface scattering, i.e., assuming infinite effective-mean-free paths corresponding to spin-dependent scattering at the interfaces, $\lambda^{\uparrow(\downarrow)}\rightarrow\infty$, we find that Eq. (13) coincides with the equation for the angular dependence of the magnetoresistance in Ref. 9. But if the magnetization of the layers is assumed to be strictly collinear ($\gamma=0,\pi$), there is no interference between coherent electron waves with different directions of the spin projection: The term that contains the difference $k^\uparrow-k^\downarrow$ and is proportional to $\sin^2\gamma$ vanishes. The expression for the magnetoresistance then coincides with the one given in Ref. 13. The results can therefore be regarded as a generalization of the previously published calculations.

To plot graphs, we use the normalized form of the magnetoresistance

$$\mathrm{GMR}=\frac{R(\gamma)-R(\gamma=0)}{R(\gamma=\pi)-R(\gamma=0)} \tag{15}$$

with realistic values of the electron scattering parameters and the Fermi wave vector $k_F^{\uparrow(\downarrow)}$. In particular, we assume that $(k_F^\uparrow-k_F^\downarrow)/(k_F^\uparrow+k_F^\downarrow)=0.1$, as in the experiments reported in Ref. 9. Allowance for interfacial as well as volume scattering introduces a contribution to the angular dependence of the magnetoresistance of the multilayer structure. Specifically, surface scattering can have the effect that the resistance is observed to be a maximum for other than an antiparallel configuration of the magnetizations of adjacent ferromagnetic layers (Fig. 1). This unexpected result could not happen as a consequence of previous calculations and is most likely typical of the CPP geometry only, because the CIP resistance depends linearly on cos γ, owing to the absence of interference between electronic states. Naturally, when the thickness of the magnetic layers is increased, the influence of scattering at the interfaces diminishes, volume scattering begins to play an ever-increasing role, and this effect no longer occurs (Fig. 2). The change in the surface scattering parameters for electrons with spins ↑ and ↓, the ratio of which can differ from the ratio of the mean free paths of the electrons in the bulk, $(\lambda^\uparrow-\lambda^\downarrow)/(\lambda^\uparrow+\lambda^\downarrow)\neq(l^\uparrow-l^\downarrow)/(l^\uparrow+l^\downarrow)$, also influences the value of the magnetoresistance (Fig. 3).

[*)] E-mail: pugach@magn.phys.msu.su

---

[1] M. N. Baibich, J. M. Broto, A. Fert, F. Nguyen Van Dau, and F. Petroff, Phys. Rev. Lett. **61**, 2472 (1988).
[2] R. E. Camley and J. Barnas, Phys. Rev. Lett. **63**, 664 (1989).
[3] P. M. Levy, S. Zhang, and A. Fert, Phys. Rev. Lett. **65**, 1643 (1990).
[4] X.-G. Zhang and W. H. Butler, Phys. Rev. B **51**, 10 085 (1995).
[5] A. Barthelemy, J. Childress, V. Cros, O. Durant, O. Duvail, P. Etienne, A. Fert, J. M. George, R. Loloee, R. Morel, D. N. Mosca, L. G. Pereira, F. Petroff, A. Schuhl, P. A. Schroeder, and L. Steren, Phys. Low-Dimens. Struct. **3**, 17 (1994).
[6] R. Q. Hood and L. M. Falicov, Phys. Rev. B **46**, 8682 (1992).
[7] J. Mathon, M. Villert, and H. Itoh, Phys. Rev. B **52**, R6983 (1995).
[8] A. Vedyaev, B. Dieny, N. Ryzhanova, J. B. Genin, and C. Cowache, Europhys. Lett. **25**, 465 (1994).
[9] A. Vedyayev, N. Ryzhanova, B. Dieny, P. Dauguet, P. Gandit, and J. Chaussy, Phys. Rev. B **55**, 1 (1997).
[10] K. M. Schep, P. J. Kelly, and G. E. W. Bauer, Phys. Rev. Lett. **74**, 586 (1995).
[11] P. Zahn, I. Mertig, M. Richter, and H. Eschrig, Phys. Rev. Lett. **75**, 2996 (1995).
[12] W. H. Butler, X.-G. Zhang, D. M. C. Nicholson, and J. M. MacLaren, Phys. Rev. B **52**, 13 399 (1995).
[13] A. Vedyaev, M. Chshiev, N. Ryzhanova, B. Dieny, C. Cowache, and F. Brouers, J. Magn. Magn. Mater. **172**, 53 (1997).
[14] H. E. Camblong, P. M. Levy, and S. Zhang, Phys. Rev. B **51**, 16 052 (1995).

Translated by James S. Wood

PHYSICS OF THE SOLID STATE VOLUME 41, NUMBER 10 OCTOBER 1999

Phase composition of nanocrystalline iron films deposited in a nitrogen atmosphere

G. I. Frolov,*) V. S. Zhigalov, and O. A. Bayukov

L. V. Kirenskiĭ Institute of Physics, Siberian Branch, Russian Academy of Sciences,
660036 Krasnoyarsk, Russia

(Submitted February 24, 1999)
Fiz. Tverd. Tela (St. Petersburg) **41**, 1819–1821 (October 1999)

The phase composition of iron films prepared by pulsed-plasma deposition in a controlled nitrogen atmosphere is investigated by Mössbauer spectroscopy. The observed changes in the phase composition are dictated by the nanocrystalline structure of the samples and the dynamics of the substrate temperature during film deposition. © *1999 American Institute of Physics.* [S1063-7834(99)02110-3]

The last few years have witnessed a concerted effort to find new magnetically soft magnetic thin-film materials having a large magnetic saturation induction for modern electronic devices. Compounds of the Fe–N type are of special interest in this regard, because small additives of nitrogen to iron-base thin films increase the magnetic moment, improve the corrosion properties of the films, and decrease the coercive force.[1,2]

The development of methods for the preparation of nanocrystalline materials[3] has extended the potential capabilities for the synthesis of various alloys. This trend is mainly attributable to the fact that the chemical activity of the materials exhibits a strong dependence on the dimensions of the nanocrystallites.[4] Research at the present time is aimed primarily at powders, which after deposition on a substrate are placed in some particular gas atmosphere.[5] The end result comprises complex composite formations with interesting physical properties. At the practical level, however, continuously condensed media are of greater interest. The properties of such materials can differ from the properties of the nanoparticles from which they are formed, owing to interaction effects between them.

In this paper we report a Mössbauer spectroscopy study of the phase composition of iron films as a function of the nitrogen pressure in a vacuum chamber. The films were prepared by pulsed-plasma deposition (PPD). The deposition atmosphere was established by preliminary evacuation of the vacuum system to 10^{-6} torr with freezing-out of the oil vapor, followed by the injection of spectrally pure nitrogen, whose pressure was varied from 10^{-5} torr to 10^{-2} torr. The temperature of the substrate was equal to room temperature at the start of deposition. The samples had a thickness $\sim 10^3$ Å, which was measured by x-ray fluorescence analysis. The rate of condensation of the iron film in a 100 μs pulse was $10^4 - 10^5$ Å/s.

The pulsed nature of the plasma was created by laser pulses from an LTI-207 solid-state laser and by the discharge of a capacitor bank in the vapor of the atomized target. A distinguishing feature of the film deposition process, apart from a high evaporation rate, is high-energy saturation of a plasma with iron and nitrogen as its main components.

In the proposed technology, the interaction effects of the

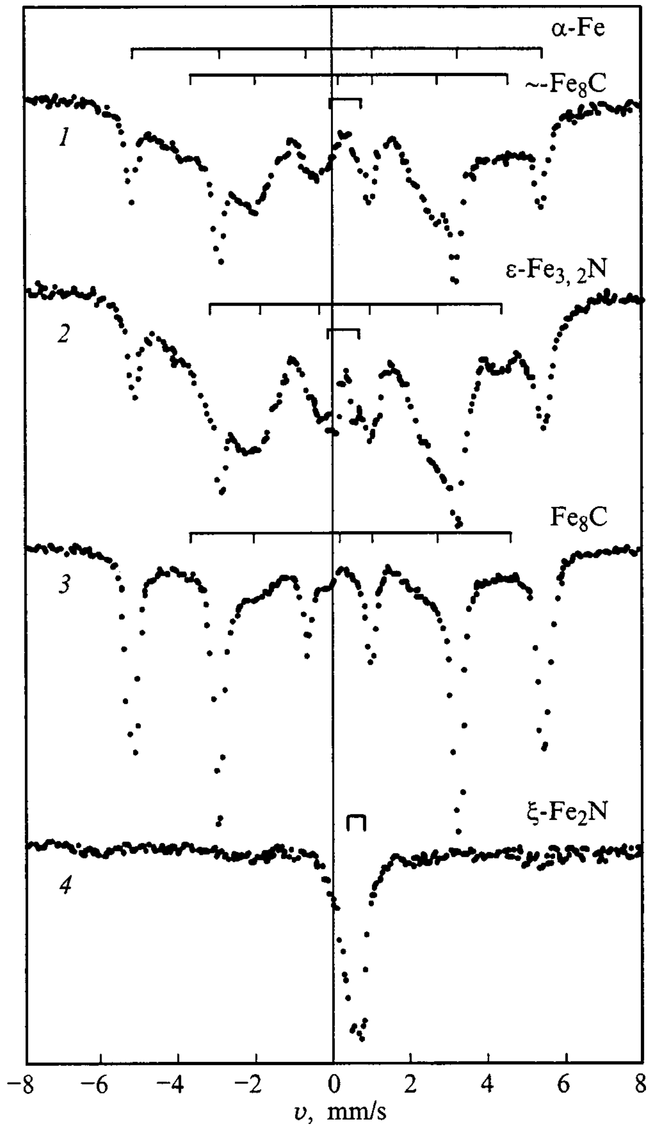

FIG. 1. Variation of the Mössbauer spectra of Fe–N films as a function of the nitrogen atmosphere pressure: (*1*) $P = 10^{-6}$ torr; (*2*) 10^{-5} torr; (*3*) 10^{-4} torr; (*4*) 10^{-2} torr.

TABLE I. Parameters of the Mössbauer spectra of Fe–N films.

No.	P, torr	H, kOe	δ, mm·s^{-1}	ε, mm·s^{-1}	S, %	Postulated composition	Literature data H, kOe	 δ, mm·s^{-1}	 ε, mm·s^{-1}	Refs.
1	10^{-6}	330	0	0	26	α-Fe,				
		~250	~0.15	0	72	~Fe_8C	245	~0.17		6, 7
		0	0.19	0.6	2					
2	10^{-5}	331	0.01	0	20	α-Fe,				
		~234	0.27	0.06	75	ε-carbonitride	230	0.24	0.10	8
		0	0.16	0.8	5	or ε-$Fe_{3.2}N$	238	0.33		9
3	10^{-4}	332	−0.01	0	76	ε-Fe,				
		251	0.16	0	24	~Fe_8C	245	~0.17		6, 7
4	10^{-2}	0	0.58	0.29	100	ε- or γ-Fe_2N	0	0.42	0.27	10

laser beam with the vapor adsorbed on the surface of the target and bombardment of the target with high-energy plasma particles in the presence of an applied electric field increase the atomic nitrogen content of the Fe–N vapor system, promoting an increase in the reactivity of the system. The results of mass spectroscopic analysis shows that the quantity of ionized atomic nitrogen increases to 15–20%.

The Mössbauer spectra of the investigated films are shown in Fig. 1, and the parameters of these spectra are summarized in Table I. The spectra were recorded with a Co^{57}(Cr) source at room temperature. The spectral lines for films prepared at $P=10^{-6}$ torr and 10^{-5} torr are very broad and evolve on a U-shaped base, as it typical of the ultradisperse or amorphous state. Electron microscope examinations of iron films prepared by PPD show that the samples consist of nanocrystallites with dimensions $\leqslant 50$ Å (Refs. 11 and 12).

The spectrum of film No. 1 contains two sextets, which can be identified with the phases αFe and iron carbide Fe_8C (Ref. 6). The formation of the second phase is caused by the high carbon content of the films (~20 at.%). Auger spectroscopy data show that this effect is quite typical of $3d$-metal films prepared by PPD.[13] The fraction of bound carbon is <10 at.% in this case.

Two sextets are also observed for film No. 2. In addition to αFe, a phase also emerges with a magnetization similar to that of Fe_8C, but with a larger isomeric shift. According to published data, these parameters are typical of the compound ε carbonitride or ε $Fe_{3.2}N$ (Ref. 9).

Unusual results are exhibited by the spectra of film No. 3: They do not contain nitride compounds. The phase composition of this sample repeats the composition of film No. 1 with the one exception that αFe is now predominant.

To explain these data, we have investigated the substrate temperature during film deposition. Our previous work with Ni–N films provided guidelines for setting up these experiments. We observed that, when nickel is spray-deposited in a nitrogen atmosphere at a pressure of 10^{-4} torr, the substrates are strongly influenced by temperature to the point of deformation.[14] To analyze the substrate temperature dynamics, we predeposited a Pd–Cu thin-film thermocouple on the substrate during the PPD process.

The results are shown in Fig. 2. In the first few minutes as the film is being deposited, the substrate temperature increases to 500–600 K. This behavior is attributable to a large quantity of heat being released on the substrate by the high current density of evaporated material. After the plasma is turned off, the substrate temperature remains constant for a certain period of time and then begins to drop exponentially. The substrate temperature is lower in low vacuum (curves *1* and *3*). A different picture is observed for film No. 3 (curve *2*): After the temperature rises to $T\sim 520$ K it suddenly jumps up to $T\sim 750$ K. This rise can be identified with heat release from the decomposition of iron nitride.

It has been shown[8] that the ε-carbonitride phase decomposes at $T=520$ K, and the $Fe_{3.2}N$ phase decomposes at $T=720$ K. We can assume that, during deposition at $P=10^{-4}$ torr, either ε carbonitride or a mixture of ε carbonitride and $Fe_{3.2}N$ forms. An ε carbonitride–$Fe_{3.2}N$ phase transition takes place when the substrate temperature rises to $T=520$ K. The heat released in this transition causes the temperature to rise sharply, and the iron nitride decomposes at $T=720-750$ K with precipitation of the αFe phase.

At $P=10^{-2}$ torr only one quadrupole doublet is observed in the Mössbauer spectrum; it is interpreted as the ε-Fe_2N or ξFe_2N phase.[10] Obviously, the nitrogen concentration in the chamber is sufficient to produce a nitrogen-enriched Fe_2N phase throughout the entire volume of the film and, at the same time, the resulting substrate temperature is lower than the temperature at which this compound decomposes.

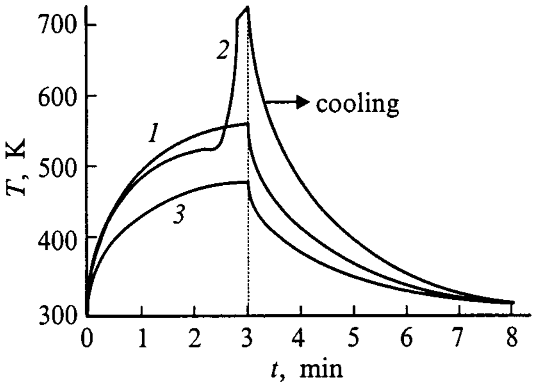

FIG. 2. Time dependence of the substrate temperature at various nitrogen atmosphere pressures: (*1*) 10^{-5} torr; (*2*) 10^{-4} torr; (*3*) 10^{-2} torr.

[*] E-mail: frolov@iph.krasnoyarsk.su

---

[1] T. K. Kum and M. Takahashi, Appl. Phys. Lett. **12**, 492 (1972).
[2] K. K. Shih, M. E. Re, and D. B. Pove, Appl. Phys. Lett. **57**, 412 (1990).
[3] W. Siegel, Nanostruct. Mater. **3**, 1 (1993).
[4] M. L. Cohen and W. D. Knight, Phys. Today **43**, 42 (1990).
[5] C.-M. Hsu, H.-M. Lin, and K.-R. Tsai, J. Appl. Phys. **76**, 8, 4793 (1994).
[6] J. M. Dubois and G. Le Gaër, Acta Metall. **25**, 609 (1974).
[7] E. Bauer-Grosse and G. Le Caër, Philos. Mag. B **56**, 485 (1987).
[8] C. A. Santos, B. A. S. Barros, J. P. Souza, and J. R. Baumvoll, Appl. Phys. Lett. **41**, 237 (1982).
[9] G. M. Chen, N. K. Jaggi, J. B. Butt, Yeh, and L. H. Schwartz, J. Phys. Chem. **87**, 5326 (1983).
[10] M. Chabanel, C. Janot, and J. P. Motte. C. R. Acad. Sci. (Paris) **222**, 13419 (1968).
[11] G. I. Frolov, V. S. Zhigalov, S. M. Zharkov, and I. R. Yarullin, Fiz. Tverd. Tela (St. Petersburg) **36**, 970 (1994) [Phys. Solid State **36**, 526 (1994)].
[12] G. I. Frolov, O. A. Bayukov, V. S. Zhigalov, L. I. Kveglis, and V. G. Myagkov, JETP Lett. **61**, 63 (1995).
[13] V. S. Zhigalov, G. I. Frolov, and L. I. Kveglis, Fiz. Tverd. Tela (St. Petersburg) **40**, 2074 (1998) [Phys. Solid State **40**, 1878 (1998)].
[14] V. S. Zhigalov, G. I. Frolov, V. G. Myagkov, S. M. Zharkov, and G. V. Bondarenko, Zh. Tekh. Fiz. **68**, 136 (1998) [Tech. Phys. **43**, 122 (1998)]

Translated by James S. Wood

PHYSICS OF THE SOLID STATE VOLUME 41, NUMBER 10 OCTOBER 1999

Long-range order and magnetic relaxation in a system of single-domain particles

S. I. Denisov*)

Sumy State University, 244007 Sumy, Ukraine

(Submitted September 18, 1998; resubmitted March 9, 1999)
Fiz. Tverd. Tela (St. Petersburg) **41**, 1822–1827 (October 1999)

The paramagnetic-ferromagnetic phase transition and distinctive characteristics of relaxation of the magnetization in a system of interacting single-domain ferromagnetic particles distributed randomly in a nonmagnetic matrix are investigated in the mean-field approximation. © *1999 American Institute of Physics.* [S1063-7834(99)02210-8]

The currently intensive experimental and theoretical research into systems of small ferromagnetic particles distributed in a nonmagnetic solid matrix is motivated by their unique properties and encouraging prospects for practical applications. In the approximation of noninteracting particles regarded as classical objects, the special attributes exhibited by the magnetic properties of such systems as a result of thermal fluctuations of the magnetic moments of the particles may be described using the approach developed by Brown.[1] It is based on the kinetic equation for the directional distribution function of the magnetic moment which, when the thermal magnetic field is modeled by white noise, reduces to the Fokker–Planck equation. In systems of particles having uniaxial anisotropy this approach has been used, in particular, to investigate, relaxation of the magnetization,[2–5] the frequency dependence of the dynamic magnetic susceptibility,[6,7] ferromagnetic resonance,[8] and stochastic resonance.[9–11] An alternative approach to the description of the statistical dynamics of the magnetic moment of single-domain particles has been proposed in recent papers,[12,13] based on the so-called inverse Fokker–Planck equation[14] and providing a means for reducing the problem of thermally induced magnetic-moment reorientation to a problem well-known in the theory of stochastic processes: the arrival of a Markov process at a given level.[15]

To account for the influence of long-range magnetic-dipole interaction on the properties of systems of single-domain particles poses a rather complex problem, for which there is no satisfactory solution at the present time, even in the mean-field approximation. For example, the role of magnetic-dipole interaction has been investigated in application to systems of single-domain particles in thermodynamic equilibrium.[16] The main result of this work is a proof of the existence of long-range ferromagnetic order in the distribution of the particle magnetic moments. However, the approximations used in Ref. 16 yield results that conflict with the general results of Luttinger and Tisza.[17] According to Ref. 17 and published numerical results,[18] in particular, the existence or nonexistence of ferromagnetic ordering in the lattice of magnetic dipoles depends on the type of lattice, whereas no such dependence follows from the results of Ref. 16. The mean-field approximation has also been used in describing phenomena resulting from the influence of magnetic-dipole interaction on the relaxation of the magnetization.[19–22] However, the mean field has been introduced without the application of appropriate procedures for averaging and establishing self-consistency, so that the results of these studies are merely qualitative.

In the present paper the mean-field approximation is used to determine the conditions for the onset of ferromagnetic order and to investigate the prominent features of magnetization relaxation in a system of interacting single-domain particles.

1. MODEL AND BASIC EQUATIONS

We consider a system of spherical single-domain ferromagnetic particles of radius r randomly distributed in a nonmagnetic solid matrix. We model the distribution of the particles in the matrix on the assumption that, with probability p, their centers occupy sites of a simple tetragonal lattice having periods d_1 (along the x and y axes) and d_2 (along the four-fold z axis). We also assume that the interaction of the particles is of the magnetic-dipole type, the particles are uniaxial, their easy axes are perpendicular to the xy plane, and the dynamics of the magnetic moment $\mathbf{m}=\mathbf{m}(t)$ of any particle is described by the stochastic Landau–Lifshitz equation

$$\dot{\mathbf{m}}=-\gamma\mathbf{m}\times(\mathbf{h}+\mathbf{n})-(\lambda\gamma/m)\mathbf{m}\times\mathbf{m}\times\mathbf{h}$$
$$(\mathbf{m}(0)=\mathbf{e}_z m). \tag{1}$$

Here $\gamma(>0)$ is the gyromagnetic ratio, λ is the dissipation parameter, $m=|\mathbf{m}|$, $\mathbf{h}=-\partial W/\partial\mathbf{m}$ is the effective magnetic field acting on the magnetic moment,

$$W=-(H_a/2m)(\mathbf{m}\cdot\mathbf{e}_z)^2-\mathbf{m}\cdot\mathbf{H}(t) \tag{2}$$

is the magnetic energy of the particle in the mean-field approximation, H_a is the magnetic anisotropy field, $\mathbf{H}(t)=H(t)\mathbf{e}_z$ is the mean dipole magnetic field at the site occupied by the particle, $\mathbf{e}_z$ is the unit vector along the z axis, and $\mathbf{n}=\mathbf{n}(t)$ is the Gaussian δ-correlated thermal magnetic field, which is given by the relations

$$\overline{n_\alpha(t)=0},\quad \overline{n_\alpha(t)n_\beta(t+\tau)}=(2\lambda kT/\gamma m)\,\delta_{\alpha\beta}\delta(\tau), \tag{3}$$

where k is Boltzmann's constant, T is the absolute temperature, $\delta_{\alpha\beta}$ is the Kronecker delta, $\delta(\tau)$ is a delta function, and the overbar signifies averaging over the realizations of $\mathbf{n}$.

Taking Eqs. (2) and (3) into account, we can associate the stochastic equation (1) interpreted according to Stratonovich,[23] with the Fokker–Planck equation

$$\frac{\partial P}{\partial t}=\frac{1}{t_r a}\frac{\partial}{\partial\theta}\left\{[a(\sin 2\theta+2b(t)\sin\theta)-\cos\theta]P+\frac{\partial P}{\partial\theta}\right\} \tag{4}$$

[$t_r=2/\lambda\gamma H_a$, $a=H_a m/2kT$, $b(t)=H(t)/H_a$] for the density function $P=P(\theta,t)$ of the probability that the vector **m** will have the polar angle θ ($0\leqslant\theta\leqslant\pi$) at time *t*. As usual, the solution of this equation must satisfy the normalization condition and the initial condition, which in the given situation has the form $P(\theta,0)=\delta(\theta)$. We are interested in the magnetization $M(t)$, which is expressed in terms of the probability density function P as follows:

$$M(t)=n\overline{m_z(t)}=nm\int_0^\pi\cos\theta P(\theta,t)\,d\theta, \tag{5}$$

where $n=p/d_1^2d_2$ is the particle number density.

Placing the origin at the site occupied by a designated particle and enumerating all others with the index *i*, we can write the mean dipole magnetic field $H(t)$ produced by these particles at the center of the designated particle in the form

$$H(t)=\left\langle\sum_i\frac{3r_{iz}^2-|\mathbf{r}_i|^2}{|\mathbf{r}_i|^5}\overline{m_{iz}(t)}\right\rangle. \tag{6}$$

Here $\mathbf{r}_i$ is the radius vector of the *i*th particle, and the angular brackets signify averaging over all possible spatial allocations (permutations) of the particles among the lattice sites. In Eq. (6) we average over the admissible particle permuations. To do so, we segregate a region of volume V in the matrix containing S lattice sites, of which $N(\leqslant S)$ are occupied by particles, and then find the probability for each permuation. Inasmuch as the total number of permuations of N distinct particles among S sites is given by the relation $R=S!/(S-N)!$, the required probability is equal to $1/R$. Consequently, by enumerating the particle permuations by the index σ and denoting the radius vectors of the particles in these permuations by $\mathbf{r}_\sigma$, we can rewrite Eq. (6) in the form

$$H(t)=\lim_{V\to\infty}\frac{1}{R}\sum_\sigma\sum_{\mathbf{r}_\sigma}\frac{3r_{\sigma z}^2-|\mathbf{r}_\sigma|^2}{|\mathbf{r}_\sigma|^5}\overline{m_{\mathbf{r}_\sigma z}(t)}. \tag{7}$$

In Eq. (7) we change from summation over σ and $\mathbf{r}_\sigma$ to summation over the radius vectors of the lattice sites $\mathbf{r}=d_1(n_1\mathbf{e}_x+n_2\mathbf{e}_y)+d_2n_3\mathbf{e}_z$ (n_1, n_2, and n_3 are integers, not simultaneously equal to zero). It is evident at once that each site is occupied by particles in $R_1=(N/S)R$ permuations. Consequently, denoting the *z* components of the particle magnetic moments at the site **r** by $m_{\mathbf{r}}^{(l)}(t)$, where the index *l* assumes values from 1 to R_1, from Eq. (7) we obtain

$$H(t)=\lim_{V\to\infty}\frac{1}{R}\sum_{\mathbf{r}}\frac{3r_z^2-|\mathbf{r}|^2}{|\mathbf{r}|^5}\left(\sum_{l=1}^{R_1}\overline{m_{\mathbf{r}z}^{(l)}(t)}\right). \tag{8}$$

Finally, bearing in mind that the expression in parentheses in Eq. (8) is equal to $R_1\overline{m_z(t)}$, taking into account the relation $\lim_{V\to\infty}R_1/R=p$, and defining the function

$$S(\xi)=\frac{1}{8}\sum_{n_1,n_2,n_3}\frac{2\xi^2n_3^2-n_1^2-n_2^2}{(n_1^2+n_2^2+\xi^2n_3^2)^{5/2}} \tag{9}$$

($\xi=d_2/d_1$), for the mean dipole magnetic field we obtain

$$H(t)=8pS(\xi)\overline{m_z(t)}/d_1^3. \tag{10}$$

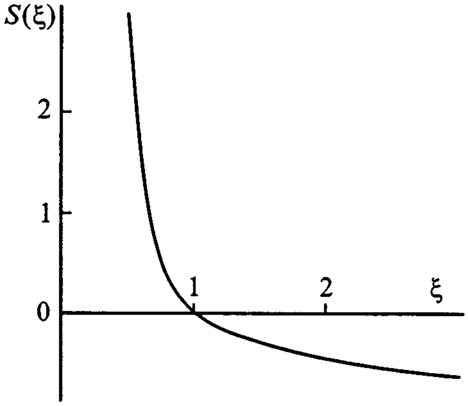

FIG. 1. Graph of the function $S(\xi)>0$.

A characteristic feature of the function $S(\xi)$, which determines the existence or nonexistence of ferromagnetic order in systems of single-domain particles, is its change of sign: $S(\xi)$ for $\xi<1$, and $S(\xi)<0$ for $\xi>1$ (Fig. 1). Since $H(t)=8\xi S(\xi)M(t)$, we can state *a priori* that ferromagnetic ordering is possible in such systems only for $\xi<1$. A two-dimensional particle distribution corresponds to the condition $\xi\to\infty$ [$S(\infty)\approx-1.129$], so that ferromagnetic order does not exist in this case.

2. PARAMAGNETIC-FERROMAGNETIC TRANSITION

We now find a steady-state solution $P_s(\theta)$ of Eq. (4) and the corresponding magnetization of the system of single-domain particles. Assuming that the probability flux is zero at the endpoints of the interval $(0,\pi)$, we obtain

$$P_s(\theta)=C^{-1}(a,2ab(\infty))e^{a(\cos^2\theta+2b(\infty)\cos\theta)}\sin\theta, \tag{11}$$

where

$$C(a,2ab(\infty))=\int_{-1}^{1}e^{a(x^2+2b(\infty)x)}dx. \tag{12}$$

We define the order parameter of the investigated system of single-domain particles as $\mu=M(\infty)/nm$. Then, making use of the relation

$$M(\infty)=nm\int_0^\pi\cos\theta P_s(\theta)\,d\theta$$

and Eqs. (11) and (12), we obtain the following equation for μ:

$$\mu=\frac{1}{2a}\left[\frac{2e^a}{C(a,3T_0\mu/T)}\sinh\left(\frac{3T_0}{T}\mu\right)-\frac{3T_0}{T}\mu\right], \tag{13}$$

where $T_0=8pm^2S(\xi)/3kd_1^3$.

An analysis shows that, for $\xi>1$ (when $T_0\leqslant0$), Eq. (13) has a unique solution at any temperature: $\mu=0$. Consequently, long-range order does not occur in this case, including a two-dimensional particle distribution. The absence of long-range order in the case $\xi = 1$, which corresponds to a simple cubic lattice, agrees with the results of Luttinger and Tisza.[17]

A nonzero solution of Eq. (13) can exist only for $\xi < 1$. As in the case of the Langevin equation $\mu = \text{cotanh}(3T_0\mu/T) - T/(3T_0\mu)$, to which Eq. (13) reduces in the limit $H_a \to 0$, it exists if the tangent to the graph of the function defined by the right-hand side of Eq. (13) is greater than unity as $\mu \to 0$. It is readily verified that this condition is satisfied if $T < T_{\text{cr}}$, where T_{cr} is the paramagnetic-ferromagnetic phase transition temperature, which is determined by solving the equation $T = 3T_0 f(a)$ $f(a) = [2\exp a/C(a,0) - 1]/2a$ for T. We note that $f(a)$, m, and hence $T_0 f(a)$ are decreasing functions of T, where $T_0 f(a) = 0$ for $T \geqslant T_C$ (T_C is the Curie temperature of the particle material). This means that the equation $T = 3T_0 f(a)$ has a unique solution, which always satisfies the condition $T_{\text{cr}} < T_C$. Inasmuch as $m = m(T)$ and $a = a(T)$, the equation is analytically solvable only in certain limiting cases. In particular, if $m(T_{\text{cr}}) \approx m(0)$ (this condition holds for values of T_{cr} not too close to T_C), then, using the expansions $f(a) = 1/3 + 4a/45$ $(a \ll 1)$ and $f(a) = 1 - 1/a$ $(a \gg 1)$, we find

$$T_{\text{cr}} = \begin{cases} T_0(1 + 4a(T_0)/15), & a(T_0) \ll 1, \\ 3T_0(1 - 1/a(3T_0)), & a(3T_0) \gg 1. \end{cases} \tag{14}$$

As the radius of the particles increases, the transition temperature T_{cr} rapidly approaches their Curie point T_C. For example, for a system of single-domain Co particles, characterized by the parameters $T_C = 1400$, $M_s = 1400G$ (M_s is the saturation magnetization), $H_a = 6400$, $p = 1$, $\xi = 0.5$, and $d_2 = 3r$, from the lower equation (14) [whose use is justified by the fact that $a(3T_0) \approx 5$ in the given situation] we obtain $T_{\text{cr}} \approx 2.18 \times 10^{-2} r^3$ ($[r] = \text{Å}$). Hence it follows that T_{cr} can differ significantly from T_C only if $r < 40$; for particles of larger radius $T_{\text{cr}} \approx T_C$.

In the vicinity of the point $T = T_{\text{cr}}$ the behavior of a number of the thermodynamic parameters of the system of single-domain particles exhibits anomalies which, in accordance with the given approximation, are typical of the mean-field theory. In particular, the magnetic susceptibility $\chi = \lim_{H \to 0} \partial M / \partial H$ (H is a static magnetic field directed along the z axis) is given by the following expressions for $m(T_{\text{cr}}) \approx m(0)$ and $a(3T_0) \gg 1$:

$$\chi = \begin{cases} 1/16\xi S(\xi)(1 - T/T_{\text{cr}}), & T < T_{\text{cr}}, \\ 1/8\xi S(\xi)(T/T_{\text{cr}} - 1), & T > T_{\text{cr}}, \end{cases} \tag{15}$$

and the magnetization $M(\infty)$ has a square root asymptotic behavior: $M(\infty) \sim (T_{\text{cr}} - T)^{1/2}$. As an illustration, Fig. 2 shows temperature dependences of the order parameter for the above-analyzed system of single-domain Co particles [at $T = 0$ the spontaneous magnetization of this system is $nm(0) \approx 54\,\text{G}$].

We note that the physical cause for the existence (for $\xi < 1$) or nonexistence (for $\xi \geqslant 1$) of ferromagnetic order in the system of single-domain particles is the competition of magnetic-dipole particle interactions. In fact, all particles surrounding the designated particle can be divided conditionally into two groups according to whether the condition $3r_{iz}^2 - |\mathbf{r}_i|^2 > 0$ or the condition $3r_{iz}^2 - |\mathbf{r}_i|^2 \leqslant 0$ is satisfied for them. According to Eq. (6), particles of the first group produce at the designated particle site a mean dipole magnetic field parallel to the magnetization, while particles of the second group produce an antiparallel field. It is obvious that ferromagnetic order corresponds to the case in which the contribution to the total dipole field from particles of the first group prevails over the contribution from particles of the second group; it follows from (9) that this is the situation for $\xi < 1$.

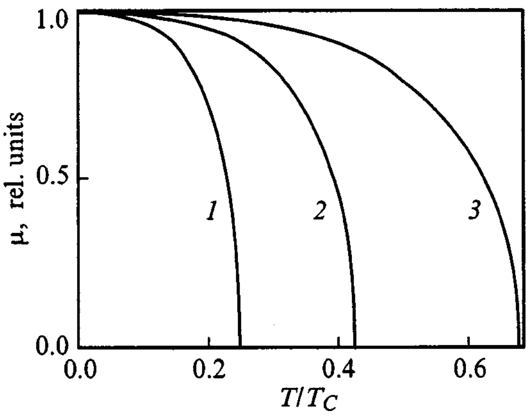

FIG. 2. Graphs of the order parameter μ as a function of the normalized temperature T/T_C for a system of single-domain Co particles, characterized by the parameters indicated in the main text and various radii: *1*) $r = 25$; *2*) $r = 30$; *3*) $r = 35$.

Experimental evidence for the existence of a paramagnetic-ferromagnetic transition in systems of single-domain particles has been obtained in several recent studies. For example, ferromagnetic ordering has been observed in a decomposing $Cu_{64}Mn_9Al_{27}$ melt[24] and in Fe powders.[25] However, the fundamental issue of the interaction responsible for ferromagnetic order is left open in these papers. We have considered it advisable therefore to formulate a number of conditions that must be satisfied by systems of single-domain particles to facilitate the experimental observation and investigation of the paramagnetic-ferromagnetic transition induced in them by magnetic-dipole particle interaction. First, to exclude the influence of the phase transition at the Curie temperature on the behavior of the phase transition at $T = T_{\text{cr}}$, the temperatures T_{cr} and T_C must be sufficiently far apart. This requires that the particle radius not exceed a certain critical value, which can be estimated from Eq. (14) and the condition $T_{\text{cr}} = T_C$. Second, since T_{cr} depends strongly on the particle size, the distribution of their radii must have a small variance. The third and final condition is that the mean distance between the particles in the plane perpendicular to the easy magnetization axis must be larger than the mean distance between the particles in the direction of the easy axis. Obviously, this condition can be met in certain situations by ''preconditioning'' the system in the presence of a sufficiently strong ($\sim H_a$) static magnetic field directed along the easy axis.

3. RELAXATION OF THE MAGNETIZATION

We now consider the distinctive characteristics of the process of magnetization relaxation in the system of single-domain particles, assuming that $a(1-|b(t)|)^2 \gg 1$ and $|b(t)<1|$. Since, according to (4), a quasi-equilibrium distribution of the magnetic moments is established in times of the order of $t_r a$, Kramers method[14] may be used to investigate the evolution of the magnetization at $t > t_r a$. In accordance with this method we seek a solution of Eq. (4) in the form

$$P(\theta,t)=V(\theta,t)\begin{cases} p_+(t)/n_+(t), & 0\leqslant\theta<\theta_0(t),\\ p_-(t)/n_-(t), & \theta_0(t)<\theta\leqslant\pi, \end{cases} \tag{16}$$

where

$$p_+(t)=\int_0^{\theta_0(t)} P(\theta,t)\,d\theta, \quad p_-(t)=\int_{\theta_0(t)}^{\pi} P(\theta,t)\,d\theta, \tag{17}$$

are the probabilities that the polar angle of the vector **m** will belong to the interval $(0,\theta_0(t))$ or $(\theta_0(t),\pi)$, respectively, $\theta_0(t)=\arccos(-b(t))$ is the angle corresponding to the maximum of the energy $W=-(1/2)H_a m\cos^2\theta - H(t)m\cos\theta$, $V(\theta,t)=\sin\theta\exp(a(\cos^2\theta+2b(t)\cos\theta))$, and

$$n_+(t)=\int_0^{\theta_0(t)} V(\theta,t)\,d\theta, \quad n_-(t)=\int_{\theta_0(t)}^{\pi} V(\theta,t)\,d\theta. \tag{18}$$

Inasmuch as the mean dipole magnetic field can be expressed in terms of the probabilities $p_+(t)$ and $p_-(t)$ for $a(1-|b(t)|)^2 \gg 1$:

$$H(t)=8nm\xi S(\xi)[p_+(t)-p_-(t)], \tag{19}$$

and $p_-(t)=1-p_+(t)$, the only unknown in Eq. (16) is $p_+(t)$.

To find the equation satisfied by the probability $p_+(t)$, we first invoke the relation

$$\frac{\partial V(\theta,t)}{\partial\theta}+[a(\sin 2\theta+2b(t)\sin\theta)-\cos\theta]V(\theta,t)=0$$

and then use it to transform Eq. (4) as follows:

$$\frac{\partial P(\theta,t)}{\partial t}=\frac{1}{t_r a}\frac{\partial}{\partial\theta}V(\theta,t)\frac{\partial}{\partial\theta}\frac{P(\theta,t)}{V(\theta,t)}. \tag{20}$$

Next, having obtained from (20) the equation

$$\int_0^{\theta_0(t)}\frac{1}{V(\theta,t)}\frac{\partial}{\partial t}\left(\int_0^{\theta}P(\vartheta,t)\,d\vartheta\right)d\theta = \frac{1}{t_r a}\int_0^{\theta_0(t)}\frac{\partial}{\partial\theta}\left(\frac{P(\theta,t)}{V(\theta,t)}\right)d\theta, \tag{21}$$

substitute (16) into it, and evaluate the integrals involved in Eq. (21). Bearing in mind that

$$\frac{\partial}{\partial\theta}\left(\frac{P(\theta,t)}{V(\theta,t)}\right)=-\left(\frac{p_+(t)}{n_+(t)}-\frac{p_-(t)}{n_-(t)}\right)\delta(\theta-\theta_0(t))$$

and that the following asymptotic $[a(1-|b(t)|)^2\to\infty]$ equations are valid:

$$n_\pm(t)=\frac{e^{a[1\pm 2b(t)]}}{2a[1\pm b(t)]},$$

$$\int_0^{\theta_0(t)}\frac{1}{V(\theta,t)}\frac{\partial}{\partial t}\left(\int_0^{\theta}P(\vartheta,t)\,d\vartheta\right)d\theta = \dot{p}_+(t)\frac{1}{2}\sqrt{\frac{\pi}{a}}\frac{e^{ab^2(t)}}{1-b^2(t)},$$

from (21) we obtain an equation for $p_+(t)$:

$$\dot{p}_+(t)=-\left(\frac{p_+(t)}{\tau_+(t)}-\frac{p_-(t)}{\tau_-(t)}\right), \tag{22}$$

where the quantities $\tau_+(t)$ and $\tau_-(t)$, defined by the relation

$$\tau_\pm(t)=\frac{t_r\sqrt{\pi/a}}{2(1-b^2(t))(1\pm b(t))}e^{a(1\pm b(t))^2}, \tag{23}$$

have the significance of the mean residence times of the magnetic moment in states with $\theta\in(0,\theta_0(t))$ and $\theta\in(\theta_0(t),\pi)$, respectively. Since the probability of transition of the magnetic moment from the first to the second state is negligible in times of the order of $t_r a$, the initial condition for Eq. (22) is $p_+(0)=1$.

According to Eq. (5), for $a(1-|b(t)|)^2\gg 1$ the magnetization of a system of single-domain particles can be written in the form $M(t)=nm\mu(t)$, where it follows from Eq. (22) that the function $\mu(t)=2p_+(t)-1$ satisfies the equation

$$\dot{\mu}(t)=-\mu(t)\left(\frac{1}{\tau_+(t)}+\frac{1}{\tau_-(t)}\right)-\frac{1}{\tau_+(t)}+\frac{1}{\tau_-(t)}. \tag{24}$$

Inasmuch as $\tau_+(t)$ and $\tau_-(t)$ depend on the time only through the normalized magnetization $\mu(t)$, Eq. (24) is an equation of the form $\dot{\mu}(t)=-F(\mu(t))$ with

$$F(\mu(t))=\mu(t)\left(\frac{1}{\tau_+(t)}+\frac{1}{\tau_-(t)}\right)+\frac{1}{\tau_+(t)}-\frac{1}{\tau_-(t)},$$

which can be solved, subject to the initial condition $\mu(0)=1$, by solving the algebraic equation

$$\int_{\mu(t)}^{1}\frac{dx}{F(x)}=t \tag{25}$$

for $\mu(t)$.

Using Eq. (25), we find the asymptotic forms of the solution of Eq. (24) in the limits $t\to 0$ and $t\to\infty$. In the first case we have $\mu(t)\to 1$, so that by replacing $F(x)$ with $F(1)=2/\tau_+(0)$ in (25) and denoting $\beta=8\xi S(\xi)nm/H_a$ we obtain $\mu(t)=1-t/\tau_0$, where

$$\tau_0=\frac{t_r\sqrt{\pi/a}}{4(1-\beta^2)(1+\beta)}e^{a(1+\beta)^2} \tag{26}$$

is the relaxation time of the initial magnetization.

To find a solution of Eq. (24) in the second case, we set $\mu(t)=\mu+\mu_1(t)$ $[\mu=\mu(\infty),\ \lim_{t\to\infty}\mu_1(t)=0]$ and rewrite Eq. (25) in the form

$$\int_0^{1-\mu-\mu_1(t)} \frac{dy}{F(\mu+\mu_1(t)+y)} = t. \tag{27}$$

Next, we make use of the fact that the order parameter μ obeys the equation $F(\mu)=0$ [as must be the case, because for $a(1-|b(t)|)^2 \gg 1$ Eq. (13) reduces to the equation $F(\mu)=0$], so that in the limit $t \to \infty$ the main contribution to the integral over y is from a small neighborhood of its lower limit of integration. Accordingly, replacing $F(\mu+\mu_1(t)+y)$ with $F'(\mu)(\mu_1(t)+y)$ (the prime denotes differentiation with respect to μ), from Eq. (27) we obtain $\mu(t)=\mu+c\exp(-t/\tau_\infty)$, where the relaxation time of the magnetization at long times, defined as $\tau_\infty = 1/F'(\mu)$, is given by the expression

$$\tau_\infty = t_t \sqrt{\frac{\pi}{a}} \frac{(1-\mu)e^{a(1+\beta\mu)^2}}{4(1+\beta\mu)[1+\beta(1-\mu^2)-\beta^2\mu^2-2a\beta(1-\beta^2\mu^2)(1-\mu^2)]}. \tag{28}$$

As for the parameter c, the Padé approximant[26] of the function $\mu(t)$:

$$\mu(t) = \mu + \frac{(1-\mu)^2 \tau_0/\tau_\infty}{\exp(t/\tau_\infty)+(1-\mu)\tau_0/\tau_\infty - 1}, \tag{29}$$

which matches the asymptotic forms of $\mu(t)$ in the limits $t \to 0$ and $t \to \infty$, gives the approximate [by virtue of the approximate character of (29)] value of the parameter $(1-\mu)^2 \tau_0/\tau_\infty$. We also note that in cases where $\xi > 1$ or $T > T_{\mathrm{cr}}$ (for $\xi < 1$) the order parameter is equal to zero, and Eq. (28) is greatly simplified:

$$\tau_\infty = t_r \sqrt{\frac{\pi}{a}} \frac{e^a}{4(1+\beta-2a\beta)}.$$

Because τ_0 is an exponential function of a, for sufficiently large values of the parameter a the condition $t \gg \tau_0$ underlying the derivation of Eq. (28) can become experimentally unattainable. In this event, the quantity of primary interest for the experimental verification of the results is the relaxation time of the initial magnetization. We first ascertain how magnetic-dipole particle interaction influences τ_0. Since the parameter characterizing this interaction is β, and $a(1-|\beta|)^2 \gg 1$, it follows from Eq. (26) that when $\beta > 0$ (i.e., when $\xi < 1$), an increase in β causes τ_0 to increase, and when $\beta < 0$ ($\xi > 1$), an increase in $|\beta|$ causes τ_0 to decrease. This behavior of τ_0 as a function of β is easily explained: In the first case the magnetization relaxes in the presence of a mean dipole magnetic field in the same direction as the magnetization, whereas in the second case the mean field and the magnetization are in opposite directions. Defining the relaxation time of the magnetization of a system of noninteracting particles as $\tau_n = t_r(\pi/16a)^{1/2}\exp a$, on the basis of Eq. (26) we obtain

$$\frac{\tau_0}{\tau_n} = \frac{e^{a\beta(2+\beta)}}{(1-\beta^2)(1+\beta)}. \tag{30}$$

According to Eq. (30), when $a(1-|\beta|)^2 \gg 1$, we have $\tau_0/\tau_n > 1$ for $\beta > 0$ and $\tau_0/\tau_n < 1$ for $\beta < 0$.

Consequently, magnetic-dipole interaction of the particles causes the relaxation time of the initial magnetization to decrease for $\xi > 1$ and to increase for $\xi < 1$ relative to the case of noninteracting particles. In particular, for the system of Co particles of radius $r = 35$ Å discussed in the preceding section, for $T/T_C = 0.2$ we obtain $a \approx 20.8$, $\beta \approx 0.1$, and $\tau_0/\tau_n \approx 73$.

Note that it is entirely realistic for the parameter β to have values of the order of unity, and the ratio τ_0/τ_n can be very large therefore. For example, if Co particles are replaced by Fe particles in the shape of ellipsoids of revolution with $M_s = 1740$ and $H_a = 1550$ (here H_a is the uniaxial geometrical anisotropy field, which corresponds to the 1.2 ratio of the polar semiaxis of the ellipsoid to the equatorial semiaxis[27]), then $\beta \approx 0.51$ and $\tau_0/\tau_n \approx 0.9\exp(1.3a)$. The recent experimental observation[28,29] of a huge excess of τ_0 over τ_n is ample corroboration of the magnetization relaxation theory developed here.

We conclude the investigation with a discussion of the main approximations used in the work and the possible consequences of their omission. The most significant approximation, of course, is the assumption that the directions of the particle magnetic moments are uncorrelated, which has permitted us to reduce the original multifrequency problem to single-frequency status. One possible consequence of taking such correlations into account could be, for example, slowing of the magnetization relaxation rate at long times. Indeed, correlation of the directions of the particle magnetic moments due to their magnetic-dipole interaction should be manifested in a tendency toward ferromagnetic order in a random particle with the magnetic moments of particles in the first group, as dictated by the condition $\sim\exp a\ 3r_{iz}^2 - |\mathbf{r}_i|^2 > 0$, and to antiferromagnetic order with the magnetic moments of particles in the second group, characterized by the condition $3r_{iz}^2 - |\mathbf{r}_i|^2 < 0$. This means that the absolute value of the mean magnetic field exerted on the designated particle by particles of the first (second) group for $t \gg \tau_0$ will be greater than (be less than or equal to) the absolute value of this field corresponding to the mean-field approximation. Thus, allowance for correlation of the directions of the magnetic moments of single-domain particles should cause the algebraic value of the resultant mean field to increase and, as a result, the relaxation rate of the magnetization to decrease for all $\xi \neq 1$.

The assumption that the system of single-domain particles is unbounded also imposes a restriction on the applicability of the results. One consequence of omitting this assumption could be the necessity of taking into account the existence of domain structure in such systems. As in the case of bulk ferromagnets,[27] domain structure will have a significant influence on the magnetic properties. Specifically, the formation of domain structure will qualitatively change the nature of the relaxation of the magnetization. However, since the onset of domain structure becomes likely only at times much larger than τ_0, the character of the relaxation of the magnetization does not change in the given situation with $a(1-|\beta|)^2 \gg 1$.

*⁾E-mail: denisov@ssu.sumy.ua

---

[1] W. F. Brown, J. Phys. Rev. **130**, 1677 (1963).

[2] L. Bessais, L. Ben Jaffel, and J. L. Dormann, Phys. Rev. B **45**, 7805 (1992).

[3] W. T. Coffey, D. S. F. Crothers, Yu. P. Kalmykov, E. S. Massawe, and J. T. Waldron, Phys. Rev. E **49**, 1869 (1994).

[4] D. A. Garanin, Phys. Rev. E **54**, 3250 (1996).

[5] W. T. Coffey and D. S. F. Crothers, Phys. Rev. E **54**, 4768 (1996).

[6] Yu. L. Raĭkher and M. I. Shliomis, Zh. Éksp. Teor. Fiz. **67**, 1060 (1974) [Sov. Phys. JETP **40**, 526 (1974)].

[7] R. S. Tekht, V. A. Ignatchenko, Yu. L. Raĭkher, and M. I. Shliomis, Zh. Éksp. Teor. Fiz. **70**, 1300 (1976) [Sov. Phys. JETP **43**, 677 (1976)].

[8] Yu. L. Raĭkher and V. I. Stepanov, Zh. Éksp. Teor. Fiz. **101**, 1409 (1991) [Sov. Phys. JETP **74**, 755 (1991)].

[9] A. Pérez-Madrid and J. M. Rubí, Phys. Rev. E **51**, 4159 (1995).

[10] Yu. L. Raikher and V. I. Stepanov, Phys. Rev. B **52**, *5*, 3493 (1995).

[11] É. K. Sadykov and A. G. Isavnin, Fiz. Tverd. Tela (St. Petersburg) **38**, 2104 (1996) [Phys. Solid State **38**, 1160 (1996)].

[12] S. I. Denisov and A. N. Yunda, Izv. Vyssh. Uchebn. Zaved. Fiz. **41**, 118 (1998).

[13] S. I. Denisov and A. N. Yunda, Physica B **245**, 282 (1998).

[14] C. W. Gardiner, *Handbook of Stochastic Methods for Physics, Chemistry, and the Natural Sciences*, (Springer-Verlag, Berlin, 1985).

[15] V. I. Tikhonov and V. I. Khimenko, *Excursions of the Paths of Stochastic Processes* (Nauka, Moscow, 1987).

[16] H. Zhang and M. Widom, Phys. Rev. B **51**, 8951 (1995).

[17] J. M. Luttinger and L. Tisza, Phys. Rev. **70**, 954 (1946).

[18] J. P. Bouchaud and P. G. Zérah, Phys. Rev. B **47**, 9095 (1993).

[19] S. Shtrikman and E. P. Wohlfarth, Phys. Lett. A **85**, 467 (1981).

[20] J. L. Dormann, L. Bessais, and D. Fiorani, J. Phys. C **21**, 2015 (1988).

[21] D. K. Lottis, R. M. White, and E. Dan Dahlberg, Phys. Rev. Lett. **67**, 362 (1991).

[22] M. El-Hilo, K. O'Grady, and R. W. Chantrell, J. Magn. Magn. Mater. **114**, 295 (1992); **114**, 307 (1992).

[23] R. L. Stratonovich, SIAM J. Control **4**, 362 (1966).

[24] G. A. Takzeĭ, L. P. Gun'ko, I. I. Sych, Yu. N. Troshchenkov, S. V. Cherepov, and I. Mirebeau, JETP Lett. **63**, 1013 (1996).

[25] L. Del Bainco, C. Ballesteros, J. M. Rojo, and A. Hernando, Phys. Rev. Lett. **81**, 4500 (1998).

[26] G. A. Baker and P. Graves-Morris, *Padé Approximants* (Addison-Wesley, Reading, Mass., 1981).

[27] S. V. Vonsovskiĭ, *Magnetism* (Nauka, Moscow, 1971), p. 787.

[28] E. N. Abarra and T. Suzuki, IEEE Trans. Magn. **MAG-33**, 2995 (1997).

[29] E. N. Abarra, P. Glijer, H. Kisker, I. Okamoto, and T. Suzuki, J. Magn. Magn. Mater. **175**, 148 (1997).

Translated by James S. Wood

PHYSICS OF THE SOLID STATE VOLUME 41, NUMBER 10 OCTOBER 1999

Concentration dependence of the compositional order–disorder phase-transition temperature in the solid solution $PbSc_{0.5}Nb_{0.5}O_3-PbSc_{0.5}Ta_{0.5}O_3$

I. P. Raevskiĭ, V. V. Eremkin, V. G. Smotrakov,*) E. S. Gagarina, and M. A. Malitskaya

Scientific-Research Institute of Physics, Rostov-on-Don State University, 344090 Rostov-on-Don, Russia

(Submitted January 19, 1999)
Fiz. Tverd. Tela (St. Petersburg) **41**, 1828–1830 (October 1999)

The degree of compositional order S of crystals of the complete series of solid solutions $(1-x)PbSc_{0.5}Nb_{0.5}O_3$-$xPbSc_{0.5}Ta_{0.5}O_3$ grown under identical conditions is determined by x-ray examination. The form of the dependence $S(x)$ and the variations of S for different compositions, after high-temperature annealing, indicate that the concentration dependence of the compositional order–disorder phase-transition temperature is close to linear in the given system of solid solutions. © *1999 American Institute of Physics.* [S1063-7834(99)02310-2]

In certain ternary oxides of the perovskite family characterized by the formula $PbB^{3+}_{0.5}B^{5+}_{0.5}O_3$ ($B^{3+}=Sc$, In, Yb, Lu, Er, Tm; $B^{5+}=Nb$, Ta, Sb), phase transitions of the compositional order-disorder type in the high-temperature range ($T_t=1000-1500\,°C$) are observed in addition to ferroelectric phase transitions.[1–4] Above T_t the ions of trivalent and pentavalent elements are randomly distributed among intraoctahedron lattice sites, whereas below this temperature the equilibrium state is an ordered state (compositional or crystallochemical order). Since the degree of compositional order S varies by a diffusion mechanism, the high-temperature state can be ''frozen'' by rapid postanneal cooling of the sample. This treatment induces a strong dependence of the properties of compositionally ordered oxides on the preparation conditions, first and foremost on the ratio between T_t and the anneal temperature of a ceramic or the growth temperature of a crystal.[1–6] At the present time the values of T_t have been determined for five ternary perovskites: $PbB^{3+}_{0.5}Nb^{5+}_{0.5}O_3$ ($B^{3+}=Sc$, In, Yb, Lu) and $PbSc_{0.5}Ta_{0.5}O_3$ (Refs. 1 and 4). On the other hand, although compositional order effects have been observed in several solid solutions of ternary perovskites,[2,7,8] data on the concentration dependence of T_t for such solid solutions are lacking. The objective of this study is to obtain data on the form of $T_t(x)$ in the system of solid solutions $PbSc_{0.5}Nb_{0.5}O_3-PbSc_{0.5}Ta_{0.5}O_3$ (PSN-PST), for which the values of T_t have been established for the extreme concentrations of the components: 1210 °C for PSN and 1450 − 1500°C for PST (Ref. 1). In contrast with previous studies of compositionally ordered solid solutions, which have been confined strictly to ceramic samples,[2,4,7,8] the present investigation has been carried out on crystals, because the relationship between the quantity S and the preparation or heat-treatment conditions in crystals is much more clearly defined than in ceramics.[5,6,9]

Crystals of the complete series of solid solutions $PbSc_{0.5}(Nb_{1-x}Ta_x)_{0.5}O_3$ were grown by bulk crystallization from the fluxed melt using a unified lead borate solvent (PbO-$0.26B_2O_3$), a single crystallization temperature range ($1160-1050\,°C$), and the same cooling rate of the melt ($5.5°/h$). The composition of the crystals was determined by means of a Camebax-Micro combination scanning microscope and microanalyzer within 2% error limits. The average value of S was determined by x-ray examinations of the powdered crystals. The methods of investigation are described in detail in Ref. 9.

An expression for T_t has been derived previously[10] from a simple thermodynamic model in application to solid solutions of compositionally ordered ternary perovskites. According to this expression, the function $T_t(x)$ must have a maximum:

$$T_{tx}=\frac{T_{t0}(1-x)+T_{t1}x}{x^2-x+1}. \tag{1}$$

Here T_{t0} and T_{t1} are the values of T_t for the extreme components of the solid solutions (corresponding to $x=0$ and $x=1$). Estimates using Eq. (1) have shown that in the system of PSN-PST solid solutions, as x increases, T_t rises abruptly and for compositions with $x>0.15$ exceeds the value of T_t for PST. The maximum value of T_t is attained for $x=0.5$ and is equal to 1900 °C (Fig. 1a). We have previously established[5,6] that PSN and PST crystals grow with disorder (even at temperatures below T_t, where the disordered state is a nonequilibrium state), and then the degree of order S begins to change by diffusion, tending to the equilibrium value S_e at the crystallization temperature. For this crystal, therefore, S depends on the ratio t/τ, where t is the crystallization time, and τ is the time required to reach by diffusion the equilibrium value S_e at the crystallization temperature T_{cr}. The time τ, in turn, depends on T_{cr}, and S_e depends on the ratio T_{cr}/T_t. It is evident from Fig. 2 that the average values of S for PST crystals grown in different temperature intervals agrees quite well with the dependence of the equilibrium value S_e on T_{cr}/T_t as calculated by the Kirkwood method.[3]

According to the above-described concepts of the growth mechanism of PSN and PST crystals, if the dependence $T_t(x)$ in the system PSN-PST is described by Eq. (1),

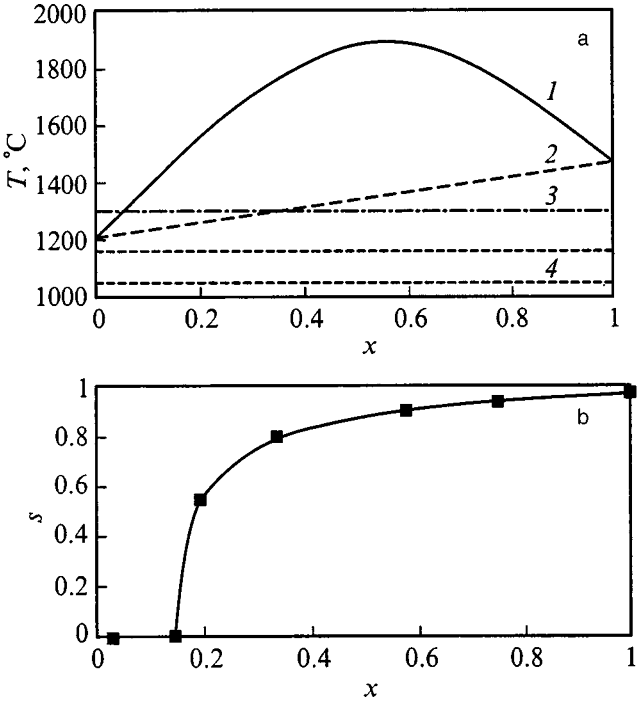

FIG. 1. (a) Relation between the temperature T_t of composition order-disorder phase transition, the anneal temperature T_a, and the crystallization temperature range of solid solutions $(1-x)\mathrm{PbSc_{0.5}Nb_{0.5}O_3}-x\mathrm{PbSc_{0.5}Ta_{0.5}O_3}$: (*1*) function $T_t(x)$ calculated from Eq. (1); (*2*) linear approximation of $T_t(x)$; (*3*) anneal temperature T_a; (*4*) crystallization temperature range. (b) Average values of the degree of compositional order S of crystals of solid solutions $(1-x)\mathrm{PbSc_{0.5}Nb_{0.5}O_3}-x\mathrm{PbSc_{0.5}Ta_{0.5}O_3}$ not further heat treated after growth.

the average values of S for crystals of solid solutions with $x>0.15$ in the crystallization temperature range used here must be no lower than for PST, and only for $x<0.1$ can S be expected to decrease as x is decreased (Fig. 1a). Thus, the average value of S remains less than 0.1 as x is increased from 0 to 0.15, but then in the interval 0.20–0.35 it increases from 0.5 to 0.8, and finally it increases more gradually with x to $S=0.97$ at $x=1$ (Fig. 1b). On the other hand, if we assume that T_t varies linearly with x in the system PSN-PST, the experimental values of S for crystals of the solid solutions are in good agreement with the calculated dependence of the equilibrium value S_e on T_{cr}/T_t (Fig. 2). The best agreement of the experimental data with the calculated dependence $S(T_{\mathrm{cr}}/T_t)$ is attained if T_{cr} is interpreted as the upper end of the crystallization temperature range for compositions with small x and as the lower end of that range for compositions with $x>0.4$. This fact can be explained on the assumption that the rate of ordering at the crystallization temperature of compositions having a high PST content is substantially higher than those close to pure PSN. This difference is more likely associated with the considerable difference in the values of T_t for PSN and PST.

To further verify the form of $T_t(x)$, we have annealed tablets pressed from powdered crystals of the solid solutions with different concentration indices x at $T_a=1310\,°\mathrm{C}$. This temperature is higher than the value of T_t for compositions with $x<0.3$ if T_t depends linearly on x. If $T_t(x)$ has the form of a curve with a maximum in accordance with Ref. 10, T_a is much lower than the value of T_t for the majority of the investigation solid solution compositions (Fig. 1a). The samples were annealed in a hermetically sealed alundum crucible packed with PST powder. The crucible was heated together with the oven to T_a, was held at this temperature for 1.5 h, and was then quenched to room temperature. X-ray examinations showed that annealing lowered the average value of S for all the compositions, and for the composition with $x=0.2$ the superlattice lines associated with order vanished. This result can be regarded as direct proof that $T_t(x)$ is close to linear in the system of PSN-PST solid solutions, because in this case T_a is higher than the value of T_t for the

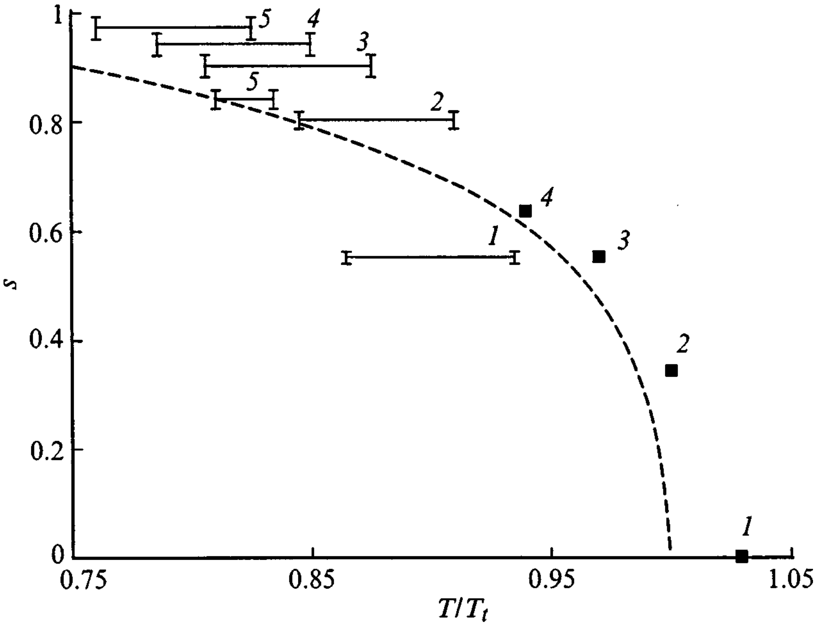

FIG. 2. Temperature dependence of the equilibrium values S_e of the degree of compositional order, calculated by the Kirkwood method[3] (dashed line). The horizontal segments *1*–*5* correspond to the crystallization temperature ranges of crystals of solid solutions $(1-x)\mathrm{PbSc_{0.5}Nb_{0.5}O_3}-x\mathrm{PbSc_{0.5}Ta_{0.5}O_3}$ (assuming that T_t depends linearly on x). The points represent the average values of the degree of compositional order S of tablets pressed from powdered crystals of the solid solutions with different values of x, after annealing at $T_a=1310\,°\mathrm{C}$: (*1*) $x=0.20$; (*2*) $x=0.34$; (*3*) $x=0.58$; (*4*) $x=0.75$; (*5*) $x=1.00$.

composition with $x=0.2$. Moreover, if T_t is assumed to be a linear function of x, the average value of S for other annealed compositions are in good agreement with the calculated dependence of S_e on T_a/T_t (Fig. 2).

To summarize, the form of the dependence $S(x)$ for PSN-PST crystals grown under identical conditions and the behavior of S for these solid solutions after a high-temperature anneal indicate that the dependence $T_t(x)$ is close to linear in the system PSN-PST. The discrepancy between the experimental dependence $T_t(x)$ and the form calculated on the basis of the model in Ref. 10 for PSN-PST solid solutions could be associated with the fact that PSN and PST are ferroelectrics in both the disordered and the ordered state, whereas all other compositionally ordered ternary perovskites known at the present time are ferroelectrics in the disordered state, but are antiferroelectrics in the ordered state.[4] Further studies of solid solutions of other compositionally ordered ternary perovskites will be needed before any final conclusions can be drawn.

This work has received partial support from the Russian Fund for Fundamental Research (RFFI Project No. 96-02-17463).

*⁾E-mail: smotr@iphys.md.runnet.ru

---

[1] C. G. F. Stenger and A. J. Burgraaf, Phys. Status Solidi A **61**, 653 (1980).
[2] Z. Chen, N. Setter, and L. E. Cross, Ferroelectrics **37**, 619 (1981).
[3] A. A. Bokov and I. P. Rayevsky, Ferroelectrics **90**, 125 (1989).
[4] A. A. Bokov and I. P. Rayevsky, Ferroelectrics **144**, 147 (1993).
[5] I. P. Raevskiĭ, A. J. Bokov, V. G. Smotrakov, S. M. Zaĭtsev, and V. P. Filipenko, Izv. Akad. Nauk SSSR, Neorg. Mater. **22**, 807 (1986).
[6] A. A. Bokov, I. P. Raevskiĭ, V. G. Smotrakov, and S. M. Zaĭtsev, Kristallografiya **32**, 1301 (1987) [Sov. Phys. Crystallogr. **32**, 769 (1987)].
[7] V. A. Isupov, E. N. Isupova, R. Yu. Sokolova, and G. A. Smolenskiĭ, Izv. Akad. Nauk SSSR, Neorg. Mater. **20**, 825 (1984).
[8] A. A. Bokov, I. P. Raevskiĭ, and V. Yu. Shonov, Izv. Akad. Nauk SSSR, Neorg. Mater. **26**, 2371 (1990).
[9] V. Eremkin, V. Smotrakov, E. Gagarina, and I. Raevski, J. Korean Phys. Soc. **32**, Suppl., S1597 (1998).
[10] A. A. Bokov, Ferroelectrics **90**, 155 (1989).

Translated by James S. Wood

PHYSICS OF THE SOLID STATE VOLUME 41, NUMBER 10 OCTOBER 1999

Domain kinetics in the formation of a periodic domain structure in lithium niobate

V. Ya. Shur*) and E. L. Rumyantsev

Scientific-Research Institute of Physics and Applied Mathematics, Ural State University,
620083 Ekaterinburg, Russia

R. G. Batchko, G. D. Miller, M. M. Fejer, and R. L. Byer

E. L. Ginzton Laboratory, Stanford University, Stanford, California 94305, USA

(Submitted November 3, 1998; resubmitted March 23, 1999)
Fiz. Tverd. Tela (St. Petersburg) **41**, 1831–1837 (October 1999)

The evolution of the domain structure in $LiNbO_3$ with polarization switching in an electric field is investigated experimentally. Special attention is given to the formation processes of a regular domain applicable to nonlinear optical devices. A new method based on the spontaneous backswitching effect is proposed for creating a regular structure with a period of 2.6 μm in $LiNbO_3$ with a thickness of 0.5 mm. © *1999 American Institute of Physics.* [S1063-7834(99)02410-7]

The formation of a periodic domain structure having micron periods in ferroelectric materials, which are useful in applications, poses a problem whose solution is particularly crucial in order to establish synchronism conditions in nonlinear optical devices.[1] Second harmonic generation in the visible and ultraviolet (UV) ranges require regular domain structures with a period less than 5 μm in substrates having a thickness of at least 0.5 mm. The feasibility of creating a regular domain structure in bulk $LiNbO_3$ placed in an electric field at room temperature was first demonstrated in 1993.[3] This technique has grown in popularity by virtue of its reproducibility and applicability to other nonlinear optical crystals. Several papers have reported applications of this technique to create a domain structure with a period of $3-4$ μm in substrates of thickness $200-300$ μm in $LiNbO_3$ (Ref. 2), $LiTaO_3$ (Refs. 3 and 4), and $KTiOPO_4$ (KTP) (Ref. 5) with the capability of generating blue and UV light. In thicker substrates, however, it is impossible to obtain structures capable of satisfying the quasi-phase synchronism condition for this spectral range. It is essential to note that the domain kinetics in $LiNbO_3$ has been investigated only for very slow switchings,[6] even though it is obvious that a systematic investigation of the stages of evolution of the domain structure in the presence of switching with characteristic times less than one second has particularly important bearing on the refinement of existing methods.

Here we report a detailed investigation of the creation and pinning of a domain structure in bulk $LiNbO_3$ samples in the presence of an electric field applied to periodic stripe electrodes. Visualization of the domain configurations by chemical etching and subsequent examination of the relief with an optical microscope and a scanning electron microscope (SEM) have been used to analyze the evolution stages of the domain structure. Special attention has been devoted to studying the domain structure kinetics in the presence of spontaneous backswitching after the field is turned off.

1. EXPERIMENTAL

The investigated samples were monodomain $LiNbO_3$ wafers of thickness 0.5 mm cut perpendicularly to the polar axis from congruent-grown, optical-quality single crystals. Periodic metal stripe electrodes (NiCr) oriented along the $[10\overline{1}0]$ direction were photolithographically deposited on the (0001) polar plane. To prevent the domains from growing beyond the limits of the electrodes, the electrode-implanted surface was coated with a thin insulator layer (Fig. 1a). The voltage pulses used to generate an above-threshold electric field (21.5 kV/mm) in the bulk of the samples were applied by means of a clamp holder (Fig. 1a) through a liquid electrolyte (LiCl solution).[7,8] Switching was performed at room temperature. The current and voltage pulses were recorded as the domain structure took shape. The parameters of the domain structure could be controlled by varying the shape and duration of the voltage pulse and the current amplitude (Figs. 1b and 1c). To analyze the domain structure obtained after partial or complete switching, the polar planes and cross sections were etched for 5–10 min in hydrofluoric acid at room temperature. The surface relief was observed by the optical and scanning electron microscopes. The preparation of tilted thin sections significantly improved the spatial resolution for examination of the domain structure in the bulk. Detailed information on the evolution of the domains during switching was obtained by comparing the domain images formed after different lengths of the switching pulses.

2. EVOLUTION STAGES OF THE DOMAIN STRUCTURE

An analysis of the domain configurations obtained after partial switchings has revealed several distinct stages in the evolution of the domains[9] (Fig. 2). The switching process begins with ‘‘nucleation’’ (the inception of new domains) on the (0001) polar surface along the edges of the electrodes (Fig. 2a) when the field attains a threshold level.[10] The second stage is characterized by growth of the domains in the polar and sidewise directions and their coalescence under the

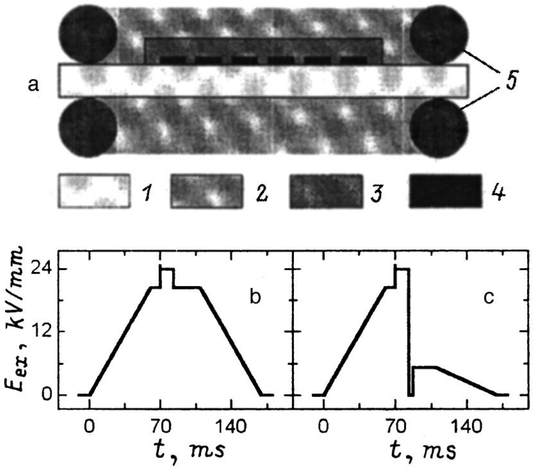

FIG. 1. a) Electrode configuration for the creation of a periodic domain structure: *1*) $LiNbO_3$ wafer; *2*) liquid electrolyte; *3*) insulator layer; *4*) periodic stripe electrodes; *5*) annular spacers; b) Shape of the switching voltage pulse in the conventional method; c) pulse shape with backswitching.

electrodes (Fig. 2b). Upon completion of this stage, laminar domains are formed all the way across the sample (Fig. 2c). In the third stage the planar boundaries of the newly formed domains move beyond the limits of the electrodes (Fig. 2d).

After a rapid decrease in the switching field the switching process stops and, depending on the pulse duration, two scenarios of domain evolution are possible: stabilization of the newly formed domain structure or partial switching of the domains back to the original stage (reverse poling or ''backswitching'').[7,11–13] In backswitching the boundaries of the switched domains move toward the electrodes; in addition, chains of wedge-shaped domains form along the edges of the electrodes (Fig. 2e).

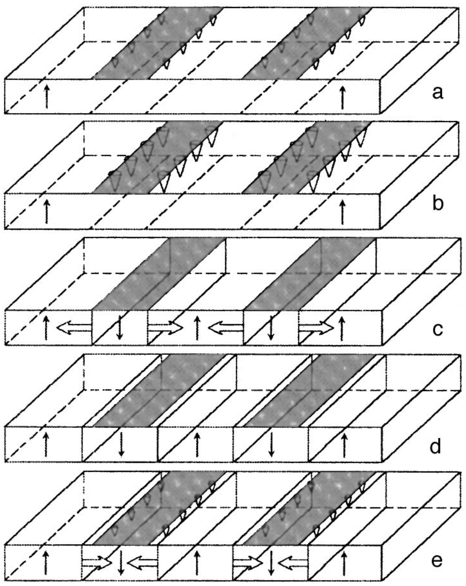

FIG. 2. Main stages of domain evolution in the switching of a monodomain wafer with stripe electrodes on (0001).

3. BASIC APPROACH

Our approach to analyzing the domain structure evolution in ferroelectrics is based on the assumption that screening effects play key role.[14,15] Switching from the single-domain state is known to be induced by the formation and growth of domains of opposite sign. The rates of formation and growth of the domains are governed by the polar component of the local electric field E_z (Refs. 10 and 15) at the nucleation sites and at the domain boundaries, respectively. The spatial distribution of the local field $E_z(r,t)$ is determined by the sum of the *z*-components of fields of various origins: 1) the external field $E_{\mathrm{ex}}(r)$ produced by the voltage applied to the electrodes; 2) the depolarizing field $E_{\mathrm{dep}}(r,t)$ produced by bound charges of the instantaneous domain configuration; 3) two types of screening fields, which compensate the depolarizing field: one external $E_{\mathrm{escr}}(r,t)$, induced by charge redistribution on the electrodes, and the other internal $E_{\mathrm{bscr}}(r,t)$, generated by various bulk mechanisms[14,16,17]:

$$E_z(r,t)=E_{\mathrm{ex}}(r)-[E_{\mathrm{dep}}(r,t)-E_{\mathrm{escr}}(r,t)-E_{\mathrm{bscr}}(r,t)]. \tag{1}$$

The depolarizing field slows domain growth, but its influence is diminished by the screening effects. As a rule, the external screening time constant is much shorter than the bulk constant and is governed by the parameters of the external circuit. Bulk screening processes are very significant, because even after the cessation of external screening a residual depolarizing field $E_{\mathrm{dr}}(r)$ (of the same order as the coercive field) still exists in the bulk, owing to the presence of a surface dielectric gap in ferroelectrics[10,11]:

$$E_{\mathrm{dr}}(r)=E_{\mathrm{dep}}(r)-E_{\mathrm{escr}}(r)\approx 0. \tag{2}$$

For an infinite, monodomain ferroelectric capacitor we have

$$E_{\mathrm{dr}}(r)=2L/d(P_S/\varepsilon_L\varepsilon_0), \tag{3}$$

where L is the thickness of the dielectric gap, d is the thickness of the sample, P_S is the spontaneous polarization, and ε_L is the dielectric permittivity of the gap.

The residual depolarizing field can be screened as a result of charge redistribution in the bulk and the orientation of charged dipole defects.[16,17] These processes are comparatively slow ($\tau\sim 10^{-1}-10^{5}$ s) (Ref. 10), so that the usually observed bulk screening delay produces various memory phenomena.[15] For example, the initial domain state can be partially or completely reconstructed after a sufficiently rapid reduction of the external field (spontaneous backswitching). This process is induced by the partially screened residual depolarizing field:

$$E_{\mathrm{bs}}(r,t)=-[E_{\mathrm{dr}}(r)-E_{\mathrm{bscr}}(r,t)]. \tag{4}$$

We have shown previously that the backswitching effect can be used to create periodic domain structures having exceptionally short periods.[9]

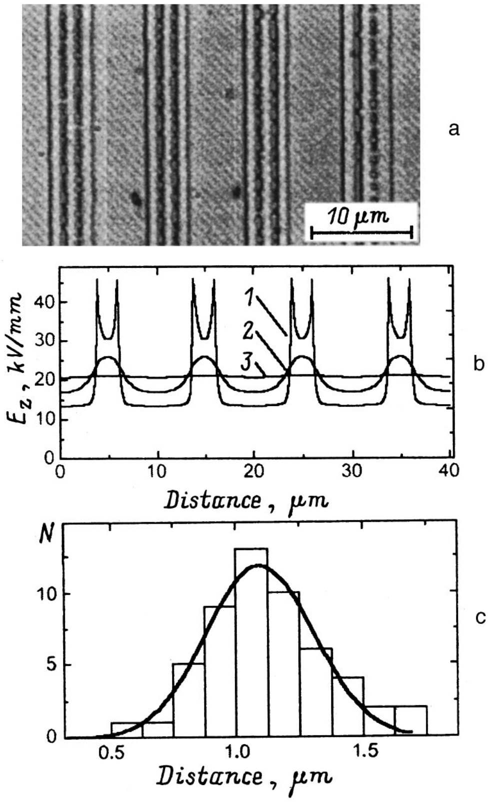

FIG. 3. a) Formation of nucleation centers near the edges of the electrodes (in backswitching); b) theoretically calculated spatial distribution of the polar field component $E_z(x)$ at various distances from the surface Δz (in fraction of the electrode period): *1*) 0.01; *2*) 0.1; *3*) 0.6; c) histogram of the distances between neighboring wedge domains and its approximation by a Gaussian curve.

4. DETAILS OF DOMAIN STRUCTURE EVOLUTION

4.1. Formation of domains on the surface

The density of nucleation centers is customarily assumed to be an important parameter, limiting the spatial frequency of periodic domain structures.[8,12] It has been established experimentally that the average density of nucleation centers in $LiNbO_3$ depends weakly on the electrode material.[12,18] Our experiments have shown that the density of newly formed, isolated wedge domains exhibits strong spatial inhomogeneity: Far from the edges of the electrodes it does not exceed $1000\,mm^{-2}$ (Ref. 8), but along the edges of the electrodes the linear density of newly formed domains attains 1100 mm^{-1} (Fig. 3a).[9]

This behavior can be attributed to the singular spatial distribution of the polar component of the local field E_z near the surface at the edges of the electrodes. It should be noted that spatial inhomogeneity of the field $E_z(x)$ exists only near the surface, and its amplitude decays rapidly with increasing depth. The field is essentially homogeneous to a depth of the order of the electrode period (Fig. 3b). Spatially inhomogeneous nucleation is attributable therefore to the inhomogeneity of the field in a thin surface layer, and the growth of the domains in the bulk takes place in a homogeneous field.

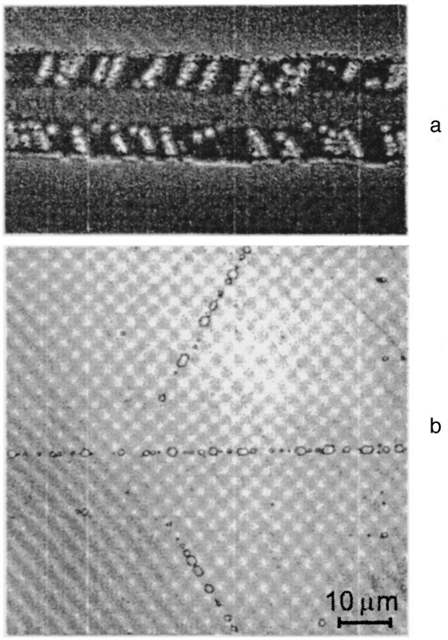

FIG. 4. a) Nanodomains formed near the edge of an electrode in backswitching; b) growth of domain chains on the $(000\overline{1})$ surface in the preferred growth directions with switching in a homogeneous field.

Our detailed investigations of the initial stage of spontaneous backswitching with SEM imaging of the domain configuration on the polar plane has revealed the existence of chains of nanodomains (Fig. 4a). These domains typically have diameters of 50–100 nm at a linear density up to $10^4\,mm^{-1}$. We assume that the usually observed wedge domains are formed as a result of the growth of these nanodomains. It is important to note that isolated needle-shaped microdomains of unknown origin with diameters less than 1 μ have been observed some time ago in $LiNbO_3$ (Ref. 19).

An analysis of the domain configurations in the first stage of backswitching shows that a correlation is observed in the spatial distribution of the wedge domains (Fig. 3c). This characteristic can be identified with a decrease in the local field near a newly formed wedge domain.[10] The modification of the spatial distribution of the electric field suppresses the growth of neighboring nucleation centers. This phenomenon imparts a quasi-regularity to the growing wedge domains, and the number of such domains is considerably smaller than the number of nanodomains.

4.2. Growth and coalescence of wedge domains under the electrodes

The newly formed wedge domains continue to grow as a result of the motion of the domain boundaries in the forward (polar) and sidewise directions. An analysis of the static domain configurations observed on tilted thin sections has shown that the rate of forward growth v_f in $LiNbO_3$ is approximately 100 times the rate of sidewise motion v_s. The velocity ratio dictates the observed vertex angles of the wedge domains, which are less than one degree.

In the case of simultaneous growth of a system of wedges, the local field $E_z(r,t)$ at the vertex of a given wedge depends on the distances to its neighbors. Consequently, if a neighbor lingers or stops altogether (as a result of being slowed down by defects), the local field near the vertex of

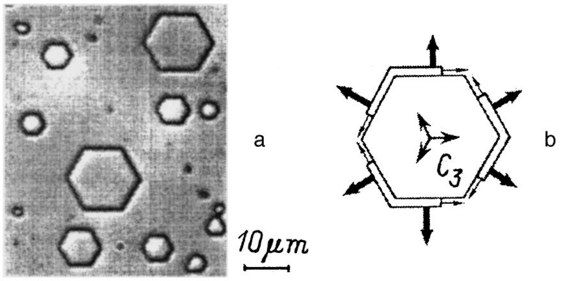

FIG. 5. Hexagonal domains in $LiNbO_3$: a) domain configuration; b) diagram of laminar domain growth. The light arrows indicate the direction of motion of the steps, and the heavy arrows indicate the direction of motion of the domain boundaries.

the moving wedge changes, causing the direction of growth to deviate. This phenomenon should create a difference between the domain configurations on different polar surfaces, as is indeed often observed in experiment.

An analysis of the domain configurations in the first stage of backswitching has shown that the growing domains in $LiNbO_3$ usually have a hexagonal shape (Fig. 5a). To explain the growth of domains having a regular geometry, we exploit the previously mentioned similarity of crystal growth and domain growth.[20,21] Domain growth (sidewise motion of the domain boundaries) is induced by the motion of individual steps along the domain boundaries (Fig. 5b). The trigonal symmetry of $LiNbO_3$ in the plane perpendicular to the polar axis causes the steps to move in the three $[10\bar{1}0]$ directions. Six planar domain boundaries are formed as a result of this growth pattern (Fig. 5b).[22] It is important to note that anisotropy is also encountered in the formation of chains of wedge domains oriented in the three $[10\bar{1}0]$ directions during switching in a homogeneous field (Fig. 4b).

The stripe electrodes are always oriented along one of the preferred growth directions (motion of the steps). Owing to this orientation, laminar growth prevails after coalescence of the chains of domains formed along the edges of the electrodes in the first switching stage, resulting in the formation of pairs of stripe domains having planar boundaries on the (0001) surface. In thick samples the coalescence of isolated domains and the formation of stripes on (0001) terminates before the vertices of the wedges grow all the way across. It has been shown experimentally that for a distance of 0.9 μm between nucleation centers the coalescence of isolated domains terminates when their vertices grow in the polar direction to depths of $50-100\,\mu$m.

The pairs of domain boundaries formed under the edges of the electrodes move opposite to one another until complete switching has taken place under the electrodes on (0001). For samples having a thickness of 0.5 mm and electrodes less than 3 μm wide this coalescence terminates before the vertices of the wedges grow clear across the sample.

Laminar through domains having a regular configuration do not form until the completion of forward growth. However, the evolution of the domain structure does not always end with this event. Pronounced unwanted broadening of the laminar domains beyond the limits of the electrodes is always observed in the final stage.

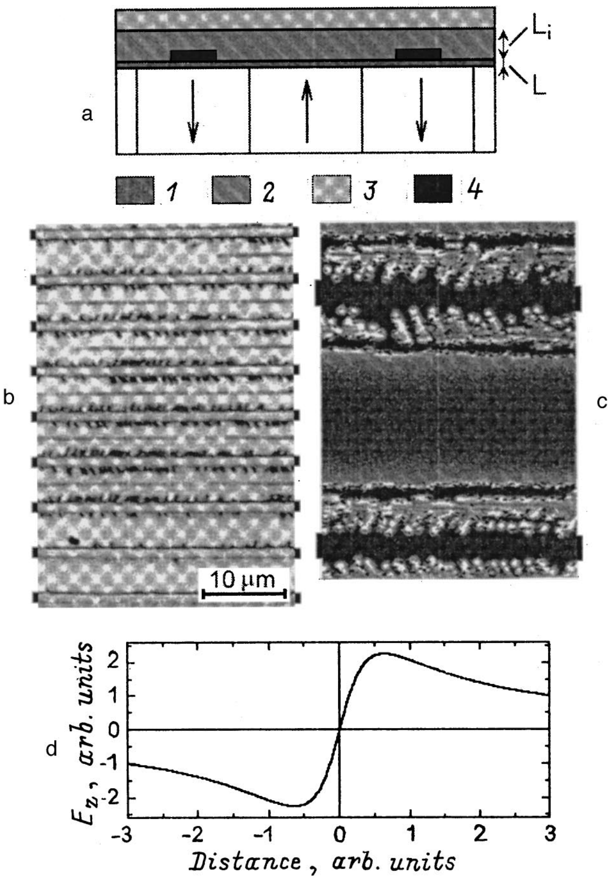

FIG. 6. a) Diagram of the surface zone of the wafer with electrodes: *1*) dielectric gap; *2*) insulator layer; *3*) liquid electrolyte; *4*) metal electrodes; b, c) domain configurations with anomalous broadening of the domains beyond the limits of the electrodes, viewed by the optical microscope (b) and SEM (c); d) theoretically calculated spatial distribution of the polar component of the local field near the surface in the vicinity of a planar domain boundary.

4.3. Motion of domain boundaries beyond the electrodes

It is obvious that, when periodic stripe electrodes are used, spatial inhomogeneity of the external field E_{ex} occurs only in a shallow surface layer having a thickness of the order of the period of the electrode structure Λ, so that the motion of the newly formed planar domain boundaries beyond the limits of the electrodes in thick samples $(\Lambda \ll d)$ takes place in an essentially homogeneous electric field.

The rate of motion of a domain boundary beyond the electrodes is determined by the polar component of the local electric field E_z (Ref. 23). The degree of compensation of the depolarizing field by external screening (redistribution of charges in the liquid electrodes) is substantially lower than under the metal electrodes (Fig. 6a). The presence of a strong residual depolarizing field and its comparatively slow bulk screening in $LiNbO_3$ at room temperature cause E_z to diminish when the boundary moves a distance Δx beyond the limits of an electrode, owing to the increase in the uncompensated fraction of the depolarizing field. The domain boundary stops when

$$E_z(\Delta x) - E_{\mathrm{th}} \approx 0, \qquad (5)$$

where E_{th} is the threshold field for sidewise movement of a planar domain boundary.

The decrease in E_z during movement of the boundary is caused by increases in $E_{\text{dr}}(\Delta x)$ and the field generated by ''attached'' charges formed during screening of the initial monodomain state, because charge redistribution can be ignored for rapid motion of the boundary. Disregarding the conductivity of the insulator layer and allowing for the fact that the thickness of the insulator layer L_i is much greater than the thickness of the dielectric gap L, for our experimental geometry (Fig. 6a) we can find the dependence on Δx of the average field in the bulk E_z if we approximate the spatial distribution of bound and screening charges by a strip of width Δx with charge density σ:

$$\begin{aligned} E_z(\Delta x) &= E_{\text{ex}} - E_{\text{dep}}(\Delta x) \\ &= U/d - \sigma(\varepsilon_i \varepsilon_0)^{-1} F(\Delta x/d), \end{aligned} \tag{6}$$

where U is the applied voltage, ε_i is the dielectric permittivity of the insulator, $F(\Delta x/d) = 1/\pi[2\arctan(\Delta x/d) + \Delta x/d \ln(1 + d^2/\Delta x^2)]$, and $\sigma = L P_S d^{-1} \varepsilon_b \varepsilon_L^{-1}(1+k)$.

The parameter k allows inclusion of the prehistories for a shift from the fully screened initial state, $k=1$, and after long residence in the biased state, $k=-1$.

The derivation of Eq. (7) and its application to analyzing experimental data of the motion of a planar domain boundary in gadolinium molybdate are described in detail in our previous work.[24]

For the given electrode geometry, Eq. (7) and condition (3) can be used to account for the movement of the domain boundaries to a certain distance beyond the limits of the electrodes and to determine the field dependence of the maximum displacement $\Delta x_{\max}(E_{\text{ex}} - E_{\text{th}})$. It should be noted that the finite conductivity of the imperfect insulator layer leads to a major increase in the displacement of the boundaries. The observed displacement of the domain boundary must depend therefore on the composition of the insulation layers and their deposition technology.

4.4. ''Anomalous motion'' of the domain boundaries

It has been observed experimentally that the displacement $\Delta x_{\max}$ in the formation of domain structures with a small period often changes from one electrode to the next, and extraordinarily large boundary displacements are observed in some regions (Figs. 6b and 6c). An attempt to ascribe this behavior to inhomogeneity of the insulating layers has been thwarted by observations showing that the motion of the domain boundary is ruled by an anomalous mechanism in this case.

To investigate the early stages of evolving of the domains in this case, we have analyzed the domain configurations obtained after very short partial backswitching. This possibility is based on the experimentally confirmed similarity of the positions of the nucleation centers in forward and reverse polings. Observations of the domain structures (etched surface relief) in the optical microscope shows that the domain kinetics in anomalous evolution consists in the formation, growth, and eventual coalescence of chains of domain ''fingers'' oriented in one of the $[10\bar{1}0]$ directions (Fig. 6b). Observations with increased spatial resolution (in the SEM) show that the optically observed domain fingers comprise strings of wedge domains approximately 10 nm in diameter (Fig. 6c; cf. Fig. 4b). The linear density of nucleation centers in the strings is greater than $10^4\,\text{mm}^{-1}$. In the formation of small-period domain structures the anomalous mechanism can lead to merging of the boundaries between the electrodes and break up the periodicity of the domain structure.

The anomalous mechanism of domain boundary motion can be analyzed by analogy with the ''correlated nucleation'' effect, which we have observed previously in lead germanate.[25,26] The effect is attributable to the long-range influence of a moving domain boundary. A calculation of $\Delta E_z(x)$ near a planar domain boundary (Fig. 6d) reveals a pronounced maximum at a distance of the order of the thickness of the surface dielectric gap.[10] In LiNbO_3 this distribution results in the formation of strings of wedge nanodomains in the surface and layer and their subsequent growth in preferred directions (Fig. 6c). The coalescence of the strings produces an inhomogeneous, anomalously large displacement of the boundaries and modifies their shape.

4.5. Evolution of domain structure in backswitching

In a departure from the conventional approach we have demonstrated the possibility of using spontaneous backswitching to create periodic domain structures. This nontraditional approach is based on notions that have been confirmed experimentally in our previous studies.[10,13,15]

The shape of the voltage pulse is changed for polarization utilizing backswitching (Fig. 1c). Under the influence of the first part of the pulse (strong field) laminar domains are formed with a width exceeding that of the electrodes. In the switched region during the stage of a weak applied field, the domain boundaries begin to move in the reverse direction (backswitching). Moreover, as in ordinary switching, wedge-shaped domains form and grow along the edges of the electrodes (Figs. 2 and 3a). The domain structure obtained through backswitching is pinned during the stage of stabilization of the polarizing voltage pulse, but in a much weaker field than in the conventional technique (Fig. 1c). Domain structures corresponding to different degrees of backswitching can be pinned by varying the duration of the weak-field stage. The monitored reverse movement of planar boundaries makes it possible to obtain domain structures clear through the sample with unprecedented short periods in thick samples by virtue of the compensation of unwanted broadening of the domains in the switching stage.

The backswitching method has enabled us to create a domain structure with a period of 2.6 μm in LiNbO_3 having a thickness of 0.5 mm (Fig. 7). It should be noted that the conventional procedure is incapable of yielding structures of this kind in such thick substrates.

4.6. Stabilization of the domain structure after switching

In conventional switching, the domain structure crated in the electric field is pinned by fairly prolonged exposure to a field somewhat below threshold (Fig. 1b). Measurements of

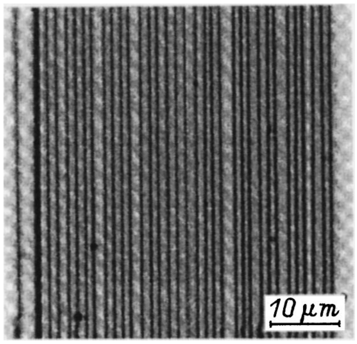

FIG. 7. Domain structure with a period of 2.6 μm obtained with backswitching in a $LiNbO_3$ wafer having a thickness of 0.5 mm; $(000\bar{1})$ surface.

the backswitching fraction (ratio of the reverse and forward poling charges, which are determined by integrating the currents) as a function of the stabilization time, $Q_{bs}(t)/Q_s$, indicate that it decreases exponentially with a time constant of 10–30 ms (Fig. 8). If backswitching is assumed to be driven by the partially screened depolarizing field, the stabilization kinetics is determined by the bulk switching time constant.[13,15,16] It is evident that a stabilization phase lasting more than 50 ms is essentially sufficient for completely blocking backswitching after the field has been turned off.[12]

4.7. Frequency multiplication

The results of our investigation of the domain kinetics associated with backswitching has enabled us to develop qualitatively new methods for the formation of regular structures with multiplication of the spatial frequency of the domain structure in contrast to the structure of the electrodes. We have achieved domain structure frequency doubling through the formation of bands of additional nonthrough domains under the electrodes on (0001) in the presence of backswitching (Fig. 9a). In the polar direction the length of the domains is usually $50-100\,\mu$m and depends on the parameters of the pulse and the width of the electrodes (Fig. 9b). Frequency tripling can be achieved by changing the switching conditions (Fig. 9c). In this case the additional stripe domains are formed under the edges of the electrodes and grow to a depth of $20-50\,\mu$m (Fig. 9d).

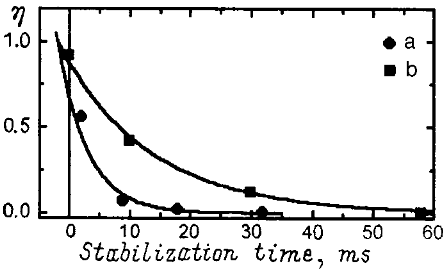

FIG. 8. Time dependence of the backswitching fraction with stabilization in various fields. The experimental points are approximated by exponential functions. a) $E_z = 24$ kV/mm, $\tau = 11$ ms; b) $E_z = 20.6$ kV/mm, $\tau = 34$ ms.

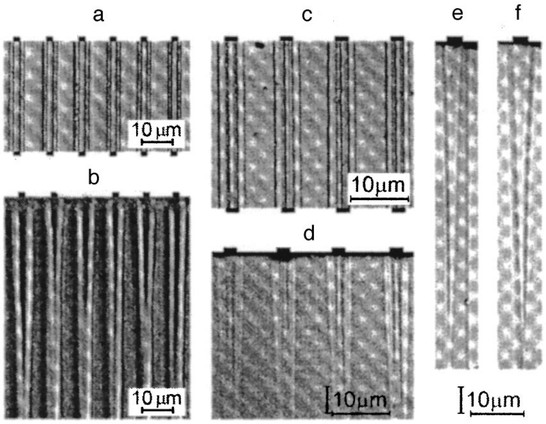

FIG. 9. Spatial-frequency multiplication of the domain structure in the presence of backswitching. Frequency doubling: a) (0001 surface; b) transverse cross section. Frequency tripling: c) (0001) surface; d) transverse cross section. e) Erasure; f) splitting (transverse cross sections).

A detailed analysis of the domain configurations in the transverse cross section indicates two possible scenarios of domain evolution with backswitching: ''erasure'' and ''splitting.'' The erasure process entails the formation of domains inside a previously switched domain without altering its outward shape (Fig. 9e). In the splitting process a domain growing in the presence of backswitching cleaves a switched domain, significantly altering its shape while approximately preserving its volume (Fig. 9f).

In summary, the reported comprehensive investigations have yielded new information about the domain structure kinetics in $LiNbO_3$ with rapid polarization switching (with a substantial delay of bulk screening) in a spatially inhomogeneous electric field. We have uncovered the phenomenon of anomalous domain broadening beyond the limits of the electrodes. We have reported the first investigation and qualitative explanation of the specific characteristics of domain structure evolution in the presence of spontaneous backswitching after removal of the external field. The level of insight achieved here has enabled us to exploit this traditionally ''undesirable'' effect as the basis of new methods for the formation of regular domain structures.

The authors are grateful to L. Eyres for performing the SEM domain structure analysis and to S. Makarov, E. Nikolaev, E. Shishkin, and D. Fursov for technical assistance.

This work has received partial support from the Russian Fund for Fundamental Research (RFFI Grant No. 96-02-19588), the Defense Advanced Research Projects Agency and Office of Naval Research (DARPA/ONR Grant N 00014-J-1903), Lawrence Livermore National Laboratory (LLNL), and the US Air Force Research Laboratory/European Office of Aerospace Research and Development under AFRL/EOARD Contract No. F61775-98-WE060.

*⁾E-mail: Vladimir.Shur@usu.ru

---

[1] R. L. Byer, J. Nonlinear Opt. Phys. Mater. **6**, 549 (1997).
[2] M. Yamada, N. Nada, M. Saitoh, and K. Watanabe, Appl. Phys. Lett. **62**, 435 (1993).
[3] K. Mizuushi and K. Yamamoto, Opt. Lett. **21**, 107 (1996).
[4] J.-P. Meyn and M. M. Fejer, Opt. Lett. **22**, 1214 (1997).
[5] W. P. Risk and S. D. Lau, Appl. Phys. Lett. **69**, 3999 (1996).

[6] Yu. S. Kuz'minov, *The Electrooptical and Nonlinear Optical Lithium Niobate Crystal* (Nauka, Moscow, 1987).

[7] L. E. Myers, R. C. Eckardt, M. M. Fejer, R. L. Byer, and W. R. Bosenberg, Opt. Lett. **21**, 591 (1996).

[8] G. D. Miller, R. G. Batchko, M. M. Fejer and R. L. Byer, in *SPIE Proceedings*, Vol. 2700: *Solid State Lasers and Nonlinear Crystals* (SPIE, Bellingham, Wash., 1996), p. 34.

[9] V. Ya. Shur, E. L. Rumyantsev, R. G. Batchko, G. D. Miller, M. M. Fejer, and R. L. Byer, Ferroelectrics (in press).

[10] V. Ya. Shur, in *Ferroelectric Thin Films: Synthesis and Basic Properties* (Gordon & Breach, New York, 1996), Chap. 6, p. 153.

[11] V. Ya. Shur and E. L. Rumyantsev, J. Korean Phys. Soc. **32**, S727 (1998).

[12] L. E. Myers, *Quasi-Phasematched Optical Parametric Oscillators in Bulk Periodically Poled Lithium Niobate*, Ph.D. Thesis (Stanford University, 1995).

[13] V. Ya. Shur, V. V. Leguchev, and I. V. Ovechkina, Fiz. Tverd. Tela (Leningrad) **26**, 3474 (1984) [Sov. Phys. Solid State **26**, 2091 (1984)].

[14] V. Ya. Shur, V. V. Leguchev, and N. V. Korovina, Fiz. Tverd. Tela (Leningrad) **26**, 781 (1984) [Sov. Phys. Solid State **26**, 471 (1984)].

[15] V. Ya. Shur and E. L. Rumyantsev, Ferroelectrics **191**, 319 (1997).

[16] P. V. Lambeck and G. H. Jonker, Ferroelectrics **22**, 729 (1978).

[17] V. M. Fridkin, *Ferroelectric Semiconductors* (Nauka, Moscow, 1976).

[18] G. D. Miller, Ph.D. Thesis (Stanford University, 1998).

[19] N. Ohnishi and T. Iisuka, J. Appl. Phys. **46**, 1063 (1975).

[20] V. Ya. Shur and E. L. Rumyantsev, Ferroelectrics **142**, 1 (1993).

[21] W. K. Burton, N. Cabrera, and F. C. Frank, Philos. Trans. R. Soc. London **243**, 299 (1951).

[22] V. Ya. Shur, A. L. Gruverman, V. V. Letuchev, E. L. Rumyantsev, and A. L. Subbotin, Ferroelectrics **98**, 29 (1989).

[23] V. Ya. Shur, A. L. Gruverman, V. P. Kuminov, and N. A. Tonkachyova, Ferroelectrics **111**, 197 (1990).

[24] V. Ya. Shur, E. L. Rumyantsev, V. P. Kuminov, A. L. Subbotin, and E. V. Nikolaeva, Fiz. Tverd. Tela (St. Petersburg) **41**, 126 (1999) [Phys. Solid State **41**, 112 (1999)].

[25] V. Ya. Shur, A. L. Gruverman, N. Yu. Ponomarev, E. L. Rumyantsev, and N. A. Tonkacheva, JETP Lett. **53**, 615 (1991).

[26] V. Ya. Shur, A. L. Gruverman, N. Yu. Ponomarev, and N. A. Tonkachyova, Ferroelectrics **126**, 371 (1992).

Translated by James S. Wood

PHYSICS OF THE SOLID STATE VOLUME 41, NUMBER 10 OCTOBER 1999

Impurity centers in a barium titanate ceramic doped with rare-earth ions

S. M. Kornienko, I. P. Bykov, M. D. Glinchuk,*) and V. V. Laguta

Institute of Materials Science, Ukrainian Academy of Sciences, 252180 Kiev, Ukraine

A. G. Belous

Institute of General and Inorganic Chemistry, Ukrainian Academy of Sciences, 252680 Kiev, Ukraine

L. Yastrabik

Institute of Physics, Czechoslovakian Academy of Sciences, Prague, Czechoslovakia

(Submitted February 3, 1999; resubmitted April 1, 1999)
Fiz. Tverd. Tela (St. Petersburg) **41**, 1838–1842 (October 1999)

The ceramic $BaTiO_3$ doped with rare-earth ions Y, La, Nd, Sm, Lu, and Dy to 0.1–0.5 at. % was studied in the temperature range $160<T<480$ K by ESR. Several ESR spectra were observed. The most intense spectra have g factors close to 5.5 and 1.96. The dependences of their intensity, g factor, and width on the concentration of rare-earth ions and temperature were studied. Analysis of the data obtained made it possible to determine the critical concentration of the rare-earth ions $x_c=0.2-0.3$ at. %. It is characterized by the fact that for $x<x_c$ or $x>x_c$ all rare-earth ions, except Lu, replace predominantly Ba^{4+} or Ti^{4+}, respectively. Models of paramagnetic centers were established: $Fe^{3+}-V_O$ ($g\approx5.5$) and $Ti^{3+}-Ln^{3+}$ ($g\approx1.96$), where V_O is an oxygen vacancy and Ln is a rare-earth ion. An abrupt change in axial symmetry to cubic for a $Fe^{3+}-V_O$ center at a phase transition from the tetragonal into the cubic phase was observed for the first time. The role of new centers in the appearance of the posistor effect is discussed. © *1999 American Institute of Physics.* [S1063-7834(99)02510-1]

The investigation of impurity centers in single and polycrystals of $BaTiO_3$ has been attracting persistent attention from investigators for many years.[1,2] This is because the impurities and structural defects strongly influence the properties of this material, leading to the appearance of semiconductor properties in $BaTiO_3$. The most striking effect is the anomalous increase in the resistance above the Curie temperature T_c in ceramic samples of barium titanate with impurities. This latter phenomenon is widely used in thermistors with a positive coefficient of resistance (posistors) to limit uncontrollable current growth.

A posistor effect is usually observed only in $BaTiO_3$ ceramic samples doped with donor impurities (for example, rare-earth ions, niobium ions, and others). It has also been established that adding fractions of a percent of acceptor impurities (for example, Mn ions) greatly increases the jump in resistance near T_c.[2] We note that transition element impurity ions, such as Mn, Fe, and Cr, are ordinarily also present in undoped $BaTiO_3$ samples,[3] so that the posistor effect is also observed in samples doped with donor impurities.

In summary, donor and acceptor centers are needed in order for ceramics to exhibit posistor properties. The need to compensate the excess charges of the impurities can change their charge state, which is accompanied by an increase in the grain size and transfer impurities from the inter- into the intragrain space,[4] and it also can lead to the appearance of lattice defects of the type Ti^{3+}, as has been shown for the doped ceramic lead zirconate-titanate.[5] On the other hand, the magnitude and sign of the excess charge of the impurities depends strongly on the type of lattice site which they occupy. In this connection, it can be expected that the location of the impurity atoms in the lattice and the number of intrinsic structural defects will depend on the concentration of the impurities introduced. Since all factors listed above should strongly influence the electrophysical properties of the material, it is necessary to study the type, charge state, and location of impurities and the intrinsic lattice defects in order to establish the nature of the observed phenomenon.

In the present work, impurity centers in the ceramic Ba TiO_3 doped only with rare-earth ions are investigated by ESR. It is shown that the observed ESR spectra are due to the Fe^{3+}, Mn^{2+}, and Ti^{3+} ions, and the most intense spectra are due to centers identified as $Fe^{3+}-V_O$ and $Ti^{3+}-Ln^{3+}$ (Ln — rare-earth ion, V_O — oxygen vacancy).

1. SAMPLES AND EXPERIMENTAL DETAILS

A series of ceramic samples $Ba_{1-x}Ln_xTiO_3$, where Ln is a rare-earth element Y, La, Nd, Sm, Lu, and Dy, was investigated. The concentrations of the rare-earth elements were 0.1, 0.2, 0.3, 0.4, and 0.5 at. %. The initial reagents were ultrapure $BaCO_3$, TiO_2, Y_2O_3, Nd_2O_3, Sm_2O_3, Dy_2O_3, and Lu_2O_3. The phase transformations were studied by thermogravimetry using a Q-1000 OD-102 apparatus. The heating rate was 10 K/min. The products obtained were identified by x-ray diffraction from the powder diffraction patterns obtained on a DRON-3M diffractometer (Cu $K\alpha$ radiation). Samples synthesized at temperatures 1340–1360 °C in air were used for the investigations.

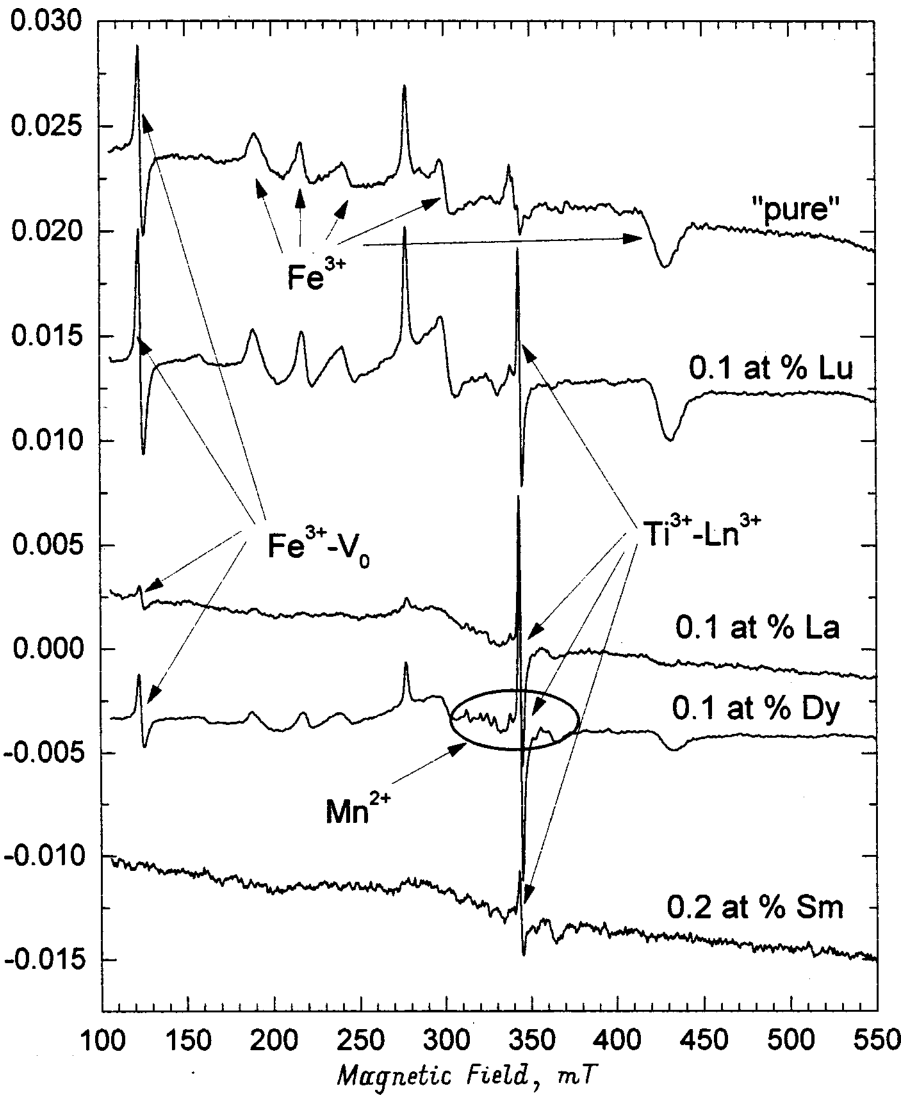

FIG. 1. ESR spectra of pure $BaTiO_3$ and $Ba_{1-x}Ln_xTiO_3$ at $T=300$ K, $f=9455.73$ MHz.

The ESR spectra were recorded in the *X* microwave band. The measurements were performed in the temperature range 160–480 K.

2. RESULTS

Figure 1 shows the ESR spectra of a series of samples at $T=300$ K. Together with the lines of the well-studied centers Fe^{3+} and Mn^{2+},[6–9] we observed intense lines with g factors close to 5.5 and 1.96.

2.1. ESR line near $g\approx 5.5$

In pure $BaTiO_3$, not doped with rare-earth ions, the line with $g=5.549$ (Fig. 1) most likely belongs to the tetragonal center $Fe^{3+}-V_O$. The spectrum of such a center is ordinarily described by an effective spin Hamiltonian $H_{\mathrm{eff}}=g_{\mathrm{eff}}\beta H S_{\mathrm{eff}}$ with effective spin $S_{\mathrm{eff}}=1/2$, since because of the large tetragonal splitting of the spin levels only one line, at $H\approx 100$ mT, is seen in the *X* range. This phenomenon is observed for all centers containing an oxygen vacancy, and it has been studied very well in $SrTiO_3$ for $Fe^{3+}-V_O$ and $Mn^{2+}-V_O$.[10] The $Fe^{3+}-V_O$ center has been previously investigated in single-crystal $BaTiO_3$,[11] but the spectrum of this center has been seen only in the orthorhombohedral phase at $T=20$ K and in iron-doped samples. In the tetragonal phase this line ($g=5.542$) has been observed in ceramic samples doped with neodymium and iron, while $Fe^{3+}-V_O$ spectrum was absent in samples additionally doped with tin the (see Refs. 12 and 13). In the present work, the spectrum of this center was observed in the tetragonal phase of ceramic samples which were not doped with iron. The behavior of the ESR line of this center as a function of temperature was investigated. The ESR line of the center $Fe^{3+}-V_O$ appeared in the tetragonal phase, and the line started to broaden at $T\approx 350$ K (Fig. 2). This broadening follows the Arrhenius law

$$\Delta B\sim 1/\tau=1/\tau_0\exp(-E_a/kT). \tag{1}$$

The parameters of the reorientational motion of an oxygen vacancy were determined from the slope of the dependence $\ln(\Delta B)=f(1/T)$: $E_a=0.5$ eV, $1/\tau_0=2.54\times 10^{13}$ Hz (inset in Fig. 2).

At a transition to the cubic phase, the line corresponding to the axial center $Fe^{3+}-V_O$ disappeared, but the ESR line of the cubic center Fe^{3+} without an oxygen vacancy appeared.

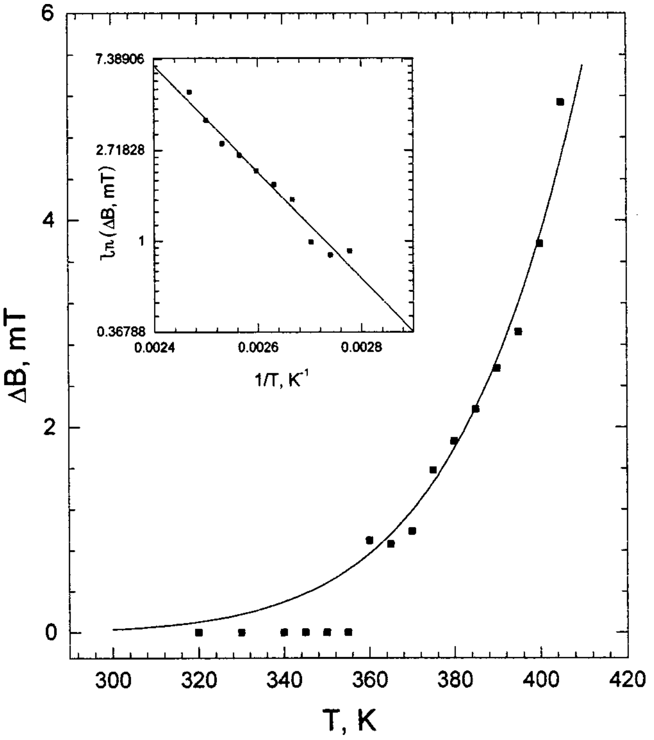

FIG. 2. Broadening ΔB of the Fe^{3+}–V_O line versus temperature. Inset: $\ln(\Delta B)$ versus $1/T$. Dots — experiment, solid line — fit of the expression (1).

This is the first observation of a jump-like change in the symmetry of such centers at a phase transition.

Aside from the temperature dependence of the linewidth, the g factor of the ESR line of the paramagnetic center Fe^{3+}–V_O depends on the type of and concentration of the impurity (Table I). The dependence of the intensity of the ESR line of the paramagnetic center Fe^{3+}–V_O on the impurity concentration is presented in Fig. 3a. It is evident in a series of samples that this line disappears as the concentration increases approximately up to 0.2 at. %, and it reappears at a higher impurity concentration. The vanishing of the spectrum is shown by an arrow in Table I.

2.2. ESR line near $g \approx 1.963$

We attribute the ESR line with $g \approx 1.963$ at a low concentration of rare-earth impurities in $BaTiO_3$ (Fig. 1) to a Ti^{3+}–Ln^{3+} center (the rare-earth ion replaces Ba^{2+}), since this line is virtually absent in pure $BaTiO_3$. For doping with rare-earth elements, the intensity of this line increases, and the g factor is close to that of centers containing Ti^{3+}, but it differs from all previously known values.[14] As the impurity concentration increases to 0.2 at. %, the g factor changes negligibly, remaining constant with a further increase of the

TABLE I. The value of the g factor of a Fe^{3+}–V_O center in $BaTiO_3$ samples with various impurities at $T = 300$ K. For pure $BaTiO_3$ $g = 5.549$.

	x, at. %				
Ln	0.1	0.2	0.3	0.4	0.5
Y	5.578	5.573	5.568	↓	↓
Lu	5.588	5.533	5.542	–	5.518
Sm	5.551	↓	–	5.493	5.479
Dy	5.584	↓	↓	5.512	5.525
Nd	5.55	↓	↓	5.424	5.437
La	5.532	–	5.481	5.516	5.423

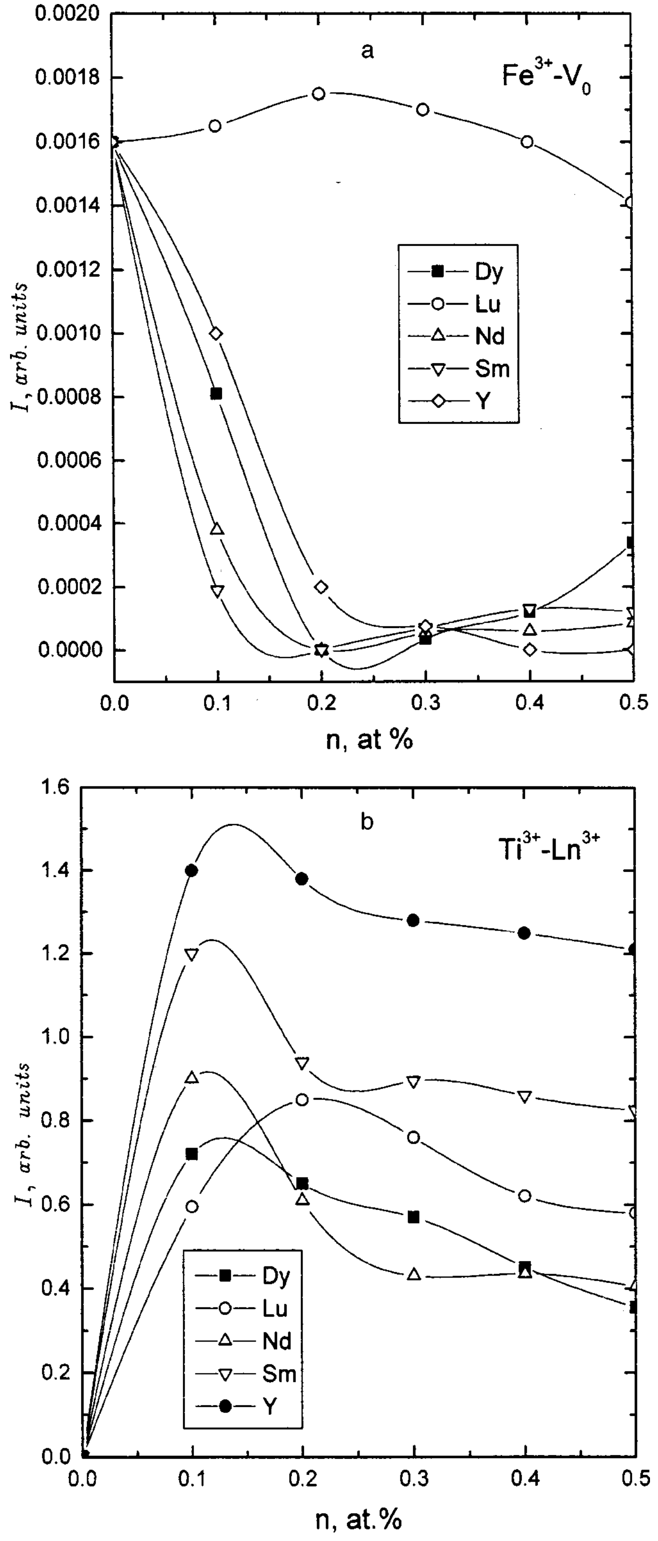

FIG. 3. ESR line intensities for Fe^{3+}–V_O (a) and $Ti^{3+}Ln^{3+}$ (b) as a function of the concentration of impurity rare-earth ions.

TABLE II. The value of the g factor for a Ti^{3+}–Ln^{3+} center in $BaTiO_3$ samples with various impurities at $T=300$ K.

	x, at. %				
Ln	0.1	0.2	0.3	0.4	0.5
Y	1.962	1.97	1.972	1.971	1.972
Lu	1.969	1.97	1.971	–	1.971
Sm	1.965	1.971	–	1.971	1.971
Dy	1.964	1.972	1.973	1.965	1.971
Nd	1.97	1.971	1.971	1.971	1.975
La	1.963	–	1.972	1.965	1.971

concentration. Table II gives the g factors of the ESR lines of the paramagnetic center Ti^{3+}–Ln^{3+} for different impurity concentrations.

3. DISCUSSION

3.1. Impurity center Fe^{3+}–V_O

The temperature dependences of the linewidth of the ESR spectrum of a center Fe^{3+}–V_O in $BaTiO_3$, which we investigated, are unusual. As has already been mentioned, in the tetragonal phase, at $T\approx 350$ K the ERS line starts to broaden, and the broadening follows the Arrhenius law (1). The parameters E_a and $1/\tau_0$ obtained are typical for activating above-barrier hops of an impurity between certain equivalent or nearly equivalent positions. Evidently, the vacancy V_O moves in the center Fe^{3+}–V_O, where the attractive Coulomb field keeps it close to the iron ion. The oxygen vacancy stays near Fe^{3+} at least up to temperature $T\approx 400$ K, i.e., up to $T\approx T_c$, since the center remains tetragonal up to these temperatures. An unusual behavior of this center is the abrupt increase of its symmetry to cubic immediately above the phase transition temperature. It is obvious that in the polar tetragonal phase the dipole moment associated with the pair defect Fe^{3+}–V_O was oriented predominantly along the direction of electric polarization. As recent theoretical calculations for $PbTiO_3$ have shown,[15] the decrease in the energy of V_O along the direction of polarizaiton can be 0.3 eV compared with the decrease in the energy in a direction perpendicular to the polarization. An increase in temperature speeds up above-barrier reorientations of the dipole Fe^{3+}–V_O, shortening the lifetime of a paramagnetic center with this distinguished orientation in accordance with the expression (1). As follows from the theory of ''motional'' averaging of ESR spectra, which describes the change in the spectrum as a result of the motion of the paramagnetic center, averaging of the tetragonal field produced by V_O, accompanying the initial ''motional'' broadening, and then narrowing of the line can be expected if $\Delta\omega\tau<1$ (narrowing) and $\Delta\omega\tau>1$ (broadening), where $1/\tau$ is the frequency of reorientations of the paramagnetic center and $\Delta\omega=(B_\parallel-B_\perp)g\beta/h$ is the total tetragonality-determined range of the spectrum. Estimates of the narrowing criterion show that it can hold for $T>500$ K, so that the vanishing of the axial spectrum and the appearance of a spectrum with cubic symmetry could be expected only when $T>500$ K, which is much higher than T_c. This explains the ESR line broadening observed up to $T=T_c$. It can be inferred that the vanishing of the electric polarization and the high permittivity in $BaTiO_3$ at temperatures $T\geqslant T_c$ catastrophically affected the energy position of the vacancy near Fe^{3+}. Specifically, it can be expected that, similarly to the results of Ref. 15, the energy of the vacancy in the polar phase is lower than in the paraelectric phase, so that the vacancy is less stable at temperatures $T>T_c$. For this reason, the transformation of a Fe^{3+}–V_O center into an Fe^{3+} center can be explained by activation, in the nonpolar phase, of processes leading to thermal freeing of vacancies followed by their diffusion through the crystal.

The dependence of the intensity of the ESR line of an Fe^{3+}–V_O center on the concentration of rare-earth ions (Fig. 3a) can be explained by assuming that, at low Ln^{3+} (Ln^{3+}, Nd^{3+}, Dy^{3+}) concentrations this impurity occupies sites of the type A^{2+} (Ba^{2+}) during which an excess positive charge is introduced and, in order to compensate this excess charge, the number of centers Fe^{3+}–V_O, likewise carrying in excess positive charge, starts to decrease. The most likely charge transfer process is Fe^{3+}–$V_O\rightarrow Fe^{2+}$–V_O, since the concentration of Fe^{3+} centers is not observed to increase (i.e., the number of vacancies does not decrease), and Fe^{2+}–V_O is not observed in the X band. Thus Fe^{3+}–V_O is an acceptor center (trap for electrons), which can be important for semiconductor properties of the ceramic. At a definite concentration (~ 0.2 at. %) the Fe^{3+}–V_O centers disappear — almost total charge transfer occurs. As the concentration increases further, the impurity rare-earth ions start to occupy not only sites of the type A^{2+}, but also sites of the type B^{4+}, thereby creating an excess negative charge. The impurities at the sites A and B can partially compensate themselves, which probably occurs for $x_c=0.2-0.3$ at. %. The Fe^{3+}–V_O centers once again appear at concentration $x>x_c$ to compensate the excess negative charge associated with the rare-earth ion at a type B site. The critical concentration x_c introduced here determines the limiting concentration for the solubility of ions at type A ($x<x_c$) or type B ($x>x_c$) sites. We note that predominant substitution for type-A sites at low La concentrations and type B sites at La concentrations greater than 4 at. % had been observed previously in the ceramic $PbZr_{1-x}Ti_xO_3$.[16] Aside from the changes in the intensity, the g factor of this center changes with the impurity concentration (see Table I). This seems to be due to the fact that the structure of $BaTiO_3$ becomes distorted as the concentration increases. On doping with Lu, the intensity of the ESR line of the Fe^{3+}–V_O center does not change much. This can be explained by the fact that Lu starts to occupy A and B sites simultaneously, compensating itself at all Lu concentrations considered. We note that in this series of rare-earth ions Lu has the smallest ionic radius, which, possibly, enables Lu to substitute at both sites simultaneously.

3.2. Impurity center Ti^{3+}–Ln^{3+}

The ESR line with $g=1.963$ and a low impurity content (up to 0.1 at. %) was previously observed in Ref. 17, where the ESR line with $g=1.963$ was attributed to a Ti^{4+}–V_O–Ti^{4+} center with an electron moving between Ti^{4+} and converting Ti^{4+} into Ti^{3+}. However, there are certain inconsistencies in this model. Two situations are possible in the complex Ti^{4+}–V_O–Ti^{4+} with a moving electron. Most of the time the electron is localized at the vacancy, and its wave function extends in the direction of Ti^{4+}. In this case this is a typical F center and its g factor should be about 2.0023. The electron spends a great deal of time localized on one of the Ti^{4+} ions, so that there will be a center Ti^{3+}–V_O. As already mentioned, the results of investigations of all centers containing Ti^{3+} are reported in Ref. 14. None of these centers has a g factor of 1.963. Therefore this model does not correspond to reality. The Ti^{3+}–Ln^{3+} model that we propose is more plausible. As one can see from Figs. 1 and 3b, the ESR line with $g=1.963$ is essentially absent in pure $BaTiO_3$. It is evident from Fig. 3b that as the impurity concentration increases to ~0.2 at. % (i.e., up $x \approx x_c$), the intensity of this ESR line increases. As the impurity concentration increases further, the intensity of the ESR line decreases negligibly. This can be explained by the fact that for $x > x_c$ the impurity occupies both sites A and B (as indicated above). The number of Ti^{3+}–Ln^{3+} centers decreases or does not change, since Ti^{3+} centers are not needed for charge compensation of Ln ions at type-B sites. The change in the g factor with the change in the impurity concentration of rare-earth ions can be explained by a distortion of the structure, just as in the case of a Fe^{3+}–V_O center, and for concentrations above 0.2 at. %, when the impurity occupies the sites A and B, strong distortion of the structure does not occur and the g factor does not change much (within the limits of experimental error) (see Table II).

Temperature measurements showed that this center appears in the orthorhombic phase and exists right up to the cubic phase. Its absence in the cubic phase could be due to the fact that Ti^{3+} has a short relaxation time at such temperatures and cannot be detected by ESR.

The Ti^{3+}–Ln^{3+} center, being a donor center, is important for the appearance of semiconductor properties in a ceramic, and the contribution of Ti^{3+} ions to the conductivity has been discussed in a number of works (see, for example, Ref. 14). Both centers investigated are of interest for understanding the posistor effect in $BaTiO_3$. It should be underscored that the ESR line of the Ti^{3+}–Ln^{3+} center exists for all concentrations of rare-earth impurities, even at concentrations where the line of the Fe^{3+}–V_O center is absent.

A more detailed comparative analysis of the characteristic features of the ESR spectra and conductivity, measured in a wide temperature range in $BaTiO_3$ samples with various concentrations of rare-earth ions, is now in progress and will make it possible to investigate in greater detail the mechanism leading to the posistor effect in the ceramic $BaTiO_3$.

*)E-mail: glin@ipms.kiev.ua

---

[1] H. Jkushima, J. Phys. Soc. Jpn. **21**, 1866 (1966).
[2] T. Miki and A. Fujimoto, J. Appl. Phys. **83**, 1592 (1998).
[3] S. Jida and T. Miki, J. Appl. Phys. **80**, 5234 (1996).
[4] M. D. Glinchuk, I. P. Bykov, V. M. Kurliand, M. Boudys, T. Kala, and K. Nejezchleb, Phys. Status Solidi A **22**, 341 (1990).
[5] I. B. Bykov, M. D. Glinchuk, V. G. Grachev, Yu. V. Martynov, and V. V. Skorokhod, Fiz. Tverd. Tela (Leningrad) **33**, 3459 (1991) [Sov. Phys. Solid State **33**, 1943 (1991)].
[6] T. Sakudo, J. Phys. Soc. Jpn. **18**, 1626 (1963).
[7] W. R. Eliot and J. L. Bjorkstam, J. Phys. Chem. Solids **25**, 1273 (1964).
[8] A. W. Hornig, R. C. Rempel, and H. E. Weaver, J. Phys. Chem. Solids **10**, 1 (1959).
[9] E. Possenriede, P. Jacobs, and O. F. Shirmer, J. Phys.: Condens. Matter **4**, 4719 (1992).
[10] E. Siegal and K. A. Muller, Phys. Rev. B **19**, 109 (1977).
[11] E. Possenriede, O. F. Shirmer, H. J. Donnerberg, G. Godefroy, and A. Mailard, Ferroelectrics **92**, 245 (1989).
[12] R. Vivekanadan and T. R. N. Kutty, Mater. Sci. Eng., B **6**, 221 (1990).
[13] P. Murugaraj and T. R. N. Kutty, J. Mater. Sci. Lett. **5**, 171 (1986).
[14] B. Scharfschwerdt, A. Mazur, O. F. Shirmer, H. Hesse, and S. Mandricks, Phys. Rev. B **54**, 15284 (1996).
[15] C. H. Park and D. J. Chadi, Phys. Rev. B **57**, R13961 (1998).
[16] A. E. Krumin', *Phase Transitions and Their Characteristic Features in Ferroelectrics* (Riga, 1984), pp. 3–63.
[17] T. R. N. Kutty, P. Murugaraj, and N. S. Gajbhaye, Mater. Lett. **2**, 396 (1984).

Translated by M. E. Alferieff

PHYSICS OF THE SOLID STATE VOLUME 41, NUMBER 10 OCTOBER 1999

LATTICE DYNAMICS. PHASE TRANSITIONS

Dynamical parameters and phonon spectrum of crystal In_4Te_3

D. M. Bercha

Uzhgorod State University, UA-294000 Uzhgorod, Ukraine; Pedagogical University, Institute of Physics, Zheshuv, Poland

K. Z. Rushchanskiĭ

Uzhgorod State University, UA-294000 Uzhgorod, Ukraine

(Submitted November 16, 1998; resubmitted February 2, 1999)
Fiz. Tverd. Tela (St. Petersburg) **41**, 1843–1847 (October 1999)

Calculations of the phonon spectrum of an In_4Te_3 crystal in the central pair-interaction model neglecting long-range forces are reported. The model developed contains 19 unknown parameters, which were determined from experimental values of the displacements of individual sublattices in the unit cell and from the change in the basis vectors as a result of hydrostatic pressure. The phonon spectrum obtained contains a large number of low-frequency optical branches, deforming the acoustic branches. © *1999 American Institute of Physics.* [S1063-7834(99)02610-6]

Investigations of the properties of heterojunctions formed by indium and gallium selenides for the purpose of producing new radiation detectors and phototransducers have been attacting special attention in the last few years.[1–6] On the other hand, crystals of the systems In–Se and In–Te[7–9] are attractive for investigating the formation of natural superstructures,[9–13] one-dimensional disorder,[14] and radiation resistance.[15] It is obvious that the paramount problem is the study of the lattice dynamics of these structures. In Ref. 16 we calculated the phonon spectrum of an In_4Te_3 crystal in the central pair-interaction model (CPIM) using limited experimental information about the elastic and thermal properties of this crystal.

In the present paper we shall show that information about the lattice parameters and the positions of the atoms in the absence and presence of hydrostatic pressure makes it possible to calculate the force constants and to obtain the phonon spectrum of an In_4Te_3 crystal, even if there are no data on the thermal and elastic properties of this crystal, as well as experimental data on the values of the vibrational frequencies.

The structure of the In_4Te_3 crystal is isomorphic to the structure of In_4Se_3 and is described in Refs. 7–9. In our calculations we used the lattice constants and atomic coordinates, given in Ref. 7, in the absence and presence of 0.5 GPa pressure (Table I). As a result of the structural isomorphism of the crystals, the group-theoretical description of the normal vibrations in In_4Te_3 is the same as in In_4Se_3.[16]

For the calculation, it is convenient to use the microscopic theory of elasticity of solids in the approximation of a slowly varying field of displacements.[17,18]

In the theory of elasticity of complex lattices, the displacement field of individual particles in the presence of deformation can be represented as a sum of the displacements s_i of the centers of gravity of all particles and the displacements u_i^μ of individual particles relative to the center of gravity (the index i determines the component of the displacement in Cartesian coordinates, and μ is the number of the particle in a unit cell).

This representation makes it possible to exclude, in the long-wavelength approximation, the displacements of the inner sublattices by means of a system of equations that in the static case has the form[17]

$$\sum_{\nu,k} \tilde{C}_{ik}^{\mu\nu} u_k^{\nu} = \sum_{k,m} \tilde{C}_{\mathrm{kim}}^{\mu} s_{k|m}\,.^{\dagger)} \tag{1}$$

The system of equations (1) relates the internal displacements u_k^ν of the sublattices with the elastic external strains $s_{k|m}$ for fixed force constants of the interatomic interaction, which determine the coefficients $\tilde{C}$. Given information about the displacements u_k^ν with prescribed external deformations $s_{k|m}$, in our case due to hydrostatic pressure, this system can be studied relative to the unknown force constants, thereby decreasing the number of independent parameters of the model. For hydrostatic pressure, the strain tensor has the form $s_{k|m}=s_k\delta_{km}$, where δ_{km} is the Kronecker δ function, $s_k=(a'_k-a_k/a_k)$, a'_k and a_k are, respectively, the lattice parameters of the deformed and undeformed crystals, and $k,m=1,2,3$. The internal displacements in the unit cell were determined using the relation $u_k^\mu=(x'_k-x_k)a'_k$, where x_k and x'_k are, respectively, the relative coordinate of the atom μ in the absence of and presence of pressure, respectively.

The CPIM is based on the representation of the force constants in the form[19–21]

$$\Phi^{h}_{\substack{\mu\nu\\ ik}} = -\frac{R_iR_k}{R^2}(A^h_{\mu\nu}-B^h_{\mu\nu})-\delta_{ik}B^h_{\mu\nu}\,, \tag{2}$$

TABLE I. The lattice constants (a_1, a_2, a_3) (in Å) for 0.1 MPa and 0.5 GPa pressures[7] and the relative coordinates (u, v, w) of the atoms in the lattice of single crystal of In_4Te_3 samples.

Pressure	a_1	a_2	a_3
0.1 MPa	15.626 (3)	12.738 (3)	4.436 (1)
0.5 GPa	15.396 (3)	12.674 (3)	4.424 (1)
Atom	u	v	w
In1	0.71543 (4) [0.7144 (4)]	0.34555 (4) [0.3456 (5)]	0
In2	0.81716 (4) [0.8174 (4)]	0.52501 (5) [0.5242 (5)]	0
In3	0.96387 (3) [0.9650 (3)]	0.64590 (4) [0.6459 (4)]	0
In4	0.42749 (4) [0.4268 (3)]	0.39773 (6) [0.3990 (5)]	0
Te1	0.90350 (3) [0.9055 (3)]	0.86013 (4) [0.8615 (4)]	0
Te2	0.77394 (3) [0.7735 (3)]	0.13745 (4) [0.1367 (4)]	0
Te3	0.42264 (3) [0.4192 (3)]	0.14809 (4) [0.1484 (4)]	0

Note: The values of the coordinates of the atoms in the lattice under a hydrostatic pressure of 0.5 GPa are displayed in the brackets. The standard deviations are given in parentheses. The data are from Ref. 7.

TABLE II. Interatomic distances and force constants of bonds taken into account in the dynamical matrix for calculations of the phonon spectra of an In_4Te_3 crystal.

l	Bond		R, Å	A_l, N/m	B_b, N/m
1	In1–Te2	In–Te	2.80402	149.47	0.00732
2	In3–Te3		2.83994	6861.0	0.04529
3	In3–Te1		2.88731	134.69	−0.19244
4	In1–Te1		2.89960	59.03	−0.12477
5	In2–Te2		2.99955	29.84	0.16289
6	In4–Te3		3.18082	81.48	−0.88233
7	In4–Te2		3.29808	11.02	−0.47175
8	In4–Te1		3.48189	8.54	−0.08629
9	In2–Te3		3.53525	6.38	0.11112
10	In4–Te1′		3.81752	6.96	−0.16435
11	In1–Te3		3.92554	2.48	−0.08113
12	In2–In3	In–In	2.76167	46.63	0.06645
13	In1–In2		2.78434	31.25	0.03453
14	In4–In4		3.45303	−2.10	−0.88177
15	In3–In3		3.88467	9.90	−0.16813
16	Te1–Te2	Te–Te	4.07151	4.71	0.53957
17	Te2–Te3		4.21678	2.75	0.35332
18	Te1–Te3		4.42667	0.7982	0.25566

Note: l is the bond index, R, the interatomic distance

where

$$\mathbf{R} \equiv \mathbf{R}^h_{\mu\nu} = \overset{\smile}{\mathbf{Ah}} + \mathbf{R}_\mu - \mathbf{R}_\nu \tag{3}$$

is the distance between the atoms μ and ν in the cell h; $\mathbf{R}_\mu$ is the radius vector of particle μ in the unit cell, and the vector $\overset{\smile}{\mathbf{Ah}}$ determines the position of the cell h in the chosen coordinate system. $A^h_{\mu\nu}$ and $B^h_{\mu\nu}$ are, respectively, the tangential and radial force constants. The parameters $B^h_{\mu\nu}$ must satisfy the following conditions of equilibrium: $\sum_{h,\mu} B^h_{\mu\nu} R^h_{\mu\nu_i} = 0$ and $\sum_{h,\mu\nu} B^h_{\mu\nu} R^h_{\mu\nu_i} R^h_{\mu\nu_j} = 0$, where $R^h_{\mu\nu_i}$ is the i-th projection of the vector (3), while the index ν in the first equation enumerates the atom which is assumed to be in the position of equilibrium. The second equation expresses the absence of initial stresses in the lattice.

Since the interatomic bonds are identical because of the symmetry of the problem, the indices (h, μ, ν) can be replaced by a single index l identifying the bond. Considering the structure of the crystal, to exclude the trivial case $B_l = 0$ the number of interatomic bonds must be greater than 17. In our case, 18 bonds are used (see Table II); this leads to a single free parameter, for example, B_{14}. In order to choose the required number of bonds we limited the bond lengths, taking account of the In–Te and In–In interactions, which occur at interatomic distances less than 4.0 and 3.9 Å , respectively. The Te–Te distances are limited by the lattice constant a_3, i.e. our analysis neglects the interaction between the symmetry-equivalent atoms belonging to neighboring cells.

Thus, to calculate the phonon spectrum it is necessary to know the force constants (2), which are determined by 18 unknown parameters A_l and one parameter B_{14}.

On account of the uncertainty in the variation of its length, the In3–Te3 bond was modeled as a rigid bond, i.e. in our calculations the relative value 0.4193324 is used for the x coordinate of the Te3 atoms under a pressure of 0.5 GPa.

Since each atom lying along the direction $\mathbf{a}_3$ is a center of inversion, for 19 unknown parameters of the model we have 14 equations of the type (1).

X-ray structural investigations of the changes in the lattice parameters under hydrostatic compression yield three additional conditions $\Sigma_k C_{iikk} s_{k|k} = -p$, $i = 1,2,3$; $p = 0.5$ GPa.

Since there are no other additional dynamical parameters for an In_4Te_3 crystal, we employed the condition of lattice stability to determine the two remaining parameters (A_{17} and A_{18}). Our investigations showed that, for the principal directions in the Brillouin zone, negative frequencies were absent for the following ratios of the parameters: $A_{16}/A_{17} = 1.7 \pm 0.01$ and $A_{16}/A_{18} = 5.9 \pm 0.1$, i.e. in very narrow ranges of these parameters.

The final computed values of the model parameters are presented in Table III. Figures 1 and 2 show the phonon spectra of an In_4Te_3 crystal calculated on the basis of the model described above.

First, we shall make some remarks concerning the results presented here. The results were obtained assuming that Hooke's law holds for deformations corresponding to a pressure of 0.5 GPa and that the central pair-interaction approximation is satisfied. Comparing the computed values of the elastic constants, presented in Table III, and the corresponding values for In_4Se_3[22] and the characteristic ratios of the components of the tensor of elastic constants for layered crystals[23] show that the values obtained seem to be realistic.

The larger mass of the tellurium atoms, as compared with selenium atoms, has the effect that the range of limiting

TABLE III. Computed values (in GPa) of the elastic moduli of an In_4Te_3 crystal and the corresponding experimental values for In_4Se_3.[22]

	C_{11}	C_{22}	C_{33}	C_{44}	C_{55}	C_{66}	C_{12}	C_{13}	C_{23}
In_4Te_3 (calc)	22.53	23.98	21.36	2.34	2.31	2.01	21.57	22.21	22.94
In_4Te_3 (exper)	38.2	66.5	64.3	16.6	26.6	19.0	10.8	30.4	22.4

frequencies in the In_4Te_3 spectrum is narrower than the range of frequencies in the vibrational spectrum of In_4Se_3.[16]

The double degeneracy of the frequencies at the boundaries of the Brillouin zone agrees with the group-theoretical analysis, performed to describe the branches in In_4Se_3.[16] A complicated intersection pattern of individual branches of the phonon spectrum is observed in the $O-Z$ direction. In the $O-Y$ direction the picture is not as complicated, indicating a weakening of the interatomic bond for this direction. The weak interlayer bond along $O-X$ is reflected in the essentially dispersion-free optical branches of the phonon spectrum for this direction.

The most interesting result are the minima in the low-energy acoustic branch with Δ_4 symmetry along the $O-Y$ direction and the low-energy acoustic and optical branches along $O-Z$. The presence of these minima can be explained by the splitting of branches with the same symmetry as a result of interaction with the low-energy optical branches, emanating from the $1\Gamma_1$ and $1\Gamma_7$ modes. As additional investigations showed, the In4–In4 bond strongly influences the positions of these modes. In our calculations this bond is described by a negative force constant, even though the bond length decreases monotonically with increasing applied pres-

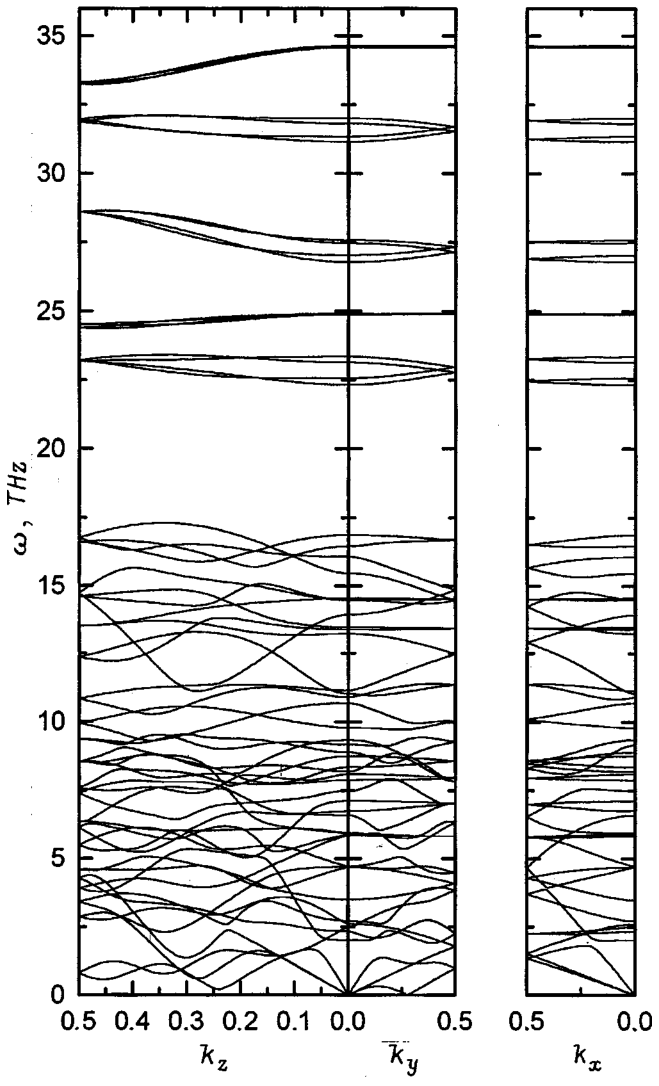

FIG. 1. General form of the phonon spectrum of an In_4Te_3 crystal along the most important directions in the Brillouin zone. The high-frequency modes corresponding to a rigid In3–Te3 bond are not shown.

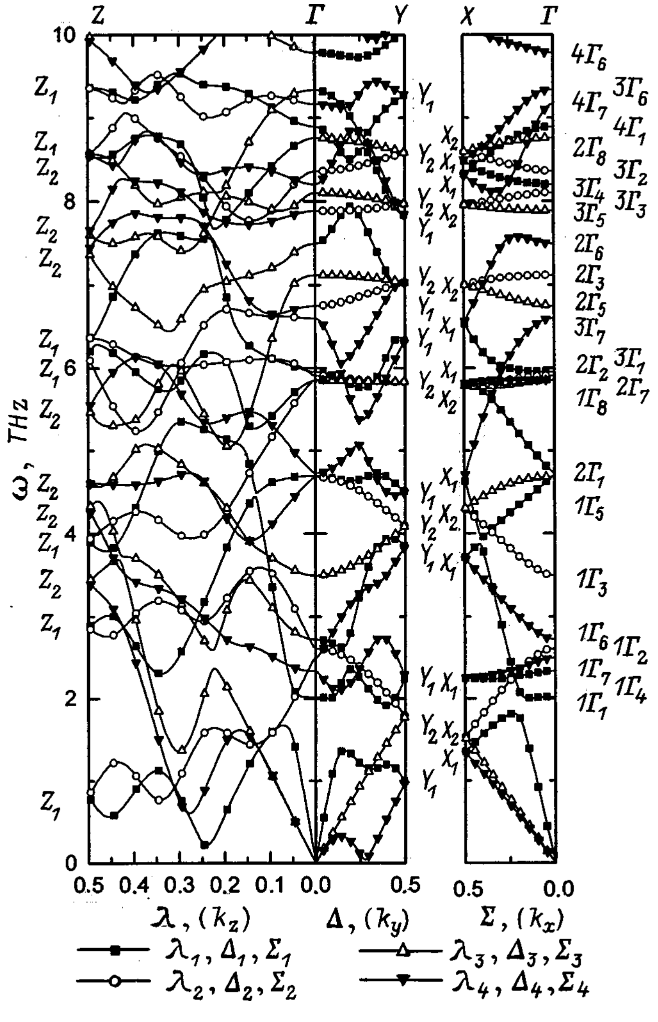

FIG. 2. Low-energy branches of the phonon spectrum of an In_4Te_3 crystal and their symmetry classification. The branches were obtained in the anisotropic force-constants model.

sure. The negligible decrease in the absolute value of the force constant A_{14} corresponding to this bond leads to substantial displacements of the positions of the $1\Gamma_1$ and $1\Gamma_7$ modes along the direction of increasing energy and to a change in the nature of the interaction with acoustic branches. The displacements of the individual sublattices calculated in this case under 0.5 GPa pressure differ strongly from the initial experimental values, both in magnitude and, in a number of cases, in sign. This observation shows that the microscopic stability of the structure is due to the nature of In4–In4 interaction, i.e. the purity of the interlayer space, which agrees indirectly with the results of Ref. 10, where the formation of the superstructure observed in the In_4Se_3 crystal is attributed to the precipitation of indium into the interlayer region. Unfortunately, such investigations have not been performed for In_4Te_3 crystals, but the fact that these two crystals have a common structure and the results obtained in the present work allow us to infer that such a superstructure can also occur in In_4Te_3 crystals.

We thank Professor H. J. Deiseroth for providing the scientific literature to us and for his interest in this work, which assisted us in choosing a method for the investigations.

1) Liebfried’s notation is used here.[17]

---

[1] S. G. Guseĭnov, G. D. Guseĭnov, G. G. Bannaeva, P. G. Ismaĭlova, G. A. Mamedova, and É. G. Abdullaev, Neorg. Mater. **29**, 781 (1993).

[2] A. A. Lebedev and V. Yu. Rud’, and Yu. V. Rud’, Fiz. Tekh. Poluprovodn. **32**, 353 (1998) [Semiconductors **32**, 320 (1998)].

[3] A. V. Simashkevich and P. A. Gashin, Neorg. Mater. **25**, 1890 (1989).

[4] V. N. Katerinchuk, M. Z. Kovalyuk, A. D. Ogorodnik, and Yu. I. Zhirko, Fiz. Tekh. Poluprovodn. **28**, 1208 (1994) [Semiconductors **28**, 689 (1994)].

[5] V. N. Katerinchuk, M. Z. Kovalyuk, A. D. Ogorodnik, and Yu. I. Zhirko, Fiz. Tekh. Poluprovodn. **28**, 2096 (1994) [Semiconductors **28**, 1153 (1994)].

[6] V. N. Katerinchuk, M. Z. Kovalyuk, A. D. Ogorodnik, and Yu. I. Zhirko, Neorg. Mater. **32**, 937 (1996).

[7] R. Walther, *Beiträge zur Strukturchemie gemischtvalenter Chalkogenide mit Elementen der 3. Hauptgruppe: Neue Verbindungen, Substitutionsversuche an bekannten Phasen, Hochdruckexperimente* (Shaker, Aachen, 1995).

[8] U. Schwarz, H. Hillebrecht, H. J. Deiseroth, and R. Walther, Z. Kristallogr. **210**, 342 (1995).

[9] L. I. Man, R. K. Karakhnyan, and P. M. Imamov, Kristallografiya **19**(6), 1166 (1974) [Sov. Phys. Crystallogr. **19**, 725 (1974)].

[10] V. M. Garamus, Ya. P. Pilat, V. P. Savchin, and A. Kh. Islamov, Fiz. Tverd. Tela (St. Petersburg) **40**, 248 (1998) [Phys. Solid State **40**, 223 (1998)].

[11] J. van Landuyt, G. van Tandeloo, and S. Amelinckx, Phys. Status Solidi A **30**, 299 (1975).

[12] E. Kress-Rogers, R. J. Nicholas, and A. Chevy, J. Phys. C **16**, 2439 (1983).

[13] G. L. Belen’kiĭ, Usp. Fiz. Nauk **156**(2), 365 (1988) [Sov. Phys. Usp. **31**, 955 (1988)].

[14] I. M. Stakhira and P. G. Ks’ondzik, Ukr. Fiz. Zh. **26**(5), 762 (1981).

[15] V. M. Koshkin and Yu. N. Dmitriev, Chem. Rev. **19**, 1 (1994).

[16] D. M. Bercha and K. Z. Rushchanskiĭ, Fiz. Tverd. Tela (St. Petersburg) **40**, 2103 (1998) [Phys. Solid State **40**, 1906 (1998)].

[17] G. Liebfried, in *Microscopic Theory of Mechanical and Thermal Properties of Crystals*, edited by B. Ya. Moĭzhes (Fizmatgiz, Moscow, 1963).

[18] Max Born and Kun Huang, *Dynamical Theory of Crystal Lattices* (Oxford Clarendon Press, Oxford, 1954; Inostr. Lit., Moscow, 1958).

[19] V. Ya. Altshul, V. K. Bashenov, D. I. Marvakov, and A. G. Petukhov, Phys. Status Solidi B **98**, 715 (1980).

[20] B. M. Powell and P. Martel, J. Phys. Chem. Solids **36**, 1287 (1975).

[21] H. G. Smiht and N. Wakabayashi, in *Dynamics of Solids and Liquids by Neutron Scattering*, edited by S. W. Lovesey and T. Springer (Springer-Verlag, New York, 1977; Mir, Moscow, 1980, p. 94).

[22] B. Ya. Kuryachiĭ, V. Yu. Bogachev, V. P. Mikhal’chenko, and I. M. Stakhira, Izv. Akad. Nauk SSSR, Neorg. Mater. **22**, 855 (1986).

[23] G. L. Belen’kiĭ, É. Yu. Slaev, and R. A. Suleĭmanov, Usp. Fiz. Nauk **155**(1), 89 (1988) [Sov. Phys. Usp. **31**, 434 (1988)].

Translated by M. E. Alferieff

PHYSICS OF THE SOLID STATE VOLUME 41, NUMBER 10 OCTOBER 1999

Spontaneous twisting of an incommensurable improper ferroelastic $Ba_2NaNb_5O_{15}$

S. A. Gridnev,*) A. V. Biryukov, and O. N. Ivanov

Voronezh State Technical University, 394026 Voronezh, Russia

(Submitted January 13, 1999)
Fiz. Tverd. Tela (St. Petersburg) **41**, 1848–1850 (October 1999)

The spontaneous twisting of a *y*-orientation single-crystal sample of barium–sodium niobate $Ba_2NaNb_5O_{15}$ at a phase transition and into an incommensurable ferroelastic phase is investigated. Anomalies are found in the temperature dependence of the torsional deformation at temperatures 453, 533, and 573 K and anomalous hysteresis of the temperature dependences of the torsional deformation, measured on heating and cooling of the sample. The results obtained are discussed on the basis of an analysis of the temperature dependence of incommensurable $1q$ and $2q$ structures and ferroelastic twins. *© 1999 American Institute of Physics.* [S1063-7834(99)02710-0]

It is well known[1–3] that the compound $Ba_2NaNb_5O_{15}$ in the solid-state temperature range undergoes several structural phase transitions. The transition occurring at the highest temperature is a ferroelectric phase transition, accompanied by a change in the point symmetry 4/mmm↔4mm and, correspondingly, the appearance of spontaneous polarization along the *c* axis.[2] The ferroelectric phase transition temperature (the Curie point) depends on the deviation from stoichiometry of the chemical composition (ratio of Ba and Na ions) of a specific sample; the Curie points most often reported in the literature are in the range 830–870 K. At ~573 K, a $Ba_2NaNb_5O_{15}$ crystal undergoes another structural phase transition 4mm↔mm2, which is an improper ferroelastic phase transition. This transition must be interpreted as a high-temperature ferroelastic phase transition, since it is assumed[4] that the ferroelastic phase is stable only in a limited temperature range 125–573 K, and below ~125 K the structure once again changes (low-temperature ferroelastic phase transition) with the 4mm point symmetry being restored. The ferroelastic properties of $Ba_2NaNb_5O_{15}$ are described by the behavior of the spontaneous shear deformation X_{12}. It should be noted that the ferroelastic phase itself is simultaneously incommensurable and, as has been reliably established recently,[5–7] at a phase transition from the normal to the incommensurate phase, the latter can be represented in a quite wide temperature range by two structural states: a $1q$ state with a single structural modulation vector and a $2q$ state with two mutually perpendicular modulation vectors. The orthorhombic $1q$ structure is ferroelastic, while the spontaneous deformation of the tetragonal $2q$ structure is zero. Under thermal cycling or prolonged annealing, restructurings of the $1q$ and $2q$ structures occur in the temperature range of the incommensurable phase. These restructurings can give rise to effects such as anomalous thermal hysteresis of various physical properties, a memory effect, and others.[8]

Since the ferroelastically active deformation is an X_{12} deformation, it is obvious that investigations of the temperature evolution of X_{12} will yield additional information about the characteristic ferroelastic behavior of $Ba_2NaNb_5O_{15}$ at the ferroelastic phase transition temperature and in the range of coexistence and restructurings of $1q$ and $2q$ structures in the incommensurable phase. Some results of such an investigation are reported in the present paper.

A Czochralski-grown $Ba_2NaNb_5O_{15}$ single crystal was used to prepare samples in the form of 2×2×18 mm bars whose long axis was oriented along the *b* axis of a tetragonal structure (*y* orientation of the sample). The experiments were performed using an apparatus based on an inverted torsional pendulum method.[9] In the course of the experiments, the bottom end of the sample was secured in a special collet chuck, and the top end was secured to a metal rod suspended on a wire. In such a system, the appearance of a torsional deformation X_y in the sample should cause the attached metal rod to rotate (for a sample with *y* orientation the change of the shear deformation X_{23} and/or X_{12} determines the behavior of the deformation X_y). The rotation angle φ of the rod was measured with special photoelectric or capacitive gauges. This made it possible to determine the torsional deformation according to

$$X=\varphi\left(\frac{4d}{3l}\right),$$

where d and l are, respectively, the transverse size and length of the sample.

Figure 1a shows the temperature dependence of the torsional deformation X_y, recorded on an $X-Y$ recorder in the temperature range 400–590 K in a regime of heating followed by cooling of the sample. It is evident that the dependence $X_y(T)$ is complicated, and possesses a number of sharp anomalies. It is observed that in the entire experimental temperature range the curves $X_y(T)$ obtained in the heating regime are not the same as those obtained in the cooling regime. Spontaneous twisting of the sample is strongest in the ferroelastic phase below 573 K, where X_{12} deformation arises spontaneously. Strictly speaking, in ferroelastics, in the absence of external mechanical stresses, the macroscopic spontaneous deformation of the entire sample should be zero because it is compensated by the formation of domains with

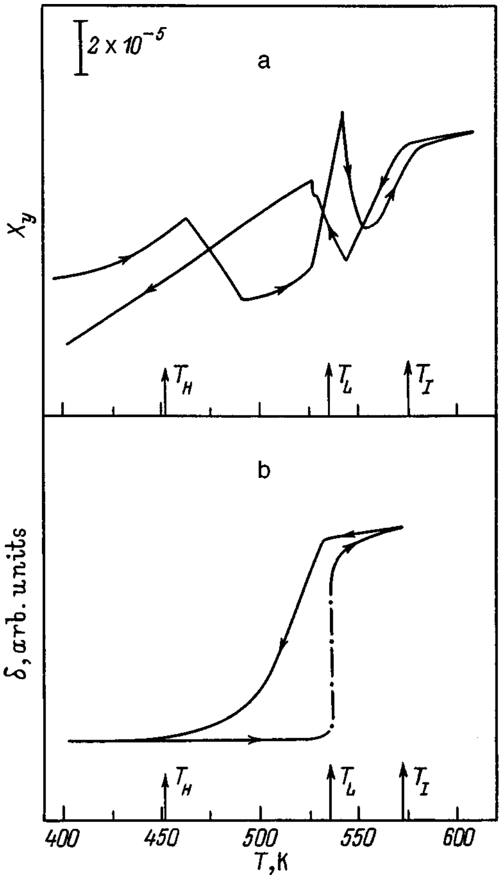

FIG. 1. Temperature dependences of the torsional deformation (a) and incommensurateness parameter[6] (b) of a $Ba_2NaNb_5O_{15}$ sample with y orientation. The arrows show the direction of variation of the temperature.

deformations of different sign. However, as a rule, macroscopic spontaneous deformation of the samples (spontaneous twisting of the samples for the case of a spontaneous shear deformation) as a result of a ferroelastic phase transition and in the absence of external mechanical stresses is observed. Such incomplete compensation of the macroscopic spontaneous deformation could be due to the presence of internal mechanical stresses arising in the sample either during growth or after mechanical working.

That the anomalies in the curves $X_y(T)$ (Fig. 1a) are related to the behavior of the spontaneous deformation X_{12} is confirmed by the fact that such anomalies do not occur in investigations of samples with z orientation (for a sample with such orientation the torsional deformation does not depend on the shear deformation X_{12}).

Let us compare the temperature dependence of X_y with the temperature evolution of the incommensurateness parameter δ, shown in Fig. 1b. The dependence $\delta(T)$ was obtained in Ref. 6 using the x-ray method. Several characteristic temperatures can be distinguished in it: the temperature of the transition from the normal into the incommensurable phase $T_I = 573$ K, at this temperature $\delta = 12\%$; the lock-in temperature $T_L = 533$ K; in the temperature range $T_L < L < T_I$ the $2q$ structure is stable, and at T_L a transition occurs between the $1q$ and $2q$ structures; the temperature $T_F = 503$ K below which only the $1q$ structure is present; the temperature of the transition into the quasicommensurable state $T_H = 453$ K, where $\delta = 1.2\%$ and does not change with further cooling.

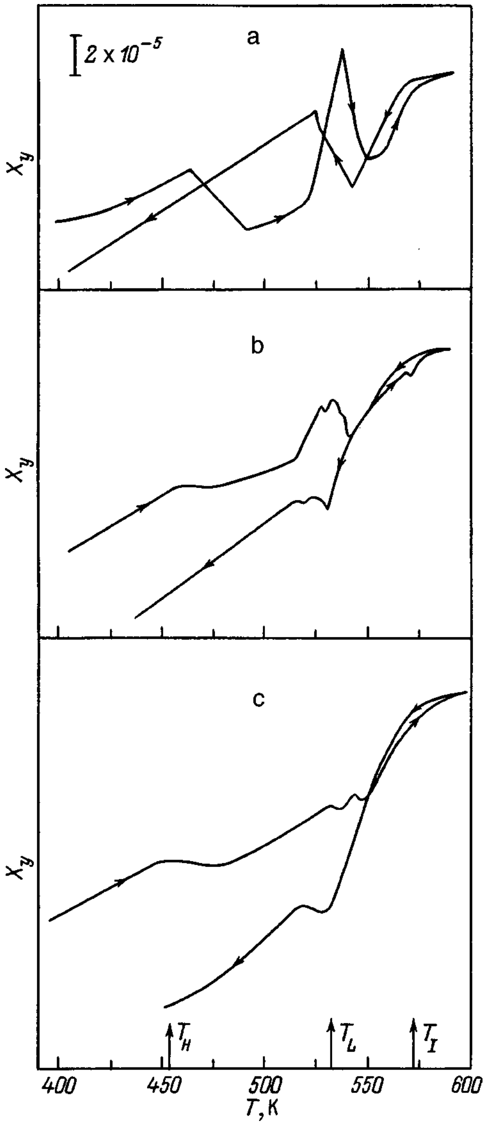

FIG. 2. Temperature dependences of X_y with different torsional mechanical stresses of different magnitudes applied to the sample: 0 (a), 1.5×10^6 (b), and 3×10^6 Pa (c).

The temperature hysteresis of $\delta(T)$ is attributed in Ref. 6 to hindered nucleation of a $1q$ structure inside a $2q$ structure during cooling of the sample.

Comparing Figs. 1a and 1b, it is easy to see that the curve $X_y(T)$ obtained during heating of the sample has anomalies near the temperatures T_H (the peak of the dependence $X_y(T)$), T_L (peak), and T_I (kink), and the analogous curve obtained in the cooling regime has anomalies near the temperatures T_L (peak) and T_I (kink). The anomalies of $X_y(T)$ at T_L are most pronounced. According to Ref. 8, the density of the walls of the ferroelastic domains, arranged along the (100) and (110) planes in the tetragonal setup, changes sharply near this temperature.

Temperature hysteresis of $\Delta(T)$ occupies a smaller temperature range than the temperature hysteresis of the curves $X_y(T)$. The hysteresis of $X_y(T)$ below $T_H = 453$ K is probably due to ferroelastic domains. It is known[10] that when a sample exists for a long time in the ferroelastic phase, the domain walls are pinned by point defects, which move from the interior volume of the domains to the boundaries of the domains. Heating above the ferroelastic phase transition temperature causes the domain walls to vanish and results in a uniform distribution of point defects throughout the volume of the sample. Under subsequent cooling from the paraelastic phase, the structure will be more labile, since a certain period of time is needed for point defects to pin the domain walls. In our case, prior to the measurements the sample was held for a long time at room temperature (ferroelastic phase) and, on heating, a ''pinned'' domain structure arose in the sample. In the subsequent cooling regime, a ''free'' domain structure formed in the sample. The difference in the degree of pinning of the domain walls can explain the presence of anomalous temperature hysteresis in $X_y(T)$ in a wide temperature range, above the temperature range of hysteresis in $\delta(T)$. It is obvious that in the range $T_H < T < T_I$ hysteresis of $X_y(T)$ could be due to a change in the system of domain walls interacting with defects as well as to changes in the $1q$ and $2q$ structures responsible for the hysteresis of $\delta(T)$.

The stress and the dependent spontaneous deformation applied to the ferroelastic can affect the ferroelastic domain structure. The results of the investigation of the effect of a torsional mechanical stress σ_y on the temperature evolution of the spontaneous twisting of the $Ba_2NaNb_5O_{15}$ sample are displayed in Fig. 2. It is evident that as the mechanical stress increases from 0 to 3×10^6 Pa, the total torsional deformation increases substantially, indicating an increase in the degree of single-domian formation in the sample in the field of the external mechanical stresses and, therefore, an increase in the macroscopic spontaneous deformation. In addition to the fact that the applied mechanical stress strongly changes the form of the anomalies in the curves $X_y(T)$, it also increases the hysteresis of the curves themselves. The peaks at the temperatures T_H and T_L (heating curves) and T_L (cooling curves) strongly decrease in magnitude and become wider on the temperature scale. The form of the dependence $X_y(T)$ at T_I is not changed much by an applied mechanical stress. Assuming that an increase in the mechanical stress results in a decrease in the concentration of domain walls in the ferroelastic, it can be concluded that the anomalous behavior of the spontaneous twisting at temperatures T_H and T_L is related to the state of the ferroelastic domains in $Ba_2NaNb_5O_{15}$.

One would expect that a decrease in the concentration of domain walls in the sample should result in a decrease of the temperature hysteresis of $X_y(T)$. However, the exact opposite was observed experimentally. One possible explanation of this contradiction is that an external mechanical stress has a different effect on the ''pinned'' (heating process) and ''free'' (cooling process) domain structure. It is reasonable to assume that the effect of the mechanical stress during cooling is to produce a greater degree of monodomain formation in the sample, while the ''pinned'' domain structure is less effectively rearranged by a mechanical stress.

It is obvious that further experiments are required to study the effect of the mechanical stress on the temperature hysteresis of the spontaneous twisting of a $Ba_2NaNb_5O_{15}$ crystal.

This work was supported by the Russian Fund for Fundamental Research (Project No. 98-02-16055).

*)E-mail: gridnev@nsl.vstu.ac.ru

---

[1] I. T. Bodnar' and V. P. Yarunichev, Fiz. Tverd. Tela (Leningrad) **29**, 614 (1987) [Sov. Phys. Solid State **29**, 354 (1987)].

[2] J. C. Toledano and L. Pateau, J. Appl. Phys. **45**, 1611 (1974).

[3] S. Mori, N. Yamamoto, Y. Koyama, and Y. Uesu, Ferroelectrics **190**, 13 (1997).

[4] J. Schneck and D. Paquet, Ferroelectrics **21**, 577 (1978).

[5] S. Mori, N. Yamamoto, Y. Koyama, and Y. Uesu, Ferroelectrics **169**, 105 (1995).

[6] J. M. Kiat, G. Galvarin, and J. Schneck, Ferroelectrics **105**, 219 (1990).

[7] X. Pan, H.-G. Unruh, and D. Feng, Ferroelectrics **105**, 225 (1990).

[8] P. Saint-Gregoire, Ferroelectrics **175**, 25 (1996).

[9] S. A. Gridnev, V. I. Kudryash, and L. A. Shuvalov, Izv. Akad. Nauk SSSR, Ser. Fiz. **43**, 1718 (1979).

[10] S. A. Gridnev, V. I. Kudrjash, B. N. Prasolov, V. T. Dybov, and R. M. Fedosyuk, Ferroelectrics **111**, Part B, 233 (1990).

Translated by M. E. Alferieff

PHYSICS OF THE SOLID STATE VOLUME 41, NUMBER 10 OCTOBER 1999

LOW-DIMENSIONAL SYSTEMS AND SURFACE PHYSICS

Localization of an electron on a one-dimensional chain of periodically arrayed random δ potentials

D. M. Sedrakyan*) and D. A. Badalyan

Erevan State University, 375049 Erevan, Armenia

A. Zh. Khachatryan†)

Armenian State Engineering University 375049 Erevan, Armenia

(Submitted July 16, 1998; resubmitted February 9, 1999)
Fiz. Tverd. Tela (St. Petersburg) **41**, 1851–1855 (October 1999)

A new method for exact averaging of the resistivity of a chain of periodically arrayed random short-range potentials has been developed. It is shown that the dependence of the average resistivity of the system on the length of a system having an arbitrary disorder at its centers is a sum of three exponential functions. The nature of the localization of the states as a function of the system's disorder parameters and the energy of the single-electron states have been investigated. © *1999 American Institute of Physics.* [S1063-7834(99)02810-5]

The transmission of electrons through layers of a randomly nonuniform medium is an important problem in the theory of disordered systems (see, for example, Ref. 1). At present the solution of this problem for two- and three-dimensional systems encounters insurmountable mathematical difficulties. At the same time, one-dimensional models are being intensively investigated (see Refs. 2–14). This is because, specifically, one-dimensional models in a number of cases admit exact solutions, which makes it possible to follow the evolution of electronic states as a function of the sample size with an arbitrary interaction force.

For a one-dimensional system, the electric conductivity at zero temperature is the reciprocal of the Landauer resistivity ρ, which in turn can be presented as[2,3]

$$\rho = R/T, \tag{1}$$

where R and T are, respectively, the electron reflection and transmission coefficients. If the nonideal region is a uniform metal with stationary random scatterers, where all electronic states are localized, then the average Landauer resistivity $\langle \rho \rangle$ can be expressed in terms of the chain length L (when $L \to \infty$) by[2–5]

$$\langle \rho \rangle = \frac{1}{2}(e^{L/\xi} - 1), \tag{2}$$

where $\hbar = e^2 = 1$ and $\langle \ldots \rangle$ denotes averaging over all possible realizations of the random field. Here ξ is the localization length of one-electron states, which depends on the electron energy and the form of the random-field potentials and does not depend on the sample length.

In Ref. 15, an exact solution was obtained for the average resistivity and the localization length was found as a function of the order parameters and the electron energy for a model of a chain consisting of periodically arranged random δ scatterers, such that the average potential is zero. In Ref. 16, a transfer matrix was used to find the general form of the solution for the average resistivity of the model studied in Ref. 15, when the average potential is different from zero.

In the present paper we propose a new, simple method which, in the general case, permits finding an exact solution for the average resistivity of a chain of random short-range potentials. It is shown that all one-electron states are localized and the dependence of the localization length on the model parameters is found for arbitrary electron energies.

1. EQUATION FOR THE AVERAGE RESISTIVITY

Let us consider a model where N random δ potentials occupy sites of a one-dimensional chain with the coordinates $x_l = la$, where a is the period of the one-dimensional structure,

$$V(x) = \sum_{l=1}^{N} V_l \delta(x - x_l). \tag{3}$$

Let the strengths of the δ potentials $V_1, V_2, \ldots, V_N$ be independent random quantities, assuming any values in the range $(-(W/2), (W/2))$ with probability density $\sim f(V_1)$ ($f(V_l)$ is a density function, $\int_{-\frac{W}{2}}^{\frac{W}{2}} f(V_l) dV_l = 1$).

Following Refs. 14 and 15, we can express the ensemble average $\langle \rho_N \rangle$ as

$$\langle \rho_N \rangle = \int_{-\frac{W}{2}}^{\frac{W}{2}} \ldots \int_{-\frac{W}{2}}^{\frac{W}{2}} (|D_N|^2 - 1) \times f(V_1) \ldots f(V_N) dV_1 \ldots dV_n, \tag{4}$$

where

$$D_N=1+\sum_{p=1}^{N}\sum_{1\leqslant j_1<j_2<\ldots<j_p}^{N}\frac{iV_{j_1}}{2k}\,\frac{iV_{j2}}{2k}\cdots\frac{iV_{jp}}{2k}\times\prod_{e=1}^{p-1}(1-\exp 2ik(x_{j_{e+1}}-x_{j_e})). \tag{5}$$

The series D_N satisfies the recurrence equation[9]

$$D_N=A_N D_{N-1}-B_N D_{N-2}, \tag{6}$$

where

$$A_N=1+B_N+C_N;\quad B_N=(V_N/V_{N-1})\exp(i\gamma),$$

$$C_N=(iV_N/2k)(1-\exp(i\gamma));\quad A_1=1+iV_1/2k,$$

$$\gamma=2ka,\quad D_0=1,\quad D_{-1}=0.$$

As follows from Eq. (4), the problem of determining the average resistivity of a chain of random δ scatterers reduces to finding the average value of $|D_N|^2$. The direct calculation and averaging of $|D_N|^2$ according to Eq. (4) is a very difficult mathematical problem. For this reason, it is necessary to obtain for $\langle|D_N|^2\rangle$ (or $\langle\rho\rangle$) an equation whose solution would make it possible to find the dependence of the average resistivity on the model parameters and the electron energy.

This equation has the form (see Appendix):

$$\langle\rho_N\rangle=(l+m)\langle\rho_{N-1}\rangle-(l-m)\langle\rho_{N-2}\rangle+\langle\rho_{N-3}\rangle+m, \tag{7}$$

where l and m are determined by the expressions

$$l=4(\cos\gamma/2+\beta\sin\gamma/2)^2-1;$$

$$m=2(\alpha-\beta^2)(1-\cos\gamma),$$

$$\alpha=\langle V_l^2\rangle/4k^2,\quad \beta=\langle V_l\rangle/2k.$$

Equation (7) is a finite-difference (recurrence) equation with the initial conditions (A.18).

We note that the solution of the equation with the conditions (A.18) is equivalent to the problem of solving an integral-type finite-difference equation

$$\langle\rho_N\rangle=(\alpha-\beta^2)N+\beta^2\frac{\sin^2(N\gamma/2)}{\sin^2(\gamma/2)}+\sum_{n=1}^{N-1}F_{N-n}\langle\rho_n\rangle, \tag{8}$$

where

$$F_n=(\alpha-\beta^2)(1-\cos n\gamma)+2(2\beta+\beta^2\tan(\gamma/2))\sin n\gamma.$$

For $\beta=0$ (the average potential is zero), equation (8) becomes an equation for $\langle\rho_N\rangle$ obtained in Ref. 15 by a different method.

2. AVERAGE RESISTIVITY OF THE SYSTEM

Following Refs. 15 and 16, we shall seek the dependence of the average resistivity of the chain on the length of the chain in the form

$$\langle\rho_N\rangle=\sum_{j=1}^{p}T_j t_j^N+T_0, \tag{9}$$

where t_j, T_j, and T_0 do not depend on N. Substituting the expression (9) in Eq. (7) [or in Eq. (8)], we obtain $T_0=-1/2$ and the characteristic equation for determining x_j

$$t_j^3-t_j^2(l+m)+t_j(l-m)-1=0, \tag{10}$$

where l and m are determined by the expression (7).

Equation (10) is a third-order equation and therefore $p=3$ in expression (9).

Substituting expression (9) into the boundary conditions (A.18) and taking account of the characteristic equation (10), we obtain a system of equations for T_j

$$\sum_{j=1}^{3}T_j t_j=\frac{1}{2}+\alpha, \tag{11}$$

$$\sum_{j=1}^{3}\frac{T_j}{1+t_j}=\frac{1}{4}+\frac{(\beta^2-\alpha)\cos^2 ka}{\cos^2\varphi}, \tag{12}$$

$$\sum_{j=1}^{3}T_j=\frac{1}{2}, \tag{13}$$

where $\cos\varphi=\cos\gamma/2+\beta\sin\gamma/2$.

The system of equations (11)–(13) can also be obtained by requiring that the solution (9) satisfy Eq. (8). The solution of the linear system of equations (11)–(13) leads to the following expressions for the coefficients T_1, T_2, and T_3:

$$T_1=\frac{1}{2}\,\frac{4b(1+l)-(1-t_1)(l+m-2a-t_1+1)}{(t_2-t_1)(t_3-t_1)}, \tag{14}$$

where

$$a=\alpha+\frac{1}{2},\quad b=\frac{1}{4}+\frac{(\beta^2-\alpha)\cos^2 ka}{16k^2\cos^2\varphi}.$$

The coefficients T_2 and T_3 are obtained from T_1 by cyclic permutation of the quantities t_1, t_2, and t_3.

Thus, the length dependence of the average resistivity of the present model of a chain in the general case can be expressed by a sum of three exponential functions of the roots of the characteristic equation (10) t_1, t_2, and t_3 with coefficients T_1, T_2, and T_3.

The roots of the cubic equation (10) can be expressed in terms of radicals

$$t_1=A+B+\frac{l+m}{3},\quad t_2,t_3=-\frac{A-B}{2}\sqrt{3}+\frac{l+m}{3}, \tag{15}$$

where

$$A=\sqrt[3]{-\frac{q}{3}+\sqrt{Q}},\quad B=\sqrt[3]{-\frac{q}{3}-\sqrt{Q}} \tag{16}$$

and

$$Q=\frac{2l}{3}\,\frac{c^2+3m^2}{9}-\frac{1}{12}\left(\frac{l^2-m^2}{3}\right)^2-\frac{l^2-m^2}{6}+\frac{1}{4},$$

$$q=-2\left(\frac{l^2+m^2}{3}\right)^3-\frac{l^2-m^2}{6}-\frac{1}{2}. \tag{17}$$

Equation (10) for $Q>0$ has one real and two complex-conjugate roots, and for $Q\leqslant 0$ all three roots are real.

Let us consider some particular cases. For the well-known Kronig–Penney model, the resistivity ρ_N can be obtained from the solution (9) by making the substitution $\alpha=\beta^2$. Indeed, we obtain from Eq. (15) in this case

$$t_1=1, \quad t_2=\exp(i\,2\varphi), \quad t_3=\exp(-i\,2\varphi). \tag{18}$$

Then, substituting expressions (18) into Eq. (15) we have

$$T_1=\frac{1}{2}\left\{\frac{\beta^2}{\sin^2\varphi}-1\right\}, \quad T_2=T_3=\frac{1}{4}\,\frac{\beta^2}{\sin^2\varphi}. \tag{19}$$

The substitution of expressions (18) and (19) into Eq. (9) immediately gives the well-known result[9]

$$\rho_N=\frac{V^2}{4k^2}\,\frac{\sin^2 N\varphi}{\sin^2\varphi}, \tag{20}$$

where $\cos\varphi=\cos ka+(V/2k)\sin ka$ and V is the strength of a single δ potential.

Let us consider a different special case, where the electron energy corresponds to the edge of an energy band ($ka=\pi$, $k^2=E$ is the electron energy) and the disorder parameters α and β can assume any values. In this case the average resistivity $\langle\rho_N\rangle$ has the form

$$\langle\rho_N\rangle=(\alpha-\beta^2)N+\beta^2N^2. \tag{21}$$

As one can see from Eq. (21), the dependence of the average resistivity of the system on the length of the system consists of terms which are linear and quadratic in N. The power-law dependence of $\langle\rho_N\rangle$ on N leads to the fact that the state $ka=\pi$ is delocalized. This is the well-known feature of the present model, related to the choice of interaction potentials in the form of δ functions.[1,9]

3. LOCALIZATION OF STATES

Before considering the asymptotic behavior of $\langle\rho_N\rangle$ in the limit $N\to\infty$, we shall determine certain properties of the roots of the characteristic equation (10).

For this we write the equation (10) in the form

$$l=\frac{t^2+t+1}{t}m-\frac{t+1}{t-1}. \tag{22}$$

We shall treat l and m as linearly independent variables and the roots t of the characteristic equation (10) as an independent parameter of Eq. (22). As one can see from the definitions of l and m (A.9), for arbitrarily fixed ka,β, and α ($\alpha\geqslant 0$, $\alpha-\beta^2\geqslant 0$) they can assume numerical values only in the intervals

$$l\in[-1,\infty) \quad \text{and} \quad m\in[0,\infty). \tag{23}$$

It can be shown that Eq. (22), which in the (l,m) plane looks like a straight line, intersects the domain of the variables l and m (23) only for certain values of x. It is obvious that the real roots of the characteristic equation possess numerical values for which the straight line (22) passes through the region (23). This happens when t assumes a value in the range

$$t\in[-1,\infty). \tag{24}$$

It follows on this basis that the characteristic equation (10) always possesses a real root which is greater than or equal to 1. For $Q>0$ the modulus of the complex root is less than 1. We note that two roots greater than 1 can also be present ($Q\leqslant 0$). Therefore the localization length, according to Eq. (2), is given by the formula

$$\xi=\frac{a}{\ln t_1}, \tag{25}$$

where t_1 is the largest real root ($t_1\geqslant 1$) of Eq. (10).

As is evident from Eq. (25), when $t_1=1$, the localization length becomes infinite, i.e. delocalization of the states occurs. Indeed, as one can see from Eq. (18), the case $t_1=1$ corresponds to the Kronig–Penney model ($\langle V^2\rangle=\langle V\rangle^2$), where the electron energy lies within an allowed zone ($|\cos\varphi|\leqslant 1$).

When the variance of the potential is different from zero, t_1 is greater than 1. Then all electronic states are localized.

We shall find the localization length for the physically interesting case where the particle energy lies within the allowed band of the Kronig–Penney model, and the variance σ^2 of the potential is much less than the average value of the potential, i.e. $\langle V^2\rangle-\langle V\rangle^2\ll V^2$. In this case t_1 is close to 1 and it can be sought in the form

$$t_1=1+\Delta t, \quad 0<\Delta t\ll 1. \tag{26}$$

Substituting expression (26) in Eq. (10) and retaining only terms linear in σ^2, we obtain for Δt

$$\Delta t=\frac{2m}{3-e}. \tag{27}$$

Substituting expression (26) in Eq. (25) and using Eq. (27) we obtain finally for the localization length

$$\xi=\frac{2ak^2}{\sigma^2}\left(\frac{\sin\varphi}{\sin ka}\right)^2. \tag{28}$$

Relative (28) determines the dependence of the localization length on the variance of the potential.

Finally, we note that the roots of Eq. (10) are equal, i.e., $t_1=t_2=t_3=1$, if $Q=0$, which corresponds to the states $ka=\pi m$ ($m=1,2,\dots$). As one can see from Eq. (25), these states are delocalized.[17,18]

In conclusion, we note that a solution was found for the average resistivity $\langle\rho\rangle$ of a one-dimensional chain of N periodically arranged random δ scatterers. The dependence of $\langle\rho\rangle$ on the chain length with arbitrary disorder on the centers is a sum of three exponential functions. In the limit of an infinitely long chain, the average resistivity for the values of the disorder parameter ($\sigma^2\neq 0$) grows exponentially, which attests to localization of all states of the one-electron spectrum.

The dependence of the localization length on the parameters of the problem was found. For the case of weak disorder, an analytic expression (28) is obtained for ξ as a function of the electron energy and the variance of the potential. As one can see from Eq. (28), in the allowed bands of the Kronig–Penney potential, the one-particle electronic states have a finite localization length, whose dependence on the

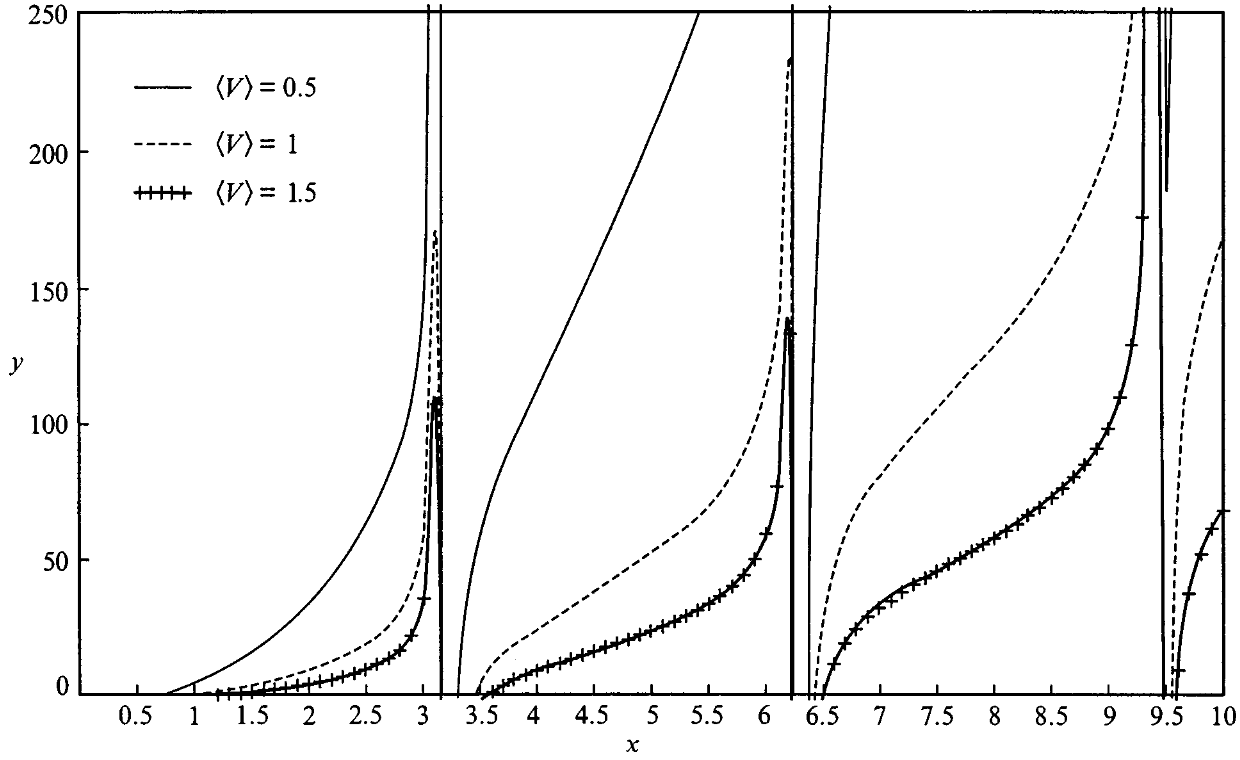

FIG. 1. $y=(\sigma^2/\langle V\rangle^2)\ (\xi/a)$ versus $x=ka$ for various values of the average potential $\langle V\rangle$ and $a=1$.

particle energy is displayed in Fig. 1. The localization length approaches infinity only at the edges of the allowed bands $k=\pi m$; this is due to the choice of the potential in the form of δ functions. As one can see from the figure, the localization length is a multivalued function of the electron energy in different bands. For an arbitrary energy k, as the average potential $\langle V\rangle$ increases, the localization length decreases.

One of us (D. A. B.) thanks V. M. Gasparyan for a discussion of the results obtained.

APPENDIX

We introduce the new function

$$S_N=D_N-D_{N-1}. \qquad \text{(A.1)}$$

Then we obtain from Eq. (6)

$$S_N=C_N D_{N-1}-B_N S_{N-1}. \qquad \text{(A.2)}$$

It is convenient to use S_N, since it can be expressed as

$$S_N=C_N f_{N-1}, \qquad \text{(A.3)}$$

where the function

$$f_{N-1}=(1+B_N/C_N)D_{N-1}-(B_N/C_N)D_{N-2} \qquad \text{(A.4)}$$

does not depend on V_N. Now, a relation between the functions D_N and f_N can be established from Eqs. (A.2) and (A.3):

$$D_{NB}=f_N-bf_{N-1}, \qquad \text{(A.5)}$$

where $b=\exp(i\gamma)$.

The dependence of $|D_N|^2$ on the functions f_N and f_{N-1} obtains from Eq. (A.5)

$$|D_N|^2=|f_N|^2+|f_{N-1}|^2-b^*f_Nf^*_{N-1}-bf^*_Nf_{N-1}. \qquad \text{(A.6)}$$

We shall find the recurrence equation for f_N. We replace N by $N-1$ in Eq. (A.5) and construct the difference D_N-D_{N-1}. Using Eqs. (A.1) and (A.3) we obtain

$$f_N=a_Nf_{N-1}-bf_{N-2}, \qquad \text{(A.7)}$$

where $a_N=1+b+C_N$. The equation (A.7) leads to the recurrence relation

$$|f_N|^2=(|a_N|^2-1)|f_{N-1}|^2+(1-|a_{N-1}|^2 - a_Na^*_{N-1}-a^*_Na_{N-1})|f_{N-2}|^2+|f_{N-3}|^2. \qquad \text{(A.8)}$$

The equation obtained is remarkable in that the function $|f_k|^2$ ($k=N-1,\ N-2$) and the corresponding coefficients do not contain the general random potentials V_l, so that they can be averaged independently of one another. From Eq. (4) we obtain

$$\langle|f_N|^2\rangle=(l+m)\langle|f_{N-1}|^2\rangle-(l-m)\langle|f_{N-2}|^2\rangle+\langle|f_{N-3}|^2\rangle, \qquad \text{(A.9)}$$

where

$$l=4(\cos\gamma/2+\beta\sin\gamma/2)^2-1;$$

$$m=2(\alpha-\beta^2)(1-\cos\gamma),$$

$$\alpha=\langle V_l^2\rangle/4k^2, \quad \beta=\langle V_l\rangle/2k.$$

Now, using Eq. (13), we obtain from Eq. (12)

$$|D_N|^2=|f_N|^2+(1-a_N-a^*_N)|f_{N-1}|^2+(a_{N-1}+a^*_{N-1})|f_{N-2}|^2-b^*f_{N-2}f^*_{N-3}-bf^*_{N-2}f_{N-3}. \qquad \text{(A.10)}$$

Replacing the index N by $N-1$ in Eq. (A.6) and using Eq. (A.10) we construct the difference $W_N=|D_N|^2-|D_{N-2}|^2$. We obtain

$$Q_N=|f_N|^2+(1-a_N-a_N^*)|f_{n-1}|^2+(1-a_{N-1}-a_{N-1}^*)|f_{N-2}|^2-|f_{N-3}|^2. \tag{A.11}$$

We now average Eq. (A.11), using Eq. (4),

$$\langle Q_N\rangle=\langle|f_N|^2\rangle+\lambda|f_{N-1}|^2-\lambda\langle|f_{N-2}|^2\rangle-\langle|f_{N-3}|^2\rangle, \tag{A.12}$$

where

$$\lambda=-(1+2\cos\gamma+2\beta\sin\gamma).$$

The averages $\langle Q_N\rangle$ satisfy the recurrence relation

$$\langle|Q_N|\rangle=(l+m)\langle Q_{N-1}\rangle-(l-m)\langle Q_{N-2}\rangle+\langle Q_{N-3}\rangle. \tag{A.13}$$

This can be verified by using Eqs. (A.12) and (A.9).

We now introduce the average $\langle P_N\rangle=\langle|D_N|^2\rangle-\langle|D_{N-1}|^2\rangle$. Then

$$\langle Q_N\rangle=\langle P_N\rangle+\langle P_{N-1}\rangle. \tag{A.14}$$

It follows from Eqs. (A.13) and (A.14) that the following equations, similar to Eqs. (A.9) and (A.12), hold:

$$\langle|P_N|\rangle=(l+m)\langle P_{N-1}\rangle-(l-m)\langle P_{N-2}\rangle+\langle P_{N-3}\rangle,$$

$$\langle|P_{N-1}|\rangle=(l+m)\langle P_{N-2}\rangle-(l-m)\langle P_{N-3}\rangle+\langle P_{N-4}\rangle. \tag{A.15}$$

Continuing Eq. (A.15) right up to the equation for $\langle P_4\rangle$, we obtain a chain of $N-3$ equations. Summing them and taking into account the fact that, by definition, $\langle P_N\rangle=\langle\rho_N\rangle-\langle\rho_{N-1}\rangle$, we obtain

$$\langle\rho_N\rangle+(l+m)\langle\rho_{N-1}\rangle-(l-m)\langle\rho_{N-2}\rangle+\langle\rho_{N-3}\rangle+C, \tag{A.16}$$

where

$$C=\langle\rho_3\rangle-(l+m)\langle\rho_2\rangle+(l-m)\langle\rho_1\rangle+\langle\rho_0\rangle. \tag{A.17}$$

The first few averages $\langle\rho_k\rangle$ $(k=0,1,2,3)$ can be easily obtained directly from Eqs. (6) and (4). We have

$$\langle\rho_0\rangle=0,\quad \langle\rho_1\rangle=\alpha,$$

$$\langle\rho_2\rangle=2\alpha+2\alpha^2(1-\cos_{\gamma})+4\alpha\beta\sin\gamma+2\beta^2\cos\gamma;$$

$$\begin{aligned}\langle\rho_3\rangle&=3\alpha+8\alpha^2+4\alpha^3+6\alpha\beta^2\\&+(4\beta^2-4\alpha^2+8\alpha\beta^2-8\alpha^3)\cos\gamma\\&+(4\alpha^3-8\alpha\beta^2-4\alpha^2)\cos^2\gamma\\&+(2\beta^2-6\alpha\beta^2)\cos2\gamma+(16\alpha^2\beta+8\alpha\beta)\sin\gamma\\&+(4\beta^3-8\alpha^2\beta+4\alpha\beta)\sin2\gamma.\end{aligned} \tag{A.18}$$

Substituting the expression (A.18) into Eq. (A.17) we obtain $C=m$.

*)E-mail: dsedrak@www.physdep.r.am

†)E-mail: akhachat@www.physdep.r.am

---

[1] I. M. Lifshitz, S. A. Gredeskul, and L. A. Pastur, *Introduction to the Theory of Disordered Systems* (Nauka, Moscow, 1982).

[2] R. Landauer, Philos. Mag. **21**, 863 (1970).

[3] F. W. Anderson, D. L. Thouless, E. Abrahams, and D. S. Fisher, Phys. Rev. B **22**, 3519 (1980).

[4] V. A. Mel'nikov, Fiz. Tverd. Tela (Leningrad) **22**, 2404 (1980) [Sov. Phys. Solid State **22**, 1398 (1980)].

[5] V. N. Prigodin, Zh. Eksp. Teor. Fiz. **79**, 2338 (1980) [Sov. Phys. JETP **52**, 1185 (1980)].

[6] G. M. Soukolis, I. V. Jose, E. N. Economou, and Ping Sheng, Phys. Lett. **50**, 786 (1983).

[7] V. I. Perel' and D. I. Polyakov, Zh. Éksp. Teor. Fiz. **86**, 352 (1984) [Sov. Phys. JETP **59**, 204 (1984)].

[8] N. Kumar, Phys. Rev. B **31**, 5513 (1985).

[9] V. M. Gasparyan, B. L. Altshuler, A. G. Aronov, and Z. H. Kasamanian, Phys. Lett. A **132**, 201 (1988).

[10] A. P. Dmitriev, Zh. Éksp. Teor. Fiz. **95**, 234 (1989) [Sov. Phys. JETP **68**, 132 (1989)].

[11] V. N. Dorokhov, Zh. Éksp. Teor. Fiz. **101**, 2001 (1992) [Sov. Phys. JETP **74**, 1071 (1992)].

[12] N. Zekri, M. Schreiber, R. Ouasti, R. Rouamranc, and A. Brezini, Z. Phys. B: Condens. Matter **99**, 381 (1996).

[13] B. N. Shalaev, Fiz. Tverd. Tela (Leningrad) **32**, 3586 (1990) [Sov. Phys. Solid State **32**, 2079 (1990)].

[14] V. M. Gasparian and Ash. Zh. Khchatrian, Solid State Commun. **12**, 1061 (1993).

[15] D. M. Sedrakyan, D. A. Badalyan, V. M. Gasparyan, and A. Zh. Khachatryan, Zh. Éksp. Teor. Fiz. **111**, 575 (1997) [JETP **84**, 317 (1997)].

[16] P. Erdos and C. Herdon, Solid State Commun. **98**, 495 (1996).

[17] Yu. A. Bychkov, JETP Lett. **17**, 162 (1973).

[18] B. Kramer, *Localization and Transport in One-Dimensional Disordered Systems*, Preprint PTB (1998).

Translated by M. E. Alferieff

PHYSICS OF THE SOLID STATE VOLUME 41, NUMBER 10 OCTOBER 1999

Quantum melting of mesoscopic clusters

A. I. Belousov and Yu. E. Lozovik*)

Institute of Spectroscopy, Russian Academy of Sciences, 142092 Troitsk, Moscow District, Russia

(Submitted February 10, 1999)
Fiz. Tverd. Tela (St. Petersburg) **41**, 1856–1862 (October 1999)

The phase diagram of a two-dimensional mesoscopic system of charges or dipoles, whose realizations could be electrons in a semiconductor quantum dot or indirect excitons in a system of two vertically coupled quantum dots, is investigated. Quantum calculations using *ab initio* Monte Carlo integration along trajectories determine the properties of such objects in the temperature–quantum de-Boer-parameter plane. At zero (sufficiently low) temperature, as the quantum fluctuations of the particles increase, two types of quantum disordering phenomena occur with increasing quantum de Boer parameter q: first, for $q\sim 10^{-5}$ the systems transform into a radially ordered but orientationally disordered state wherein various shells of the ''atom'' rotate relative to one another. For much larger $q\sim 0.1$, a transition occurs to a disordered state (a superfluid in the case of a system of bosons). [S1063-7834(99)02910-X]

The study of the properties of a mesoscopic systems with a small number of particles is becoming increasingly important in connection with the continuing decrease in the characteristic sizes of electronic devices. The development of microlithography in semiconductor technology now makes it possible to perform experiments with extremely small structures containing only several electrons or excitons. The investigation of such systems has led to the development of single-electronics[1,2] and to substantial progress in the study and construction of various kinds of mesoscopic objects,[3] regarded as an elemental base for electronic-computing and measurement systems of the future.

In the present paper we study the phase diagram of a finite system of particles (a cluster) confined in a two-dimensional harmonic potential. This model can be used, for example, to describe electrons in a semiconductor quantum dot[1,4] and a system of indirect excitons in vertically coupled quantum dots.[3–6] The existing experimental techniques make it possible to control the number of particles N in such an ''atom'' and to prepare classical clusters with fixed N as well as systems whose behavior is governed by quantum effects. This makes it possible to investigate a number of interesting problems in the physics of mesoscopic systems.

One of the most interesting phenomena occurring in small classical clusters is orientational disordering of clusters (''orientational melting,'' see Refs. 7–10), in which relative orientational disorder in different regions of the system occurs at temperatures several orders of magnitude lower than the temperature for complete disorder (breakdown of the shell structure and onset of particle transfer between shells). Different pairs of shells of a cluster rotate as a whole relative to one another, losing their relative orientational order.

In studying clusters, wherein quantum fluctuations of the particles are comparable to the average interparticle distance, the question of the existence of a quantum analog of classical orientational melting is of interest. It is obvious that, as the role of quantum effects increases, the temperature $T_{s_1 s_2}$ of orientational melting of the shells $\{s_1,s_2\}$ should decrease and, one would think, their ''zero'' orientational melting should occur at a certain critical magnitude of the quantum fluctuations.

What determines the position of the point $q_{s_1 s_2}$ of ''zero'' orientational melting? Ordinarily, the quantum phase-transition point is estimated as the point where the energy $\hbar/ma^2$ of quantum fluctuations of a particle is equal to the energy $k_b T_c$ of its thermal vibrations at the temperature T_c of classical disorder (in other words, when at temperature T_c the wavelength of a thermal de Broglie wave is equal to the average distance a between the particles). How does this estimate change in application to quantum orientational melting of small clusters? What will be the relative arrangement of the regions of existence of orientational order for various pairs of shells in a multishell cluster? What is the role of exchange effects in the phenomenon under consideration?

In the present work we attempted to answer these questions by calculating the properties of artificial ''atoms,'' formed by electrons and excitons in quantum dots, using the quantum Monte Carlo method of integration along trajectories. The general structure of this paper is as follows: In Sec. 1 the mathematical model is introduced and the computational algorithm employed is briefly described. In Sec. 2 a description and discussion of the obtained results are presented.

1. MODEL. COMPUTATIONAL ALGORITHM

The mesoscopic clusters whose properties we wish to investigate can be regarded as two-dimensional systems with a finite number N of particles with mass m in a quadratic confining potential of strength α. The general form of the Hamiltonian of such systems is

$$\hat{H}=\frac{\hbar^2}{2m}\sum_{i=1}^{N}\left(\frac{\partial^2}{\partial x_i^2}+\frac{\partial^2}{\partial y_i^2}\right)+\alpha\sum_{i=1}^{N}(x_i^2+y_i^2)+\sum_{i<j}U(r_{ij}). \tag{1}$$

The following functions were considered for the pair interaction potential U of the particles: 1) for a system of electrons e in a semiconductor quantum dot the particles interacted according to the Coulomb law, i.e. $U(r_{ij})=e^2/r_{ij}$, $r_{ij}=|\mathbf{r}_i-\mathbf{r}_j|$; 2) the interaction of indirect magnetoexcitons in a double quantum dot was viewed as an interaction of parallel dipoles:[6] $U(r_{ij})=d^2/r_{ij}^3$, where the dipole moment $d=he$ is determined by the distance h between the quantum dots.

The Hamiltonian (1) can be reduced to a dimensionless form by expressing all distances and energies in units of r_0 and $E_0=\alpha r_0^2$, where $r_0=e^{2/3}/\alpha^{1/3}$ for a system of electrons (Coulomb cluster, Coul) and $r_0=d^{2/5}/\alpha^{1/5}$ for a cluster of magnetoexcitons (dipole cluster D). As a result, the Hamiltonian (1) becomes

$$\hat{H}=q^2\sum_{i=1}^{N}\left(\frac{\partial^2}{\partial x_i^2}+\frac{\partial^2}{\partial y_i^2}\right)+\sum_{i=1}^{N}(x_i^2+y_i^2)+\sum_{i<j}U(r_{ij}),$$

$$U(r_{ij})=\{1/r_{ij},(\mathrm{Coul});\quad 1/r_{ij}^3,(\mathrm{D})\}. \tag{2}$$

Here the quantum de Boer parameter $q=\hbar/(m^{1/2}\alpha^{1/2}r_0^2)$ determines the magnitude of the quantum fluctuations of the particles. The other dimensionless parameter determining the state of the system (2) is the dimensionless temperature $T=k_bT/(\alpha r_0^2)$.

We used the quantum Monte Carlo method of integration along trajectories (see, for example, the review in Ref. 11) to calculate the properties of the system (2). In this method the properties of the initial two-dimensional quantum system $\{\hat{\mathbf{r}}_i\}$, $i=\overline{1...N}$, are calculated along a fictitious three-dimensional $\{\mathbf{r}_i^p\}$, $p=\overline{0\ldots P-1}$ trajectory, obtained by ‘discretizing’ the functional integrals. The required accuracy in making such a substitution, controlled by the dimensionless parameter $\tau=q/(PT)$, was achieved by choosing the number of layers P in the three-dimensional system such as to best satisfy the condition $\tau=0.3$.

The derivation of the state of a cluster at each point $\{q;T\}$ investigated in the plane of the controlling parameters was based on a calculation of a number of quantities: the radial particle distribution function in a trap and the radial mean-square displacements

$$u_r^2=\frac{1}{NP}\sum_{i=1}^{N}\sum_{p=0}^{P-1}[\langle(r_i^p)^2\rangle-\langle r_i^p\rangle^2]. \tag{3}$$

The orientational disorder of a cluster was investigated using the relative orientational order parameter[10]

$$g_{s_1s_2}=\langle\psi_{s_1}\psi_{s_2}^*\rangle. \tag{4}$$

The ‘‘orientational order parameter’’ ψ_s of a shell s containing N_s particles is determined by $\psi_s=(1/N_s)\Sigma_{i_s}^{N_s}\times\exp(\tilde{j}N_s\varphi_{i_s})$, where the sum extends over all particles in a given shell s.

The variance of the trajectories in imaginary time, i.e., the degree of ‘‘smearing’’ of the trajectories over an angle φ and radius r, was also studied:

$$l_\varphi=\frac{1}{NP}\left\langle\sum_{i=1}^{N}\sum_{p=0}^{P-1}\left(\varphi_i^p-\frac{1}{P}\sum_{p=0}^{P-1}\varphi_i^p\right)^2\right\rangle, \tag{5}$$

$$l_r=\frac{1}{NP}\left\langle\sum_{i=1}^{N}\sum_{p=0}^{P-1}\left(r_i^p-\frac{1}{P}\sum_{p=0}^{P-1}r_i^p\right)^2\right\rangle. \tag{6}$$

2. COMPUTATIONAL RESULTS

We consider first the behavior of classical clusters (for $q=0$). The main configuration of a classical system of 10 dipoles (for $T\ll 1$) in a confining harmonic potential has two distinct shells with the inner shell containing three particles: $D_{10}(3,7)$. Figure 1 shows that, as temperature increases, at first the relative orientational order of the shells is lost. This occurs at a very low temperature $T_{21}\approx 5.4\times 10^{-6}$. The total disordering of a cluster D_{10} with particle transfer between the shells occurs at a much higher temperature $T_f\approx 0.01$.

It is obvious that, for a small cluster consisting of several shells, a number of orientational melting phenomena will occur, each one corresponding to relative orientational disordering in different pairs of shells. This feature of small clusters can be seen in Fig. 2, which shows the temperature dependences of the radial fluctuations (3) and of the orientational parameter (4) of different pairs of shells of a three-shell Coulomb cluster Coul_{25}, which in the ground state has the configuration $\mathrm{Colu}_{25}(3,9,13)$. The arrows in the figure mark the temperatures $T_{32}\approx 3\times 10^{-5}$ and $T_1\approx 1.25\times 10^{-3}$ of the orientational disorderings and the temperature $T_f\approx 7\times 10^{-3}$ of total melting of the system. The data in Fig. 2 confirm that the temperatures $T_{s_1s_2}$ of orientational disordering of the pairs of shells s_1,s_2 are a function of the distribution function of the particles over shells (N_{s_1},N_{s_2}) and are maximum for the pair of shells that form closed groups of sites of an ideal two-dimensional triangular lattice (i.e. when $(N_{s_1},N_{s_2})=(3,9),(4,10),(6,12),\ldots$).[8,10]

In the cases considered above, the temperature range $T_{s_1s_2}<T<T_f$ can be regarded as the region where the shells $\{s_1,s_2\}$ of a cluster, which retains its internal order, rotate relative to one another, losing the mutual orientational order. In a $2\times N$ dimensional configuration space, the system moves in a narrow region — ‘‘ravine’’ — on the potential energy surface, different points of which correspond to different values of the order parameter $g_{s_1s_2}$. Figures 1 and 2 show that such motion is accompanied by ‘‘breathing’’ of the shells of a cluster, which sharply increase the radial mean-square fluctuations u_r^2 at the points $T_{s_1s_2}$ of orientational disorderings.

Let us see how the state of the ‘‘atoms’’ with $T=\mathrm{const}$ changes with an increase in the quantum fluctuations. Figure 2a shows the behavior of the relative orientational order parameter g_{21} of the dipole cluster D_{10} for motion along the line $T=3\times 10^{-6}$. The sharp change in g_{21} at the point $q_{21}\approx 8\times 10^{-4}$ attests to a quantum fluctuations induced transition from an orientationally ordered state (OO, for $q<q_{21}$) to

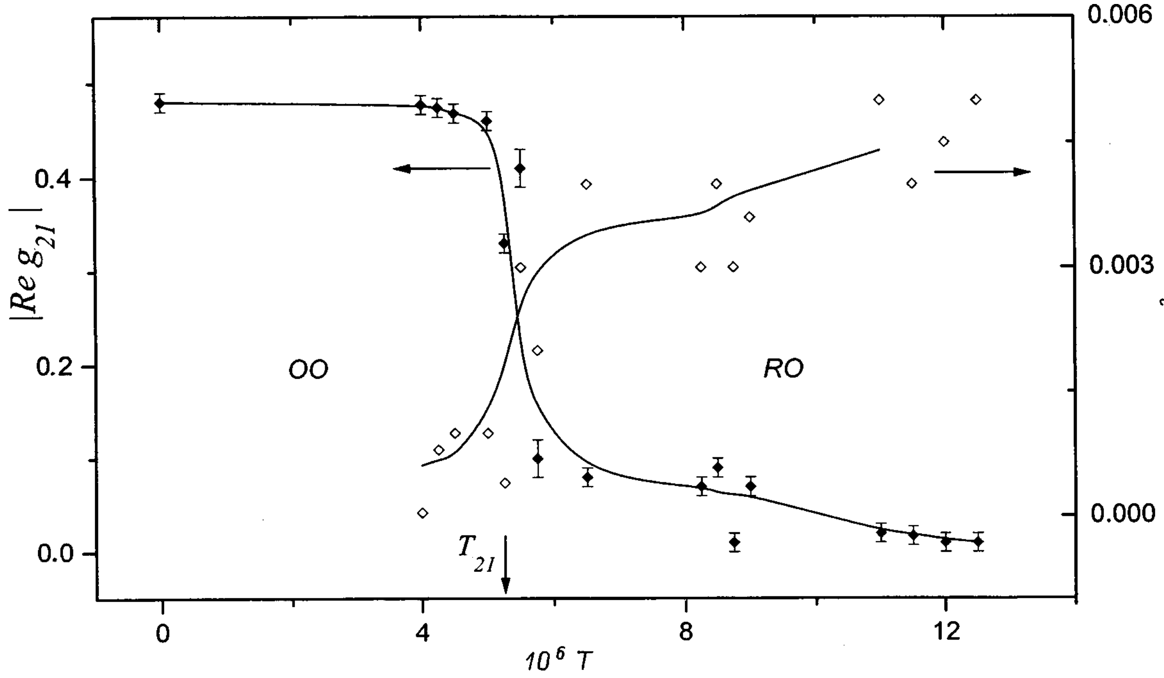

FIG. 1. Vanishing of the relative orientational order parameter g_{21} (4) attests to a transition from an orientationally ordered (OO) to an orientationally disordered but radially ordered state (RO). The sharp increase of the mean-square radial fluctuations u_r^2 (3) at the point $T_{21}\approx 5.5\times 10^{-6}$ of orientational disorder is caused by "breathing" of the shells in a cluster D_{10} as the shells rotate relative to one another.

an orientationally disordered but radially ordered state (RO, $q>q_{21}$). The dependences of the angular and radial dispersion of the particle trajectories in imaginary time (5) and (6) on the quantum parameter q are presented in Fig. 2b. The inset in Fig. 2b shows the instantaneous projection of the trajectories $\mathbf{r}_i^0\rightarrow\mathbf{r}_i^0\rightarrow\dots$ of a three-dimensional classical system in the OXY plane, giving an idea of the trajectories of an orientational disoriented system in imaginary time. The figure shows that the quantum fluctuations are sharply anisotropic. As the quantum parameter increases, the angular fluctuations of the particles increase sharply at the point q_{21} where the mutual orientational order vanishes, while the radial fluctuations of the particles as a function of q do not have any features.

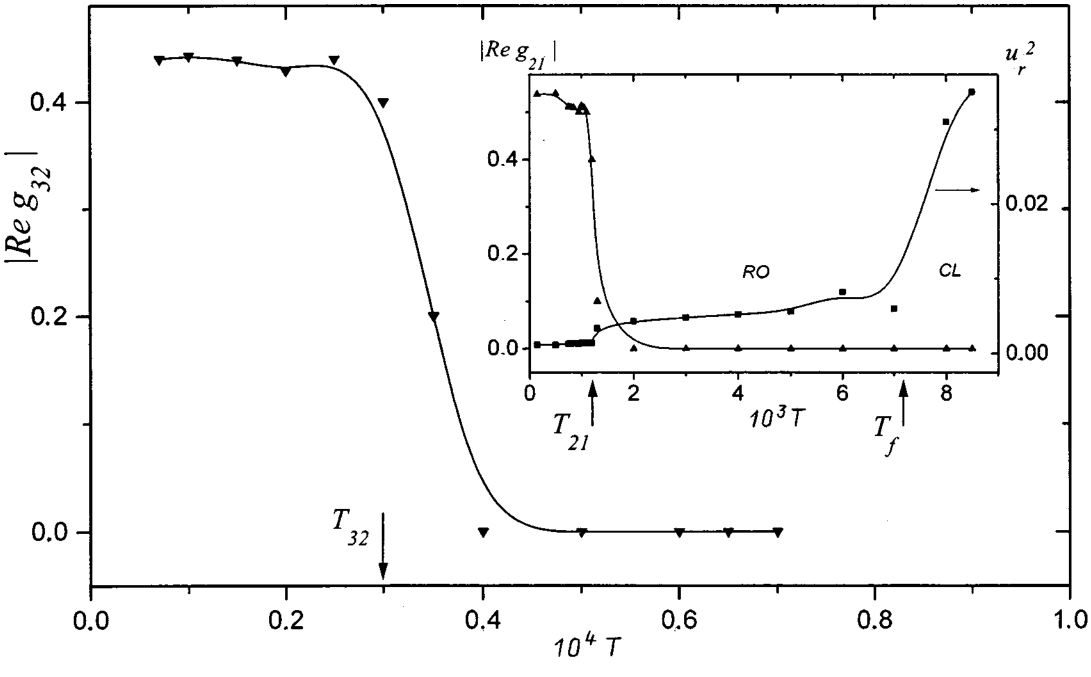

FIG. 2. Orientational melting of different pairs of shells of a three-shell Coulomb cluster $Coul_{25}$. The arrows mark the temperatures T_{32} and T_{21} of orientational disordering of the pairs {3,2} and {2,1} of the cluster as well as the temperature T_f of complete melting of the clusster — a transition from the RO state to a state of a classical liquid (CL).

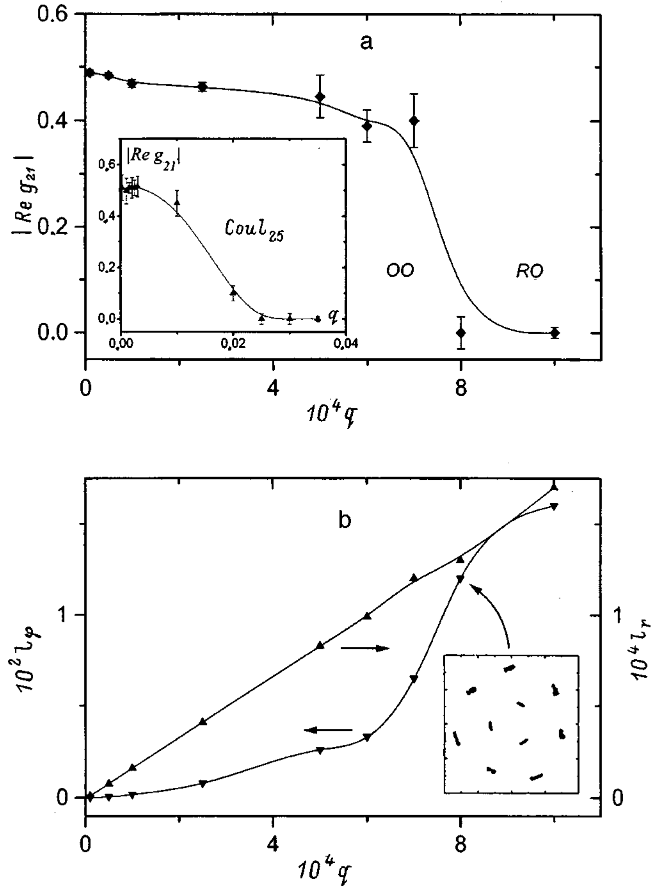

FIG. 3. Quantum orientational melting of a dipole cluster at $T=3\times10^{-6}$ and a Coulomb cluster (inset to Fig. 3a) at $T=5\times10^{-3}$. a — Relative orientational parameter g_{21} as a function of the quantum parameter q; b — measured of quantum particle fluctuations: radial l_r and angular l_φ dispersion of particle trajectories in imaginary time. The region of sharp changes in the angular fluctuations is identical to the region of vanishing of the relative orientational order of the shells. Inset: Instantaneous projection of the trajectories of cluster D_{10} on the OXY plane at the point $\{q,T\}=\{8\times10^{-4}, 3\times10^{-6}\}$.

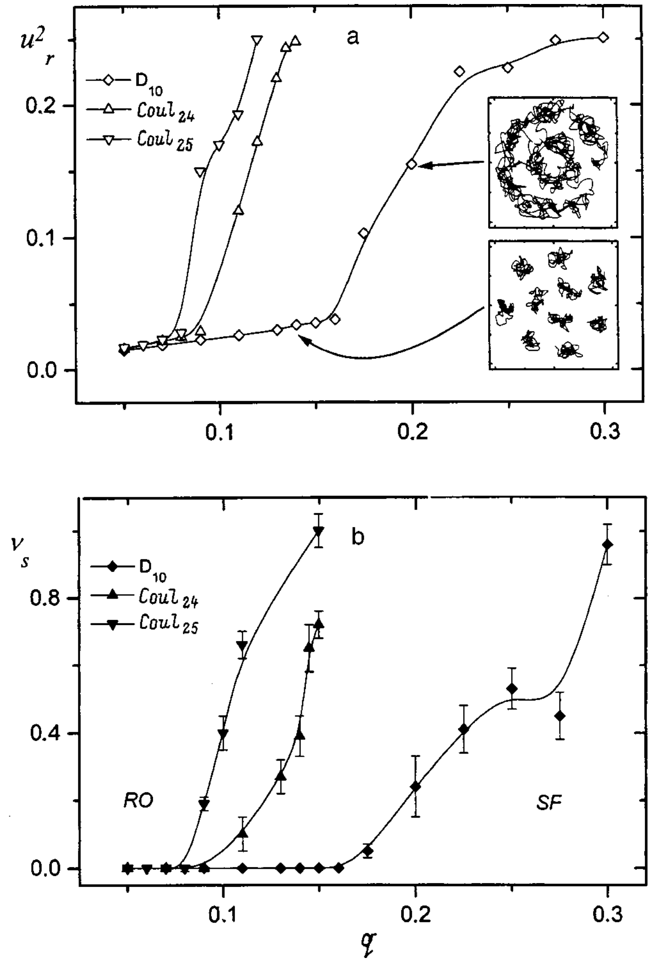

FIG. 4. $T=5\times10^{-3}$. a — Mean-square radial fluctuations u_r^2 of particles as a function of the quantum parameter q. The insets show the characteristic patterns of the trajectories (spline interpolation of their projections on the OXY plane) before ($q=0.13$) and after ($q=0.2$) a transition to a radially ordered superfluid state. b — Superfluid component fraction ν_s as a function of the quantum parameter q.

Similar results were obtained for the Coulomb cluster Coul_{25} and are presented in the inset in Fig. 3a. The results correspond to the temperature $T=3\times10^{-4}$. At this temperature, the second and first shells of a cluster lose orientational order at $q\approx0.01$. The quantum orientational melting of the third and second shells occurs at much smaller values of the quantum parameter $q_{32}\approx8\times10^{-3}$.

The computational results examined above show that the characteristic scales of the quantum particle motions at the quantum orientational melting point become equal to the average angle between the closest particles from the pair of shells considered. A characteristic feature of quantum orientational melting of mesoscopic systems is that, at sufficiently low temperatures, the main direction of particle motion corresponding to a classical system is determined by a narrow and high ''ravine'' formed by the multidimensional potential-energy surface. The existence of such a ravine leads to anisotropy in the quantum fluctuations and strongly distinguishes the role of angular quantum motions. We also note that, for Coulomb and dipole clusters, the quantum orientational melting of any pair of shells occurs in the region of controlling parameters $\{q,T\}$ where the role of exchange effects is negligibly small. This feature is clearly shown in the inset in Fig. 3b, which shows a picture of the trajectories of an orientationally disordered ''atom'' in imaginary time.

We shall now briefly consider the effect of a further increase in quantum fluctuations for $q\geqslant0.05$. The simplest estimates show (see above) that, in the region of the phase diagram under study, for $q>\sqrt{T}$, exchange effects start to play an important role. To simplify the calculations we assumed that the particles forming the ''atom'' are bosons. Strictly speaking, this assumption is valid only for a system of indirect magnetoexcitons in double quantum dots,[6] i.e., for a dipole cluster. The system of electrons in a semiconductor quantum dot satisfies Fermi statistics and the model under consideration is not valid for large quantum fluctuations. However, investigation of a Coulomb boson cluster has definite methodological interest and makes it possible to observe certain general regularities in the behavior of mesoscopic bosonic systems (see below).

Figure 4a shows the computational results for the mean-square radial fluctuations of particles in dipolar and Coulomb

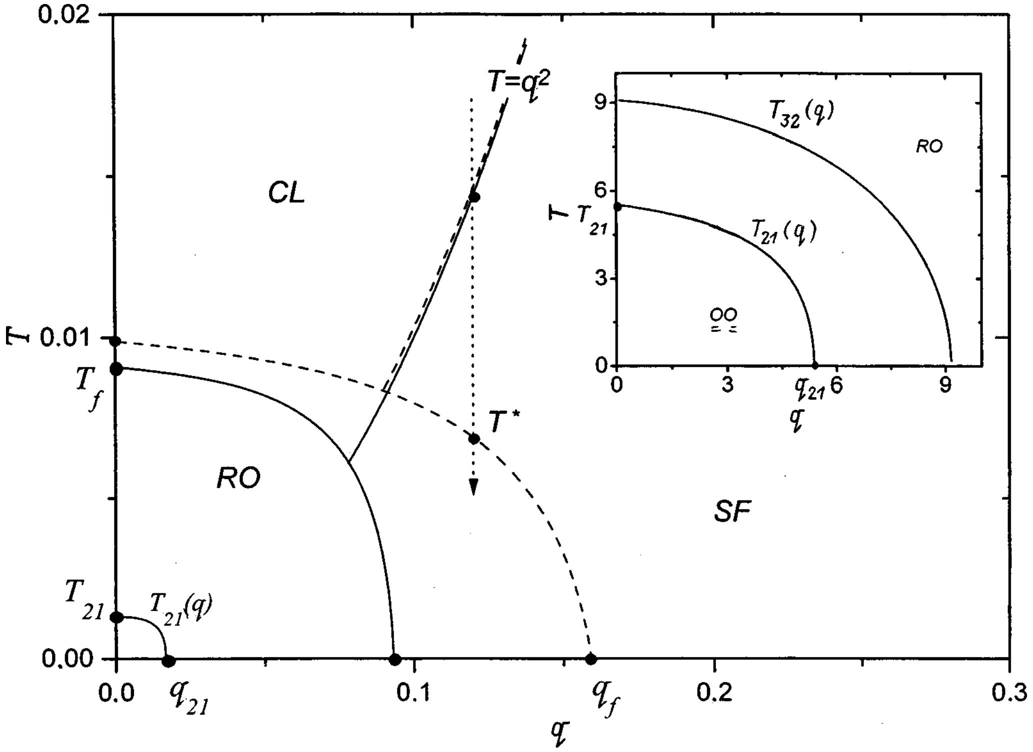

FIG. 5. Resulting phase diagram of an ''artificial atom'' in quantum dots (see text for notation). The dashed lines correspond to a dipole cluster D_{10}, the solid lines correspond to a Coulomb cluster Coul_{25}. The region of a transition from the OO to the RO state is shown qualitatively on an enlarged scale. In regions of substantial quantum fluctuations with decreasing temperature, the superfluid state can vanish at a certain temperature T^* in a system of a small number of bosons.

bosonic clusters as a function of the quantum parameter q at $T=5\times10^{-3}$. The statistics of the particles are taken into account using a multilevel block method, described in detail, for example, in Ref. 11. As follows from the analysis performed above (Figs. 1–3), mesoscopic clusters in the controlling-parameter region under study are in an orientationally disordered state. Therefore, a sharp increase in mean-square radial fluctuations attests to complete melting.

Comparing the results of measurements of the radial fluctuations u_r^2 (Fig. 4a) and the relative superfluid component fraction ν_s of a cluster (Fig. 4b) shows that this disorder corresponds to a transition from a radially ordered (RO) to a superfluid (SF) state.1) As an illustration, the characteristic patterns of particle trajectories in imaginary time are displayed in the inset in Fig. 4a (the spline interpolation of their instantaneous projections on the OXY plane is shown). We note that the fraction of particles participating in nonidentity permutations sharply increases at the point q_f of disordering and appearance of superfluidity in the system. Since the temperature of complete disorder in the corresponding classical systems is $T_f\approx0.01$, which is two times higher than the temperature to which the results of Fig. 4 pertain, the values of q_f of total disorder can be taken as fairly good estimates for points of the corresponding quantum transitions $(T=0)$.

Combining the results presented above, we can draw a phase diagram of mesoscopic clusters in the $\{q;T\}$ plane (Fig. 5). The calculations showed that the system can be in one of the following sharply distinguished states: in an ordered state (OO) with a distinct shell structure and the presence of mutual orientational order between shells; in orientationally disorderd but radially ordered (RO) states, in each of which there is no mutual orientational order of any pair of shells in the cluster; in a state of a ''classical liquid'' (CL) — a disordered state where the role of quantum fluctuations is small. Moreover, for bosonic clusters (clusters of indirect excitons) a region of superfluid (SF) state can exist.

Of course, for systems with a small number of particles it is impossible to talk about the existence of sharp boundaries between the above-mentioned states of the system, if these boundaries are viewed as lines $T(q)$ of phase transitions of one or another kind (more likely, this is a crossover region). However, as one can see from Figs. 1–4, analysis of the properties of a system with even such a small number of particles makes it possible to determine clearly the presence of such regions and to show qualitatively their relative arrangement in the $\{q;T\}$ plane.

The relative arrangement of various regions of the phase diagram obtained is controlled by the following ratios (Fig. 1–5). 1) The ratio between the temperature of the system and the characteristic height of the potential barriers for relative rotation of different pairs of shells determines the region of the transition from an orientationally ordered state to a state with no orientational order for these pairs of shells. Such transitions can occur at different temperatures $T_{s_1s_2}$ for each pair of shells $\{s_1s_2\}$. 2) A further increase of temperature (in the region of small quantum particle fluctuations) leads to complete disordering of the system for $T>T_f$ and a transition of the system to the classical-liquid state. This transition is controlled by the ratio of the temperature of the system and the characteristic particle interaction energy (i.e. the dimensionless temperature T in our variables). 3) For $T > T_f$, as the quantum fluctuations increase, when the de Broglie wavelength becomes comparable to the characteristic interparticle distance in the liquid, a transition occurs to the superfluid state. In our dimensionless variables this transition occurs along the line $T(q) = q^2$. 4) The point q_f (at $T = 0$) of quantum melting of a cluster — its transition from a radially ordered to a superfluid (in the case of a cluster of bosons) state — is controlled by the ratio of the energy of the quantum fluctuations and the characteristic interaction energy of the particles in the cluster. 5) Comparing the energy of quantum particle fluctuations with the characteristic height of the potential barrier for relative rotation of a pair of shells $\{s_1; s_2\}$ in a cluster makes it possible to estimate the position of the point $q_{s_1 s_2}$ of quantum orientational disorder.

In concluding this section, we note one other interesting feature of the behavior of the systems we are investigating. Considering the computational results for the dipole cluster D_{10}, we note that the simplest estimate q_f^{est} of the quantum melting point of the system as $q_f^{\mathrm{est}} = \sqrt{T_f}$ (for explanation see above) in our case would give a much too-low result, $q_f^{\mathrm{est}} \approx 0.1$, instead of the computational result obtained $q_f \approx 0.16$. This observation allows us to infer that, for sufficiently strong quantum fluctuations (for example, for $q \approx 0.13$ in our case, Fig. 5) as temperature decreases and the line $T(q) = q^2$ is crossed, a superfluid state is established and then, at some finite temperature T^*, it vanishes (reentrant) and clearly distinguished shells of the cluster appear. A more detailed investigation of this feature of the behavior of small systems showed that, as the number of particles in a cluster increases, the estimate $q_f \approx \sqrt{T_f}$ works quite well (Fig. 4) and the phenomenon under discussion does not occur.

So, in the present work, using the quantum Monte Carlo method, we investigated the properties of small clusters of electrons in a quantum semiconductor dot (''Wigner islands'') or indirect magnetoexcitons in coupled quantum dots. The ''phase diagram'' of the system was constructed in the $\{q, T\}$ plane (quantum de Boer parameter—temperature). Regions with sharply different properties of a mesoscopic cluster are clearly distinguished in this diagram: regions of an ordered state with a pronounced shell structure and the presence of mutual orientational order between the shells; regions of orientationally disordered but radially ordered state, in each of which there is no mutual orientational order of any pair of shells in the cluster; regions of a classical liquid — disordered state in which quantum fluctuations and (for bosonic clusters of indirect excitons) regions of a superfluid state play a small role. It was found that volume effects do not play any role in determining the boundary of the orientationally ordered state of the system.

At zero temperature, as the quantum particle fluctuations increase, two types of quantum disordering phenomena occur with increasing quantum parameter q: first, the system transforms into a radially ordered but orientationally disordered state, where different shells of an ''atom'' rotate relative to one another. The transition to the disordered state (superfluid in the case of a system of bosons) occurs at a much higher intensity of quantum fluctuations, and the position of the point of this transition q_f for systems with a sufficiently large number of particles ($N > 20$) can be obtained by the standard estimate $q_f \approx \sqrt{T_f}$.

This work was supported by grants from the Russian Fund for Fundamental Research, INTAS, and the program ''Physics of Solid-State Nanostructures.''

*) E-Mail: lozovik@isan.troitsk.su

[1] The fraction ν_s of superfluid component was measured in terms of the response of the system of bosons to an infinitely slow rotation of the system.[11]

---

[1] R. C. Ashoori, Nature (London) **379**, 413 (1994).

[2] R. C. Ashoori, H. L. Stormer, J. S. Weiner, L. N. Pfeiffer, S. J. Pearton, K. W. Baldwin, and K. W. West, Phys. Rev. Lett. **68**, 3088 (1992); R. C. Ashoori, H. L. Stormer, J. S. Weiner, L. N. Pfeiffer, K. W. Baldwin, K. W. West, Phys. Rev. Lett. **71**, 613 (1993).

[3] *Proceedings of the Conference on Mesoscopic and Srongly Correlated Electronic Systems, Chernogolovka-97*; Usp. Fiz. Nauk **168**, No. 2 (1998).

[4] A. A. Koulakov and B. I. Shklovskii, Phys. Rev. B **57**, 2352 (1998).

[5] A. Zrenner, L. V. Butov, M. Hagn, G. Abstreiter, G. Bohm, and G. Weimann, Phys. Rev. Lett. **72**, 3382 (1994); L. V. Butov, A. Zrenner, G. Abstreiter, A. V. Petinova, K. Eberl, Phys. Rev. B **52**, 12 153 (1995); V. F. Timofeev *et al.*, to be published.

[6] Yu. E. Lozovik, O. L. Berman, and V. G. Tsvetus, JETP Lett. **66**, 594 (1997).

[7] Yu. E. Lozovik, Usp. Fiz. Nauk **153**, 356 (1987) [Sov. Phys. Usp. **30**, 912]; Yu. E. Lozovik and V. A. Mandelshtam, Phys. Lett. A **145**, 269 (1990); **165**, 469 (1992).

[8] V. M. Bedanov and F. M. Peeters, Phys. Rev. B **49**, 2662 (1994); V. Shweigert and F. M. Peeters, Phys. Rev. B **51**, 7700 (1995); I. V. Shweigert, V. A. Shweigert, and F. M. Peeters, Phys. Rev. B **54**, 10 827 (1996).

[9] Yu. E. Lozovik and E. A. Rakoch, Phys. Lett. A **235**, 55 (1997); Yu. E. Lozovik and E. A. Rakoch, Phys. Rev. B **57**, 1214 (1998).

[10] A. I. Belousov and Yu. E. Lozovik, in *Conference on Computational Physics ''CCP-1998''*; preprint cond-mat/9803300; A. I. Belousov and Yu. E. Lozovik, JETP Lett. **68**, 858 (1998).

[11] D. Ceperley, Rev. Mod. Phys. **67**, 279 (1995).

Translated by M. E. Alferieff

PHYSICS OF THE SOLID STATE VOLUME 41, NUMBER 10 OCTOBER 1999

Copper-induced diamond formation in amorphous carbon

V. I. Ivanov-Omskiĭ and S. G. Yastrebov*)

A. F. Ioffe Physicotechnical Institute, Russian Academy of Sciences, 194021 St. Petersburg, Russia

(Submitted December 24, 1998; resubmitted February 18, 1999)
Fiz. Tverd. Tela (St. Petersburg) **41**, 1863–1866 (October 1999)

Diamond formation in hydrogenated amorphous-carbon films containing ultradisperse copper has been studied by measuring IR absorption at two-phonon diamond frequencies. The anomalously high two-phonon absorption observed in the experiments has permitted improving the sensitivity of the method. Mechanisms of the two-phonon absorption enhancement are discussed in terms of the theory of a medium containing nanosized copper-doped graphite fragments. It is shown that the observed enhancement of two-phonon absorption is caused by electrical induction of the local fields induced by irradiation in diamond nanocrystals acting on adjoining copper-doped graphite fragments. © *1999 American Institute of Physics.* [S1063-7834(99)03010-5]

Studies of the initial stages in nucleation and growth are limited by the spatial resolution of the currently available diagnostics. Attempts at resolution improvement by increasing the energy of the probing (e.g., electron) beams may cause destruction of structural details. The giant enhancement of two-phonon absorption discussed in this work offers a possibility of using phonon spectroscopy[1] to probe the diamond nanocrystals forming in the amorphous carbon matrix under nonequilibrium conditions of plasma cosputtering of copper and graphite.

The problem of diamond nanocrystal nucleation in an amorphous carbon medium may be considered in connection with the growth of nanosized structures and with the characteristics of their electrophysical properties. The components of the heterostructures formed in this case are the same in chemical composition (carbon) while differing in lattice symmetry. Indeed, there have been repeated attempts to discuss the mechanisms of diamond nucleation on graphite,[2] the fragments of its planes being an essential component of the structure of amorphous carbon, including its hydrogenated species (a-C:H).[3] This work shows how this mechanism of diamond nucleation may account for the giant enhancement of IR absorption at two-phonon vibrational frequencies, which is observed to occur in hydrogenated carbon containing finely dispersed copper (a-C:H:Cu).

1. EXPERIMENTAL TECHNIQUE

a-C:H:Cu films were grown by planar-magnetron cosputtering of a copper and a graphite target in an argon-hydrogen plasma ($80\%\,\mathrm{Ar}^{+}20\%\,\mathrm{H}_2$) on a Si(100) substrate at 200 °C. The cosputtering was carried out in a working gas flow at pressures from 5 to 15m Torr and magnetron power of 350–450W (for a pressure of 8–9m Torr, the voltage was 360–380V). As shown earlier,[3] the films prepared in such conditions are enriched in a diamond-like component (tetrahedral carbon). The layers thus prepared were annealed in vacuum for one hour at 220 °C.

The layers were studied by IR absorption spectroscopy in the region of vibrational frequencies of the C–C and C–H bonds in a-C:H. To improve the contrast, we complemented the study of one-transit absorption at normal incidence by measuring two-transit absorption in reflection geometry at a 45° incidence angle.

2. RESULTS OF THE EXPERIMENT

Figure 1 presents a typical two-transit absorption spectrum of the grown layers modified by the presence of copper. The intensity of the characteristic hydrogen-bond vibrational frequencies ($3000-2800\,\mathrm{cm}^{-1}$) is seen to be considerably reduced by the introduction of the metal. A still more important consequence of copper doping is the appearance of new bands in the region of two-phonon diamond absorption ($2000-2200\,\mathrm{cm}^{-1}$, Ref. 1) and of the graphite Raman frequencies (the G band at $1575\,\mathrm{cm}^{-1}$ and band D with a poorer determined frequency around $1400\,\mathrm{cm}^{-1}$, Ref. 4). Table I lists for comparison published data on the characteristic features of two-phonon absorption bands for bulk diamond and the parameters of the copper-induced absorption bands in a-C:H in the same spectral region. The number of characteristic spectral features in our case is smaller, but the fairly accurate matching of the band frequencies observed in an a-C:H:Cu film with the two-phonon bulk-diamond bands gives one grounds to call them, for the sake of brevity, pseudodiamond bands.

The fact itself of this matching suggests diamond formation in amorphous carbon containing ultradisperse copper. The nanoscopic dimensions of the copper clusters (~ 3 nm, Ref. 5) enhance their activity as catalysts of diamond nucleation. Thus the diamond formation temperature decreases from 800–900 °C required for the standard industrial vapor-phase epitaxy process down to 200 °C.

The bands in Table I are numbered in accordance with Fig. 2, which shows in a greater detail the absorption in the two-phonon region both before and after the sample annealing. One readily sees that after an anneal at a temperature

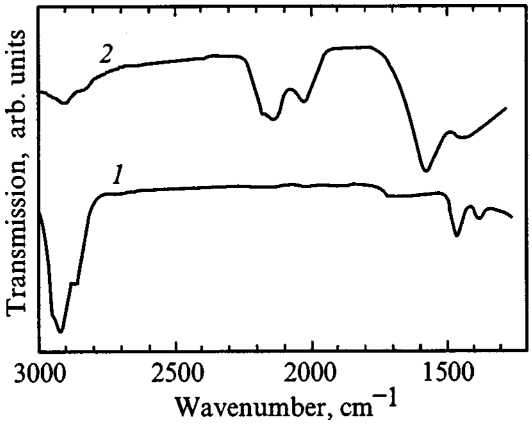

FIG. 1. Two-transit IR absorption spectrum of (*1*) a-C:H and (*2*) a-C:H:Cu.

only slightly in excess of the film growth temperature the spectrum is dominated by band I coinciding in frequency with the bulk-diamond absorption band, whose nature is not fully clear and which corresponds to a two-phonon combination in the asymmetric Brillouin band.[6] Bands III and IV also coincide well in position with their counterparts of bulk diamond. Band II, which is seen clearly in a-C:H:Cu only prior to annealing, shifts to lower frequencies by $\sim 16\,\mathrm{cm}^{-1}$. The same relates to band V, which, by contrast, becomes observable only after the annealing. As for the activation of the graphite Raman frequencies in the optical absorption spectrum, this effect was already reported[7] and assigned to graphite-fragment intercalation by copper. For brevity, we shall call the corresponding bands pseudo-Raman. The same phenomenon was observed in a-C:H doped by a number of other elements.[4] As evident from Fig. 2, the halfwidth of the dominant band at $2177\,\mathrm{cm}^{-1}$ is $30\,\mathrm{cm}^{-1}$, which yields an estimate of the BZ edge dispersion corresponding to a diamond nanocrystal about 2 nm in size.

3. DISCUSSION

Estimation of the absorption coefficient at the maximum of the pseudodiamond bands yields a few hundred cm^{-1}, which is considerably in excess of $14\,\mathrm{cm}^{-1}$, the figure for bulk diamond.[1] This is all the more remarkable if one takes into account that the diamond nanophase does not fill all of the available space. Thus the observation itself of two-phonon absorption in such thin films argues for the existence of a mechanism of giant enhancement. This effect appears apparently as a result of heteroepitaxial diamond growth on the (0001) surface of graphite fragments. The resultant heterostructure is displayed in Fig. 3. By multiply repeating such structural units, one approaches the model of insulating medium, which serves as a basis for our theory of the giant enhancement of two-phonon absorption.

TABLE I. Parameters of the diamond two-phonon absorption bands.

Band No.	I	II	III	IV	V
Wave number (experiment), cm^{-1}	2210	2177	2137	2024	1977
Wave number (literature), cm^{-1}	2210	2177	2153	2024	1968

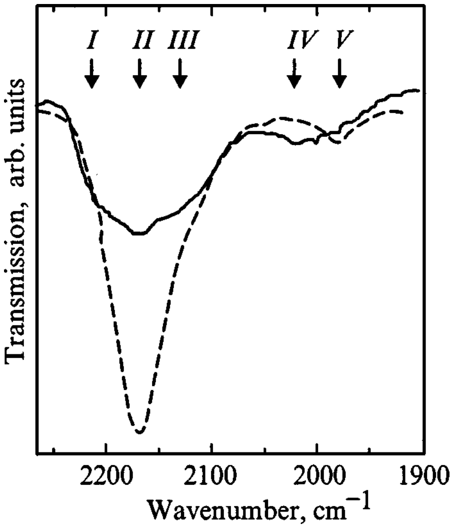

FIG. 2. Parts of an IR absorption spectrum of a a-C:H:Cu film in the as-grown state (solid line) and after annealing for one hour at $T = 220\,^{\circ}\mathrm{C}$ (dashed line).

As already pointed out,[5] cosputtering of graphite and copper produces an insulating medium containing copper-based conducting clusters. It was shown also that such a medium can be described satisfactorily in terms of the effective-medium approximation including the weighted contributions of all possible Lorentzian oscillators. We shall assume the multiply repeated heterostructure displayed in Fig. 3 to be the main structural unit of the material. We also take into account that the concentration of π electrons in graphite increases as a result of its intercalation with copper.[8] Thus graphite-fragment intercalation with copper gives rise to the dependence of the fragment plasma frequency on intercalation efficiency (which depends, in its turn, on temperature) and on the copper concentration. The dielectric permittivity of a medium ε can be written in terms of the adapted model in the form[5]

$$\varepsilon=(1-\theta)\varepsilon_G+\frac{\theta(\varepsilon_D-\varepsilon_G)\varepsilon_G}{\varepsilon_D-\varepsilon_G+f(\varepsilon_D-\varepsilon_G)}, \tag{1}$$

where ε_G and ε_D are the permittivities of the graphite and diamond components, respectively, θ is the diamond-phase bulk concentration, and f is a form factor, which, considering the quasitwo-dimensional nature of the diamond-graphite structural units, is 1/2. As follows from the available data on the dielectric permittivity of a-C:H:Cu films, at copper concentrations less than 15% the dispersion of ε outside the two-phonon absorption region is practically zero, so that ε may be assumed equal to $\varepsilon_a = 4.2$ (for 14% Cu).[5] Using this as a starting point, we applied the simplified Kramers–Kronig transformation procedure and narrowed the limits of integration to the spectral range $\nu \in (1900-2300)\,\mathrm{cm}^{-1}$ of interest to us here:

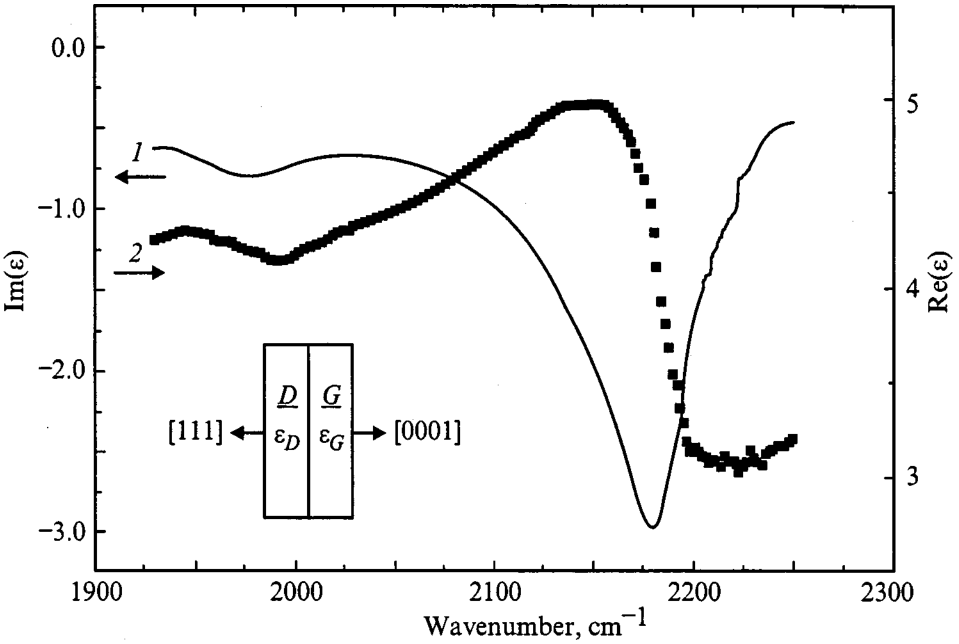

FIG. 3. Dispersion relations of the real and imaginary parts of the a-C:H:Cu dielectric permittivity after annealing, which were calculated based on the experimental data of Fig. 2 using the Kramers–Kronig procedure. Inset: model of a diamond–graphite heteroepitaxial structure representing a building block of the investigated medium.

$$n(\nu_0)=C+\frac{2}{\pi}\int_A^B\frac{k(\nu)\nu d\nu}{\nu^2-\nu_0^2},$$

$$C=\varepsilon_a^{1/2};\quad A=1900\,\mathrm{cm}^{-1};\quad B=2300\,\mathrm{cm}^{-1},\tag{2}$$

where $k(\nu)$ is the extinction coefficient. The $k_1(\nu)$ coefficient for the films studied by us was calculated from the experimental data presented in Fig. 2, ε_D in Eq. (1) was found using the relation $\varepsilon_D=n^2(\nu)$, and $n(\nu)$ was derived, in its turn, from Eq. (2) with the coefficient $C=2.4$ equal to the refractive index of bulk diamond in the visible and near IR regions. For the extinction coefficient of bulk diamond one used the data[1] on $k_v(\nu)$ in the two-phonon spectral range.

The results of the calculation of the real and imaginary parts of the film permittivity are presented in Fig. 3. We readily see that the imaginary part obtained by us reproduces quite well the main features of the starting spectrum (Fig. 2), while the real part exhibits anomalous dispersion in the interval of interest. It should be pointed out that the model does not have any fitting parameter except the bulk fraction of the diamond nanophase, which is rather small (0.1–0.2). Note that the two-phonon absorption coefficient reaches a maximum at 2177 cm^{-1}, in full agreement with experiment.

Using the data on ε_D and the calculated film permittivity, one can obtain from Eq. (1) the permittivity of the graphite component of the film ε_G, whose imaginary part is displayed in Fig. 4 for different contents of the diamond phase. It has been established by simulation that the nanodiamonds forming on graphite fragments cause an anomalously high dielectric response in the graphite phase at the frequency of two-phonon absorption. This response grows with increasing bulk diamond concentration. To analyze the enhancement factor, we describe the response of the graphite component by the following Lorentzian:

$$\varepsilon_G(\omega)=\varepsilon_0+\frac{\omega_{p0}^2\tau_0}{(\omega_0^2-\omega^2)\tau_0+i\omega},\tag{3}$$

where ω_p is the plasma frequency of the copper-doped graphite component, ω_0 is the characteristic frequency corresponding to the two-phonon absorption frequency, τ_0 is the oscillator relaxation time, and ε_0 is the low-frequency dielectric permittivity of graphite. Copper intercalation of graphite fragments results in their plasma frequency becoming dependent on the intercalation efficiency (which depends, in its turn, on temperature) and on the bulk copper concentration. Thus the mechanism of the absorption enhancement consists in excitation of plasma waves at the diamond-graphite interface, with their subsequent relaxation. The coefficient of electromagnetic-wave phonon absorption enhancement can be written

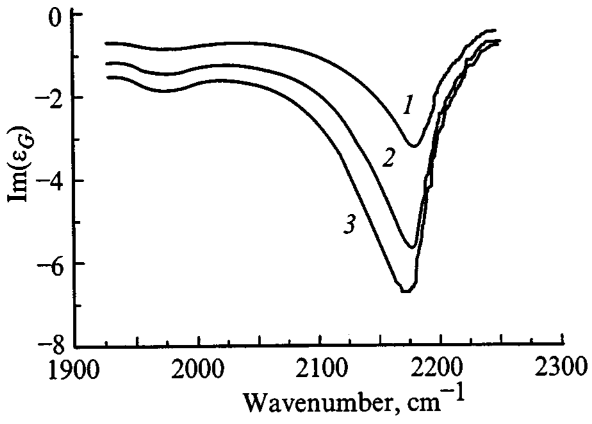

FIG. 4. Reconstruction of the dielectric permittivity ε_G for the copper-doped graphite component of a-C:H:Cu made in the effective-medium approximation for different diamond-phase volume fractions θ: *1*—0.1, *2*—0.2, *3*—0.5.

$$A=\frac{\tau_0}{\tau_1}\frac{\omega_{p0}^2}{\omega_{p1}^2}. \tag{4}$$

Equation (4) was obtained by directly comparing the imaginary parts of the dielectric permittivity of the oscillators excited in a diamond nanocrystal by the two-phonon absorption mechanism (subscript 1) and by the oscillator of a graphite fragment (subscript 0) excited by oscillator 1 through electromagnetic induction. An analysis of two-phonon absorption data[1] yields the following oscillator parameters for bulk diamond: $\nu=2177\,\mathrm{cm}^{-1}$, $\tau_1=1.6\times10^{-11}\,\mathrm{s}$, and $\omega_{p1}=2.3\times10^{11}\,\mathrm{s}^{-1}$.

For diamonds formed on a graphite nanocluster the data of Fig. 2 yield $\tau_0=1.1\times10^{-12}\,\mathrm{s}$ and $\omega_{p0}=3\times10^{13}\,\mathrm{s}^{-1}$. These two sets of parameters can be used to obtain from Eq. (4) an order-of-magnitude estimate of the value of A, which was found to be 10^3. This value is in a good agreement with experiment. According to Eq. (4), annealing increases the plasma frequency of copper-intercalated graphite, which can be assigned to a higher intercalation efficiency of graphite fragments by copper atoms in annealing.

Thus it has been demonstrated experimentally that the anomalous enhancement of two-phonon absorption in nanodiamonds embedded in an amorphous-carbon matrix containing nanosized inclusions of a conducting phase permits one to obtain valuable information on the early stages of diamond nucleation. Moreover, the uniqueness of the two-phonon absorption bands may serve as a reliable indication of the presence of diamonds.

Support of the Russian Fund for Fundamental Research (Grant 97-02-18110) is gratefully acknowledged.

*)E-mail: Yastrebov@pop.ioffe.rssi.ru

---

[1] F. A. Johnson, Prog. Semicond. **9**, 181 (1965).
[2] J. C. Angus, A. Argoitia, R. Gat, M. Sunkara, L. Wang, and Y. Wang, Philos. Trans. R. Soc. London, Ser. A **342**, 195 (1993).
[3] V. I. Ivanov-Omskii, V. I. Siklitsky, A. A. Sitnikova, A. A. Suvorova, A. V. Tolmatchev, T. K. Zvonariova, and S. G. Yastrebov, Philos. Mag. B **76**, 973 (1997).
[4] J. F. Kaufman, S. Metin, and D. Saperstein, Phys. Rev. B **39**, 13053 (1989).
[5] V. I. Ivanov-Omskii, A. V. Tolmatchev, and S. G. Yastrebov, Philos. Mag. B **73**, 715 (1996).
[6] G. Dolling and R. A. Cowley, Proc. Phys. Soc. London **88**, 463 (1966).
[7] V. I. Ivanov-Omskii and G. S. Frolova, Zh. Tekh. Fiz. **65**(9), 186 (1995) [Tech. Phys. **40**, 966 (1995)].
[8] E. A. Smorgonskaya and V. I. Ivanov-Omskii, in *Diamond-Based Composites and Related Materials*, edited by N. Prelas, A. Benedictus, L. T. S. Lin, G. Popovici, and P. Gielisse, NATO ASI Ser. 3, Vol. 38 (Kluwer, Dordrecht, 1997), p. 203

Translated by G. Skrebtsov

PHYSICS OF THE SOLID STATE VOLUME 41, NUMBER 10 OCTOBER 1999

Electronic resonances in a quantum well having a periodically uneven boundary

V. A. Pogrebnyak*)

Institute of Radio Physics and Electronics, Ukrainian Academy of Sciences, 310085 Khar'kov, Ukraine

(Submitted October 2, 1998; resubmitted March 5, 1999)
Fiz. Tverd. Tela (St. Petersburg) **41**, 1867–1870 (October 1999)

The spectrum of the electronic states in an infinitely deep two-dimensional potential well, where one wall is periodically uneven, is investigated theoretically. It is shown that in non-Bragg type resonances — standing electron wave resonances, which are modes of different spatial harmonics of the electron wave function — arise in such a well. The resonances occur in a wide range of energies, starting at values close to the bottom in each 2D subband. The resonance interaction splits the energy spectrum and results in the appearance of gaps, giving the electron spectrum a miniband character. The properties of the electron gas vary substantially in accordance with the new characteristics of the spectrum. © *1999 American Institute of Physics.* [S1063-7834(99)03110-X]

Analysis of the electronic states in two-dimensional systems is of considerable interest for the extensive use of 2D systems in microelectronics devices as well as for the close relation of this problem to investigations of the quantum Hall effect and HTSCs.[1–3] In microelectronic devices, the coupling between the electron 2D subsystem and external fields or an external circuit is often effectuated by depositing a lattice on the surface of a film with the 2D gas.[4–6] In this case, the electrons are subjected to an external periodic potential, which makes it possible to investigate the electron spectrum in such a system. Similar problems appear in the investigation of the properties of a two-dimensional electron gas at the boundary of a heterojunction in the presence of misfit dislocations or at grain boundaries in mosaic crystals. In the first case the additional periodic potential arises because of the presence of misfit dislocations,[7] and in the second case it arises on account of edge dislocations forming the grain boundary and the 2D channel on it.[8,9]

Of course, this is by no means a complete list of cases leading to the problem of the spectrum of electronic states in a 2D quantum well with periodically varying parameters. The bibliography on this problem is large, since it includes an enormous number of works on waveguide theory. This is because the formulations of problems mathematically for electronic, electromagnetic, and acoustic wave processes are in many respects equivalent. Investigations of wave processes in bounded periodic media have been conducted to greater extent in the theory of electromagnetic and acoustic waveguides.[10–13]

Investigations of this problem for an electronic system as well as for waveguides have focused primarily on wave processes near Bragg resonances, since it was assumed that the most effective interaction of waves with a lattice occurs only in this energy range. The problem was usually solved in the approximation of the coupled-mode equation,[14,15] describing the behavior of a system near Bragg resonances. This approximation has been used quite often to investigate wave processes in bounded periodic structures.[11–15] Much less attention has been devoted to the study of the behavior of a system at energies below the energy of a Bragg resonance, since it was assumed that the interaction of waves with a lattice at these energies is weak and it results only in a negligible shift of the 2D levels.[16–18]

However, the present analysis of the problem in the multimode approximation shows that resonances of a different, non-Bragg type, caused by the interaction of modes of various spatial harmonics of the electron wavefunction, arise in the indicated energy range. These resonances substantially alter the spectrum of a 2D system, and therefore they lead to the appearance of qualitatively new physical properties of the resonances, creating prerequisites for expanding the functional possibilities of microelectronics devices employing such 2D structures.

The electronic states for a half-space bounded by a similar periodically uneven boundary are analyzed in Refs. 19 and 20.

1. INITIAL EQUATIONS

We shall investigate the electronic states in an infinitely deep potential well of width d, where one wall has one-dimensional periodic corrugations described by the function $y(x)=\xi\cos(qx)\equiv y_0(x)$, where $q=2\pi/a$ and ξ and a are the amplitude and period of the corrugations. Thus, an electron is in a well bounded by a two-dimensional potential $U(x,y)$

$$U(x,y)=\begin{cases}0, & d>y>y_0(x),\\ \infty, & y\geqslant y_0(x), \quad y\leqslant d.\end{cases} \tag{1}$$

The wave functions $\Psi(x,y,z)$ and the energies E of the electron are found by solving the three-dimensional stationary Schrödinger equation

$$\Delta\Psi+\frac{2m}{\hbar^2}[E-U(x,y,z)]\Psi=0 \tag{2}$$

together with boundary conditions at both boundaries

$$\Psi(x,y_0(x),z)=\Psi(x,d,z)=0. \tag{3}$$

Since the boundary is periodic, we shall seek the solution in the form of a Fourier series

$$\Psi=\sum_n (a_n\cos(k_y y)+b_n\sin(k_y y))$$
$$\times\exp[i(k_x+nq_z)x+ik_z z], \tag{4}$$

where k_x, k_y, and k_z are the components of the electron wave vector $\mathbf{k}$. From the Schrödinger equation and Eq. (4) follows a relation between E and $\mathbf{k}$

$$k_{yn}^2=\frac{2\pi E}{\hbar^2}-(k_x+nq_x)^2-k_z^2, \tag{5}$$

and the boundary conditions (3) impose a relation between the quantities k_x, k_z, and k_{yn}, thereby determining the dispersion $E(\mathbf{k})$ of a particle.

Substituting $\Psi(x,y_0(x),z)$ and $\Psi(x,d,z)$ into the boundary conditions, we obtain a system of linear algebraic equations for the coefficients a_n and b_n. Equating to zero the determinant of this system permits finding the allowed values of k_{yn}. For small corrugations $\xi/d\ll 1$, $\xi d\ll 1$, it is sufficient to retain the first ten harmonics a_0, b_0, $a_{\pm 1}$, and $b_{\pm 1}$, and so on, neglecting harmonics $\sim\xi^2$. As a result, we obtain the following characteristic equation for the allowed values of k_{yn}:

$$\tan(dk_0)=\frac{\xi^2}{4}\left\{\frac{k_0k_{-1}}{\tan(dk_{-1})}+\frac{k_0k_1}{\tan(dk_1)}+\tan(dk_0)\right.$$
$$\left.\times\left[\frac{k_1k_2}{\tan(dk_1)\tan(dk_2)}+\frac{k_{-1}k_{-2}}{\tan(dk_{-1})\tan(dk_{-2})}\right]\right\}. \tag{6}$$

In Eq. (6) and below we drop the index y in the wave numbers k_{yn}. We shall seek the solution of Eq. (6) by the method of successive approximations with respect to ξ,[19] i.e. $k_0=k_0^0+\delta k_0+\ldots$. For $\xi=0$ we have from Eq. (6) $\tan(dk_0)=0$ and therefore

$$k_0^0=\frac{s\pi}{d}\equiv k_{0s}, \quad s=1,2,3\ldots,$$

$$E=E_s+\frac{\hbar^2(k_x^2+k_z^2)}{2m}, \quad E_s=\frac{\hbar^2s^2\pi^2}{2md^2}. \tag{7}$$

These are well-known 2D subbands in a smooth quantum well.

In the next approximation, for $\xi\neq 0$, we obtain the desired quantity δk_0, which will describe the effect of a periodic boundary.

We shall seek the solution of Eq. (6) in individual ranges of variation of the wave number k_x. First, we examine the region $k_x=k_z=0$, i.e. the shift of the energy levels will be found. Next, for small k_x ($k_x\ll q$) we describe the change in the spectrum in terms of the effective mass, and finally, in the most interesting and important case, $k_x\sim d$, $k_x\sim q$, the resonance of standing electronic waves and the miniband character of the electron spectrum will be described.

2. SHIFT OF THE ENERGY LEVELS

For $k_x=k_z=0$ the characteristic equation (6) becomes

$$\tan(dk_0)=\frac{\xi^2}{2}k_1\cot(dk_1)[k_0+k_2\tan(dk_0)\cot(dk_2)],$$

$$k_1=\sqrt{k_0^2-q^2}, \quad k_2=\sqrt{k_0^2-4q^2}. \tag{8}$$

Substituting into the right-hand side of this equation the zeroth-order solution (7), we find the corrections δk_0 to the wave numbers and the new positions of the energy levels. The behavior of the system is qualitatively different in the regions $k_0>q$. For $k\leqslant q$ we have

$$\delta k_{0s}=\frac{\xi^2}{2d}k_{0s}k_{1s}\coth(dk_{1s}), \quad k_{1s}=\sqrt{q^2-k_{0s}^2},$$

$$E=E_s\left[1+\frac{\xi^2}{d}k_{1s}\coth(dk_{1s})\right]. \tag{9}$$

For $k_0>q$ the corresponding formulas are

$$\delta k_{0s}=\frac{\xi^2}{2d}k_{0s}k_{1s}\cot(dk_{1s}), \quad k_{1s}=\sqrt{k_{0s}^2-q^2},$$

$$E=E_s\left[1+\frac{\xi^2}{d}k_{1s}\cot(dk_{1s})\right]. \tag{10}$$

The qualitative difference in the solutions for the regions $k_0\leqslant q$ and $k_0>q$ is due to the fact that for $k_0\leqslant q$ the wave number $k_{\pm 1}$ of the first harmonic is an imaginary number. The harmonic is a nonuniform wave; it leads to a shift of the energy level but does not contribute to interference phenomena. For $k_0>q$ the wave number k_1 becomes real, and the harmonic under consideration describes a wave process, which, as one can see from Eqs. (10) and (8), assumes a resonance character for $k_{1s}=r\pi$, $r=1, 2, 3, \ldots$. If the geometric dimensions of the quantum well are such that for a certain quantum state s, the relation $k_{1s}=r\pi$ or, expressed in terms of the geometric dimensions of the well,

$$(2d/a)^2=s^2-r^2, \quad s>r \tag{11}$$

is satisfied for any integer r, then such an s-th electronic state is a resonance state. Equation (8) reduces in this case to a quadratic equation, and its solution describes the splitting of this energy level into two levels

$$E^{\pm}=E_s\left(1\pm\sqrt{2}\frac{\xi}{d}\frac{r}{s}\right), \tag{12}$$

the splitting being determined by the relation

$$\delta E=2\sqrt{2}\frac{\xi}{d}\frac{r}{s}E_s. \tag{13}$$

We underscore once again that the resonance state (12) arises for a quantum well with specially chosen geometric dimensions, satisfying the relation (11). For arbitrary dimensions of the well such a state will not arise.

3. REGION OF SMALL k_x, $k_x \ll k_{1s}$

If the expression (6) is expanded in powers of the small parameter, then using Eqs. (8)–(10) we obtain the dispersion law near a minimum of the s-th 2D subband in the form

$$E(k_x,k_z)=E_s\left[1+\frac{\xi^2}{d}k_{1s}\coth(dk_{1s})\right]+\frac{\hbar^2k_x^2}{2m^*}+\frac{\hbar^2k_z^2}{2m}. \tag{14}$$

The effect of a periodic boundary reduces to changing the electron mass, which now depends not only on the period of the corugations but also on the width of the quantum well

$$m^*=m\left\{1-\frac{\xi^2q^2k_{0s}^2}{2k_{1s}^2}\left[\frac{dk_{1s}}{\tanh(dk_{1s})}\left(\frac{1}{\sinh^2(dk_{1s})}+\frac{1}{d^2k_{1s}^2}\right)-\frac{3}{2}\,\frac{1}{\sinh^2(dk_{1s})}\right]\right\}. \tag{15}$$

As expected, the effective mass m^* is less than the free-electron mass, since the expression in brackets in Eq. (15) is always positive.

In the resonance case (11) the effective mass becomes much smaller

$$m^*=m\left(1-\frac{8}{15}\xi^2q^2k_{0s}^2d^2\right), \quad k_xqd^2\ll 1, \tag{16}$$

because of the more effective interaction of the electron with the periodic boundary in the resonance case.

4. RESONANCE REGION, $k_x \sim d$, $k_x \sim q$

We shall now analyze the characteristic equation (6) in the resonance region. In the zeroth-order approximation with the wave numbers $k_{\pm 1}$, appearing on the right-hand side of Eq. (6), can be written as

$$k_{\pm 1}=\sqrt{\frac{s^2\pi^2}{d^2}\mp 2k_xq-q^2}. \tag{17}$$

It is evident from Eqs. (6) and (17) that for $k_x=\pm q/2$ the conventional Bragg resonances, the same as resonances in unbounded periodic structures, arise in all 2D subbands. For this reason, we shall not dwell on this, but rather we shall investigate the properties which are due to particle motion in the y direction.

As is evident from Eqs. (6) and (17), the general condition for resonances is

$$k_\pm=\frac{l\pi}{d}, \quad l=1,2,3\ldots. \tag{18}$$

Comparing Eqs. (7) and (18) shows that these conditions express a resonance of standing waves, which are different modes of the zeroth and first spatial harmonics of the electron wave function.

Substituting expression (17) into Eq. (18) we find the values of the wave numbers $k_x^\pm$ for which standing wave resonances arise between the zeroth and $n=+1$ or $n=-1$ harmonics, respectively,

$$k_x^\pm=\mp\frac{q}{2}(1+\gamma_{sl}), \quad \gamma_{sl}=\frac{(l^2-s^2)\pi^2}{(dq)^2}. \tag{19}$$

The quantity γ_{sl} depends on the parameters d and a of the potential well and the quantum numbers s and l, and it can vary over a wide range of positive and negative numbers. In this connection, the resonances $k_x^\pm$ can assume the values $k_x^\pm\to 0$ as $\gamma_{sl}\to -1$, in contrast to Bragg resonances, for which $k_x^\pm=\mp q/2$ are fixed. Near resonances Eq. (6) reduces to the quadratic equation

$$\delta k_0^2-\frac{\xi^2}{4d^2}\left(\frac{l\pi}{d}\right)^2=0, \tag{20}$$

which gives two roots

$$\delta k_0^\pm=\pm\frac{\xi}{2d}\,\frac{l\pi}{d}. \tag{21}$$

The solution (21) describes the splitting of the spectrum at resonance into two levels E_{sl}^+ and E_{sl}^-

$$E_{sl}^\mp=E_s\left(1\pm\frac{\xi}{d}\,\frac{l}{s}\right)+E_B(1+\gamma_{sl})^2+\frac{\hbar^2k_z^2}{2m} \tag{22}$$

and the appearance of a gap δE_{sl}

$$\delta E_{sl}=E_{sl}^+-E_{sl}^-=2\frac{\xi}{d}\,\frac{l}{s}\,\frac{\hbar^2k_{0s}^2}{2m}. \tag{23}$$

In the expression (22), the notation $E_B=\hbar^2q^2/8m$ has been introduced. In Eqs. (18)–(23) the number l is the number of the resonance for the s-th 2D subband.

It is evident from Eq. (22) that for $\gamma_{sl}\to -1$ and $k_z=0$ the resonance energies measured from the bottom in each 2D subband vanish, i.e., the resonances occur in a wide range of energies, starting with zero.

The gap width ΔE corresponding to the energy range between l and $l+1$ resonances in the s-th 2D subband can be found from Eq. (22) as

$$\Delta E=\frac{2(2l+1)\pi^2E_B}{(qd)^2}\left\{1+\frac{\pi^2|l^2+(l+1)^2-2s^2|}{2(qd)^2}\right\}. \tag{24}$$

It is evident from Eqs. (23) and (24) that the energy spectrum of electrons in a quantum well with a periodic boundary assumes a miniband character resembling a Wannier–Stark ladder.[21] For a wide well, $qd\gg 1$, the width of one miniband is small $\Delta E\ll E_B$, i.e. there will be a large number of minibands in the energy range $0-E_B$.

The investigation performed above shows that, in a two-dimensional quantum well having a periodically corrugated wall with low amplitudes of the corrugations, the electron wave function can be represented as a superposition of three spatial harmonics. Each harmonic is characterized by longitudinal k_x and transverse k_y wave numbers. In contrast to a smooth quantum well, where k_x and k_y are quantum numbers, in a corrugated well k_x and k_y are related with one another by the characteristic equation (6).

The wave numbers k_{0y} and $k_{\pm 1}$, corresponding to the zeroth and first harmonics, respectively, can assume quasidiscrete values, determined by the solution of the characteristic equation (6). These values k_{yn} determine the set of partial states of an electron in a quantum well with a periodically corrugated boundary.

The wave number k_{0y} deviates negligibly from the discrete values assumed in a smooth quantum well. The wave number $k_{\pm 1y}$ of the first harmonic varies over wide limits, assuming real and imaginary values as k_x varies.

For certain values of k_x the wave numbers k_{0y} and $k_{\pm 1y}$ can be equal to one another. In this case, a resonance interaction of the corresponding partial waves arises. Since the electronic states in the direction of the y axis are described by standing waves, this resonance is a resonance of partial standing waves. The de Broglie wavelength associated with the motion of an electron in the direction of the y axis is determined by the corresponding value of k_{yn}. A resonance arises between states for which the quantum well width d is a multiple simultaneously (with different integers) of de Broglie half-wavelengths associated with both k_{0y} and $k_{\pm 1y}$. These resonances lead to splitting of the energy levels with the corresponding values of the wave numbers k_x and the appearance of gaps. Thus, the spectrum of each 2D subband is divided into minibands, which substantially changes the physical properties of the electron gas in such a quantum well.

*⁾E-mail: vpog@ire.kharkov.ua

---

[1] T. Ando, A. B. Fowler, and F. Stern, Rev. Mod. Phys. **5**, 437 (1982).

[2] V. M. Loktev, Fiz. Nizk. Temp. **22**, 3 (1996) [Low Temp. Phys. **22**, 1 (1996)].

[3] *The Quantum Hall Effect*, edited by R. Prange and S. Girvin (Spinger-Verlag, New York, 1987).

[4] S. J. Allen, D. C. Tsui, and R. A. Logan, Phys. Rev. Lett. **38**, 980 (1977).

[5] T. N. Theis, J. P. Kotthaus, and P. J. Stiles, Solid State Commun. **26**, 603 (1978).

[6] D. C. Tsui, E. Gornik, and R. A. Logan, Solid State Commun. **35**, 875 (1986).

[7] N. L. Boborov, L. F. Rybal'chenko, V. V. Fisun, I. K. Yanson, O. A. Mironov, S. V. Chistyakov, V. V. Sorchenko, A. Yu. Sipatov, and A. I. Fedorenko, Fiz. Nizk. Temp. **16**, 1531 (1990) [Sov. J. Low Temp. Phys. **16**, 862 (1990)].

[8] V. A. Pogrebnyak, D. D. Khalameĭda, and V. M. Yakovenko, JETP Lett. **46**, 210 (1987).

[9] V. A. Pogrebnyak, I. M. Rarenko, D. D. Khalameĭda, and V. M. Yakovenko, Fiz. Tekh. Poluprovodn. **32**, 319 (1998) [Semiconductors **32**, 288 (1998)].

[10] B. Z. Katsenelenbaum, *Theory of Irregular Waveguides with Slowly Varying Parameters* (Soviet Academy of Sciences, Moscow, 1961).

[11] D. Marcuse, *Integrated Waveguides* (IEEE Press, New York, 1973; Mir, Moscow, 1974).

[12] S. Solimenko, B. Krozin'yani, and P. di Porto, *Diffraction and Wave Propagation of Optical Radiation* (Mir, Moscow, 1989).

[13] *Integrated Optics*, edited by T. Tamir (Springer-Verlag, Berlin, 1975; Mir, Moscow, 1978).

[14] S. E. Miller, Bell Syst. Tech. J. **33**, 661 (1954).

[15] H. Kogelnik, Bell Syst. Tech. J. **48**, 2909 (1969).

[16] T. Tamir, H. C. Wang, and A. A. Oliner, IEEE Trans. Microwave Theory Tech. **12**(3), 323 (1964).

[17] C. Elachi and C. Yeh, J. Appl. Phys. **45**(8), 3494 (1974).

[18] V. F. Borul'ko, Radiotekh. Elektron. **30**, 1873 (1985).

[19] V. A. Pogrebnyak, V. M. Yakovenko, and I. V. Yakovenko, Phys. Lett. A **209**, 103 (1995).

[20] V. A. Pogrebnyak, V. M. Yakovenko, and I. V. Yakovenko, Fiz. Tverd. Tela (St. Petersburg) **39**, 1875 (1997) [Phys. Solid State **39**, 1677 (1997)].

[21] G. H. Wannier, *Elements of Solid State Theory* (Cambridge University Press, London, 1959).

Translated by M. E. Alferieff

Radiation-induced conduction in quantum-confined p^+-n silicon junctions

A. N. Andronov and S. V. Robozerov

St. Petersburg State Technical University, 195251 St. Petersburg, Russia

N. T. Bagraev, L. E. Klyachkin, and A. M. Malyarenko

A. F. Ioffe Physicotechnical Institute, Russian Academy of Sciences, 194021 St. Petersburg, Russia

(Submitted March 22, 1999)
Fiz. Tverd. Tela (St. Petersburg) **41**, 1871–1874 (October 1999)

Electron-beam diagnostics are used to study the radiation-induced conduction of supershallow p^+-n silicon junctions obtained by nonequilibrium boron diffusion. Current–voltage $(I-V)$ characteristics of radiation-induced conduction of a both forward- and reverse-biased p^+-n junction are demonstrated for the first time, which has been made possible by the presence of self-organized transverse quantum wells inside a supershallow p^+ diffusion profile. The variation of the dark-current $I-V$ characteristics with electron irradiation dose shows that formation of self-organized longitudinal quantum wells inside supershallow p^+ diffusion profiles favors an increase of the breakdown voltage in p^+-n silicon junctions. © *1999 American Institute of Physics.* [S1063-7834(99)03210-4]

Application of dopant drag by excess fluxes of vacancies or intrinsic interstitials generated efficiently near the $\mathrm{Si-SiO_2}$ interface to silicon planar-diffusion technology made possible creation of supershallow (5–20 nm) boron diffusion profiles on n-type Si(100) and Si(111) surfaces.[1] As follows from the angular dependences of the optically induced electron and hole cyclotron resonance, as well as from $I-V$ characteristics obtained in a crystallographically oriented electric field, supershallow p^+ diffusion profiles represent various combinations of transverse (Fig. 1a) and/or longitudinal (Fig. 1b) self-organized n- and p-type quantum wells between δ-doped barriers $[N(\mathrm{B})\approx 10^{21}\,\mathrm{cm}^{-3}]$, which form, accordingly, perpendicular or parallel to the p^+-n junction plane, depending on the actual stimulated impurity-diffusion mechanism.[2,3] Studies of the $I-V$ characteristics of quantum-confined conduction revealed that self-organized quantum wells transform in a longitudinal electric field into a system of dynamic quantum wires due to electrostatic ordering of the $\mathrm{B^+-B^-}$ impurity dipoles with negative correlation energy, which, as follows from ESR and thermopower investigations, make up predominantly δ-doped diffusion barriers.[2,3] Such dynamic quantum wires with isolated quantum dots served as a basis for fabricating transistor structures possessing various single-hole localization and transport effects.[2] Besides, diffusion-produced superlattices made up of quantum-confined p^+-n junctions (Fig. 1) are of considerable interest for development of IR silicon lasers operating on intraband transitions,[3,4] as well as for studies of the effect of self-organized nanostructures on radiation-induced conduction in both forward- and reverse-biased p^+-n junctions, which was the objective of the present work and which is impossible in principle when using continuous $p-n$ junctions.

The starting material for fabricating supershallow p^+-n junctions was 350-μm thick n-Si(111) single-crystal plates with a resistivity $\rho\cong 90\,\Omega\cdot\mathrm{cm}$. The process started by oxidizing both sides of a plate in dry oxygen at 1150 °C, followed by making photolithographically dia. 3-mm circular windows in the oxide layer on the working side of the plate, into which boron was diffused for a short time (4 min) from the gas phase. The diffusion temperature was varied (800, 900, and 1100 °C) in the course of the investigation at a constant thickness of the predeposited oxide layer, which

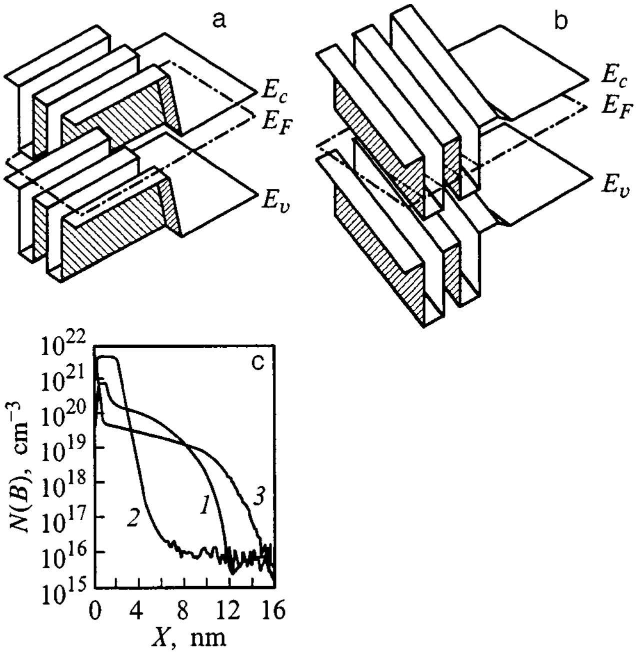

FIG. 1. Three-dimensional image of one-electron band diagram of supershallow p^+-n junctions consisting of (a) transverse and (b) longitudinal quantum wells. (c) Boron concentration profiles in p^+-n silicon junctions prepared at diffusion temperatures (°C): *1* — 800, *2* — 900, *3* — 1100 on (111)Si doped by phosphorus to a concentration $N(\mathrm{P})=5\times 10^{13}\,\mathrm{cm}^{-3}$.

permitted simulation of the conditions prevailing in the impurity-diffusion vacancy mechanisms.[1,5] Note that the thickness of the predeposited oxide on both sides of the plate was in excess of $d_0 \cong 0.44\,\mu$m, thus stimulating additional vacancy injection from the Si–SiO$_2$ interface during the impurity diffusion.[1] Besides, the high concentration of the nonequilibrium vacancies responsible for the dopant drag effects was provided in the course of diffusion by additionally feeding dry oxygen and chlorine-containing compounds into the boron-containing gas phase. In the final stage of the technological process, ohmic contacts were produced around the perimeter of the windows and on the back side of the plate. The dopant concentration profiles were measured by SIMS (Fig. 1c).[6]

When diffused at $T_{\mathrm{dif}} = 800\,°$C, boron penetrates into silicon by silicon vacancy drag, whereas at $T_{\mathrm{dif}} = 1100°$C impurity diffusion is stimulated by exchange interaction of the dopant with silicon interstitials (the kick-out mechanism[5]). In both cases one observes acceleration of the impurity diffusion process (see curves *1* and *3* in Fig. 1c). Boron diffusion is seen to slow down abruptly at the diffusion temperature $T_{\mathrm{dif}} = 900\,°$C (curve *2* in Fig. 1c), where the rates of the above diffusion mechanisms become comparable because of intensive annihilation of interstitials and vacancies in the vicinity of working surface of the silicon plate.[1–3] The shape of the diffusion depth profiles obtained under short-term nonequilibrium diffusion differs from the classical one. Note that extremely steep boron profiles are observed both in the case of suppressed impurity diffusion and under its acceleration, which implies a fractal mechanism of diffusion doping under conditions of strong interaction of the impurity with intrinsic defect flows, whose intensity is determined by the shape of the deformation potential at the Si–SiO$_2$ interface.[1,5]

The small depth of the p^+ diffusion profile (5–20 nm) in supershallow p^+-n junctions makes the use of a focused electron beam probing the near-surface region by low- and medium-energy electrons attractive for the investigation of radiation-induced conduction.[7] By varying properly the electron-beam energy E_p within the range of 0.1 to 3.0 keV, one can change smoothly the probing depth from 2 to 250 nm.[7] To separate the dark from induced current, $I-V$ measurements of the radiation-induced conduction coefficient were carried out under sine modulation of the primary electron beam at a frequency of 1 kHz. As shown by reference dc experiments, at such frequencies the radiation-induced conduction coefficient γ does reach its steady-state level.[7]

Figure 2 presents $I-V$ curves of the radiation-induced conduction of supershallow p^+-n junctions fabricated at low boron-diffusion temperatures on an *n*-type Si(111) surface. The $I-V$ curve of radiation-induced conduction of a p^+-n junction prepared at $T_{\mathrm{dif}} = 900\,°$C is seen to be obtained only under reverse bias. Note that the γ coefficient depends on neither the primary current nor the bias voltage. When measured under forward bias, the radiation-induced conduction current drops sharply to zero as a result of intensive nonequilibrium-carrier recombination at the p^+-n junction boundary (curve *6* in Fig. 2).

An unexpected result was obtained when taking an $I-V$ curve of radiation-induced conduction of a p^+-n junction prepared at the diffusion temperature $T_{\mathrm{dif}} = 800\,°$C. In this case the radiation-induced conduction is observed to occur under both reverse and forward bias, and it does not decrease even when a current of the order of 10 mA flows through the conducting diode, which implies a substantial increase of the excited-carrier lifetime (curves *1–5* in Fig. 2). Such a decrease of recombination efficiency could be due to the electron and hole flows becoming spatially separated by the presence of self-organized transverse quantum wells (Fig. 1a). As shown by studies of the angular dependences of the electron and hole cyclotron resonance, as well as of the crystallographically dependent hole conduction,[2,3] the p^+ diffusion profiles obtained in the conditions of dominant vacancy diffusion mechanisms ($T_{\mathrm{dif}} = 800\,°$C) do indeed consist of transverse quantum wells, whereas longitudinal quantum wells were found to exist inside p^+-n Si junctions fabricated under equally competing kick-out and vacancy impurity-diffusion mechanisms, a condition reached at $T_{\mathrm{dif}} = 900\,°$C (Fig. 1b). The presence of transverse quantum wells reduces the dark current (curve *1* in Fig. 3a) because of the formation of natural channels for nonequilibrium carriers (Fig. 1a), while at the same time favoring spatial separation of excited electrons and holes across the p^+-n junction plane. Therefore the radiation-induced conduction of p^+-n junctions containing self-organized transverse quantum wells can be detected under both forward and reverse bias (curves *1–5* in Fig. 2). The potential relief, which is due to the transverse quantum wells and is responsible for such electron and hole spatial separation, can become smoothened out with increasing current as a result of the ohmic drop at the p^+-n junction interface, which should become particularly manifest in

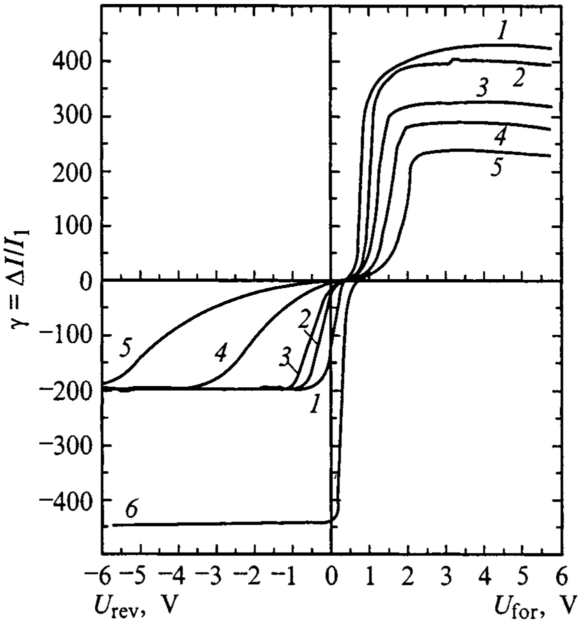

FIG. 2. $I-V$ characteristics of the radiation-induced conduction coefficient γ of p^+-n junctions prepared at diffusion temperatures of 800 and 900 °C on (111)Si doped by phosphorus to a concentration $N(\mathrm{P}) = 5 \times 10^{13}\,\mathrm{cm}^{-3}$: $\gamma = \Delta I / I_1$, where $\Delta I = I - I_1$ and I is the radiation-induced current. *1–5* — $T_{\mathrm{dif}} = 800\,°$C, primary current I_1, μA: *1* — 0.5, *2* — 1.0, *3* — 1.9, *4* — 5.0, *5* — 10; *6* — $T_{\mathrm{dif}} = 900\,°$C, primary current $I_1 = 1.0\,\mu$A.

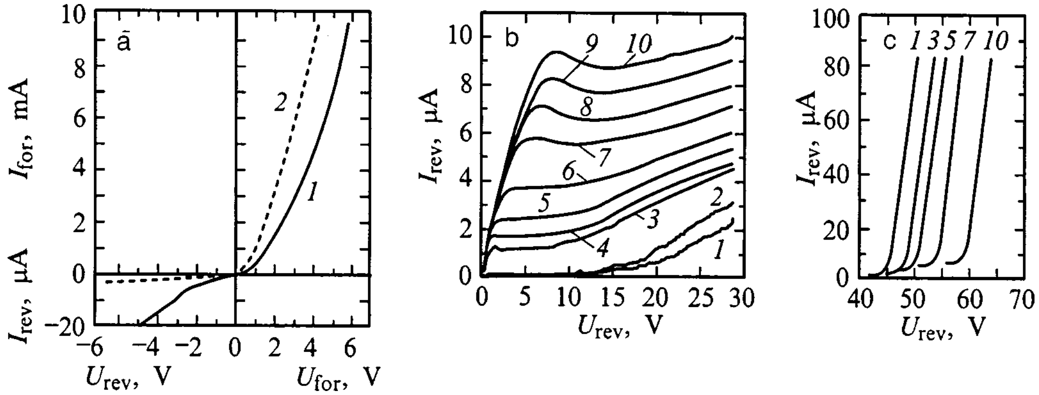

FIG. 3. $I-V$ characteristics of the p^+-n junctions prepared at diffusion temperatures (a) 800 °C and (a,b,c) 900 °C on (111)Si doped by phosphorus to a concentration $N(\mathrm{P})=5\times10^{13}\,\mathrm{cm}^{-3}$. (a) Original I-V characteristics: *1* — $T_{\rm dif}=800\,°$C, *2* — $T_{\rm dif}=900\,°$C; (b,c) reverse $I-V$ branches after 2-keV electron-beam irradiation; (c) p^+-n junction breakdown region. Irradiation dose $\Phi\times10^{-20}\,(\mathrm{cm}^{-2})$: *1* — 3, *2* — 6.6, *3* — 8.2, *4* — 9.4, *5* — 12.6, *6* — 14.4, *7* — 16.0, *8* — 17.2, *9* — 22.0, *10* — 28.4.

structures with a high-resistance substrate. Indeed, a forward-biased p^+-n junction exhibits a decrease of γ with increasing primary current I_1, starting with the level at which the excited-carrier current ΔI becomes comparable to the dark current, which evidences an increase in the rate of carrier recombination (Fig. 2). At the same time, in the case of a reverse-biased p^+-n junction, with no majority-carrier current present, the radiation-induced conduction coefficient does not depend on the primary current, which affects only the voltage corresponding to saturation of the radiation-induced $I-V$ curve (see curves *1–5* in Fig. 2).

Supershallow p^+-n silicon junctions made up of longitudinal quantum wells are characterized by low dark currents (curve *2* in Fig. 3a) because of the presence of intrinsic potential barriers for minority carriers (Fig. 1b). However no spatial separation of excited electrons and holes takes place in this case across the p^+-n junction plane, which results in a sharp vanishing of radiation-induced conduction through a forward-biased p^+-n junction (curve *6* in Fig. 2). An essential factor accompanying the formation of self-organized longitudinal quantum wells is the creation of an internal longitudinal electric field (Fig. 1b), which, as shown by studies of the cyclotron resonance and $I-V$ characteristics of quantum-confined conduction,[2,3] is caused by dopant distribution fluctuations at the quantum-well boundaries and is conducive to spatial separation of electrons and holes along the p^+-n junction plane. Under conditions in which an electron beam generates nonequilibrium electrons and holes, the internal electric field may grow gradually in strength, which accounts for the increase of the dark current and breakdown voltage with increasing irradiation dose (Fig. 3b and 3c).

Thus electron irradiation has been used to study $I-V$ characteristics of radiation-induced conduction through self-organized quantum wells, which form spontaneously in the course of fabrication of supershallow p^+-n silicon junctions under nonequilibrium impurity diffusion. $I-V$ characteristics of radiation-induced conduction were observed to exist under both forward and reverse bias of a p^+-n junction consisting primarily of transverse quantum wells which stimulate spatial separation of nonequilibrium electrons and holes perpendicular to the p^+-n junction plane, while longitudinal quantum wells inside supershallow p^+ diffusion profiles favor the onset of radiation-induced conduction only through a reverse-biased p^+-n junction because of the electrons and holes becoming spatially separated along the p^+-n junction plane.

Support of the projects “Physics and Technology of Nanostructures” (Grant 97-1040), “Promising Technologies for Nanoelectronics” (Grant 02.04.301.89.5.2), and “Integration” (Grant 75:2.1) is gratefully acknowledged.

[1] N. T. Bagraev, W. Gehlhoff, L. E. Klyachkin, and A. Näser, Defect Diffus. Forum **143-147**, 1003 (1997).
[2] N. T. Bagraev, I. E. Klyachkin, A. M. Malyarenko, and W. Gehlhoff, Superlattices Microstruct. **23**, 1333 (1998).
[3] N. T. Bagraev, E. I. Chaikina, L. E. Klyachkin, I. I. Markov, and W. Gehlhoff, Superlattices Microstruct. **23**, 338 (1998).
[4] N. T. Bagraev, E. I. Chaikina, W. Gehlhoff, L. E. Klyachkin, I. I. Markov, and A. M. Malyarenko, Solid-State Electron. **42**, 1199 (1998).
[5] W. Frank, U. Gösele, H. Mehrer, and A. Seeger, *Diffusion in Crystalline Solids* (Academic, New York, 1984), p. 63.
[6] P. S. Zalm, Rep. Prog. Phys. **58**, 1321 (1995).
[7] A. N. Andronov, N. T. Bagraev, L. E. Klyachkin, and S. V. Robozerov, Fiz. Tekh. Poluprovodn. **32**, 137 (1998) [Semiconductors **32**, 124 (1998)].

Translated by G. Skrebtsov

Total-current spectroscopy of layered rare-metal dichalcogenides under electron excitation

S. A. Komolov

Institute of Physics, St. Petersburg State University, 198904 St. Petersburg, Russia

O. F. Panchenko*) and L. K. Panchenko

Donetsk Physicotechnical Institute, Ukrainian Academy of Sciences, 340114 Donetsk, Ukraine

(Submitted March 10, 1999)
Fiz. Tverd. Tela (St. Petersburg) **41**, 1875–1878 (October 1999)

A theoretical interpretation is given of the fine structure in the total-current spectra obtained from the (0001) plane of MoS_2, ZrS_2, and $NbSe_2$ single crystals. The calculations took into account the energy dependences of band energy-level broadening and of the density of unfilled electronic states which become occupied by electrons entering a solid. The dominant contribution of the bulk band structure to the spectra is demonstrated. © *1999 American Institute of Physics.* [S1063-7834(99)03310-9]

Comprehensive investigation of near-surface phenomena has been made possible by the recent development of new experimental methods and of devices capable of determining the composition of a substance and its geometric and electronic structure. Among these methods is the low-energy total-current spectroscopy, which possesses a high surface sensitivity and is non-destructive.[1–6] An experimentally measured spectrum is the derivative of the total (integrated) current in the sample circuit with respect to primary electron (PE) energy obtained under the condition of total secondary-electron detection.[7,8] Besides the traditional application to the analysis of elementary excitations and near-surface states in a solid, this method is used presently to monitor surface cleanness during purification from impurities,[9] for studies of the photovoltaic effect in thin films on the surface of semiconductors,[10] and so on. The physical nature of the fine structure in total-current (TC) spectra is determined by the mechanisms of low-energy electron interaction with the surface of a solid. Theoretical analysis of the fine structure in TC spectra encounters difficulties because of the need to take into account the diverse nature of the physical processes occurring in the near-surface region of crystals. The main features in the fine structure are believed to be connected primarily with the bulk band structure of the crystal.[5,6] This conclusion is supported by theoretical calculations invoking the dynamic theory of low-energy electron diffraction (LEED).[4]

The specific features of the crystal and electronic structure produce a number of unique properties in rare-metal dichalcogenides, as a result of which the materials based on these compounds do not have analogs and cannot be equivalently replaced. Among these substances are layered binary compounds with strongly anisotropic atomic interactions, which accounts for their anomalous behavior and the diverse nature of many of their properties, specifically of the structure of the intrinsic energy levels, such as the fine structure, splitting, overlap, and mutual position in **k** space. The numerous theoretical band-structure calculations of the rare-metal dichalcogenides are contradictory (particularly in what concerns the conduction-band structure) and do not offer a detailed explanation of the nature of the experimentally established features in optical and photoemission (PE) spectra. The band widths and gaps quoted in different papers differ by several times. In connection with this, investigation of TC spectra of rare-metal dichalcogenides appears to be of a certain interest, because data on the threshold characteristics of transition excitation in these elements permit one to obtain new information on the electronic properties of strongly hybridized *d*, *p*, and *s* states.

The present work aims to investigate and interpret the fine structure in TC spectra of layered rare-metal dichalcogenides based on their bulk band structure, and develop a data processing technique to extract as much information as possible on electron dispersion above the vacuum level E_{vac}. The samples studied were $2H-MoS_2$, $2H-ZrS_2$, and $2H-NbSe_2$ single crystals, which possess hexagonal structure with trigonal-prismatic coordination. ZrS_2 has the highest ionicity (it is an ionic crystal with $4d^2 5s^2$ electronic configuration of the Zr outer shells), MoS_2 is a low-ionicity covalent crystal (Mo configuration $4d^5 5s$), and $NbSe_2$ is a semimetal ($4d^4 5s$ in Nb) with metallic-type bonding.

The TC spectra were measured in superhigh vacuum [the residual gas pressure in the working chamber $\sim(0.5-1)\times 10^{-7}$ Pa]. A detailed description of the method can be found in Refs. 1 and 6, The width of the secondary-electron energy distribution was ~ 0.5 eV, and the electron energy was modulated with a frequency ~ 400 Hz and amplitude ~ 0.1 eV. The signal proportional to the total-current derivative was isolated by lock-in detection. Prior to measurements, the samples were subjected to a prolonged high-temperature (up to 1200 K) annealing. The surface was cleaned by ion milling (0.4-keV Ar^+ ions). In the course of cleaning, one followed the evolution of TC spectra, moni-

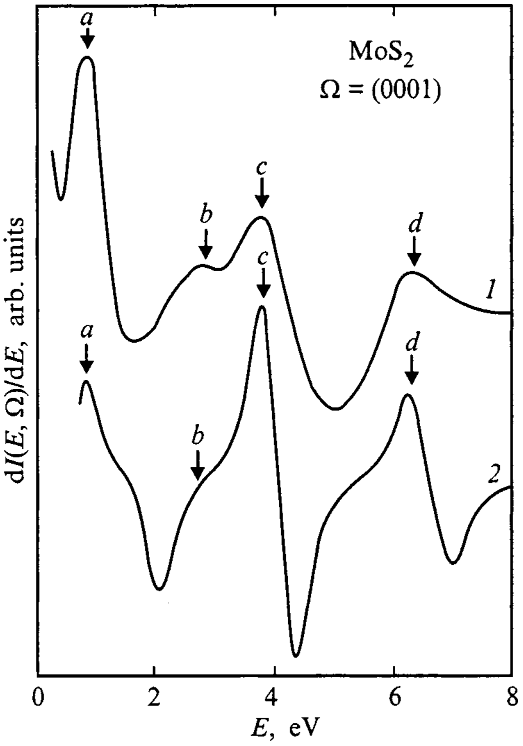

FIG. 1. TC spectra obtained along the normal to the (0001)MoS_2 plane. *1* — Experiment, *2* — theory. The curves are shifted vertically in an arbitrary manner. The energy E is reckoned from E_{vac}. The arrows with symbols identify the main features in the TC spectra.

tored the variation of the surface potential, and measured Auger electron spectra. The criterion of good surface cleaning was the reproducibility of the shape of TC spectra, of the surface potential in a series of consecutive high-temperature heatings, and the absence of Auger signals of oxygen, carbon, and other impurities. The current in the sample circuit $I=I_p-I_s$, where I_p is the primary-electron flux with energy E_p along the normal to the (0001) surface studied, and I_s is the current of the electrons leaving the sample, both elastically and inelastically scattered. Among the latter are the inelastically scattered primary electrons, highly excited electrons of the solid, Auger electrons, and the secondary electrons themselves, whose appearance depends substantially on the magnitude of E_p. For low primary-electron energies ($E_p > 10\,\mathrm{eV}$), the elastic (quasielastic) scattering (caused by electron interaction with the lattice atoms and ions) is dominant,[6] and it becomes comparable to the inelastic component for $E_p \leqslant 40\,\mathrm{eV}$. Within the energy domain of up to 100 eV, the fraction of elastic scattering is a few per cent, and it is dominated by electron-electron scattering involving excitation of interband transitions. Besides the interband transitions, the spectra may exhibit threshold characteristics of the electron-induced excitation of the solid, namely, plasma oscillations, impurity atom and vacancy states, etc. However it is the features reflecting the fundamental properties of the material under study that constitute the main structure of the spectrum.

Figures 1–3 (curves *1*) present the $dI(E,\mathbf{\Omega})/dE$ TC spectra measured on the (0001) plane of MoS_2, ZrS_2, and $NbSe_2$ single crystals, respectively. The fine-structure intensity in the spectra is $\sim 1\%$ of the maximum in the primary-electron distribution (not shown in the figures), which appears at the energy at which electrons start to impinge on the sample.

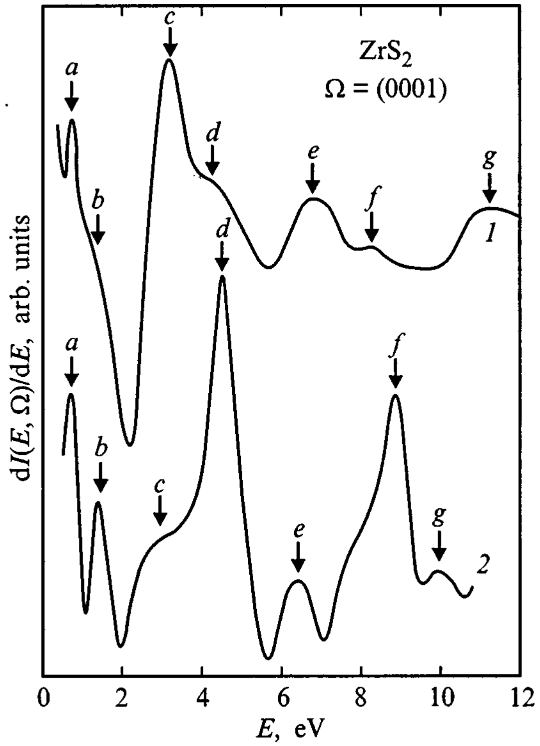

FIG. 2. Same as in Fig. 1 for the (0001)ZrS_2 plane.

Our theoretical analysis of the TC spectra obtained considered the scattering of electrons with a given momentum

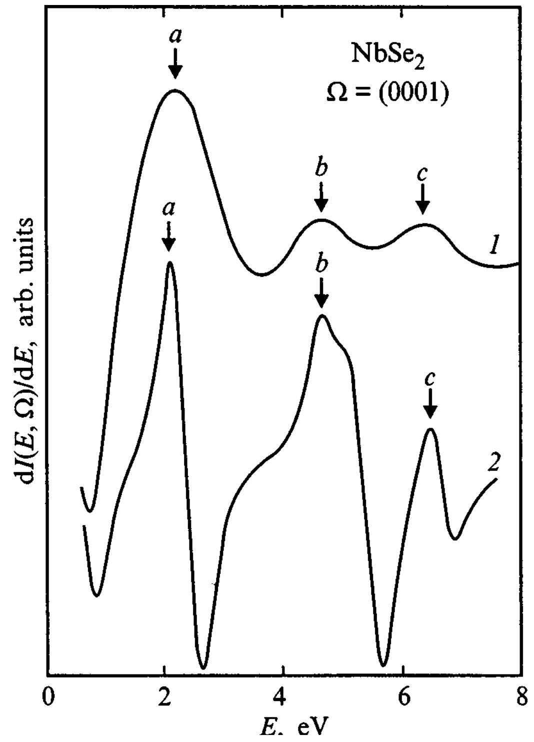

FIG. 3. Same as in Fig. 1 for the (0001)$NbSe_2$ plane.

from a crystal in an approximation where the scattering probability is proportional to the number of final states at a given energy level E with a prescribed direction of the quasimomentum $\mathbf{\Omega}$. The current through the sample can be written[11,12]

$$I(E,\mathbf{\Omega})\sim\frac{1}{V}\sum_{n\mathbf{k}}\left[1-f_F(E_{n\mathbf{k}})\right]\left|\frac{1}{\hbar}\nabla_{\mathbf{k}}E_{n\mathbf{k}}\right|\times\delta(E-E_{n\mathbf{k}})\,\delta(\mathbf{\Omega}-\mathbf{\Omega}_{n\mathbf{k}}),\qquad(1)$$

where $E_{n\mathbf{k}}$ is the electron dispersion relation, $\mathbf{\Omega}_{n\mathbf{k}}$ is the unit vector along the $\nabla_{\mathbf{k}}E_{n\mathbf{k}}$ direction, $f_F(E_{n\mathbf{k}})$ is the equilibrium Fermi–Dirac occupation function, which for $E>E_{\mathrm{vac}}$ is zero, and V is the crystal volume. Replacing the summation over $\mathbf{k}$ with integration over the constant-energy surface $E_{n\mathbf{k}}=E$ yields

$$I(E,\mathbf{\Omega})\sim\frac{1}{(2\pi\hbar)^3}\int dE'\,N(E',\mathbf{\Omega})\times\frac{1}{2\pi}\frac{\hbar\Gamma(E')}{(E-E')^2+\hbar^2\Gamma^2(E')/4},\qquad(2)$$

where $N(E,\mathbf{\Omega})$ is the number of energy bands along the $\mathbf{\Omega}$ direction for which the $E=E_{n\mathbf{k}}$ equality is met. We have taken here into account the finite width $\hbar\Gamma(E)=\hbar/\tau(E)$ of electronic levels by replacing the δ function in energy in Eq. (1) with the corresponding Lorentzian. The excited-state lifetime was determined from[13,14]

$$\hbar/\tau(E)\simeq7.23\times10^{-4}\sqrt{E-E_0}\quad(E-E_F)^2,\qquad(3)$$

where E_F is the midgap energy, and $E_0=0$ is the valence-band bottom position.

Equation (2) is valid if $\mathbf{\Omega}$ coincides with the crystal symmetry axis (under normal incidence of the electron beam on the sample). To construct the $N(E,\mathbf{\Omega})$ step function as this was done in Refs. 15–17, we used the bulk band-structure calculations of $E_{n\mathbf{k}}$ for $\mathrm{MoS_2}$, $\mathrm{NbSe_2}$ (obtained by the layer-by-layer technique in Refs. 18 and 19, respectively, which is based on the method of scattering from layers developed in LEED studies) and $\mathrm{ZrS_2}$ (obtained[20] by a self-consistent OPW method). It should be pointed out that the valence-band calculations[19] made for $\mathrm{NbSe_2}$ agree well with the PE angular dependences,[21] despite the strong line broadening (similar to the TC spectrum *1* in Fig. 3) because of the high free-electron concentration in $\mathrm{NbSe_2}$.

Taking into account surface effects, which contribute to $N(E,\mathbf{\Omega})$, can be considered in the following way. The specific features in the surface electronic spectrum of rare-metal dichalcogenides are associated with the fact that the electronic spectrum characteristic of the bulk is practically undistorted in the near-surface region, with only local states appearing on it. This is confirmed by numerous PE measurements. LEED studies showed that the bulk geometric structure of $2H-\mathrm{NbSe_2}$ persists on the surface as well, and with the same lattice parameters, whereas $2H-\mathrm{MoS_2}$ revealed compression of up to 5% of interlayer separation.[22] A study of $\mathrm{MoS_2}$, $\mathrm{ZrS_2}$, and $\mathrm{NbSe_2}$ surfaces obtained by high-vacuum cleavage (8×10^{-7} Pa) or 3-keV $\mathrm{Ar^+}$ ion milling made use of electron Auger spectroscopy.[23] The experiment showed formation of imperfections at the basal surface (defects and ''edge'' atoms), without any significant distortion of the bulk structure. Ion milling also contributes to surface distortions; little is known, regrettably, about their nature.

The calculations of TC spectra are presented in Figs. 1–3 (curves *2*). The positions of the characteristic maxima in the curves are denoted by symbols $a,b,c,\ldots$ in the order of increasing energy. The differences in position of the features in the experimental and theoretical curves are related, on the one hand, with the approximate nature of the band calculations for high levels. One needs a self-consistent band theory which would take into account correctly the strong anisotropy of rare-metal dichalcogenide lattices, interband hybridization of states ($d-p$ and $p-s$ coupling), spin-orbit and interlayer effects, and the unusual features in the d states of Mo, Zr, and Nb. On the other hand, there are experimental errors associated with the production of a collimated electron beam in the low-energy region, complete collection of secondary electrons, deviation of the electron beam from the normal in the case of inaccurately oriented crystal faces, and the high surface sensitivity of TC spectra, which is determined not only by the small depth of the region to be analyzed but by the strong dependence on the physicochemical processes on the surface as well[6,9]. For instance, the low-energy maximum at $E\simeq1.3$ eV in the TC spectrum from the Si(111) face is assigned[24] to the existence of a band of surface states near the valence-band edge. The intensity of this maximum (as that of maximum a in Fig. 1, curve *1*) decreases after oxygen adsorption. Maximum b ($\mathrm{MoS_2}$) is displaced by adsorption toward lower energies by approximately 0.8 eV. The presence on the surface of an adsorbant or of foreign atoms, of fairly high concentrations of impurities between the layers, as well as the trend to formation of layer stacking faults in the course of crystallization of the rare-metal dichalcogenides gives rise to large-angle elastic scattering, which opens new channels for electron penetration into a crystal.

The agreement between the main features in the experimental and theoretical TC spectra evidences a dominant role of bulk band structure in the formation of a spectrum. This offers a possibility of experimental investigation of the electron dispersion relation and of using TC spectral data as reference points for refined band calculations capable of indicating which bands are responsible for a particular feature in a spectrum. Investigation and interpretation of experimental TC spectra obtained at various primary-electron incidence angles can provide direct information on specific features of the bulk band structure throughout the Brillouin zone. It can be employed in direct and inverse PE spectroscopy. The dependence of the fine structure in TC spectra on the geometric structure and degree of order in the crystals under study has been confirmed. The above method permits one to separate bulk from surface TC effects, as well as to describe the fine-structure features in experimental dependences of the secondary electron-emission coefficient $\sigma(E_p)=I_s/I_p$, as this was done, for example, in Refs. 25 and 26, without invoking the cumbersome formalism of the LEED dynamical theory.

Support of the State Foundation for Basic Research of Ukraine is gratefully acknowledged.

---

[*] E-mail: panch@host.dipt.donetsk.ua

[1] S. A. Komolov and L. T. Chadderton, Surf. Sci. **90**, 359 (1979).
[2] P. J. Møller and M. H. Mohamed, J. Phys. C **15**, 6457 (1982).
[3] P. J. Møller and J.-W. He, Surf. Sci. **162**, 209 (1985).
[4] E. Tamura, R. Feder, J. Krewer, R. E. Kirby, E. Kisker, E. L. Garwin, and F. K. King, Solid State Commun. **55**, 543 (1985).
[5] I. Schäfer, M. Schlüter, and M. Skibowski, Phys. Rev. B **35**, 7663 (1987).
[6] S. A. Komolov, *Integrated Secondary-Electron Surface Spectroscopy* (LGU, Leningrad, 1986).
[7] S. A. Komolov and L. T. Chadderton, Philos. Mag. B **39**, 13 (1979).
[8] S. A. Komolov and O. M. Artamonov, Vestn. Leningr. Univ., Ser. 4: Fiz., Khim. **10**, No. 2, 47 (1979).
[9] V. I. Silant'ev and N. A. Shevchenko, Vysokochist. Veshch. **4**, 197 (1988).
[10] S. A. Komolov, K. Schamburg, N. B. Gerasimova, and A. O. Morozov, Zh. Tekh. Fiz. **66**, No. 7, 185 (1996) [Tech. Phys. **41**, 734 (1996)].
[11] S. A. Komolov, O. F. Panchenko, and V. M. Shatalov, Fiz. Tverd. Tela (St. Petersburg) **34**, 1259 (1992) [Phys. Solid State **34**, 665 (1992)]; *ibid.* **34**, 3489 (1992) [Phys. Solid State **34**, 1867 (1992)].
[12] O. F. Panchenko and L. K. Panchenko, Phys. Lett. A **192**, 289 (1994).
[13] V. M. Shatalov and O. F. Panchenko, Solid State Commun. **69**, 937 (1989).
[14] O. F. Panchenko and L. K. Panchenko, Solid State Commun. **101**, 483 (1997).
[15] V. M. Shatalov, O. F. Panchenko, O. M. Artamonov, A. G. Vinogradov, and A. N. Terekhov, Solid State Commun. **68**, 719 (1988).
[16] V. V. Korablev, Yu. A. Kudinov, O. F. Panchenko, L. K. Panchenko, and V. M. Shatalov, Fiz. Tverd. Tela (St. Petersburg) **36**, 2373 (1994) [Phys. Solid State **36**, 1290 (1994)].
[17] S. A. Komolov, O. F. Panchenko, L. K. Panchenko, and V. M. Shatalov, Pisma Zh. Tekh. Fiz. **19**, No. 3, 17 (1993) [Tech. Phys. Lett. **19**, 77 (1993)].
[18] K. Wood and J. B. Pendry, Phys. Rev. Lett. **31**, 1400 (1973).
[19] G. Wexler and A. M. Woolley, J. Phys. C **9**, 1185 (1976).
[20] H. M. Isomäki and J. von Boehm, Phys. Lett. A **89**, 89 (1982).
[21] F. Minami, M. Sekita, M. Aono, and N. Tsuda, Solid State Commun. **29**, 459 (1979).
[22] B. J. Mrstik, R. Kaplan, and T. Reinecke, Nuovo Cimento Soc. Ital. Fis., B **38**, 387 (1977).
[23] R. H. Williams, J. G. Higginbotham, and M. A. Whittaker, J. Phys. C **5**, L191 (1982).
[24] S. A. Komolov, Zh. Tekh. Fiz. **51**, 1909 (1981) [Sov. Phys. Tech. Phys. **26**, 1108 (1981)].
[25] O. F. Panchenko and L. K. Panchenko, Fiz. Tverd. Tela (St. Petersburg) **35**, 3164 (1993) [Phys. Solid State **35**, 1560 (1993)].
[26] O. F. Panchenko, Fiz. Tverd. Tela (St. Petersburg) **39**, 1727 (1997) [Phys. Solid State **39**, 1537 (1997)].

Translated by G. Skrebtsov

PHYSICS OF THE SOLID STATE VOLUME 41, NUMBER 10 OCTOBER 1999

POLYMERS. LIQUID CRYSTALS

Spin exchange in iodine-doped polydiacetylene

M. K. Kerimov

Radiation Research Division, Azerbaĭdzhan Academy of Sciences, 370143 Baku, Azerbaĭdzhan

(Submitted January 18, 1999)
Fiz. Tverd. Tela (St. Petersburg) **41**, 1879–1881 (October 1999)

It is shown that the observed transformation of the ESR spectrum in polydiacetylene films upon doping with iodine agrees with an exchange interaction between the spin systems of localized paramagnetic centers (S) and polaron states (P) by means of which current-carrier transport occurs. The data obtained indicate carrier transport in the form of uncorrelated hops with probability determined by the lifetime of an exchange-coupled ($S-P$) pair. © *1999 American Institute of Physics.* [S1063-7834(99)03410-3]

A characteristic feature of organic semiconductors based on polymers with conjugate multiple bonds is a distinct relation between electric conductivity and their paramagnetism.[1] The mechanism of such an interrelation and the interaction between systems of current carriers and paramagnetic centers (PCs) have never been completely determined. Thus, although existing mechanisms based on soliton or polaron–bipolaron ideas make it possible to interpret qualitatively the correlated changes in the density of PCs and the electric conductivity, for example, on doping of the polymer with donor or acceptor impurities, they cannot explain the changes observed in the ESR spectra of the material investigated.

To determine the mechanism of these changes we investigated the ESR spectra and electric conductivity of films of dissolved polydiacetylene–polydiphenyldiacetylene (PDPDA) in the process of doping in situ with iodine molecules. Doping was performed directly in the cavity of a RÉ-1306 ESR spectrometer with simultaneous detection of the ESR signal and the electrical resistance of the sample. In addition, the dependence of the resistance of the polymer on the intensity of the constant magnetic field used in ESR was investigated.

Figure 1 shows the dependences of the amplitude of the ESR signal and electric conductivity of PDPDA on the duration of iodizing at room temperature. It is evident that the concentration of PCs increases monotonically, while the electric conductivity stabilizes after doping for 6 h. In addition, the conductivity increases by 7 orders of magnitude, whereas the PC density increases by only a factor of 5, reaching $3.5\times10^{19}\,\mathrm{cm}^{-3}$. At the same time, transformation of the ESR signal from the initial line of a mixed form with $g=2.0035$ and width $\Delta H_{pp}=0.8mT$ to a narrower, Lorentzian line with $g=2.0027$ and $\Delta H_{pp}=0.4mT$ is observed (Fig. 2). The samples show a dependence of the electric resistance on the external magnetic field strength, as shown in Fig. 3. Such a dependence is characteristic for a process with participation of pairs of paramagnetic particles, whose rate depends on the relative orientation of the spins of these particles.[2] It is shown in Refs. 3 and 4 that the effect of a magnetic field in the conductivity is due the spin-dependent transport of current carriers along a system of localized PCs

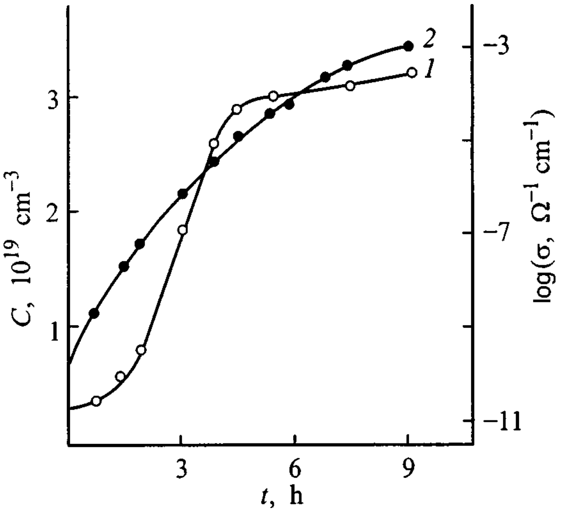

FIG. 1. Electric conductivity (*1*) and spin density (*2*) versus the duration of doping of PDPDA with iodine molecules.

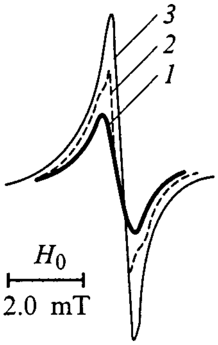

FIG. 2. ESR spectra of PDPDA samples: initial (*1*) and doped for 2 (*2*) and 8 (*3*) h.

and the character of singlet–triplet evolution of spins in pairs under the action of a magnetic field.

The observed changes in the position, width, and shape of the ESR line in the process of doping PDPDA with iodine molecules as well as the magnetic sensitivity of the electrical resistance of the polymer attest to the presence of an interaction between the PCs and the current carriers. This interaction can be explained by considering the spins of the PCs and current carriers to be a dynamically coupled spin system. In addition, such a coupling occurs by means of exchange interactions of the spins of the PCs and the current carriers.

It is known that in polyconjugated polymers positively charged spin-1/2 polaron states (P), through which charge-carrier transport occurs,[5] are formed when an electron is captured by an acceptor impurity (I_2). Moving along the localized states, including along the system of PCs (S), the polarons enter with the latter into bimolecular spin-exchange processes $(S+P)$. In the process, depending on the ratio of the exchange rate and the difference of the resonance frequencies of the spins of the interacting partners, spin exchange produces qualitatively different changes in the spectra of the ESR particle under observation.[6]

Thus, if the exchange rate exceeds the rms deviation in the ESR frequency from the average value ω_0, $\omega_e > \sqrt{\langle\Delta\omega^2\rangle}$ (fast exchange), then exchange narrowing of the ESR line is observed, and the absorption spectrum acquires a Lorentzian form[7]

$$g(\omega)=\frac{T_2^{-1}+\langle\Delta\omega^2\rangle/\omega_e}{(\omega-\omega_0)^2+(T_2^{-1}+\langle\Delta\omega^2/\omega_e\rangle)^2}, \tag{1}$$

where T_2^{-1} is the transverse spin relaxation rate.

It follows from expression (1) that, as the exchange rate increases, the ESR linewidth should decrease. Since in accordance with the theory of pair collisions the exchange rate is proportional to the concentration C of the colliding spins, $\omega_e = kC$, expression (1) also describes the dependence of the linewidth on the concentration of paramagnetic particles. Specifically, the ESR linewidth should decrease with increasing spin concentration as

$$\Delta\omega_e=\frac{\langle\Delta\omega^2\rangle}{kC}. \tag{2}$$

It is noteworthy that the exchange interaction of spins also produces a shift of the resonance frequency of a PC, as follows from the solution of the kinetic equations describing the process of spin exchange between paramagnetic systems having different Zeeman frequencies. Using the spin Hamiltonians for the Zeeman interaction of the spins s_S and s_P with a magnetic field, and the spin Hamiltonian for exchange interaction, it was shown in Ref. 6 that, as a result of exchange interaction, the resonance frequency of the spins s_S under study will not be ω_S but

$$\omega_S-\frac{1}{2}\tau_c kC(\omega_P-\omega_S), \tag{3}$$

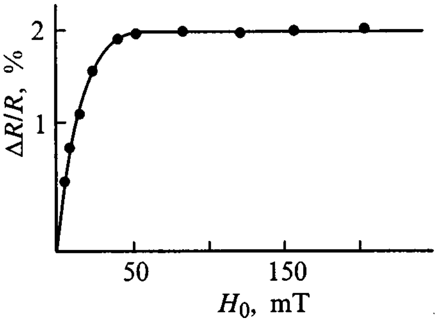

FIG. 3. Relative change in the electrical resistance of PDPDA as a function of the magnetic field intensity.

where τ_c is the average duration of a collision of the spins s_S and s_P. Therefore the shift of the resonance frequency is linear in the spin density, just as in the case of exchange narrowing.

In summary, the observed changes in the ESR spectrum of PDPDA upon doping with iodine molecules can be explained qualitatively on the basis of an exchange interaction between the spin systems of localized polarons and the PCs of the polymer. Moreover, the proposed mechanism makes it possible to determine a number of important parameters characterizing this interaction. Comparing these parameters with theoretical estimates could attest to the validity of this approach.

Specifically, the spin exchange rate constant and the exchange interaction length can be found from relation (2) using the concentration dependence of the ESR linewidth. Thus, switching from measuring the linewidth in frequency units to measurement in units of the magnetic induction, and taking account of the fact that $\langle\Delta\omega^2\rangle=\Sigma_i I_i(U_i+1)a_i^2/3$, where a_i is the HFS constant from the i-th nucleus and I_i is the spin of this nucleus, expression (2) can be rewritten[7]

$$\delta(\Delta H_{pp})=3.39\times10^6 g\sum_i I_i(I_i+1)\frac{a_i^2}{kC}. \tag{4}$$

Proceeding from the structure of PDPDA, where the unpaired electron is distributed in the same way over protons of the phenyl ring, for which HFS constant is $a_i=0.38mT$, we find from the narrowing $\delta(\Delta H_{pp})=0.4mT$ of the ESR line that the spin exchange constant is

$$k=2.6\times10^{-12}\,\mathrm{cm}^3\cdot\mathrm{s}^{-1}.$$

According to the pair-collision mechanism, in the continuous diffusion model the effective exchange rate constant is related with the exchange radius r_{ex} as

$$k=4\pi r_{ex}D, \tag{5}$$

where D is the sum of the diffusion coefficients of the collision partners, $D=D_P+D_S$. Since $D_P \gg D_S$, the constant k will be determined, in practice, by the mobility of the current carriers, which is related with the diffusion coefficient D_P as

$$D_P=\mu\frac{kT}{e}. \tag{6}$$

Therefore we find from Eqs. (5) and (6)

$$r_{ex} = \frac{ke}{4\pi\mu kT}. \tag{7}$$

In PDPDA the carrier mobility $\mu = 3\times10^{-5}\,\mathrm{cm^2/V\cdot s}$. We then find the exchange interaction radius between the PCs and the carriers $r_{ex} = 2.7\times10^{-7}$ cm.

Since spin exchange is the mechanism determining the singlet–triplet evolution of the spins in pairs $(S\ldots P)$ under the action of external or internal magnetic fields, it is completely obvious that the efficiency of the evolution will be determined by the lifetime τ of the exchange-coupled pair: it must be long enough so that there is enough time for evolution to occur, but it must be shorter than the spin relaxation time T_1 so that the spin states do not reach an equally probable population. For polymers with conjugate multiple bonds this condition reduces to the time interval $10^{-9} < \tau < 10^{-7}$ s.

In accordance with the theory of Brownian motion

$$\tau = \frac{r_{ex}^2 e}{6\mu kT}.$$

Hence, substituting the values for r_{ex} and μ at $T = 300$ K we obtain $\tau = 1.6\times10^{-8}$ s, which falls within the range of the indicated interval, making possible the observed magnetic spin effect in the electrical conductivity of PDPDA.

It is interesting to note that the average duration τ_c of contact between the spins, calculated from the shift of the ESR signal according to Eq. (3), is 2×10^{-8} s, which is very close to the value of τ. Apparently, such close values of τ_c and τ indicate that the duration of the contact of the spins is actually determined by the diffusion time of a carrier through the exchange-interaction region. On the other hand, the fact that this time is equal to the lifetime of $S-P$ pairs could be due to the fact that polaron diffusion occurs by large hops, so that they fall within the region of interaction or leave this region as a result of one hop. This assumption agrees with the established mechanism of current-carrier transport in polydiacetylenes in the form of a sequence of uncorrelated hops of a polaron along localized states,[5] if the probability of a hop $\sim \tau_c^{-1}$.

In this way, the analysis of the interaction of localized PCs with current carriers in iodized samples of PDPDA from the standpoint of the spin exchange mechanism enables us not only to interpret the observed changes in the ESR spectrum qualitatively but also to determine a number of kinetic parameters, which agree with the experimental prerequisites, describing current-carrier transport in a polymer.

Obviously, an additional argument in favor of the mechanism considered above could be provided by investigations of the effect of temperature and electric field intensity on the nature of the interaction between the PCs and current carriers in a polymer. We hope to devote our next report to these questions.

We thank I. D. Akhmedov for providing the PDPDA samples and E. Z. Aliev for performing certain ESR measurements.

[1] N. A. Bakh, A. V. Vannikov, and A. D. Grishina, *Electric Conductivity and Paramagnetism of Polymer Semiconductors* (Nauka, Moscow, 1971).

[2] Ya. B. Zel'dovich, A. L. Buchachenko, and E. L. Frankevich, Usp. Fiz. Nauk **155**(1), 3 (1988) [Sov. Phys. Usp. **31**, 385 (1988)].

[3] E. L. Frankevich, A. I. Pristupa, and V. M. Kobryanskiĭ, JETP Lett. **40**, 733 (1984).

[4] E. L. Frankevich, D. I. Kadyrov, I. A. Sokolik, A. I. Pristupa, V. M. Kobryanskii, and N. Y. Zurabyan, Phys. Status Solidi **132**, 283 (1985).

[5] N. A. Cade and B. Movaghar, J. Phys. C **16**, 539 (1983).

[6] K. I. Zamarev, Yu. N. Molin, and K. M. Salikhov, *Spin Exchange* (Nauka, Novosibirsk, 1977).

[7] P. W. Anderson and P. R. Weiss, Rev. Mod. Phys. **25**(1), 269 (1953).

Translated by M. E. Alferieff

PHYSICS OF THE SOLID STATE VOLUME 41, NUMBER 10 OCTOBER 1999

Theoretical description of fluctuations in free-standing smectic-*A* films including spatial non-uniformity of their elastic characteristics

L. V. Mirantsev

Institute for Problems in Mechanical Engineering, Russian Academy of Sciences, 199178 St. Petersburg, Russia

(Submitted November 27, 1998; resubmitted February 25, 1999)
Fiz. Tverd. Tela (St. Petersburg) **41**, 1882–1889 (October 1999)

A theoretical study is reported of fluctuations in smectic layer displacements and of the correlations between them in free-standing smectic-*A* films formed of liquid-crystal compounds with smectic-*A*–isotropic liquid (Sm-*A*–*I*) and Sm-*A*–nematic (Sm-*A*–*N*) bulk phase transitions. The study took into account the dependence of the elastic constants for bending, *K*, and tension (compression), *B*, of smectic layers on distance to the free film surfaces. The calculations are compared with the results obtained within Hołyst's model for spatially uniform, free-standing smectic-*A* films. It has been established that, below the temperature at which smectic order in the bulk of a liquid crystal disappears, taking into account the profiles of the elastic moduli *K* and *B* does not produce noticeable differences from this model. However, at temperatures considerably above the Sm-*A*–*I* and Sm-*A*–*N* phase transitions, their inclusion results in considerable discrepancies from the predictions of Hołyst's model. © *1999 American Institute of Physics.* [S1063-7834(99)03510-8]

A unique property of smectic liquid crystals is their capability of forming free-standing films. The area of such films, which may be considered as stacks of smectic layers with two free surfaces, can reach as high as $\sim 1\,\mathrm{cm}^2$,[1] and their thickness varies from a few hundred to two and even one smectic layer.[2,3] In thin free-standing films, the effects associated with the finite size of the system combine with surface effects. This combination gives rise to phenomena not observed in the bulk phase of liquid crystals (LC). First, the temperatures of phase transitions in free-standing films can differ substantially from those of similar transitions in the bulk of an LC[4–10] and, if a film is thin enough, first-order transitions become continuous (i.e. second-order). Second, in free-standing films of some LCs there can exist smectic phases not observed in thick samples of the same compounds altogether.[11–13] Finally, a quite recent study revealed that free-standing smectic-*A* (Sm-*A*) films of some LC compounds, rather than rupturing when heated above the temperature at which smectic order disappears in the bulk of the LC, undergo a series of stepped layer-by-layer thinning transitions.[14–18] Due to such jumps, the thickness of free-standing films can decrease successively from a few tens to two smectic layers, and the temperature at which two-layer films can exist may exceed by $\sim 10-20\,\mathrm{K}$ that of the Sm-*A*–isotropic (Sm-*A*–*I*) or Sm-*A*–nematic (Sm-*A*–*N*) phase transition in thick samples of the same mesogens. For this reason, as well as because by properly varying the film thickness one can study the crossover in behavior from three- to two-dimensional physical systems, free-standing smectic films have been for the recent 15–20 years subjects of intensive experimental[1–28] and theoretical[29–39] investigation.

The most complete information on the structure of free-standing smectic films can be obtained from small-angle x-ray-scattering experiments, which provide data both on their equilibrium characteristics (the number of smectic layers, layer thickness, the type of molecular packing in a layer),[11–13,22–24] and on fluctuations in films.[18,24–28] Measurements of the specular reflection coefficient of a film can be used to derive the profile of smectic-layer displacement fluctuations, and investigation of diffuse reflectivity, the correlations between the displacements of various layers in a film.[26–28] It should be pointed out, however, that measurements of the x-ray intensity reflected from a film can yield this information only if one has a theoretical model capable of adequately describing thermal fluctuations of smectic-layer displacements in a free-standing film. A simple discrete model to describe such fluctuations in a free-standing Sm-*A* film, which takes into account not only compression and transverse bending of smectic layers but surface tension as well, was proposed by Hołyst.[31,32] A continuum version of this theory, which is more convenient for description of experimental data, was subsequently developed.[33,34] It provides a fairly good interpretation of the measurements of specular and diffuse x-ray reflection coefficients for free-standing films of some LC compounds.[26,27] Hołyst's model assumes a free-standing smectic-*A* film to be spatially uniform and characterized only by four physical parameters: the number of smectic layers *N*, the surface tension coefficient γ, and the elastic moduli for transverse bending *K* and tension (compression) *B* of smectic layers. The latter two quantities are assumed to be the same for all layers in a film, irrespective of their position, and equal to the corresponding elastic constants for the bulk of the smectic-*A* phase. This assumption is physically valid only for free-standing films studied at temperatures substantially below the phase-transition points of the Sm-*A*–*N* or Sm-*A*–*I* transitions in the LC bulk. Because the Sm-*A* structure sets in under these conditions throughout the bulk of the film, the orientational and translational ordering of molecules in the inner and surface layers of the film differ little from one another. Assuming the transverse bending modulus K in free-standing films, as well as in bulk LC samples, to be proportional to the square of the orientational order parameter s, and the tension (compression) modulus of smectic layers B, proportional to the square of the translational order parameter τ,[40,41] these moduli should also be practically the same for all layers in a film.

However free-standing smectic films of some LCs are capable of existing, as already mentioned, at temperatures considerably in excess of those at which smectic order disappears in the bulk of a mesogen. According to the microscopic model,[35,36,39] which reproduces fairly well the behavior of free-standing films under heating above the Sm-A–N and Sm-A–I phase transitions, both orientational and translational ordering in the inner layers of the film can be substantially lower in this case than that near the free bounding surfaces. This theoretical result was confirmed experimentally[18] by measurements of the x-ray specular reflection coefficients on smectic-*A* films of various thicknesses above the Sm-A–N phase-transition point in the bulk of the LC. Hence the moduli of transverse bending and tension (compression) of smectic layers in such films should decrease with distance from the free surface, to reach the minimum value at the film center. Because neither Hołyst's model[31,32] nor its continuum modifications[33,34] take such profiles of the elastic moduli into account, they must yield wrong values for the smectic-layer displacement fluctuations and the correlations between them. Note also that while the x-ray structural measurements[26,27] of smectic-*A* films, performed at temperatures substantially below the level at which smectic order in the bulk of the LC disappears, could be well fitted by the model of Ref. 34, a similar study[18] of free-standing films made in the vicinity of the Sm-A–N phase transition revealed serious discrepancies between the predictions of this model and experimental data.

The present work proposes a straightforward generalization of Hołyst's discrete model[31,32] which takes into account the dependences of the elastic constants for transverse bending K and tension (compression) B of smectic layers on the distance to the bounding surfaces of the film. These relations are found by means of a microscopic model[35,36,39] developed for free-standing smectic-*A* films. The profiles of fluctuations in smectic-layer displacements and the correlations between these fluctuations are calculated for free-standing film of LC compounds exhibiting Sm-A–I and Sm-A–N bulk phase transitions. In both cases the calculations were performed for temperatures both substantially lower than the corresponding phase-transition points and the highest at which free-standing films of a given thickness still exist. The calculations are compared with the results obtained within Hołyst's model. It is shown that, below the temperature at which smectic order in the bulk of liquid crystals disappears, taking the profiles of the K and B elastic moduli into account, does not entail any noticeable discrepancies from this model. However, at temperatures substantially higher than the Sm-A–I and Sm-A–N phase-transition points, their inclusion results in considerable deviations from the predictions of Hołyst's model.

1. DISCRETE MODEL FOR DESCRIPTION OF LAYER-DISPLACEMENT FLUCTUATIONS IN A FREE-STANDING SMECTIC-*A* FILM

Consider a free-standing smectic-*A* film consisting of N discrete layers. Denote by $u_n(x,y)$ the fluctuating displacements of smectic layers from their equilibrium positions $z_n = (n-1)d$ along the z axis perpendicular to the layer plane. Here d is the thickness of the smectic layer, and n is its number. To such a film-layer displacement corresponds an excess free energy F made up of a surface, F_S, and a bulk, F_B, contribution. Hołyst's model[31,32] proposes the following expression for the surface energy F_S associated with an increase in the area of the two free film surfaces

$$F_S=\frac{1}{2}\gamma\int[|\nabla_\perp u_1(\mathbf{R})|^2+|\nabla_\perp u_N(\mathbf{R})|^2]d\mathbf{R}, \tag{1}$$

where γ is the surface tension coefficient of the free surface of a smectic-*A* film, $\mathbf{R}$ is the position vector in the smectic-layer plane ($R^2=x^2+y^2$), $\nabla_\perp$ is the projection of the $\boldsymbol{\nabla}$ operator onto the (x,y) plane. As for the bulk contribution F_B to the film strain energy F, it consists of two parts, namely, the energy $F_B^{(1)}$ of transverse bending strain of the director $\mathbf{n}$ and the energy $F_B^{(2)}$ of smectic-layer tension (compression). Denoting by K_n the transverse bending modulus in the nth layer of the film, we can write the $F_B^{(1)}$ energy in terms of the discrete model used, by analogy with the expression for the density of transverse-bending strain energy in the bulk smectic-*A* phase,[40,41] in the form

$$F_B^{(1)}=\frac{1}{2}\sum_{n=1}^{N}K_n d\int[\Delta_\perp u_n(\mathbf{R})]^2 d\mathbf{R}, \tag{2}$$

where $\Delta_\perp$ is the Laplace two-dimensional operator in the (x,y) plane. Using again the analogy with the expression for the tension (compression) strain energy in the bulk of the smectic-*A* phase,[40,41] we write the $F_B^{(2)}$ energy as

$$F_B^{(2)}=\frac{1}{2}\sum_{n=1}^{N-1}\left(\frac{B_n+B_{n+1}}{2d}\right)\int[u_{n+1}(\mathbf{R})-u_n(\mathbf{R})]^2 d\mathbf{R}. \tag{3}$$

Here B_n is the tension (compression) modulus of the nth layer in a free-standing smectic-*A* film. Adding F_S, $F_B^{(1)}$, and $F_B^{(2)}$ yields the total excess energy F of the film associated with fluctuations in the displacement of its layers:

$$F=\frac{1}{2}\int\left\{\sum_{n=1}^{N-1}\frac{B_n+B_{n+1}}{2d}[u_{n+1}(\mathbf{R})-u_n(\mathbf{R})]^2 +\sum_{n=1}^{N}K_n d[\Delta_\perp u_n(\mathbf{R})]^2+\gamma|\nabla_\perp u_1(\mathbf{R})|^2 +\gamma|\nabla_\perp u_N(\mathbf{R})|^2\right\}d\mathbf{R}. \tag{4}$$

It should be pointed out that, in the case of spatially uniform, free-standing smectic-*A* film, where the moduli for transverse bending, K_n, and tension (compression), B_n, of all its layers are the same and equal to K and B, respectively, Eq. (4) for the excess film energy F coincides with the similar expression obtained within Hołyst's model.[31,32]

By using continuous Fourier transform

$$u_n(\mathbf{R})=(2\pi)^{-2}\int u_n(\mathbf{q}_\perp)\exp(i\mathbf{q}_\perp\mathbf{R})d\mathbf{q}_\perp \tag{5}$$

one can obtain a simple, compact expression for the excess free energy F

$$F=\frac{1}{2}\sum_{k,n=1}^{N}\int u_k(\mathbf{q}_\perp)M_{kn}u_n(-\mathbf{q}_\perp)d\mathbf{q}_\perp\,, \tag{6}$$

where M_{kn} are elements of a symmetric ribbon-type matrix. In such a matrix, only the diagonal and the first neighboring elements are nonzero:

$$M_{11}=M_{NN}=\gamma q_\perp^2+K_1 d q_\perp^4+(B_1+B_2)/2d=b_1=b_N\,, \tag{7}$$

$$M_{nn}=K_n d q_\perp^4+(B_{n-1}+2B_n+B_{n+1})/2d=b_n\,,$$

$$n=2,\ N-1\,, \tag{8}$$

$$M_{n+1\,n}=M_{n\,n+1}=-(B_n+B_{n+1})/2d=c_n\,,$$

$$n=1,\ N-1\,. \tag{9}$$

Knowing the elements M_{kn} of the direct matrix, one can readily determine the elements $(M^{-1})_{kn}$ of the reciprocal matrix, and use them to calculate the average fluctuations of film layer displacements $\sigma_n=\langle u_n^2(0)\rangle^{1/2}$ and the correlations $g_{k,n}(R)=\langle u_k(\mathbf{R})u_n(0)\rangle/(\sigma_k\sigma_n)$ between them. According to Refs. 31, 32

$$\sigma_n^2=\langle u_n^2(0)\rangle=\frac{k_BT}{(2\pi)^2}\int (M^{-1})_{nn}d\mathbf{q}_\perp\,, \tag{10}$$

$$\langle u_k(\mathbf{R})u_n(0)\rangle=\frac{k_BT}{(2\pi)^2}\int (M^{-1})_{kn}\exp(i\mathbf{q}_\perp\mathbf{R})d\mathbf{q}_\perp\,, \tag{11}$$

where k_B is the Boltzmann constant, and T is the absolute temperature of the system. The lower limit of integration on the right-hand sides of Eqs. (10) and (11) is determined by the transverse dimensions of the film L, and the upper limit, by the molecule diameter a $(2\pi/L\leqslant|q_\perp|\leqslant 2\pi/a)$. The reason for this lies in that transverse modes with a wavelength smaller than the diameter of the molecule and larger than the film transverse size cannot be excited in a film. If a free-standing film has macroscopic transverse dimensions (with L of the order of 1 cm), the lower limits of integration in (10) and (11) can be put equal to zero.

As already mentioned, the transverse bending modulus K in the bulk of an LC is proportional to the square of the orientational order parameter $s=\langle\frac{3}{2}\cos^2\vartheta-\frac{1}{2}\rangle$,[40,41] where ϑ is the polar angle between the long axis of the LC molecules and the director $\mathbf{n}$, and $\langle\ldots\rangle$ denotes averaging over all molecules in a small, but macroscopic volume, and the tension (compression) modulus B of smectic layers in the bulk of a smectic LC is proportional to the square of the translational order parameter $\tau=\langle\cos(2\pi z/d)\rangle$. If one assumes that the relations connecting the elastic constants with the orientational and translational order parameters in free-standing films are the same as in the bulk of the mesophases throughout the range of the film existence, including the temperatures in excess of the Sm-$A-N$ or Sm-$A-I$ phase transitions in the bulk of an LC, then these relations will provide a possibility of finding the elastic moduli K_n and B_n in Eqs. (7)–(9) for smectic layers in a free-standing smectic-A film by means of the microscopic model proposed in Refs. 35, 36, 39. This model permits one to determine the order parameters $s_n(T)$ and $\tau_n(T)$ for each film layer of an arbitrary thickness and for any temperature T within the domain of the film existence. Besides, in the case of very thick films ($N\rightarrow\infty$) it yields the values of these parameters at the film center, which fully coincide with the results obtained for a bulk smectic-A phase using the well-known theory of McMillan.[42] If one knows the values of the elastic constants K and B in the bulk of a smectic-A phase at some temperature T_0 $[K(T_0)\equiv K_0,B(T_0)\equiv B_0]$ below the Sm-$A-I$ or Sm-$A-N$ phase-transition point, then one can find the order parameters $s(T_0)\equiv s_0$ and $\tau(T_0)\equiv\tau_0$ at this temperature using the model of Refs. 35, 36, 39, after which the relations

$$K_n(T)=K_0[s_n(T)/s_0]^2\,, \tag{12}$$

$$B_n(T)=B_0[\tau_n(T)/\tau_0]^2\,, \tag{13}$$

make it possible to determine the elastic constants K_n and B_n for all layers of a film of the given thickness for any temperature within the region of its existence.

2. RESULTS OF NUMERICAL CALCULATIONS AND THEIR DISCUSSION

The numerical calculations of the smectic-layer displacement fluctuations σ_n and correlations $g_{k,n}(R)$ were carried out for two free-standing smectic-A films consisting of $N=24$ layers. It was assumed that one of them is made of an LC undergoing a strong first-order transition from the isotropic to smectic-A phase. In McMillan's model[42] for a bulk smectic-A phase, as well as in the model of Refs. 35, 36, 39 for free-standing smectic-A films, this case corresponds to a model parameter $\alpha=2\exp[-(\pi r_0/d)^2]\geqslant 0.98$. Here r_0 is the characteristic interaction radius for a model pair intermolecular potential used in the theory of McMillan. We used in the calculations $\alpha=1.05$. The second free-standing smectic-A film was assumed to be made from an LC with a weakly pronounced Sm-$A-N$ first-order phase transition. To this case corresponds a model parameter $\alpha\leqslant 0.98$. Our calculations were performed with $\alpha=0.871$. This choice of the model parameters can be explained by the fact that it is in such free-standing films that the smectic-layer displacement fluctuations and the correlations between them were studied by small-angle x-ray scattering in Refs. 18, 26–28. In Refs. 26, 27, the studies were performed on free-standing smectic-A films prepared of the FPP mesogen (4-heptyl-2-[4-(2-(perfluorhexylethyl)phenyl]-pyrimidine), which exhibits a strong Sm-$A-I$ first-order phase transition, and Refs. 18, 28 investigated free-standing films of the 7AB liquid crystal (4,4′-diheptylazoxybenzene) undergoing a Sm-$A-N$ second-order (or a weakly pronounced first-order) phase transition. In both cases the layer displacement fluctuations in a free-standing smectic-*A* film and the correlations between them were calculated for two temperatures; the first of them, $T_1^{(1,2)}$, was substantially lower than the Sm-$A-I$ (Sm-$A-N$) bulk phase-transition point, and the second, $T_2^{(1,2)}$, slightly lower than the upper limiting temperature for the existence of a free-standing film of a given thickness. For the first film, $T_1^{(1)}=0.205\,(V_0/k_B)$, and $T_2^{(1)}=0.2298\,(V_0/k_B)$. Here V_0 is the molecular interaction constant in McMillan's theory.[42] By this theory, at $\alpha=1.05$ the Sm-$A-I$ bulk phase-transition temperature is $T_{AI}=0.2249\,(V_0/k_B)$. On the other hand, according to the model of Refs. 35, 36, 39 for free-standing smectic-*A* films, at $\alpha=1.05$ the limiting temperature of existence of a 24-layer free-standing film $T_c^{(1)}(N=24)=0.2299\,(V_0/k_B)$. Above this temperature a film either ruptures or undergoes a stepwise thinning transition by an integral number of smectic layers. For the second film ($\alpha=0.871$), the first temperature was taken $T_1^{(2)}=0.204\,(V_0/k_B)$ [by Ref. 42, at $\alpha=0.871$ the Sm-$A-N$ transition temperature in the LC bulk is $T_{AN}=0.2091\,(V_0/k_B)$], and the second, $T_2^{(2)}=0.21035\,(V_0/k_B)$ [by the model of Refs. 35, 36, 39, at $\alpha=0.871$ the upper temperature of the film existence is $T_c^{(2)}(N=24)=0.21036\,(V_0/k_B)$]. The molecular interaction constant V_0 for the first film was chosen such that the absolute temperature T_{AI} of the Sm-$A-I$ bulk phase transition in the LC coincides with the experimentally found temperature (396 K, Refs. 26, 27) of this transition in the FPP liquid crystal. Similarly, the constant V_0 for the second film was chosen so as to fit the absolute temperature T_{AN} of the Sm-$A-N$ phase transition in the bulk of the liquid crystal to the temperature (326 K, Refs. 18, 28) at which this transition was found to occur in the 7AB liquid crystal. The ordering action of the free film surface on the LC molecules was assumed to be strong enough. The ratio of the interaction constant *W*, which in the model of Refs. 35, 36, 39 determines the strength of the effective external field simulating this action, to the molecular interaction constant V_0 was taken equal to 1.6. According to this model, at such a strong ordering action of the free surface on LC molecules, heating a free-standing smectic-*A* film to the upper temperature of its existence should result not in its rupture but rather in its jumplike thinning by an integral number of layers. It is this effect that was observed in experiments with the 7AB liquid crystal.[18,28] As for the FPP liquid crystal studied in Refs. 26, 27, it belongs to mesogens whose molecules have partially fluorinated alkyl tails. According to Refs. 14, 16, films of such LCs, rather than rupturing under heating, also exhibit a jumplike thinning. The transverse bending modulus K_0 for the bulk LC phase at a temperature lower than T_{AI} or T_{AN} (for an LC with a Sm-$A-I$ phase transition this temperature was assumed to coincide with $T_1^{(1)}$, and for an LC undergoing a Sm-$A-N$ transition, with $T_1^{(2)}$) was set in both cases equal to $K_0=10^{-6}$ dyn (a typical value for most LCs[40,41]). As for the smectic tension (compression) moduli B_0, which for the sake of simplicity were also assumed to be defined at the $T_1^{(1)}$ and $T_1^{(2)}$ temperatures, for the first LC one used the value found in Refs. 26, 27 ($B_0=7.5\times10^9$ dyn/cm^2), and for the second, that measured in Ref. 28 ($B_0=10^8$ dyn/cm^2). The surface tension coefficients γ for the free film surface, also taken from Refs. 26–28, were put equal to $\gamma=13$ and 25 dyn/cm for the first and second film, respectively. The thickness *d* of smectic layers in a film was assumed temperature-independent and equal to the molecule length $l=30$ Å, and the molecule diameter *a* was taken equal to 4 Å (typical dimensions for LC molecules[40,41]).

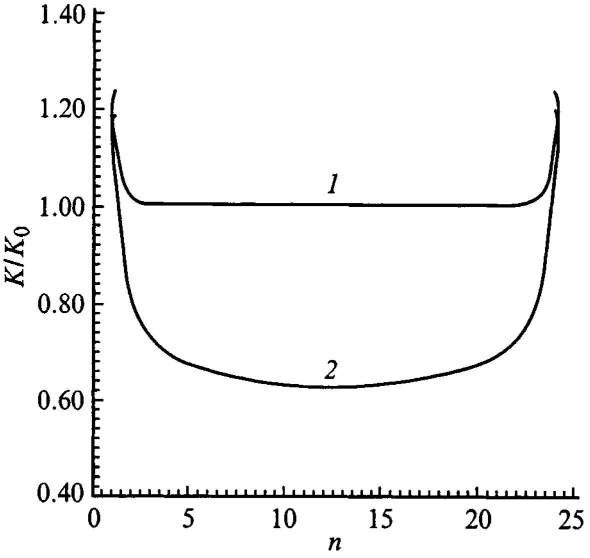

FIG. 1. Profiles of the elastic constant for bending *K* for the first free-standing smectic-*A* film for temperatures below the Sm-$A-I$ phase-transition point and for the highest temperature at which it still exists. $N=24$, $\alpha=1.05$, $W/V_0=1.6$. *1* — $T=T_1^{(1)}=0.205\,(V_0/k_B)$, *2* — $T=T_2^{(1)}=0.2298\,(V_0/k_B)$.

First of all, we calculated the profiles of the elastic moduli *K* and *B* for both free-standing films using the model of Refs. 35, 36, 39. These profiles are shown for the first of them in Figs. 1 and 2, respectively. One readily sees (curves *1*) that below the Sm-$A-I$ phase-transition point ($T=T_1^{(1)}$)

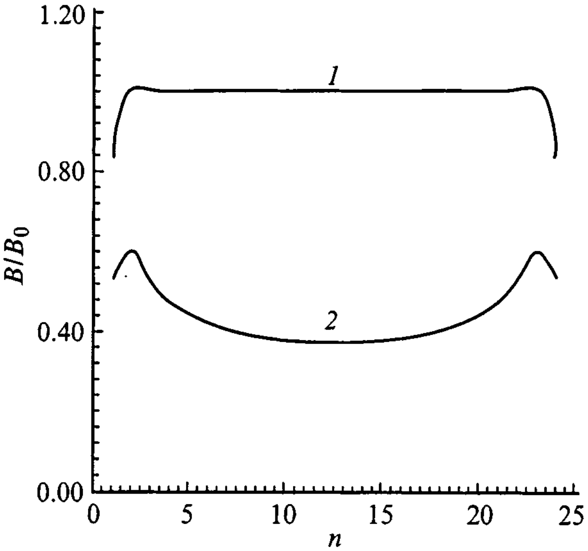

FIG. 2. Profiles of the elastic constant for tension (compression) *B* for smectic layers in the first free-standing film obtained for the conditions of Fig. 1. *1* — $T=T_1^{(1)}=0.205\,(V_0/k_B)$, *2* — $T=T_2^{(1)}=0.2298\,(V_0/k_B)$.

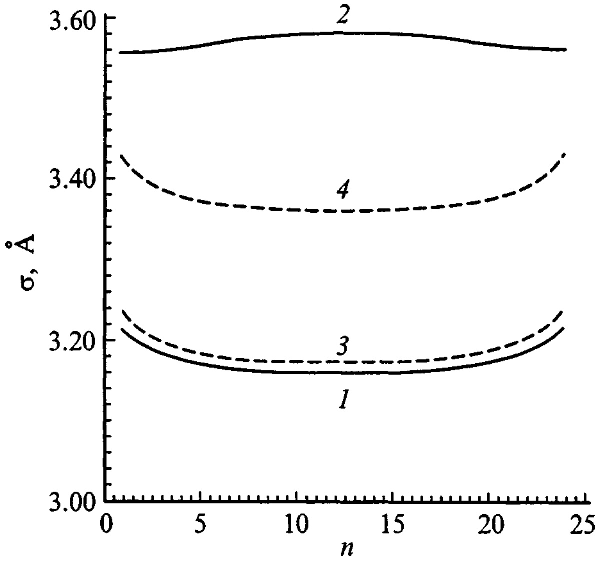

FIG. 3. Profiles of smectic-layer displacement fluctuations in the first free-standing smectic-*A* film calculated taking into account the *K* and *B* elastic-constant profiles (curves *1* and *2*) and within Hołyst's model[31,32] (curves *3* and *4*). $K_0=10^{-6}$ dyn, $B_0=7.5\times 10^9$ dyn/cm^2, $\gamma=13$ dyn/cm. Same parameters as in Figs. 1 and 2. *1* — $T=T_1^{(1)}=0.205\,(V_0/k_B)$, *2* — $T=T_2^{(1)}=0.2298\,(V_0/k_B)$, *3* — Hołyst's model for $T=T_1^{(1)}$, *4* — same model for $T=T_2^{(1)}$.

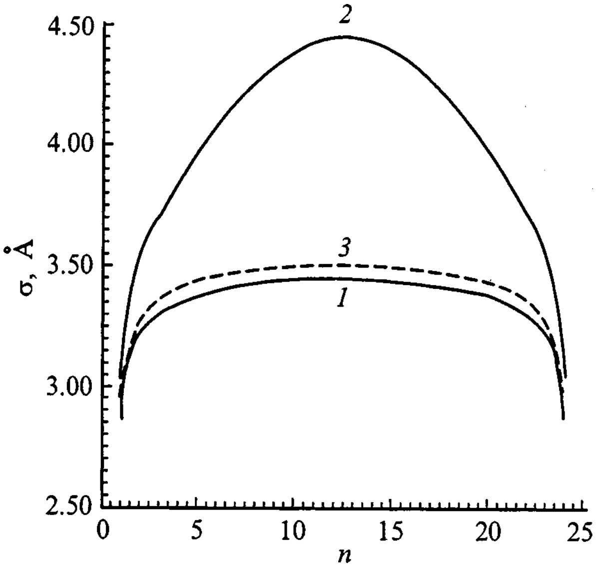

FIG. 4. Profiles of smectic-layer displacement fluctuations in the second free-standing smectic-*A* film ($N=24$, $\alpha=0.871$, $W/V_0=1.6$, $K_0=10^{-6}$ dyn, $B_0=10^8$ dyn/cm^2, $\gamma=25$ dyn/cm). Curves *1* and *2* — our calculations made for $T=T_1^{(2)}=0.204\,(V_0/k_B)$ and $T=T_2^{(2)}=0.21035\,(V_0/k_B)$, respectively; curve *3* — Hołyst's model for $T=T_2^{(2)}$.

both elastic moduli are the same for all film layers (with the exclusion of the first and last surface layers). In this case the free-standing smectic-*A* film is indeed spatially uniform (or nearly uniform), and Hołyst's model[31,32] should yield close to our results. However near the limiting temperature of the existence of a free-standing film of a given thickness ($T=T_2^{(1)}$) the film is no longer spatially uniform (curves *2*), and the elastic moduli *K* and *B* at its center are considerably smaller than those near the free surface. It is in this case that the difference between our results and the predictions of Hołyst's model[31,32] should be appreciable. Note that the profiles of the elastic moduli *K* and *B* for the second free-standing film, which are not shown here, are similar to those in Figs. 1 and 2.

The profiles of the elastic moduli *K* and *B* obtained in this way were subsequently used to calculate those of the smectic-layer displacement fluctuations σ_n for the two free-standing films. The results of these calculations are displayed graphically in Figs. 3 and 4, respectively. Also shown (dashed lines) are the profiles of the displacement fluctuations σ_n obtained within Hołyst's model[31,32]. As should be expected, at $T=T_1^{(1)}$ for the first film and $T=T_1^{(2)}$ for the second our results practically do not differ from the calculations made by this model (in Fig. 4, the σ_n profile obtained for $T=T_1^{(2)}$ by the model of Refs. 31, 32 is even not shown, because it nearly coincides with the profile calculated taking into account the film spatial nonuniformity). However, in the vicinity of the limiting temperatures for both free-standing films ($T=T_2^{(1,2)}$), inclusion of the dependence of the elastic moduli *K* and *B* on distance from the free surface of the films results in a substantial deviation from the predictions of Hołyst's model.[31,32] For instance, the difference between the values of σ_n for the first free-standing film (Fig. 3) calculated for $T=T_1^{(1)}$ and $T=T_2^{(1)}$ with due account of the profiles of the *K* and *B* moduli shown in Figs. 1 and 2, accordingly, exceeds by about two times that obtained when calculating σ_n on this model. Besides, by Refs. 31, 32, an increase in film temperature should result only in an increase of the absolute value of σ_n and would not change the shape of the smectic-layer displacement fluctuation profile [the quantity σ_n has a maximum at the surface and a minimum at film center (Fig. 3, curves *3* and *4*)]. At the same time our calculations, which take into account the thermally-induced changes in the *K* and *B* profiles, show that heating a film to the limiting temperature $T_2^{(1)}$ at which it still exists not only increases σ_n in absolute magnitude but affects the shape of the smectic-layer displacement fluctuation profile as well [the value of σ_n at film center becomes larger than that near the free surfaces (curves *1* and *2* in Fig. 3)]. As for the second free-standing film, the differences between our results and the predictions of Hołyst's model obtained in the region near its limiting temperature ($T=T_2^{(2)}$) are still larger. As in the preceding case, this model predicts only an insignificant change in the smectic-layer displacement fluctuation profile σ_n with increasing film temperature (curve *3* in Fig. 4). By contrast, our calculations yield a completely different result (curve *2* in Fig. 4). First, at $T=T_2^{(2)}$ the absolute magnitude of the displacement fluctuations σ_n at film center is found to be larger than that at $T=T_1^{(2)}$ by about 30%. Second, the displacement fluctuation profile, originally fairly flat, becomes bell-shaped at $T=T_2^{(2)}$. It should be noted that it is such a substantial change in the fluctuation profile with increasing temperature that was observed in small-angle x-ray scattering measurements[18,28] made on 7AB LC free-standing films (similar experiments[26,27] on FPP liquid-crystal films were carried out at a temperature substantially below the Sm-*A*–*I* phase-transition point). Thus our results fit appreciably

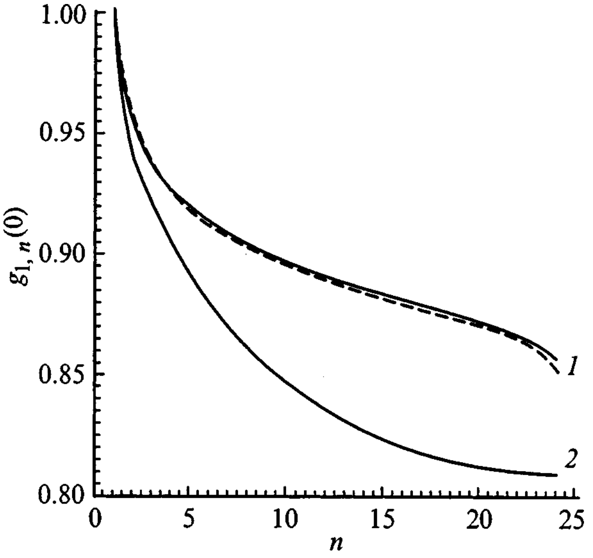

FIG. 5. $g_{1,n}(0)$ correlations between displacement fluctuations of the first and the other ($n=1,24$) smectic layers of the first free-standing film. Parameters N, α, W/V_0, K_0, B_0, and γ are the same as in Fig. 3. Curves *1* and *2* — our calculations made for $T=T_1^{(1)}=0.205\,(V_0/k_B)$ and $T=T_2^{(1)}=0.2298\,(V_0/k_B)$, respectively. Dashed curve — Hołyst's model.

better the experimental data of Refs. 18, 28 than those predicted by the model of Refs. 31, 32.

We calculated also the correlations $g_{k,n}(R)$ between the displacement fluctuations in free-standing smectic-*A* films. The results of these calculations of the correlations between the displacement fluctuations of the first ($k=1$) and the other ($n=1,24$) layers in the first and second films (for $\mathbf{R}=0$) are presented in Figs. 5 and 6, respectively. In both cases the results obtained by us (curves *1* in Figs. 5 and 6), for temperatures below the breakdown of smectic order in the bulk of the LC [$T=T_1^{(1,2)}$], practically coincide with those based on Hołyst's model[31,32] (the dashed lines in both figures). Both models predict for the first film a fairly small weakening of correlations between the displacement fluctuations of the layers with increasing distance between them and a substantial decrease in the $g_{1,n}(0)$ correlation with increasing number n for the second film. Indeed, as seen from Fig. 5, in the first free-standing film the correlation $g_{1,24}(0)$ between the displacement fluctuations in the first and last layers are only smaller by 10% than the $g_{1,2}(0)$ correlation between the displacement fluctuations in the first and second layer. One could say that all layers of this film fluctuate in phase. As for the second free-standing film (curve *1* in Fig. 6), the correlation between the displacement fluctuations in the first and last layers is almost one half that between neighboring (first and second) layers. In other words, the displacement fluctuations of two sufficiently remote layers in this film are only weakly connected with one another. This difference in the behavior of the films under study is associated with the fact that the tension (compression) moduli of smectic layers in the first of them are almost two orders of magnitude larger than those in the second. Due to the larger stiffness of the layers in the first film, the fluctuating displacement of one of them transfers to other layers better than that in the second.

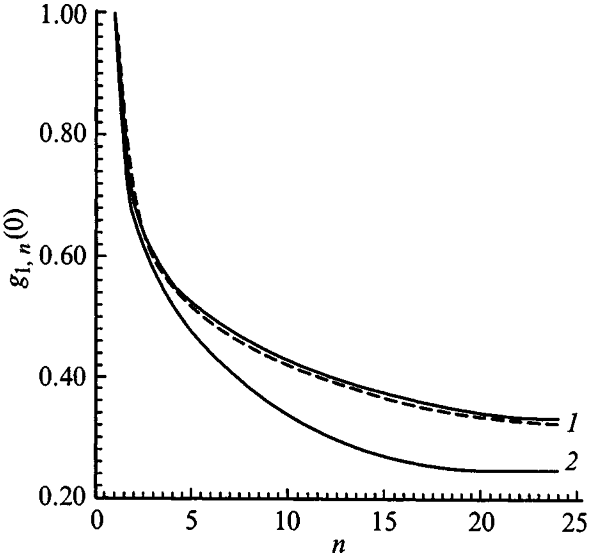

FIG. 6. Same correlations as in Fig. 5 but for the second free-standing smectic-*A* film. Parameters N, α, W/V_0, K_0, B_0, and γ are the same as in Fig. 4. Curves *1* and *2* — our calculations made for $T=T_1^{(2)}=0.204\,(V_0/k_B)$ and $T=T_2^{(2)}=0.21035\,(V_0/k_B)$, respectively. Dashed curve — Hołyst's model.

Turning now to the case of the highest temperatures at which both free-standing films still can exist ($T=T_2^{(1,2)}$), the correlations $g_{1,n}(0)$ between the displacement fluctuations of their layers obtained by us (curves *2* in Figs. 5 and 6) differ noticeably from the predictions of the model of Refs. 31, 32. According to this model, an increase of film temperature should practically not affect the magnitude of these correlations [the dependences of the $g_{1,n}(0)$ correlations on number n at $T=T_2^{(1,2)}$ are represented in Figs. 5 and 6 by the same dashed lines as for $T=T_1^{(1,2)}$]. By contrast, our calculations show that an increase in film temperature practically does not change the correlations between the displacement fluctuations of only neighboring (first and second) smectic layers. As for fairly remote layers, increasing the temperature of a free-standing film weakens the correlation between their displacement fluctuations. The decrease in the correlation is the strongest for the most remote, first and last, layers of a film. For instance, for the first film (Fig. 5) the correlation $g_{1,24}(0)$ at $T=T_2^{(1)}$ is about 6% smaller than that obtained for the initial temperature $T=T_1^{(1)}$, and for the second film (Fig. 6), $g_{1,24}(0)$ decreases by nearly 34% from its initial value as the temperature increases from $T=T_1^{(2)}$ to $T=T_2^{(2)}$. This decrease in the $g_{1,24}(0)$ correlation is caused by the substantial decrease of the elastic moduli K and B in the central part of the films as they are heated to the highest temperatures of their existence, $T=T_2^{(1,2)}$ (Figs. 1 and 2), which is totally disregarded in Hołyst's model[31,32]. Because fluctuation displacement of smectic layers near one of the free film surfaces is transmitted to the layers near the other free surface through the central layers, a decrease in the stiffness of the latter should weaken the correlations between the displacement fluctuations of the two surface layers.

Support of the Russian Fund for Fundamental Research (Grant 98-03-32448) is gratefully acknowledged.

[1] P. Pieranski, L. Beliard, J. P. Tournellec, X. Leoncini, C. Furtlehner, H. Dumoulin, E. Riou, B. Jouvin, J. P. Fenerol, Ph. Palaric, J. Heuving, B. Cartier, and I. Kraus, Physica A **194**, 364 (1993).
[2] C. Rosenblatt, R. Pindak, N. A. Clark, and R. B. Meyer, Phys. Rev. Lett. **42**, 1220 (1979).
[3] M. Veum, C. C. Huang, C. F. Chou, and V. Surendranath, Phys. Rev. E **56**, 2298 (1997).
[4] C. Rosenblatt and N. M. Amer, Appl. Phys. Lett. **36**, 432 (1980).
[5] S. Heinekamp, R. A. Pelcovits, E. Fontes, E.Y. Chen, R. Pindak, and R. B. Meyer, Phys. Rev. Lett. **52**, 1017 (1984).
[6] R. Pindak, D. J. Bishop, and W. O. Sprenger, Phys. Rev. Lett. **44**, 1461 (1980).
[7] J. C. Tarczon and K. Miyano, Phys. Rev. Lett. **46**, 119 (1981).
[8] D. J. Bishop, W. O. Sprenger, R. Pindak, and M. E. Neubert, Phys. Rev. Lett. **49**, 1861 (1982).
[9] Ch. Bahr and D. Fliegner, Phys. Rev. A **46**, 7657 (1992).
[10] I. Kraus, P. Pieranski, E. Demikhov, H. Stegemeyer, and J. Goodby, Phys. Rev. E **48**, 1916 (1993).
[11] J. Collett, P. S. Pershan, E. B. Sirota, and L. B. Sorensen, Phys. Rev. Lett. **52**, 356 (1984).
[12] E. B. Sirota, P. S. Pershan, L. B. Sorensen, and J. Collett, Phys. Rev. Lett. **55**, 2039 (1985).
[13] E. B. Sirota, P. S. Pershan, L. B. Sorensen, and J. Collett, Phys. Rev. A **36**, 2890 (1987).
[14] T. Stoebe, P. Mach, and C. C. Huang, Phys. Rev. Lett. **73**, 1384 (1994).
[15] E. E. Demikhov, V. K. Dolganov, and K. P. Meletov, Phys. Rev. E **52**, R1285 (1995).
[16] V. K. Dolganov, E. I. Demikhov, R. Fouret, and C. Gors, Phys. Lett. A **220**, 242 (1996).
[17] P. M. Johnson, P. Mach, E. D. Wedell, F. Lintgen, M. Neubert, and C. C. Huang, Phys. Rev. E **55**, 4386 (1997).
[18] E. A. L. Mol, G. C. L. Wong, J. M. Petit, R. Rieutord, and W. H. de Jeu, Physica B **248**, 191 (1998).
[19] C. Y. Young, R. Pindak, N. A. Clark, and R. B. Meyer, Phys. Rev. Lett. **40**, 773 (1978).
[20] R. Geer, C. C. Huang, R. Pundak, and J. W. Goodby, Phys. Rev. Lett. **63**, 540 (1989).
[21] P. Mach, S. Grantz, D. A. Debe, T. Stoebe, and C. C. Huang, J. Phys. II **5**, 217 (1995).
[22] J. D. Brock, R. J. Birgenau, J. D. Litster, and A. Aharony, Contemp. Phys. **30**, 321 (1989).
[23] S. Amador, P. S. Pershan, H. Stragier, B. D. Swanson, D. J. Tweet, L. B. Sorensen, E. B. Sirota, G. E. Ice, and A. Habenschuss, Phys. Rev. A **39**, 2703 (1989).
[24] E. B. Sirota, P. S. Pershan, S. Amador, and L. B. Sorensen, Phys. Rev. A **35**, 2283 (1987).
[25] S. Gierlotka, P. Lambooy, and W. H. de Jeu, Europhys. Lett. **12**, 341 (1990).
[26] J. D. Shindler, E. A. L. Mol, A. Shalaginov, and W. H. de Jeu, Phys. Rev. Lett. **74**, 722 (1995).
[27] E. A. L. Mol, J. D. Shindler, A. N. Shalaginov, and W. H. de Jeu, Phys. Rev. E **54**, 536 (1996).
[28] E. A. L. Mol, G. C. L. Wong, J. M. Petit, F. Rieutord, and W. H. de Jeu, Phys. Rev. Lett. **79**, 3439 (1997).
[29] C. Rosenblatt and D. Ronis, Phys. Rev. A **23**, 305 (1981).
[30] J. V. Selinger and D. R. Nelson, Phys. Rev. Lett. **61**, 416 (1988).
[31] R. Hołyst, D. J. Tweet, and L. B. Sorensen, Phys. Rev. Lett. **65**, 2153 (1990).
[32] R. Hołyst, Phys. Rev. A **44**, 3692 (1991).
[33] A. Poniewierski and R. Hołyst, Phys. Rev. B **47**, 9840 (1993).
[34] A. N. Shalaginov and V. P. Romanov, Phys. Rev. E **48**, 1073 (1993).
[35] L. V. Mirantsev, Phys. Lett. A **205**, 412 (1995).
[36] L. V. Mirantsev, Liq. Cryst. **20**, 417 (1996).
[37] T. Krancj and S. Žumer, J. Chem. Phys. **105**, 5242 (1996).
[38] Y. Martínez-Ratón, A. M. Somoza, L. Mederos, and D. E. Sullivan, Phys. Rev. E **55**, 2030 (1997).
[39] L. V. Mirantsev, Phys. Rev. E **55**, 4816 (1997).
[40] P. G. de Gennes, *The Physics of Liquid Crystals* (Oxford University Press, London, 1974; Mir, Moscow, 1977).
[41] S. Chandrasekhar, *Liquid Crystals* (Cambridge Univ. Press, London, 1977; Mir, Moscow, 1980).
[42] W. L. McMillan, Phys. Rev. A **4**, 1238 (1971).

Translated by G. Skrebtsov

FULLERENES AND ATOMIC CLUSTERS

Structure of ultradisperse diamonds

V. D. Andreev*) and Yu. I. Sozin

Institute of Superhard Materials, Ukrainian Academy of Sciences, 254074 Kiev, Ukraine

(Submitted March 15, 1999)
Fiz. Tverd. Tela (St. Petersburg) **41**, 1890–1893 (October 1999)

The structure of crystallites (regions of coherent scattering — RCS), which comprise the grains of ultradisperse diamond (UDD) powder, was investigated by x-ray crystallography and coordination-sphere diffractometry. It was established that the RCS have an average size $\overline{L}=42\pm 2$ Å and that these regions are themselves UDD grains with the structure of a diamond lattice and a negligible content of clusters of carbon atoms distributed throughout the volume that do not form a lattice and are mainly located at interatomic distances ~ 1.5 Å. The clusters of carbon atoms, for which the distribution of interatomic distances is close to Gaussian, which may indicate an amorphous structure of the boundary layers, lie along grain boundaries. © *1999 American Institute of Physics.* [S1063-7834(99)03610-2]

Ultradisperse diamonds (UDDs) obtained by explosion synthesis are now attracting increasing attention from investigators. In the present work we investigated the structure of utradisperse diamonds (ALIT Company) by analysis of the total width of the x-ray diffraction lines[1] and by coordination-sphere diffractometry (CSD).[2] All diffraction patterns were obtained in the conventional Bragg–Brentano arrangement.

The x-ray diffraction pattern of UDD powder characterizes the experimental powder as a diamond phase with no lonsdalite and graphite impurities. The substructure of the powder was investigated by total-width analysis[1] using two diffraction lines (111) and (220) of diamond obtained with Cu $K\alpha$ radiation. The physical broadening of the lines B_{phi} was determined according to $B_{phi}=B_{mi}-(B_{oi}/B_{mi})^2$, where B_{mi} is the measured linewidth and B_{oi} is the instrumental linewidth (for ASM 7/5 diamond).

The ratio of the physical widths B_{phi} of the analytical lines was found to be the same as the reciprocal of the ratio of the cosines of the angles corresponding to these lines. This shows that the physical broadening of the lines is due only to the dispersity of the subgrains in the absence of microdistortions of the lattice ($\Delta d/d=0$). For this reason, the average subgrain size was determined as $L=\lambda/(\rho B_{phi}\cos\theta_j)$, where $\lambda=\lambda(\mathrm{Cu}\,K\alpha)=1.54$ Å, and ρ is a factor for conversion into radians. A calculation using the (111) line gave $L_1=43$ Å and, correspondingly, a calculation using the (220) line gave $L_2=45$ Å. The average value for the two lines is $\overline{L}=44$ Å, which corresponds to dislocation density $\overline{N}=3/\overline{L}^2=1.6\times 10^{13}\,\mathrm{cm}^{-2}$. These data are reproduced well for several batches of UDD powders, and their average values are $\overline{L}=42\pm 2$ Å and $\overline{N}=(1.7\pm 0.1)\times 10^{13}\,\mathrm{cm}^{-2}$. The value $\overline{L}=43$ Å was obtained in Ref. 3 by a similar method.

The spectra obtained from UDD powder, ASM 28/20 powder, and single-crystal diamond ($7\times 4.5\times 1.5$ mm wafer cut parallel to the (001) plane) were used to analyze the structure of the UDD powder by the CSD method. In addition, the background spectrum was measured. In accordance with theory, the CSD method[2,4] is based on the Debye equation and the Ehrenfest equation related with it,[5] allowing investigating the radial distribution of the cluster of identical objects (atoms, molecules, structural groups, and so on) lying in pairs at some fixed distances from one another.1)

The identification of the CSD spectra as a sum of Debye scattering functions[5] was made by Fourier analysis using the final expression in the form of a Fourier transform of these functions in direct space, representing the distribution of the coordination numbers on the corresponding coordination spheres (CSs). The calculations were performed by a numerical method using the Mathlab 5.2 software. The degree of adequacy of calculating the physical analog by the method of Fourier analysis of the spectrum covering a portion of the total angular range $2\theta=[0,\pi]$ depends on the angular range of the experimentally detected spectrum; this must be kept in mind when analyzing and interpreting the computational results. In the case at hand the CSD spectrum from a single crystal was obtained in the angular range $2\theta=[6°,55°]$ and from the ASM 28/20 and UDD powders in the ranges $2\theta=[6°,40°]$ and $2\theta=[6°,37°]$, respectively (the decrease in the maximum grazing angle compared with the spectrum from the single crystal is explained by the superposition of the lines of the powder diffraction pattern of diamond). It is obvious that the solution giving the closest description of the experimental object can be obtained by recording the CSD spectrum itself in the full angular range $2\theta=[0,\pi]$, which, unfortunately, is technically not feasible.

To obtain the computed curve corresponding to the experimental CSD spectrum from a single crystal (Fig. 1a), the tabulated data (Fig. 1b) for 48 CSs (1371 atoms) of the diamond lattice were used. The use of more than 48 CSs and the

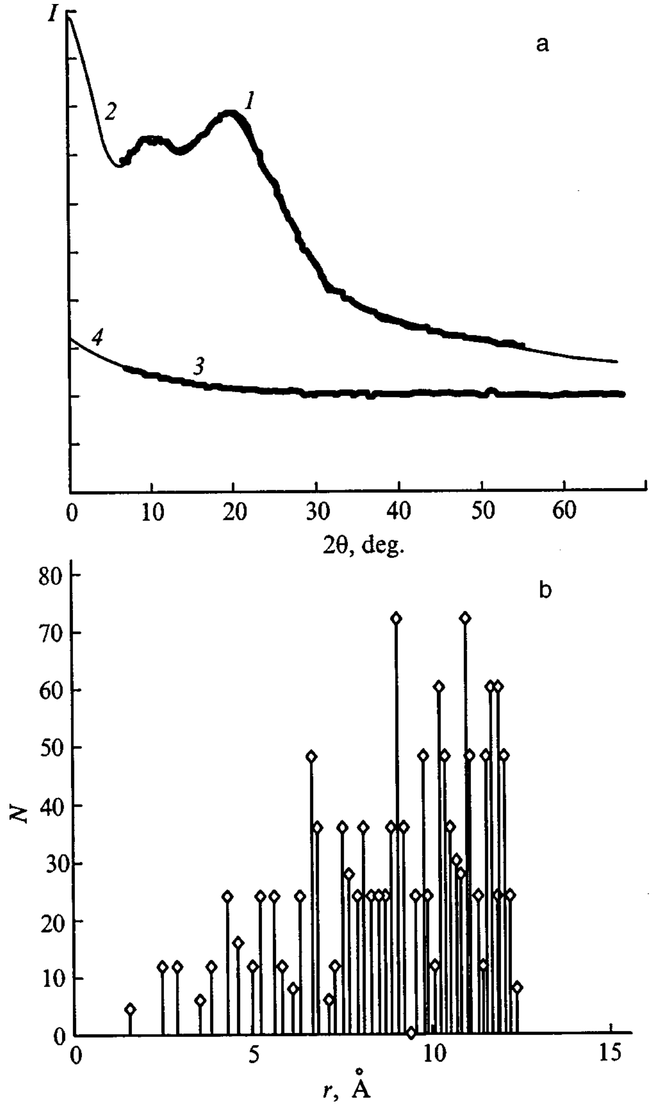

FIG. 1. Identification of the CSD spectrum from a diamond single crystal: a — experimental (*1*) and computed (*2*) CSD spectra from a diamond single crystal, the background spectrum (*3*) and its fit (*4*); b — distribution of coordination spheres and coordination numbers that corresponds to the computed CSD spectrum from a diamond single crystal.

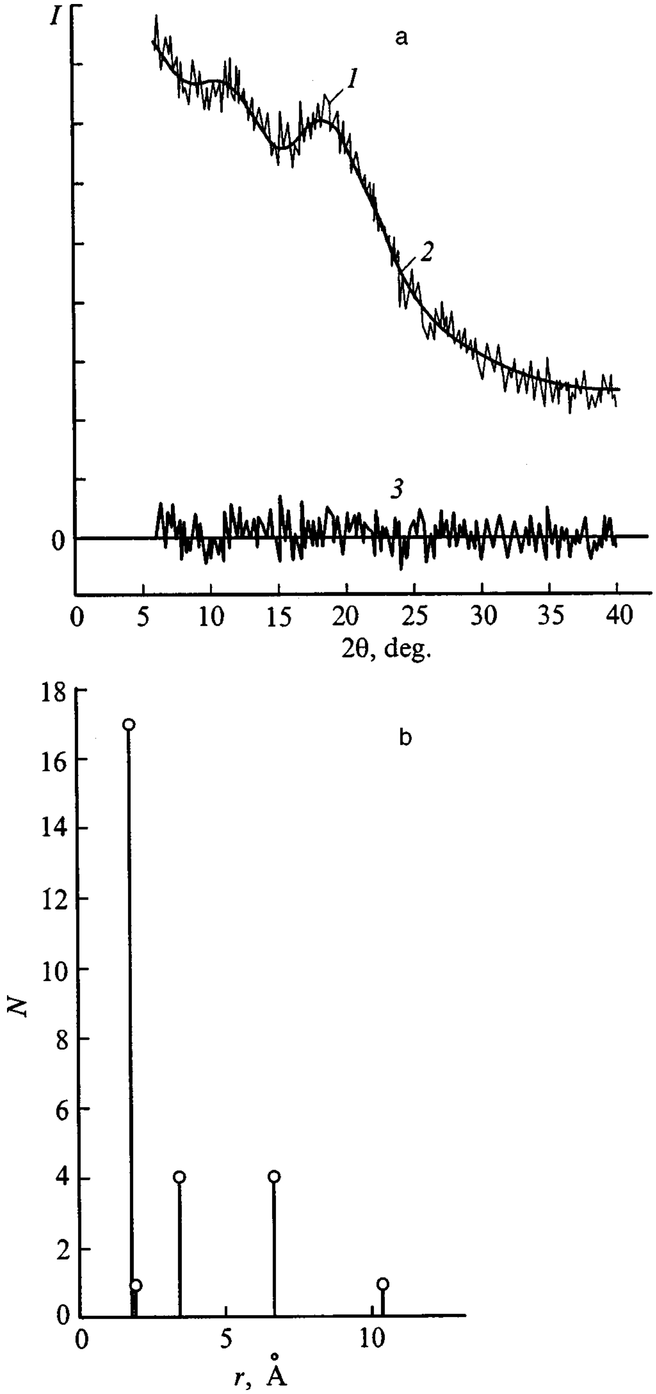

FIG. 2. Identification of the CSD spectrum from ASM 28/20 diamond powder: a — experimental (*1*) and computed (*2*) CSD spectra from ASM 28/20 diamond powder, the difference between the experimental spectrum and the computed curve (*3*); b — computed distribution of coordination numbers and coordination spheres that corresponds to the structural component corresponding to the distribution of atoms that are not part of the composition of an ideal diamond lattice in grains of ASM 28/20 powder.

corresponding number of atoms in the calculation does not affect the accuracy of the computational approximation of the experimental CSD spectrum from the diamond single crystal, since the agreement obtained is limited by the experimental accuracy.

The identification of the CSD spectra from ASM 28/20 and UDD powders is based on extracting the component of the spectrum of these powders that distorts the ideal spectrum of the single crystal and then Fourier analyzing this component. It is obvious that such a component of the CSD spectrum will be determined by atoms which are not part of the ideal structure of the lattice, but rather by atoms disseminated over the volume, surface, and grain boundaries of the powder. The computed curve was fitted to the experimental data for 48 tabulated CSs of an ideal diamond lattice and for the auxiliary CSs, which do not fit in the diamond structure and are distributed every 0.1 Å for interatomic distances ranging from 1.5 to 25 Å for ASM 28/20 (i.e., 236 CSs) and from 1.5 to 55 Å for UDD (i.e., for 536 CSs), with *N* rounded off to integer values in the calculation of CSs.

Figure 2 shows the results of the identification of the CSD spectrum from ASM 28/20 powder, whose grains consist of fragments and concretions of single crystals. The more ‘‘agitated’’ nature of the spectrum, as compared to the spectra from a single crystal, UDD, and the background is interesting. It could be due to a large number of atoms with uncompensated bonds located on the cleavage surfaces of the powder grains. The fit of the computed curve to the experimental spectrum is quite good (Fig. 2a). Of the 236 auxiliary CSs introduced into the calculation, only five were found to be nonzero (i.e. CN $\neq 0$) (Fig. 2b). From the final result of the solution, presented in the form of a distribution of the CSs and CNs of the ideal lattice, similar to Fig. 1b and the distributions of clusters of atoms which are not part of the structure of the ideal lattice (Fig. 2b), it follows that most of the atoms distributed through the volume and over the surface are clusters located at interatomic distances close to 1.54 Å. As the interatomic distance increases, the number of atoms in the clusters decreases rapidly and is zero at ~ 10 Å.

According to electron microscopy, UDD powder consists of agglomerates of grains with average size in various batches of powders 30–80 Å. The grains in the clusters are coupled to one another by the low-order form of carbon, which is arranged in the form of a binding matrix over the boundaries of the diamond grains. The thickness of the interlayers between the grains, estimated from the electron micrographs in Ref. 6, is $\sim 10-20$ Å. Individual grains are repeatedly twinned. Together with the particles of multiple twinning, there also exist single-crystal agglomerates. Most grains, however, are monoblock grains.

A diffraction pattern of UDD, which contains a halo at $2\theta \approx 17°$, is presented in Ref. 3. Comparing this halo with the CDS spectrum in Fig. 3a (curve 1) of the present work shows that both spectra are identical in the corresponding range of angles. This allows us to conclude that the CSD spectrum in Ref. 3 was recorded from UDD powder. The authors of Ref. 3 believe that the halo which they examined is characteristic for disordered amorphized structures and that it cannot be related to diffraction by macrostructures with long-range order. As will be shown below, the interpretation of this spectrum from the standpoint of the CSD method gives a better interpretation of the UDD structure.

The results of the analysis of the CSD spectrum obtained in the present work from UDD powder are displayed in Figs. 3a–c. The degree to which the calculation fits the experiment (Fig. 3a), just as in the case of the CSD spectrum from ASM 28/20 powder (Fig. 2a), is also high. Of the 536 auxiliary CSs introduced into the calculation, 40 were found to be nonzero, and the distribution of atoms on the nonzero CSs differs substantially from that in the grains of the ASM 28/20 powder (Fig. 3b). In the present case, besides the distribution of CSs of the ideal diamond lattice, similar to Fig. 1b, two clusters of atoms, which are actually not connected to one and which, according to the calculation, are responsible for the distortion of the ideal CDS spectrum of diamond that corresponds to the experiment, are actually observed.

One of these distributions is similar to the distribution of clusters of atoms in grains of AS 28/20 powder that are not part of the structure of an ideal lattice. Most of the clusters are distributed throughout the volume of the powder grains at interatomic distances close to 1.54 Å; the number of atoms in the clusters decreases sharply as the interatomic distance increases to $\sim 10-15$ Å.

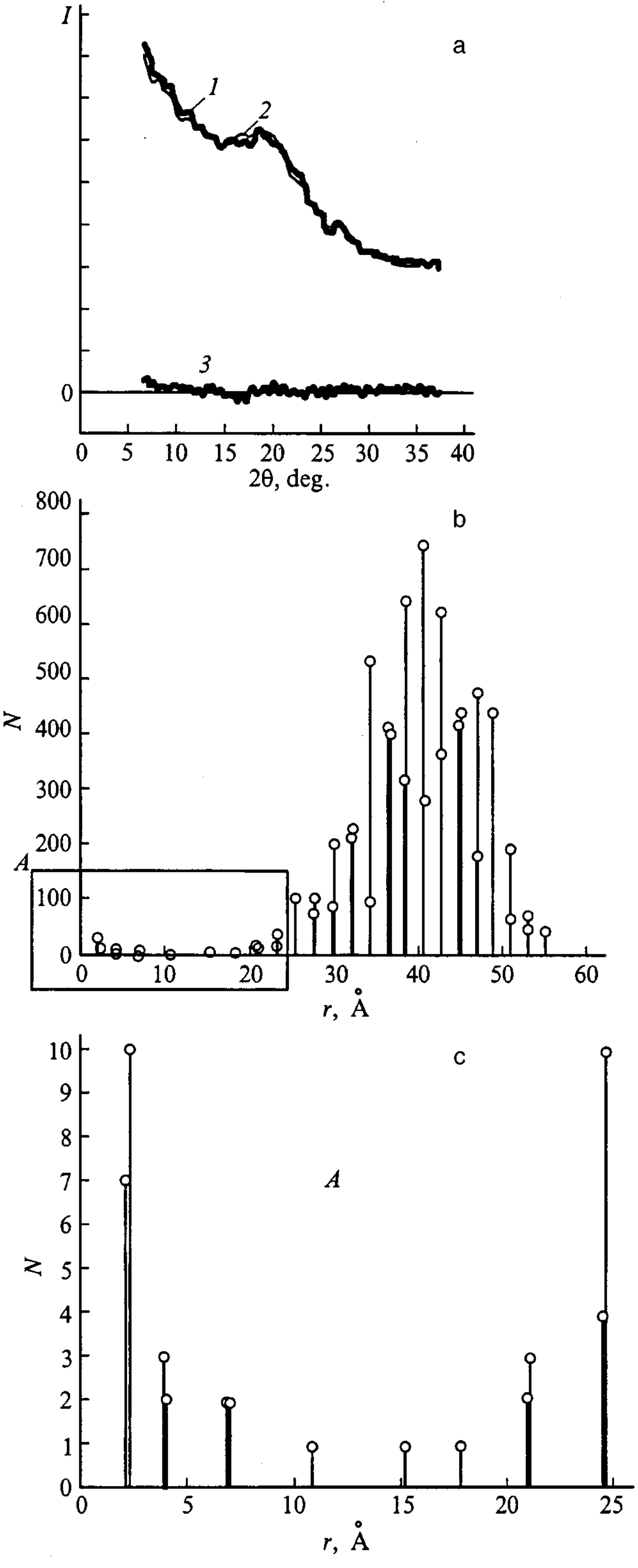

FIG. 3. Identification of the CSD spectrum from UDD powder: a — experimental (*1*) and computed (*2*) CSD spectra from UDD powder, the difference between the experimental spectrum and the computed curve (*3*); b — computed distribution of coordination numbers and coordination spheres that corresponds to the structural component corresponding to the distribution of the atoms that are not part of the ideal diamond lattice in grains of UDD powder; c — section *A* of the distribution of CSs and CNs from (b).

The second distribution of clusters of atoms which are not part of the structure of the ideal lattice is a nearly Gaussian distribution with a maximum at interatomic distance ~40 Å and half-width ~20 Å. According to these characteristics, this distribution of atoms can be referred to structureless (amorphous) carbon intergrain interlayers described in Ref. 6. The average interatomic distances obtained for this distribution are the same as the sizes of the RCS $\overline{L}=42 \pm 2$ Å, determined from the broadening of the diffraction lines. In turn, this testifies that the average size of subgrains with the structure of a diamond lattice and a negligible content of clusters of carbon atoms distributed through the volume that do not form a lattice, and are mainly located at interatomic distances ~1.5 Å, is the same as the average sizes of the powder grains themselves as determined from electron micrographs in Ref. 6.

In summary, the results obtained show that different investigation methods give, in agreement with and supplementing one another, information about the structure of ultradisperse diamonds.

*⁾E-Mail: andreyev@andr.kiev.ua

[1] For the lattice of a single crystal, the degree of deviation from isotropy of the spatial distribution of reflection from coordination spheres is, obviously, determined by the degree of deviation of the polyhedron, whose vertices correspond in number to the atoms (CN) corresponding to a given coordination sphere, as well as the number of fixed spatial positions (i.e., rotation angle) of such polyhedra in the lattice as a whole, inscribed in a given coordination sphere. For a diamond lattice, the largest difference from a sphere occurs for a four-vertex polyhedron (tetrahedron) for the first CS, six-vertex polyhedra (octahedra) for the fourth and sixteenth coordination spheres, and finally eight-vertex polyhedra (cubes), for the 12th and 48th coordination spheres. All other polyhedra have 12, 24, 28, 36, 48, and so on vertices. The tetrahedron for the first coordination sphere possesses at least four spatial sites in the lattice for which its vertices in each position do not coincide with one another. This decreases the degree of nonisotropy of reflection from the first coordination sphere, corresponding to the degree to which the 16-vertex polyhedron differs from a sphere. The situation is similar for other coordination spheres of a diamond lattice. Thus, for the spatial distribution of reflection from the coordination sphere of a diamond lattice, the degree of nonisotropy is negligibly small, falling within the range of the experimental accuracy of the diffraction patterns obtained in the present work. It is possible that such nonisotropy can be detected with better experimental methods in specially designed experiments.

---

[1] Yu. I. Sozin, A. R. Kryuchkova, E. S. and Cherepenina, in *Apparatus and Methods of X-Ray Analyis* (SKTBRA, Leningrad, 1971).
[2] Yu. I. Sozin, Kristallografiya **39**, 10 (1994) [Crystallogr. Rep. **39**, 6 (1994)].
[3] A. E. Aleksenskiĭ, M. V. Baĭdakova, A. Ya. Vul', V. Yu. Davydov, and Yu. A. Pevtsova, Fiz. Tverd. Tela (St. Petersburg) **39**, 1125 (1997) [Phys. Solid State **39**, 1007 (1997)].
[4] Yu. I. Sozin and V. D. Andreev, Kristallografiya **42**, 431 (1997) [Crystallogr. Rep. **42**, 385 (1997)].
[5] A. Guinier, *Théorie et Technique de la Radiocristallograhie* (Dunod, Paris, 1956; Fizmatgiz, Moscow, 1961).
[6] G. I. Savvakin, V. A. Kotko, N. F. Ostovskaya, and A. V. Kurdyumov, Poroshkovaya Metallurgiya, No. 1, 78 (1988).

Translated by M. E. Alferieff